Advanced Rotor Blade Design based on High-Fidelity Computational Fluid Dynamics

Thomas Alexander Fitzgibbon

Submitted in fulfilment of the requirements for the
Degree of Doctor of Philosophy

James Watt School of Engineering
College of Science and Engineering
University of Glasgow

January 2021

Abstract

This thesis is aimed at expanding the current state of the art in rotor design by combining high fidelity CFD and optimisation methods. Such methods are associated with extremely high computational costs, when optimisation of unsteady flow fields is required such as those encountered by a rotor in forward flight. For this reason, the majority of studies in literature resort to lower fidelity models for forward flight optimisation. To maintain the high fidelity of the Navier-Stokes equations at modest computational costs, an optimisation framework based on an overset adjoint harmonic balance method was developed within the present research, which is the primary novelty of the thesis.

Firstly, however, the CFD solver is validated for a range of rotor designs in hover and forward flight, by comparing the performance predictions with available experimental data, and thereby verifying the findings obtained in the rotor design study. The CFD validation also includes a sensitivity analysis of various numerical modelling parameters on the performance predictions including effects of computational setup, grid resolution and turbulence models. The validation studies highlighted the need for more accurate and higher quality experimental data.

Based on the CFD validation results, the use of standard performance metrics such as figure of merit and lift-to-drag ratio was assessed for comparing different rotor designs, showing that a dimensional thrust and torque comparison is more informative. A blade solidity study was also performed to inform the correct use of different solidity parameters, in particular, thrust-weighted solidity. The comparison of the different designs used for CFD validation highlighted the subtle aerodynamics involved in advanced planform shapes and the need for numerical optimisation.

The developed optimisation framework was applied to the AH-64A rotor blade and showed that significant performance benefits are available through blade planform shape modifications. The final design was validated in hover and forward flight using time-marching calculations. The differences between the harmonic balance and time-marching simulations are analysed in detail along with the sources behind the performance gains for the optimised blade. Finally, a discussion of the favourable rotor design features is conducted along with suggestions for improvements of the optimisation framework.

List of Publications

In Journals

Fitzgibbon, T., Barakos, G., and Woodgate, M., "Validation of the Steady State Hover Formulation for Accurate Performance Predictions," *AIAA Journal*, Vol. 57, No. 12, 2019, pp. 5293-5308, DOI: 10.2514/1.J058408

Fitzgibbon, T., Barakos, G., and Woodgate, M., "Assessment of current rotor design comparison practices based on high-fidelity CFD methods," *The Aeronautical Journal*, Vol. 124, No. 1275, 2020, pp. 731-766, DOI:10.1017/aer.2019.162

Barakos, G.N., Fitzgibbon, T., Kusyumov, A.N., Kusyumon, S.A. and Mikhailov, S.A., "CFD simulation of helicopter rotor flow based on unsteady actuator disk model," *Chinese Journal of Aeronautics*, 2020, DOI:: 10.1016/j.cja.2020.03.021 (Early Online Publication)

Fitzgibbon, T., Barakos, G., Woodgate, M., and Markiewicz, R., "Rotor Blade Planform Design based on an Overset Harmonic-Balance Adjoint Optimisation Framework," *AIAA Journal*, (Submitted)

In Conference Proceedings

Fitzgibbon, T., Barakos, G., Woodgate, M., and Jimenez-Garcia, A., "Numerical Simulation of Different Rotor Designs in Hover and Forward Flight," *Proceedings of the 44th European Rotorcraft Forum*, 18-21 September 2018, Delft, Netherlands.

Fitzgibbon, T., Barakos, G., Woodgate, M., and Jimenez-Garcia, A., "Numerical Simulation of Various Rotor Designs in Hover and Forward Flight," *Proceedings of the 2019 SciTech AIAA Forum*, 7-11 January 2019, San Diego, CA, USA.

Fitzgibbon, T., Barakos, G., and Woodgate, M., "Assessment of current CFD performance pre-

diction capabilities for novel rotor blade planforms," *Proceedings of the 75th Annual Forum of the American Helicopter Society*, 13-16 May 2019, Philadelphia, USA.

Fitzgibbon, T., Barakos, G., and Woodgate, M., "Assessment of the Harmonic Balance Method for Rotor Blade Performance Predictions," *Proceedings of the 45th European Rotorcraft Forum*, 17-19 September 2019, Warsaw, Poland.

Conference (to be presented)

Lim, J., Jain, R., Potsdam, M., Widjaja, R., Barakos, G., and Fitzgibbon, T., "High Fidelity Code-to-Code Comparison of Rotor Performance Predictions for Hover and Forward Flight," *76th Annual Forum of the American Helicopter Society*, 6-8th October 2020, Virginia Beach, USA.

In Conferences without Proceedings

Fitzgibbon, T. and Barakos, G., "Assessing different rotor designs based on Navier-Stokes CFD-predictions," *4th Vertical Lift Network Workshop*, 7-9 April 2019, Cheshire, UK.

Contents

List of Tables

List of Figures

Acknowledgements

I would like to devote my deepest gratitude to my supervisor Prof. George Barakos for his guidance, support and technical expertise. He continuously passed on his passion and enthusiasm for rotorcraft and computational fluid dynamics on to me, thereby motivating me during the project.

Special thanks to Dr Mark Woodgate, who shared his expertise on numerical methods, and unselfishly devoted time to answer any questions devoted to code development and the HMB3 solver. I would also like to thank all the CFD Lab Members for making the PhD experience much more enjoyable.

Many thanks to Dr Richard Markiewicz and Bryan Finlay for making the effort to review my work and providing valuable input to the real-world applications of the present research.

The financial support from DSTL (Defence Science and Technology Laboratory), under Project No. 74260 is also gratefully acknowledged as well as the use of the Cirrus UK National Tier-2 HPC Service at EPCC (http://www.cirrus.ac.uk) and the ARCHER UK National Supercomputing Service (http://www.archer.ac.uk). I would also like to acknowledge the TTCP collaboration project, TTCP AER CP13.A1, Next Generation Rotor Blade Design, under which a part of technical work has been completed.

Most importantly, I would like to thank my parents and sister, Jola, Gerald and Kitty, for their support, love, and giving me the belief that I can achieve anything in life. Last but not least, I would like to express my gratitude to Maureen, for her continuous love, for always being there for me during this long journey and making me smile when I most needed it.

Declaration

I certify that the thesis presented here for examination for a PhD degree of the University of Glasgow is solely my own work other than where I have clearly indicated that it is the work of others (in which case the extent of any work carried out jointly by me and any other person is clearly identified in it) and that the thesis has not been edited by a third party beyond what is permitted by the University's PGR Code of Practice.

I declare that the thesis does not include work forming part of a thesis presented successfully for another degree.

I declare that this thesis has been produced in accordance with the University of Glasgow's Code of Good Practice in Research.

I acknowledge that if any issues are raised regarding good research practice based on review of the thesis, the examination may be postponed pending the outcome of any investigation of the issues.

January 2021

.....

Thomas Fitzgibbon

Nomenclature

Latin symbols

a	lift curve slope or speed of sound
A	area $[m^2]$
AR	rotor blade aspect ratio, $\frac{R}{c_{ref}}$
c	chord $[m]$
C_D	drag coefficient, $\frac{D}{\frac{1}{2}\rho V_\infty^2 S}$
C_F	skin friction coefficient, $\frac{\tau_w}{\frac{1}{2}\rho V_\infty^2}$
C_L	lift coefficient, $\frac{L}{\frac{1}{2}\rho V_\infty^2 S}$
C_M	pitching moment coefficient, $\frac{M}{\frac{1}{2}\rho V_\infty^2 c S}$
C_{Mx}	non-dimensional rotor rolling moment coefficient (US), $\frac{M_x}{\rho_{ref}(V_{inf})^2\pi(AR)^3}$
C_{My}	non-dimensional rotor pitching moment coefficient (US), $\frac{M_y}{\rho_{ref}(V_{inf})^2\pi(AR)^3}$
C_{Mz}	non-dimensional rotor torque (US), $\frac{M_z}{\rho_{ref}(V_{inf})^2\pi(AR)^3}$
C_P	pressure coefficient, $\frac{p-p_\infty}{\frac{1}{2}\rho(\Omega r)^2}$
C_{Pz}	non-dimensional rotor thrust coefficient, $\frac{P_z}{\rho_{ref}(V_{inf})^2\pi(AR)^2}$
C_q	blade section torque coefficient, $\frac{dQ/dr}{\frac{1}{2}\rho c_{ref} R(\Omega r)^2}$
C_Q	torque coefficient (US), $\frac{Q}{\rho(\Omega R)^2\pi R^3}$
C_t	blade section thrust coefficient, $\frac{dT/dr}{\frac{1}{2}\rho c_{ref}(\Omega r)^2}$
C_T	thrust coefficient (US), $\frac{T}{\rho(\Omega R)^2\pi R^2}$
d	distance $[m]$
D	drag force $[kgm/s^2]$ or Fourier collocation derivative operator
E	energy per unit mass $[m^2/s^2]$ or harmonic balance transformation matrix or Young's modulus $[kg/(ms^2)]$
f	frequency $[1/s]$
f_D	vehicle equivalent parasite drag area $[m^2]$
$\mathbf{F}$	flux vector in x direction
F_z	non-dimensional rotor vertical force
FoM	figure of merit, $\frac{C_T^{3/2}}{\sqrt{2}C_Q}$

g	optimisation inequality constraints
G	shear modulus $[kg/(ms^2)]$
$\mathbf{G}$	flux vector in y direction
h	optimisation equality constraints
$\mathbf{H}$	flux vector in z direction
H_{out}	source-sink model distance of outflow region from rotor disk plane
I	optimisation objective function
I_c, I_f	chordwise/flapwise moment of area $[m^4]$
J	Jacobian matrix, $\frac{\partial R}{\partial W}$ or torsion constant
k	turbulent kinetic energy per unit mass $[m^2/s^2]$ or reduced frequency of oscillation, $\frac{fc}{2V_\infty}$ or number of restarted Krylov eigenvectors in GMRES-DR method
k_h	heat transfer coefficient
L	lift Force $[kgm/s^2]$ or length $[m]$
$\mathscr{L}$	Lagrangian of the optimisation problem
m	flow equation pseudo-time step level or number of inequality constraints or number of Krylov vectors in the GMRES method
M	Mach number or weight per unit length $[kg/m]$
M_x	rotor disk rolling moment $[kgm^2/s^2]$
M_y	rotor disk pitching moment $[kgm^2/s^2]$
M^2C_d	blade section drag coefficient (rotor disk in-plane force), $\frac{D}{\frac{1}{2}\rho a^2 c}$
M^2C_l	blade section lift coefficient (rotor disk normal force), $\frac{L}{\frac{1}{2}\rho a^2 c}$
M^2C_m	blade section pitching moment coefficient, $\frac{M_y}{\frac{1}{2}\rho a^2 c^2}$
n	flow equation real time step level or number of design variables
$\mathbf{n}$	unit normal vector
N	mesh metrics vector
N_b	number of blades
N_{crit}	critical amplification factor
N_H	number of harmonic balance modes
N_T	number of harmonic balance snapshots, $N_T = 2N_H + 1$
p	pressure $[kg/(ms^2)]$ or number of equality constraints
P	preconditioner or rotor power $[kgm^2/s^3]$, ΩQ
q	heat flux vector
Q	rotor torque $[kgm^2/s^2]$ or Q-criterion
r	radial position along blade span $[m]$
R	rotor radius $[m]$
R_{out}	source-sink model outflow region radius
$\mathbf{R}$	flow residual vector

R_{sp}	specific gas constant $[m^2/(s^2K)]$
Re	Reynolds number, $\frac{V_\infty c_{ref}\rho}{\mu}$
Re_θ	transition onset momentum thickness Reynolds number
Ret	turbulent eddy viscosity ratio, $\frac{\mu_t}{\mu}$
S	area $[m^2]$
$\mathbf{S}$	source term vector
S_{ij}	strain rate tensor
t	time $[s]$
t^*	non-dimensional time
T	rotor thrust $[kgm/s^2]$ or time $[s]$ or temperature $[K]$ or oscillation period, $\frac{2\pi}{\omega}$
T_s	Sutherland Temperature $[K]$
u_τ	friction velocity, $\sqrt{\frac{\tau_w}{\rho}}$
U	velocity $[m/s]$
$U=(u,v,w)^T$	cartesian velocity vector $[m/s]$
$\mathbf{v}$	arbitrary vector
V	velocity $[m/s]$ or cell volume $[m^3]$
$\mathbf{W}$	vector of conserved variables
X_S	surface mesh
X_V	volume mesh
y	chordwise position $[m]$
y^+	non-dimensional wall distance, $\frac{yu_\tau}{\upsilon}$
W	non-dimensional rotor downwash velocity or weight $[kg]$
W_{in}	source-sink model inflow velocity
W_{out}	source-sink model outflow velocity
x,y,z	spacial coordinates in cartesian system $[m]$
$x=(x,y,z)^T$	fluid position vector $[m]$
z	vertical distance from rotor disk plane $[m]$

Greek symbols

α	angle of incidence $[deg]$ or adjoint design variable vector
α_s	rotor shaft angle
β_0	rotor coning angle $[deg]$
β_{1c}	rotor longitudinal flapping angle $[deg]$
β_{1s}	rotor lateral flapping angle $[deg]$
γ	shear rate $[1/s]$ or turbulence intermittency factor or specific heat ratio or rotor Lock number
δ_{ij}	Kronecker delta

ε	turbulent energy dissipation rate
Θ	rotor twist angle $[deg]$
θ_0	rotor collective angle $[deg]$
θ_{75}	rotor pitch angle at 75% radius
θ_{1c}	rotor lateral cyclic angle $[deg]$
θ_{1s}	rotor longitudinal cyclic angle $[deg]$
λ	rotor inflow factor or adjoint variable vector
μ	dynamic Viscosity $[kg/(ms)]$, $\frac{\tau}{\gamma}$ or rotor advance ratio, $\frac{M_\infty}{M_{tip}}$
μ_t	turbulent eddy viscosity $[kg/(ms)]$
ρ	density $[kg/m^3]$
σ, σ_N	nominal rotor solidity, $\sigma_N = N_b/(\pi R/c_{ref})$
σ_G	geometric rotor solidity, $\sigma_G = \int_0^1 \sigma(r)dr$
σ_T	thrust-weighted rotor solidity, $\sigma_T = 3\int_0^1 \sigma(r)r^2dr$
τ	shear stress $[kg/(ms^2)]$
τ_{ij}	viscous shear stress tensor
τ_{ij}^R	Reynolds shear stress Tensor
τ_w	wall shear stress $[kg/(ms^2)]$
υ	kinematic viscosity $[m^2/s]$
υ_t	turbulent kinematic viscosity $[m^2/s]$
ψ	azimuthal position $[deg]$
ω	specific dissipation rate of turbulent kinetic energy $[1/s]$ or frequency $[1/s]$
Ω	rotor rotational speed $[rad/s]$

Acronyms

ABC	Advancing Blade Concept
ACRB	Advanced Chinook Rotor Blade
ADAM	Aerofoil Design and Analysis Methodology
ADT	Alternating Digital Tree
AGB	Advanced Geometry Blade
AH	Attack Helicopter
AIAA	American Institute of Aeronautics and Astronautics
ALE	Arbitrary Lagrangian-Eulerian
AMG	Algebraic Multi Grid
AMR	Adaptive Mesh Refinement
AoA	Angle of Attack
AR	Aspect Ratio
ARO	US Army Research Office
ATIC	Advanced Technology Institute of Commuter-Helicopter

ATR	Advanced Technology Rotor
AW	Agusta Westland
BCFD	Boeing Computational Fluid Dynamics code
BERP	British Experimental Rotor Programme
BFGS	Broyden-Fletcher-Goldfarb-Shanno
BILU	Block Incomplete Lower Upper
BMESH	Background Mesh
BVI	Blade Vortex Interaction
CAD	Computer-Aided Design
CAMRAD	Comprehensive Analytical Model for Rotor Aerodynamics and Dynamics
CFD	Computational Fluid Dynamics
CFL	Courant-Friedrichs-Levy condition
CG	Centre of gravity offset
CH	Cargo Helicopter
CHANCE	Complete Helicopter AdvaNced Computational Environment
CHARM	Comprehensive Hierarchical Aeromechanics Rotorcraft Model
CLOR	China Laboratory Of Rotorcraft
CMRB	Composite Main Rotor Blade
CONGRA	CONjugate GRAdient Optimization
CONMIN	CONstrained function MINimization
COPTER	COmprehensive Programme for Theoretical Evaluation of Rotorcraft
CPU	Computer Processing Unit
CSD	Computational Structural Dynamics
CVC	Constant Vorticity Contour
DASA	Deutsche Aerospace AG
DDES	Delayed Detached Eddy Simulation
DDR	Dynamic Deflated Restarting
DES	Detached Eddy Simulation
DL	Disk Loading
DLR	Deutsches zentrum fur Luft- und Raumfahrt
DNS	Direct Numerical Simulation
DoE	Design of Experiment
DR	Deflated Restarting
DSTL	Defence Science & Technology Laboratory
EAL	Exact Arithmetics Library
EC	EuroCopter
EGO	Efficient Global Optimisation
EHPIC	Evaluation of Hover Performance using Influence Coefficients

elsA	Ensemble Logiciel pour a Simulation en Aerodynamique
ENO	Essentially Non-Oscillatory
ERATO	Etude d'un Rotor Aeroacoustique Technologiquement Optimise
ERF	European Rotorcraft Forum
FARA	Future Attack Reconnaissance Aircraft
FEA	Finite Element Analysis
FEM	Finite Element Method
FGMRES	Flexible Generalised Minimal RESidual method
FF	Forward Flight
FLRAA	Future Long-Range Assault Aircraft
FMESH	Foreground Mesh
FoM, FM	Figure of Merit
FPI	Fixed Point Iteration
FPR	Full Potential Rotor
FS	Full Scale
FVL	Future Vertical Lift
FW-H	Ffwocs-Williams and Hawkings
GCR	Generalised Conjugate Residual
GMRES	Generalised Minimal RESidual method
GOAHEAD	Generation Of Advanced Helicopter Experimental Aerodynamic Database
GRP	Generalised Rotor Performance
HART	Higher harmonic control Aeroacoustics Rotor Test
HB	Harmonic Balance
HELIOS	HELIcopter Overset Simulations
HH	Hughes Helicopters
HHC	Higher Harmonic Control
HIMARCS	High Manoeuvrability Agility Advanced Rotor Control System
HMB	Helicopter Multi-Block solver
HOST	Helicopter Overall Simulation Tool
HPC	High Performance Computing
I/O	Input/Output
IDW	Inverse-Distance Weighting
ILU	Incomplete Lower Upper
KKT	Karush-Kuhn-Tucker conditions
LBERP	Langley BERP blade
LBL	Langley Baseline blade
LE	Leading Edge
LES	Large Eddy Simulation

LSAF	Lifting Surface aerodynamics and performance analysis in Axial Flight
LU-SGS	Lower-Upper Symmetric Gauss-Seidel
MAC	Mean Aerodynamic Chord
MBB	Messerschmitt-Bolkow-Blohm
MGIV	Modified GIVens method
MTOW	Maximum Take-Off Weight
MUSCL	Monotone Upwind Schemes for Conservation Laws
MVBB	Minimum Volume Bounding Box
NA	Neutral Axis
NACA	National Advisory Committee for Aeronautics
NASA	National Aeronautics and Space Administration
NFAC	National Full-scale Aerodynamics Complex
NSGA	Nondominated Sorting Genetic Algorithm
OMS	Overset Mesh Search
ONERA	Office National d'Etudes et de Recherches Aerospatiales
OPT	Optimisation
OVERFLOW	OVERset grid FLOW solver
PA	number of Points around Aerofoil
PDE	Partial Differential Equation
PIV	Particle Image Velocimetry
PN	number of Points in blade Normal direction
POD	Proper Orthogonal Decomposition
PROTEGE	Pale pRincipale ecOlogique en composiTe de nouvellE GEneration
PS	number of Points in Spanwise direction
PSP	Pressure Sensitive Paint
RAE	Royal Aircraft Establishment
RANS	Reynolds-Averaged Navier-Stokes
RBF	Radial Basis Functions
RCAS	Rotorcraft Comprehensive Analysis System
ROBIN	ROtor Body INteraction
RPM	Revolutions Per Minute
SLSQP	Sequential Least-Squares Quadratic Programming
SNOPT	Sparse Nonlinear OPTimizer
SQP	Sequential Quadratic Programming
SST	Shear Stress Transport
SU	Stanford University
TM	Time Marching
TMESH	Total Mesh

TRAM	Tilt Rotor Aeroacoustic Model
TSD	Transonic Small Disturbance
TSP	Transonic Small Perturbation
TTCP	The Technical Cooperation Program
TURNS	Transonic Unsteady Rotor Navier-Stokes
UH	Utility Helicopter
UK	United Kingdom
UMARC	University of Maryland Advanced Rotor Code
VFS	Vertical Flight Society
WAVES	Without Artificial Viscosity Euler Solver
WDIST	Wall DISTance
WENO	Weighted Essentially Non-Oscillatory

Subscripts

e	equivalent
hb	harmonic balance
i, j, k	indices
imp	implicit
max	maximum
p	pressure term
ref	reference value
rms	root-mean-square
tip	tip value
tot	total
v	viscous term
∞	freestream value

Superscripts

i	inviscid
T	transpose
v	viscous

Chapter 1

Introduction

1.1 Motivation

Helicopters are complex, unique machines that serve many roles in the modern world and are present in the military, civilian, medical emergency and firefighting duties. The uniqueness of rotorcraft comes from their extreme manoeuvrability, ability to hover and take-off and land vertically. However, with helicopter design (single main rotor and tail rotor) come severe challenges and complexities. The rotor blade as it rotates has a velocity variation across it, leading to a non-uniform lift distribution. In hover, the speed of the rotor varies from zero at the hub to a maximum value at the blade tip. This leads to strong tip vortices that affect the rotor loads on the blade, and hence blade performance. In forward flight, the free-stream velocity contributes to the local rotor velocity value. This leads to an asymmetric velocity field where a maximum velocity is seen on the advancing blade of the rotor whereas the minimum flow velocity is seen on the retreating side. To maintain uniform lift across the rotor disk blade feather (altering the blade pitch) and flapping motions are introduced. This has aerodynamic and dynamic issues such as advancing blade compressibility effects as the flow becomes transonic during high speed forward flight and retreating blade stall if the angle of attack (AoA) is too high. On top of these flow physics phenomena, rotorcraft have to deal with blade-tip vortex interactions (BVI) which lead to increased noise and increased vibration, complex blade dynamics and main rotor/tail rotor interaction. These features lead to a very complex flow field as can be seen in Figure 1.1 [220]

The aforementioned challenges lead to difficulties in the design of helicopter rotor blades. However, understanding the phenomena associated with helicopter flight can lead to improved designs and enhanced performance - which is a requirement in any area of engineering. Since rotorcraft are unique machines that go through many flight states such as hover, forward flight, ascent and climb, it is difficult to design a rotor blade that will be optimum across the entire flight envelope. The complex rotor flow field leads to the coupling of multiple disciplines, which must be considered for practical rotor design such as: aerodynamics, aeroelasticity, structures,

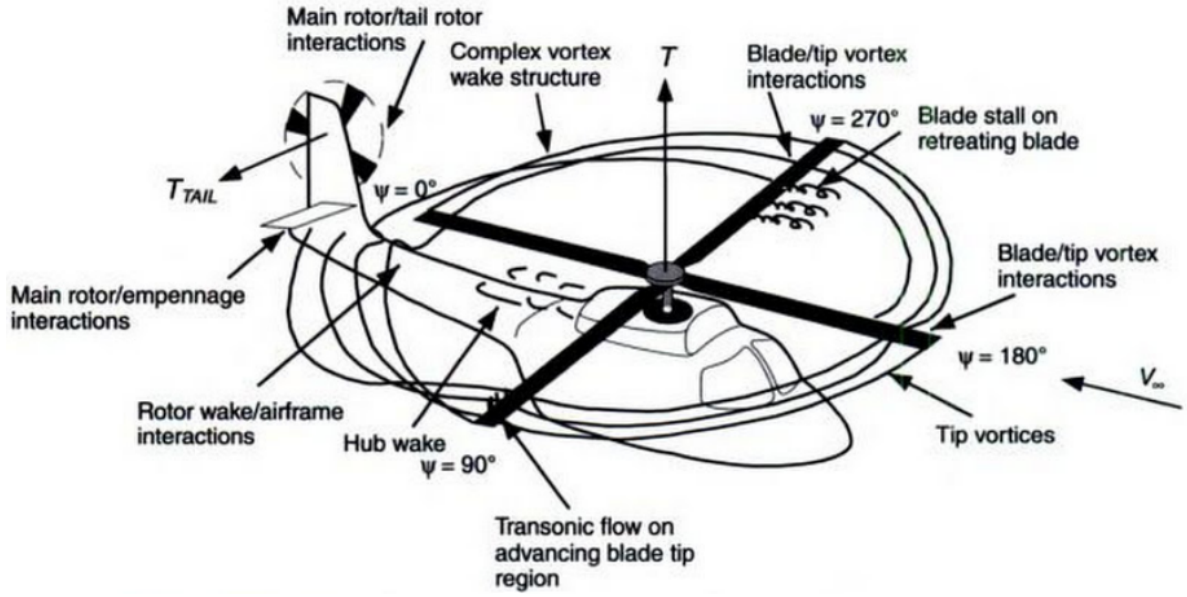

Figure 1.1: Complex helicopter flow field showing the need for advanced aerodynamic design [220]

dynamics, acoustics, manoeuvrability, flying qualities and safety.

The main motivation for this project comes from the need for higher performance and safer helicopters. In the age where environmental aspects are important, there are additional requirements for reduced fuel consumption as well as reduced noise and vibration levels. Another aspect is expanding the helicopter flight envelope, whether it is the lifting capability or maximum forward flight speed. The main rotor design is key to achieving these goals, in particular the aerodynamic blade design, which is the main focus of this work. This research is also motivated by the fact that many different rotor blade planform and tip shapes are currently used around the globe. A BERP (British Experimental Rotor Programme) planform is used nearly solely in the UK, whereas other regions of the world tend to use simpler designs such as a swept/swept-tapered or a parabolic tip [64]. The emergence of more radical rotor designs such as the Blue-Edge blade [39] or the Advanced Chinook Rotor Blade (ACRB) [54] further shows that rotor design is still progressing. CFD has become an important tool to promote this advancement and in conjunction with optimisation methods can be used to further develop the current state of the art in rotor design.

1.2 Literature Survey

A literature review is performed to assess the current research performed in the area of rotor design, and determine the aims and objectives for the present research. The literature survey was conducted by searching popular scientific databases such as Scopus, Science Direct, Aerospace Research Central and the NASA Technical Reports Server, using keywords related

to each subtopic in the literature survey. Additionally, conference proceedings of the Vertical Flight Society (VFS) and European Rotorcraft Forum (ERF) were consulted, as these are not available in these scientific databases. The present research is focused on the rotor design using numerical methods. Therefore, the literature survey has been divided into two key sections: CFD validation and Advanced rotor blade design. The first section aims to assess the current capabilities of CFD codes to predict the performance rotor blade designs, which is key before using numerical methods in rotor design studies. For the optimisation phase of the project to be valid, the uncertainty on the accuracy of the performance prediction must be much lower than the performance benefit obtained for a better design. The advanced design reviews in detail the manner in which rotor blades were designed in the past and in industry today. An overview of rotor design optimisation studies in current literature is given, along with a discussion of their current limitations.

1.2.1 CFD Validation

This section discusses current practices in the validation of CFD methods with experimental data and assesses the solver fidelity required for accurate performance predictions, in view of using the prediction method for a rotor design study. First, the available experimental data for validation studies will be reviewed in order to determine which data sets should be used for validation and the optimisation study within this research. Following, an analysis of literature regarding CFD validation for rotor flows is presented.

1.2.1.1 Available Experimental Data

The available experimental data is key for validation of numerical methods, in particular CFD. The experimental data must be of high quality with few uncertainties, to be usable CFD validation studies. The geometry of the blade must be well defined, as well as the flow conditions. The scatter between the experimental data test points should also be minimal for higher certainty of the CFD results. Finally, comparisons of multiple quantities give higher confidence in the CFD solutions, as validation through integrated loads alone may not be valid due to potential cancelling errors. These quantities can include blade surface pressures, sectional and azimuthal loads and vortex trajectories, however, such data is scarce in literature, especially regarding wake measurements. An analysis of the available experimental data is performed to determine which rotor blades will be studied within this work for CFD validation and later, during the optimisation process. Several rotor blades are considered for this task, shown in Tables 1.1-1.2. These rotors are chosen based on available data in the public domain. The available flight test data for a number of rotors is presented in Table 1.1, whereas the wind tunnel data is presented in Table 1.2.

Based on the available data shown in Tables 1.1-1.2, it is clear that the most-well tested rotor

Table 1.1: Available data flight test data for selected blades

Blade	Measurements
UH-60A [59]	Instrumented blade data with 242 pressure transducers and various strain gauges. Forward flight and hover integrated loads, section lift and moment in forward flight, pitch link loads, various measurements in climb, descent and manoeuvring flight [59], surface pressure data [204], further airloads and performance data [91].
S-76 [181]	Non-instrumented blade data. Performance in forward flight along with vibratory loads data [172], Noise measurements data [277], BVI acoustic measurements data [424].
AH-64A [40]	Non-instrumented blade data. YAH-64 data for hover and forward flight performance as well as flight and vibration characteristics [40].
CH-47 [41]	Non-instrumented blade data. Hover and forward flight performance, autorotational performance, flight and vibration characteristics [41], Acoustic measurements [278].
Lynx Metal blade [211]	Blade instrumented with bending moment gauges. Forward flight performance [211], Extensive blade and hub loads data at various conditions available [211], [212].
AH-1 [254]	Instrumented blade data with 144 pressure transducers and a number of strain gauges. Forward flight performance and flight characteristics [107], blade loads [385], hover performance [200], further blade loads, surface pressure data, blade displacements and acoustic data [94]

blades are the UH-60A and S-76, as flight test data is available as well as model and full scale wind tunnel test data. The UH-60A flight test data [59] is the primary source for CFD validation of rotors in forward flight, especially for CFD/CSD frameworks, as the flight test blades were instrumented and a wide range of data was measured. The UH-60A has also been studied in hover, however, the main dataset used in literature for hover validation are the model-scale S-76 rotor blade experiments [32] as part of the AIAA Hover Prediction Workshop [137]. The UH-60A and S-76 rotors, although have extensive experimental datasets, have also significant CFD validation studies in literature as will be shown in the next section, and hence are not considered for the present research. Other instrumented flight test data for the AH-1 [254] and Lynx Metal Blade [211], has perhaps received less attention due to the simple rectangular rotor geometry. Flight test data for the CH-47 [41] and YAH-64 [40] also have very few validation studies, as the blades were uninstrumented. A much wider range of data is available from wind tunnel experiments, especially at model-scale. Most of these experiments, however, are for simple blade geometries such as the Caradonna & Tung rotor blade, or only report integrated loads. In fact, the only available data for a more advanced planform are the model-scale tests of Yeager et al. [429] for a BERP-like planform. A rectangular planform was also tested, with the same radius, twist distribution and aerofoils. This experimental dataset is, therefore, valuable for the present research even though only integrated loads are reported. This is due to the fact that CFD validation can be performed for an advanced planform, but also the data also can be used to validate the differences in performance between rotors with rectangular and BERP-like planforms. A number of geometric uncertainties, however, exists for the BERP-like blade such as the exact blade tip geometry. Furthermore, a certain degree of experimental data scatter exist in the hover performance data. For the same reason, flight test data is also disregarded for CFD validation in hover, as the experimental data scatter can approach 3-5 counts (1 count =

Table 1.2: Available wind tunnel test data (model and full-scale) for selected blades

Blade	**Measurements**
UH-60A [59],	1:5.73 model scale chordwise surface pressure and airloads in forward flight, BVI event positions [230], Model scale hover performance with various tip shapes [32, 33], Full-scale hover and low-speed forward flight performance [284, 344], Full-scale forward flight performance, airloads, dynamic stall tests [283], Full-scale blade displacements in forward flight [35], Slowed rotor performance and loads [101].
S-76 [181]	1:5 model scale hover performance with tip Mach number trends [34], 1:4.71 model scale hover performance with different tip shapes [32, 33], 1:6 model scale hover performance [196], Full-scale hover and forward flight performance, blade loads with different tip shapes [181, 368, 369], Full-scale hover and low speed forward flight performance, dynamic loads data [342, 343], Full-scale forward flight performance [31], Acoustic measurements [264]
AH-64 [40]	0.27 model-scale hover performance at different blade tip Mach numbers, forward flight performance [190, 191], 0.27 model-scale structural blade loads data in forward flight [47], Full-scale whirl tower hover data [168]
CH-47 [41]	1:6 model-scale hover and forward flight performance [195], Full-scale whirl tower hover performance [195]
AH-1 [254]	1:4 scale forward flight performance and oscillatory loads data [216], 1:4 scale acoustic measurements [146]
XV-15 [119]	8% Model-scale flow field and acoustic measurements [304], Full-scale hover performance at different blade tip Mach numbers, rotor wake dynamic pressure distributions [119], Full-scale hover and forward flight performance [48], Full-scale acoustic measurements [90], Full-scale acoustic measurements and performance in hover and forward flight [224], Full-scale skin friction measurements in hover [394].
HIMARCS [282]	Model-scale rotor with LE slats/TE flap; hover performance and forward flight performance, pitch-link and vibratory loads [282]
HART-II [382]	Model-scale B0-105 rotor with HHC 3/rev pitch actuation and instrumented blade with pressure transducers and strain gauges. Pressure distributions, acoustic data, blade loads, vorticity development along with vortex flight path data [382], Blade displacements, structural loads, tip vortex trajectories in forward flight [383].
PSP [291]	Instrumented blade with pressure transducers, and the PSP technique for comparison. Model-scale hover performance, surface pressure field and chordwise pressure data in hover and forward flight [419, 420], Model-scale hover performance with transitional effects [291], Model-scale forward flight performance integrated loads [227]
BERP-like [429]	Model-scale hover and forward flight performance, normalised pitch-link and vibratory loads [429]
Caradonna & Tung [73]	Surface pressure data, sectional loads and vortex trajectories in hover [73]

0.01) in Figure of Merit (FoM), as shown for example in the YAH-64 data [40]. The accuracy required by CFD methods is significantly higher than the experimental data scatter. For this reason, the more modern dataset of the model-scale PSP rotor blade [291] is also used, as the integrated loads uncertainty is fairly low, and the blade geometry is well defined. Comparisons of surface pressure data and sensitivity due to transitional effects also give higher confidence in the CFD results. This blade is also to be tested in the future at a slightly higher blade tip Mach number in the large NASA NFAC facility [164] to reduce wind tunnel wall effects and provide a comprehensive dataset for hover validation, including wake measurements and PIV data. This blade is also the current focus for the AIAA Hover Prediction Workshop [136]. Furthermore, forward flight performance data was provided for this project as part of the TTCP collaboration [227]. Therefore, the data of Yeager et al. [429] with a rectangular and BERP-like planform, and the PSP data of Overmeyer [227, 291] will be used for CFD validation of rotors in hover and forward flight in the present research.

The performance of the rotor blade chosen as a baseline for the optimisation process should also be validated. The blade selection is based on the availability of the baseline geometry and experimental data, and whether the rotor blade can be attributed to a real aircraft. The available experimental data for a number of rotor blades was presented in Tables 1.1-1.2 from which the baseline blade for the optimisation process is selected. State of the art rotor blades such as the Blue-Edge blade [39], BERP III [298] and BERP IV [141] are not considered, due to the unavailability of the experimental data and blade geometry. However, as the project aims to further examine the aerodynamics of BERP-like rotor blades, the disk loading parameter is also of importance, as it indicates the role of the helicopter as well as having an effect on the ratio between induced and profile power [313]. The disk loading values for a number of helicopters are compared to rotorcraft that have main rotor blades with a BERP tip in Table 1.3.

Table 1.3: Disk loading of various production helicopters showing the high disk loading on rotors with a BERP tip.

Helicopter	**NoB**	σ	**R**	**S**	**MTW**	**DL**
UH-60A	4	0.0826	$26.8ft$	$2,260ft^2$	$20,250lbs$	$8.96lb/ft^2$
S-76	4	0.0704	$22ft$	$1,520ft^2$	$11,700lbs$	$7.69lb/ft^2$
Lynx Metal blade	4	0.078	$21ft$	$1,385ft^2$	$7,998lbs$	$5,77lb/ft^2$
Sea King	5	0.084	$31ft$	$3,020ft^2$	$21,000lbs$	$6.95lb/ft^2$
AH-64	4	0.092	$24ft$	$1,809.5ft^2$	$23,000lbs$	$12.71lb/ft^2$
CH-47	2x3	0.085	$32ft$	$5,655ft^2$	$50,000lbs$	$8.84lb/ft^2$
AH-1G	2	0.0651	$22ft$	$1,520ft^2$	$9,500lbs$	$6.25lb/ft^2$
XV-15	2x3	0.089	$12.5ft$	$981.7ft^2$	$13,000lbs$	$13.24lb/ft^2$
Helicopters with a rotor that utilizes a BERP planform						
AW101 (Merlin)	5	-	$30.5ft$	$2,992.5ft^2$	$32,188lbs$	$10.75lb/ft^2$
AW159	4	-	$21ft$	$1,385ft^2$	$13,228lbs$	$9.55lb/ft^2$
Super Lynx	4	-	$21ft$	$1,385ft^2$	$11,750lbs$	$8.48lb/ft^2$

As can be seen in Table 1.3 the blades with a BERP blade have relatively high disk loading of order 8-11 lb/ft^2. It is generally understood that the BERP blade has more optimal performance at higher disk loading, as proven by the current helicopter designs. To examine rotor designs under similar conditions as rotorcraft with blades that utilize a BERP tip, the baseline blade for the optimisation process must also operate at high disk loading. From the rotors listed in Table 1.3, only the AH-64A and UH-60A helicopters have a disk loading in this region, however, they are usually operated at a lower loading than max-takeoff weight. The operational disk loading for the AH-64A helicopter is 9.75 lb/ft^2, whereas the UH-60A operates with a disk loading of $7.71lb/ft^2$. The CH-47 operates also operates at a high disk loading however, this aircraft has a tandem configuration which is not of interest in this work. The AH-64A has a comparable disk loading to the AW159/AW101 helicopters that utilize a BERP IV blade tip. Another benefit of the AH-64A helicopter is the operation of these aircraft in the UK, hence being of interest to the project sponsor, DSTL. Based on these, observations, the AH-64A rotor blade is selected as a baseline blade for the optimisation process and validation studies within this work will also include comparisons with the YAH-64 flight test data [40] and the full-scale whirl tower data in hover [168].

1.2.1.2 Rotor Performance Validation Studies

The review of current validation practices is performed based on the utilized numerical models from low-fidelity to high-fidelity Navier-Stokes methods. Performance prediction sensitivity studies are also discussed to determine which modelling aspects are important for accurate performance predictions. The analysis is split into two segments corresponding to the two key flight conditions: hover and forward flight.

Hover Flight

Significant efforts have been performed in the rotorcraft community to study the flow field around a rotor in hover and develop the predictive capabilities of numerical codes. The key performance indicator in hover is represented by the Figure of Merit (FoM), which is the primary measure of a rotors efficiency. Today, design tolerances in industry are nearing 0.5% in FoM, which represents a payload of one passenger [75], and hence such predictions must be obtainable through CFD.

Analytical models such as actuator disk theory and blade element momentum theory were very quickly seen to have a major drawback - a lack of modelling fidelity of the blade-vortex interaction and the detailed effects of the rotor wake. This led to the emergence of prescribed wake models [198, 209] based on empirical relationships derived from experimental data. An example of combining prescribing wake models with blade element momentum theory for performance calculations was given by Young [436]. At the same time, free-wake analysis methods were also gaining popularity [89, 210], which rely on an iterative re-calculation of the rotor wake geome-

try and circulation strength. These wake models were often coupled with potential flow solvers, which were in development during the late 1970s and 1980s. These methods were primarily aimed at transonic flow predictions although, have also been successfully used in validation of hovering rotor flows [2, 9, 73]. The aforementioned methods are considered as low fidelity and are used still today for preliminary performance estimates in comprehensive rotor codes such as CAMRAD [182, 183] or EHPIC [314]. They do not, however, rigorously account for the effects of tip shape, nonlinear blade twist and flow separation.

Modern CFD analyses, based on Euler and Navier-Stokes methods were in development in the mid-1980s and were seen as a promising alternative to widely used potential flow solvers. These methods were computationally very expensive at the time, but had an advantage of direct modelling of the tip vortex roll-up process and wake convection. One of the key issues for these methods (and still present today) was significant numerical diffusion. Often various approximations were used to obtain meaningful solutions at reduced computational costs, for example, coupling with free-wake analyses as in the work by Roberts [320] or Agarwal and Deese [4]. Other methods included applying a correction to the geometric angle of attack to account for wake effects, as in the work of Srinivasan and McCroskey [8]. The fact that the rotor wake is key to accurately predict the hover performance of a rotor, was widely recognised.

However, since then CFD methods have undergone significant developments, including numerical algorithms, grid generation as well as a rapid growth in computational power. In the past, only single-block grid systems were generated, and most numerical schemes relied on explicit time-stepping methods, limiting the allowable time-step. RANS methods became more accessible in the 1990s, with the introduction of implicit methods, such as the LU-SGS scheme developed by Yoon and Jameson [7] allowing the use of larger time steps, which was later used in the TURNS code [10]. TURNS was later applied to the UH-60A rotor blade [10] in hover showing good agreement with the experiments of Lorber [230]. A source-sink model for imposing the farfield boundary conditions was used for the first time, with no external wake model. The importance of including viscous effects was also highlighted by comparing RANS and Euler solutions [10]. A BERP blade was also simulated with the tip vortex formation and roll-up process shown in Figure 1.2 [354]. Lower fidelity methods, cannot give such insight into the behaviour of the flow field around the tip of the blade, showing the benefits of high-fidelity Navier-Stokes simulations.

Further developments in the 1990s and early 2000s, were focused on grid generation techniques, solution acceleration and reducing the numerical diffusion. The introduction of the overset grid method [357] allowed generation of much smoother and less skewed grids, compared to the single-block grids used previously. This method uses multiple overlapping grid systems and uses interpolation to transfer the solution between the grids. This meant that fine body conforming grids could be generated, along with more regularly spaced background grids, to capture the rotor wake. This method was applied to hovering rotors by Duque and Srini-

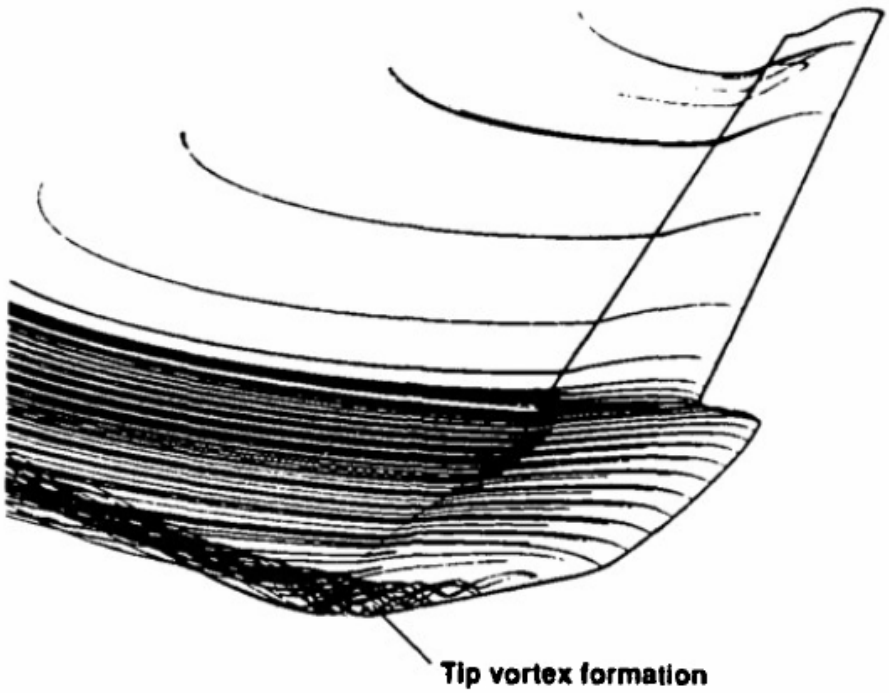

Figure 1.2: Tip vortex formation and roll-up process around a BERP blade, showing the capability of Navier-Stokes based methods in predicting design critical flow field phenomena [354].

vasan [110]. Various solution acceleration techniques were introduced into CFD solvers at the time such as local time-stepping, multi-grid, residual smoothing and preconditioning. This allowed faster calculation turnaround times, or larger grid sizes to be used. To reduce numerical diffusion, higher order numerical schemes were investigated by several researchers. This included 5th and 7th order accurate in space ENO and WENO schemes [5, 139, 434] as well as 4th order MUSCL schemes [6, 175], which led to a better preservation of the rotor tip vortices and rotor wake. Other vortex preservation methods were also investigated such as the vorticity confinement technique [361] or a vorticity transport model [3].

Even though vorticity based techniques were promising, the rotorcraft community continued to use RANS based solvers. In the 2000s, overset grid methods became fairly standard, although other methods such as sliding planes were also in use [358]. The most commonly used computational setup was based on a steady-state solution using a source-sink model as in the work by Srinivasan [354]. With growth in computational power, however, the close to 1 million points used by Srinivasan [354] for a fine grid simulation become 64 million points as in the work used by Strawn and Djomehri [1]. Here, the UH-60A rotor experimental data [230] is used once again and simulated using OVERFLOW, with the study aimed at performance sensitivity due to grid resolution. The wake resolution was found to have a minor sensitivity on the integrated blade loads, and the loading at the blade tip was more sensitive to the employed turbulence model than the grid resolution. Further grid resolution studies were performed by Potsdam and Strawn [308]

for the TRAM rotor in hover and showed a performance sensitivity of under 1 count in FoM for grid sizes from 11 to 37 million cells.

The resolution of the tip vortex, in particular, accurate tip vortex formation and reduction in core size growth, was tackled through adaptive mesh refinement (AMR). An example of the use of AMR in a mixed prism/tetrahedral mesh using the Helios framework was shown by Wissink et al. [416]. The method was demonstrated for the TRAM rotor in hover and showed little improvement to the blade loads predictions with increasing grid size, but improved the rotor wake resolution. Hollst and Puliam [149], also examined the TRAM rotor in hover at high thrust (14 deg collective) using AMR for grids between 64 and 448 million cells and high order schemes. Building on this study, Chaderijan [75] performed further simulations using AMR, up to grid sizes of 1.2 billion cells and concluded that resolving the rotor wake to such a degree had little impact on the predicted rotor performance. Using a DES turbulence model (Detached Eddy Simulation) and/or near-body 5th order spatial accuracy led to much larger improvements in the performance predictions. The effect of changing the grid size on the rotor wake through AMR is shown in Figure 1.3 [75]. The difference in the coarse and fine grid solutions in this study was only 0.2 counts in FoM.

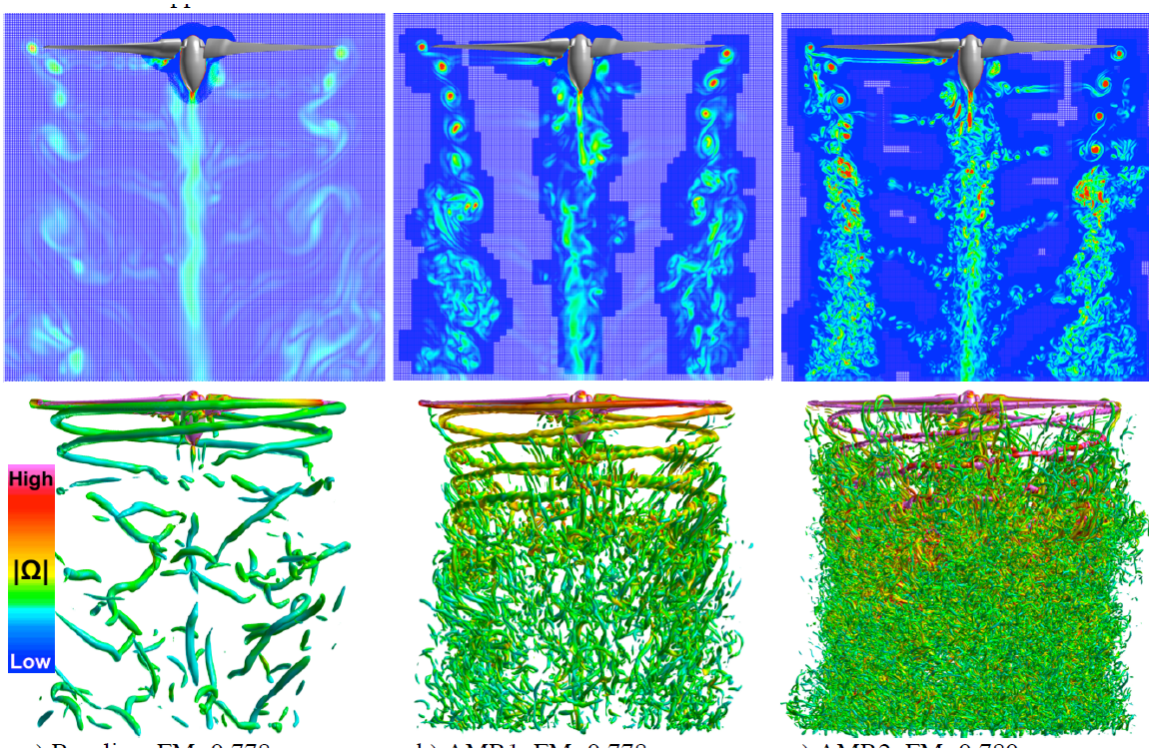

Figure 1.3: Effect of AMR on the rotor wake for the TRAM rotor at 14 degrees collective, with varying grid size from 34 million to 670 million cells, showing a negligible effect on performance prediction [75].

Therefore, accurately capturing the tip vortex formation and the roll-up process is much more important than resolving the far-field rotor wake. Other key issues highlighted were, that

RANS solutions tend to lead to high levels of turbulent viscosity in the rotor wake, leading to an underprediction of the FoM. This was solved by switching off the viscous terms on the background grid or using the DES turbulent model. The 5th order near-body and off-body RANS solution, however, predicted a similar performance as the DES solution. The work of Potsdam and Puliam [307] for the TRAM rotor blade, also demonstrated similar findings and showed a higher sensitivity of the near-body solver order than the background grid turbulence treatment. Wake instabilities were also seen in the computed solutions and were attributed by the author to shear layer rollup [75], also seen in experiments [127, 128]. Further evidence of these secondary structures in the rotor wake have also been demonstrated by more recent experiments [418]. These structures, however, overload the entire wake in many numerical solutions, for unknown reasons, which is an ongoing topic of research [133, 134]. In general, however, treatment of the off-body region as RANS rather than laminar has a stabilizing effect on these flow phenomena due to higher turbulent eddy viscosity present in the flowfield [435]. Other vortex properties such as vortex core size and circulation are also important, however, to capture these characteristics accurately very large grid sizes are required along with high-order numerical schemes and AMR, with little benefit for performance predictions.

The current state of the art of hovering rotor calculations is represented by the studies within the AIAA Hover Prediction Workshop formed in 2014 [135]. The selected test case was the S-76 rotor which was experimentally tested by Balch [32], and was chosen due to availability of data for different tip shapes - swept-tapered, rectangular and anhedral. Hence, the accuracy of the performance predictions could be compared not only for the swept-tapered S-76 rotor but also, based on the changes due to tip geometry, which are more important when considering rotor design. Code comparisons were made using various solvers of different orders of accuracy, meshing techniques and turbulence models. Various levels of hover performance prediction accuracy were obtained with a number of studies nearing performance predictions within one count (0.01) in FoM. However, a wide degree of scatter was observed in the blade sectional loads, vortex strength and displacements. Only code to code comparisons could be performed, as only experimental integrated loads were reported. Due to the lack of experimental data clear conclusions on which methodologies showed most promise could not be made. Full-Navier Stokes simulations, however, generally gave more accurate predictions, in terms of FoM [138], although at much higher computational costs compared to hybrid techniques or comprehensive analyses. This workshop highlighted the need for a more comprehensive experimental dataset in order to perform more in-depth CFD validation. For this reason, future tests are planned for the PSP (Pressure Sensitive Paint) rotor blade in hover at the NASA NFAC wind tunnel facility.

One key statement was highlighted by Egolf et al. [114], that due to many modelling simplifications (simulation method, and also modeling the rotor as isolated), compensating errors may be introduced into the results, thus giving a perception of good agreement with experimental data. For these reasons, it is important to distinguish which elements of the numerical hover

simulation, have a large impact on the overall solution. Transitional effects have been examined by a number of researchers [163,296,387] for the PSP rotor blade using the experiments of Overmeyer [291]. Flow transition was seen to have a noticeable impact on the performance for the model scale PSP blade, especially at low thrust conditions where profile drag has a much larger contribution compared to high loading conditions. However, such a sensitivity is not expected in real-life due to higher Reynolds number and free-stream turbulence as well as the presence of the erosion shield which could promote early transition on the upper surface of the blade. For correlation with model scale data, transitional effects may be important, however, the fully-turbulent boundary layer assumption has given good predictions in many CFD validation studies in literature. Turbulence model sensitivity studies have also been performed during the AIAA workshop for the S-76 rotor blade. In particular, the blade loading at which stall is first seen on the rotor blade has been seen to be turbulence model sensitive [340,421], leading to performance prediction differences at high thrust. Jain [163] highlighted that the k-ω SST turbulence model can lead to premature stall when compared to experiments or other turbulence models. An example study [215] for the S-76 rotor blade using Spalart-Almaras and Spalart-Almaras DDES models showed major differences in the separation patterns at the blade tip, shown in Figure 1.4. This was mainly attributed to the very high turbulent eddy viscosity levels seen in the wake for the Spalart-Almaras predictions.

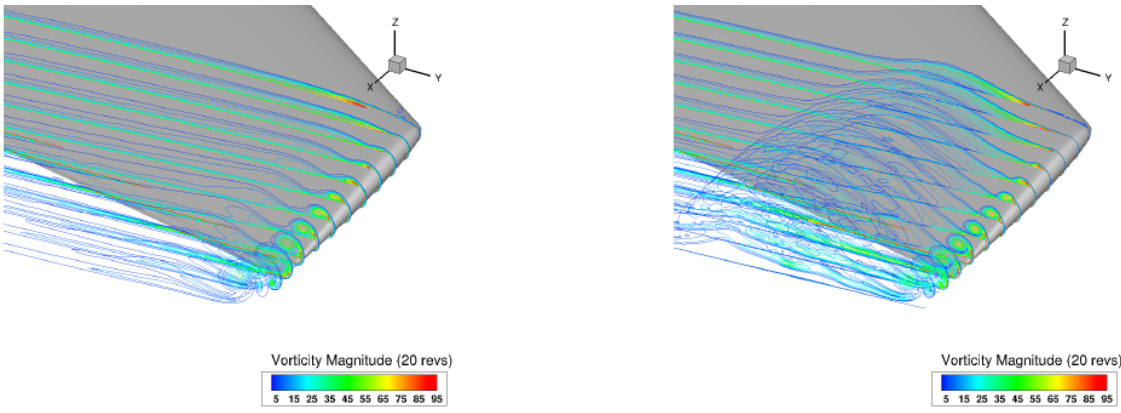

Figure 1.4: Differences between the Spalart-Almaras (left) and Spalart-Almaras DDES (right) turbulence models, tip vortex formation process predictions, showing a separated flow region for the Spalart-Almaras DDES turbulence model [215].

Accurate representation of separated flow fields is still a challenge for CFD methods, mainly due to inaccuracies of employed turbulence models. More recently, further sensitivity analyses have also been performed such as due to aeroelastic or installation effects [163, 164]. The inclusion of the fuselage for the PSP rotor blade was found to increase the FoM by approximately 1.5 counts due to an upwash induced by the fuselage, whereas aeroelastic effects were found to be minor for the PSP blade FoM prediction, but had an impact on the blade loading achieved at a given collective due to elastic blade twist. Aeroelastic effects could, however, have a larger sensitivity at full scale or for more advanced planform shapes. Jain [164] also examined the

effect of the facility walls and test stand in view of the future PSP experiments at the larger NFAC facility (80 by 120ft), and found that these effects are rather minor, within 1 count in FoM. Another study for the UH-60A rotor blade in hover [76] reported similar findings for the NFAC facility, but found a much higher sensitivity for the Rotor Test Cell of the NASA Langley Research Center due to flow recirculation.

The sensitivity analyses for performance predictions, however, must also take into account computational costs. For example, modelling the facility walls and test stand, while having a low sensitivity on the integrated loads, will lead to a large increase in computational costs. Similarly, with installation effects, the performance sensitivity can be of significance, however, for simulations with the fuselage, the flowfield can no longer be treated using the steady-state hover formulation. Periodic boundary conditions and simulating the flow field as steady rather than unsteady can lead to major computational cost reductions. In fact, this is how most simulations were performed back in the 1990s and early 2000s when the computational resources available were much lower than today. The steady hover formulation becomes inadequate if large separated flow regions are seen in the domain. A study by Narducci [269] compared the unsteady and steady hover solutions for the S-76 rotor with different tip shapes, and found comparable performance predictions except at high thrust levels, where the steady-state formulation predicted pre-mature stall, which is the main limitation of this method. However, this method required only 3% of the resources used by unsteady simulations. Other possible solutions for reducing the computational costs include coupled Free Wake/Navier-Stokes codes as in [162] or [255].

Another important aspect to highlight is the fact that while CFD methods and more accurate hover performance predictions are obtained, the accuracy of flight test data and wind tunnel data is not sufficient to validate high-fidelity CFD methods. The typical scatter of various experimental and flight test measurements in terms of FoM or power coefficient versus thrust coefficient is shown in Figure 1.5.

The typical scatter seen in the flight test data, representing a real-life scenario approaches 5 counts in FoM, while wind tunnel tests are generally able to obtain predictions within 2-3 counts. Scaling effects including Mach number, Froude number and Reynolds number effects as well as the use of different facilities, increase the scatter between each wind tunnel test data set. CFD predictions are nearing a scatter within 1-2 counts, even with many sensitivity analyses. With the uncertainties from full-scale experimental/flight test performance measurements, more accurate predictions may be unachievable at this time, and it is difficult to assess the accuracy of modern CFD methods. Therefore, the use of higher fidelity turbulence models and/or numerical schemes along with large grid sizes as in the studies of Chaderijan [75] may not be fully justifiable for CFD validation. The use of the unsteady simulation technique, especially away from high loading conditions, may also not be worthwhile. RANS methods compared to lower fidelity models are, however, are key to accurately capture tip vortex formation and roll-up effects. Despite, the large scatter in experimental data, these types of methods are useful for ro-

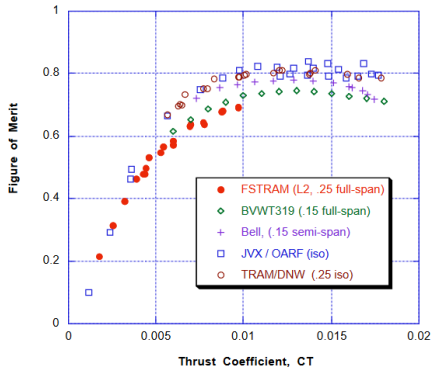

(a) TRAM rotor experiments [247] (corrected for Re No. effects)

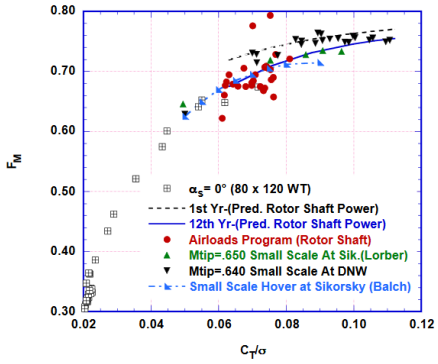

(b) UH-60A rotor experiments [344] (uncorrected)

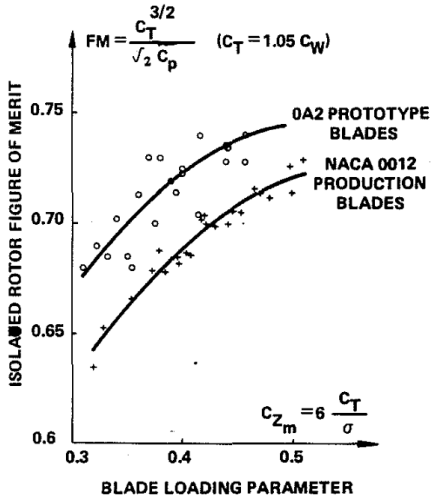

(c) SA-365N Dauphin 2 flight tests [323] (two blades tested)

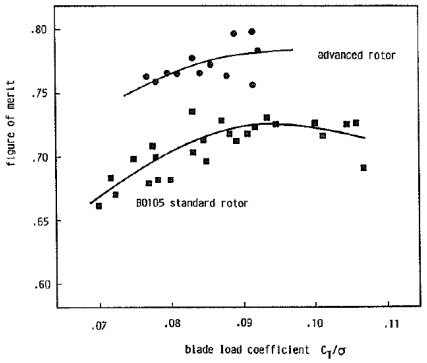

(d) B0-105 flight tests [306] (two blades tested)

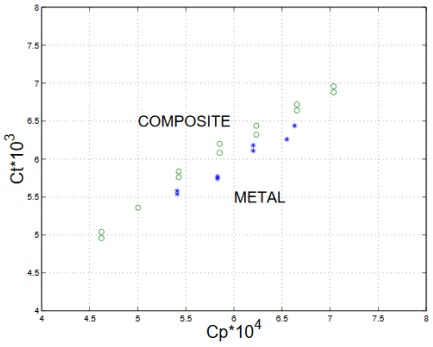

(e) S-61 flight tests [95] (composite & metal blades)

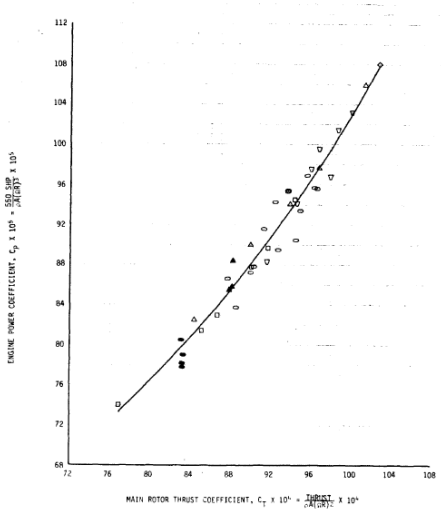

(f) YAH-64 IGE flight tests [263]

Figure 1.5: Experimental hover performance predictions, showing the wide degree of scatter between the measurement points, especially for flight test data.

tor design purposes, where simulation speed is crucial, and accurate predictions of performance improvements due to planform changes are of major significance. As indicated by Figures 1.5 (c) and 1.5 (d), an improvement rotor design is still clear from the experimental data scatter as the noticeable shift in the FoM values is seen.

Forward Flight

Many of the observations in terms of CFD solver developments described in the hover simulation section apply to forward flight simulations. The main difference between hover and forward flight simulations is the necessity to treat the flow as unsteady, and apply time-varying rotor control inputs in the form of pitching and flapping. The importance of CFD/CSD modelling, especially for comparisons with flight-test data is also highlighted in the reviewed validation studies for rotors in forward flight.

For forward flight validation studies, potential methods emerged first, and received significantly more attention than for hover simulations. The first studies were based on the transonic small-disturbance equations and were primarily aimed at advancing side pressure predictions [71, 72]. These methods went through significant developments from two-dimensional and quasi-steady for non-lifting rotors to three-dimensional and unsteady applied to lifting rotors [365]. Methods based on the small-disturbance transonic equations were also replaced by full-potential equations tools. An example of an early application of the full-potential equations to a lifting rotor was presented by Arieli and Tauber [22]. The lack of wake modelling, however, was very quickly seen as a major drawback. Sankar and Pritchard [331] developed a full conservative potential code and coupled it with a free wake model to include wake effects. This tool also captured aeroelasticity and used an implicit solution procedure allowing larger time steps, leading to a reduction in computational costs [330]. Egolf and Sparks [115] developed a tool that used the full potential equations in the near-blade region, and a vortex lattice method in the outer domain. A prescribed wake based on free-wake predictions was used to calculate the wake geometry with a vortex embedding technique used for the inner domain. Another example is the well-known Full-Potential Rotor (FPR) code [367], which was coupled to the boundary integral method, CAMRAD [182] to include rotor trim and wake modeling effects. CAMRAD was used to specify the equivalent angles of attack along the rotor blade. This method was later used in the correlation of blade loads for the PUMA rotor blade [366] with flight test data and the transonic perturbation methods of RAE (TSP) and ONERA (TSD). A comparison of surface pressure isolines for the advancing side of the PUMA blade is shown in Figure 1.6, showing the capabilities of potential flow methods in transonic loading predictions. The full-potential code also predicts a larger extent of the supercritical region inboard of the blade tip. Further comparisons of the FPR code with various lifting line/wake modeling approaches were given in [61].

Higher fidelity CFD methods were also in development during the mid-1980s, and applied

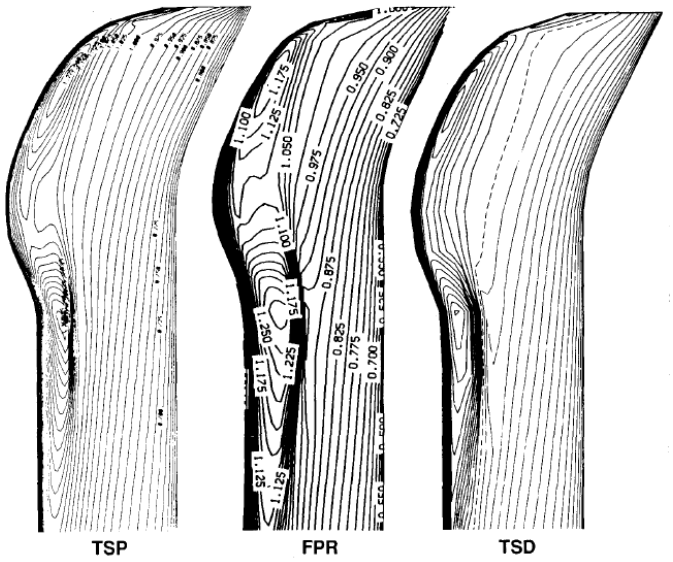

Figure 1.6: Comparison of the transonic pressure distributions for the advancing side of the PUMA blade, between the ONERA TSD code, RAE TSP code and US Army FPR code [366].

to rotors in forward flight. Wake et al. [397] compared predictions from the unsteady Euler equations based on a semi-implicit solution approach with quasi-steady potential code results and experimental data for a generic rotor blade. Further results were presented by Sankar and Tung [332] for the 1/7 scale Cobra blade and a generic 3-bladed rotor. Here, a coupled approach was used where a free-wake model was used in the farfield, and angle of attack corrections were employed as a boundary condition at the blade surface of the near-body grid. A similar approach was adopted by Chang and Tung [80] who presented results for non-lifting and lifting rotor blades, although the solution was based on the explicit Runge-Kutta scheme (with implicit residual smoothing). Wake and Sankar [395], later extended their implementation to the Navier-Stokes equations. Another example of a Free-Wake Navier-Stokes (thin-layer approximation used here) method was implemented in the TURNS solver by Srinivasan and Baeder [354]. Chen et al. [82] also developed an unsteady Euler solution methodology, based on an upwind solution algorithm and the LU-SGS numerical scheme [166]. Berezin and Sankar [43], later applied a inner-outer domain Navier-Stokes/Potential method to the UH-60A rotor in forward flight, and compared the predictions with full Navier-Stokes calculations. Many of the calculations during this time were performed using hybrid methods due to the extremely high computational costs of full Navier-Stokes methods and high numerical diffusion. However, the importance of capturing the correct physics, in terms of tip vortex formation, and interaction of the advancing blade shockwave with the boundary layer was recognised.

Full Navier-Stokes calculations of rotors in forward flight started becoming routine in the mid-1990s and early-00s. Ahmad and Dueque [13] showed predictions for the AH-1G rotor in forward flight, using the overset grid method. Although a coarse grid by today's standards of 1.6M cells was used, the comparison with experimental data was encouraging, even though

aeroelastic effects were neglected. The research focus very quickly moved to coupled CFD/CSD analyses based on 1D-beam structural dynamics. The UH-60A flight test data supported this research and provided a basis for validation of such methods. A first attempt at CFD/CSD analysis was performed by Bachau and Ahmad [25] for the UH-60A rotor blade in forward flight, using OVERFLOW and DYMORE. Comparisons were made between rigid and elastic calculations, and showed the importance of modelling aeroelastic effects, however, comparisons with flight test data required further improvements. Many further studies using the UH-60A data were published to compare different CFD/CSD modeling approaches. Potsdam et al. [309] coupled OVERFLOW with CAMRAD, and compared the high-fidelity solutions with the CAMRAD lifting-line/free-wake predictions. Even though the resolution of the wake was quite poor by today's standards, the loads were well captured at high-speed conditions as shown in Figure 1.7. This shows that fine grids (over 50 million cells) are not required to capture the loading on the blades. However, the agreement at high-thrust conditions was of poorer quality.

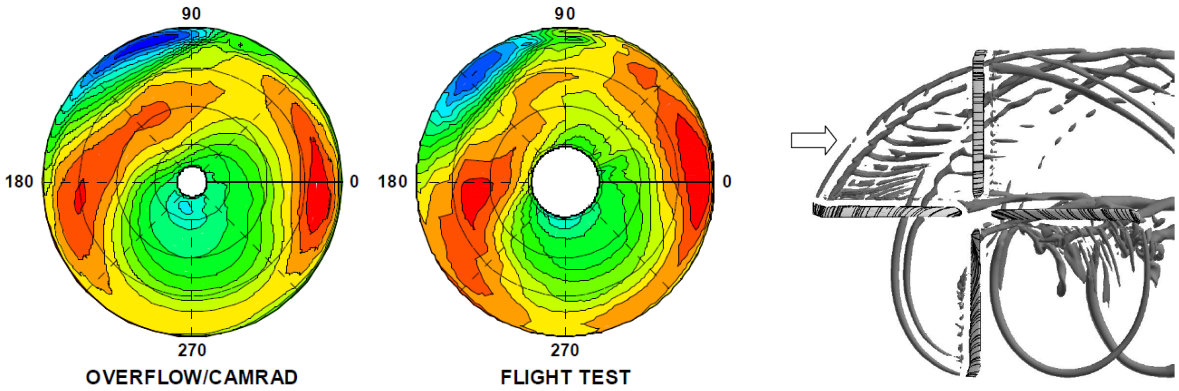

(a) Disk normal force (b) Rotor wake

Figure 1.7: Disk loading and wake resolution for the UH-60A rotor blade calculations [309] at $\mu = 0.37$ and $C_T/\sigma = 0.084$.

Sitaraman et al. [348, 349] performed TURNS/UMARC calculations and also compared the CFD analyses with lifting-line predictions. Here, however, the full wake was not captured and a free-wake analysis was used to minimize computational costs. The TURNS/UMARC framework was also later used to examine vibratory loads [100], dynamic stall [98] and structural load predictions [99]. The majority of these studies used a loose-coupling approach between structure and aerodynamics, where the aerodynamic and structural deformations are exchanged once per revolution or a fraction of a revolution based on the number of blades. With growth in computational power, predictions for CFD/CSD analyses in forward flight were further refined on finer grids. Ahmad and Chaderijan [12] performed coupled OVERFLOW/CAMRAD calculations on grids of 69 million cells, and obtained significantly better agreement with flight test data compared to the first calculations by Bachau and Ahmad [25]. Biedron and Lee-Rausch [51] performed grid, turbulence and time-step sensitivity studies using the unstructured FUN3D CFD

solver and CAMRAD. The results indicated a very low sensitivity for the high-speed case, with a higher effect of modelling inputs for the dynamic stall condition predictions. In Europe, coupling aerodynamic analyses with CSD analyses appeared before full Navier-Stokes calculations became routine. Beaumier [37] coupled an unsteady full potential code with the R85 dynamics code. Later the Euler code WAVES was coupled with the comprehensive rotor code HOST (developed based on R85) [339]. Results were presented for the 7A and 7AD ONERA model rotors and compared with experimental data. This dataset was used within the European collaboration project CHANCE [293]. Pahlke et al. [294] presented results using the CFD code FLOWER coupled with the S4 dynamics code at DLR. Euler and Navier-Stokes solutions were compared, and showed the importance of including viscous effects. Further work using FLOWER and the HOST code compared weak and strong coupling approaches [19]. The impact of including the test stand in the CFD calculations was also evaluated [293]. As shown in Figure 1.8, the test stand can have an effect on the rotor loads in the inboard locations.

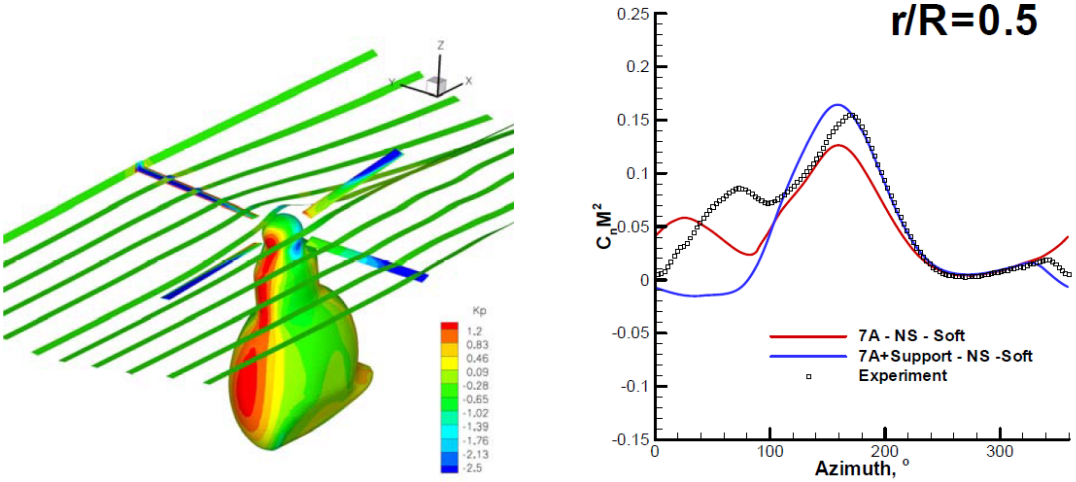

(a) Flow and pressure fields for the 7A rotor with test-stand

(b) Normal force at r/R = 0.5

Figure 1.8: Pressure and flow field for the 7A rotor blade with model support and sensitivity of the test stand on the normal force prediction [293]

Another collaboration project aimed at CFD/CSD analyses was the HART-II international workshop [352], with a focus on cases with strong blade-vortex interactions and HHC pitch control inputs aimed at minimizing noise and vibration. Very good agreement was seen between the project participants in the blade loads with a larger scatter in the vortex locations, and strength of BVI events (which also impact the loading predictions). The GOAHEAD collaboration workshop is another European effort aimed at CFD validation of flows around a complete helicopter. First pre-test predictions were compared between participants for a large range of flow conditions [56]. Comparisons included surface pressure predictions, velocity fields for low-speed, high-speed and highly loaded cases. Further results were presented post-test [336] with a focus

on main-rotor surface predictions and visualisation of the flow separation behind the fuselage rear door. Results were also computed within this workshop using the HMB3 solver, used in this research [360].

The US CFD validation efforts past 2010 shifted to the new full-scale UH-60A wind tunnel tests [283] at the NASA NFAC facility. These tests provided further data compared to the flight test data including blade displacements and deformations as well as PIV wake measurements. Additional conditions were also tested such as a slowed rotor at high advance ratios. Chang et al. [79] performed pre-test predictions and examined facility effects. Various other correlation studies for rotor loads were performed to validate high-fidelity CFD/CSD analyses [78,218,242], although the new data led to further validation studies, giving higher confidence in the predictions. Biedron and Lee-Rausch [52] compared blade displacements and elastic deformations with experimental data. Potsdam et al. [310] performed predictions for a slowed-rotor at high advance ratios. Jayaraman and Potsdam [170] compared the PIV wake measurements with CFD predictions and examined facility and installation effects on the results. Very fine grids were used here, of up to 500 million grid points, with sample vorticity comparisons with experimental data at 5 degrees ahead of the advancing side shown in Figure 1.9. Very good qualitative agreement is seen with experimental data, with the CFD predicting a stronger shear layer and a weaker outboard trim tab vortex.

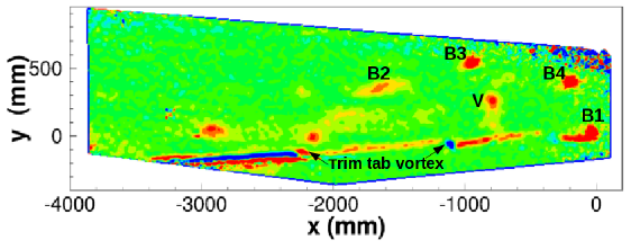

(a) PIV data

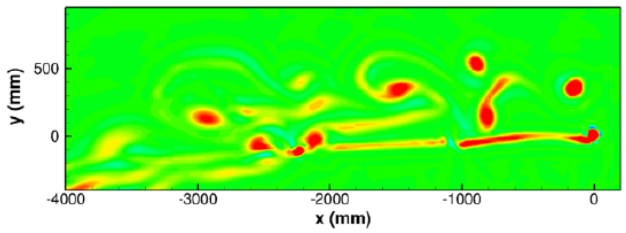

(b) CFD prediction (with fuselage and wind tunnel model)

Figure 1.9: Comparison of streamwise vorticity fields between CFD and PIV data at $\Delta\psi = 5^o$ ahead of the advancing side for the UH-60A rotor in forward flight [170].

Alongside high-fidelity analyses, lower fidelity tools, given the term as comprehensive rotor analyses, have also been in significant development due to much faster turn-around times. These methods are typically based on boundary integral methods, or so called "panel methods", hence lifting-line/lifting-surface representations of the rotor blade, with aerodynamic coeffi-

cients based on 2D aerofoil look-up tables, and are typically coupled with various wake models. They also often include aeroelastic effects, trimming routines and other multidisciplinary analyses. Although they do not rigorously model the actual flow physics of the rotorcraft flowfield, comprehensive analyses are often used in preliminary design studies. A complete overview of comprehensive rotor codes was given by Johnson [184]. Early applications of such methods include predictions for the PUMA rotor blade using various lifting-line/wake modelling approaches [61] or model scale UH-60A rotor predictions using the RotorCRAFT tool (precursor of CHARM) [377]. Later, Yeo and Johnson [431] assessed the CAMRAD II comprehensive rotor code for a number of rotor blades for blade load predictions. Structural load predictions were also examined [432]. Datta and Chopra used the UMARC code for comparisons with the UH-60A flight test data [97]. Wachspress et al. [393] assessed a CHARM and RCAS coupled analysis for the same blades studies by Yeo [431], whereas Bousman and Norman [60] performed an assessment of current predictive capabilities of various comprehensive rotor codes. The HART-II data was also used for comprehensive code predictions with results compared by various approaches [383]. The majority of studies highlighted similar predictive capabilities of these low/mid-fidelity tools. Compared to fully-resolved CFD, these methods cannot accurately predict highly nonlinear effects such as dynamic stall and/or advancing blade aerodynamics. This is due to the difficulty in capturing unsteady transonic effects, higher harmonic loading and flow separation. Higher-fidelity analyses are required to capture these effects more accurately. A recent validation study [433] for the ONERA 7A blade compared the HOST and RCAS predictions with coupled elsA/HOST and Helios/RCAS analyses, confirmed these observations, although no dynamic stall model was used in the comprehensive analyses. Sample results for the normal force and pitching moment predictions are shown in Figure 1.10 at r/R = 0.915 at $\mu = 0.3, C_L/\sigma = 0.10$. The comprehensive rotor codes either miss the stall events or predict significantly weaker stall. Truong [378], showed that the comprehensive rotor code predictions significantly improve with a stall model, however, still far from the agreement of CFD/CSD analyses.

Another approach for reducing the computational costs of full Navier-Stokes time-marching calculations is the use of time-spectral methods. These methods, maintain the high-fidelity of Navier-Stokes equations and represent an unsteady problem as a large steady problem with an unsteady source term. These methods have primarily been applied to other applications such as predictions of limit cycle oscillations [125, 376, 426] and turbomachinery [131, 345, 384], although a number of studies also exist for rotorcraft problems. The key assumption of flow periodicity in frequency domain methods makes them well suited to many rotorcraft problems. First solutions for flow fields around helicopter rotors started appearing in the late 2000s, although these were mainly aimed at proving the methodology. Ekici et al. [116] used an inviscid harmonic balance method for the Caradonna-Tung rotor in hover and forward flight. The method utilised steady-state acceleration techniques such as local time stepping and multigrid acceler-

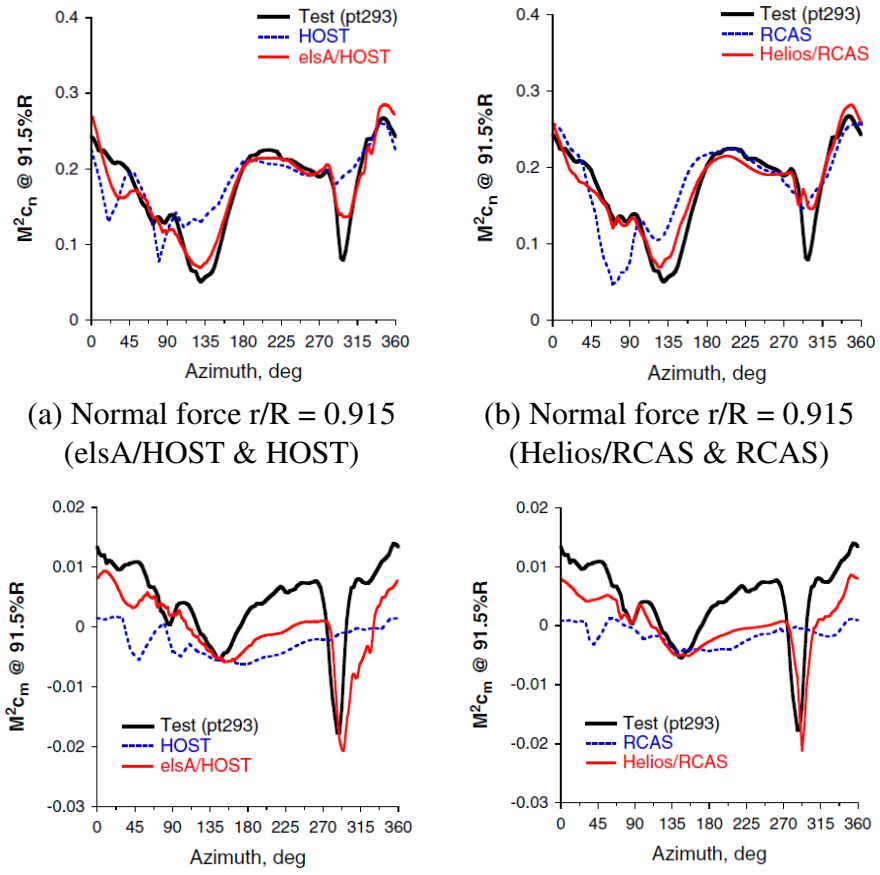

(a) Normal force r/R = 0.915 (elsA/HOST & HOST)

(b) Normal force r/R = 0.915 (Helios/RCAS & RCAS)

(c) Pitching moment r/R = 0.915 (elsA/HOST & HOST)

(d) Pitching moment r/R = 0.915 (Helios/RCAS & RCAS)

Figure 1.10: Comparison of normal force and pitching moment predictions from CFD/CSD and comprehensive rotor code analyses and experimental data [433].

ation. Gopinath and Jameson [126] developed a time-spectral method for the Navier-Stokes equations using a spectral Fourier collocation matrix. The method used explicit treatment of the source term with artificial dissipation and was later applied to rotorcraft flows by Butsuntorn and Jameson [167] for the Caradonna Tung rotor. The current state of the art for time-spectral predictions for rotorcraft is shown by Choi et al. [84] who used the same time-spectral formulation as Gopinath and Jameson [126] for the UH-60A rotor blade at three flight conditions. Blade deformations were prescribed from coupled CFD/CSD analyses using the time-marching solver. Full rotor simulations were performed along with single-blade calculations coupled with free wake analysis to further reduce computational costs. A blade loads sensitivity analysis was also performed for the number of time-spectral instances. Sample full-rotor disk normal force predictions for the UH-60A at high thrust (flight counter 9017) conditions using 15 time-instances (7 harmonic balance modes) are shown in Figure 1.11. The agreement with flight test data and time-marching calculations is excellent, although the pitching moment predictions were less accurate. This due to the fact that spectral methods are not well suited in predicting short-lived flow phenomena such as dynamic stall.

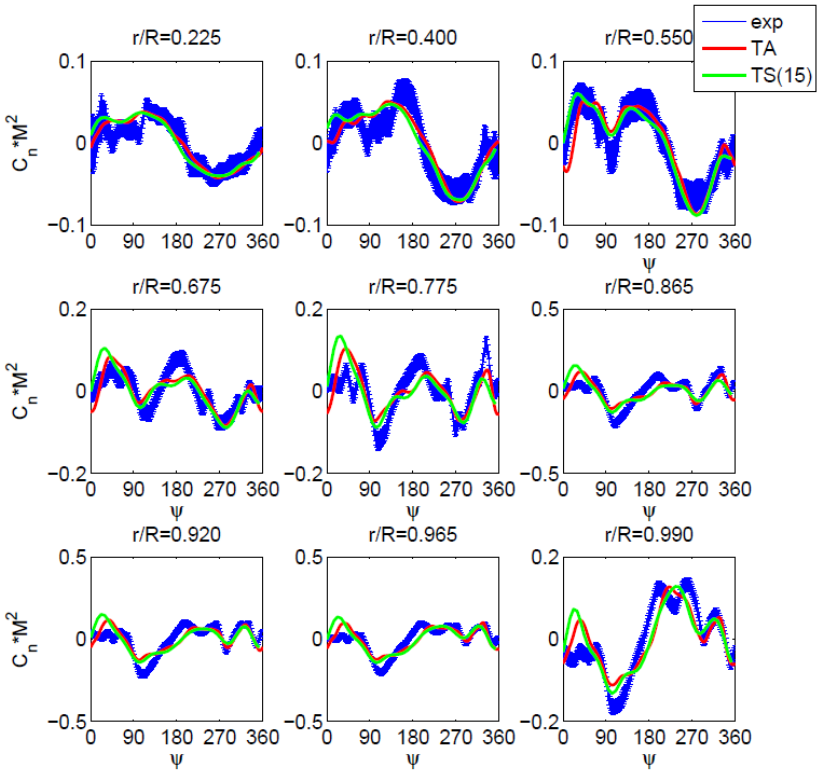

Figure 1.11: Comparison blade normal force predictions for the UH-60A rotor blade at high thrust conditions (flight counter 9017), between time-spectral, time-accurate predictions and flight test data [84].

Further studies by Choi and Datta [86] examined the method for vibratory load predictions and also coupled the time-spectral solver with a comprehensive analysis code, UMARC [85]. The majority of these methods, however, are explicit in nature. Woodgate and Barakos [422] developed a fully-implicit harmonic balance method (also used in the present research) and applied it to a range of cases including the UH-60A rotor in forward flight. This method was also used by Johnson and Barakos [179] for optimisation of a rotor blade with a British Experimental Rotor Programme (BERP)-like blade tip using artificial neural networks as a metamodel and genetic algorithms. Research in harmonic balance methods for overset grids has also been a growing subject of research. Various approaches are used to obtain a valid solution for cells that switch from non-computational to computational in different harmonic balance snapshots. Mavriplis et al. [246], used a Poisson equation solver for non-computational cells to ensure solution smoothness. A different approach was used by Leffell [219] who implemented a Barycentric rational interpolation routine. Im et al. [154, 155] also developed an overset time-spectral method, however, the treatment of non-computational cells was not elaborated on.

Research for validation of CFD predictions continues aimed at specific flow phenomena or more complex configurations. In particular, dynamic stall is still an important topic in rotorcraft research. Chaderijan [76] performed predictions for the UH-60A rotor blade at high thrust con-

ditions using AMR with grids up to 1.3 billion cells. Although greater details of the vortical structures during the dynamic stall were resolved using finer grids, the effect on the rotor loads was not significant. Other dynamic stall predictions were performed by Richez [74, 318] for the ONERA 7A blade in light-stall and deep-stall conditions. Further research in this area was part of the 2019 ARO Dynamic Stall Workshop with results to be presented in the future [351]. Other current research topics for CFD validation of rotors in forward flight include coupled CFD/CSD analyses based on 3D FEM rotor blade models, rather than 1D-beam models, as used in the majority of studies. The 3D FEM analyses lead to higher fidelity predictions, but also provide structural design data, such as internal axial and bending stresses, which could be used for safety constraints. Preliminary studies demonstrating the capabilities of such methods were performed by Ortun et al. [287] for the 7A rotor blade, and Staruk [356] for the Metatail proprotor. Interactional effects for more advanced rotorcraft configurations are also under investigation including rotor loading in the presence of a wing [120, 370], proprotors [57, 120, 362] or for full configurations [120, 286, 407] and coaxial rotorcraft [62, 197, 297]. These investigations, however, often were purely computational due to unavailable experimental data.

1.2.1.3 CFD Validation - Summary

The review of CFD validation efforts in both hover and forward flight showed the need for higher quality validation data. In hover, future tests are planned for the PSP rotor blade in the NFAC facility, to provide a more comprehensive dataset for CFD validation, whereas in forward flight, the majority of studies refer to the UH-60A flight test data [59] or full-scale wind tunnel data [283]. Further testing is required for more advanced rotor blade planforms. The CFD validation studies have shown that grid refinement and resolution of the rotor wake has a low sensitivity on the rotor loads as long as the first vortex passage is well captured. Furthermore, the steady-state approach in hover has shown to be promising to significantly reduce computational costs. In forward flight, the harmonic balance method offers a good compromise between lower fidelity models and full Navier-Stokes time-marching calculations. Coupled CFD/CSD analyses have become the norm, and are required for accurate analyses of full-scale rotor blades, however, elastic effects may be less important at model scale. Very little CFD validation has been performed for more advanced rotor blades, mainly due to the lack of experimental data in open literature. The present work will aim to build on these validation efforts, by comparing CFD predictions with experimental data for a number of rotor blades, including a more advanced planform, with modest computational resources.

1.2.2 Advanced Rotor Blade Design

This review is aimed at investigating the current state of the art in rotor design. As highlighted in the introduction, many different planform geometries are used across the globe. This may

be due to mismatched design objectives used by different manufacturers, however, new rotor designs are still emerging, which proves that rotor design is an ongoing topic of research. The main objective of this section is to determine what features of a blade design have a large effect on the rotor performance and to assess the current rotor design methodologies.

Throughout the design of the main rotor for a helicopter, a variety of parameters have to be decided. Values for design features such as rotor diameter, disk loading and tip speed usually come from the general sizing of the helicopter and various constraints on the helicopter operability, more than the aerodynamic performance of the helicopter. Parameters such as tip speed, solidity and number of blades are chosen based on from noise and vibration level limits, as well as autorotational performance requirements. The main design feature that has a direct influence on the aerodynamic performance is the blade shape, including blade twist, tip shape and aerofoils used. In the past, a large number of studies have been conducted to investigate the effect of these parameters on the performance of a helicopter, and have successfully shown that modifications in the planform design can lead to performance improvements. This led to a large number of production helicopter rotor blade planform designs as can be seen in Figure 1.12 [178].

Figure 1.12: A wide range helicopter rotor blade planforms showing the variety of used designs based on [178].

As can be seen from Figure 1.12, a large variety of rotor designs have been proposed by various researchers and been used on production helicopters. Simple, rectangular planforms have mainly been used in the past and are still presently in use. Today, this is attributed to low manu-

facturing costs and ease of maintainability. However, advanced planforms (non-rectangular) and use of more advanced aerofoils (other than the NACA 0012) - are more prominent today with the use of composite materials and the need for higher performance rotors. The improved knowledge on the flow physics around helicopters, constantly improving measurement techniques as well as numerical methods such as CFD models allow an in-depth study of more advanced rotor blade planforms. Although a large amount of studies have been performed in the past, today, the performance of an advanced rotor planform can be determined with much greater accuracy - both numerically and experimentally. An extensive literature review on helicopter tip shapes as well as the use of CFD methods to capture the effect of tip geometry has been written by Brocklehurst and Barakos [64]. However, since this review was written more novel tip shapes have emerged such as the Advanced Chinook Rotor Blade (ACRB) [55]. This indeed, shows that the optimum tip shape is not yet well defined. The following subsections review the key elements of rotor design. First, experimental and numerical studies are analysed, which formed a basis of trends in rotor designs and were focused on exploratory studies of planform shape effects on the rotor blade performance. Next, different approaches to rotor design in industry are reviewed based on information in open literature. Finally, research based on the use of optimisation methods in rotor design, as well as the limitations in current design methodologies are discussed.

1.2.2.1 Experimental studies

In the early years of advanced rotor design (1970s-1980s), performance predictions were predominantly obtained through experimental studies - flight and wind tunnel testing. With the developments in CFD methods as well as computational power in the last 40-50 years, today experimental studies are mainly used for generation of validation data for CFD, examining new flow phenomena as well as validating new blade designs from computational studies. However, over the years a vast amount of experimental studies were performed to gain insight into the physics of helicopter flows and the effect of blade design parameters on the performance of the rotor.

A large number of experimental studies have been conducted in the past concerning rotor blade shapes. Especially in the 1970s and 1980s, many studies looked at incorporating features such as sweep, taper and anhedral into the blade tip design, use of blade twist and more advanced aerofoils. These ideas, however, were not novel and were adopted from fixed-wing aircraft. The majority of these studies, however, only measure the rotor loads using strain-gauge balances and do not examine the rotor flow field in greater detail. This makes it difficult to analyse the reasons behind better rotor designs, in terms of flow physics. In the USA, following the development of the UH-60A and S-76 rotors in the 1970s, a number of studies were conducted to examine the effect of tip shape on the performance of the rotor. Stroub et al. [368] performed wind tunnel tests for the full-scale S-76 rotor blade in forward flight with variations in tip sweep

and taper, and found certain dependencies with thrust and propulsive force. The same blade along with the UH-60A blade was used in the hover experiments of Balch [32] using various tip shapes. Another study by Weller [406] examined tip shape effects on the rotor performance and blade structural loads for a generic model-scale rotor blade with sweep, taper and anhedral. Similar studies were performed by Yeager and Mantay [427] with a focus on the impact of tip shape on the torsional loads and correlations with the rotor performance. The fundamental design considerations of tip sweep and taper were confirmed in these studies. Tip sweep leads to reduced compressibility effects by increasing the local drag divergence Mach number. Another action of sweep is the aft movement of the centre of gravity, leading to an azimuthally varying blade torsional load. Tip taper was generally found to improve the rotor performance through a reduction in profile drag, by reducing the planform area, as well as, improved lift distribution, by reducing the loading at the blade tip. Tip taper, however, can also lead to a much sharper stall at higher thrust coefficients as shown by McVeigh [249]. The hover performance curves with blade loading from this study for various tip shapes are presented in Figure 1.13. The rotor blades examined maintained geometric solidity and had different thrust-weighted solidities.

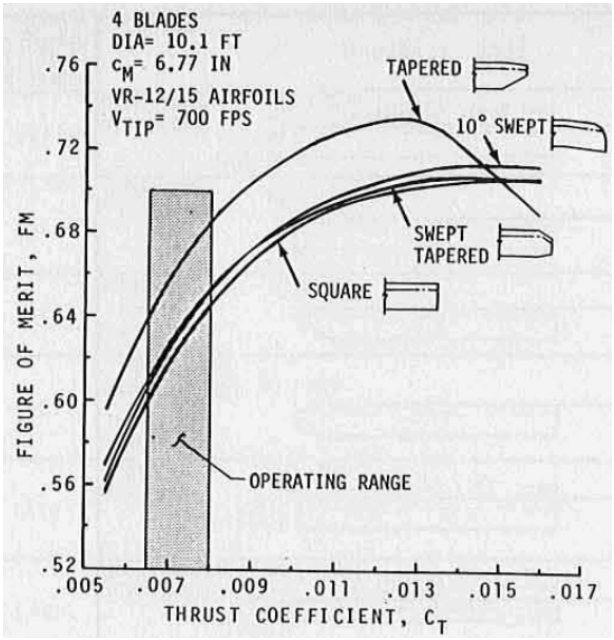

Figure 1.13: Effect of tip geometry on the hover performance, showing a sharp performance deterioration with blade loading for the tapered blade tip [249].

Anhedral was thought to have an impact on the vertical miss distance between the blade and preceding tip vortex [427], leading to improved performance in hover and lower advance ratios, although this was not fully confirmed experimentally. Regarding, the observations with respect to trends on the structural and control loads, care must be taken when interpreting experimental data at model scale, due to a potential mismatch in aeroelastic effects occurring for the full-scale blade. Although it is evident that the correct use of sweep and anhedral could lead to a predesigned control of the blade twist in forward flight. Very little information, however, is

present in open literature regarding the use of anhedral on different tip geometries.

Blade twist effects were also studied by various researchers [63,194,315]. Blade twist effects on the performance in hover and forward flight from the study of Keys [194] are shown in Figure 1.14.

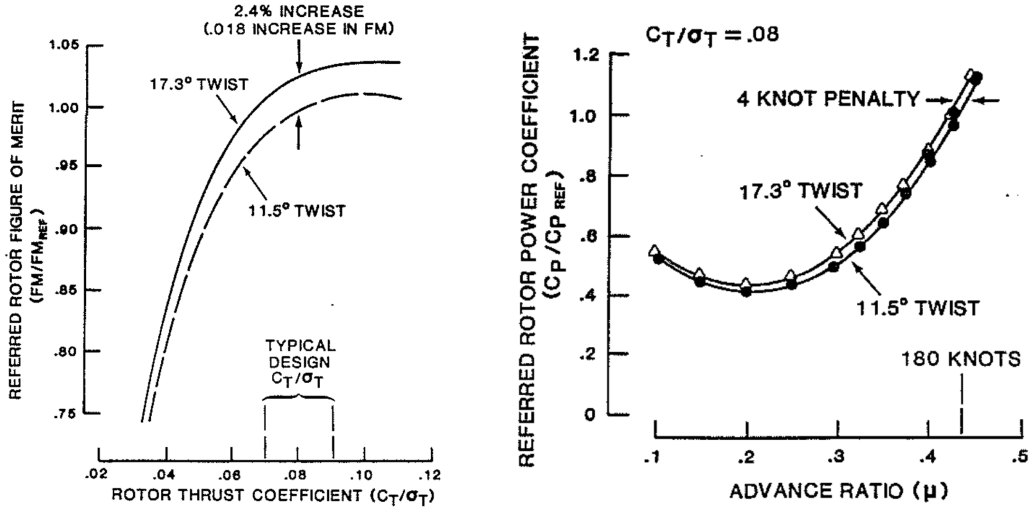

(a) Hover performance (b) Forward flight performance

Figure 1.14: Effect of blade twist on the performance of a model scale rotor in hover and forward flight [194].

Figure 1.14 indicates that higher values of blade twist are beneficial in hover, but detrimental in forward flight in terms of performance. The high blade twist primarily affects the advancing side in forward flight, as a higher region of negative lift is produced at the tip of the blade. Keys [194] also found that high blade twist can have a negative impact on the control loads and vibration. This could be the main reason why rotors such as the AH-64A or S-76 have fairly low values of blade twist (9-10 degrees). In comparison, the UH-60A has a much higher value of 16 degrees, although a non-linear twist distribution is used to increase the loading at the blade tip. The exact optimum twist value that combines hover and forward flight requirements tends to be in the range of -10 to -14 degrees and will depend on the rotor blade planform shape. A high amount of experimental research has also been conducted for advanced rotorcraft aerofoils [53, 280, 281, 374, 408]. Modern rotorcraft aerofoils have a higher lift to drag ratio over a range of Mach numbers. More modern rotor designs also utilise more than one aerofoil along the blade span, with the main lifting section in the region of 70%-90%R and a thin section outboard of 90%. The main requirements of newer generation aerofoils are high values of $C_{L_{MAX}}$, low drag values over a range of C_L and Mach numbers and low pitching moments. However, due to difficulties in certification, the majority of helicopter manufacturers utilize a number of trusted aerofoils on newer rotor designs.

Many of the experimental studies in the USA, combined the use of blade tip shape, twist and advanced aerofoils. These efforts were focused at a number of potential rotor upgrade pro-

grammes including the UH-1 [45, 46], AH-64 [190, 191] and UH-60A [302], [428] rotors. A particular focus was put on tapered planforms, that included taper further inboards than within the region usually called as the blade tip, for example starting from 50% radius, leading to significant performance improvements in combination with blade twist and more advanced aerofoils. The majority of these experiments, were however, performed at model scale and did not enter high loading conditions where such blade planforms may suffer performance degradation due to pre-mature flow separation. Furthermore, this also means that the studies were performed at lower Reynolds numbers with a mismatch in aeroelastic effects. Finally, the majority of comparisons were performed on a thrust-weighted solidity basis, which may be incorrect as examined by Perry [299], which will also have an impact on the obtained performance metrics (lift-to-drag ratio and FoM). This is discussed further in the analysis of the BERP rotor design (in Section 1.2..2.3: Rotor Design in Industry).

Experimental studies on rotor blade tips were also performed in Europe. ONERA and RAE performed research on swept rotor blade tips as part of a collaboration programme. ONERA performed the model scale wind tunnel tests [410] for a planform with a parabolic swept blade tip and compared the performance data with a rectangular blade over a range of thrust coefficients and advance ratios. Flight tests were performed by RAE [319], for a fully-instrumented rotor blade with a swept blade tip and a leading edge extension to keep the centre of pressure close to the elastic axis, reducing torsional deflections. Both blade tips, from the model scale experiments and flight tests, are shown in Figure 1.15.

As anticipated, the swept blade tip led to performance improvements, that increased with forward flight speed, but also blade loading. The swept tip reduces the profile drag coming from an increase in the drag divergence Mach number. This leads to a weaker shock on the advancing blade and a reduced maximum local Mach number. The model scale experiments, however, were performed without cyclic pitch control and for fairly stiff rotor blades, hence aeroelastic effects were not fully accounted for. The flight tests performed by Riley and Miller [319], could not fully verify the performance improvements as, only blade with a blade tip was used, with the main goal to obtain pressure measurements for both rectangular and advanced swept tip rotor blades. These were then compared with numerical calculations (using a transonic small perturbation approximation). The benefits of the swept tip, were however, confirmed in reducing compressibility effects.

ONERA also performed model scale wind tunnel tests for a more advanced parabolic swept blade tip, known as PF2 [303]. The performance improvements in hover and forward flight were confirmed through flight tests [129] on the Dauphin-365N helicopter. However, the new blade tip led to an increase in the static control loads, through the production of a high nose-down pitching moment lead to high elastic blade torsion, which prohibited tests at high-speeds. Additionally, the blade tip led to reduced noise levels. Further studies examined the use of anhedral [104], showing even greater potential benefits at higher blade loading (above $C_T/\sigma = 0.07$), and also

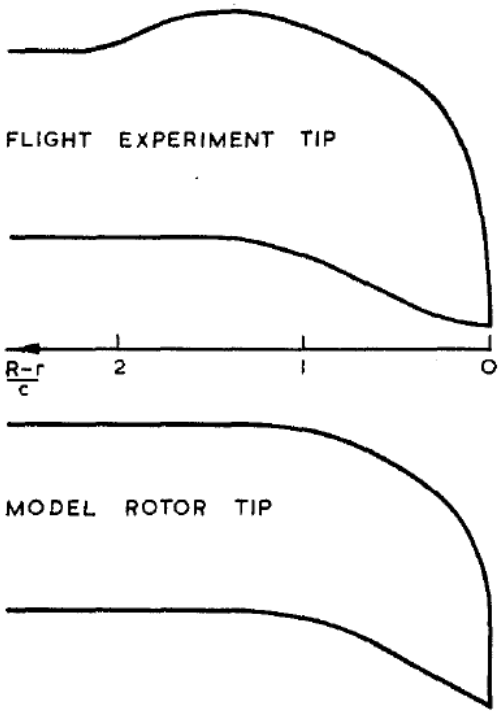

Figure 1.15: Blade tips used in the research on swept rotor blade tips during the model scale experiments of ONERA and RAE flight tests [410].

examined trim law effects [102]. The addition of anhedral, however, was once again only studied for a single blade tip geometry.

Another use of wind tunnel experiments and flight tests in the developments of an advanced rotor blade design was seen at MBB [306] who developed an upgrade for the B0-105 rotor blade. The final design labeled as AGB IV utilised a parabolic blade tip, with planform taper initiated from 0.8R and advanced aerofoils, as shown in Figure 1.16. Although many of the developments were supported through numerical calculations, the most promising concepts in terms of aerofoils and planform design were tested experimentally. The new design was flight tested on the B0-105 helicopter and confirmed significant performance benefits, including reduced vibration levels.

Experimental studies were also performed aimed to evaluate BERP-like rotor blades. The blade designed by Westland Helicopters [298] was aimed at managing conflicting advancing and retreating side requirements. This rotor design was used on the Westland Lynx that obtained the helicopter rotor speed record in 1986 [298]. This design is analysed in more detail in Section 1.2.2.3: Rotor Design in Industry. The unique BERP design, however, sparked a lot of controversy in the rotorcraft community due to the unusual paddle-shaped blade tip. Experiments were performed by Yeager et al. [429] to compare rectangular and BERP-like rotor blade planforms, which are shown in Figure 1.17.

The two blades were tested at model-scale in a Freon-based medium to provide better match-

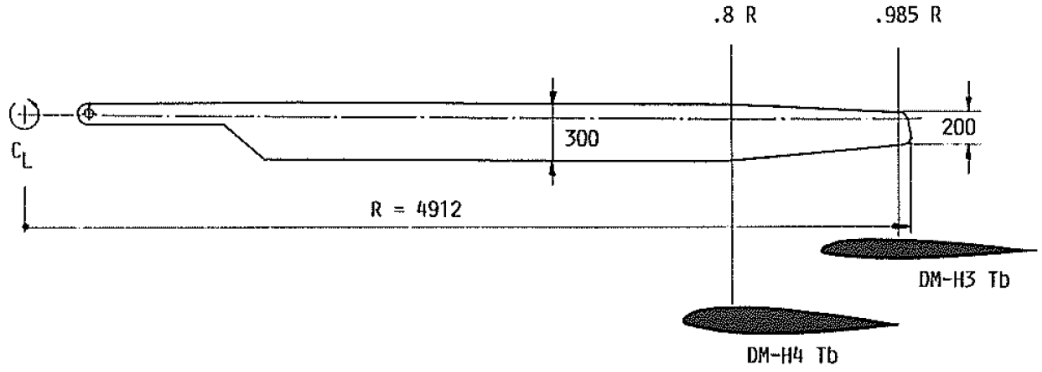

Figure 1.16: Advanced rotor blade planform designed at MBB [306].

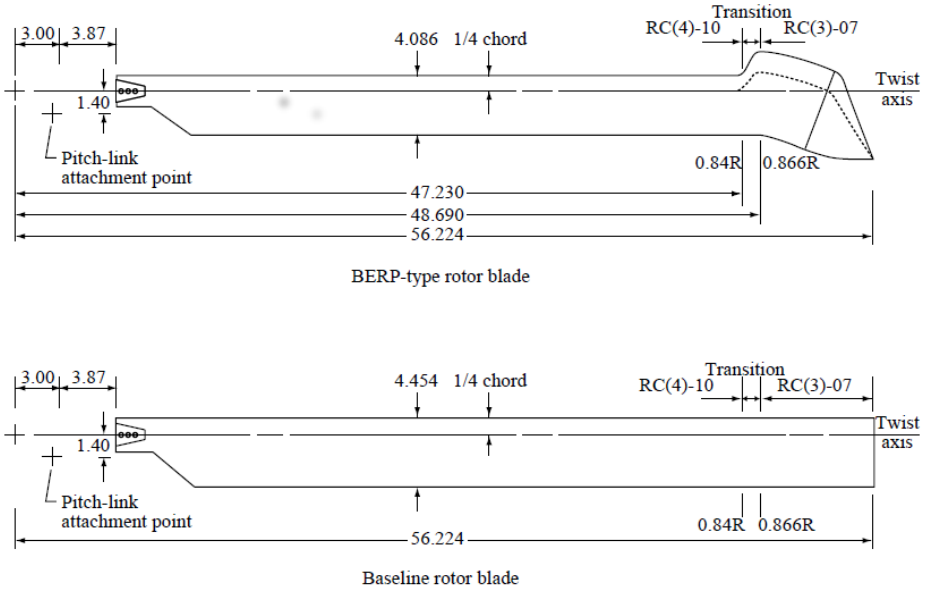

Figure 1.17: Rectangular and BERP-like blade planforms tested by Yeager et al. [429].

ing of the full-scale Reynolds number. Both planforms had the same rotor radius, used the same aerofoils (RC-series [280, 281]) and same nominal blade twist ((9^o linear twist). The only differences were the tip shape and the inboard chord which was lower for the BERP-like blade to match the thrust-weighted solidity. Based on Perry [299], the matching of thrust-weighted solidity may favour the rectangular blade. The performance data showed better performance across hover and forward flight conditions for the rectangular blade. These findings, however, may be due to the lower chord used by the BERP-like blade. Furthermore, the BERP blade designed by Westland [298], was not a blade tip design but a whole planform design, which combined blade tip shape, aerofoils and blade twist.

The research on rotor design at ONERA, also continued, aimed at reducing acoustic footprint. Polascek and Lafon [305] compared rectangular and swept-parabolic anhedral blade tips (known as the 7A and 7AD rotor blades) in aerodynamic performance and acoustics. In-depth acoustic data was obtained for these rotors within the HELISHAPE project including vortex tra-

jectories and differential pressure maps [335]. This research later led to double-swept ERATO planform through the use of numerical tools [312]. The ERATO planform was compared to the 7AD blade [353] through experimental tests and showed significantly reduced noise levels (more on this planform in the next section). Various other more radical concepts were tested experimentally (and evaluated numerically) aimed at noise reduction such as the Vane Tip [66], Canard Tip [289] aimed at generating twin tip vortices, or variations of BERP-like tips within the Japanese ATIC project [201,266]. These concepts, however, were never put into production.

1.2.2.2 Numerical Studies

With developments in numerical methods, analytical tools and CFD codes have also been used in rotor design research. They allow the possibility of investigating more arbitrary planform shapes and provide the entire flow-field solution in the case of resolved CFD methods. Today, this is the primary method used for design purposes, whether conducting parametric design sensitivity studies or using formal optimisation methods. The fidelity of the numerical model, however, must accurately capture the performance improvements due to design changes. Due to high computational costs of Navier-Stokes CFD methods, the majority of numerical studies conducted in the past, aimed at exploratory rotor design, have been performed using lower fidelity models. Higher-fidelity models, are however, seeing greater use with growing computational power.

A number of the experimental studies on advanced rotor design discussed in the previous section were supported by numerical calculations. The PUMA blade flight test data was used for validation of CFD codes, however, comparisons between the rectangular and swept blade tips were also performed [319]. Advancing side surface pressure isobars for both blades using a solver based on the transonic small perturbation equations are shown in Figure 1.18 a). Research at ONERA on swept-blade tips [103] also used a similar solver for theoretical predictions with pressure contours shown in Figure 1.18 b), based on unsteady non-lifting calculations.

The pressure contours clearly show the benefits of tip sweep on the advancing side, as the strength of the shockwave is reduced. The parabolic blade tips indicate much weaker bunching of the pressure isobars. Another important feature of the parabolic tip is the prevention of shock delocalisation, which also leads to significant noise reduction. Numerical modelling was also present during the rotor upgrade programme at MBB [306], although a much simpler approach was used based on blade element theory [151]. Calculations were performed for a simple rectangular blade, AGB III and AGB IV tip designs, as well as various other swept tip configurations. Flight characteristics were also examined, showing the need for careful structural design (mass balance) for more advanced planforms. Such calculations, however, could not predict such features accurately, hence an extensive experimental and flight-testing campaign was required.

Another study by Scott et al. [338] used an unsteady full-potential solver to evaluate a variety of rotor blade tips for high-speed forward flight. However, only the advancing blade was

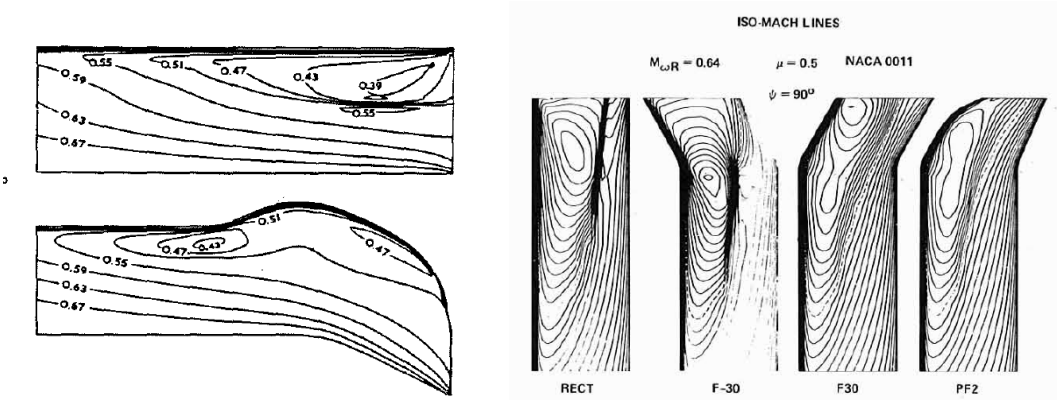

(a) PUMA blade tip [319] (b) ONERA blade tips [103]

Figure 1.18: Research on swept tips by ONERA and RAE, showing the effect of tip sweep on the surface pressure contours [103, 319]

simulated. This paper, however, also investigated the retreating side characteristics through experiments. The blade tips used in the computational study are shown in Figure 1.19.

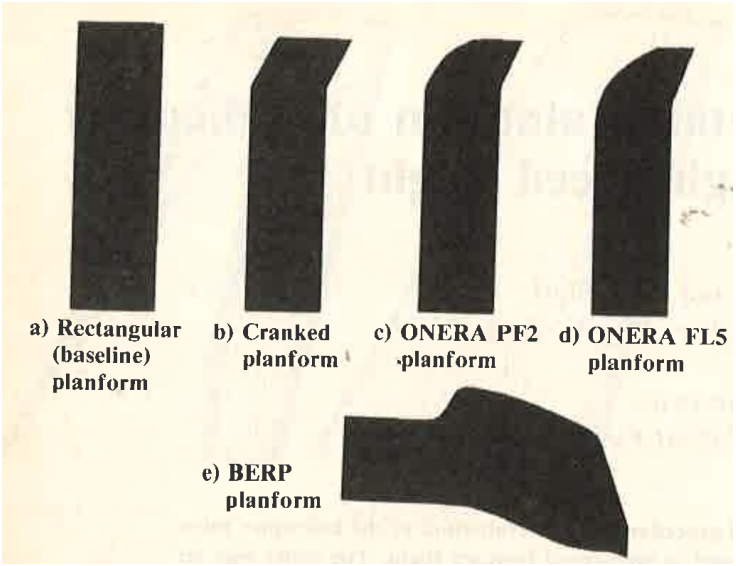

Figure 1.19: Advanced rotor blade tip designs used by Scott et al. to investigate high-speed flight performance [338]

The computational study examined a number of advanced blade tips using a constant airfoil (NACA 64A-010) for each of the geometries to examine the physics of the transonic flow solely based on planform geometry. The ONERA geometries were found to decrease the shock strength, however, the BERP tip was found to be best at diffusing the advancing blade shockwave. This tip also decreased the shock strength further inboards than the other tips. The BERP-like tip spreads the pressure recovery over a larger portion of the chord, leading to improved performance. Further conclusions, however, could not be made as only one flight condition was examined, and due to the predictive capability of potential flow solvers.

Calculations for BERP rotor blade planforms and other blade tips were also performed by

Duque [109], using the full-potential FPR code [2] and the LANS3D code [285] based on the thin-layer Navier-Stokes equations. Although the calculations were performed in fixed-wing mode, the capability of the BERP design to delay the onset of separation at high angles of attack and suppress advancing shockwave formation across the blade tip in transonic conditions was confirmed. However, at lower angles of attack, the blade with the BERP tip exhibited higher values of induced drag compared to the rectangular, swept-tapered or PUMA blade. The study also showed the necessity of including viscous effects at high angles of attack, to accurately capture separated flow regions. The complex separation pattern of the BERP blade showing attached flow across the blade tip is shown in Figure 1.20.

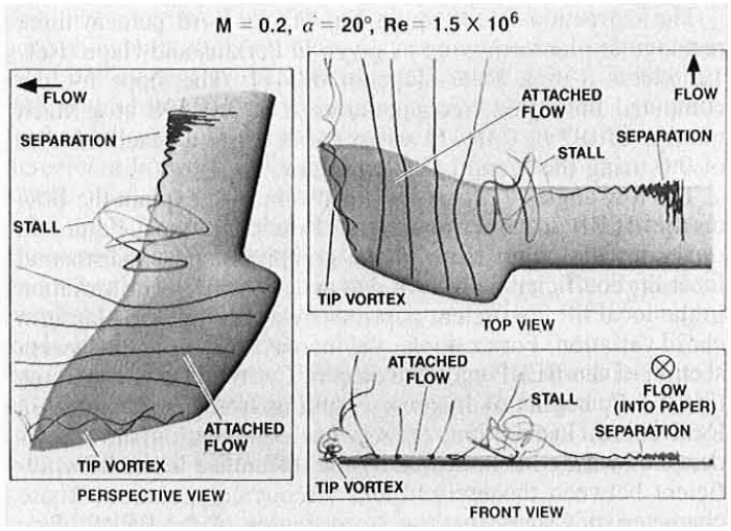

Figure 1.20: Complex separation pattern of the BERP blade, showing attached flow across the blade tip [109].

The pressure distributions, loading distribution and separation patterns were also compared with experimental data [65] and showed fairly good agreement. Other CFD studies for BERP rotor blades were performed by Srinivasan [354] who performed comparisons with the UH-60A blade in hover conditions based on Navier-Stokes predictions. The UH-60A blade exhibited slightly better performance (in terms of FoM) for a given collective, however, the BERP blade produced a much higher thrust coefficient, through much lower shock-induced separation across the blade tip. Early CFD studies, for BERP rotor blades, showed the potential of the planform at the extremes of the flight envelope.

Other studies using higher fidelity methods based on the Euler and Navier-Stokes equations continued focusing on transonic conditions and moved towards acoustics. Aoyama et al. [21] studied a number of fairly exotic tip shapes incorporating sweep and taper using Euler's equations, aimed at advancing side reduction of compressibility effects. Baeder [26] also examined a wide range of tip shapes using CFD based on an Euler solver, for reduced high-speed impulsive noise. These studies, however, only examined transonic conditions and proposed tip shapes that were unrealistic for use on practical rotor designs.

The ERATO programme [312] was also primarily aimed at noise reduction. This programme featured lower-fidelity calculations using DLR and ONERA comprehensive rotor codes. Parametric studies were performed for blades featuring different chord, sweep, thickness and twist distributions. Rotor design was performed with the main objective to minimize noise, using the 7AD blade as a baseline. No formal optimisation method was utilised, and the design was iterated based on engineering judgement. Significant improvements in noise emissions were obtained and validated through wind tunnel tests. Higher-fidelity computations using CFD (FLOWER and FP3D codes) were also performed for the ERATO blade, to ensure that the blade is free of shock delocalisation. The initial 7AD and final ERATO planforms are shown in Figure 1.21.

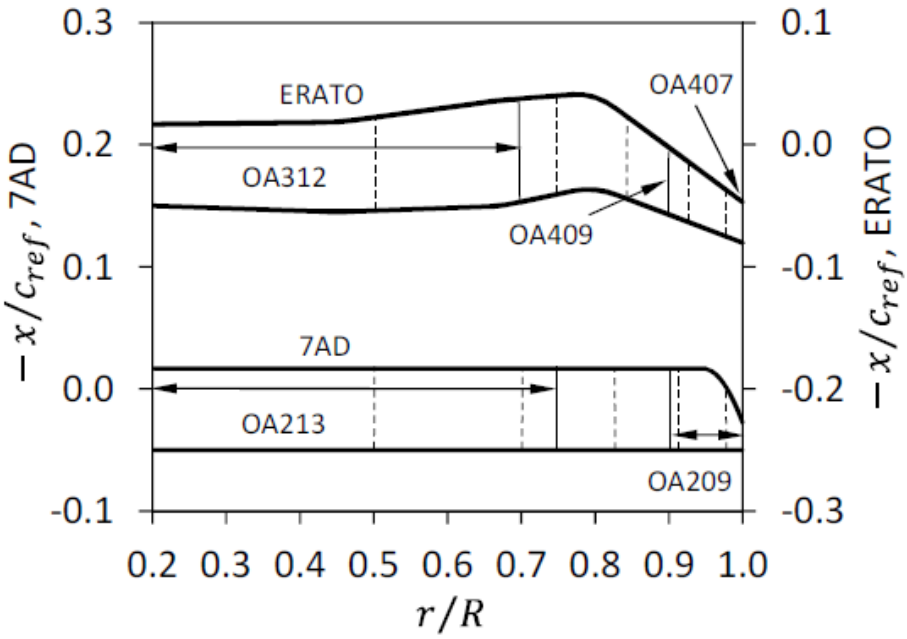

Figure 1.21: Planforms of the 7AD and ERATO rotor blades [38].

The ERATO blade compared to the 7AD blade, distributes the BVI interaction in time and space, due to the fact that the blade leading edge is parallel to the preceding tip vortex core axis over a shorter period of time. In combination with a weaker emitted tip vortex, this leads to significant noise reduction. The ERATO disk loading also sees more dynamic content which has an effect on the tip vortex trajectories. The blade also saw performance improvements in forward flight due to the highly swept blade tip, although this was not a design goal. A drawback of the ERATO planform was earlier and sharper stall at high loading in hover. This was later addressed by Airbus Helicopters in the design of the Blue-Edge planform [38], discussed in Section 1.2.2.3, Rotor Design in Industry. Various other approaches reducing BVI are discussed in a summary article by Yu [437].

While the numerical research on swept blade tips has heavily been focused on transonic

characteristics and acoustics, very little research has been done on the effects of sweep on the retreating side. Visbal and Garmann [388] examined dynamic stall phenomena for a fixed-wing with various sweep angles using LES. Lutke [235] and Muller [265] show a double-swept rotor blade design similar to the ERATO planform aimed at dynamic stall investigations. Numerical investigations were performed by Kaufmann et al. [189] for this design, using the DLR TAU solver, and compared the results with a parabolic tip design. Although the thrust coefficients obtained by the two geometries were similar, different evolutions of the dynamic stall flow structures were observed, as shown in Figure 1.22.

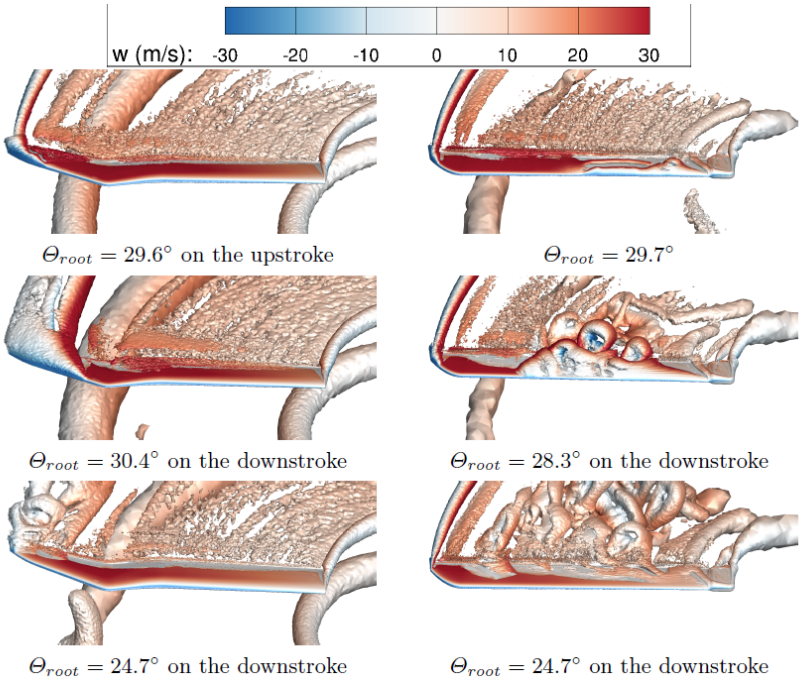

Figure 1.22: Evolution of the dynamic stall flow structures on double-swept and parabolic tip rotor blades [189].

The dynamic stall vortex starts at the blade tips for the double-swept configuration, and spreads inboards with increasing angle of attack. For the parabolic tip, the dynamic stall vortex starts at the root and spreads towards the blade tip. The flow across the blade tip, however, remains fully attached for the parabolic design. The double-swept rotor blade also exhibited much larger pitching moment variations along the blade span. These findings, however, examined only one condition at a fairly low Reynolds number of 3.5×10^5, for comparisons with model-scale experiments. Hence it is uncertain whether these findings would translate to full-scale rotor blades. The research in this area is ongoing, as still not much is known regarding the effect of double-swept and other planforms on the retreating side aerodynamics.

Anhedral effects have also been the subject of a number of numerical studies. Zhou et al. [443] examined anhedral effects in hover for the S-76 rotor blade. The addition of anhedral led to a more uniform inflow distribution leading to reduced induced power and improved performance. The anhedral tip, produced a weaker tip vortex, with a large miss distance with the

next rotor blade, reducing BVI effects. These calculations, were however, performed at fairly low thrust coefficients. Another study by Hollands et al. [147] examined various tip shapes using coupled CFD/CSD analyses and found anhedral to be the most sensitive tip shape parameter on the performance of the rotor blade. This was examined in more detail [148], including effects of anhedral/dihedral radial position and magnitude. Anhedral was found to be beneficial in hover, whereas dihedral led to performance improvements in forward flight. Moderate values of anhedral/dihedral were better than high values in both hover and forward flight, whereas the radial position had little effect. The addition of anhedral was found to increase the negative lift region on the advancing side in forward flight. The anhedral study, however, only examined one type of planform geometry with an increased chord at 0.8R and highly tapered blade tip without any sweep. For more highly loaded blade tips, the addition of anhedral may have had a lower impact in forward flight. As discussed by Brocklehurst and Barakos [64], the addition of up to 20 degrees of anhedral on a BERP tip had no impact on the rotor forward flight performance. In fact, anhedral induces a beneficial pitching moment variation compensating for sweep effects leading to a reduction in control loads. The effects of anhedral for different rotor designs (for example BERP vs conventional planforms) have not been studied in literature.

Due to the noticeable effects of tip shape on the blade dynamics and structural behaviour, this area of research was also examined in literature. Yen [430] evaluated sweep and taper effects, based on comprehensive rotor code analyses. The swept-tapered tip leads to a reduction in pitch-link loads at high advance ratios and reduced nose-down elastic blade twist on the advancing side due to reduced compressibility effects. However, as the thrust-weighted solidity was matched, a 5.4% increase in blade mass was reported. Furthermore, the present analytical model did not fully capture tip shape trends in terms of pitch-link loads when compared with test data, although the difference between the rectangular and swept-tapered tips was predicted well. Another study by Kim and Chopra [6] used a transonic small-disturbance potential code to examine tip shape trends on the aeroelastic response. Tip sweep was found to increase the torsional frequency and reduce the torsional/lag response at the tip, whereas the flap response was increased. Tip anhedral mainly had an effect on the flap response, although also led to a reduction in the torsional response. More recently, Kumar and Venkatesan [206, 207] performed similar studies, and observed similar observations, although trim controls and vibrational loads were also examined. In particular, tip sweep reduced the collective requirement due to the nose-down elastic blade twist and increased vibratory content. Anhedral also increased vibratory content and had an effect on the lateral cyclic control angle. Finally, Lim [225] included dynamic effects of tip shapes in a rotor design study, showing the detrimental effects of introducing dihedral and sweep on the steady torsional and chordwise bending moments. Introducing these parameters further outboard (0.85R compared to 0.7R), with a reduction in the inboard dihedral angle, solved many of the structural load problems. The final planform featured a double-swept planform with a dihedral-anhedral distribution, which led to significant performance improvements

in forward flight and minor benefits in hover and reduced vibration. The study, however, was conducted using a comprehensive rotor code, which is less reliable in such high-fidelity aspects as structural and vibratory loads.

Other examples of parametric CFD analyses for rotor design, were performed as preliminary studies precursory to design with optimisation methods. Zhao and Xu [440] evaluated a number of conventional planform shapes with a new unconventional CLOR blade tip in terms of aerodynamics and aeroacoustics, based on a coupled Navier-Stokes/Potential/Free-Wake solver. The pressure distributions for the conventional blade tips and CLOR blade tips in hover at $M_{tip} = 0.85$ and $\theta_0 = 8^o$ are shown in Figure 1.23

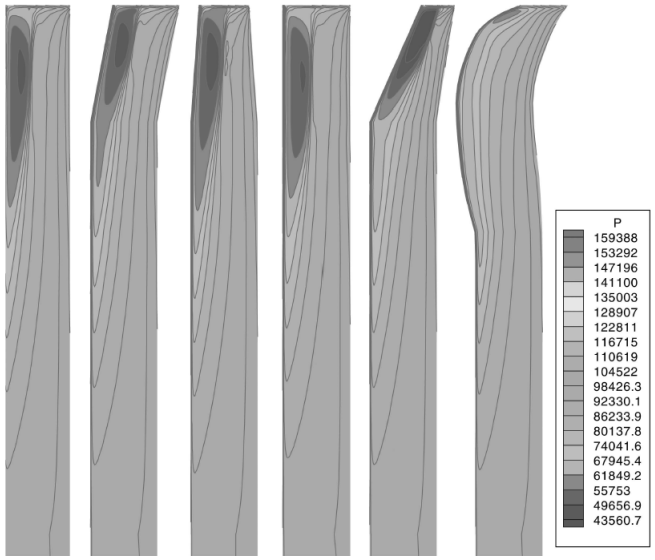

Figure 1.23: Pressure distributions in hover at $M_{TIP} = 0.85$ and $\theta_0 = 8^o$ for a number of blade tips from left to right: rectangular, swept, tapered, rectangular-anhedral, swept-tapered and CLOR [440].

The blended forward-backward swept planform shows a much smoother pressure distribution in hover compared to the more conventional blade tips, with no presence of a shockwave. Similar observations were made in forward flight conditions, as the CLOR blade also showed improved advancing side characteristics. This led to improvements in performance as well as noise reduction. Further studies presented an improved CLOR-II version [400]. Wilke [412] examined parametric twist, chord, sweep, anhedral effects using numerical models of varied fidelity, showing the significant differences between blade element/panel methods and higher fidelity Euler/Navier-Stokes predictions. The main parameter that showed significant differences between Euler and Navier-Stokes predictions was the performance sensitivity due to tip sweep. As was seen from this study, higher fidelity methods are required to accurately capture the rotor design sensitivities, however, as will be seen in the next section, the majority of industry continues to use lower fidelity models in rotor design.

1.2.2.3 Rotor Design in Industry

This section is aimed at analysing the past and current rotor design approaches by the largest rotorcraft manufacturers. This includes the methodologies used to obtain better designs, primary objectives and trends regarding planform and tip shapes. The analysis is performed based on open literature, hence the accuracy of the discussion may be questioned in certain cases, however, this is due to the fact that the majority of the design processes used in industry are proprietary. In fact, very few papers on rotor design exist in literature, regarding case studies in industry. Despite this, however, certain conclusions can still be made, that aid forming the objectives of the present research. The following rotorcraft manufacturers are analysed in this section: Leonardo, Airbus Helicopters, Boeing, Sikorsky and Bell.

Leonardo

The Leonardo company was formed from two different rotorcraft manufacturers: Westland Helicopters of the UK and Agusta of Italy. Due to this fact, two distinctly different rotor design approaches have arisen. The UK rotor technology is based around the BERP blade, whereas Italian blade designs are based around parabolic swept tips with anhedral. The two approaches are discussed in more detail in the following paragraphs.

The BERP blade design emerged through significant research on rotorcraft aerofoils and swept blade tips. The BERP blade tip actually has certain similarities to the PUMA tip [319] which was studied in a collaboration programme between RAE and ONERA on swept tips research. Although a research programme, the UK MOD also needed a replacement rotor blade for the Sea King. The first prototypes of the blade focused on demonstrating composite technology and the initial aerodynamics of a BERP tip [409]. The BERP III rotor blade is the design that obtained the helicopter world speed record in 1986 [298]. The novel blade design was aimed at managing conflicting advancing and retreating side aerodynamics, especially at edge of the envelope flight conditions. The advanced geometry of this planform is shown in Figure 1.24 along with the aerofoils used and the expected formation characteristics.

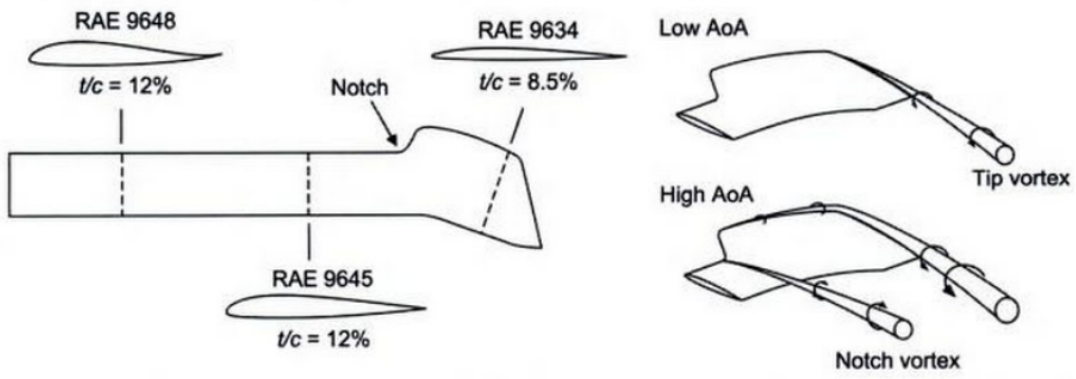

Figure 1.24: Advanced BERP tip geometry by Leishman [220] adapted from Perry [298].

The BERP blade design features a characteristic blade tip shape and new generation advanced aerofoil sections which also contributed to the success of the BERP blade. During the design phase of the rotor blade, it was recognised that the main section contributing to the rotor lift was at the 70-85%R section [132]. A high lift aerofoil with moderate camber and nose droop was used in this region. To balance the pitching moments (and reduce control loads) coming from the high lift section, a reflexed section is used inboards. A thin aerofoil section with low camber and good transonic characteristics is used across the swept blade tip. The blade tip shape has been designed taking into consideration both aerodynamic and aeroelastic characteristics. The BERP tip has a progressively increasing sweep to keep the Mach number normal to the leading edge approximately constant [220]. However, tip sweep has some adverse effects, as it increases nose-down pitching moments and can lead to early pitching-moment stall. The blade pitching moments are minimized by the forward offset at the notch to keep the aerodynamic centre, and centre of gravity close to the elastic axis. The notch also has aerodynamic benefits, both in transonic and low-speed stall conditions. On the advancing side, a sharp decrease in aerofoil thickness to chord ratio, suppresses the advancing blade shockwave, whereas, on the retreating side, a notch vortex is formed which acts as an aerodynamic fence, preventing flow separation across the blade tip. Another feature of the raked blade tip was the formation of a stable separated vortex flow [298] at high incidence, leading to improved aerodynamic performance. The BERP III rotor blade was first flown on a Lynx Aircraft, and comparisons in performance were shown with the rectangular datum metal rotor blade [298]. The BERP planform leads to an expansion of the blade stall envelope by approximately 35% at high loading. Significant performance improvements were seen at high loading, with no losses at lower loading [132]. The datum rectangular blade and BERP rotor were compared directly without a scaling with solidity. This fact sparked controversy, as to whether the main benefit of the BERP blade came from the additional geometric area across the blade tip, and that two rotors should be compared on a thrust-weighted solidity basis [20]. However, Perry [299] claimed that the definition of thrust weighted solidity does not account for three dimensional effects at the blade tip, hence reducing the planform effectiveness [299]. Perry proved his point by examining the rotor thrust envelopes for BERP and tapered tip rotors based only on the blade planform. The resultant of the blade loading based on nominal and thrust-weighted solidities can be seen in Figure 1.25 [299].

As can be seen from Figure 1.25 the definition of thrust-weighted solidity is misleading. Based on nominal solidity the BERP blade can generate 7.5% more thrust than a tapered tip blade, whereas when the thrust-weighted solidity parameter is used, the tapered tip seems to have a much larger thrust envelope. A similar conclusion can be made for a rectangular versus a BERP blade, however the difference will be smaller in magnitude. In terms of performance, the main drawback of the BERP blade compared to the tapered blade is the additional weight coming from the additional area of the tip. Perry claims that the weight increase is of second order due to the outer structure of the blade only being a light fairing [299]. However, to generate the same

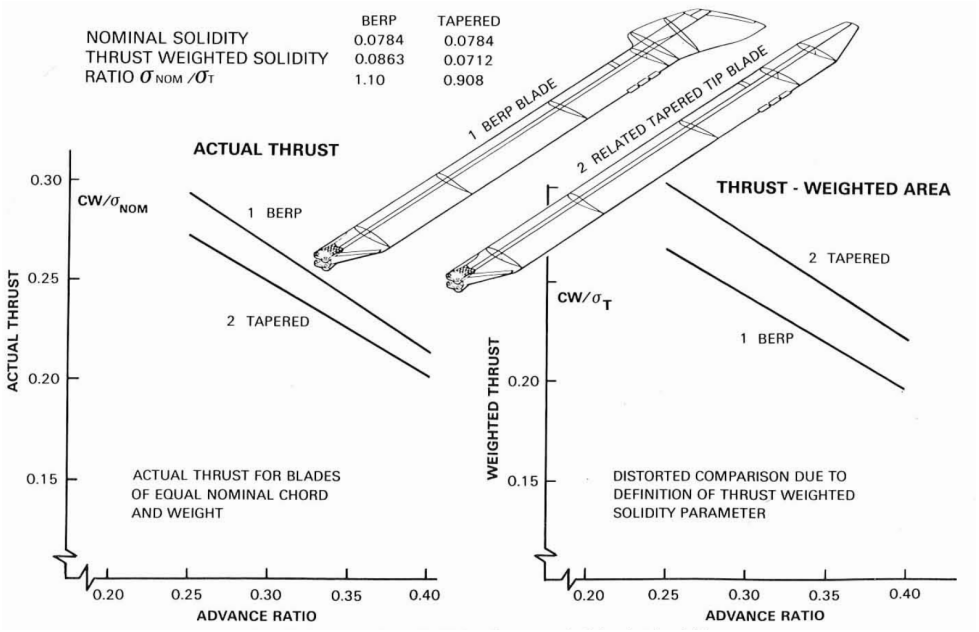

Figure 1.25: Thrust envelopes of a BERP and tapered tip rotor based on two different definitions of solidity [299].

thrust, the blade chord of the tapered blade would have to be increased by 7.5 % which would incur much more significant weight penalties. Further implications of matching thrust-weighted solidity between different blade designs will have an impact on key performance metrics such as FoM and lift-to-drag ratio. The claims made by Perry [299], however, have only been supported by data from low-fidelity analytical calculations.

Further characteristics of the BERP blade were examined by various Westland engineers. Hansford [132] presented blade loads and vibration results using the R85 dynamics code of Westland, and found that the BERP planform has reduced control loads and vibration at high speed but increased at lower speed, compared to the rectangular planform. Vibration reduction at high-speed was primarily attributed to the careful dynamic design of the blade, through mass distribution modifications. The design also led to a more shallow increase in control loads and vibration with flight-speed when compared with the datum Lynx blade. Isaccs and Harrison [160], confirmed the lifting vortex flow phenomenon around the BERP tip and the high incidence capability, through flight test pressure transducer measurements, whereas Brocklehurst and Duque [65] confirmed the formation of the notch vortex at high angles of attack. Later anhedral was also introduced on the BERP design to improve hover performance and reduce 1/rev control loads in forward flight [64].

As detailed by Wilby [409], CFD methods had a certain level of impact in the development of the BERP blade. In particular, aerofoil design was based on 2D transonic codes that included boundary layer effects, whereas full blade simulations were performed using inviscid potential codes in a fixed-wing configuration. The primary methods of design were, however, low-fidelity models such as the R85 dynamics code [132] based on a lifting-line blade model,

an incidal model to include unsteady effects and a vortex ring wake model, as well as extensive experimental and flight-test campaigns. Since the BERP III campaign CFD methods have undergone significant developments and have seen much wider use in industry. The BERP III blade, however, has seen great success on the EH101 (now known as AW101) and the Westland Lynx helicopters, even with fairly low-fidelity design tools, and the design primarily driven by engineering judgement.

A more recent effort of Leonardo (Agusta Westland at the time) is the BERP IV programme [141], with aerodynamic, aeroelastic and structural developments over the BERP III rotor blade. The aerodynamic design included modifications in the blade twist, planform shape and aerofoils [321]. The blade twist was increased to 16^o, to improve hover performance, whilst managing the risk of high vibration. A wide range of tip shapes were evaluated parametrically using panel methods, Euler and Navier-Stokes CFD calculations as well as non-rotating wind tunnel tests. The blade tips evaluated along with the final BERP IV blade tip design (and BERP III for comparison) are shown in Figure 1.26.

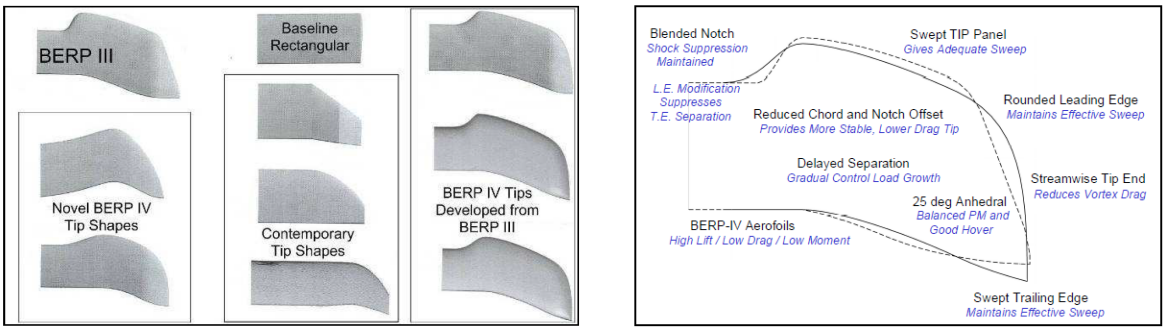

(a) Various blade tips examined (b) BERP IV and BERP III blade tips

Figure 1.26: Blade tips evaluated during the BERP IV programme and comparison of the BERP III and BERP IV blade tips [321].

The blade tips shown in Figure 1.26 were evaluated using model-scale, non-rotating, wind tunnel tests and numerical methods including panel, Euler and Navier-Stokes. The data presented by Robinson [321] focuses on Euler predictions using the HMB3 code for rotor calculations in forward flight, although Fluent was also used based on sheared Mach number computations. The final blade tip design improves the detailed aerodynamics of the BERP III blade, by better management of the tip vortex, reduced planform area, and more blended smoother tip shape (notch, raked tip). New aerofoils were also used on this blade design with significantly reduced pitching moments, with the design based on aerofoil codes such as MSES and BVGK as well as unsteady Navier-Stoked CFD using HMB and wind tunnel testing. The surface pressure distributions for the BERP III and IV blades in hover is shown in Figure 1.27, based on Euler calculations [321]. The surface pressure contours validate the design features of the BERP IV blade, through a reduction in the high suction regions and smoother pressure distribution.

The final design leads to significant improvements in both hover and forward flight, vali-

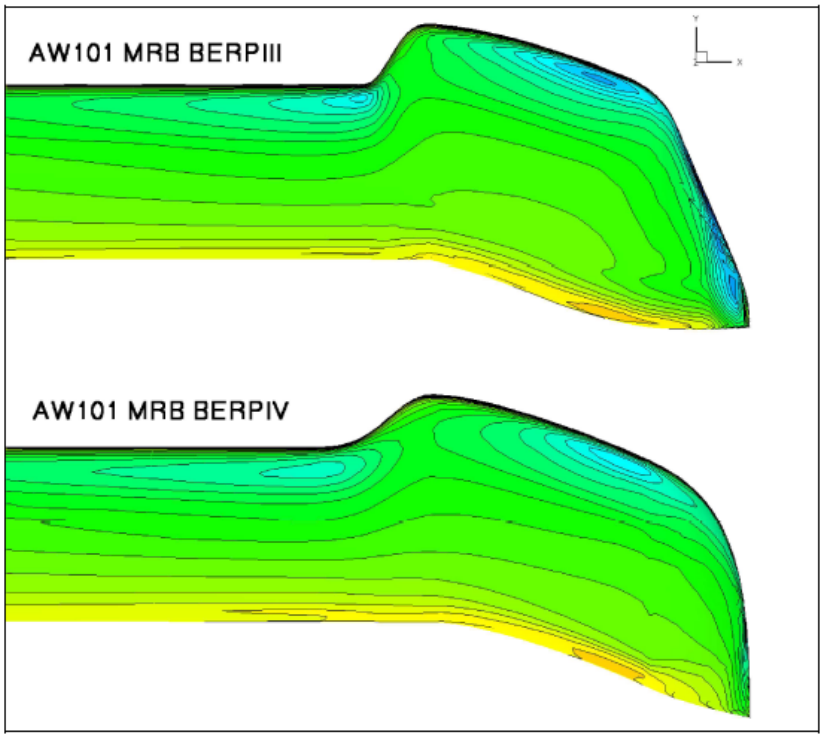

Figure 1.27: Comparison of BERP III and BERP IV pressure distributions in hover, based on Euler calculations [321].

dated through flight tests. The blade structural and dynamic design, however, also received a lot of attention [259]. The high blade twist of the BERP IV blade initially led to an increase in vibration and vibratory control loads compared to the BERP III blade based on R150 dynamic code predictions. These were significantly reduced through structural optimisation and aeroelastic tailoring, and validated through model scale rotor tests. The main objective behind aeroelastic tailoring was to couple the flap and torsion modes, thereby eliminating the vibration at the source, and was successful in reducing vibration for the Lynx aircraft, but less effective for the AW101. For the AW101, aeroelastic tailoring was found the reduce the vibratory control loads at low speed, however, a minor increase (within limits) was observed in high-speed forward flight, when compared to the BERP III blade. The BERP IV rotor blade is currently used on the AW101 aircraft and the recently upgraded Lynx, known as the AW159 Wildcat.

Other aircraft of Leonardo, follow a different design philosophy, focused on rotor blades with swept parabolic blade tips with anhedral as on the AW159, AW169 and AW189 rotor blades. The main difference between these types of designs compared to a BERP tip is a significantly less loaded blade tip. The BERP blade design has quite high loading at the blade tip, making it suitable for heavy-lift applications. The parabolic blade tip design aims to improve the performance by reducing the loading outboard, leading to a more uniform lift distribution and a weaker tip vortex, which can also have a negative impact on noise levels and vibration. However, not much information is available in open literature regarding the parabolic blade designs

of Leonardo or the methods used to design these blades. Future concepts, have included BERP rotor blades with thrust compounding as shown in [409], however, the future attack helicopter AW249, aimed to replace the AW129 rotorcraft, features a parabolic blade tip [222].

A few studies were published, that describe the rotor design methodologies used at Leonardo for generic rotors. Massaro et al. [245] optimised a rectangular rotor blade using a surrogate-assisted memetic algorithm. The aerodynamic predictions were based on mid-fidelity tools such as ADPANEL (3D panel tool with CVC free-wake) and CAMRAD (lifting-line). The final planform shapes, are actually very similar to the blades currently used on Leonardo products such as the AW159 or AW169 helicopters, although anhedral was not part of the optimisation study. In another study Massaro and D'Andrea [244], used a similar optimisation algorithm for optimisation of tiltrotor blades, starting from the XV15 design. Once again, ADPANEL and CAMRAD are used for aerodynamic predictions, with the final design based on a parabolic tip shape with anhedral. No high-fidelity tools were used during these studies, although Navier-Stokes CFD has been used at Leonardo for predictive studies using Fluent [333] and HMB [36, 123]. Based on studies in open literature, Leonardo had started implementing formal optimisation methods into the aerodynamic design framework in the early 2010s, however, only in conjunction with low/mid-fidelity aerodynamic tools. No formal optimisation methods were used in the aerodynamic design of the BERP III and IV blades, with limited application of higher-fidelity CFD methods. Not much information is given in open literature regarding the current numerical rotor design capabilities at Leonardo.

Airbus

The developments in rotor design at Airbus (formerly Eurocopter) age back to the times of Aerospatiale and DASA (formerly MBB). An example early rotor design study at Aerospatiale includes the rotor upgrade for the SA 365N Dauphin 2 helicopter [323] which featured more advanced OA-series aerofoils compared to a NACA0012 aerofoil and a tapered tip. The previously mentioned advanced rotor blade for the B0105 helicopter [306] or the development of the B0108 technology demonstrator [152] are examples of a early rotor design at MBB. These efforts, highly contributed to the EC135 design [187, 447], the first helicopter developed by Eurocopter. The design featured a similar blade to the B0108, with a parabolic tip shape, however, the inboard blade taper was removed, as there was a demand for increased MTOW, which led to a need for increased blade area and different aerofoil radial positions. Following, the EC145 helicopter [153] was developed, based on the BK117 aircraft and using the new technologies of the EC135 aircraft. The rotor blade was based on the ATR (Advanced Technology Rotor) [39], and is shown in Figure 1.28 and featured newly developed aerofoils, inverse taper along the blade span and a parabolic blade tip.

The design of the ATR blade was based on parametric studies of the blade twist, tip shape and aerofoil positions, through engineering judgement. The inverse taper was used to increase

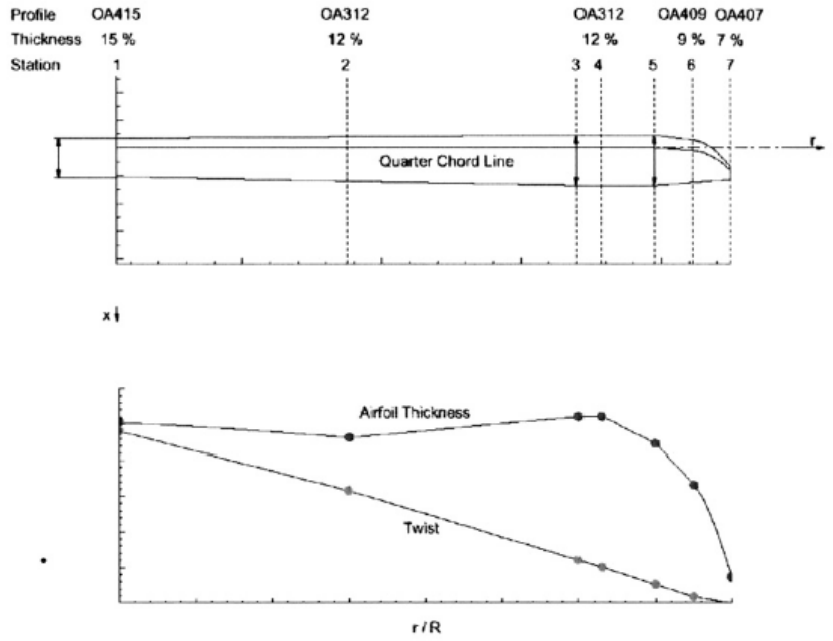

Figure 1.28: Advanced EC145 rotor blade based on the Advanced Technology Rotor [153].

the chord in the main lifting region of the rotor blade (75-85%R) for higher performance at high loading. The parabolic blade tip was used to reduce compressibility effects on the advancing side and in hover as well as reduce noise, based on previous experience with the EC135 design. A forward trailing-edge sweep is also used to minimise torsional loads. A similar blade design was used on the EC155 helicopter [18], whereas the parabolic blade tip is used on many other products such as the Eurocopter Tiger, NH90 (joint design with Agusta Westland and Fokker Aerostructures) or the EC 225 Super Puma (now known as H225). Many of these designs also incorporate blade tip anhedral for additional lifting-capability, especially for heavy-lift applications. A more recent design, the EC175, medium/heavy-lift helicopter incorporates a parabolic blade tip, though no anhedral is used.

Key developments in rotor design technology at Eurocopter emerged with the introduction of the Blue-Edge blade [316]. This design was primarily aimed at noise reduction, building on the experience from the ERATO programme between ONERA/DLR. The main objectives of the design were to improve hover performance at high loading, as the ERATO blade design exhibited early blade stall, whilst maintaining favourable acoustics, blade dynamics and forward flight performance. Based on the ERATO blade, a number of forward-backward swept designs were evaluated in hover using CFD as a starting point, shown in Figure 1.29.

All the proposed designs had a higher blade tip chord compared to the ERATO blade, to delay the onset of separation at the blade tip during high loading conditions. The C4 blade design was selected for a more in-depth study, although this blade tip showed the poorest hover performance at the highest examined loading when compared with the C0 reference design. The anhedral and twist laws were optimised across the blade tip (outboard of 0.9R), using an optimisation

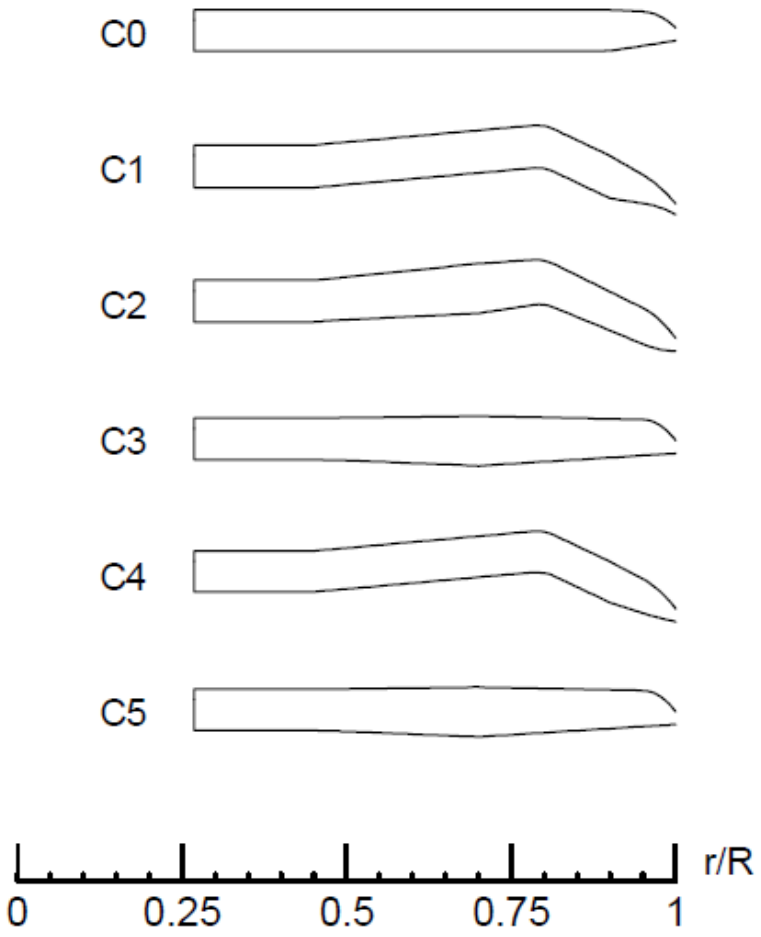

Figure 1.29: Initial designs evaluated in hover during the Blue-Edge programme [316].

algorithm with high-fidelity CFD. Although the details of the optimisation process were not given, this is the first time, an optimisation process has been used with high-fidelity CFD in an industrial rotor design. The selection of the optimal design, was however, performed outside the optimisation loop. The blade design was later altered to minimize torsional deformations and control loads in high-speed forward flight, with the spanwise extension of the backward swept portion of the blade reduced and altered sweep angles. The final Blue-Edge planform is shown in Figure 1.30, and compared with the ERATO blade.

The Blue-Edge planform features a more advanced sweep distribution compared to the ERATO design, as well as a lower blade area inboard of the tip. The tip region area is increased and tapered off further outboard. The final planform shape was evaluated using modern CFD methods in hover, forward flight and descent conditions. The blade was also designed using structural optimisation based on 2D FEA, including torsional stiffening for strength and improved dynamic behaviour as well as careful placement of the centre of gravity locations along the span to stabilize flap/torsion coupling. The altered sweep angles of the final design ensured that the structural and dynamic constraints were met. Detailed analysis was then performed including the 3D FEM model coupled with a 3D CFD analysis. The blade was first flight-tested on

Figure 1.30: Final Blue-Edge planform compared to the ERATO planform shape [124].

the EC155 demonstrator aircraft and confirmed the benefits in hover as well as the significantly reduced noise emissions, without losses in forward flight performance. Additionally, the blade exhibited lower static loads, high-loading dynamic loads and vibration. The Blue-Edge design was also demonstrated on the H160 helicopter in terms of noise [130] and dynamics [350], with this configuration going into serial production and currently going through the certification process [15]. Other applications of the Blue-Edge blade include the EC135 [15], H175 [130] and H225 [15] aircraft with appropriate rescaling of the blade size to match the specific helicopter class.

The Blue-Edge rotor blade design is a key example that shows the benefits of using high-fidelity numerical methods in the design process. Dietz and Dieterich [106], summarised the use of CFD methods at Eurocopter with a more recent focus on coupled CFD/CSD analyses. However, the use of high-fidelity CFD within the optimisation process was performed for the first time in an industrial setting for the Blue-Edge blade and highly contributed to the success of the design. In a later study, Leusink et al. [223] elaborate more on the optimisation framework used at Eurocopter for aerodynamic rotor design. The framework is based on a genetic algorithm with response surface approximations and an update based on a surrogate model to minimize computational costs. Aerodynamic evaluations are performed using high-fidelity CFD in hover (elsA) and comprehensive rotor code analyses in forward flight (HOST). A demonstration of the framework is shown for the redesign of the 7A blade in terms of chord and twist distributions. A comparison is also made between the response surface surrogate modelling strategy and a full genetic algorithm, showing good agreement between the two approaches for HOST-only evaluations. A reduction from 1600 simulations to 180 is achieved using these approximations, however, such a number is still high if high-fidelity methods were to be used in forward flight as well. The inclusion of high-fidelity CFD (only hover) in the surrogate model alters the optimum design twist distributions (reduced blade twist) due to the inclusion of three-dimensional effects near the blade tip. This study shows the importance of including high-fidelity models in the optimisation process to ensure that the optimal design behaviour is reproduced in reality.

A similar optimisation approach was used in a further study for the Blue-Edge rotor blade planform [15] as part of the PROTEGE project, aimed at improving forward flight performance whilst maintaining current hover performance and the characteristic forward-backward swept planform shape. The study was also focused on high loading conditions and applied the optimisation process to the H225 aircraft at MTOW in hover and hot & high conditions in forward flight. Twenty-one design parameters were used altering the chord and twist distributions (through the use of Bezier curves) and the radial aerofoil positions. A constraint was also imposed on the Mean Aerodynamic Chord (MAC), which may not be correct as examined by Perry [299]. A total of 6400 HOST evaluations were performed to generate the multi-objective Pareto front (hover, forward flight). The optimal chord law showed the largest variation with flight conditions, with the optimal hover design preferring a higher chord inboard, and forward flight blades at approximately 0.7R. The final PROTEGE planform shown in Figure 1.31 has a more advanced chord law compared to the Blue-Edge design as well as an improved EOM-series inboard aerofoil. Although direct comparisons with the Blue-Edge blade were not performed, significant benefits were seen compared to the standard H225 blade in both performance and acoustics.

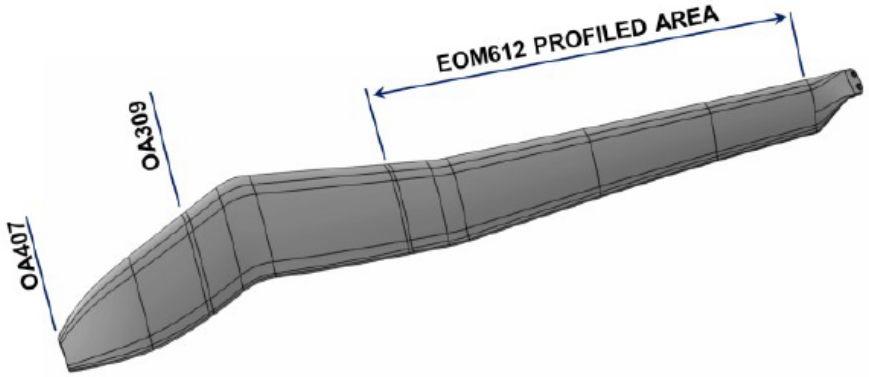

Figure 1.31: Advanced PROTEGE planform design [15].

More recent developments in the optimisation framework at Airbus were shown by Desvigne et al. [105] who included dynamically-adapted structural properties within the optimisation process. The structural properties are adapted through the use of a sample design space using a specified number of donor planforms, extrapolation to new designs and tailoring of the internal structure for optimal eigenfrequency placement. The aim of the study was to minimize high-speed dynamic blade loads whilst maintaining hover performance. A NSGA-II type algorithm was used along with Bezier curve parameterisation of the chord, sweep and twist laws and a constraint on the MAC. Once again HOST is used for aerodynamic evaluations due to the large number of runs required (25 generations of 400 + 60 generations of 200 per population). A discontinuous Pareto front was obtained with two families of rotor blades with similar hover performance and forward flight pitch link loads. The two families differed in twist rates, chord

and sweep distributions as hover and forward flight loads optima followed different trends. A compromise design was selected as optimum, which is in fact similar to Leonardo style blades with a parabolic blade tip. The optimal structural design was compared with the tailored design from the donor blade and show certain differences in the eigenfrequencies which led to increased dynamic loads. A high-fidelity elsA CFD computation in hover also revealed an increase in hover power required, even when compared to the reference blade. The optimisation methodology was successfully demonstrated, however, the need to include high-fidelity CFD methods is demonstrated with a too high number of evaluations required for practical design.

A wide range of studies was published in open literature regarding the rotor design methodologies at Airbus. These moved from parametric studies based on engineering judgement to incorporating formal optimisation methods within the design process over the years. The majority of studies were based on genetic algorithms with HOST comprehensive rotor code analyses. In hover, the elsA CFD code has also been used as part of the optimisation process. However, no high-fidelity forward flight optimisation was performed due to too the high number of evaluations required by non-gradient based optimisation methods. Despite this, the use of optimisation methods using low-fidelity methods have still been successful as demonstrated through the Blue-Edge and PROTEGE designs, however, certain deviations from high-fidelity analyses and real-life operation were observed.

BOEING

The rotor design at BOEING is built on legacy helicopters such as the CH-47 and AH-64 aircraft, which are based on 1970s technology. The CH-47 aircraft has a non-advanced rectangular blade planform, which went through an upgrade from a metal blade to a blade made out of composite materials. BOEING was not involved in the baseline AH-64 design, as it was developed by McDonnell-Douglas, who later merged with BOEING. Despite this, these two aircraft remain the most successful BOEING products (along with the V-22 Osprey tiltrotor in collaboration with Bell). However, compared to Airbus, much less information about the rotor design methodologies used at BOEING is published in open literature. This is perhaps, due to the primary design focus on military helicopters and strong collaboration with US Army.

Despite this, a comprehensive rotor design paper was published regarding the design of the composite main rotor blade (CMRB) for the AH-64 aircraft in 2003 [168]. The need for a new rotor blade was recognised due to growing payload requirements (AH-64A vs AH-64D), and reduced performance of the baseline design at high loading. The objective of the study was to design a rotor blade for an operating weight of 19,000 lbs (AH-64A is 14,766 lbs), for improved hover and forward flight performance whilst maintaining a low risk design in terms of loads and vibration. Constraints were imposed on the rotor diameter and tip speed with free parameters including blade twist, tip shape and aerofoil distributions. The aerodynamic codes were based on comprehensive rotor analyses including LSAF and EHPIC for hover calculations

and CAMRAD in forward flight. The design process started with a predetermined blade solidity value and preliminary selection of aerofoils. As a starting point, a 15 degrees twist value was selected along with tip shapes based on parametric studies and engineering judgement. The initial designs are shown in Figure 1.32 for four-bladed and five-bladed configurations, leading to significant benefits in FoM in hover and L/D_E ratio in forward flight.

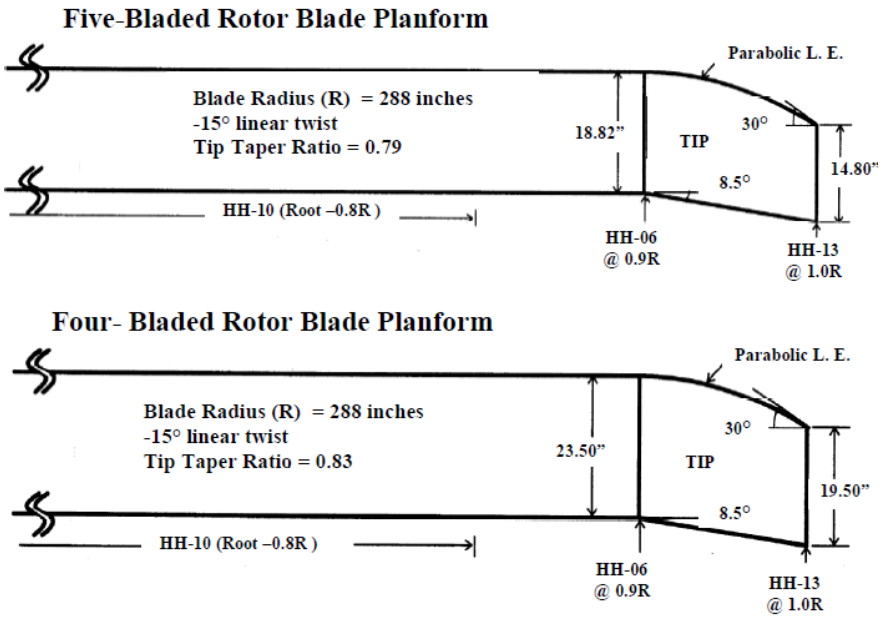

Figure 1.32: Optimal 4-bladed and 5-bladed new Apache planform designs for improved performance [168].

The twist value was refined for the initial blade using a formal optimisation process for the 5-bladed design, leading to an even higher twist value with constant twist across the blade tip, giving a FoM value of 0.8. Further design studies for the 5-bladed configuration re-examined the baseline solidity value and further aerofoil investigations including the VR-series aerofoils. The twist value was also revisited with increased risk of high vibratory loads in forward flight for high twist values, and reduced to 12 degrees linear twist with a constant twist outboard of 0.92R, similar as on the Comanche rotor blade. The blade stiffness and mass distributions were optimised to minimise the dynamic blade loads in forward flight. However, eventually a decision was made to reduce the tip sweep from 30 to 20 degrees to minimize control loads and implement a simplified linear sweep for ease of manufacturability. The five-bladed rotor was later disregarded due to higher costs and suitability with a more powerful engine configuration. Further studies were performed for the 4-bladed configuration including modification of the inboard VR-22 aerofoil section with a 1-inch tab to increase the blade solidity. This procedure was validated using CFD and wind tunnel testing. As with the 5-bladed rotor, the final design was simplified and the final twist value was reduced to 12 degrees. The final four-bladed rotor blade planform is shown in Figure 1.33.

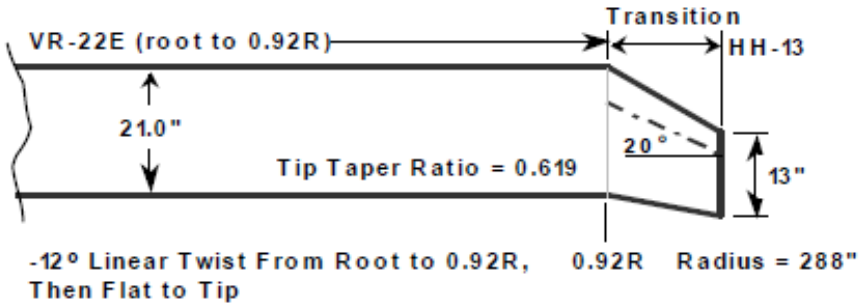

Figure 1.33: Final 4-bladed advanced Apache planform design [168].

The final design achieved the programme goals, however, due to the low-fidelity tools used for performance predictions many of the design choices were based on safety and forward flight vibration/control load constraints. A more advanced planform could have been developed if higher-fidelity tools were used as these constraints could be directly validated. Finally, the design was mainly driven by engineering judgment with limited use of formal optimisation algorithms. Higher-fidelity CFD tools, however, have seen much wider use at BOEING in recent years. Narducci and Tadghighi [270] used Helios coupled with CAMRAD for evaluations of the AH-64E rotor blade in hover and forward flight, whereas Meadowcroft and Jain [250] applied coupled Helios/RCAS and RCAS analyses to the H-47 tandem aircraft. Another study [268] compared the Helios and BCFD codes for A160 fuselage predictions. Ducted fan predictions using Helios were also presented. Tadghighi [372] and Narducci [269] also evaluated the S-76 rotor blade with various tip shapes as part of the AIAA Hover Prediction Workshop. The use of high-fidelity methods in current rotor design processes, however, is unknown.

A more recent conceptual design study [363] aimed at investigation of the use of active devices on the AH-64E blade performed high-fidelity CFD in hover (OVERFLOW) and comprehensive rotor code predictions in forward flight (CAMRAD). Evaluations were also performed by Georgia Tech and the University of Maryland. Certain aspects of the design utilized optimisation processes such as the rotor design in hover and optimum blade deflection profiles for minimised noise. These were found to be more effective in finding better designs than parametric studies. The use of high-fidelity CFD/CSD was seen to be too costly within formal optimisation frameworks, but was seen useful to gain further insight into the final designs. The current research at BOEING is focused on demonstrating the advanced compound version of the AH-64 helicopter [67] with the new CMRB rotor design used in the configuration with a wing and an auxiliary thruster. Wind tunnel testing was also performed using a CMRB blade with anhedral. Moreover, BOEING recently developed a new Advanced Chinook Rotor Blade (ACRB) [54] for the CH-47 aircraft. Currently, little is known about the details of the design, however, the blade features a smoothed dihedral-anhedral shape, shown in Figure 1.34, which is likely to have come from a numerical parametric study or optimisation process.

BOEING is also involved in the FVL programme, including the FLRAA SB-1 Defiant coax-

Figure 1.34: New advanced rotor blades for the CH-47 rotorcraft [54].

ial compound aircraft proposal with Sikorsky currently in the phase of flight testing. The aerodynamic design, however, is driven by Sikorsky with BOEING responsible for the mission systems design. BOEING also submitted a proposal for the FARA role, however, the six-bladed concept with a pusher propeller was not selected for the next phase. Due to the fairly recent emergence of these designs, information about the design processes used in the development of the FVL concepts is unavailable.

Sikorsky

Similarly, like for BOEING, very few studies have been published regarding rotor design, although a significant amount of papers can be found in open literature regarding the use of high-fidelity CFD methods for validation and comparison with experimental data. Furthermore, certain assumptions can be made regarding the design methodologies from various studies. Sikorsky started investigating more advanced rotor blade designs very early in the 1970s with the development of the legacy UH-60A and S-76 rotor blades, with swept and swept-tapered blade tips. However, over the past decades, Sikorsky has developed significant experience for more advanced coaxial rotorcraft configurations, with a large current focus on such designs.

Despite this, Sikorsky continues to also develop rotorcraft with the standard main rotor/tail rotor configuration. The S-76 civil aircraft went through a series of upgrade programmes, including a main rotor and tail rotor upgrades for the S-76D version [161]. The new rotor blade features more advanced aerofoils, tip sweep and taper as well as a modified structural twist distribution leading to an increase in lifting capability and forward flight performance. No anhedral was incorporated into the final design. Details of the design methodology, however, are not presented. Another Sikorsky civil aircraft design includes the S-92 aircraft with swept-tapered rotor blades and sharp anhedral.

Heavy-lift helicopters have also been of interest at Sikorsky with the CH-53 aircraft [234] going through a series of upgrade programmes from the CH-53D Sea Stallion, the CH-53E

Super Stallion to the CH-53K King Stallion aircraft. Very little information, however, has been published about the design of these aircraft. The CH-53E Super Stallion design included 7 rotor blades compared to the 6 of the CH-53D version as well as a third engine, to further increase the lifting capability of the aircraft. The CH-53K upgrade featured new composite main rotor blades and new engines leading to a significant expansion of the flight envelope (increase in maximum payload of nearly three times compared to the CH-53D, to 88,000 lbs). Not much is known about the rotor blade design methodology, however, Lorber [234] states that a parametric rotor design wind-tunnel test program was launched internally that evaluated advanced blade tip designs for four-bladed and seven-bladed rotors, with the best design adapted to the CH-53K aircraft. However, as seen on Figure 1.35, the CH-53K blade is only a minor upgrade in terms of planform shape compared to the CH-53E blade, as a simple taper is replaced by a slightly more advanced tip profile. The CH-53K blade, also features new advanced aerofoils, a modified twist distribution and a significant amount of anhedral, which also highly contributed to the increased lifting capability. The use of optimisation methods in this design programme, however, is unknown.

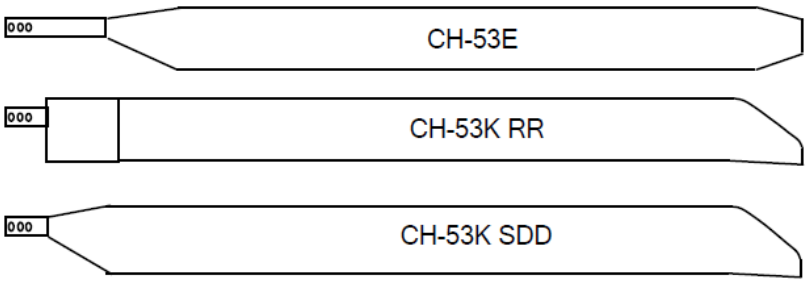

Figure 1.35: Comparison of the CH-53E and CH-53K planform shapes [234].

Recently, Sikorsky has also been involved in several programmes that developed coaxial rotorcraft technology. Building on the experience of the Advancing Blade Concept (ABC) [83], which was demonstrated on the X-59A aircraft [326] in the 1970s, a revived interest in these technologies has arisen at Sikorsky, due to the need for even higher-speed rotorcraft. The basic principle included rigid coaxial rotor blades with slowed RPM at high flight speeds which lead to offloaded retreating blades and an additional propulsive force provided by a rear propulsor. The X2 programme was launched to demonstrate the compound rotorcraft technology, whilst including newer advancements since the X-59A programme. The only detailed rotor design paper at Sikorsky found in open literature was presented by Bagai [27], detailing the aerodynamic design of the X2 rotor blades. The blade design was based on GRP analyses (Generalised Rotor Performance) based on rigid lifting surface models with non-uniform inflow with loads based 2D aerofoil look-up tables. The interference between the two rotor disks was not modeled as the two disks were analysed as co-planar. The design evolved through parametric studies of the effects of blade twist, chord distribution, aerofoil shape and thickness, as well as previous

experience with the X-59A design. Despite, the limitations of the simple analytical model, the predictions correlated fairly well with experimental data for isolated rotor cases in high-speed forward flight. The final design for the X2 rotor planform is shown in Figure 1.36 and compared with the X-59A planform.

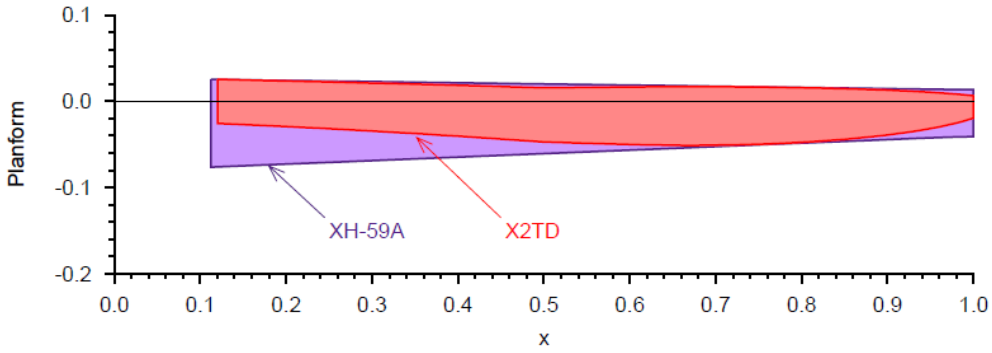

Figure 1.36: Final X2 planform shape design, compared to the X-59 blade [27].

The final planform design features an elliptic planform shape centred around 70%R. The low inboard chord is due to the use of double-ended aerofoils with blunt trailing edges to improve retreating blade performance, where a large portion of the blade is in reverse flow. The minimal chord was limited by structural constraints. A high-lifting section was used in the region of the maximum chord, with super-critical aerofoils towards the blade tip. A positive 14^o linear twist is used in the inboard region (up to 40%R) with a standard negative -9^o linear twist used outboard. The new blade design showed significant performance benefits compared to the X-59A rotor blade, however, advanced concepts such as lift-offset predictions need to be approached carefully, due to the low-fidelity numerical model.

Building on the X-2 programme, further aircraft have been developed including the S-97 RAIDER [232] aircraft aimed at further technology demonstration as well as the SB-1 Defiant [231] and Sikorsky RAIDER-X aircraft submitted as FVL FLRAA and FARA proposals. The information regarding the design methodologies in open literature, for these aircraft, however, is scarce. A number of studies at Sikorsky have, however, used higher-fidelity CFD methods for predictive investigations for the S-97 RAIDER aircraft [62], S-92 [233] as well as UH-60A [255]. A summary article of the analytical tools used at Sikorsky for the Joint Multi-Role programme was published by Tuozzo et al. [379], from lifting line/surface free wake comprehensive rotor codes to coupled CFD/CSD analyses using OVERFLOW/RCAS. The tool correlation activities highlighted primary use of lower fidelity analyses for forward flight performance and vibratory loads though highlighted the benefits of using CFD/CSD predictions. Tuozzo et al. [379] stated that one of the objectives was to mature CFD analyses to support design processes of future FVL programmes, hence it is likely that the design was primarily driven by lower fidelity tools.

Bell

Bell has developed many types of rotorcraft including a wide range of civil aircraft as well as military aircraft - both standard main rotor/tail rotor as well as tiltrotor configurations. Bell has significant experience in rotor design, perhaps due to the adoption of numerical methods into the design process in the early years of CFD.

Early helicopter performance methodologies are described by Kocurek et al. [199] and Harris et al. [140], with calculations largely based on lifting surface representations of the blade coupled with a wake model. Harse et al. [142] described the driving technologies at Bell Helicopter in the 1970s/80s and highlighted the use of numerical methods in the advancement of rotor designs. These included inverse aerofoil design tool (ADAM [275]) which was used for the design of the V-22 aerofoils, transonic potential codes coupled with boundary layer models and various panel methods (VSAERO in particular). These methodologies contributed to the design of the Bell 412 rotor blades which used four different aerofoils along the blade span at carefully selected radial positions, and the AH-1W rotor blades. The use of aeroelastic tailoring was also highlighted in the development of the Bell 680 rotor blade to minimize vibration.

Higher fidelity CFD methods were implemented at Bell, during the years where Navier-Stokes methods were still maturing. As early as 1989, a Navier-Stokes CFD solver was implemented in BELLTECH (Bell CFD code) [238], based on the work of Wake and Sankar [396]. The solver was then used in an inverse aerofoil design code [239] based on a residual correction technique and was demonstrated for correlations with swept blade tips [337], retreating side aerodynamics [273] and the full V-22 configuration [274]. New inboard aerofoils were developed for the BA609 tiltrotor blade using the inverse design tool, as well as improved wing-fuselage fairing aerodynamics using parametric three-dimensional Navier-Stokes CFD [272]. A mid-fidelity optimisation framework using a genetic algorithm based on response surface methods, the COPTER comprehensive rotor code at Bell, a transonic full potential method and an aeroacoustic method was presented by Xue et al. [423]. The framework was applied to the Bell 407 rotor blade and showed benefits of re-designing the blade tip shape. CFD was also used in the design of the Bell 429 rotor blade [271, 276] including aerofoils designed using the inverse design tool, and the planform shape based on parametric studies in hover using 3D CFD (TURNS code), starting from the Bell 427 planform. This is a development in rotor design technology, as the Bell 427 blade was designed using lifting surface with prescribed wake [276]. The new planform shape Bell 429 is shown in Figure 1.37.

The Bell 429 rotor blade features a parabolic blade tip which leads to improvements in lifting capability and hover performance compared to the Bell 427 blade. Although not included in the design objectives, high-speed forward flight performance was also improved. In particular, the maximum loading before stall was increased by a considerable amount, which is not surprising due to more advanced aerofoils, and higher blade area in the blade tip region. The rotor dynamics developments based on the COPTER comprehensive rotor code and the Myklestad method were

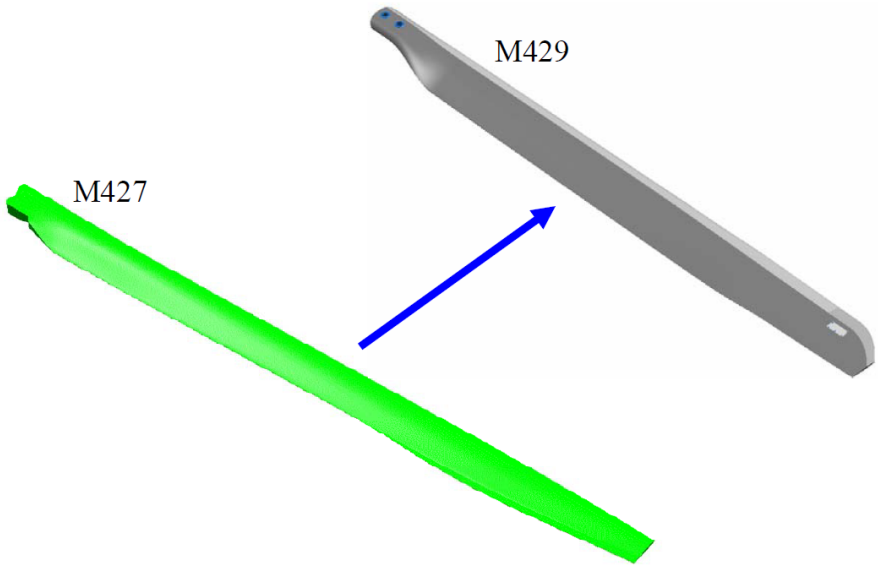

Figure 1.37: Comparison of the Bell 427 and 429 rotor blade planforms [276].

also presented.

Further developments in the computational methodology at Bell include the integration of the DYMORE code of Georgia Institute of Technology and comparisons with the current COPTER/Myklestad method [261]. The DYMORE code was also coupled with the OVERFLOW CFD solver for CFD/CSD analyses and integrated within Bell [262], with predictions shown for the UH-60A and Bell 427 rotor blades. In a subsequent study [11], CFD/CSD analyses were also performed for the Bell 429 rotor blade and comparisons were made with flight test and lower fidelity analyses (COPTER, DYMORE).

Despite the use of higher fidelity methods for rotor analyses, the use in current rotor design is unknown. Since the development of the Bell 429 rotor blade, Bell has launched the 505 Jet Ranger aircraft with a fairly simple rectangular rotor blade planform. The 525 Relentless Aircraft is also currently in development with a 5-bladed rotor and a parabolic tip shape. A similar design (4-bladed) is to be used on the Bell 360 Invictus Aircraft submitted for the FVL FARA category. Following the V-22 experience in tiltrotor technology Bell is also developing the V280 Valor for the FVL FLRAA category, and the future V-247 Vigilant large tiltrotor aircraft.

Summary - Rotor Design in Industry

Based on the industrial rotor design practices of the major companies in the rotorcraft industry, it can be stated that there is a growing use of CFD and optimisation methods. The majority of rotor design studies in industry, still use the numerical tools in a parametric manner [27,168,276,321]. The use of formal optimisation methods in industrial rotor design is still scarce, and has mainly been used in conjunction with low/mid fidelity tools as in the studies of Leonardo [245] and Bell

[423]. Eurocopter has shown the use of higher fidelity methods in optimisation studies [223], which were also used in the Blue-Edge [316] and PROTEGE [15] designs. However, in the studies of Eurocopter, Navier-Stokes based optimisation has only been used in hover condition, with forward flight optimisation based on comprehensive rotor code analyses (HOST). Based on the findings of Leusink [223] and Desvigne [105], there is a need for high-fidelity optimisation across all flight conditions, including forward flight. Certain research in this direction has been performed in academia and research centres, which is discussed in the next section.

1.2.2.4 Rotor Design Using Optimisation Methods

The following section will discuss work performed in literature concerning rotor design using optimisation methods, with a particular focus on aerodynamic design. As seen from previous sections, many of the rotors that fly today, have been designed based on parametric studies, by sequentially varying certain design features of the rotor and studying the impact on the performance. The design changes were widely based on engineering judgement, hence relied on the experience of the designer. Optimisation methods allow to explore a wider design space and detach the designer from selecting the optimal shape of the blade, which also allows for exploration of more novel blade designs. Based on the last 20 years of rotor design in industry, where more advanced planform shapes have emerged and a growing use of CFD was seen, more novel planform shapes are likely to be obtained through use of optimisation methods. Typical optimisation frameworks, however, are still currently limited by model fidelity, which is directly linked to computational costs. The parameterisation of the blade surface and choice of the objective/constraint functions have to be pre-selected and will have an impact on the final design. The parameterisation should be selected to cover a wide design space and allow for exploration of novel designs, whereas the objective function must include conflicting design conditions - hover and forward flight, for realistic rotor designs. Furthermore, multiple disciplines should be included for an industrially viable design, such as aerodynamics, aeroelastics, structures, vibration and noise. Finally, the choice of the optimisation method will also drive the design changes, impact the achieved performance benefits and the computational costs required to optimal design. Two key optimisation approaches have been identified in literature and will be described in the next subsections along with applications to rotor design.

Non-Gradient Based Methods

The majority of research regarding the use of optimisation methods in rotor design has been performed using non-gradient based methods. These methods are typically based on genetic algorithms and guarantee reaching the global optimum within a given design space. However, they require a high number of evaluations to reach the final design, as the optimisation cost scales with the number of design parameters. Non-gradient based methods are considered as computationally expensive making them more suitable with low/mid fidelity performance prediction

methods. To minimize computational costs, various approximations are typically used such as response surface methods or surrogate models, which reduce the accuracy of the optimisation process. However, even with such methods employed, the computational costs are still high compared to gradient-based methods. Despite this fact, these methods have been successfully been demonstrated in literature for rotor design in many studies.

Non-gradient methods have been applied to many aspects of rotor design. A number of studies [118, 121, 122, 217, 243, 355, 439] used genetic algorithms for the design of rotorcraft aerofoils using low-fidelity models or based on 2D Navier-Stokes CFD. However, typically, whilst improvements are obtained targeted at specific conditions, the optimal aerofoil is not validated for off-design conditions or when applied to a three-dimensional rotor flow field. The work of Fusi [121, 122], showed the importance of including uncertainty effects in the design optimisation, however, all the work was based on 2D aerofoil simulations. Stanko [355] used a high-fidelity CFD method to generate a 2D look-up table for a low-fidelity comprehensive code, aimed at improving advancing blade aerodynamics. A code based on blade element momentum theory, however, is unlikely to capture the correct aerodynamics of shock-boundary layer induced separation. Due to the importance of three-dimensional effects, significantly more research has been performed for rotor blade optimisation, sometimes including aerofoil modifications.

Sun and Lee [371] used a response surface approach to modify the rotor aerofoils and tip shape for a rotor in subsonic and transonic hover conditions based on Navier-Stokes methods. Over 180 evaluations are required to form the response surface. The aerofoil impact on the rotor performance was found to be more sensitive in transonic than subsonic conditions, however, greater benefits were obtained through tip shape modifications, with the final geometry having maximum linear twist and tip anhedral. Vu [390–392] also performed modifications of the aerofoils and planform shape, using DoE for sampling of the design space and a surrogate model based on kriging interpolation. In this work, both hover and forward flight conditions were considered, however, a low/mid fidelity comprehensive rotor code was used with 2D aerofoil aerodynamics based on various models (from panel to Navier-Stokes). Over 220 function evaluations were required to reach an optimum shape with a tapered blade tip. The final shape is fairly simple, perhaps due to the low-fidelity model employed for aerodynamic evaluations.

Higher fidelity CFD methods were also used by various researchers in non-gradient based optimisation studies. Imiela [156, 158] presented a high-fidelity optimisation framework based on Navier-Stokes CFD methods including aeroelastic effects. First, the performance of three different optimisation methods was presented, gradient-based on finite differences (CONGRA), genetic pattern search algorithm (Subplex) and a surrogate model using a predictor technique and an expected improvement function to update the design (EGO). The EGO algorithm was found to be most successful and was applied to the re-design of the 7A model rotor including collective, twist, anhedral, chord and sweep design variables for FoM optimisation. Over 200

iterations were performed to obtain a hover optimised design with an increased twist angle, negative tip sweep, reduced tip chord and tip anhedral. The optimiser, however, drove the design to very high collective angles (over 20^o), as the objective function was set to maximise the FoM, which attains higher values at higher thrust coefficients. Forward flight and multi-objective hover-forward flight optimisations were also carried out, however, a single blade assumption was used to reduce computational costs, neglecting unsteady wake effects, and only the twist design variable was considered. In subsequent work [157], a comparison of rigid and elastic blade assumptions was carried out for hover optimisation, showing a high influence of aeroelasticity on the final planform shape as shown in Figure 1.38.

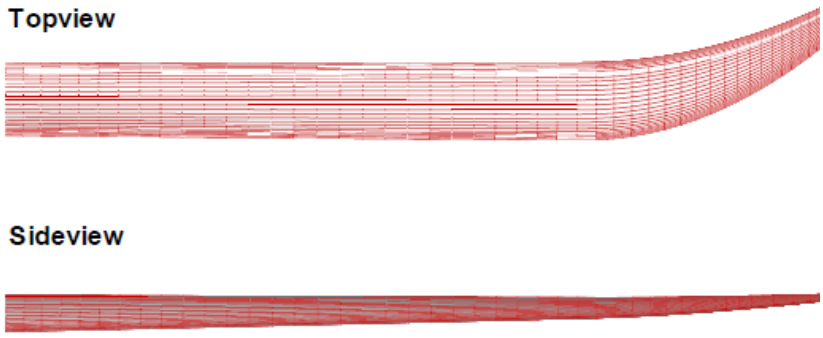

(a) Rigid optimum

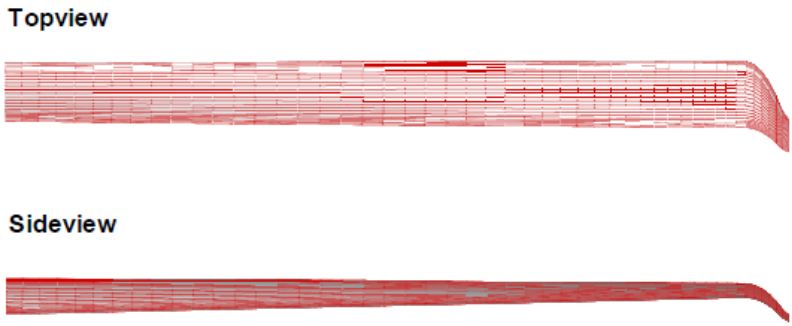

(b) Elastic optimum

Figure 1.38: Effect of aeroelastic effects on the optimum planform shape in hover [157].

The inclusion of aeroelastic effects slightly increased the collective and blade twist angles due to an elastic torsion effect. The influence of aeroelasticity had a much higher impact on the sweep and anhedral distributions. The rigid optimal shape is indeed surprising, and contrary to what is seen in other studies in literature [214, 221], however as stated by the author the shape is driven by a more optimal loading distribution rather than reduced compressibility. Furthermore, these parameters were seen to have a low impact on the objective function and exhibit multiple

optima for the rigid blade optimisation. The elastic shape is better behaved and drives the optimiser to a moderate sweep angle and minor anhedral. Another aspect of note is the high elastic torsion values, of up to 15 degrees at the tip seen during the optimisation, showing the planform shape may be driven by a more optimal elastic deformation, leading to a more optimal loading distribution. Further studies by Imiela [159] examined hover and forward flight optimisation at a constant thrust coefficient and assessed optimal blade designs at off-design conditions. Forward flight optimisation studies included twist optimisation based on a single blade assumption and multi-variable (chord, twist, sweep, anhedral) optimisation based on multi-fidelity approach of Wilke [413], with a primary use of Euler methods. The optimisation leads to a backward-swept tip with minor dihedral, giving a power benefit of 2.2% and suffering degraded hover performance at high-loading. These studies highlighted the high computational cost of forward flight optimisation which limited the number of design variables and/or the fidelity of the CFD model. The studies of Imiela [156–159], also imposed a constraint on constant thrust-weighted solidity, which may not be correct for more advanced planforms [299] and drive the designs to higher inboard blade area to delay stall effects.

Building on this work, Wilke [412] developed a multi-fidelity optimisation approach applied for the 7A blade to minimise computational costs. Initial design parameter studies showed that generally, the modelling fidelity was more sensitive in hover conditions than in forward flight. The methods that utilised a wake model seemed to overpredict the impact of the planform shape on the rotor power than other employed methods. Optimisations which used a direct genetic algorithm were performed in hover and forward flight for all methods. In hover, methods of varied fidelity predicted different levels of performance improvement, however, after validation with high-fidelity CFD, the blade with the highest performance was the optimal blade generated using Navier-Stokes based CFD. A similar observation was made for forward flight optimised blades. Similarly as in the work of Imiela [158], the hover optimised blade leads to a blade tip with dihedral and forward sweep, even though aeroelastic effects were included, whereas the forward flight optimised blade shows backward swept tips for the full Navier-Stokes simulations. A methodology is shown to use multi-fidelity simulations in a surrogate model based on the variable Kriging method, based on Hierarchical Kriging, where the optimal solution from the low fidelity model is sample in the high-fidelity DoE, leading to significant reductions in computational costs and similar optimal designs. Further studies included coupled hover forward flight multi-objective optimisation studies [413], using a differential evolutionary algorithm to drive the Pareto front. The full optimisation, however, still required a high number of evaluations (for example DoE size of 256 Euler simulations), even though a variable approach was used. In this case, the planform shapes were fairly similar. As shown in Figure 1.39.

All planforms had a backward sweep and taper towards the blade tip. A highly twisted blade with anhedral was preferable in hover, whereas a blade with a lower twist angle and dihedral was better in forward flight. In general, the improvements were much higher than in the work

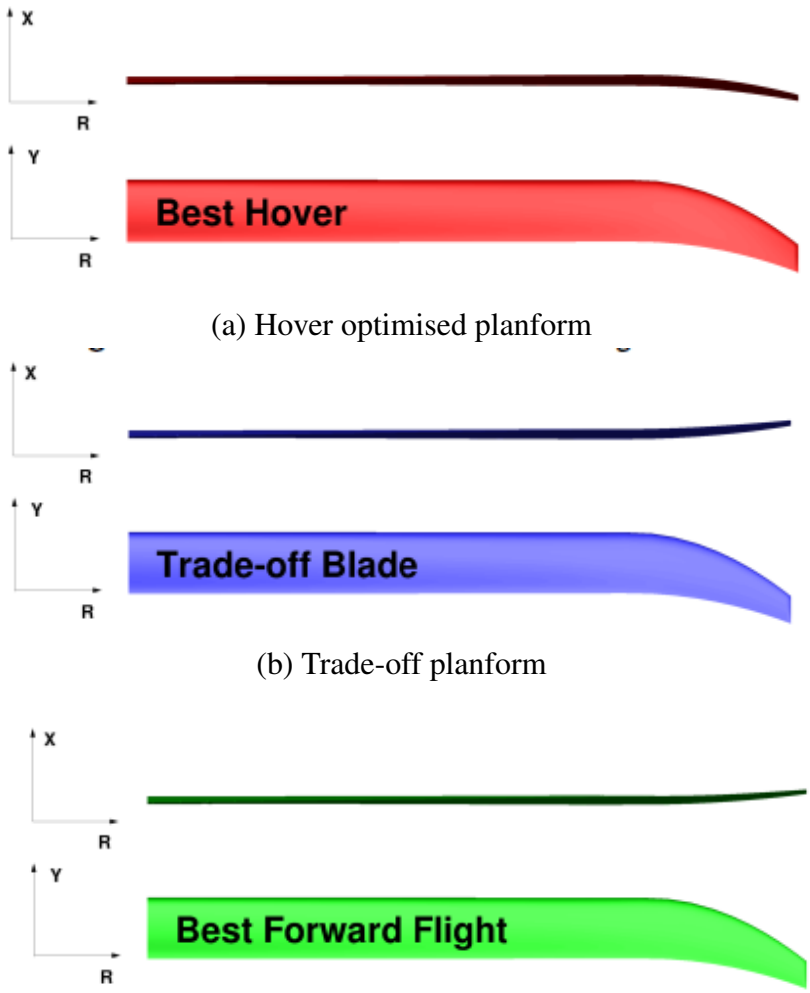

(a) Hover optimised planform

(b) Trade-off planform

(c) Forward-flight planform

Figure 1.39: Optimised planform shapes by Wilke et al. [413] in hover and forward flight showing similar features.

of Imiela [159], approaching 9% power reduction in hover and forward flight for the trade-off blade. The optimisation was, however, performed at a fairly low thrust coefficient (approx. 0.0065). Subsequent studies [414] for the 7AD rotor blade at higher blade loading, yielded significantly different planforms with a much higher area at the blade tip and high dihedral in hover and forward flight, with significantly lower benefits of approx. 2%. The work of Wilke [412–414], shows the high-dependency of the flight conditions and initial geometry on the obtained performance improvements and final geometry. Furthermore, despite the reduced cost of the variable-fidelity approach, the importance of including full Navier-Stokes simulations in the design process is highlighted.

Similar findings regarding solution fidelity are found by Bailly and Bailly [28, 29] who optimised the sweep distributions for a reference rotor blade in forward flight using lifting line and Navier-Stokes methods. Similarly as in the studies of Wilke [412, 413], the EGO algorithm was used along with a Kriging/Co-Kriging based surrogate models. The low fidelity model im-

provements were not reproducible once a high fidelity model was applied. The optimal blade shapes, however, had unrealistic sweep distributions, which would lead to high structural and control loads. Following studies [30], included twist and anhedral optimisation in forward flight based on Navier-Stokes methods and chord/sweep optimisation using HOST with an update of the structural properties. The structural data, however, was extrapolated from data based on a parametric study, and led to significant errors in a number of the structural properties when compared to the actual values of the 7AD blade. Fairly exotic blade shapes were obtained, even when the structural data update was included. Other studies at ONERA were performed by Leon et al. [221, 322] who used an optimisation algorithm based on Nash games. First, a hover optimised blade using Navier-Stokes CFD was obtained based on a gradient-based method. Then a multi-objective hover and forward flight optimisation was performed with the forward flight simulations based on HOST computations and hover evaluations based on a kriging surrogate model. Similarly as in the work of Bailly and Bailly [28], unrealistic S-shaped blade designs were obtained by Leon et al. [322], as shown in Figure 1.40, due to the low-fidelity model employed in forward flight. Once again, a constraint was also imposed on the thrust-weighted solidity.

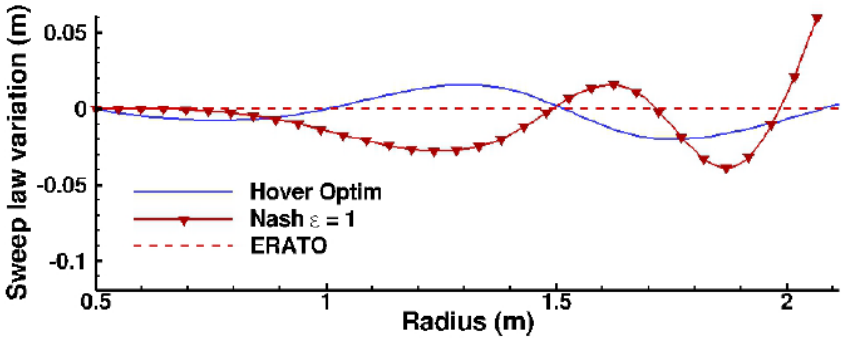

Figure 1.40: Unrealistic S-shaped planform shapes obtained by Leon et al. [322].

Various other studies exist in literature [77, 441, 444] based on Navier-Stokes methods using surrogate models based on Kriging or Radial basis functions (RBF). These studies typically used more advanced parameterisation techniques with polynomial expressions of the leading and trailing edge curves, leading to more advanced planform shapes. The studies by Zhu et al. [444] and Chae et al. [77] predicted benefits of a leading edge notch-like feature leading to a reduction in induced power for multi-objective aerodynamic/aeroacoustic optimisation studies despite different flight conditions (hover/forward flight), as shown in Figure 1.41.

These studies show that the parameterisation may play a key role in obtaining more advanced planforms which exhibit more similar features across different studies and flight conditions. One solution to improved blade surface parameterisation representations was suggested by Sinsay and Alonso [347] who used a heuristic approach to update the parameterisation during the optimisation process. Despite using surrogate models, many of the studies investigated in this

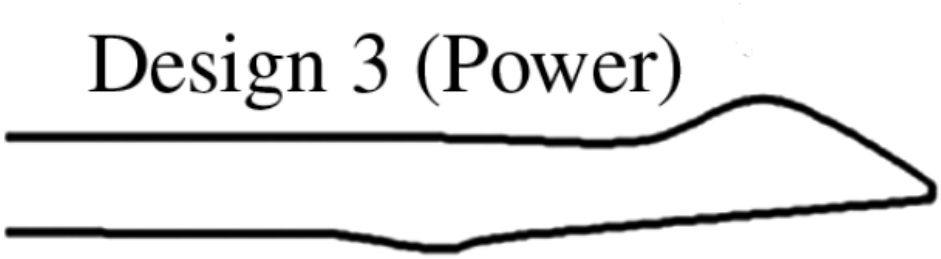

(a) Optimal planform (power objective) obtained by Chae et al. [77]

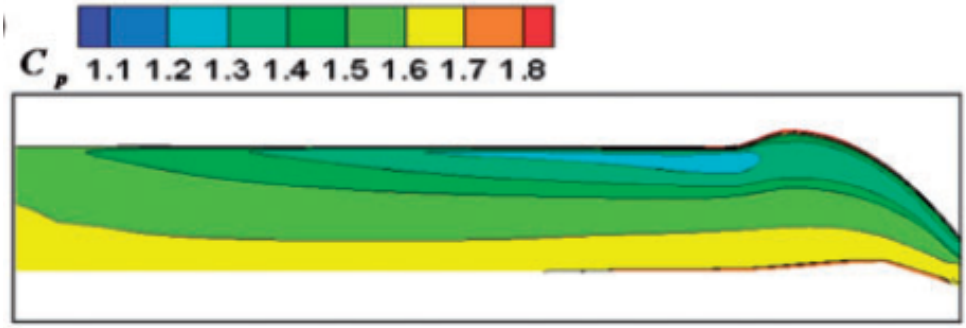

(b) Optimal planform obtained by Zhu et al. [444]

Figure 1.41: Optimised planform shapes by Chae et al. [77] and Zhu et al. [444] showing a protrusion shape feature aimed at reducing induced power.

section still required a high number of evaluations (over 100). However, with large enough DoE sample size, genetic based methods guarantee finding a global optimum within a given design space. An additional benefit of non-gradient based methods in multi-objective formulations is the presence of the entire Pareto front, leading to a possible choice of the final design based on engineering judgement and required weighting between multiple objective functions.

Gradient Based Methods

Gradient-based methods are significantly cheaper, computationally, compared to non-gradient based methods, however, due to their local nature, they do not guarantee finding a global optimum. The optimal design will be dependent on the starting point and may be a local minimum in the given design space. These methods are based on the computation of the design sensitivities and use of a gradient-based optimiser to compute the search step size and direction within a given design space. The sensitivity analysis can be computationally costly when using standard methods such as finite differences or complex step methods, as the cost scales with the number of design variables N (2N+1 computations required). However, with adjoint methods, the sensitivities of all the design variables can be computed at the cost of a base flow solution independent of the number of design variables. This means that these methods are more suitable for dealing with large design spaces compared to non-gradient based methods. The power of the adjoint method has been demonstrated in the fixed-wing community where nearly 1000

variables have been used [193]. Finally, compared to genetic algorithms where N^3 evaluations are required (without the use of surrogate models), adjoint methods require significantly fewer iterations, and can usually obtain a better design within the first 10 iterations.

Finite Difference Method Gradient-based optimisation based on standard gradient evaluation such as finite differences received attention much sooner than non-gradient based or adjoint based optimisation. In the early 1990s, a number of optimisation studies were performed for various rotors using the CONMIN optimiser [68, 81, 398, 399, 445, 446]. These studies typically used low-fidelity models such as CAMRAD or R85 due to limited computational power available at the time, but also included multidisciplinary aspects of rotor design such as noise, vibration, structure and aeroelastic stability. The low iteration count very quickly made these optimisation methods suitable for high-fidelity CFD methods, however, due to the use of finite differences, the optimisation cost was still dependent on the number of design parameters.

High-fidelity gradient based optimisation was first performed by Le Pape and Beaumier [214] in hover. In this study, the 7A/7AD and ERATO rotor blades were optimised using Navier-Stokes methods with chord, twist, anhedral and sweep design variables. Design features such as backward sweep, tip taper and anhedral were all proven to be beneficial. When applied to the ERATO blade, a slightly higher blade tip area with a minor anhedral led to benefits of over 4 counts in FoM, however, the optimal blade was not simulated in forward flight. The study also imposed a constraint on the thrust-weighted solidity, which could have an impact on the area at the blade tip. Further studies by Le Pape [213] included forward flight optimisation and compared gradient and non-gradient-based optimisation approaches. However, due to the high computational costs of unsteady simulations, the forward flight evaluations were based on a comprehensive rotor code prediction (HOST). The gradient-based method obtained similar performance benefits with significantly fewer evaluations (39 compared to 200 in forward flight). The use of a high-fidelity CFD model (elsA) also yielded higher benefits compared to optimisation using only HOST. The multi-objective optimal shape is actually quite similar to the hover optimised shape of the ERATO blade [214] as seen in Figure 1.42, with a slightly sharper forward sweep inboard and lower blade twist.

However, despite the rather minor differences in the planform shapes, the multi-objective optimised blade does not give such large performance benefits in hover. Based on the findings, the twist distribution is a major contributor to high hover performance.

Another study by Allen [17] examined hover performance optimisation for the Caradonna & Tung rotor blade based on Euler methods. Here, a mesh parameterisation approach was used with 63 design variables including planform shape, twist and aerofoil thickness, with the grid deformed based on a radial basis function approach. The final shape also had the forward notch-like feature seen in other studies [77, 444] leading to significant reductions in torque. Finally, another study [404] that used finite differences for gradient-based optimisation re-designed the

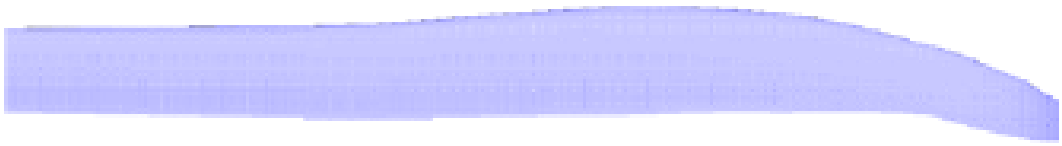

(a) Hover optimised planform

(b) Forward flight optimised planform

Figure 1.42: Comparison of hover and forward flight optimised shapes obtained by Le Pape et al. [213, 214]

aerofoil of the SA349/2 rotor blade aimed at reducing dynamic stall phenomena. Compared to other aerofoil design studies, this study also validated the optimal aerofoil through the three-dimensional calculation of the rotor in hover and forward flight.

Despite the low number of iterations required by gradient-based methods, the computational costs of the optimisation can become excessive when using finite differences for a large number of design variables. A significant improvement in the efficiency of computing the design sensitivities is offered by the adjoint method, which is reviewed along with applications to rotor design in the next section.

Steady Adjoint-Based Method Adjoint methods compute the gradients of all the design variables by solving an additional stiff linear system at the cost of a baseline flow solution. This means that the optimisation cost scales with the number of explicitly defined objective/constraint functions, as each of these functions will require a new adjoint solution. Two key adjoint approaches exist in literature: discrete and continuous. The main differences are that for the continuous approach, the equations are derived directly from the flow equations and then discretised, whereas for the discrete approach, the adjoint equations are derived from the discretised flow equations. The discrete approach gives exact gradients and typically is implemented through the use of automatic differentiation, whereas the continuous approach gives an approximation of the gradients and is usually hand-coded (though simpler). Due to the complexity in developing adjoint solution frameworks [237] and solution of stiff linear systems, very few studies have used adjoint methods for rotor design optimisation.

The use of the adjoint method for steady-state problems can be achieved in hover conditions

by solving the flow in the non-inertial reference frame. This approach has been adopted in the present HMB3 solver which was used by Jimenez-Garcia and Barakos [177] for optimisation of the XV-15 rotor blade and by Biava and Barakos [49] for hybrid-air vehicle design. These studies showed the benefits of using adjoint methods, as they required only 20-30 design cycles for convergence using the optimisation SLSQP algorithm. Jones [186] performed optimisation for the TRAM tiltrotor blade based on unstructured meshes (FUN3D code) and also reported a similar number of iterations for convergence. However, here a large number of design variables was used (123) including aerofoil thickness and camber changes, based on the SNOPT optimisation algorithm. The design improvements showed minor changes in performance (FoM in hover and propulsive efficiency in propeller mode) for a constant thrust, which increased without the thrust constraint, especially in propeller mode. Another adjoint framework was developed at ONERA within the elsA solver and was applied to the 7A and ERATO rotor blades in hover [108]. Similar findings and optimal blade shapes were reported as in non-adjoint gradient based studies [214], however, the authors reported a computational cost reduction by a factor of 7 compared to first-order finite differences. Another study at Stanford University [112] applied a continuous adjoint approach to the design of the Caradonna & Tung rotor blade with the solution approach based on the Euler equations and required 20 design iterations to reach an optimal shape. The adjoint surface torque sensitivity solution along with the pressure distribution from this study is shown in Figure 1.43 showing the high influence of blade shape in the vicinity of the shockwave and round the leading edge. These types of sensitivity maps can inform design decisions even without the use of formal optimisation algorithms.

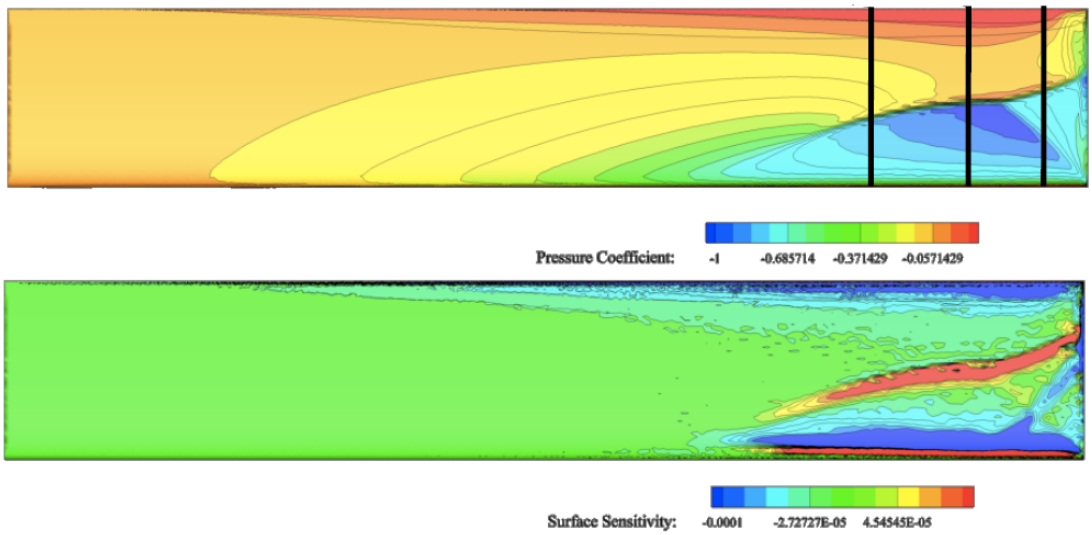

Figure 1.43: Surface pressure distribution and adjoint surface sensitivity map with respect to torque for the Caradonna & Tung rotor blade in hover [112].

Adjoint methods have shown significant improvements in computational costs when compared to finite differences or non-gradient based methods. However, steady-adjoint methods can

only be used for rotors in the non-inertial reference frame and hence are limited to steady hover and/or propeller mode optimisation. A limited number of unsteady adjoint optimisation frameworks, which allow for forward flight optimisation, have also been developed in literature, and are analysed next.

Time-Marching Adjoint Method The only high-fidelity time-marching adjoint optimisation frameworks applied to rotor design have been developed at NASA [279] and University of Wyoming [117]. This is due to the extremely high computational costs associated with unsteady adjoint solutions. The framework of NASA [279] was implemented within the FUN3D CFD solver and was first demonstrated for the TRAM tiltrotor in a pitch-up manoeuvre and the F-15 aircraft with aeroelastic effects (prescribed grid motion). For the tiltrotor case, the optimisation converges in six iterations, however, the flow solution storage requirements for a grid size of 30 million tetrahedral elements and 360 time steps per revolution approach 1.5 terabytes. This is one of the limitations of the time-accurate adjoint, as the entire time history of the solution is required for the adjoint solution (backward integration) which leads to a large disk I/O overhead and storage requirements. These facts make these methods unsuitable for industrial scale optimisation. Certain efforts in literature have been applied to minimize these issues such as advanced checkpoint techniques [403] or solution compression using POD [42]. The methodology was later extended to overset meshes and coupled CFD/CSD analyses, and applied to rotor cases [401, 402] using FUN3D coupled with DYMORE. The optimisation framework considers trim constraints, including the control angles within the design variables and accounts for aeroelastic deformation by solving the coupled adjoint system. The structural sensitivities with respect to the aerodynamic loads were computed using a complex-step approach. Demonstrations are given for the HART-II rotor in terms of forward flight performance [401] and acoustics [402]. In both studies over 70 design parameters are used with a low amount of iterations to achieve a better design (under 12). However, as the optimisation mainly considered localised aerofoil and twist changes, the benefits for the optimal shape, are fairly low (3% reduction in torque) considering the high fidelity of the solution framework. The impact of more drastic changes on the blade shape such as an advanced tip shape was not examined.

A similar framework was developed at the University of Wyoming also based on unstructured meshes, and first applied to unsteady aerofoil optimisation under dynamic stall conditions [240]. The time-marching adjoint framework was also extended to include aeroelastic effects based on coupled NSU3D and beam analysis formulation [257, 258]. The framework was demonstrated for the HART-II rotor blade in hover in both rigid and elastic conditions. A very coarse mesh of 2.32 million grid points was used with a two degree time step, due to the high computational costs associated with unsteady adjoint methods. Similarly as in in the work of NASA [401, 402], only local aerofoil shape and twist changes were considered leading to fairly low objective improvements (2%). Further studies [117] performed optimisation of the

HART-II rotor in forward flight and included aeroacoustics in the adjoint problem based on the FW-H equations. The acoustic optimisation leads to an increase in the required torque, through a significant increase in the thickness in of the inboard aerofoils. Another optimisation was presented with a constraint imposed on the torque coefficient, leading to more realistic aerofoil shapes.

Preliminary research into time-marching adjoint methods has also been performed at Stanford University [93]. An inviscid continuous time-marching adjoint method was developed within the SU2 solver and coupled with UMARC. The method was applied to the UH-60A rotor blade, however, the study was mainly aimed at proving the functionality of the method. Despite, this an improved design was obtained leading to a reduction in torque by 7% compared to the baseline design, with a dihedral-anhedral shape and significantly increased twist at the blade tip. Further extensions of this framework included coupling with dynamic meshes [113] and aeroacoustics [442], although only results for pitching 2D aerofoils and 3D wings were presented.

Time-Spectral Adjoint Method To reduce the computational costs associated with unsteady adjoint-based design time-spectral methods have received particular attention. These methods allow to treat the solution as a large steady problem by assuming periodicity in time, with an additional unsteady source term. The harmonic balance method first gained popularity in the field of turbomachinery [131, 345, 384] but has also been applied to rotorcraft problems [84, 116, 422], as shown in the validation section. While the accuracy and computational costs are directly dependent on the number of harmonic balance modes used in the solution, significant improvements in simulation times are obtainable with only a minor decrease in accuracy when compared to time-marching simulations [267, 422]. The nature of frequency-domain methods also make them attractive for adjoint optimisation studies, as the steady adjoint solver (with certain modifications) can be used. The use of harmonic balance-adjoint methods is still an ongoing subject of research as indicated by recent relevant literature. An inviscid harmonic balance adjoint method has been applied in turbomachinery studies by [150] and was primarily applied to two-dimensional simulations. More recently, Rubino [324, 325] developed a fully-turbulent time-spectral adjoint in SU2, and also applied it only to two-dimensional turbomachinery flows. Following this work, Vitale et al. [389] demonstrated the developed method for three-dimensional studies of multi-stage turbomachinery design. Time-spectral adjoint has also been applied in 2D aerofoil flutter studies [144,311] and 2D aerofoil optimisation under periodic wakes [145].

Very few applications of time-spectral adjoint solvers related to rotor design are present in current literature. This is due to the complexity of edgewise rotor flows, including many complex flow phenomena such as strong compressibility effects, retreating blade separation and multiple near-blade vortex interactions. These aspects make harmonic-balance adjoint systems

difficult to solve due to the high linear system stiffness and requirement for advanced linear solvers. Tatossian et al. [373] applied a Non-Linear Frequency Domain Adjoint method based on the Euler equations to re-design the Caradonna & Tung rotor in hover. In this work, as the hover condition can be considered as steady, only one harmonic balance mode was required. The surface mesh points were directly used as design variables leading to a high number of 4128 variables, with optimiser convergence achieved after 85 iterations. No optimisation results were presented for forward flight conditions. The adjoint equations were derived by hand and solved using a similar pseudo-spectral approach as for the flow solution. In another study, Nadarajah [267], compared time-spectral and time-marching adjoint approaches for optimisation of a pitching aerofoil. Similar optimal shapes were obtained, however, a relative cost of 1:362 was seen between the time-spectral and time-marching adjoint solutions, showing the significant benefits of using time-spectral methods.

The only application of time-spectral adjoint methods to the optimisation of rotor blades in forward flight was presented by Choi et al. [87]. Preliminary studies were conducted regarding performance sensitivity due to the number of harmonic balance modes [84] and design gradient validation [88]. A hover optimisation study for the UH-60A blade was also performed using one harmonic balance mode [88]. The developed framework was then applied to forward flight conditions [87]. The UH-60A blade was optimised in high-speed forward flight using 100 design variables including chord, sweep and twist distributions as well as Hicks-Henne bump functions to alter the aerofoil shapes. Aeroelastic effects were included through a prescribed deformation. Key simplifications were, however, made to reduce the computational cost and reduce the system complexity. Viscous effects were neglected with the CFD solution based on the Euler equations. Only one blade was simulated, thereby, neglecting unsteady wake effects. The framework also employed fairly stringent bounds on the design variables due to the robustness of the mesh generator. A fairly coarse matched grid of 0.5 million nodes was used. Trim constraints were also not considered, as only the thrust was constrained. These simplifications were mainly imposed to reduce the numerical modelling complexity, leading to improved robustness and convergence properties. During the optimisation process, nine time-spectral instances were used and the adjoint linear system was solved using an ILU preconditioned GMRES solver. The authors also noted that this solver stagnated for larger problems and required additional multigrid preconditioning to restore good convergence properties. The optimal blade shape with a reduced tip area, as shown in Figure 1.44 led to a reduction of 7.4% in torque compared to the baseline UH-60A blade. The performance improvement reduced to 5% after validation with a high-fidelity Navier-Stokes CFD method and four-bladed solution. The highly-tapered design was not evaluated in hover conditions and could potentially lead to a more abrupt stall at higher thrust coefficients, typical for tapered designs.

More recently, Kim et al. [6] extended the framework developed by Choi [87] to include coupled fluid-structure interaction, although no formal optimisation study was shown. The study

(a) Baseline UH-60A planform

(b) Optimised planform

Figure 1.44: Baseline and forward flight optimised UH-60A planforms with a reduced blade tip area [87]

of Choi et al. [87] showed that the inclusion of viscous and unsteady wake effects within the time-spectral adjoint framework could be beneficial increasing the fidelity of the optimisation process.

1.2.2.5 Current Limitations in Rotor Design

The majority of rotor blades that fly today, were mainly designed using low-fidelity analytical tools and experimental studies. The use of higher-fidelity methods in industry is increasing, however, these are still rarely coupled with formal optimisation methods. Typically, rotor design has been performed in a parametric manner with design changes based on engineering judgement. This was also the case for advanced BERP IV, Blue-Edge and CMRB planforms (twist distributions optimised for Blue-Edge and CMRB). Optimisation frameworks, however, have also been of interest in industry and have been developed at Leonardo [245], Airbus [223] and Bell [423]. Elements of optimisation were also present in studies at BOEING [168]. The majority of these studies, however, were based on low-fidelity methods in hover and forward flight or high-fidelity methods only in hover, as the flow can be solved as steady. The information regarding design processes in industry is fairly scarce in open literature, and significant developments may have occurred aimed at improving the fidelity of the optimisation frameworks. However, the problem of optimising unsteady flows, required for forward flight conditions, is still a challenge even in the rotorcraft research community, and hence it is unlikely that such methods are used in industry. Forward flight optimisation has been performed in industry [223, 245] based on low/mid fidelity models, however, as shown by Wilke [412] and Bailly [28], these models can give significantly different optimal designs when compared to high-fidelity CFD analyses. High-fidelity unsteady optimisation frameworks are usually associated with extremely high computational costs, as in the case of non-gradient based optimisation or time-marching adjoint methods, making them unsuitable for industrial rotor design. Frameworks based on the time-spectral adjoint method offer a good compromise between solution cost and accuracy, however, these methods

have not been developed to a level required for high-fidelity rotor design optimisation.

The current use of optimisation frameworks in industry and research institutes, still heavily relies on engineering judgement, and this is unlikely to change in the near future, due to the complexity of rotor design. Engineering expertise is required for selecting the blade surface parameterisation, objective and constraint functions which drive the optimisation process. The design space and variables are usually selected based on known design features that have a large impact on the performance such as blade twist, sweep, anhedral, chord and aerofoil shape. The majority of studies in literature simply minimize power whilst constraining thrust, whereas multi-disciplinary aspects such as vibration, noise, aeroelastic stability and control loads are not considered. The optimal aerodynamic design is typically validated using a high-fidelity CFD method or experiment and altered through engineering judgment to ensure that key design constraints at met, which were not considered during the optimisation process. High-fidelity CFD methods are required within optimisation frameworks to ensure that the optimal blade design achieves the expected aerodynamic performance improvements and shows potential problems with the new design early in the design process. For example, the neglection of unsteady wake effects by Choi et al. [87] would not have taken into account changes in loading due to near blade-vortex interaction. However, due to the nature of time-spectral methods, localised effects such as BVIs and dynamic stall are difficult to capture and require a high number of harmonic balance modes. Furthermore, the importance of including viscous effects has been shown in many CFD prediction studies [10, 109, 294], and is especially significant for advanced planform shapes. The neglection of viscosity may lead to planforms with higher blade area, due to the neglection of profile power.

Another aspect is the issue of thrust-weighted solidity. This parameter was disregarded by Perry [299] based on low-fidelity predictions, however, is still constrained to be constant in many optimisation studies [108, 158, 214, 221]. A blade with higher thrust-weighted solidity may obtain higher performance, simply from an aerodynamic perspective. For example, increasing the local thickness to chord ratio leads to weaker compressibility effects on the advancing side, but due to the higher chord will also lead to higher local loading and profile drag. The interaction of these aerodynamic features will not be captured correctly if thrust-weighted solidity is maintained, and will typically lead to blade tips with lower blade area. The misuse of thrust-weighted solidity, however, has not been validated using high-fidelity CFD methods.

Based on the current studies in literature, fully coupled multi-disciplinary optimisation frameworks that include aerodynamic and structural design variables as well as safety, acoustic and dynamic constraints are unlikely to appear in the near future, especially when considering unsteady flow problems. This is due to the excessive modelling complexity and excessive computational costs. In terms of aerodynamic design, time-spectral methods offer a good compromise between solution fidelity and solution cost. It is difficult to propose a design methodology that will capture all the necessary design objectives and constraints at a range of conditions. How-

ever, the use of high-fidelity aerodynamic models within the optimisation framework, will inform better decisions based on engineering judgement regarding other disciplines and will lead to more practical rotor designs.

1.3 Aims and Objectives of Thesis

The main aim of this thesis is to expand the current knowledge of rotor design through the use of high-fidelity CFD and optimisation methods. Based on the findings of the literature review, the thesis objectives were set as follows:

1. Validate the HMB3 solver for performance predictions in hover and forward flight using modest computational resources including a range of modelling sensitivity studies.
2. Examine different rotor designs in terms of disk loading, advancing and retreating side features and assess the impact of blade anhedral on the rotor performance.
3. Assess the validity of different performance metrics and the thrust-weighted solidity parameter when comparing different rotor designs.
4. Develop an overset fully-turbulent adjoint harmonic balance optimisation framework for optimisation of unsteady rotor flows.
5. Apply the newly developed optimisation framework in a real-life rotor design study.

1.4 Novelty of Current Research

The primary novelty of the research is the development of an optimisation framework based on an overset fully-turbulent adjoint harmonic balance method. The framework builds on the work of Choi et al. [87] where viscous and unsteady wake effects were neglected, and simulations were performed for matched grids. The demonstration of the framework is performed for a real-life rotor design (AH-64A) and includes hover and forward flight requirements.

Secondary novelty is obtained through examination of different performance metrics, solidity effects and analysis of various rotor designs. The findings of Perry [299] regarding thrust-weighted solidity are examined in the present research through a solidity study using the rotor blades from the experiments of Yeager et al. [429]. Further analysis of different rotor designs and the optimisation results show the benefits and drawbacks of rotor designs with an off-loaded blade tip, anhedral effects on the rotor loads and influence of blade geometry on the strength of the advancing blade shockwave (in particular regarding the rectangular and BERP-like blade tips). The identification of novel features for use on blades such as anhedral/dihedral, forward-backward sweep and variable non-linear blade twist are also adding to the novelty of thesis.

1.5 Structure of Thesis

The structure of the thesis is as follows:

Chapter 1 presents the motivation behind the current research and a detailed literature review on current performance validation and current rotor design methodologies used in industry and research institutes. The review on rotor design includes experimental and numerical parametric studies, industrial rotor design and the use of optimisation methods in rotor design.

Chapter 2 describes the HMB3 solver including the CFD solver formulation, turbulence modelling, hover formulation, rotor trimming routines and the overset grid method.

Chapter 3 presents the high-fidelity rotor optimisation framework including, the adjoint, harmonic balance methods and coupling with the overset grid method. Other components of the framework are also presented, such as the blade surface parameterisation, gradient-based optimiser and mesh deformation method.

Chapter 4 presents the CFD modelling strategy including different blade geometries (LBL, LBERP, PSP, AH-64A), grid generation and computational setups for hover and forward flight simulations

Chapter 5 analyses CFD validation of different rotor blades in hover along with turbulence modelling and solution methodology sensitivity studies.

Chapter 6 describes CFD validation of different rotor blades in forward flight along with turbulence modelling, grid refinement, installation effects and shaft angle sensitivity studies.

Chapter 7 presents preliminary design analyses based on the CFD simulations used for validation. Firstly, typically used performance metrics, such as figure of merit and lift-to-drag ratio are assessed for comparing different rotor designs. Next, a solidity study is performed for the LBL and LBERP blades, examining the effect of matching the thrust-weighted solidity parameter. Finally, the different rotor designs simulated for CFD validation, are compared in terms of rotor loads, wakes and advancing/retreating side aerodynamic characteristics.

Chapter 8 presents preliminary investigations using the overset fully-turbulent adjoint harmonic balance optimisation framework. Firstly, a sensitivity study is performed regarding the number of harmonic balance modes required to accurately capture the rotor blade loads. Secondly, design variable gradient validation is performed, by comparing the adjoint sensitivity results with finite differences. Finally, a demonstration of the framework is shown for the optimisation of the HH02 aerofoil in DM/DT mode.

Chapter 9 presents the application of the optimisation framework to a real-life rotor blade design - the AH-64A rotor blade. Firstly, the blade is optimised in high-loading hover conditions. Following this, forward-flight optimisation is performed whilst constraining the key design features responsible for performance improvements in hover. Finally, the final design is validated using time-marching CFD methods.

Chapter 10 describes the conclusions of the thesis and future work.

Chapter 2

HMB3 Solver

This chapter describes the HMB3 flow solver including the discretisation method and turbulence modeling. The hover formulation along with rotor trimming routines in hover and forward flight are also described. Finally, the overset grid method, procedure for DM/DT calculations and quantities used for wake visualisation are presented.

2.1 Solver Formulation

All simulations within this work a performed using the Helicopter Multi-Block (HMB) solver [358, 359]. The solver is based on a control volume based method and was initially developed for solving rotorcraft problems on structured grids. However, over the years, HMB3 has been used for a variety of flows and has been extended to handle overset grids, sliding planes as well as unstructured meshes. The HMB3 solves the compressible Navier-Stokes equations in the 3D Cartesian frame of reference (with a space transformation for curvilinear grids). The Navier-Stokes equations consist of Partial Differential Equations (PDEs) describing the laws of conservation:

- Conservation of mass (Continuity equation)
- Conservation of momentum (Newton's 2nd Law)
- Conservation of energy (1st Law of Thermodynamics)

The continuity equation states that the mass must be conserved. In Cartesian coordinates, x_i, this is written as:

$$\frac{\partial \rho}{\partial t} + \frac{\partial (\rho u_i)}{\partial x_i} = 0 \tag{2.1}$$

Newton's 2^{nd} Law states that linear momentum must be conserved, and is expressed as:

$$\frac{\partial(\rho u_i)}{\partial t} + \frac{\partial(\rho u_i u_j)}{\partial x_j} = \rho f_i - \frac{\partial p}{\partial x_i} + \frac{\partial \tau_{ij}}{\partial x_j}, \tag{2.2}$$

where f_i represents any acting body force, and τ_{ij} is the viscous stress tensor, which is defined as:

$$\tau_{ij} = \mu \left[\left(\frac{\partial u_i}{\partial x_j} + \frac{\partial u_j}{\partial x_i} \right) - \frac{2}{3} \delta_{ij} \frac{\partial u_k}{\partial x_k} \right], \tag{2.3}$$

where μ is the molecular viscosity and δ_{ij} the Kronecker delta, which is defined as:

$$\delta_{ij} = \begin{cases} 1, & \text{if } i = j, \\ 0, & \text{if } i \neq j. \end{cases} \tag{2.4}$$

For viscosity, Sutherland's law is used:

$$\mu = \mu_0 \left(\frac{T}{T_{ref}} \right)^{\frac{3}{2}} \left(\frac{T_{ref} + T_S}{T + T_S} \right) \tag{2.5}$$

where T is the temperature of the fluid, T_{ref} is a reference temperature ($T_{ref} = 273.15K$), μ_{ref} is the viscosity at that reference temperature ($\mu_{ref} = 1.716 \times 10^{-5} kg/ms$) and T_S is the Sutherland temperature ($T_S = 110.4K$).

The 1^{st} Law of Thermodynamics states that the total energy of an isolated system is constant. This can be written as:

$$\frac{\partial \rho E}{\partial t} + \frac{\partial}{\partial x_j} \left[u_j (\rho E + p) \right] - \frac{\partial}{\partial x_j} \left(u_i \tau_{ij} - q_{ij} \right) = 0, \tag{2.6}$$

where E is the total energy of the fluid per unit mass, and $\mathbf{q}$ is the heat flux vector. The total energy per unit mass is defined as:

$$E = \left[e + \frac{1}{2} u_i u_i \right], \tag{2.7}$$

where $\frac{1}{2} u_i u_i$ represents the kinetic energy per unit mass. The heat flux vector is calculated using Fourier's Law:

$$q_i = -k_h \frac{\partial T}{\partial x_i}, \tag{2.8}$$

where k_h is the heat transfer coefficient. An ideal gas approximation is assumed and is used to relate pressure and density. By default dry air is considered, with a specific gas constant, R_{sp}, of 287.058 $\frac{J}{KgK}$.

$$p = \rho R_{sp} T \tag{2.9}$$

2.1.1 Vector Form of Conservation Laws

These three laws of conservation can be combined and written as follows:

$$\frac{\partial \mathbf{W}}{\partial t} + \frac{\partial \left(\mathbf{F}^i + \mathbf{F}^v\right)}{\partial x} + \frac{\partial \left(\mathbf{G}^i + \mathbf{G}^v\right)}{\partial y} + \frac{\partial \left(\mathbf{H}^i + \mathbf{H}^v\right)}{\partial z} = \mathbf{S}, \tag{2.10}$$

where $\mathbf{W}$ is the vector of conserved variables:

$$\mathbf{W} = \left(\rho, \rho u, \rho v, \rho w, \rho E\right)^T, \tag{2.11}$$

In the above ρ is the density, u, v and w are the components of velocity given by the Cartesian velocity vector $\mathbf{U} = (u, v, w)$. Finally, E is the total energy per unit mass. The superscripts i and v are used to denote the inviscid and viscous components of the flux vectors $\mathbf{F}$, $\mathbf{G}$ and $\mathbf{H}$, in three directions (x,y,z).

The inviscid flux vectors F^i, G^i and H^i are given by:

$$\mathbf{F}^i = \left(\rho u, \rho u^2 + p, \rho uv, \rho uw, u\left(\rho E + p\right)\right)^T \tag{2.12}$$

$$\mathbf{G}^i = \left(\rho v, \rho uv, \rho v^2 + p, \rho vw, v\left(\rho E + p\right)\right)^T \tag{2.13}$$

$$\mathbf{H}^i = \left(\rho w, \rho uw, \rho vw, \rho w^2 + p, w\left(\rho E + p\right)\right)^T \tag{2.14}$$

while the viscous flux vectors, F^v, G^v and H^v, contain terms for the heat flux and viscous forces exerted on the body and can be represented by:

$$\mathbf{F}^v = \frac{1}{\mathrm{Re}}\left(0, \tau_{xx}, \tau_{xy}, \tau_{xz}, u\tau_{xx} + v\tau_{xy} + w\tau_{xz} + q_x\right)^T \tag{2.15}$$

$$\mathbf{G}^v = \frac{1}{\mathrm{Re}}\left(0, \tau_{xy}, \tau_{yy}, \tau_{yz}, u\tau_{xy} + v\tau_{yy} + w\tau_{yz} + q_y\right)^T \tag{2.16}$$

$$\mathbf{H}^v = \frac{1}{\mathrm{Re}}\left(0, \tau_{xz}, \tau_{yz}, \tau_{zz}, u\tau_{xz} + v\tau_{yz} + w\tau_{zz} + q_z\right)^T \tag{2.17}$$

where the term τ_{ij} represents the viscous stress tensor and q_i the heat flux vector. In equation 2.10, S is the source term, which is set to 0 in most calculations. However, for rotors in hover and axial flight, typically a non-inertial reference frame is used, and a source term is added (hover formulation described later).

The HMB3 solver uses a non-dimensional form based on four reference variables: length L_{ref} , a density ρ_{ref}, a velocity U_{ref} and a temperature T_{ref}. The values of the reference variables are arbitrary, and are usually chosen depending on the nature of the problem. The following non-dimensionalisation procedure is used:

$$x = \frac{x^*}{L^*}, \qquad y = \frac{y^*}{L^*}, \qquad t = \frac{t^*}{L^*/V_\infty^*},$$

$$u = \frac{u^*}{V_\infty^*}, \qquad v = \frac{v^*}{V_\infty^*}, \qquad \mu = \frac{\mu^*}{\mu_\infty^*},$$

$$\rho = \frac{\rho^*}{\rho_\infty^*}, \qquad p = \frac{p^*}{\rho_\infty^* V_\infty^{*2}}, \qquad T = \frac{T^*}{T_\infty^*}, \qquad e = \frac{e^*}{V_\infty^{*2}}. \tag{2.18}$$

2.1.2 Discretisation Method

The Navier-Stokes equations used in the Helicopter Multi-Block solver which written in differential form of equation 2.10 can also be written in the Arbitrary Lagrangian Eulerian (ALE) formulation for time-dependent domains with moving boundaries:

$$\frac{d}{dt}\int_{V(T)} \mathbf{W} dV + \int_{\partial V(T)} (\mathbf{F^i}(\mathbf{W}) - \mathbf{F^v}(\mathbf{W}))\mathbf{n} dS = S \tag{2.19}$$

The above equations form a system of conservation laws for any time-dependent control volume $V(T)$ with boundary $\partial V(T)$ and outward unit normal $\mathbf{n}$. F^i and F^v are the inviscid and viscous fluxes respectively. The fluxes include the effect of a time-dependent domain, i.e. a mesh velocity is included in the contra-variant velocity components. In the absence of volume forces and in an inertial frame of reference, the source term S = 0. For hovering rotors, a non-inertial frame of reference is used for which S $\neq$ 0.

The Navier-Stokes equations 2.10 are discretised using a cell-centred finite volume approach on structured multi-block grids. The spatial discretisation leads to a series of differential equations in time,

$$\frac{d}{dt}\left(\mathbf{W}_{i,j,k} V_{i,j,k}\right) = -\mathbf{R}_{i,j,k}\left(\mathbf{W}\right). \tag{2.20}$$

where **W** and **R** are the vectors of cell conserved variables and residuals respectively. The convective terms are discretised using Osher's upwind scheme (Osher et al. [288]) for its robustness, accuracy, and stability properties. MUSCL variable extrapolation [386] is used to provide second-order accuracy with the Van Albada limiter [380] to prevent spurious oscillations around shock waves. The central differencing spatial discretisation method is used for the viscous terms. Boundary conditions are set using ghost cells in the exterior of the computational domain.

2.1.3 Steady State Solver

The system of equations defined in Equation 2.20 is integrated in time to reach a steady state solution using an implicit time-marching scheme, defined by

$$\frac{\mathbf{W}_{i,j,k}^{n+1} - \mathbf{W}_{i,j,k}^{n}}{\Delta t} = -\frac{1}{V_{i,j,k}} \mathbf{R}_{\mathbf{i,j,k}} \left(\mathbf{W}_{i,j,k}^{n+1} \right), \tag{2.21}$$

where $n+1$ denotes the time $(n+1) * \Delta t$. Equation 2.21 represents a system of non-linear algebraic equations and to simplify the solution procedure, the flux residual $\mathbf{R}_{\mathbf{i,j,k}} \left(\mathbf{W}_{\mathbf{i,j,k}}^{\mathbf{n+1}} \right)$ is linearised in time as follows,

$$\begin{aligned} \mathbf{R}_{\mathbf{i,j,k}} \left(\mathbf{W}^{n+1} \right) &= \mathbf{R}_{\mathbf{i,j,k}} \left(\mathbf{W}^{n} \right) + \frac{\partial \mathbf{R}_{\mathbf{i,j,k}}}{\partial t} \Delta t + O(\Delta t^2) \\ &\approx \mathbf{R}_{\mathbf{i,j,k}}{}^{n} \left(\mathbf{W}^{n} \right) + \frac{\partial \mathbf{R}_{\mathbf{i,j,k}}}{\partial \mathbf{W}_{\mathbf{i,j,k}}} \frac{\partial \mathbf{W}_{\mathbf{i,j,k}}}{\partial t} \Delta t \\ &\approx \mathbf{R}_{\mathbf{i,j,k}}{}^{n} \left(\mathbf{W}^{n} \right) + \frac{\partial \mathbf{R}_{\mathbf{i,j,k}}}{\partial \mathbf{W}_{\mathbf{i,j,k}}} \Delta \mathbf{W}_{\mathbf{i,j,k}}, \end{aligned} \tag{2.22}$$

where $\Delta \mathbf{W}_{\mathbf{i,j,k}} = \mathbf{W}_{\mathbf{i,j,k}}{}^{n+1} - \mathbf{W}_{\mathbf{i,j,k}}{}^{n}$. Equation2.21 now becomes the following linear system

$$\left[\frac{V_{i,j,k}}{\Delta t} \mathbf{I} + \frac{\partial \mathbf{R}_{\mathbf{i,j,k}}}{\partial \mathbf{W}_{\mathbf{i,j,k}}} \right] \Delta \mathbf{W}_{\mathbf{i,j,k}} = -\mathbf{R}_{i,j,k}^{n} \left(\mathbf{W}^{\mathbf{n}} \right). \tag{2.23}$$

Solving this linear system of equations using a direct method is prohibitive as the number of equations becomes large. To avoid this problem, an iterative Generalised Conjugate Residual (GCR) method is used as it is capable of solving large systems of equations efficiently in term of time and memory requirements. This is used in conjunction with a Block Incomplete Lower-Upper (BILU) factorisation method [24] used as a pre-conditioner for the system of equations. At the initial stages of the solution, a number of explicit iterations are performed to smooth out the initial flow. An approximate flux Jacobian is used (first order discretisation) leading to reduced CPU time and memory requirements [70], through a reduced size of the linear system and a more diagonally dominant Jacobian. To improve parallel efficiency, the BILU preconditioner is applied in a decoupled manner between grid blocks to reduce the parallel communication overhead.

The steady state solver for the turbulent case is formulated and solved in an identical manner to that described above for the mean flow. For the turbulence model equations the flux residual also contains the dissipation source term, however, the production term is solved explicitly. The eddy viscosity is calculated from the turbulent quantities as specified by the model and is used to advance both mean flow and turbulence solutions.

2.1.4 Unsteady State Solver

The implicit dual-time stepping method of Jameson [165] is used for time-accurate calculations. The residual is redefined to obtain a steady state equation which can be solved using acceleration techniques. Using a three-level discretisation of the time derivative, the updated flow solution is calculated by solving

$$\mathbf{R}^*_{i,j,k} = \frac{3\mathbf{w}^{n+1}_{i,j,k} - 4\mathbf{w}^{n}_{i,j,k} + \mathbf{w}^{n-1}_{i,j,k}}{2\Delta t} + \mathbf{R}_{i,j,k}(\mathbf{w}^{k_m}_{i,j,k}, \mathbf{q}^{k_t}_{i,j,k}) = 0 \tag{2.24}$$

$$\mathbf{Q}^*_{i,j,k} = \frac{3\mathbf{q}^{n+1}_{i,j,k} - 4\mathbf{q}^{n}_{i,j,k} + \mathbf{q}^{n-1}_{i,j,k}}{2\Delta t} + \mathbf{Q}_{i,j,k}(\mathbf{w}^{l_m}_{i,j,k}, \mathbf{q}^{l_t}_{i,j,k}) = 0. \tag{2.25}$$

Here k_m, k_t, l_m and l_t give the time level of the variables used in the spatial discretisation. If $k_m = k_t = l_m = l_t = n+1$ then the mean and turbulent quantities are advanced in real time in a fully coupled manner. However, if $k_m = l_m = l_t = n+1$ and $k_t = n$ then the equations are advanced in sequence in real time, i.e. the mean flow is updated using frozen turbulence values and then the turbulent values are updated using the latest mean flow solution.

This non-linear system of equations can be solved by introducing an iteration through pseudo-time, τ to the steady state. This is given by:

$$\frac{\mathbf{w}^{n+1,m+1}_{i,j} - \mathbf{w}^{n+1,m}_{i,j}}{\Delta\tau} + \frac{3\mathbf{w}^{k_m}_{i,j} - 4\mathbf{w}^{n}_{i,j} + \mathbf{w}^{n-1}_{i,j}}{2\Delta t} + \mathbf{R}_{i,j}(\mathbf{w}^{k_m}_{i,j}, \mathbf{q}^{k_t}_{i,j}) = 0 \tag{2.26}$$

$$\frac{\mathbf{q}^{n+1,m+1}_{i,j} - \mathbf{q}^{n+1,m}_{i,j}}{\Delta\tau} + \frac{3\mathbf{q}^{l_t}_{i,j} - 4\mathbf{q}^{n}_{i,j} + \mathbf{q}^{n-1}_{i,j}}{2\Delta t} + \mathbf{Q}_{i,j}(\mathbf{w}^{l_m}_{i,j}, \mathbf{q}^{l_t}_{i,j}) = 0. \tag{2.27}$$

where the $m-th$ pseudo-time iteration at the $n+1th$ real time step are denoted by $\mathbf{w}^{n+1,m}$ and $\mathbf{q}^{n+1,m}$ respectively. The unsteady formulation recovers the steady state solver if the residual term $\mathbf{R}^*_{i,j,k}$ is replaced $\mathbf{R}_{\mathbf{i,j,k}}$ term in equation 2.26.

2.2 Turbulence Modelling

To account for turbulence, the full Navier-Stokes equations must be solved (known as Direct Numerical Simulation). This means that the smallest turbulent length and time scales in the solution must be resolved, which leads to extremely high computational costs due to grid spacing and temporal discretisation requirements. In rotary-wing flows, the turbulent length scale may approach an order of rotor radii in the rotor wake (which is larger than the largest turbulent eddies in the flowfield) [75], whereas very small length scales approaching the Kolmogorov scale are present in the rotor boundary layer dominated by viscous dissipation. The presence of large turbulent length scales in the rotor wake can lead to an imbalance between the turbulence production and dissipation terms in the rotor wake [75], leading to high eddy viscosity values. The ratio between the inertial and viscous forces known as the Reynolds number, which also governs

the ratio between the smallest and largest length scales present in the flowfield ($Re^{3/4}$). This limits its DNS simulations to very low Reynolds numbers (order of $Re^{9/4}$ grid points required) based on today's computational resources. A simplification can be made in the form of Large-Eddy Simulation (LES), where the small-length scales (assumed to be isotropic) are modelled through a sub-grid scale model and the large scale structures are directly resolved. This technique, however, is still too computationally expensive due to spatial and temporal spacing requirements. The most common modelling approach today, is through the Reynolds Averaged Navier-Stokes (RANS) equations, due to reduced computational costs. The RANS equations, described in the next subsection, are based on a statistical description of all the turbulent scales. This method has many limitations, including high numerical diffusion and need for empirical relationships to model turbulence. To bridge the gap between LES and RANS simulations, hybrid turbulence models such as Detached Eddy Simulation (DES) can be used and have seen some success in rotary-wing flows [75]. The DES model switches between RANS in the near-body region and LES in the rotor wake region, based on a grid length scale. However, due to multiple flow solutions required in rotor design in conjunction with optimisation methods, the present research will be limited to the RANS modelling approach (although DES, LES approaches are also available within the HMB3 solver).

2.2.1 Reynolds Averaging

To present the Reynolds-Averaged Navier-Stokes approach, concepts such as the Reynolds Decomposition and Reynolds Averaging need to be introduced. The Reynolds Decomposition represents each quantity as the sum of a mean value and a fluctuating component:

$$\phi = \overline{\phi} + \phi^{'} \tag{2.28}$$

This formulation is then inserted into the conservation equations and a process known as Reynolds Averaging is performed. A Favre (density-weighted) based averaged is used to avoid flucutations between density and other variables, denoted at $\hat{\phi} = \overline{\rho\phi}/\overline{\rho}$ where $\phi = \overline{\phi} + \phi^{'} = \hat{\phi} + \phi^{''}$. By time-averaging the mass, momentum and energy equations the Reynolds-Averaged Navier-Stokes (RANS) equations are obtained:

$$\frac{\partial \overline{\rho}}{\partial t} + \frac{\partial (\overline{\rho}\hat{u}_j)}{\partial x_j} = 0 \tag{2.29}$$

$$\frac{\partial (\overline{\rho}\hat{u}_i)}{\partial t} + \frac{\partial (\overline{\rho}\hat{u}_i\hat{u}_j)}{\partial x_j} = -\frac{\partial \overline{p}}{\partial x_i} + \frac{\partial}{\partial x_j}(\overline{\tau_{ij}} + \tau_{ij}^R) \tag{2.30}$$

$$\frac{\partial \overline{\rho}\hat{E}}{\partial t} + \frac{\partial [u_j(\overline{\rho}\hat{E} + \overline{p})]}{\partial x_j} = \frac{\partial}{\partial x_j}(\overline{\tau_{ij}}\hat{u}_i + \overline{\tau_{ij}u_i^{''}}) - \frac{\partial}{\partial x_j}(\overline{q_j} + c_p\overline{\rho u_j^{''}T^{''}} - \hat{u}_i\tau_{ij}^R + \frac{1}{2}\overline{\rho u_i^{''}u_i^{''}u_j^{''}}) \tag{2.31}$$

The continuity equation remains the same since it is linear with respect to velocity. However, extra terms appear in the momentum and energy equations due to the non-linearity of the convection term. These terms include the Reynolds Stresses τ_{ij}^R, which are defined in tensor notation as being equivalent to $-\overline{\rho u_i'' u_j''}$. The calculation of the terms in the Reynolds Stress Tensor from known mean quantities is the main problem of turbulence modelling, due to a higher number of unknowns than the number of equations, which is known as the turbulence closure problem. Other terms in the energy equation that require further modelling include the turbulent heat flux, molecular diffusion and turbulent transport terms.

One common approach to close the RANS equations is based on the Boussinesq approximation, which assumes that the Reynolds Stress Tensor is aligned with and proportional to the mean rate of strain tensor, through the introduction of eddy viscosity μ_t as follows:

$$\tau_{ij}^R = -\overline{\rho u_i'' u_j''} = 2\mu_t S_{ij} - \frac{2}{3}\delta_{ij}k \tag{2.32}$$

where k is the specific kinetic energy of the fluctuations and S_{ij} is the traceless strain rate tensor:

$$S_{ij} = \frac{1}{2}\left(\frac{\partial u_i}{\partial x_j} + \frac{\partial u_j}{\partial x_i} - \frac{2}{3}\delta_{ij}\frac{\partial u_k}{\partial x_k}\right) \tag{2.33}$$

Eddy viscosity, μ_t, is a scalar and consequently, the Reynolds stress components are linearly proportional to the mean strain-rate tensor. The six unknowns of the Reynolds stress tensor are now represented as a single unknown μ_t. To compute the eddy viscosity, further modeling is required, and is typically computed by solving additional transport equations.

Various turbulence modelling formulations exist in literature, however, the present research primarily uses the two-equation k-ω SST turbulence model [251], due to its known good performance in adverse pressure gradients and flows with mild separation. Comparisons with the baseline k-ω model of Wilcox [411] are presented for a rotor in hover in Chapter 5.1.2, whereas transitional effects using the three-equation k-ω SST-γ turbulence model [252] are presented in Chapter 5.1.5. The k-ω SST and k-ω SST-γ turbulence models are discussed in more detail in the next subsections.

2.2.2 The k-ω SST Turbulence Model

In 1988, Wilcox [411] developed the popular k-ω turbulence model to close the RANS equations with two transport equations for turbulent kinetic energy k and the k-specific rate of dissipation ω. The eddy viscosity is obtained by,

$$\mu_t = \rho\frac{k}{\omega} \tag{2.34}$$

In 1994, Menter [251] proposed the blending between of the k-ω and the k-ε turbulence models. The aim was to combine the robust and accurate formulation of the k-ω model near the wall with the lack of sensitivity to free-stream values of the k-ε model far away from it. The

transport equations for k-ω type models are as follows:

$$\begin{aligned}\frac{\partial}{\partial t}(\rho k)+\frac{\partial}{\partial x_j}(\rho U_j k) &= \frac{\partial}{\partial x_j}\left[\left(\mu+\frac{\mu_t}{\sigma_\omega}\right)\frac{\partial k}{\partial x_j}\right]+\rho\left(P_k-\beta^*\omega k\right)\\ \frac{\partial}{\partial t}(\rho\omega)+\frac{\partial}{\partial x_j}(\rho U_j \omega) &= \frac{\partial}{\partial x_j}\left[\left(\mu+\frac{\mu_t}{\sigma_\omega}\right)\frac{\partial \omega}{\partial x_j}\right]+\rho\left(\frac{\alpha}{\upsilon_t}P_\omega-\frac{\beta}{\beta^*\omega^2}\right)+\rho S_l\end{aligned} \tag{2.35}$$

Menter's baseline k-ω model [251] (compared to the k-ω Wilcox model [411]) switches between the k-ω and k-ε turbulence models through a blending function which is set to one in the near-wall region and zero away from the surface. Additionally, the k-ω SST model makes use of the Bradshaw assumption, which assumes that the shear stress in the boundary layer is proportional to the turbulent kinetic energy. This assumption is implemented through a limiter on the eddy viscosity and is only invoked in the boundary layer region through a blending function. The presence of this eddy viscosity limiter in the k-ω SST model significantly improves turbulent shear stress predictions for adverse pressure gradients [251]. A detailed description of the formulation of the baseline k-ω and k-ω SST turbulence models can be found in [251] including boundary conditions and closure coefficients.

2.2.3 The k-ω SST-γ Turbulence Model

To model transitional effects, Menter developed models based on the local correlation concept, which uses experimental correlations within the transport equations through local variables [252]. Initially, a four-equation model was developed including two additional transport equations for turbulence intermittency, γ, and transition onset momentum thickness Reynolds number, Re_θ [253]. Later the equation for Re_θ was avoided and the transition onset was computed algebraicly [252]. The turbulent intermittency factor was used to control the onset of transition and varies for 0 (laminar flow) to 1 (turbulent flow). The additional transport equation for γ is as follows:

$$\frac{\partial}{\partial t}(\rho\gamma)+\frac{\partial}{\partial x_j}(\rho U_j\gamma)=P_\gamma-E_\gamma+\frac{\partial}{\partial x_j}\left[\left(\mu+\frac{\mu_t}{\sigma_\gamma}\right)\frac{\partial\gamma}{\partial x_j}\right] \tag{2.36}$$

The full formulation of the k-ω SST-γ model can be found in [252]. The model implemented within HMB3 is calibrated for low-Mach number flows as in [92] and neglects cross-flow transition terms, however, the model is still proven to give reasonable results as presented in Chapter 5.1.5.

2.3 Hover Formulation

Periodicity of the flow in azimuthal direction can be used to reduce the computational expense, i.e. for N-bladed rotor a $1/N$ segment of the complete domain with periodic boundary conditions can be modelled [359]. To account for the rotor rotation, a non-inertial reference frame is used. A combination of a mesh velocity in the ALE formulation of the Navier-Stokes equations and source terms for the momentum equations are used to represent the centripetal and Coriolis accelerations. The mesh velocity corresponds to mesh rotation in the direction of the rotor, i.e a reference velocity $\vec{u_{ref}} = \omega \times \vec{r}$ is introduced, where $\vec{r}$ is the position vector of a cell. A source term for the momentum equations is also introduced and has the form:

$$S = [0, -\rho\,\omega \times \vec{u_h}, 0]^T \tag{2.37}$$

where $\vec{u_h}$ is the velocity field in the present rotor-fixed frame of reference.

The source-sink model is used to impose boundary conditions for rotors in hover. In this boundary model, the rotor flow-field is computed using a three-dimensional source-sink singularity, with a strength determined from the rotor thrust and simple momentum theory. The singularity is located on the rotor axis of rotation and at the rotor disk plane. The sink pulls the flow from the surrounding into the computational domain resulting in a velocity given by:

$$W_{in} = -\frac{1}{8}\sqrt{C_{T_{UK}}}\left(\frac{R}{d}\right)^2 \tag{2.38}$$

where $d^2 = x_p^2 + y_p^2 + z_p^2$ is the distance of an arbitrary point (x_p, y_p, z_p) from the rotor centre of rotation. The magnitude of the total incoming velocity W_{in} is normalised with the rotor tip speed M_{tip}. Assuming that the far-field exit velocity is uniform, its magnitude can be determined from 1-D momentum theory, by relating the outflow momentum to the rotor thrust coefficient, $C_{T_{UK}}$ by:

$$W_{out} = -\sqrt{\frac{C_{T_{UK}}}{4}}\Big/\left(\frac{R_{out}}{R}\right)^2 \tag{2.39}$$

where the radius of the outflow region is set through an empirical relationship given by:

$$R_{out} = R(0.78 + 0.22e^{H_{out}/R}) \tag{2.40}$$

where H_{out} is the distance of the outflow boundary from the rotor plane. The strength of the sink is chosen to balance the mass flow into, and out of the computational domain, through setting a target thrust coefficient, $C_{T_{UK}}$ based on experimental measurements or user estimated values.

2.4 Trimming Methods

Trimming methods are key in rotorcraft computations, to ensure that a target thrust coefficient is met, and that the aircraft does not undergo excessive pitching or rolling moments at the examined flight condition. The hover and forward flight trimming routines are described in the following subsections.

2.4.1 Hover Trimming Method

The trimming method is used within selected hover simulations to obtain a blade loading. The trimmer alters the rotor coning and collective angles to achieve the target thrust coefficient. At start-up, an initial estimate of the trim state is computed using the following equation for the collective pitch,

$$\theta_0 = \frac{6}{\sigma a} C_T + \frac{3}{2}\sqrt{\frac{C_T}{2}} \tag{2.41}$$

In this case, the inflow factor λ can be obtained directly from the equation:

$$\lambda = -\sqrt{\frac{C_T}{2}} = -\frac{\sigma a}{16}\left(\sqrt{1+\frac{64}{3\sigma a}\theta_0} - 1\right) \tag{2.42}$$

assuming a constant inflow in the rotor disk.

The coning angle β_0 is then:

$$\beta_0 = \frac{\gamma}{8}\left(\theta_0 + \frac{4}{3}\lambda\right) \tag{2.43}$$

where γ is the blade lock number. The mesh is then deformed to account for the new rotor blade incidence and position, or as in the case with overset grids, the blade component is rotated with respect to the background grid. A steady flow simulation is then performed until a prescribed level of convergence is reached. The collective is updated after a prescribed number of iterations using the following relations:

$$\delta\theta_0 = \left(\frac{C_{T,\text{target}} - C_T}{\frac{dC_T}{d\theta_0}}\right)\frac{dC_T}{d\theta_0} = \frac{\sigma a}{6}\left(1 - \frac{1}{\sqrt{1+\frac{64}{3\sigma a}\theta_0}}\right) \tag{2.44}$$

The collective and coning angles are then updated until the target thrust coefficient is reached.

2.4.2 Forward Flight Trimming Method

The forward flight trimming method is based on a matrix-trimming method. In this case, a Newton-Raphson iteration method is used based on a (3×3) sensitivity matrix. A target thrust value and the requirements of vanishing rotor-averaged roll and pitching moments provide three

target values. The unknowns in the system are the rotor collective θ_0, the lateral cyclic θ_{1c} and the longitudinal cyclic θ_{1s}. The elements of the sensitivity matrix are derived from the approximate equations for the aero-mechanics based on blade-element aerodynamics.

The rotor shaft angle α_s is fixed and assumed based on a specified propulsive force (from a force triangle), along with assumed values for the coning angle β_0 and first flapping harmonics β_{1s} and β_{1c}. The thrust and moment coefficients are then expressed as a function of collective and cyclic pitch angles:

$$C_T = C_T(\theta_0, \theta_{1c}, \theta_{1s}) \tag{2.45}$$

$$C_{M,x} = C_{M,x}(\theta_0, \theta_{1c}, \theta_{1s}) \tag{2.46}$$

$$C_{M,y} = C_{M,y}(\theta_0, \theta_{1c}, \theta_{1s}) \tag{2.47}$$

where $C_{M,x}$ and $C_{M,y}$ are the non-dimensional moments about the x-axis (rotor disk rolling moment) and y-axis (rotor disk pitching moment), respectively.

$$\begin{pmatrix} \Delta\theta_0 \\ \Delta\theta_{1s} \\ \Delta\theta_{1c} \end{pmatrix} = \begin{pmatrix} \frac{\partial C_T}{\partial \theta_0} & \frac{\partial C_T}{\partial \theta_{1s}} & \frac{\partial C_T}{\partial \theta_{1c}} \\ \frac{\partial C_{M,x}}{\partial \theta_0} & \frac{\partial C_{M,x}}{\partial \theta_{1s}} & \frac{\partial C_{M,x}}{\partial \theta_{1c}} \\ \frac{\partial C_{M,y}}{\partial \theta_0} & \frac{\partial C_{M,y}}{\partial \theta_{1s}} & \frac{\partial C_{M,y}}{\partial \theta_{1c}} \end{pmatrix}^{-1} \begin{pmatrix} C_{T,target} - C_T \\ C_{M_x,target} - C_{M_x} \\ C_{M_y,target} - C_{M_y} \end{pmatrix} \tag{2.48}$$

This approach has been used in [295, 381, 425]. Yang et al. [425] used a lifting-line technique external to the flow solver to obtain the derivatives of the rotor performance parameters. In [295, 381], the flow solver is used to determine the derivatives of the rotor performance parameters by repeating the simulation with slightly different values of the angles θ_0, θ_{1c} and θ_{1c} in succession. An accurate estimate of the derivatives requires a converged flow solution for each of these different control settings. The matrix trimming method uses Equation (2.48) to trim the rotor. The elements of the sensitivity matrix in Equation (2.48) are the derivatives of C_T, $C_{M,x}$ and $C_{M,y}$ according to blade-element theory. Assuming a constant inflow factor λ and fixed flapping harmonics, the sensitivity matrix reads:

$$\begin{pmatrix} \frac{\partial C_T}{\partial \theta_0} & \frac{\partial C_T}{\partial \theta_{1s}} & \frac{\partial C_T}{\partial \theta_{1c}} \\ \frac{\partial C_{M,x}}{\partial \theta_0} & \frac{\partial C_{M,x}}{\partial \theta_{1s}} & \frac{\partial C_{M,x}}{\partial \theta_{1c}} \\ \frac{\partial C_{M,y}}{\partial \theta_0} & \frac{\partial C_{M,y}}{\partial \theta_{1s}} & \frac{\partial C_{M,y}}{\partial \theta_{1c}} \end{pmatrix} = \frac{\sigma a}{4} \begin{pmatrix} \left(\frac{2}{3} + \mu^2\right) & -\mu & 0 \\ \frac{2}{3}\mu & -\frac{1}{4}\left(1 + \frac{3}{2}\mu^2\right) & 0 \\ 0 & 0 & \frac{1}{4}\left(1 + \frac{1}{2}\mu^2\right) \end{pmatrix} \tag{2.49}$$

The control angles are updated as follows:

$$\begin{aligned}
\delta\theta_0 &= \left[\frac{\partial C_T}{\partial\theta_0}\frac{\partial C_{M,x}}{\partial\theta_{1s}} - \frac{\partial C_T}{\partial\theta_{1s}}\frac{\partial C_{M,x}}{\partial\theta_0}\right]^{-1}\left(\frac{\partial C_{M,x}}{\partial\theta_{1s}}\left(C_{T,target}-C_T\right) + \frac{\partial C_T}{\partial\theta_{1s}}C_{M_x}\right) \\
\delta\theta_{1s} &= \left[\frac{\partial C_T}{\partial\theta_0}\frac{\partial C_{M,x}}{\partial\theta_{1s}} - \frac{\partial C_T}{\partial\theta_{1s}}\frac{\partial C_{M,x}}{\partial\theta_0}\right]^{-1}\left(-\frac{\partial C_{M,x}}{\partial\theta_0}\left(C_{T,target}-C_T\right) - \frac{\partial C_T}{\partial\theta_0}C_{M_x}\right) \\
\delta\theta_{1c} &= -C_{M_x}/\frac{\partial C_{M,y}}{\partial\theta_{1c}}
\end{aligned} \tag{2.50}$$

2.5 Overset Method

The overset method [357] is based on the division of the computational domain into independently generated, overlapping, non-matching sub-domains. These sub-domains are referred to as levels and are sorted hierarchically, with higher levels having priority. The exchange of data between levels is performed through interpolation, following the level hierarchy. Typically, for rotor computations a foreground near-body grid is generated for the rotor which overlaps the background far-field domain (an intermediate background level can also be used). The use of overset grids for rotorcraft has a number of advantages including, ease of grid generation and reduced cells counts. Local refinements do not need to be propagated to the far-field as they can be constricted within an overset grid level. Additionally, mesh motion is simpler, as rotor articulation can be applied directly to the overset foreground grid. An example of an overset grid for a 2D aerofoil is shown in Figure 2.1, where Level 1 is shown in red as the foreground aerofoil grid and Level 0 is shown in black as the background grid.

Figure 2.1 (a) shows a typical overset grid layout for a 2D aerofoil calculation. The key challenge in overset grid methods involves the establishment of inter-grid communication methods and the use of high-order interpolation techniques between the grids. Firstly, a localisation procedure is carried out that identifies the block and solid minimum volume bounding boxes (MVBB) based on the second moment of area matrix. Then an Overset Mesh Search (OMS), is conducted through a range-tree algorithm to identify the cells within the MVBBs, and an Exact Arithmetics Library (EAL) is used to ensure that any point can only be located in one cell of a level that is it localised against. The main aim of this step is to determine the number of nodes of cell located in a higher level grid, based on which the cell flagging procedure is performed. The cells can be classified into three main groups:

- holes: do not need interpolation because they are overlapped by either with a hierarchically higher level cell or a solid,
- interpolation cells: those that require interpolated flow information from the grid they overlap,
- normal or computational cells: do not need any special treatment.

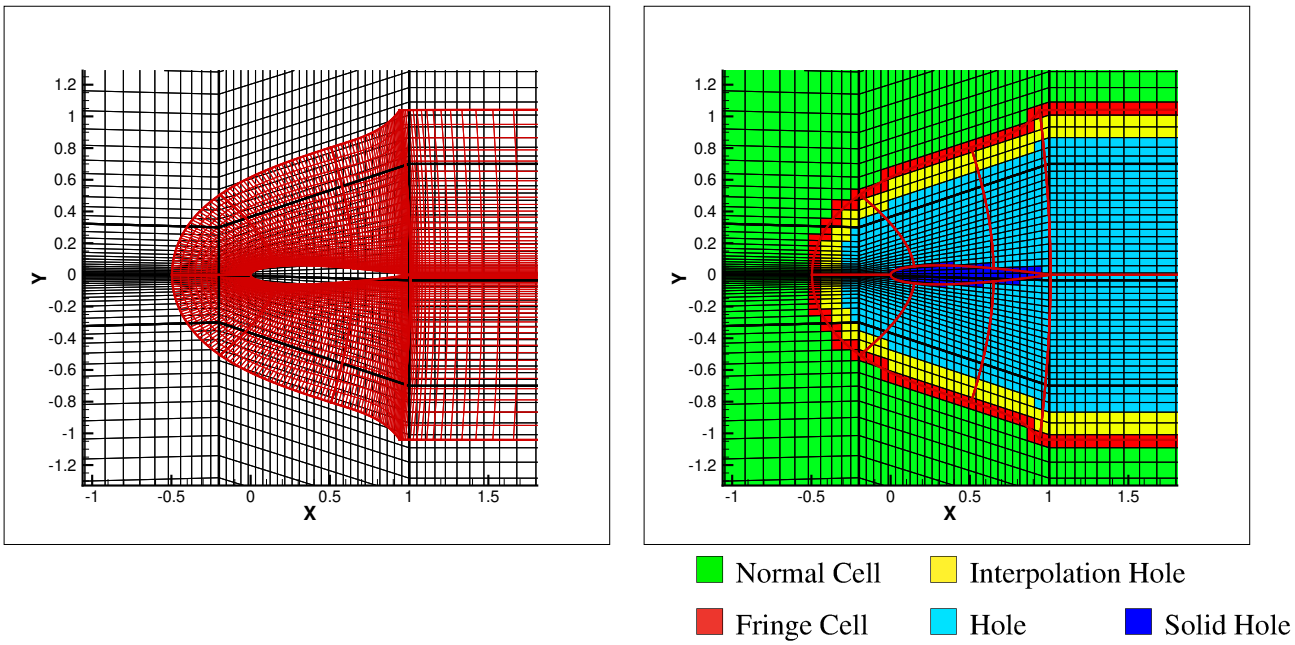

(a) Overset grids for a 2D aerofoil (background->black, foreground->red)

(b) Cell flags on background grid after hole cutting procedure

Figure 2.1: Example overset grid setup for a 2D aerofoil including background and foreground grid layouts along with background grid cell flags.

Figure 2.1 shows the localisation and cell flags for Level 0 (background). The computational cells are shown in green with the last layer of computational cells shown in red (known as the overset fringe cells). The yellow cells are interpolation cells that require information from a higher level grid, in this case, the foreground. Typically, two layers of interpolation cells are used, regardless of the flow solution model (viscous MUSCL stencil contains 9 cells). These cells are flagged recursively, as the cells neighbouring the fringe cells. The holes are indicated in light blue, whereas the holes that overlap the solid are shown in dark blue.

Three interpolation methods are available in HMB2: zero order method, least square method and inverse distance method. In the first one, the nearest neighbours value are copied to the interpolation cell. The second method uses a quadratic polynomial for the interpolation. The latter considers a cloud of nearest points and assigns larger weights to those closer to the interpolation cell and it is the approach employed in this work. Finally, it must also be noted that two-way coupling is used between the foreground and background grids. Hence, interpolation cells obtain information from the foreground grid, whereas information from the background grid is used to update the data in the two rows of halo cells on the foreground grid. These cells are then used in the flux calculation of the foreground grid cells on the overset mesh boundary. Further details of the overset grid method and its implementation in HMB3 are provided in [169].

2.6 DM/DT Procedure

A DM/DT calculation procedure is implemented within HMB3, to allow 2D unsteady calculations of aerofoil sections undergoing harmonic pitching motion, whilst including azimuthal local Mach number variation. This procedure allows to include the effects of the rotational and free-stream velocities that a 2D section sees along a specified local radial station of a rotor blade, and is included through a harmonic translation of the aerofoil section. The harmonic pitching and translation motion can be described as follows (based on one harmonic):

$$x = x_0 + x_s sin(2kt^*) + x_c cos(2kt^*) \tag{2.51}$$

$$\theta = \theta_0 + \theta_s sin(2kt^*) + \theta_c cos(2kt^*) \tag{2.52}$$

where x_0 is the initial position, θ_0 is the initial pitch, k is the reduced frequency of the first harmonic, t^* is the non-dimensional time ($t^* = \omega t/(2k)$), x_s and x_c are the translation motion coefficients of the sine and cosine components and θ_s and θ_c are the pitching motion coefficients of the sine and cosine components.

The Mach number variation at a local section r/R along a rotor blade with a known free-stream Mach number M_∞ and tip Mach number M_{tip} can be described as follows:

$$M = M_{tip}\frac{r}{R} + M_\infty sin(2kt^*) \tag{2.53}$$

Taking a reference Mach number as $M_{ref} = M_{tip}\frac{r}{R}$ and introducing advance ratio $\mu = M_\infty/M_{tip}$, equation 2.53 can be written as:

$$\frac{M}{M_{ref}} = 1 + \mu\frac{R}{r}sin(2kt^*) \tag{2.54}$$

where the term $\mu\frac{R}{r}sin(2kt^*)$ corresponds to the grid velocity, and is also equal to dx/dt. After integrating, the expression for the translational motion can be found:

$$x^* = x_0 + \frac{\mu}{2k}\left[1 - cos(2kt^*)\right] \tag{2.55}$$

where the reference reduced frequency and advance ratio used in the calculations are given by:

$$k = \frac{c_{ref}f}{2U_{ref}} = 2\pi\frac{c_{ref}}{4\pi r}, \quad \mu = \frac{M_{inf}}{M_{tip}}\frac{R}{r} \tag{2.56}$$

The reference Mach and Reynolds numbers are based on the values at the local radial station ($M_{\omega R}^{r/R}$ and $Re^{r/R}$). The pitching motion is also prescribed using a single harmonic based on the collective and cyclic control angles.

2.7 Visualisation of Vortical Structures

For wake visualisation, isosurfaces of Q-criteria are used. This quantity defines vortices as the region with a positive second invariant of velocity gradient tensor, ∇u [171], which is defined as follows:

$$Q = \frac{1}{2}(\hat{\Omega_{ij}}\hat{\Omega_{ij}} - \hat{S_{ij}}\hat{S_{ij}}) \tag{2.57}$$

where $\hat{\Omega_{ij}}$ and $\hat{S_{ij}}$ are the antisymmetric and symmetric parts of the velocity gradient, as follows:

$$\hat{\Omega_{ij}} = \frac{1}{2}\left(\frac{\partial \hat{u_i}}{\partial x_j} - \frac{\partial \hat{u_j}}{\partial x_i}\right), \quad \hat{S_{ij}} = \frac{1}{2}\left(\frac{\partial \hat{u_i}}{\partial x_j} + \frac{\partial \hat{u_j}}{\partial x_i}\right) \tag{2.58}$$

The Q-criterion quantity represents a local balance between vorticity magnitude (vortex rotation) and strain rate (vortex stretching). This quantity is also used to determine the positions of the rotor blade tip vortices versus azimuth in hover. Finally, the Q-criterion value used in HMB3 is non-dimensionalised as follows:

$$\widetilde{Q} = Q\left(\frac{L_{ref}}{V_{ref}}\right)^2 \tag{2.59}$$

Chapter 3

High-Fidelity Rotor Optimisation Framework

This chapter details the methodologies used within the optimisation framework. Firstly, the optimisation workflow is presented. Following this, key components of the framework are described including the harmonic balance and adjoint methods (and coupling with Chimera) as well as the SLSQP optimiser, the mesh deformation and the blade surface parameterisation methods.

3.1 Optimisation Workflow

The complete rotor design optimisation workflow is shown in Figure 3.1 and can be summarised as follows:

1 The flow around the aerodynamic surface S to be optimised (*e.g.* aerofoil, blade, etc.) is solved using the steady-state solver or the harmonic balance method for unsteady flows.

2 The objective function I and the constraints $g_j,\ j \in \{1,\ldots,m\}$, $h_k,\ k \in \{1,\ldots,p\}$, are evaluated from the flow solution.

3 The adjoint problem is solved to compute the gradients $\mathrm{d}I/\mathrm{d}\alpha$, $\mathrm{d}g_j/\mathrm{d}\alpha,\ j \in \{1,\ldots,m\}$, $\mathrm{d}h_k/\mathrm{d}\alpha,\ k \in \{1,\ldots,p\}$.

4 The cost functional, the constraints and their gradients are fed to the gradient based optimiser, which produces a new set of design variables α, corresponding to a design candidate in the search direction.

5 Based on the new values of the design variables α, an external parameterisation software computes the updated points vector $\mathbf{X}_{|S}$ describing the surface S, and the derivatives of these points with respect to the design variables $(\partial\mathbf{X}/\partial\alpha)_{|S}$.

6 The mesh deformation algorithm computes the new volume mesh points positions $\mathbf{X}$, and the derivatives $\partial\mathbf{X}/\partial\alpha$.

Steps 1-6 are repeated for several design cycles until determined convergence criteria are met. Usually, these criteria include checks on the objective function gradient module, checks on the variation of the design variables and the objective function between successive cycles of the optimisation process. The entire workflow is driven by a bash script executing each of the tools within the optimisation workflow sequentially. Bash scripts for non-automated optimisation have also been written for use with optimisation cases where the CFD solver HMB3 is ran on external HPC clusters.

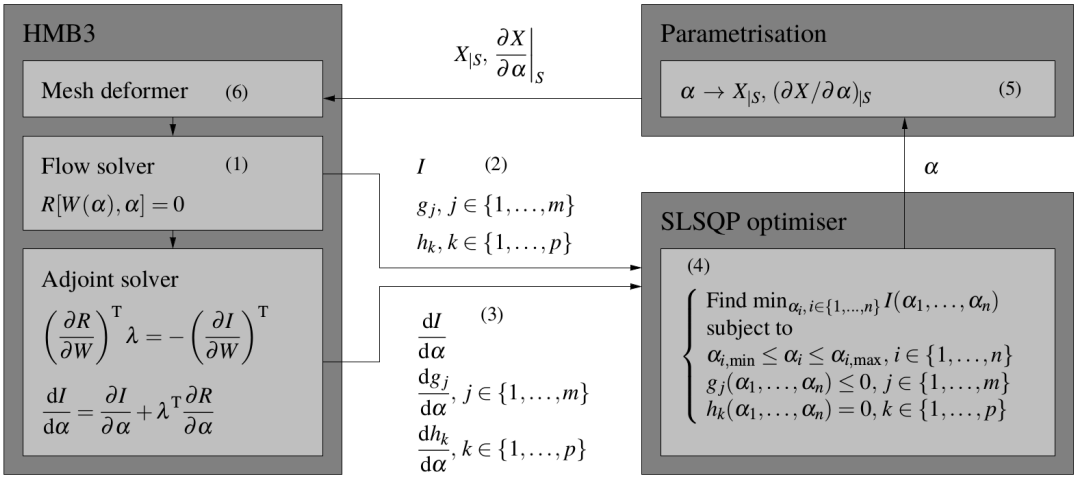

Figure 3.1: The full HMB3 optimisation workflow.

The described framework can be used to efficiently optimise the shape of two and three-dimensional aerodynamic surfaces. New developments within the framework included coupling with the harmonic balance method for optimisation of unsteady flows and coupling with the overset grid method. The gradient based optimisation algorithm guarantees that a very small number of flow evaluations is required compared to gradient-free methods [236]. The use of the adjoint solver limits the overhead for computing the necessary flow gradients, compared to finite differences. However, for harmonic balance problems, the adjoint problem may be memory intensive and is currently limited to fairly coarse problems or solutions with a low number of harmonic balance modes. The use of the mesh deformation technique avoids the necessity of remeshing, and interfacing the optimisation framework with a Computer-Aided Design (CAD) and a meshing software. The limit of the method is the assumption that, for every shape generated by the parameterisation, a new volume mesh can be obtained by deforming the mesh for the baseline shape. This excludes problems where the shape modifications allowed by the parameterisation are very large, so that the deformation of the baseline mesh may lead to highly distorted mesh elements (or even to elements with negative volume).

In the following subsections, the harmonic balance method for unsteady flow solutions and the adjoint method are described in more detail. The coupling of the adjoint, harmonic balance and overset methods is also analysed. Finally, the blade surface parameterisation method, gradient-based optimiser and mesh deformation methods are presented.

3.1.1 Harmonic Balance Method

The harmonic balance method represents the flow solution and residual vectors as a truncated Fourier series, by assuming a periodicity in time with a frequency, ω. The flow is represented by N_H harmonic balance modes and is split into $N_T = 2N_H + 1$ subintervals, which are coupled using the Fourier collocation derivative operator, D. This leads to a significant reduction in computational costs compared to time-marching simulations, as the flow-field can be solved as a large $(N_T \times N_T)$ steady state problem. This work follows the implementation used by Woodgate and Barakos [422].

By starting from the standard system of ordinary differential equations:

$$I(t) = V\frac{dW(t)}{dt} + R(t) = 0 \tag{3.1}$$

and representing as a truncated Fourier series, we can write:

$$W(t) = \sum_{k=-N_H}^{N_H} \hat{W}_k e^{ik\omega t} \tag{3.2}$$

$$R(t) = \sum_{k=-N_H}^{N_H} \hat{R}_k e^{ik\omega t} \tag{3.3}$$

$$I(t) = \sum_{k=-N_H}^{N_H} \hat{I}_k e^{ik\omega t} \tag{3.4}$$

Using the orthogonality of the Fourier terms for each wave number k we can write:

$$\hat{I}_k = i\omega k V\hat{W}_k + \hat{R}_k = 0 \tag{3.5}$$

The system is of $N_T = 2N_H + 1$ equations for N_H harmonics and which can be written as:

$$\omega A\hat{W} + \hat{R} = 0 \tag{3.6}$$

where matrix A is a N_T x N_T matrix. Various approaches exist of solving equation 3.6 directly in the frequency domain. The first approach is based on forming an analytical expression between $\hat{W}$ and $\hat{R}$, however, this leads to a complex series of convolution sums to calculate $\hat{R}$ from $\hat{W}$ and a significant increase in computational costs (quadratic scaling with N_H). For this reason, this approach has been discarded by many researchers [116, 131, 248, 422]. A more commonly used

approach is the pseudo-spectral approach of Hall [131], which solves the equations in the time-domain. The Non-Linear Frequency Domain method of McMullen et al. [248], used a similar pseudo-spectral approach, but solved the equations directly in the frequency domain, with the residual formulated in the time-domain. This led to the requirement of Fast Fourier Transforms (FFT) and Inverse Fast Fourier Transforms (IFFT) within the iterative process. The approaches used by Gopinath and Jameson [126] and Hall [131] formulate the residual in the time-domain, and solve the equations directly in the time-domain, avoiding the FFT and IFFT operations.

In the present work, the approach of Hall [131] is followed, where equation 3.6 is transformed back into the time domain. The solution is split into $2N_H + 1$ discrete, equally spaced subintervals over the period $T = 2\pi/\omega$:

$$W_{hb} = \begin{pmatrix} W(t_0 + \Delta t) \\ W(t_0 + 2\Delta t) \\ \vdots \\ W(t_0 + T) \end{pmatrix}, \quad R_{hb} = \begin{pmatrix} R(t_0 + \Delta t) \\ R(t_0 + 2\Delta t) \\ \vdots \\ R(t_0 + T) \end{pmatrix} \tag{3.7}$$

By using a transformation matrix E, such that $\hat{W} = EW_{hb}$ and $\hat{R} = ER_{hb}$ we can write:

$$\begin{aligned} \omega AEW_{hb} + ER_{hb} = 0 = \omega E^{-1}AEW_{hb} \\ + E^{-1}ER_{hb} = \omega DW_{hb} + R_{hb} \end{aligned} \tag{3.8}$$

where D = $E^{-1}AE$ and is defined as:

$$D_{i,j} = \frac{2}{N_T} \sum_{k=1}^{N_H} k sin(2\pi k(j-i)/N_T) \tag{3.9}$$

Pseudo-time marching is then applied to the equation 3.10:

$$\frac{W_{hb}}{d\tau} + \omega DW_{hb} + R_{hb} = 0 \tag{3.10}$$

The equation is solved using an implicit method with an implicit treatment of the source term (to increase the attainable CFL number) which is solved as follows:

$$\omega DW_{hb}^{n+1} = \omega DW_{hb}^{n} + \omega D(\Delta W_{hb}) \tag{3.11}$$

The full harmonic balance equation then becomes:

$$\frac{W_{hb}^{n+1} - W_{hb}^{n}}{\Delta\tau} = -\left[\omega DW_{hb}^{n+1} + R_{hb}(W_{hb}^{n+1})\right] \tag{3.12}$$

This implementation of the unsteady source term couples all variables at all N_T solution snapshots. An approximate Jacobian matrix is used within the linear system based on first order

discretisation of the residual function, to improve the conditioning of the system. The system is then solved using a Krylov subspace method with BILU factorisation. This leads to the solution of the following preconditioned system:

$$P\Big[\frac{V}{\Delta\tau}+J_{IMP}\Big]\Delta W_{hb}=-PR^{n}_{hb}-P\omega DW^{n}_{hb} \tag{3.13}$$

where V is the cell volume, P is the preconditioner and the implicit Jacobian matrix J_{IMP} that couples all the solution snapshots is defined as:

$$J_{IMP}=\begin{bmatrix} \dfrac{\partial R}{\partial W}\Big|_{t_0+\Delta t} & \omega D_{1,2} & \dots & \omega D_{1,N_T} \\ \omega D_{2,1} & \dfrac{\partial R}{\partial W}\Big|_{t_0+2\Delta t} & & \\ \vdots & & \ddots & \\ \omega D_{N_T,1} & \omega D_{N_T,2} & & \dfrac{\partial R}{\partial W}\Big|_{t_0+T} \end{bmatrix}, \tag{3.14}$$

The present approach is the main difference between the majority of harmonic balance/time-spectral implementations seen in literature based on explicit methods [87, 116, 126] or implicit methods with an explicit treatment of the time-derivative source term [96, 375]. An implicit method with an implicit treatment of the source term is unconditionally stable, whereas, the use of an explicit source term requires a stabilisation technique. Furthermore, the implicit source term allows the use of higher CFL numbers. Other examples of studies with implicit source term treatment include [346, 405].

The main drawback of the harmonic balance method is the requirement to store $2N_H+1$ solutions which can be memory intensive for a high number of harmonic balance modes. To reduce the memory footprint of the fully-implicit method, the off-diagonal terms in the Jacobian matrix are not stored explicitly but added to the right-hand side of the linear system during the matrix-vector multiply. This, however, still leads to a memory requirement of $2N_H+1$ baseline steady solutions due to the nature of the method. Various implementations exist in literature aimed at reducing the memory footprint, including a fully segregated time-spectral approach [145], leading to slower convergence compared to the fully coupled approach. Another promising technique is the adaptive harmonic balance method [260], where the number of modes required is determined on a cell by cell basis based on the cell normalised wave amplitude. This approach leads to improvements in speed and memory overhead. However, due to implementation difficulties arising from the need to correct the cell fluxes across temporally mismatched interfaces [260], adaptive harmonic balance methods have seen limited use.

3.1.2 Harmonic Balance Method with Overset Grids

The overset grid method implemented within HMB [169] is used for ease of grid generation and to allow for the relative motion between mesh components in forward flight cases. Overset grids also typically generate smoother meshes, especially when a mesh deformation routine is used, leading to improved solution accuracy and robustness. Typically for time-marching simulations, three types of cells are distinguished in the overset fringe, including computational cells where the flow is solved, interpolation cells with interpolated values from a higher overset grid level and cells flagged as holes where no solution is obtained. In the harmonic balance formulation, the holes will change dynamically between the solution snapshots, leading to a lack of information about the flow field for certain time steps. Various approaches have been used in literature to obtain a valid solution for the dynamically changing holes, including a Poisson solver [246] or Barycentric interpolation [219]. In the present research, to deal with the rotational movement of the rotor blades, an intermediate disk overset level is included in the grid that rotates with the blades, keeping the cell flagging constant. The pitching and flapping motions are solved by flagging holes that dynamically change between snapshots as an interpolation cell. This will give a valid solution as long as the holes representing the solid body do not move out of the foreground grid in any snapshot of the solution, hence they are more constrained by high flapping harmonics rather than pitching. An example of the cell flagging procedure for harmonic balance solutions is shown for a pitching 2D NACA0012 aerofoil ($\alpha = 15^\circ + 10^\circ sin(\omega t)$) in Figure 3.2. Here, the holes are shown in blue and dark-blue, the interpolation cells are shown in yellow, whereas the computational cells are shown in green. The key issue with harmonic balance overset implementations, is that between each snapshot of the solution, the cells flagged as holes (blue and -dark blue) will be different. Therefore, cells that were previously non-computational (blue) with freestream solution values will become computational (green/red). One solution to this problem is to flag all holes that become computational in any snapshot of the solution as interpolation cells (yellow). This can be seen in Figure 3.2, as the layers of interpolation cells vary with each snapshot of the solution (for standard solutions, there are only two layers of interpolation cells), ensuring that all cells that become computational have a valid solution.

3.1.3 Adjoint Method

The adjoint method offers an efficient way to produce the design variable gradients, which are used in conjunction with a gradient-based optimiser in an optimisation process. Compared to finite differences, where the gradient computation is dependent on the number of variables, the adjoint method generates the gradients of all the design variables at the cost of a base flow solution. The basic idea is to write the objective function as a function of the flow variables and a variable of interest (optimisation design variable in this case). We assume that the flow

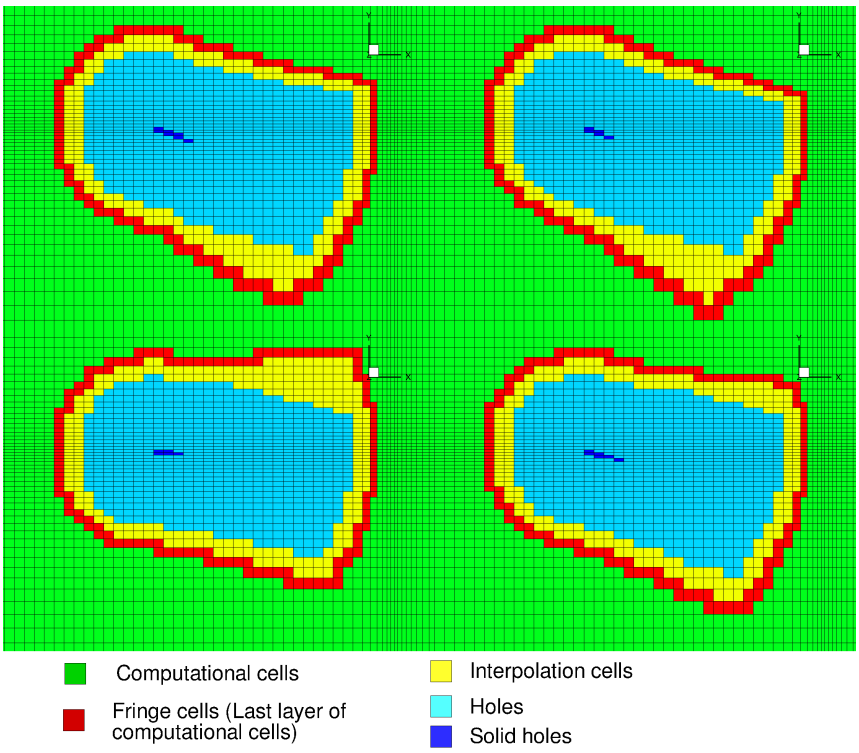

Figure 3.2: Example interpolation cell flagging for a pitching 2D NACA0012 aerofoil ($\alpha = 15^\circ \pm 10^\circ$). Cell flagging shown for four of the five snapshots of a two mode harmonic balance computation.

variables satisfy the Navier-Stokes equations (or any other set of equations), hence:

$$R\left[W(\alpha), \alpha\right] = 0 \tag{3.15}$$

Formally, taking the derivative of the adjoint objective function, I with respect to α we obtain:

$$\frac{\mathrm{d}I}{\mathrm{d}\alpha} = \frac{\partial I}{\partial \alpha} + \frac{\partial I}{\partial \mathbf{W}} \frac{\partial \mathbf{W}}{\partial \alpha}. \tag{3.16}$$

By introducing the adjoint variable λ as the solution of the following linear system:

$$\left(\frac{\partial \mathbf{R}}{\partial \mathbf{W}}\right)^{\mathrm{T}} \lambda = -\left(\frac{\partial I}{\partial \mathbf{W}}\right)^{\mathrm{T}}, \tag{3.17}$$

equation (3.16) can be rewritten as:

$$\frac{\mathrm{d}I}{\mathrm{d}\alpha} = \frac{\partial I}{\partial \alpha} + \lambda^{\mathrm{T}} \frac{\partial \mathbf{R}}{\partial \alpha}, \tag{3.18}$$

The computational cost of the dual sensitivity problem (3.17)-(3.18) scales with the number of outputs, since the right-hand side of (3.17) depends on I, but it is independent of the input parameters. The adjoint form of the sensitivity equation is particularly efficient for cases where

the number of (output) cost functionals is small, while the number of (input) design variables is large. For the inverse case, where the number of (output) cost functionals is larger, the tangent solver can be used. For rotor design optimisation problems the adjoint method, therefore, makes more sense and removes the limitation on the number of design variables (subject to the optimiser algorithm convergence).

The linear system shown in equation 3.17 is difficult to solve due to the high stiffness of the Jacobian matrix, $J = \partial\mathbf{R}/\partial\mathbf{W}$. Various approaches exist in literature of solving this system, with two techniques having the greatest success: those based around the duality preserving fixed-point iteration (FPI) and those based on Krylov subspace methods, as discussed in the overview of sensitivity analyses given by Peter [301]. The first principle is based around the fact that if the FPI converges asymptotically for a non-linear problem, the exact same rate of convergence should be obtained for the linearised problem. However, to apply this methodology, the linearisation needs to be exact, which is often not the case in many CFD codes, with approximate Jacobians. A second issue may arise if the primal non-linear problem does not converge using the FPI. For these reasons many adjoint implementations have adopted a strategy based on Krylov methods, however, the duality preserving FPI approach has been successfully demonstrated in the SU2 solver [14]. Krylov solvers have also been used as a stabilisation technique for the FPI approach, using recursive projection methods (RPM) as in [69, 111, 300]. The most commonly used solution technique for the adjoint linear system, however, is based on preconditioned Generalised Minimum Residual (GMRES) methods [329]. Kenway et al. [192] developed a GMRES method with a nested preconditioning strategy based on Additive Schwartz as a global preconditioner and apply multiple ILU preconditioning locally using Richardsons method. Mani and Mavriplis [241] apply a line-implicit linear multigrid preconditioned restarted GMRES algorithm whereas Choi et al. [87] used an ILU preconditioned GMRES for smaller problems and included an additional multigrid preconditioner for larger solutions. A similar approach is used in Star CCM+ [438] where Algebraic Multi-Grid (AMG) is used as a preconditioner for the GMRES algorithm.

In the present research, the linear system shown in equation 3.17 is solved using a Krylov-subspace solver based on a nested GMRES solver [329] with Deflated Restating (DR). GMRES is a robust method for the solution of a non-symmetric linear system, based on the minimisation of the equations residual over a Krylov subspace generated using Arnoldi's method [23]. A well known theoretical result states that GMRES is guaranteed to converge in at most n steps, where n is the dimension of the system matrix [328]. The drawback of the method is its memory requirements, since it needs to store all the base vectors of the Krylov subspace, whose size increases by one at each Arnoldi's iteration. To limit the memory demand, whilst ensuring good convergence, Deflated Restarting is employed (denoted as GMRES-DR), where the Krylov subspace is discarded after a predefined number m of Arnoldi's iterations, and the process is restarted from the last solution. To improve the convergence, during the restart, k approximate

eigenvectors associated with the smallest eigenvalues are extracted from the Krylov subspace, and used to augment the subspace at the next cycle. The GMRES solver is implemented in a nested fashion where a GMRES-DR solver is used as a preconditioner for the (outer) GMRES-DR cycles. To allow for this, a flexible variant of the outer solver was needed [327], at the cost of higher memory requirement, since two vectors need to be stored at each Arnoldi's iteration. The inner GMRES-DR solver inverts the preconditioning matrix $\hat{J}$, and uses, in turn, the decoupled ILU(0) preconditioner. The whole scheme may be denoted as FGMRES-DR(m,k)-GMRES-DR(m_p,k_p). This nested Krylov-subspace solver proved to be able to converge tough adjoint problems, as required for stiff harmonic-balance adjoint solutions. The main limitation of the method is the memory requirements, especially for larger problems where a larger number of Krylov vectors may be needed, limiting the present method to moderate grid sizes or a low number of harmonic balance modes. Advanced GMRES methods with Dynamically Deflated Restarting (DDR) are a current topic of research in literature [82], leading to both reduced memory demands and computational costs.

The adjoint method was developed within HMB3 through source code differentiation, using the tool TAPENADE [143]. The individual functions of the solver are differentiated and used to compute the partial derivatives required for the sensitivity equation 3.18. The implementation of the nested Krylov-subspace solver does not explicitly require the Jacobian matrix $\mathbf{J}$, but only the matrix-vector product $\mathbf{J}^{\mathrm{T}}\mathbf{v}$. Therefore, $\mathbf{J}$ is never stored explicitly, and the product $\mathbf{J}^{\mathrm{T}}\mathbf{v}$ is computed by means of automatically differentiated code of the residual function. Further details on the computation of the required partial derivatives for aerodynamic sensitivities and the matrix-vector product $\mathbf{J}^{\mathrm{T}}\mathbf{v}$ is given in [50]. For sensitivities of the design variables, the term $\frac{\partial \mathbf{R}}{\partial \alpha}$ is obtained in the following manner:

$$\frac{\partial \mathbf{R}}{\partial \alpha} = \frac{\partial \mathbf{R}}{\partial \mathbf{N}} \frac{\partial \mathbf{N}}{\partial \mathbf{X_v}} \frac{\partial \mathbf{X_v}}{\partial \mathbf{X_s}} \frac{\partial \mathbf{X_s}}{\partial \alpha} \tag{3.19}$$

This represents the computation of the residual vector sensitivity with respect to the design variable, and is dependent on the surface mesh sensitivities with respect to each design variable $\frac{\partial \mathbf{X_s}}{\partial \alpha}$ which are obtained from the blade parameterisation tool, the volume mesh sensitivities with respect to the surface mesh $\frac{\partial \mathbf{X_v}}{\partial \mathbf{X_s}}$, the mesh metrics sensitivities with respect to the volume mesh $\frac{\partial \mathbf{N}}{\partial \mathbf{X_v}}$ and finally, the residual sensitivities with respect to the mesh metrics $\frac{\partial \mathbf{R}}{\partial \mathbf{N}}$.

3.1.4 Coupling Adjoint and Overset Harmonic Balance Methods

The harmonic balance adjoint method uses many functions developed in the steady-state adjoint. Similarly as for the steady state method, the adjoint dual-sensitivity problem must be solved shown in equations 3.18 and 3.17. As for the steady state method, the large linear system

3.17 is solved using the Krylov-subspace method based on the Generalised Minimum Residual (GMRES) method. However, now instead of one steady solution, the linear system is $2N_H + 1$ larger, as it contains each of the snapshots of the harmonic balance solution. The harmonic balance residual computation is also slightly different. Here, the steady residual computation is used for each of the snapshots and then the Fourier collocation derivative operator is added. The differentiated harmonic balance residual computation is, therefore, based on the explicit source term. The partial derivatives required in equation 3.18 are computed for each snapshot and averaged over the number of snapshots to produce an averaged gradient value for the entire rotor revolution. The baseline set of surface sensitivities used in the computation of the $\partial \mathbf{R}/\alpha$ term are generated at a reference position. Hence, additional transformations are also applied to the surface sensitivities for moving meshes including effects of azimuth, pitch, flap and lag. The coupling of the adjoint harmonic balance method with overset grids also requires specific treatment. Typically, the contributions of the non-computational cells are removed from the Jacobian matrix rows and right-hand side for standard HMB3 solver calculations. The adjoint problem, however, uses the transpose of the Jacobian, hence both the rows and columns are set to zero for the overset grid cells flagged as holes. Finally, the dynamic holelist required for overset harmonic balance calculations was also implemented in the adjoint code.

3.1.5 SLSQP Optimiser

The general optimisation problem can be formulated as follows:

$$\begin{cases} \text{Find } \min_{\alpha_i, i\in\{1,\ldots,n\}} I(\alpha_1,\ldots,\alpha_n) \text{ subject to} \\ \alpha_{i,\min} \leq \alpha_i \leq \alpha_{i,\max},\ i \in \{1,\ldots,n\} \\ g_j(\alpha_1,\ldots,\alpha_n) \leq 0,\ j \in \{1,\ldots,m\} \\ h_k(\alpha_1,\ldots,\alpha_n) = 0,\ k \in \{1,\ldots,p\} \end{cases} \tag{3.20}$$

That is minimise/maximise an objective function I such as drag or power, subject to a number of equality (h) and inequality (g) constraints such as thrust or pitching/rolling moments over a design space $\alpha_{i,\min}$ to $\alpha_{i,\max}$. The current optimisation problem is solved using a Sequential Least-Square Quadratic Programming (SLSQP) algorithm [202, 203], with the implementation based on the software library NLopt [180]. The optimiser code is a standalone tool outside the HMB3 solver, hence other optimisation algorithms could also be easily implemented within the optimisation framework.

The main objective of any gradient-based algorithm is to update the design variables to drive the objective to an optimal value. Therefore, the optimiser must evaluate an optimal search direction based on the solution gradients and the step size. The SLSQP optimisation algorithm solves a sequence of subproblems, each of which optimises a quadratic model of the objective function subject to a linearisation of the constraints. SLSQP uses the Hans-Powell quasi-Newton (based on approximate second order information) method with the Broyden-Fletcher-Goldfarb-

Shanno (BFGS) [228] method to update the Hessian matrix. The approximate Hessian matrix is built based on the function and gradient values from previous iterations. SQP methods can also be thought of as an application of the Newton method to the Karush-Kuhn-Tucker (KKT) optimality conditions [188,205], which find an optimal search direction d to the following quadratic programming subproblem:

$$\begin{aligned} &\min_d f(x_k) + \nabla f(x_k)^T d + \tfrac{1}{2}\nabla^2_{xx}\mathscr{L}(x_k,\lambda_k,\sigma_k)d \\ &s.t. g(x_k) + \nabla g(x_k)^T d \geq 0 \\ &h(x_k) + \nabla h(x_k)^T d \geq 0 \end{aligned} \tag{3.21}$$

where f(x) is the value of the objective function I, g(x) and h(x) and the values of the inequality and equality constraints and $\mathscr{L}$ is the Langrangian of the optimisation problem of the form $\mathscr{L}(\S,\lambda,\sigma) = f(x) - \lambda g(x) - \sigma h(x)$, where λ and σ are Lagrange Multipliers.

3.1.6 Blade Surface Parameterisation

A deformative blade surface parameterisation method is used, where the movement of the blade surface mesh points is described analytically, and the volume mesh is updated using an Inverse Distance Weighting (IDW) method. The parameterisation tool lies outside the CFD solver and can be easily adapted to many different design parameterisations. In this case, the parameterisation setup used in the optimisation studies for the AH-64A blade, presented in Chapter 9, is described.

The parameterisation of the AH-64A blade is composed of twist, chord, sweep and anhedral design variables. The twist law is parameterised using a Bernstein polynomial function [44] with seven coefficients. The chord is altered at four radial stations of r/R = 0.5, 0.75, 0.943 and 1.0; whereas the sweep and anhedral angles are changed at the three outboard radial stations of r/R = 0.75, 0.943 and 1.0. Linear distributions are imposed inboard of 0.943, with parabolic distributions of the blade chord, sweep and anhedral angles across the blade tip region from 0.943 R to 1.0 R. This leads to a total of 17 design parameters. The blade planform parameterisation is shown graphically in Figure 3.3.

As a deformative method is used, the parameters are applied as a delta to the baseline surface mesh. Here, the blade tip sweep is removed before applying the new set of parameters, hence a rectangular blade with -9 degrees linear blade twist is used. The design parameter boundaries are shown in Table 3.1.

The twist is applied on top of the nominal -9 degrees linear twist angle giving the maximum possible blade twist of -19 degrees. The sweep and anhedral perturbations are applied in terms of chord magnitude. This equates to a maximum possible blade tip backward sweep angle 43 degrees and anhedral angle of 18.4 degrees in the case of the AH-64A blade.

The implemented blade surface parameterisation considers the key geometric features of twist, chord, sweep and anhedral, however, the radial location and distribution of the examined

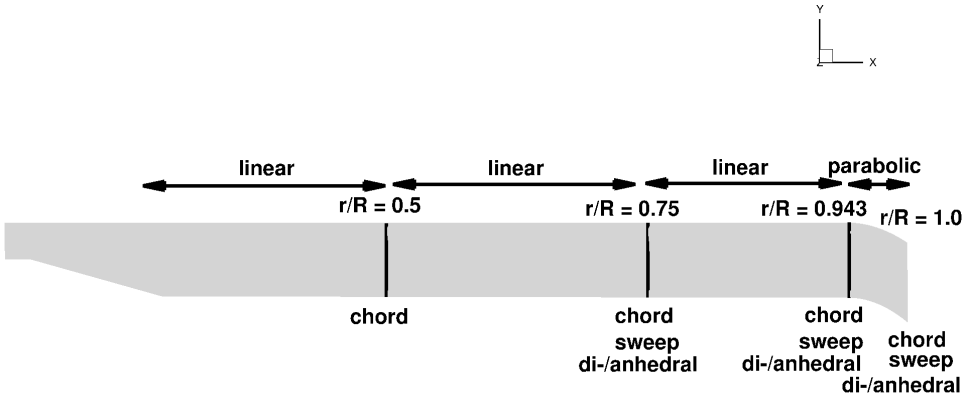

Figure 3.3: Blade surface parameterisation used within the optimisation studies of the AH-64A blade.

Table 3.1: Design parameter upper and lower boundaries for optimisation studies of the AH-64A blade.

Design Parameter	Boundary values
TWIST1 - TWIST7	$\pm$ 5 deg
CHORD at r/R = 0.5	[0.8c,1.4c]
CHORD at r/R = 0.75	[0.8c,1.4c]
CHORD at r/R = 0.943	[0.8c,1.4c]
CHORD at r/R = 1.0	[0.3c,1.5c]
SWEEP at r/R = 0.75	[-0.3c,0.4c]
SWEEP at r/R = 0.943	[-0.3c,0.4c]
SWEEP at r/R = 1.0	[-0.7c,0.4c]
ANHEDRAL at r/R = 0.75	[-0.1c,0.25c]
ANHEDRAL at r/R = 0.943	[-0.1c,0.25c]
ANHEDRAL at r/R = 1.0	[-0.25c,0.1c]

parameters are pre-defined. The shape of the aerofoil sections also remains fixed. A more elaborate parameterisation based on Bezier curves was also developed shown in Appendix A. However, the design parameter and gradient scaling require further testing with the SLSQP optimiser for the more complex Bezier parameterisation. This is due to different orders of magnitude between different gradient values.

3.1.7 Volume Mesh Deformation Method

To adapt the volume mesh to the surface generated by the parameterisation software at each optimisation cycle, an advanced mesh deformation algorithm has been implemented in HMB3, based on Inverse Distance Weighting (IDW) [341]. IDW is an interpolation method that calculates the values at given points with a weighted average of the values available at a set of known points. The weight assigned to the value at a known point is proportional to the inverse of the

distance between the known and the given point.

Given N samples $\mathbf{u}_i = u(\mathbf{x}_i)$ for $i = 1,2,...,N$, the interpolated value of the function $\mathbf{u}$ at a point $\mathbf{x}$ using IDW is given by:

$$\mathbf{u}(\mathbf{x}) = \begin{cases} \dfrac{\sum_{i=1}^{N} w_i(\mathbf{x})\mathbf{u}_i}{\sum_{i=1}^{N} w_i(\mathbf{x})}, & \text{if } d(\mathbf{x},\mathbf{x}_i) \neq 0 \text{ for all } i \\ \mathbf{u}_i, & \text{if } d(\mathbf{x},\mathbf{x}_i) = 0 \text{ for some } i \end{cases} \tag{3.22}$$

where

$$w_i(\mathbf{x}) = \frac{1}{d(\mathbf{x},\mathbf{x}_i)^p}. \tag{3.23}$$

In the above equations, p is any positive real number (called the *power parameter*) and $d(\mathbf{x},\mathbf{y})$ is the Euclidean distance between $\mathbf{x}$ and $\mathbf{y}$ (but any other metric operator could be considered as well).

The method in its original form tends to become extremely expensive as the sample data set gets large. An alternative formulation of the Shepard's method, which is better suited for large-scale problems, has been proposed by Renka [317]. In the new formulation, the interpolated value is calculated using only the k nearest neighbours within the R-sphere (k and R are given, fixed, parameters). The weights are slightly modified in this case:

$$w_i(\mathbf{x}) = \left(\frac{\max(0, R - d(\mathbf{x},\mathbf{x}_i))}{R d(\mathbf{x},\mathbf{x}_i)} \right)^p, \quad i = 1,2,...,k. \tag{3.24}$$

If this interpolation formula is combined with a fast spatial search structure for finding the k nearest points, it yields an efficient interpolation method suitable for large-scale problems.

The modified IDW interpolation formula is used in HMB3 to implement mesh deformation in an efficient and robust way. The known displacement of points belonging to solid surfaces represents the sample data, while the displacements at all other points of the volume grid are computed using equation (3.22) with the weights computed using equation (3.24). For a fast spatial search of the sample points, an Alternating Digital Tree (ADT) data structure [58] is used. A blending function is also applied to the interpolated displacements, so that they smoothly tend to zero as the distance from the deforming surface approaches R.

Chapter 4

Blade geometries and CFD Modelling Strategy

This chapter describes the blade planforms which were used for CFD validation. This includes the Langley BERP (LBERP) and Langley Baseline (LBL) blades which were tested by Yeager et al. [429] and are used here, for advanced planform validation. The PSP rotor blade tested by Wong et al. [420] is simulated for comparisons with a more modern experimental data set, whereas the performance of the baseline AH-64A blade [40] is validated prior to an optimisation study of this planform. Within this chapter, details of the CFD computational setup for rotors in hover and forward flight are also given.

4.1 Blade Geometries

The planforms of the simulated blade geometries scaled to a unit chord can be seen in Figure 4.1, whereas the twist distributions are shown for all four blades in Figure 4.2. The main rotor geometric properties are presented in Table 4.1. A detailed description of the geometric properties and necessary assumptions are given in the following subsections.

4.1.1 Langley BERP and Langley Baseline

The Langley BERP (LBERP) and Langley Baseline (LBL) blades were tested at model scale, by Yeager et al. [429] with the main aim of assessing a blade with a BERP-like tip shape - the LBERP blade, against a conventional rectangular blade design - the LBL blade. Both blades have the same nominal twist, radius of 56.225 inches and aerofoil sections along the span. The two blades only differ in the tip shape and chord which was increased by 9% for the LBL blade to match the rotor thrust-weighted solidity. Based on the discussion between Perry and Amer [20, 299], the matching of thrust weighted solidity may favour the LBL blade, due to higher geometric solidity (0.101 for LBL compared to 0.096 for the LBERP blade). This as-

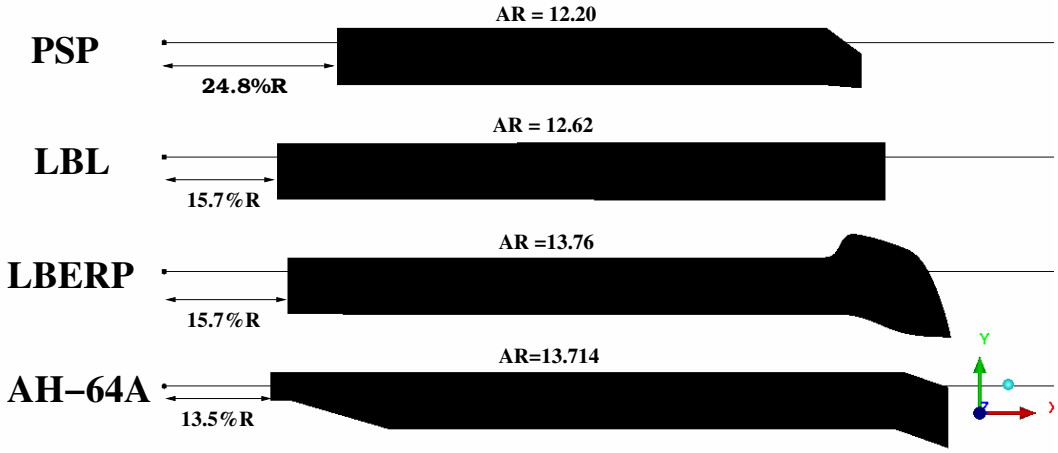

Figure 4.1: Blade planforms of the PSP [420], LBL [429], LBERP [429] and AH-64A [40] blades scaled to a unit chord used for CFD validation.

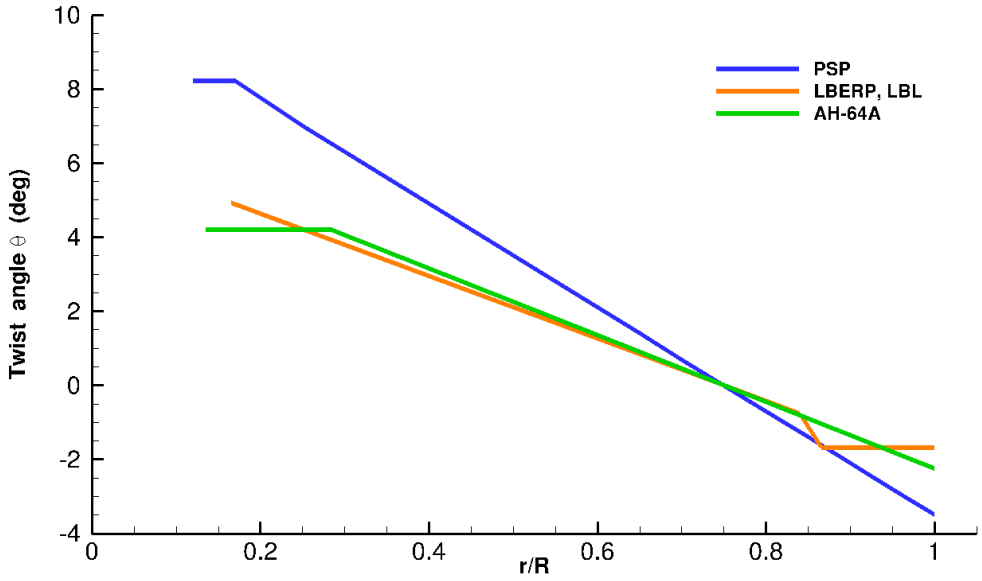

Figure 4.2: Twist distributions for the PSP [420], LBL [429], LBERP [429] and AH-64A [40] rotor blades

sumption is analysed further in a rotor solidity study in Chapter 7. The RC(4)-10 aerofoil is used inboards of the tip section up to 0.84R, whereas a scaled RC(3)-08 section to 7% thickness was used across the blade tip (RC(3)-07), from 0.86R. The aerodynamics of these two aerofoils are described by Noonan [280], [281]. For both blade designs, a linear twist of approximately 9^o was used, with a constant twist outboard of 0.866R as shown in Figure 4.2. In terms of geometry, a few assumptions had to be made. The exact shape of the BERP-tip along with its thickness distribution is not fully defined. Furthermore, the curvature of the aerofoil transition region is also not known. For these reasons, different blade geometries were generated for both blades, based on the user interpretation of the data within the report by Yeager et al. [429]. Geometries for both blades, were generated at Glasgow University, labelled as Glasgow LBERP and Glas-

Table 4.1: Geometric properties for the LBL [429], LBERP [429], PSP [420] and AH-64A [40] rotor blades, FS=Full Scale.

Parameter	LBL	LBERP	PSP	AH-64A
Number of blades, N_b	4	4	4	4
Rotor radius, R	56.224 in.	56.224 in.	66.50 in.	77.76 in. (288 in. FS)
Ref. blade chord, c_{ref}	4.454 in.	4.086 in.	5.45 in.	5.67 in. (21 in. FS)
Aspect ratio, R/c_{ref}	12.62	13.76	12.2	13.714
Rotor solidity (nominal), σ_N	0.101	0.925	0.1044	0.0928
Rotor solidity (thrust-weighted), σ_T	0.101	0.101	0.1033	0.093
Rotor solidity (geometric), σ_G	0.101	0.096	0.1033	0.093
Linear twist angle, Θ	-9.5°	-9.5°	-14°	-9°
Aerofoils	RC(4)-10	RC(4)-10	RC(4)-12	HH-02
	RC(3)-07	RC(3)-07	RC(4)-10	NACA64A006
			RC(6)-08	

gow LBL, whereas, additional geometries were obtained through The Technical Collaboration Program (TTCP) activity and are labelled as TTCP LBERP and TTCP LBL.

The Glasgow blade geometries were generated using ICEM-HEXA. For both blades, the root cutout section was omitted (low dynamic pressure in this region), and the blade root started at approximately 15.7%R. Both blades were scaled to a chord of 1.0 meaning, that the Langley BERP blade, was simulated on a slightly higher radius (equal to the aspect ratio), as seen in Figure 4.1. The rotor blade twist is referenced to the 75%R station, meaning that there is 0^o pitch angle at 75%R. The planform geometry was generated using a C program which used the parameterisation of a BERP type tip demonstrated by Johnson and Barakos [179]. An approximation of the exact planform shape was made for the LBERP blade, based on the shape outline in the report by Yeager et al. [429]. For both blades, a blunt trailing edge of 0.4% chord was used. For the LBL blade, a sigmoidal thickness distribution was assumed in the aerofoil transition region. The thickness distribution was also assumed for the LBERP blade to keep the aerofoil thickness constant (7%c) across the BERP tip. The blade thickness was then tapered off (linearly) from 0.96R to match the 0.4%c thickness of the trailing edge at the tip.

Certain differences were observed between the Glasgow and TTCP blade geometries. For the LBL blade, differences were observed in the thickness distribution across the aerofoil transition region. The TTCP LBL blade geometry assumed a linear distribution, whereas the Glasgow LBL geometry used a sigmoidal distribution. As will be seen later, this change is not significant in the blade performance predictions. Greater differences are observed for the LBERP blades. While the tip shape planform is fairly similar, the thickness distribution across the blade tip shows major differences. A thinner trailing edge thickness was also assumed for the TTCP LBERP blade (0.15%c compared to 0.4%c) Furthermore, the TTCP LBERP has a slight blade tip anhedral (corresponding to approximately 7 degrees), which is shown in Figure 4.3. The differences in the Langley BERP blade thickness distributions, mainly come from a different

assumption in the aerofoil orientation. The Glasgow geometry assumed aerofoils normal to the pitch axis, whereas the TTCP geometry, used aerofoils normal to the leading edge. For such an orientation, however, a number of aerofoil sections will intersect each other especially, those coming from the swept region of the blade. An assumption must be made on the shape of the blade here, ensuring surface smoothness. The effect of the different blade shape is analysed in hover in Chapter 5, CFD Validation in Hover.

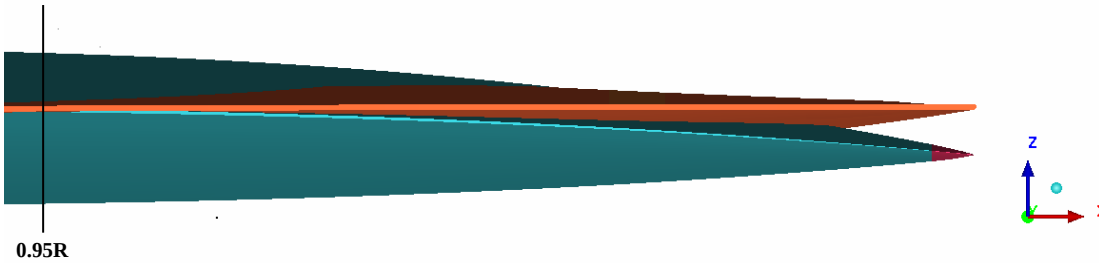

Figure 4.3: Differences between the Glasgow LBERP blade (in orange) and the TTCP LBERP blade (in green) at the very tip of the blade, showing the slight anhedral for the TTCP geometry.

The effect of anhedral is also examined for the Glasgow geometries in Chapter 7, Rotor design - Pre-Optimisation Considerations. The blade geometries were not generated manually, as a blade surface parameterisation method was used along with a mesh deformation method. An anhedral of 15 degrees was applied at 0.945 radius (start of the LBERP raked tip). A parabolic anhedral distribution was assumed. The geometry of the LBERP blade with anhedral is shown in Figure 4.4.

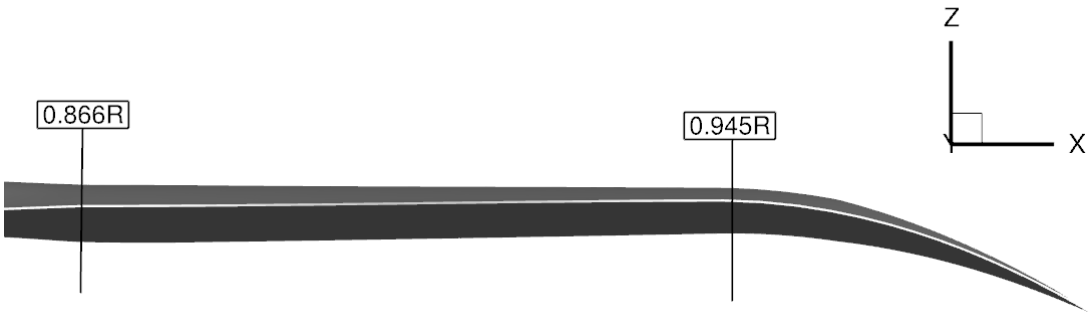

Figure 4.4: Geometry of the LBERP blade with 15 deg parabolic anhedral, viewed in the streamwise direction.

4.1.2 PSP Rotor Blade

The PSP rotor blade [420] is better defined compared to the Langley geometries with no uncertainties in the blade geometry. The PSP rotor blade has a swept-tapered tip and a linear twist angle of 14 degrees. The blade includes three aerofoil sections within the design: the RC(4)-12 is used up to 65% R, the RC(4)-10 aerofoil is used from 70% R to 80% R, and the RC(6)-08

is used from 85% R to the tip of the blade. The main lifting section, RC(4)-10 is the same aerofoil as used within the LBERP and LBL blade designs. The aerodynamic characteristics of these aerofoils can be found in [280, 281]. The exact geometry was obtained through the AIAA Hover Prediction Workshop, and hence is exactly the same as seen in the majority of publications found for this rotor blade. The geometry used within this work neglects the root cutout, and hence the blade starts at 24.8% R. A detailed structural model was also provided for this blade design [290], with uncertainties only present in the stiffness, area and mass near the root cuff region.

4.1.3 AH-64A Rotor Blade

For the full-scale AH-64A rotor blade, the majority of planform properties are based on the model scale wind tunnel tests by Berry [47] and optimisation study by JanakiRam et al. [168]. The AH-64 rotor blade has a swept tip, a linear nominal blade twist of 9 degrees and an aspect ratio of 13.714. The blade is composed of two aerofoil sections, the HH-02 section up to 0.943R and the NACA64A006 section at the tip of the blade. Information about the aerodynamic characteristics of these aerofoils can be found in [417] and [229] respectively. Based on this information, the geometry of the blade has been generated in ICEM-CFD. Uncertainties, however, exist regarding the orientation of the aerofoil section where the sweep is introduced, and the manner in which the two aerofoils are blended. The HH-02 aerofoil has a trim tab, whereas the NACA64A006 section does not. The thickness of the trailing edge for each of the aerofoils is also slightly different. The thickness of the blunt trailing edge for the NACA64A006 section was increased to match the inboard, HH-02 section. This was done by deleting the points in the last 10% of the aerofoil, increasing the thickness of the trailing edge and then fitting a spline through the remaining points. The planform was designed based on the information in [47]. In particular, the sweep initiation positions near the blade tip are slightly different at the blade leading and trailing edges (0.931R and 0.943R respectively), which was incorporated within the tip design. The aerofoil orientation was assumed to be normal to the blade feathering axis. The blade twist was applied about the quarter chord point of each section, not the twist axis, hence the generated planform does not exhibit dihedral. Finally, the initiation of the root cutout was assumed to begin at 0.16R, and the chord at the root was assumed to be half the reference blade chord. The structural properties are also fairly well defined for this blade, and can be found in [47].

4.2 Mesh Generation and Computational Setup

The computational meshes for each of the rotor blade geometries were also generated within ICEM-HEXA, based on a multi-block structured approach. For each of the rotor blades, the

overset grid technique was used, hence a foreground was generated to resolve the blade geometries, with a background grid to capture the farfield wake geometry. This type of method allows for grid deformation, due to blade flapping and pitching in forward flight, without affecting the grid quality. For the majority of cases, the simulations were performed for isolated rotors, without modelling the fuselage, test stand or facility walls to minimize computational costs. The rotors were also modelled as rigid, as for most cases the experimental data was obtained from model scale tests, hence aeroelastic effects were not expected to be significant. However, structural models have been generated for the PSP and AH-64A blades for future CFD/CSD coupled analyses with the structural modelling approach shown in Appendix B. All cases were performed using the k-ω SST turbulence model unless specified otherwise.

4.2.1 Hover - Computational Setup

In hover the flow is solved using the steady state hover formulation. Only a quarter of the computational domain was meshed, assuming periodic conditions for the flow field in the azimuthal direction. This assumption is valid if the wake generated by the rotor is assumed periodic and the blades do not experience deep stall. A source/sink model is used for the simulations with a Froude boundary condition imposed at the inflow and outflow. A typical computational domain for hover simulations is shown in Figure 4.5. The distances between the rotor blades and the inflow/outflow surfaces are based on experience from previous studies using the HMB3 solver [359]. The hub is modelled as a flat plate across the entire domain, to ease the application of boundary conditions in the solver. This representation is not very realistic, however, due to the low dynamic pressure in this region, it does not have a significant effect on the overall CFD solution.

4.2.2 Forward Flight - Computational Setup

In forward flight, the full rotor disk is modelled with four blades as the flow is highly unsteady. The hub is modelled as a generic ellipsoidal surface. The flow is solved in a cylindrical domain with farfield boundary conditions. The typical domain used is shown in Figure 4.6. For the AH-64A rotor blade cases, the rotor blade is inserted in an intermediate background rotor disk to allow a larger computational domain, without increasing the grid sizes and for overset harmonic balance calculations as shown in Figure 4.7.

4.2.3 Mesh Topologies

For the blades, a C-topology around the leading edge of the blade was selected, whereas an H-topology was employed at the trailing edge. For the LBERP blade, an O-grid is used around the tip of the blade due to the rounded blade tip, whereas the PSP, LBL and AH-64A blades are

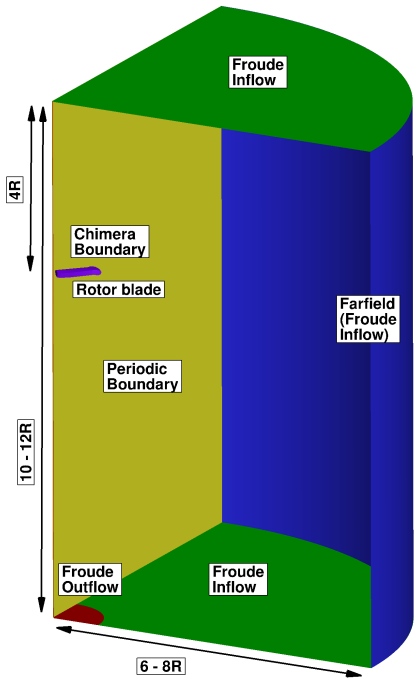

Figure 4.5: Typical computational domain used for hover simulations.

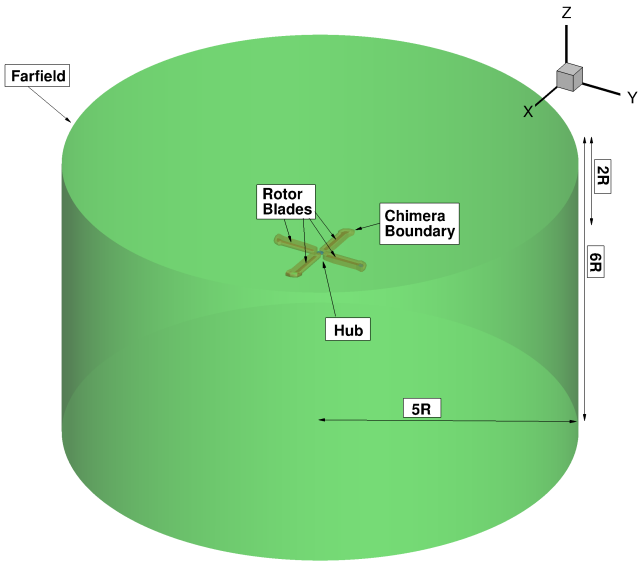

Figure 4.6: Typical computational domain used for forward flight simulations.

closed off using a H-type topology due to the sharp blade tip. The mesh topologies for the four blades are shown in Figure 4.8. The same grids were used for the TTCP and Glasgow blade geometries. The grids for the LBERP and LBL blades with anhedral are generated using a mesh deformation method (based on Inverse Distance Weighting). The grid sizes for the four rotor blades in hover and forward flight are shown in Table 4.2. A second grid is generated with finer wall normal spacing for the PSP rotor blade, to examine the effect of a transitional turbulence

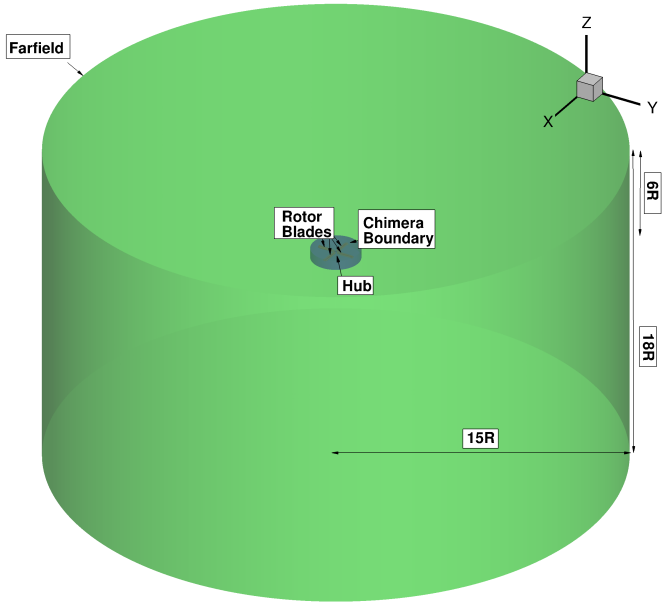

Figure 4.7: Computational domain for used forward flight simulations of the Apache rotor blade.

model. The effect of a finer grid was also examined for the Langley Baseline blade in low-speed forward flight. Finally, a coarser grid is used for the optimisation study of the AH-64A blade in forward flight, labelled as AH-64A OPT. The root cutout was also ignored in the AH-64A OPT grid. The nominal AH-64A grid is used for hover optimisation, the same grid as for CFD validation.

Table 4.2: Grid sizes in millions of cells for the simulated rotor blades in hover and forward flight. H = Hover, FF = Forward Flight, PA = points around aerofoil, PN = points normal to the blade, PS = points in the spanwise direction, WDIST = wall distance, FMESH = number of cells in foreground mesh, BMESH = number of cells in background mesh, TMESH = total number of cells in mesh.

BLADE	PA	PN	PS	WDIST	FMESH	BMESH	TMESH
PSP - H (Mesh I)	252	56	215	$1.0 \cdot 10^{-5} c_{\text{ref}}$	5.2M	7.2M	12.4M
PSP - H (Mesh II)	252	101	215	$1.0 \cdot 10^{-6} c_{\text{ref}}$	8.1M	7.2M	15.3M
LBL - H	234	64	118	$1.0 \cdot 10^{-5} c_{\text{ref}}$	3.9M	4.9M	8.8M
LBERP - H	222	66	185	$1.0 \cdot 10^{-5} c_{\text{ref}}$	4.6M	4.9M	9.5M
AH-64A - H	230	70	165	$1.0 \cdot 10^{-6} c_{\text{ref}}$	5.4M	5.3M	10.7M
PSP - FF	198	46	145	$1.0 \cdot 10^{-5} c_{\text{ref}}$	12.2M	20M	31.2M
LBL - FF (Mesh I)	234	64	118	$1.0 \cdot 10^{-5} c_{\text{ref}}$	15.7M	27.8M	43.5M
LBL - FF (Mesh II)	338	74	142	$1.0 \cdot 10^{-5} c_{\text{ref}}$	39.5M	62.2M	101.7M
LBERP - FF	222	66	185	$1.0 \cdot 10^{-5} c_{\text{ref}}$	18.4M	27.8M	46.2M
AH-64A - FF	230	70	165	$1.0 \cdot 10^{-6} c_{\text{ref}}$	21.6M	11.4M + 3.1M	36.1M
AH-64A - OPT	182	56	109	$1.0 \cdot 10^{-6} c_{\text{ref}}$	9.5M	3.2M + 0.4M	13.1M

The used mesh sizes also come from experience and are mainly limited by computational

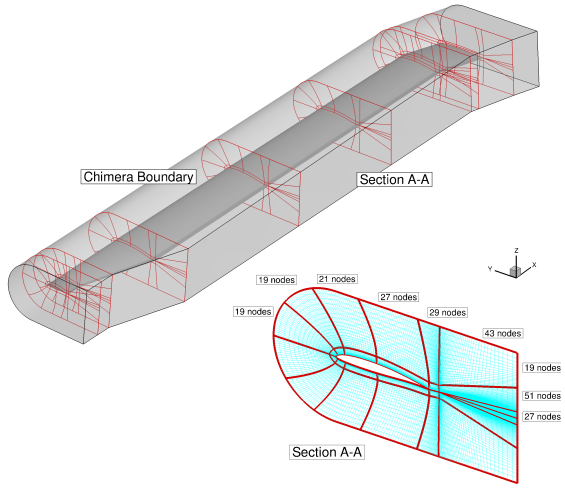

(a) Apache blocking

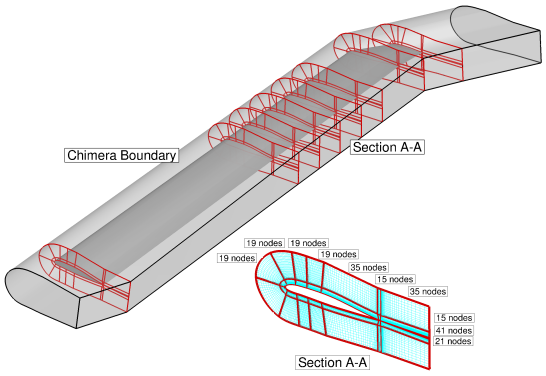

(b) PSP blade blocking

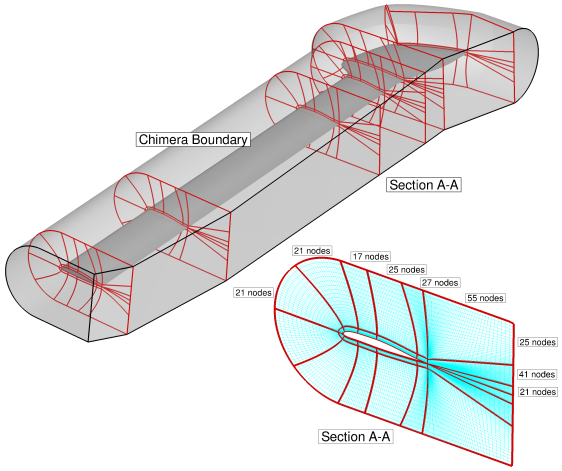

(e) Langley BERP blocking

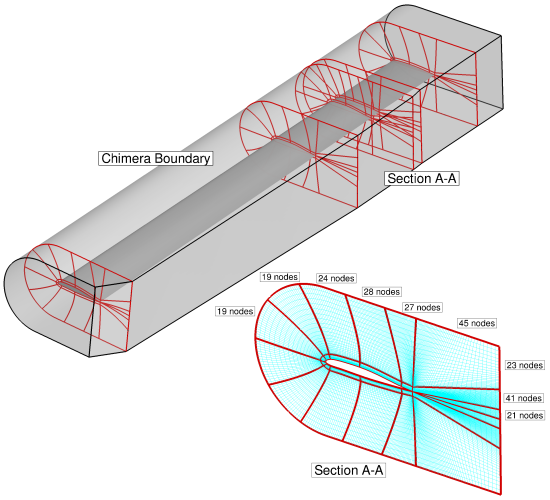

(f) Langley Baseline blocking

Figure 4.8: Foreground grid multi-block mesh topologies for each of the simulated rotor blades

resources, but also given the validation results shown in the present research, are proven to be adequate for blade loads predictions. As can be seen from Table 4.2, the LBERP foreground mesh has a higher number of cells than the LBL, due to the necessity to resolve the notch and highly swept tip geometry. The PSP mesh is the same as used by Jimenez and Barakos [176], with both foreground and background grids coarsened for forward flight simulations. The AH-64A blade grid uses a finer wall normal spacing (full-scale Reynolds number) and more efficient background grid topology as stated previously. The AH-64A forward flight optimisation grid is mainly limited by the memory demands of the adjoint-harmonic balance method. For all blades, a typical foreground blade grid uses 220-250 points around the aerofoil (PA), 50-70 points normal to the blade (PN), 120-210 points along the span (PS), depending on the geometry complexity. The typical wall distance (WDIST) used is $1.0 \cdot 10^{-5} c_{\text{ref}}$, which ensures a near wall $y^+ <= 1$ for most cases. Typically 4 to 5 millions cells are used for the near-blade grid (FMESH) with 5 to 7 million cells used in the background grid (BMESH), giving total mesh

sizes (TMESH) of 9 to 12 million cells. The size of the foreground mesh is dictated by resolving the correct surface pressure and skin friction distributions, hence blade loading, whereas the background grid resolution is determined by the wake resolution and preservation of vortex properties.

Chapter 5

CFD Validation in Hover*

This chapter presents CFD validation of the HMB3 solver for different rotor blades in hover conditions. Firstly, the test conditions are presented for the four examined rotor blades, LBL, LBERP, PSP and AH-64A. Next, various sensitivity analyses are performed focused on the effect of typical assumptions when comparing CFD results with experimental data including geometric and numerical modelling considerations. Following, performance predictions from the CFD analyses are compared with experimental data for the LBERP, LBL, PSP and AH-64A blades. Finally, surface pressure results are compared for the PSP blade with data from pressure transducers and the PSP technique.

5.1 Test Conditions

The test conditions for performance predictions in hover are replicated in the CFD simulations for the four examined rotor blades: LBL, LBERP, PSP and AH-64A are presented in Table 5.1. Details of the different examined conditions in the sensitivity analyses are presented in each of the relevant subsections.

The LBL and LBERP blades were tested by Yeager et al. [429] in minor ground effect, which was neglected in the CFD simulations. The experiments were performed in a Freon medium which has a higher density than air, allowing model scale tests at higher Reynolds numbers. The correct Reynolds number was modelled within the CFD simulation, however, the effect on the gas specific heat ratio was neglected. This has a negligible effect as will be seen in the Freon sensitivity subsection. The AH-64A blade is simulated at the full-scale Reynolds number, whereas the other three blades (LBL, LBERP, PSP) are simulated at model-scale. For all blades, a collective sweep is performed for performance predictions, with an additional point at $C_T = 0.008$ aimed at comparison of the different designs, which will be shown in Chapter 7,

*A large portion of the work presented in this Chapter is published in T. Fitzgibbon et al., "Validation of the Steady State Hover Formulation for Accurate Performance Predictions," *AIAA Journal*, Vol. 57, No. 12, 2019, pp. 5293-5308, DOI: 10.2514/1.J058408.

Table 5.1: Test conditions in hover for the LBL, LBERP, PSP and AH-64A rotor blades examined in the CFD simulations.

Blade	M_{TIP}	**Re No.**	**Other**	**CFD θ_0/C_T**
LBERP	0.628	2.51×10^6	Minor ground effect z/d=0.83 and Freon medium (neglected)	$\theta_0 = 9^o, 10.5^o, 12^o, 13.5^o$ $C_T = 0.008$
LBL	0.628	2.74×10^6	Minor ground effect z/d=0.83 and Freon medium (neglected)	$\theta_0 = 9^o, 10.5^o, 12^o, 13.5^o$ $C_T = 0.008$
PSP	0.58	1.94×10^6	N/A	$\theta_0 = 6^o, 8^o, 10^o, 11^o$ $C_T = 0.008$
AH-64A	0.65	7.99×10^6	Full-scale blade	$\theta_0 = 6^o, 8^o, 10^o, 11^o$ $C_T = 0.008$

Rotor Design - Pre-Optimisation Considerations. All Reynolds numbers given in Table 5.1 are based on the reference chord equal to the chord of the first aerodynamic section.

5.2 Sensitivity Analyses

In this section, a number of sensitivity analyses for hover calculations are presented. Firstly, a geometric sensitivity is presented for the LBL and LBERP blades regarding the blade geometry assumptions based on the report by Yeager et al. [429]. Two blade geometries were generated for the LBL and LBERP blades labelled as the TTCP geometries and Glasgow geometries. Next, the sensitivity of different fully-turbulent k-ω turbulence models is presented, as well as a comparison of the hover performance prediction in freon and in air. For the PSP blade, the solution methodology is assessed by comparing the steady state formulation with predictions from an unsteady solution. Finally, due to available experimental data, transitional effects are also examined for the PSP rotor blade.

5.2.1 Geometric sensitivity for the LBL and LBERP blades

The sensitivity of two different geometries, generated based on the same data within the report by Yeager et al. [429] is examined. As shown in Chapter 4.1 Blade Geometries, certain geometric differences exist between the planforms generated at Glasgow and within the TTCP collaboration. The integrated loads are shown in Table 5.2 at two collectives of 9^o and 12^o for the LBERP and LBL geometries.

As can be seen in Table 5.2, the differences for the LBL blade are not significant and are under one count in Figure of Merit. Similar differences can be obtained using different turbulent models, computational setups or solution methodologies. The difference for the LBERP blade is much larger. A performance difference of five counts in FoM is significant, considering the minor differences in blade geometry. For this reason, the sectional loads were extracted from

Table 5.2: Differences in integrated loads predictions for the TTCP and Glasgow geometries for the LBERP and LBL blades

Blade	θ_0	C_T	C_Q	FoM
LBL (Glasgow)	9.0	0.00730	0.000658	0.671
LBL (TTCP)	9.0	0.00736	0.000659	0.677
LBL (Glasgow)	12.0	0.01037	0.001144	0.652
LBL (TTCP)	12.0	0.01047	0.001140	0.664
LBERP (Glasgow)	9.0	0.00720	0.000689	0.626
LBERP (TTCP)	9.0	0.00724	0.000649	0.671
LBERP (Glasgow)	12.0	0.01045	0.001215	0.622
LBERP (TTCP)	12.0	0.01048	0.001130	0.671

the solution for further analysis and are presented in Figure 5.1.

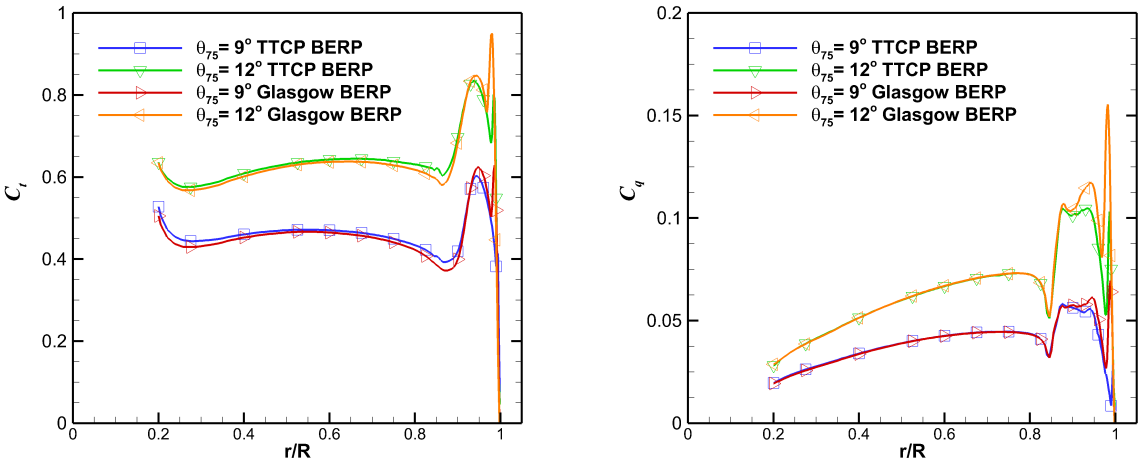

(a) Sectional thrust distribution

(b) Sectional torque distribution

Figure 5.1: Sectional loads the LBERP TTCP and Glasgow geometries at two collectives of 9 and 12 degrees.

Figure 5.1 shows the more favourable performance of the TTCP LBERP geometry compared to the Glasgow geometry. The peak thrust at the tip of the blade is reduced, whereas the thrust is slightly higher inboard of the blade tip. The main differences, however, occur in the torque distribution, where a reduced torque is seen across the paddle tip, as well as at the very tip of the blade. The source of these differences is examined further at 9 degrees collective. The surface pressure distributions for the TTCP and Glasgow blade geometries are shown in Figure 5.2. The differences in the shapes of the local aerofoil sections are also presented.

The surface pressure distributions, show more detail regarding the nature of the blade loading. At the most inboard section and across the notch, the pressure distributions are fairly similar due to the similar aerofoil sections used here. The typical pressure distribution can be seen across the notch, with a reduced stagnation pressure due to a larger cross flow velocity component. Fur-

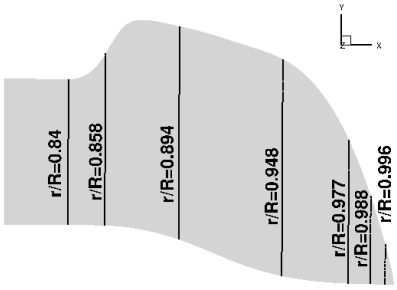

(a) Radial stations

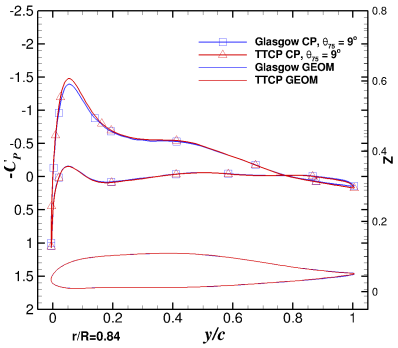

(b) r/R = 0.84

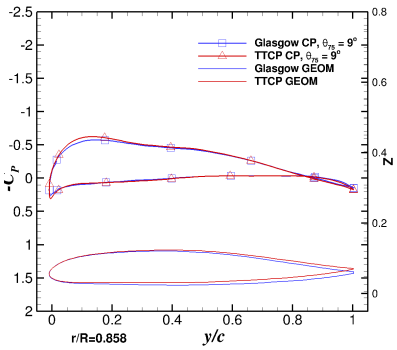

(c) r/R = 0.858

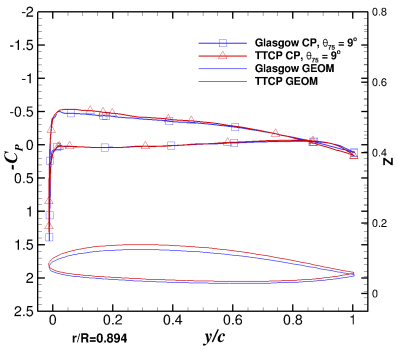

(d) r/R = 0.894

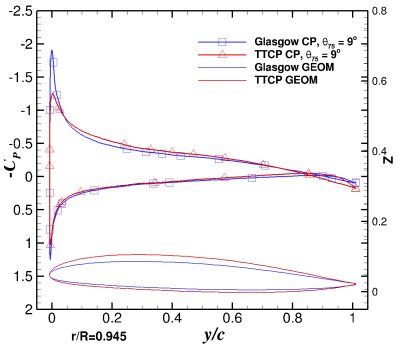

(e) r/R = 0.948

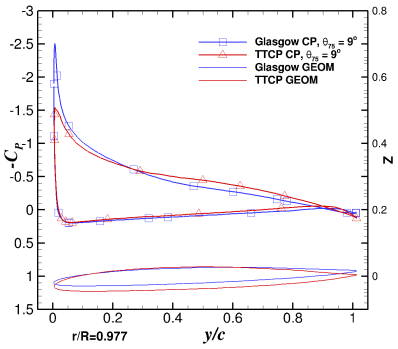

(f) r/R = 0.977

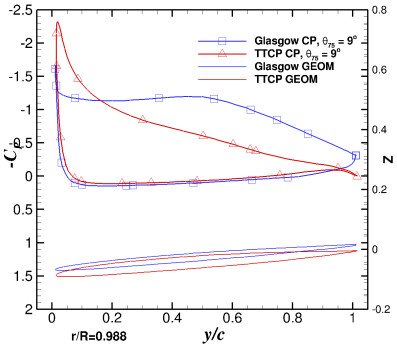

(g) r/R = 0.988

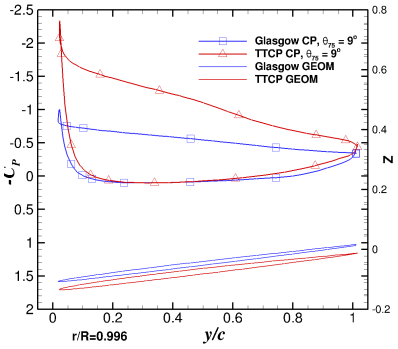

(h) r/R = 0.996

Figure 5.2: Surface pressure distributions at seven radial stations for the LBERP TTCP and Glasgow geometries at 9 degrees collective. Aerofoil geometries also shown, taken normal to blade pitch axis.

ther outboards, the TTCP blade geometry has a higher aerofoil thickness when compared with the Glasgow geometry hence larger differences are seen. The suction peak at r/R = 0.948 and r/R = 0.977 is reduced for the TTCP blade geometry leading to performance improvements. At r/R = 0.988, the tip vortex for the Glasgow geometry separates from the blade surface, whereas the vortex of the TTCP blade geometry remains attached to the blade surface, and is separated at the most outboard examined section. This behaviour at the very tip of the blade increases the thrust and leads to a torque reduction improving the integrated blade performance. The tip vortex formation process is shown in Figure 5.3 through contours of vorticity magnitude.

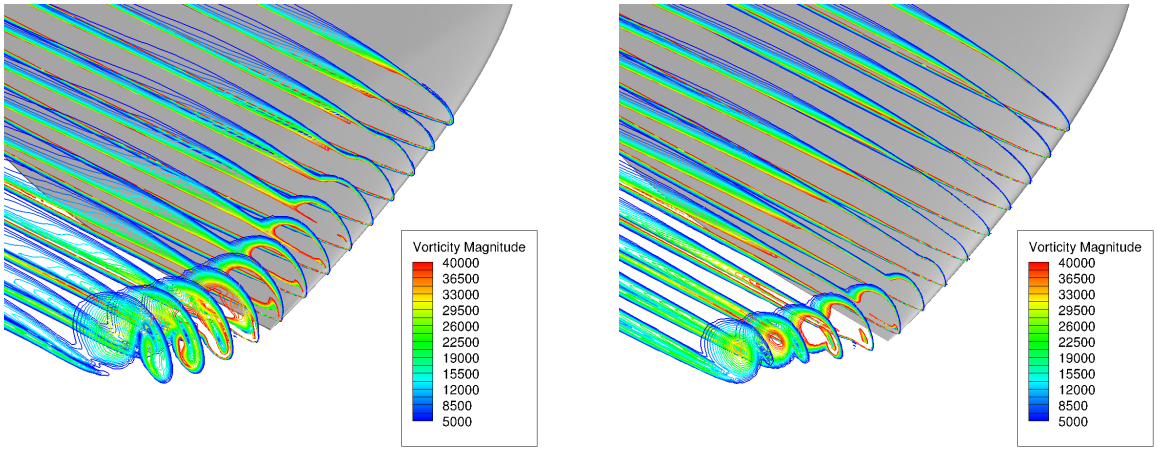

(a) Glasgow LBERP (b) TTCP LBERP

Figure 5.3: Tip vortex formation for the LBERP TTCP and Glasgow geometries at 9 degrees collectives using contours of vorticity magnitude.

Figure 5.3 shows are much cleaner tip vortex for the TTCP LBERP blade. The vortex fully-develops at a chordwise location, that is closer to the trailing edge compared to the Glasgow geometry. The secondary structure within the tip vortex, quickly disappears, whereas for the Glasgow geometry is present for a larger distance behind the blade. These flow features show that mild changes in geometry such as minimal anhedral and a different thickness distribution across the blade tip can significantly affect the performance of the blade. The tip vortex formation process is key in achieving a more optimal blade loading, especially at the tip of the blade. Here, the tip shape led to reduced loading at the tip, and hence higher performance.

5.2.2 Turbulence model sensitivity

A turbulence model sensitivity study was performed for the TTCP LBERP blade at a thrust coefficient of 0.008. The hover trimming routine was used for each of the cases to achieve the required thrust level. Three turbulence models were examined: the Menter k-ω SST model [251], Menter k-ω SST [251] with a turbulence production limiter (pk limiter) and the Wilcox

baseline k-ω model [411]. The integrated loads results for the three cases are shown in Table 5.3.

Table 5.3: Integrated loads sensitivity due to different turbulence models for the TTCP LBERP blade at $C_T = 0.008$.

Blade	Turb. model	θ_0	β_0	C_T	C_Q	FoM
LBERP (TTCP)	Menter k-ω SST	9.56	3.45	0.00794	0.000742	0.674
LBERP (TTCP)	Menter k-ω SST with pk lim.	9.58	3.47	0.00799	0.000728	0.693
LBERP (TTCP)	Wilcox baseline k-ω	9.61	3.45	0.00799	0.000754	0.669

A low sensitivity on the FoM value can be seen between the Wilcox baseline k-ω [411] and Menter k-ω SST [251] turbulence models. The addition of the pk limiter has a larger impact on the FoM prediction, leading to a difference of 2 counts. The pk limiter adds a clip on the turbulence production term to 20 times the destruction term as suggested by Menter [251]. This avoids excessive growth of turbulence eddy viscosity especially seen in the wake and vortex cores within many rotor simulations [75, 307]. Here for performance predictions, we use the k-ω SST turbulence model without the pk limiter term due to good correlation with experimental data seen for many other rotors [173, 174, 177]. In low speed forward flight, however, where many near blade vortex interactions occur, the pk limiter was seen to improve correlation with experimental data as seen in the next chapter on CFD validation in forward flight.

5.2.3 Freon Sensitivity - Effect of Specific Heat Ratio

The TTCP Langley BERP blade at $C_T = 0.008$ is also considered for the integrated loads sensitivity due to specific heat ratio. For both cases, the same Reynolds number of 2.51×10^6 was used based on Freon properties, and only the effect of specific heat ratio γ was examined. The integrated loads results are presented in Table 5.4.

Table 5.4: Integrated loads sensitivity due to different specific heat ratio (freon vs air) for the TTCP Langley BERP blade at $C_T = 0.008$.

Blade	γ	θ_{75}	β	CT	CQ	FoM
LBERP (TTCP)	1.4	9.56	3.45	0.00794	0.000742	0.674
LBERP (TTCP)	1.128	9.56	3.45	0.00795	0.000737	0.680

The impact on the rotor loads is not significant, as a difference of less than 1 count in FoM is seen. When examining the flow solution in more detail, the differences occurred due to a stronger compression in the blade tip region at the leading edge for the case with a higher specific heat ratio, as shown in Figure 5.4. This leads to reduced performance due to a slightly more highly loaded blade tip.

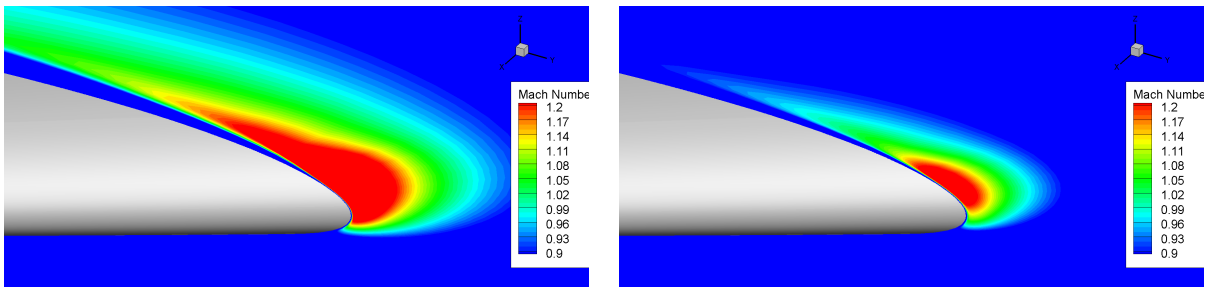

(a) Air (b) Freon

Figure 5.4: Sensitivity of the local Mach number near the leading edge at r/R=0.988 due to air and freon specific heat ratios.

5.2.4 Solution Methodology Sensitivity

In this section, a comparison is performed between the steady state hover formulation and an unsteady simulation. The test case under consideration for this comparison is the PSP rotor blade at 9 degrees collective and blade tip Mach number 0.65. The exact same grid is used, for both simulations of 13.5 million cells. For the unsteady case, the simulation is also run using periodic boundary conditions, so that only one blade is modelled. Farfield conditions (pressure boundary conditions) are used at the inflow and outflow boundaries. This is the main reason for the much higher computational cost of the unsteady simulations, as it takes much longer for the wake to develop. Here, 0.5 degree steps are used in azimuth and the simulation is ran for 30 revolutions. 120 pseudo-time steps are used within each azimuthal time step to achieve good convergence. In comparison, the steady-state simulation is fully converged after 120,000 iterations. The differences in rotor performance are shown in Table 5.5. The integrated loads for the unsteady simulation are averaged from one revolution.

Table 5.5: Comparison of integrated loads between the steady and unsteady simulations for the PSP blade at 9 degrees collective and 0.65 blade tip Mach number.

CFD Method	C_T	C_Q	*FoM*	**% difference**
Steady	0.00759	0.000666	0.702	-
Unsteady	0.00760	0.000665	0.704	+0.28%

The performance results for the steady and unsteady formulations are in very good agreement. The difference in FoM is within 1 count. For the unsteady case, a slightly lower torque and higher thrust are predicted. The differences between the two solutions are discussed further by analysing the surface pressure distributions and sectional loads. For the unsteady case, the data is averaged over one revolution.

The surface pressure coefficient is extracted at two radial stations (r/R= 0.75 and 0.95) for both solutions and is normalised by the local flow velocity. The comparison for the steady and unsteady cases is shown in Figure 5.5

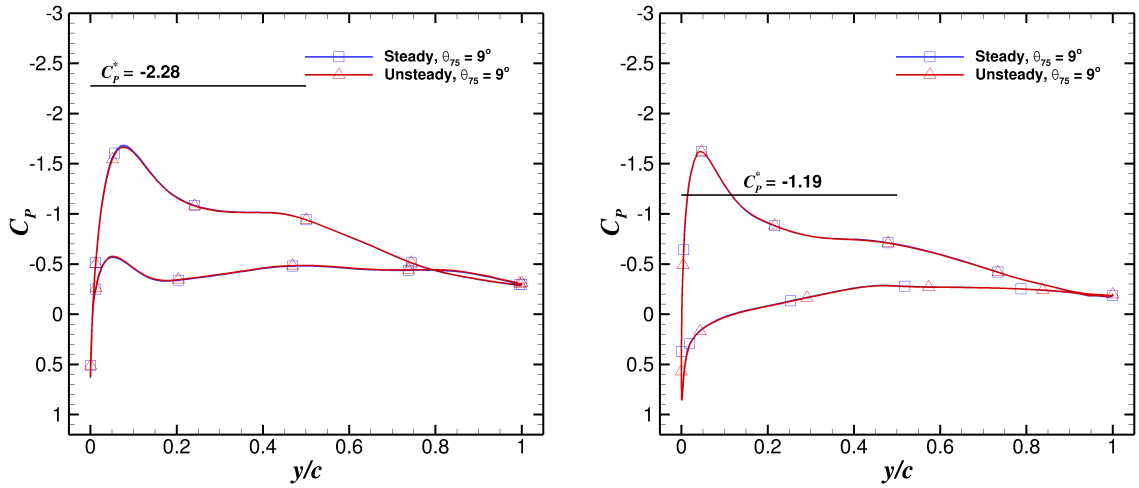

(a) 0.75R (b) 0.95R

Figure 5.5: Comparison of chordwise surface pressure coefficient (normalised by local flow velocity) distributions for PSP blade computed using steady and unsteady CFD formulations.

The surface pressure distributions are in very good agreement. Minor differences can be seen in the magnitude of the suction peaks at the two radial stations, however, these are unlikely to affect the net blade performance to a considerable degree. To analyse the difference in blade loading, the sectional thrust and torque distributions are compared. These are plotted in Figure 5.6 based on rotor tip velocity.

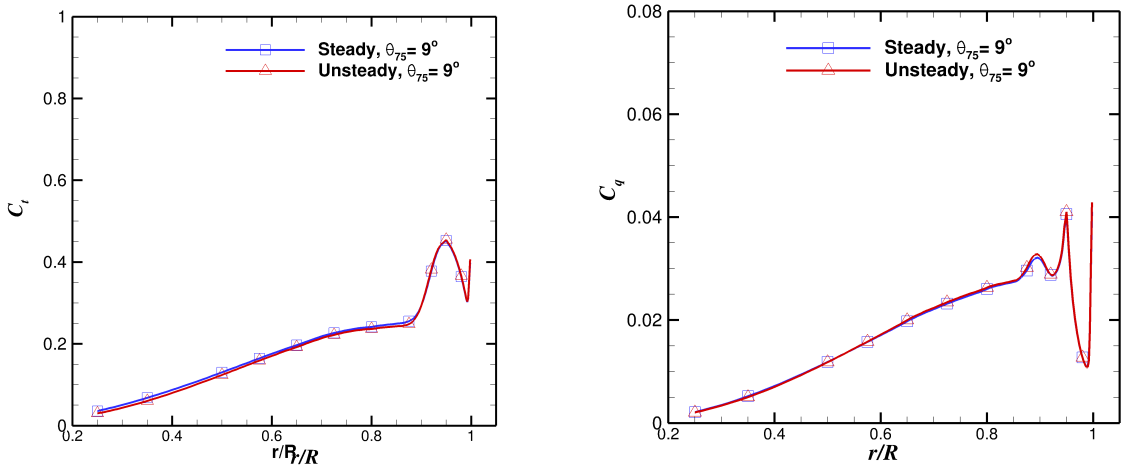

(a) C_T vs r/R (b) C_Q vs r/R

Figure 5.6: Comparison of sectional load distributions based on tip velocities for the PSP blade computed using steady and unsteady CFD formulations.

The sectional loads for the steady and unsteady formulations are in good agreement. A slightly higher thrust can be seen inboards for the steady case. A stronger root vortex is emitted for the unsteady case. Some unsteadiness is also seen in the root region, as the downwash field

indicates variation with time. The main cause of this is attributed to the unrealistic representation of the hub geometry (flat plate along the entire domain) potentially leading to unsteady flow features near the root. Due to the agreement of the sectional torque distributions, the root flow features are not considered to have a significant impact on the net performance of the blade or the flow field in the outboard region. The outboard thrust distribution is also in very good agreement. To highlight the similarity in both solutions, the wake is visualised in Figure 5.7.

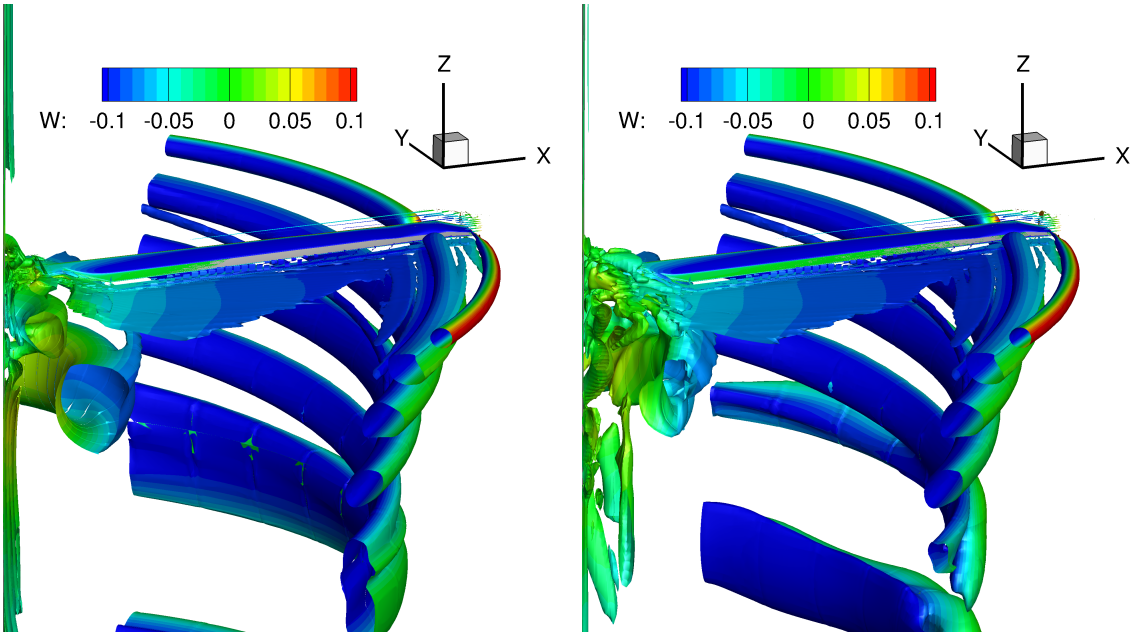

(a) Steady formulation (b) Unsteady formulation

Figure 5.7: Comparison of wake geometries visualised using Q-criterion (value of 0.0005) coloured with downwash velocity for the PSP blade in hover computed using steady and unsteady CFD formulations.

The near-blade wake geometries for both formulations exhibit similar features. A cleaner root vortex can be seen in the steady case compared to the unsteady case, however, the impact on the predicted performance is not significant as shown earlier. In the unsteady simulation, in the farfield, the rotor tip vortices are more distorted compared to the steady wake geometry. The background mesh is, however, coarse in this region, and the rotor tip vortices disappear from the flow field through the action of numerical diffusion. No clear wake breakdown can be seen in either of the cases, a phenomenon that exists in many simulations in literature [114]. Due to the farfield boundary conditions, the wake does not connect to the outflow, and the flow recirculates into the domain which could also have a minor impact on the blade performance predictions.

The comparison between the steady and unsteady formulations show the validity of the steady state method for accurate hover performance predictions. The steady formulation is able to obtain a similar solution in terms of integrated loads as the unsteady case at a significantly lower computational cost. A further assessment of the two methods should be performed at higher loading conditions, where greater flow separation is observed.

5.2.5 Transition Modelling Sensitivity

For the PSP rotor blade, a sensitivity analysis was also performed due to transitional effects. For the purposes of examining transition effects on the blade performance, the transitional turbulence model is used, the k-ω SST-γ model of Menter [252]. The integrated loads comparison with experimental data for both fully-turbulent and transitional turbulence models is presented in the next section. Here, we examine the effect of wall normal spacing on the FoM and transition location predictions, as well as the effect of transition on the integrated loads, sectional loads and surface pressure coefficients. For this purpose, the PSP rotor is trimmed to three thrust coefficients of $C_T = 0.005$, 0.007 and 0.009.

For the investigation of the wall normal spacing, the baseline PSP mesh, used for fully-turbulent calculations was refined, to reduce the wall normal expansion ratio. A y^+ of 1 near the wall is obtained in both employed grids. The integrated loads predictions, including the viscous and pressure terms, are shown for both grids in Table 5.6.

Table 5.6: Effect of wall-normal spacing on the hover performance of the PSP blade using the k-ω SST-γ turbulence model, where 1 count = 0.01

Case	C_{Q_p} **in %**	C_{Q_v} **in %**	*FoM*	*FoM* **error**
$C_T = 0.005$ (EXP)	-	-	0.662	-
$C_T = 0.005$ (Mesh I)	82.45%	17.55%	0.686	+2.4 counts
$C_T = 0.005$ (Mesh II)	82.07%	17.93%	0.681	+1.9 counts
$C_T = 0.007$ (EXP)	-	-	0.738	-
$C_T = 0.007$ (Mesh I)	89.21%	10.79%	0.749	+0.9 counts
$C_T = 0.007$ (Mesh II)	88.87%	11.13%	0.742	+0.4 counts
$C_T = 0.009$ (EXP)	-	-	0.778	-
$C_T = 0.009$ (Mesh I)	91.80%	8.20%	0.765	-1.3 counts
$C_T = 0.009$ (Mesh II)	91.85%	8.15%	0.769	-0.9 counts

Based on Table 5.6, it can be stated, that at lower loading, increasing the number of points in the boundary layer, increases the profile drag contribution leading to closer correlation with experimental data. At higher thrust, the viscous and pressure terms of the torque have a similar contribution for both grids. The improved comparison with experimental data, comes from a reduced torque leading to a slightly higher FoM. The differences in the FoM, however, are not significant as a sensitivity within 0.5 counts is observed. These differences are mainly due to different predictions in the transition locations at low blade loading at two radial stations. At low thrust, the bottom surface of the rotor blade remains laminar for a larger portion of the chord for the grid with coarser wall normal spacing as shown in Figure 5.8. This leads to a reduction in the viscous torque term. With increasing thrust, the section where differences can be seen in the transition locations moves further outboards. Therefore, it can be stated, that the transition location predictions may be highly sensitive to the number of points in the near-wall region.

An indicative result for the transition location predictions along the blade span is presented

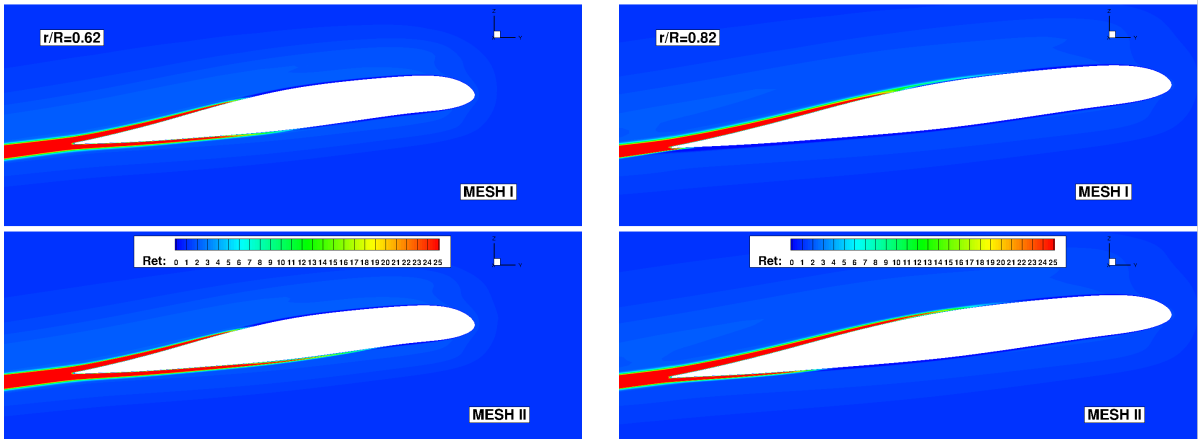

(a) C_T= 0.005, r/R =0.62 (b) C_T= 0.007, r/R =0.82

Figure 5.8: Eddy viscosity ratio contours at two thrust coefficients showing differences in the transition locations between the two grids employed.

for the low thrust case at C_T/σ = 0.048. The results for the grid with finer wall spacing are presented in Figure 5.9. The predictions from HMB3 are compared with experimental data of Overmeyer and Martin [291] and results from Star CCM+ [387].

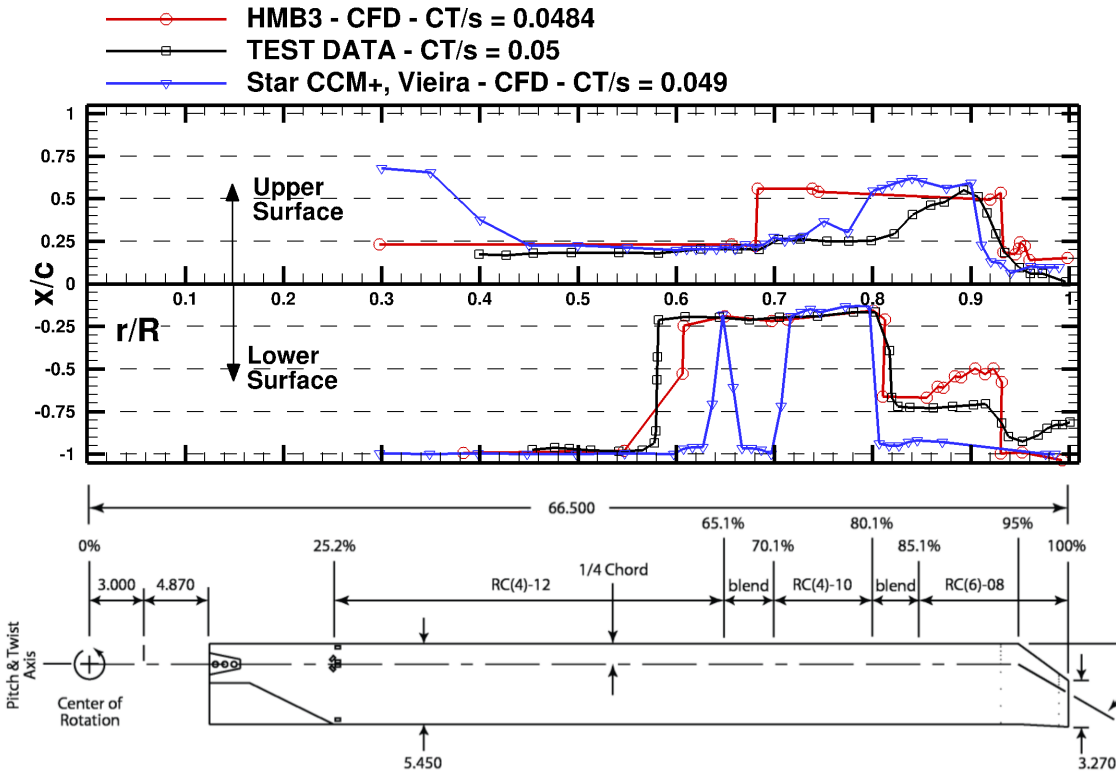

Figure 5.9: Predicted transition locations at C_T/σ=0.0484 and comparison with test data [291] and Star CCM+ predictions [387].

Figure 5.9 shows good agreement for the transition location compared with experimental data. On the upper surface, the transition location moves downstream, further inboard (r/R= 0.68) compared to the test data (r/R=0.84). On the lower surface, the HMB3 predictions show excellent agreement with experiment. Both CFD results predict a laminar flow across the blade tip, whereas the experimental data measured transition before the trailing edge of the blade. The neglection of cross flow instabilities in the transitional turbulence model may introduce errors in the transition location predictions. Further sources of error include turbulence model calibration and freestream turbulence values, which were not reported by experiment. The freestream values used in this work included critical N-factor of 9 and eddy viscosity ratio of 1. In particular, the value of the critical N-factor was found to have an impact on transition location predictions in literature [292].

The effect of transition is examined further by comparing the sectional blade loads for the fully-turbulent and transitional cases. The sectional thrust and torque distributions are shown in Figure 5.10. The pressure and viscous contributions to the total torque are also shown. The loads are scaled by the blade tip velocity and reference blade chord (equal to the chord of the first aerodynamic section).

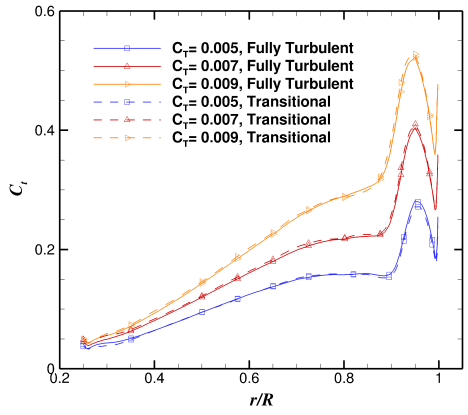

(a) Sectional total thrust distribution

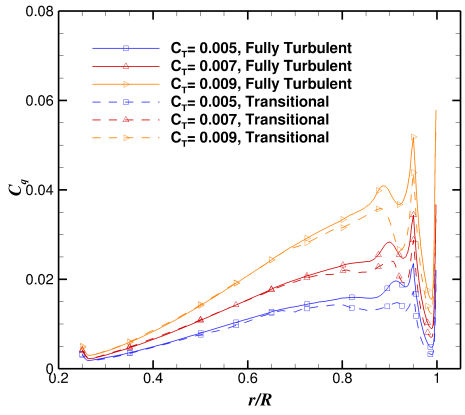

(b) Sectional total torque distribution

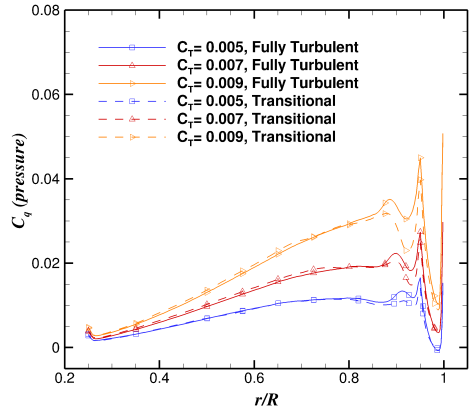

(c) Sectional pressure torque distribution

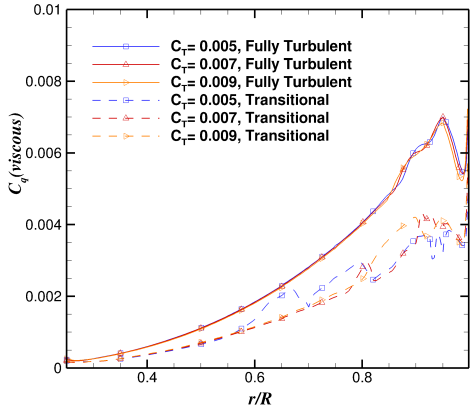

(d) Sectional viscous torque distribution

Figure 5.10: Effect of transition on the sectional thrust and torque distributions for the PSP rotor blade in hover and three thrust coefficients.

The overall torque is reduced when accounting for flow transition as expected. This is especially visible in the region where the preceding blade tip vortex interacts with the blade at r/R = 0.85-0.9, which is mainly due to the pressure torque term as seen from Figure 5.10 c). The viscous torque contribution is also reduced, especially at inboard locations and across the lower side, as transition location predictions indicated a near fully laminar lower surface. The thrust coefficient distributions do not vary as significantly as the sectional torque. Slight differences can be seen inboard, where a slightly higher thrust is seen for the transitional cases. The peak in the thrust also changes with transition, with a minor increase in thrust at higher loading, and reduction at low loading. The effect of transition on the blade loading is examined further by comparing the chordwise pressure distributions at four radial stations of $r/R = 0.75$, 0.85, 0.95 and 0.975, which are presented in Figure 5.11.

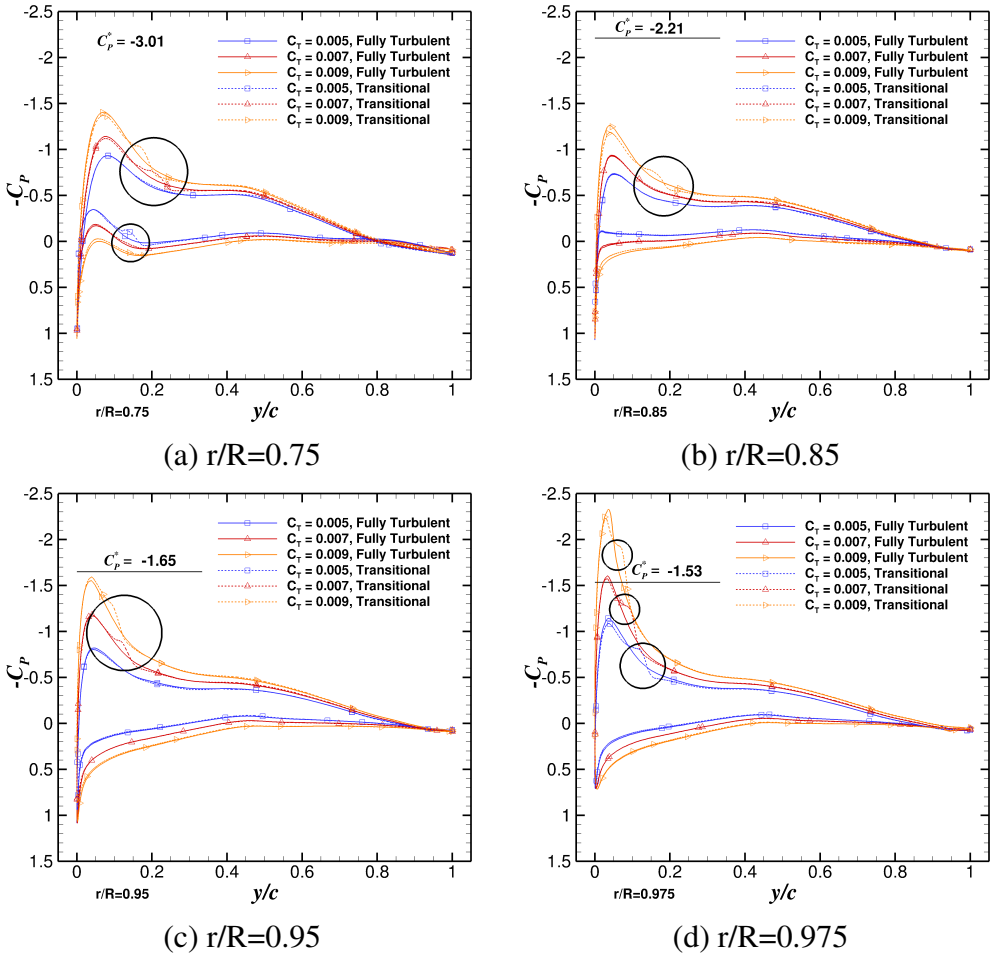

(a) r/R=0.75 (b) r/R=0.85

(c) r/R=0.95 (d) r/R=0.975

Figure 5.11: Effect of transition on the chordwise surface pressure coefficient at four radial stations for three thrust coefficients

The changes in the surface pressure due to transition are subtle. The transition location can clearly be identified on the surface pressure graphs, especially on the upper surface at higher loading, where an abrupt change in the adverse pressure gradient is seen. These features are highlighted in Figure 5.11, by black circles. Changes in the magnitude of the suction peak

are mainly noticeable at the highest thrust coefficient, especially in Figure 5.11 (b). This is in agreement with the sectional loads, where the reduction in suction leads to a reduction in torque due to pressure, at this location. The effect of transition on the surface pressure is not very large, and thus the torque due to pressure does not change as much as the viscous torque term, which approaches as much as 40%, as shown in Figure 5.10 (d). This is due to a significantly reduced overall skin friction for the transitional cases. The skin friction contour plots for the upper surface at two thrust coefficients are shown in Figure 5.12.

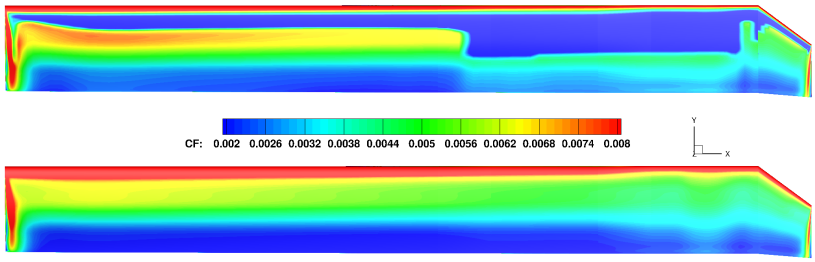

(a) $C_T = 0.005$

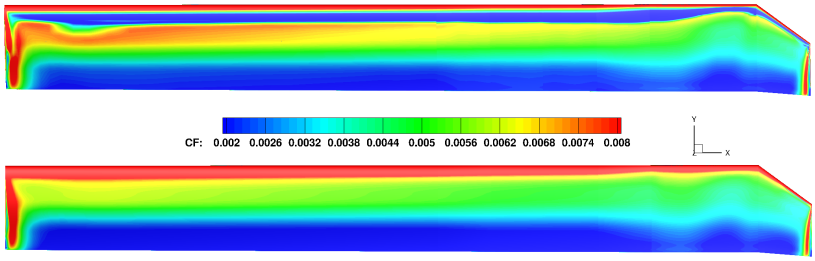

(b) $C_T = 0.009$

Figure 5.12: Effect of transition on the surface skin friction coefficient at low and high thrust, fully-turbulent boundary layer (bottom) and transitional case (top) at each thrust coefficient.

Based on these findings, it can be stated that transitional flow effects may be significant for correlation with experimental data at model scale. The importance of including these effects in the CFD simulations, however, varies between each experimental dataset, and depends on the extent of laminar flow encountered on the rotor blade surface. The magnitude of transitional effects will be dependent on factors such as rotor disk loading, rotor geometry, test section turbulence levels and test Reynolds number. Nevertheless, the studies presented here, as well as many CFD predictions in literature obtain good agreement with experimental data using the fully-turbulent boundary layer assumption. For this reason, the information regarding the freestream turbulence conditions and whether the flow was tripped in experimental studies is crucial to obtain good predictions using CFD. In the cases above, a very low freestream turbulent intensity was used based on a N_{crit} value of 9 and eddy viscosity ratio of 1. Such conditions would not be encountered for full-scale helicopters in flight, due to much higher atmospheric turbulence. Furthermore, vibration, surface roughness and erosion would promote early transition leading to

much lower performance improvements as seen for the model scale PSP rotor blade, which was tested in idealised conditions.

5.3 Performance Predictions in Hover - CFD Validation

The CFD performance predictions for the LBL, LBERP, PSP and AH-64A blades in hover are compared with experimental data in Figures 5.13-5.16. The performance is compared for the different designs in Chapter 7, Rotor design - pre-optimisation considerations, with the present discussion focused on CFD validation.

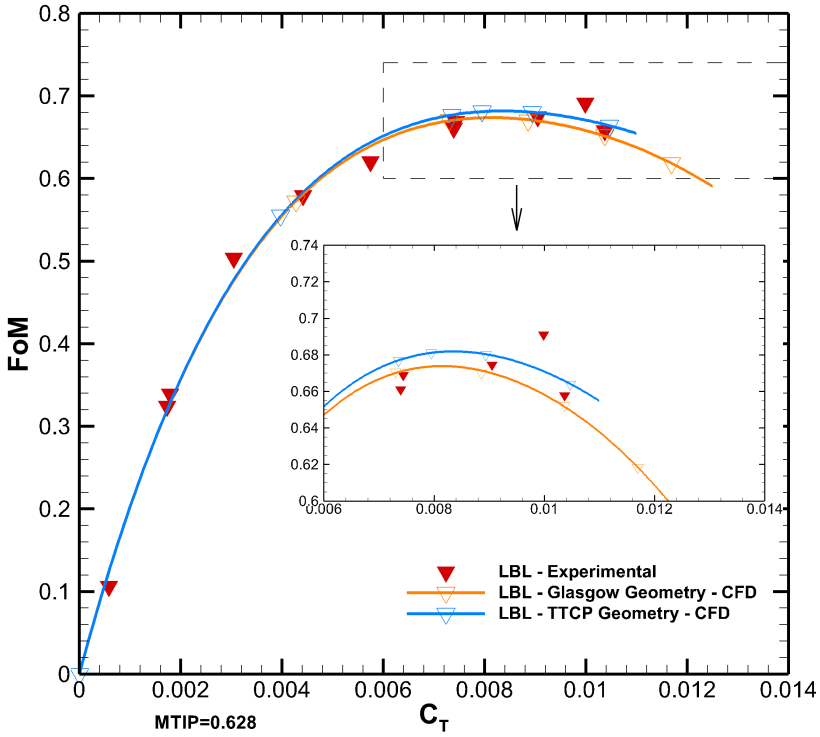

Figure 5.13: Performance predictions for LBL blade (TTCP & Glasgow) in hover and comparison with experimental data of Yeager et al. [429].

The hover performance predictions show very good agreement with experimental data for the Langley blade designs. For the LBL blade, both TTCP and Glasgow geometries are very close to the test data points. The experimental data, however, shows a large degree of scatter. The CFD simulations indicate, that at high thrust the performance of this blade rapidly deteriorates, however, there is no experimental data to compare with CFD at such high C_T. The LBERP blade predictions are also very close to experimental data for the Glasgow geometry. The performance for the TTCP geometry is highly overpredicted. This shows the high sensitivity of geometric features for such blade planforms, indicating the need for optimisation. Furthermore, for CFD validation, the exact shape must be simulated to gain full confidence in the results. A certain degree of experimental data scatter is also observed for this blade, approaching 2 counts in

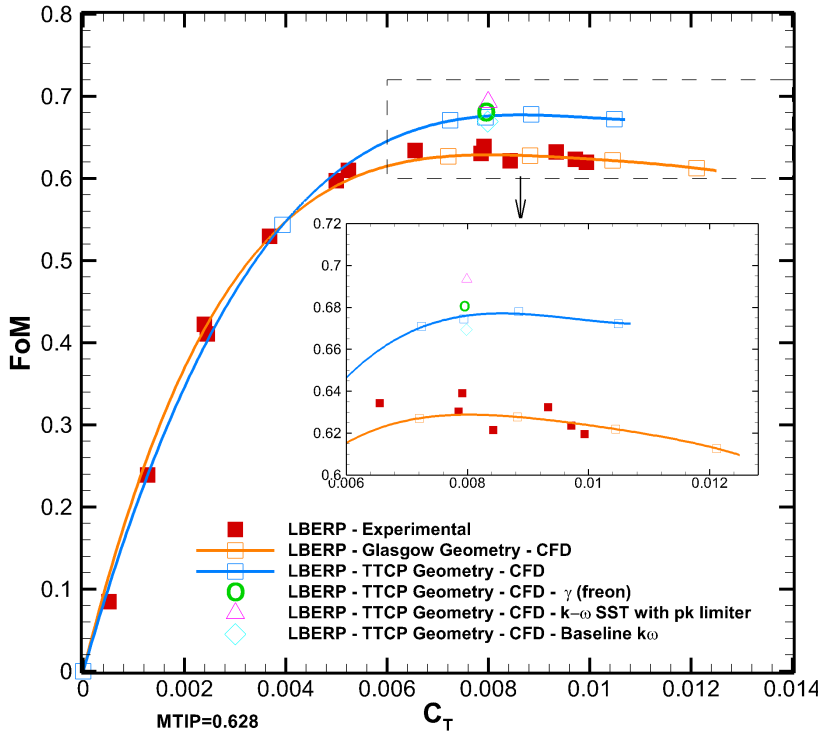

Figure 5.14: Performance predictions for LBERP blade (TTCP & Glasgow) in hover and comparison with experimental data of Yeager et al. [429].

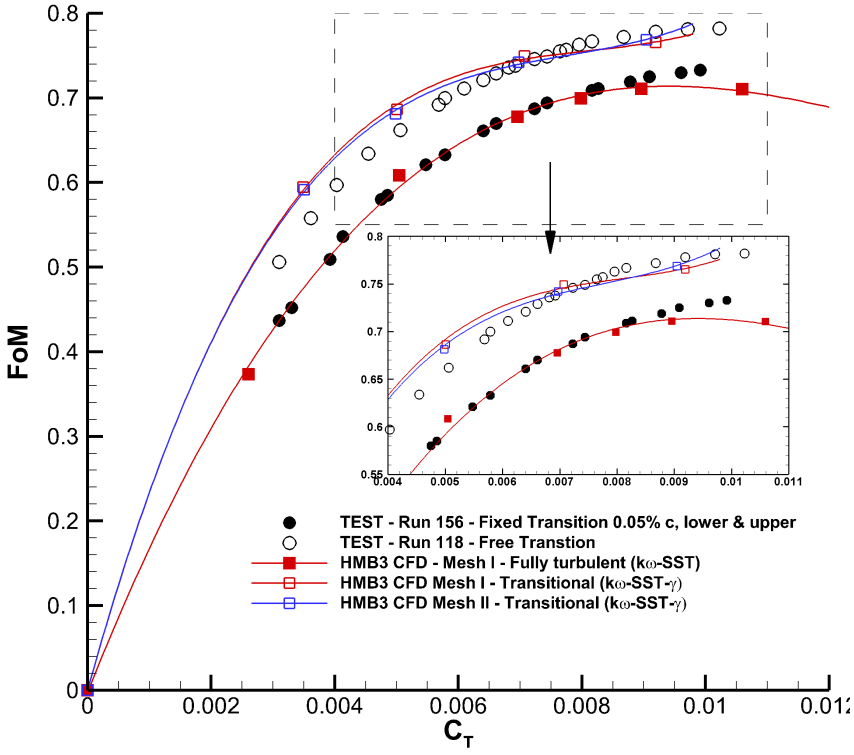

Figure 5.15: Performance predictions for PSP blade in hover and comparison with experimental data of Overmeyer and Martin [291].

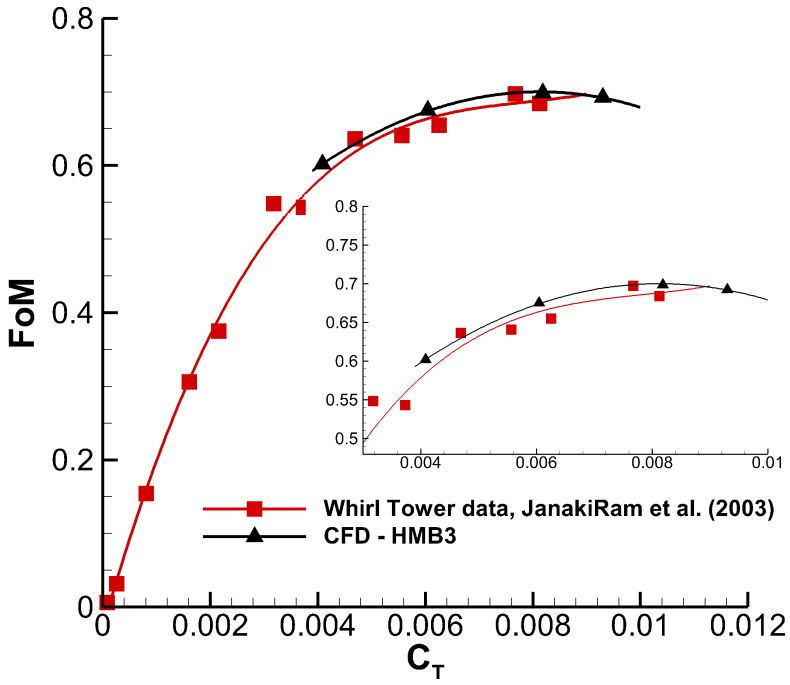

Figure 5.16: Performance predictions for AH-64A blade in hover and comparison with experimental data of JanakiRam et al. [168].

FoM at moderate thrust coefficients. The sensitivity analyses are also attached, and show a comparable scatter in the FoM predictions. Even though only integrated loads are reported, the typical behaviour of a BERP-like blade is well captured within the hover performance curve, as this planform is able to operate at higher blade loading without significant losses in performance [298], [338].

For the PSP cases, good agreement is seen for both fully-turbulent and transitional calculations. At low thrust, it can be seen that all CFD computations are in close agreement with experiments. Good correlation is seen for the fully-turbulent boundary layer cases, whereas the transitional predictions are slightly overpredicted. At these thrust levels, there is a high contribution of profile torque to the total torque, hence the predictions of the transitional locations will have a large impact on the performance prediction. Such thrust levels, are not however, attributable to any real-life scenario as for many helicopters, this loading is under the empty weight of the vehicle. At medium thrust levels, the predictions agree very well with experimental data for both fully-turbulent and transitional cases. At high thrust, the fully-turbulent HMB3 predictions underpredict the FoM compared to experimental data. Jain [163] evaluated the effect of rotor installation on the FoM, and found that the installed-rotor FoM attains higher values (around 1.4 counts of FoM) when compared with the isolated rotor at $C_T/\sigma \approx 0.094$ ($C_T = 0.0098$). This is perhaps, one of the main sources of discrepancy, at high thrust, between HMB3 and experiments. Another potential source of discrepancy could be due to aeroelastic

wind up which was not considered here. The transitional cases, however, show better agreement with experiment. The finer mesh in the wall normal direction improves the predictions at all thrust levels, leading to a reduced performance at low loading and increased FoM at high thrust levels. The PSP rotor is also found to have a high performance sensitivity due to transition effects, as the performance is improved by 7.5 counts in FoM at low thrust and 5 counts at higher thrust levels. Such large performance benefits would not be expected on full-scale helicopters in flight as discussed in Section 5.2.5, Transition Modelling Sensitivity. For correlation with wind tunnel test data, transitional effects may be significant, although many studies in literature report predictions of high accuracy with the fully-turbulent boundary layer assumption. This will highly be dependent on the experimental setup, especially regarding the use of a boundary layer trip.

For the AH-64A blade, the performance predictions show very good agreement with experimental data. A scatter of approximately 2 counts can be seen in the whirl tower data, with the HMB3 predictions predicting a FoM towards the upper limit at low and moderate thrust coefficients (up to C_T= 0.008). No experimental data is reported at high thrust coefficients, however, the HMB3 results predict reduced hover performance with the maximum FoM value occurring at approximately $C_T = 0.008$. The high-fidelity HMB3 code is shown to capture the overall rotor performance across the flight envelope, with further verification required at high thrust coefficients.

Unfortunately, no further experimental data is available for further CFD validation of rotor blade in hover, apart from the experimental surface pressure for the PSP rotor blade at two radial stations (shown in the next subsection). The results are analysed further from a rotor design perspective in Chapter 7, Rotor Design - Pre-Optimisation Considerations. Based on the FoM predictions shown in Figures 5.13-5.16, it can be stated that the steady-state formulation is able to obtain hover performance predictions within experimental data accuracy. However, the experimental data currently available in literature has a large degree of scatter, and hence the use of more advanced CFD methods is not fully justified. Furthermore, for full validation, other quantities must be compared, such as sectional loads, surface pressure distributions and vortex displacements. Such experimental data does not exist for more advanced planforms such as the LBERP blade and is scarce for simpler designs. For this reason, further experimental tests are planned for the PSP blade in the large NASA NFAC facility (80 by 120 ft wind tunnel) to provide a comprehensive experimental data set for hover validation [164] and lead to improvements in CFD prediction capabilities.

5.4 PSP Surface Pressure Predictions in Hover - CFD Validation

The PSP rotor blade was selected for CFD validation in hover due to available experimental surface pressure data. Sample results are shown in this section as these were presented previously by Jimenez [174]. The CFD predictions are compared with experimental data of Wong et al. [419] at two radial stations (r/R= 0.93 and 0.99) on the blade upper surface. The C_P is computed based on the local velocity at each radial station:

$$C_p = \frac{p - p_\infty}{1/2\rho_\infty(\Omega r)^2}. \tag{5.1}$$

Regarding the experiments, two techniques were used to measured C_P distributions, the Kulite pressure transducers (square symbols) and the PSP technique (dashed lines) in Figure 5.17.

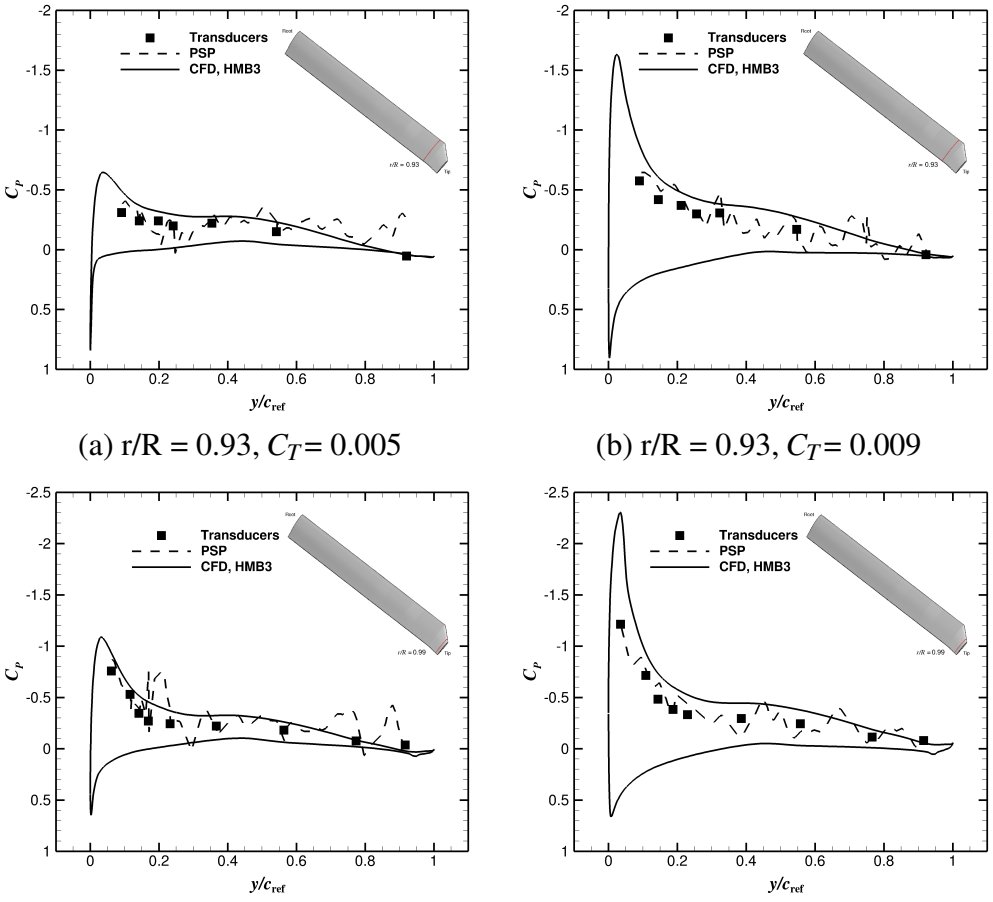

(a) r/R = 0.93, C_T= 0.005 (b) r/R = 0.93, C_T= 0.009

(c) r/R= 0.99, C_T= 0.005 (d) r/R = 0.99, C_T= 0.009

Figure 5.17: C_P profile comparisons between experimental data using the PSP technique (dashed line) and pressure tap (square symbols) [419, 420] and CFD (solid line) at radial stations $r/R = 0.93$ and $r/R = 0.99$ (Figure from Jimenez [174]).

A reasonable agreement is seen by both techniques for both stations at the two thrust coefficients considered here; C_T= 0.005 and 0.009. CFD results are able to predict the overall distribution of C_P at both stations, and the pressure at the trailing edge is also well captured. However, an overprediction in terms of the C_P magnitude is observed, primarily attributed to missing aeroelastic effects. Aeroelastic blade torsion, for example, could lead to an offloaded blade tip and hence leading to a lower C_P in the blade tip region, and improving the correlation with experimental data.

Chapter 6

CFD Validation in Forward Flight

This chapter presents CFD validation of the HMB3 solver for different rotor blades in forward flight conditions. Firstly, the test conditions are presented for the four examined rotor blades: LBL, LBERP, PSP and AH-64A. Next, various sensitivity analyses are presented including, geometric sensitivities for the LBL and LBERP blades, grid refinement, turbulence modelling, shaft angle and installation effects. Following, performance predictions from the CFD analyses are compared with experimental data for all four blades. Finally, similarly as in hover conditions, the surface pressure predictions are compared for the PSP blade with experimental data.

6.1 Test Conditions

Firstly, the test conditions are presented which were used for CFD validation of the performance predictions for each of the rotor blades, shown in Table 6.1. The trim states for these calculations are presented in Table 6.2. The simulations for the sensitivity analyses are described further in each of the relevant subsections.

The forward flight tests for the LBERP and LBL blades were also performed by Yeager et al. [429] in a freon-12 medium, which is included in the forward flight simulations (freon specific heat ratio of 1.128). A moderate propulsive force ($f_D = 29.94 ft^2$) is chosen for CFD validation, with the shaft angle calculated based on the thrust/drag force triangle. An advance ratio sweep is performed at $C_T = 0.0081$ for both blades. Two sets of simulations were performed for the PSP blade. The first set was computed for surface pressure prediction comparisons with the experimental data of Wong et al. [420]. For these comparisons, a thrust sweep was performed at a constant advance ratio of 0.35 and a rotor shaft angle of 6^o. The second set was performed for integrated load predictions and compared with the experimental data of Overmeyer [227]. Here, an advance ratio sweep was performed at $C_T/\sigma = 0.08$ ($C_T = 0.00826$). For these simulations, the Heyson corrected shaft angles gave the best agreement with experimental data. The Heyson correction applies a correction to the rotor shaft angle due to recirculation effects, which reduces the obtained propulsive force, caused by the size of the experimental facility (14 by 22ft).

Table 6.1: Forward flight test conditions for the LBL, LBERP, PSP and AH-64A blades used within the CFD calculations.

μ	C_T	M_∞	Re_∞	Other
LBL blade				
0.2	0.0081	0.1256	5.47×10^5	
0.3	0.0081	0.1884	8.21×10^5	Freon $\gamma = 1.128$, $f_D = 29.94 ft^2$
0.4	0.0081	0.2512	1.094×10^6	
LBERP blade				
0.2	0.0081	0.1256	5.02×10^5	
0.3	0.0081	0.1884	7.53×10^5	Freon $\gamma = 1.128$, $f_D = 29.94 ft^2$
0.4	0.0081	0.2512	1.004×10^6	
PSP blade - surface pressure validation				
0.35	0.004	0.203	6.79×10^5	
0.35	0.006	0.203	6.79×10^5	Assumed $\alpha_s = 6^o$
0.35	0.008	0.203	6.79×10^5	
PSP blade - performance validation				
0.2	0.00826	0.116	3.88×10^5	
0.25	0.00826	0.145	4.85×10^5	
0.3	0.00826	0.174	5.82×10^5	α_s based on Heyson correction.
0.35	0.00826	0.203	6.79×10^5	
AH-64A blade				
0.2	0.00903	0.13	1.598×10^6	Full scale, $f_D = 33.8 ft^2$
0.3	0.00903	0.195	2.397×10^6	

Finally, the AH-64A blade is also simulated, as it was selected as the baseline blade for the optimisation process. The computations are performed at $C_T = 0.00903$ and $\mu = 0.2, 0.3$, and compared with the experimental data of JanakiRam et al. [168] (which was found to be consistent with the YAH-64 data [40]). A level of uncertainty is present in the experimental data, as the engine power coefficient was reported which needs to be corrected for tail rotor power, auxiliary power and transmission losses. Similarly as for the LBL and LBERP blades, the shaft angle is determined from the thrust/drag force triangle based on a flat plate drag area of $33.8 ft^2$, which was reported by Kelley [191] (as well as Kunz [208]) for flight test data comparisons with the 8-HELLFIRE missile configuration.

For all four rotor blades, the simulations were performed using the k-ω SST turbulence model with the pk limiter unless otherwise stated. The computations for the LBL, LBERP and AH-64A blades used a 0.5 degree step in azimuth, whereas the PSP simulations were performed using a 0.25 degree step in azimuth. For all blade designs, a matrix trimming routine [359] based on Blade Element Theory was used for computing the elements of the sensitivity matrix, to achieve the target thrust and reduce rolling and pitching moments. The collective angle and pitching harmonics were updated in the trimming routine with a fixed shaft angle, coning angle and flapping harmonics. The rotor coning angle and flapping harmonics were assumed for most

Table 6.2: Forward flight trim states for the LBL, LBERP, PSP and AH-64A blades computed using the rotor trimming routine within the CFD simulations. Note, negative Fourier series used.

μ	$C_{T_{trim}}$	C_{M_x}	C_{M_y}	α_s	θ_0	θ_{1s}	θ_{1c}
LBL blade							
0.2	0.00810	2.423×10^{-6}	-4.732×10^{-6}	-1.874	6.918	4.373	-3.935
0.3	0.00812	3.249×10^{-5}	-1.871×10^{-5}	-4.208	8.780	7.002	-3.834
0.4	0.00808	9.132×10^{-5}	-2.562×10^{-5}	-7.449	12.535	10.437	-4.022
LBERP blade							
0.2	0.00807	5.138×10^{-6}	-3.713×10^{-5}	-1.874	7.249	4.489	-4.149
0.3	0.00817	9.216×10^{-6}	-3.962×10^{-5}	-4.208	9.043	7.122	-4.121
0.4	0.00808	2.332×10^{-5}	-1.614×10^{-5}	-7.449	12.920	10.891	-4.229
PSP blade - surface pressure validation							
0.35	0.00406	3.574×10^{-5}	-4.049×10^{-5}	-6.0	6.117	4.536	-2.558
0.35	0.00600	1.265×10^{-6}	-9.642×10^{-7}	-6.0	8.324	6.840	-3.392
0.35	0.00804	2.660×10^{-5}	-9.498×10^{-6}	-6.0	10.560	8.956	-4.732
PSP blade - performance validation							
0.2	0.00828	-5.185×10^{-6}	1.022×10^{-6}	-3.363	7.292	3.716	-2.695
0.25	0.00828	-1.631×10^{-6}	2.350×10^{-6}	-3.463	7.668	4.719	-2.657
0.3	0.00831	2.867×10^{-6}	-8.609×10^{-6}	-3.594	8.318	5.986	-2.503
0.35	0.00829	1.113×10^{-5}	-1.242×10^{-4}	-3.7126	9.069	7.410	-2.722
AH-64A blade							
0.2	0.00898	-6.0826×10^{-5}	-5.392×10^{-4}	-2.371	8.145	4.444	-3.309
0.3	0.00906	3.454×10^{-6}	2.045×10^{-5}	-5.341	10.413	7.421	-3.072

simulations, with the LBERP and LBL blades using values of $\beta_0 = 3.43^o$, $\beta_{1s} = -1.0^o$ and $\beta_{1c} = -0.7^o$. The PSP and AH-64A blades were trimmed to zero flapping with rotor coning angles of $\beta_0 = 1.4 - 1.6^o$ for the PSP blade and $\beta_0 = 3.5^o$ for the AH-64A blade. As can be seen in Table 6.2, the simulations are trimmed to a thrust coefficient close to the ones reported in experimental data, as well as close to zero pitching and rolling moments. The rotor collective and longitudinal cyclic angles increase with increasing advance ratio and thrust coefficient due to an increased propulsive force requirement and larger local Mach number imbalance between the rotor advancing and retreating side, whereas the lateral cyclic primarily increases with increasing thrust coefficient.

6.2 Sensitivity Analyses

In this section, sensitivity analyses are performed in forward flight. Firstly, similarly as in hover, the differences between the TTCP and Glasgow Langley blade geometries are analysed. Next, the effects of grid refinement and turbulence modelling are examined, focused on the low advance ratio case for the LBL blade (due to greatest differences in the integrated loads predictions with experimental data). Finally, shaft angle and installation effects are examined for the PSP

rotor blade.

6.2.1 Geometric Sensitivity for the LBL and LBERP Blades

The geometric sensitivity between TTCP and Glasgow geometries are analysed first. The low advance ratio case at $\mu = 0.2$ is chosen for these comparisons due to poorest agreement with experimental data (as will be seen later). The integrated loads for the LBL and LBERP blades at $\mu = 0.2$ are presented in Table 6.3 for both TTCP and Glasgow blade geometries.

Table 6.3: Comparison of integrated loads for the TTCP and Glasgow Langley blade geometries at low advance ratio $\mu = 0.2$

Blade	C_T	C_Q
LBL (Glasgow)	0.00810	0.000465
LBL (TTCP)	0.00813	0.000460
LBERP (Glasgow)	0.00810	0.000471
LBERP (TTCP)	0.00813	0.000465

Minor differences are seen in the integrated blade loads between the Glasgow and TTCP geometries. The TTCP geometries have slightly higher performance as both an increase in thrust and reduction in torque can be seen. The changes are, however, negligible when concerning rotor design and CFD validation. As seen previously, the differences in hover were much more significant, especially for the LBERP blade. Due to a low geometric sensitivity, all further results are presented for the geometries generated at Glasgow.

6.2.2 Grid Refinement Sensitivity

The effect of grid refinement is examined next. The Glasgow LBL blade is simulated at $\mu = 0.2$ on the nominal and a finer grid using a different computational setup, with intermediate background grid levels for improved capturing of the key flow features. The computational setup for the fine grid is shown in Figure 6.1, whereas the nominal grid setup was shown in Chapter 4.2, Mesh Generation and Computational Setup. A 0.25 deg time-step is also used for the fine grid simulation (compared to 0.5 deg for the nominal grid).

For the fine grid mesh, a fine near blade background grid (Component 1) is used of approximately 47M cells. A medium level refinement (Component 2) is used to better resolve the farfield wake, using an additional 12M cells. Finally, a very coarse background grid (Component 3) is used of 3.2M cells. A finer blade grid is also used with a reduced foreground overset boundary giving 40M cells for four rotor blades. The total mesh size for the fine grid setup leads to approximately 102M cells. The main purpose of the finer grid was to better capture the near blade tip vortices, leading to reduced near-blade vortex interaction. The grid refinement effect

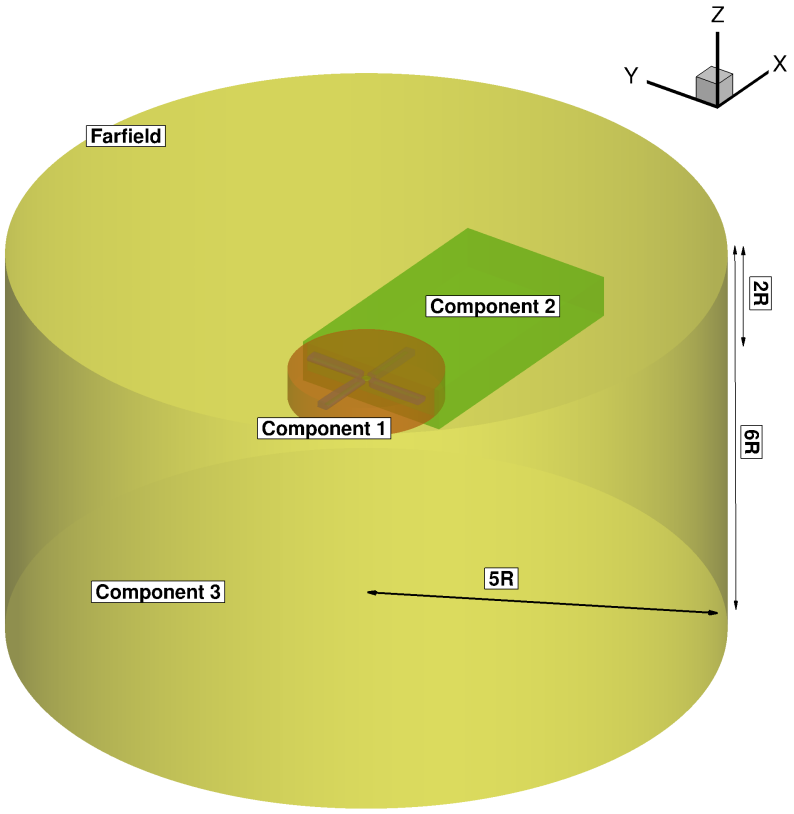

Figure 6.1: Forward flight computational grid setup for the fine grid LBL simulation at $\mu = 0.2$.

on the integrated blade loads is shown for the LBL blade at $C_T = 0.0081$ and $\mu = 0.2$ in Table 6.4.

Table 6.4: Integrated loads using the nominal and fine grid setups for the Langley Baseline blade at $C_T = 0.0081$ and $\mu = 0.2$.

Mesh	C_T	C_{Q_p}	C_{Q_v}	$C_{Q_{TOT}}$
Nominal grid	0.00810	0.000354	0.000111	0.000465
Fine grid	0.00802	0.000351	0.000104	0.000455

The integrated loads, show a low sensitivity due to grid refinement, proving that the nominal grid is fine enough for forward performance predictions. The fine grid leads to a slightly lower torque but also lower thrust. The main driver of the differences is the viscous torque contribution. However, these differences are minimal. The finer grid provides better matching between the background and foreground grids behind the trailing edge of the blade. This leads to a tighter capturing of wake structures behind the blade, which is shown in Figure 6.2 for an example contour of turbulent eddy viscosity at r/R = 0.8, with the blade at $\psi = 0^o$.

As can be seen from Figure 6.2, the fine grid setup leads to an improved solution across the overset boundary which provides a more refined representation of the rotor wake. The improved

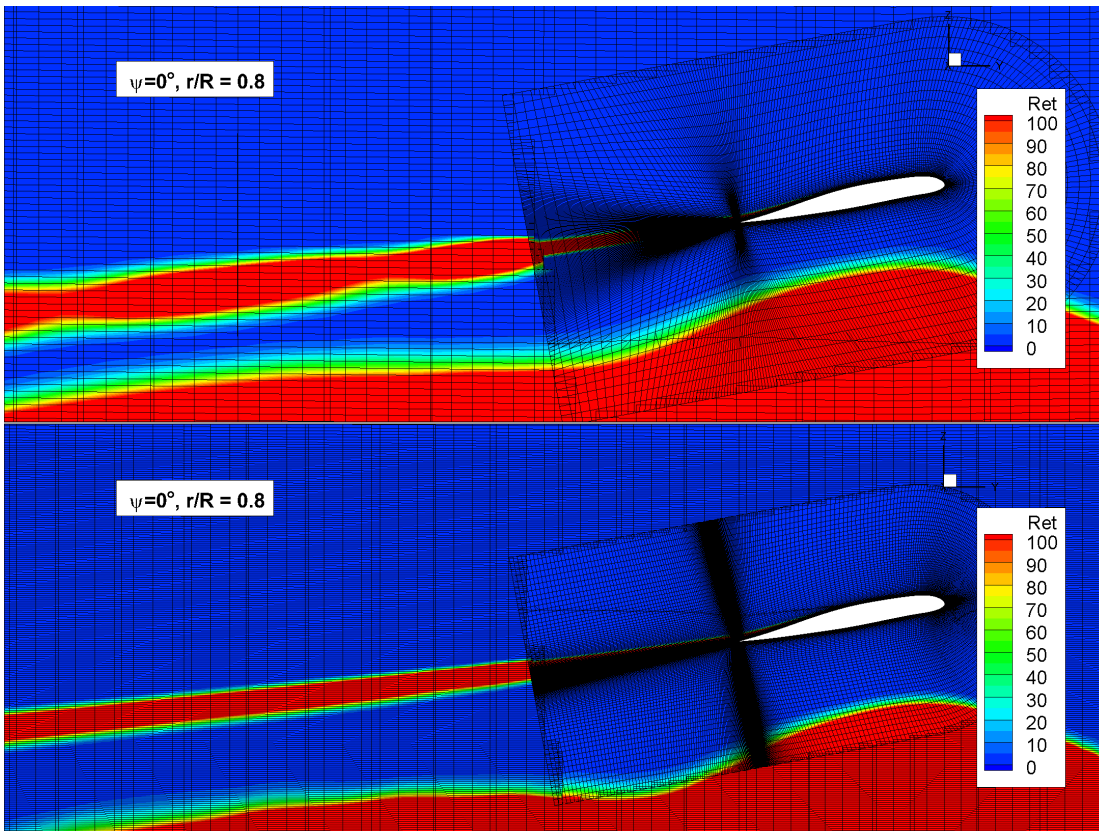

Figure 6.2: Differences in the turbulent eddy viscosity contours at r/R=0.8 and $\psi = 0^o$ for the nominal (top) and fine (bottom) grids for the LBL blade in forward flight at $C_T = 0.0081$ and $\mu = 0.2$.

capturing of the vortical structures also leads to slightly higher vorticity in the vortex cores. The near blade-vortex interaction is also reduced in many areas of the flowfield. At r/R=0.8 and $\psi = 0^o$, the finer grid indicates a larger distance between the rotor blade and shed wake, leading to a slightly reduced integrated torque. The main effect of the finer grid, however, are finer wake structures in the near-field and a much better resolved far-field wake. The comparison of the wake geometries is shown in Figure 6.3 using isosurfaces of Q-criterion (value of 0.002) coloured by downwash velocity.

The wake structures are better resolved for the finer grid. This can be especially seen at the front of the rotor disk, as well as in the hub region. In the farfield, the wake structures are dissipated after 3-4 revolutions for the fine grid, nearly reaching the edge of the domain, whereas for the nominal grid, only 2-3 vortex passages are visible. However, as seen by the integrated loads sensitivity, better resolution of the farfield wake structures does not impact the blade loads significantly.

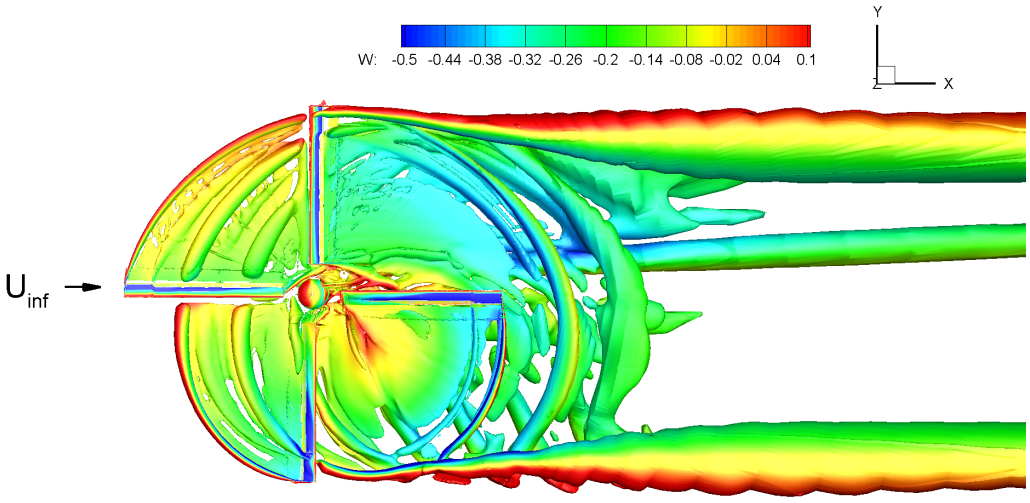

(a) Nominal grid

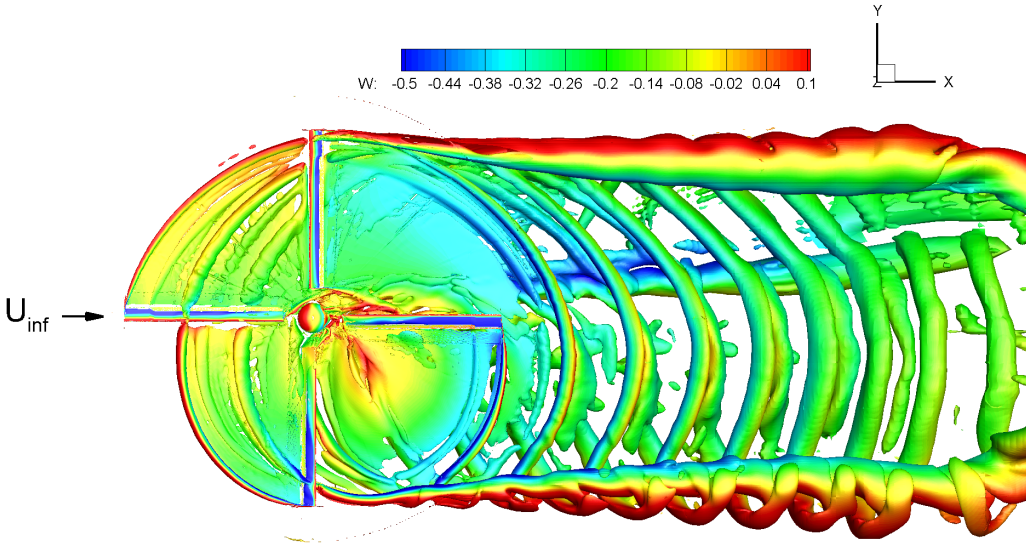

(b) Fine grid

Figure 6.3: Sensitivity of the wake structures due to grid refinement for the LBL blade in forward flight at $C_T = 0.0081$ and $\mu = 0.2$ using isosurface of Q-criterion (value of 0.002), coloured by downwash velocity.

6.2.3 Turbulence Modelling Sensitivity

Similarly as in hover, the effect of the turbulence production term limiter was assessed for simulations in forward flight. Cases were performed for the LBL and BERP blades at low and moderate advance ratios ($\mu = 0.2, 0.3$). The LBL blade was also simulated using the fine grid setup with the production term limiter. In most cases, the simulations were performed for two additional revolutions leading to a single re-trim to slightly lower collective and longitudinal cyclic angles. The effect of the pk limiter on the integrated loads is shown in Table 6.5.

The effect of the pk limiter is more significant than grid refinement. In unsteady RANS

Table 6.5: Sensitivity of integrated loads due to the pk limiter at low and medium advance ratios for the LBERP and LBL blades.

Blade	C_T	C_Q
LBL $\mu = 0.2$, k-ω SST	0.00810	0.000465
LBL $\mu = 0.2$, k-ω SST, pk limiter	0.00811	0.000425
LBL Fine grid, $\mu = 0.2$, k-ω SST	0.00802	0.000455
LBL Fine grid, $\mu = 0.2$, k-ω SST, pk limiter	0.00812	0.000429
LBL $\mu = 0.3$, k-ω SST	0.00814	0.000574
LBL $\mu = 0.3$, k-ω SST, pk limiter	0.00814	0.000551
LBERP $\mu = 0.2$, k-ω SST	0.00810	0.000470
LBERP $\mu = 0.2$, k-ω SST, pk limiter	0.00821	0.000442
LBERP $\mu = 0.3$, k-ω SST	0.00810	0.000588
LBERP $\mu = 0.3$, k-ω SST, pk limiter	0.00811	0.000569

simulations with multiple nearby blade vortex interactions, an artificial growth of turbulent eddy viscosity can be observed, which has also been seen by other researchers [307], [12]. The pk limiter reduces the eddy viscosity in these regions, through a clip on the turbulence production term (20 times the turbulence destruction terms) [251], leading to a less viscous flow. This in turn leads to a slightly higher produced thrust and lower torque. Other possible solutions for a more physical turbulence field include the use of a rotational correction term, use of non-Boussinesq or DES based turbulence models. In the Helios code, RANS simulations are often computed with laminar off-body solutions, to reduce the eddy viscosity levels in the rotor wake [75, 307]. Euler off-body solution may, however, give rise to underpredicted turbulence levels in the near-field and also potentially give rise to numerical instabilities due to the lack of viscous damping in the wake. Another aspect is that, the application of the pk limiter and fine grid together, does not change the torque prediction significantly. Both these effects improve the viscous term prediction, however, the individual effects are not additive. The effect of the pk limiter reduces with increasing advance ratio, as reduced blade vortex interaction is observed. An example effect of the pk limiter is shown in Figure 6.4 for the LBL blade at $\mu = 0.2$ using the nominal grid, by extracting a contour of turbulent eddy viscosity at $x/R = 0.0$, with the blades at $\psi = 0, 90, 180, 270^o$.

As can be seen from Figure 6.4, the turbulent eddy viscosity ratio levels are reduced with the pk limiter in the near-field and far-field wake regions. The reduction in the power required (both pressure and viscous terms) is primarily caused by lower turbulent eddy viscosity in the regions of near blade-vortex interactions. However, even with the pk limiter, fairly high eddy viscosity levels are observed in the far-field wake, showing the need for a DES simulation or the use of a rotational correction term. The far-wake turbulent eddy viscosity, however, will have a negligible impact on the rotor loads. All CFD forward flight performance prediction comparisons with experimental data are shown for simulations with the pk limiter switched on.

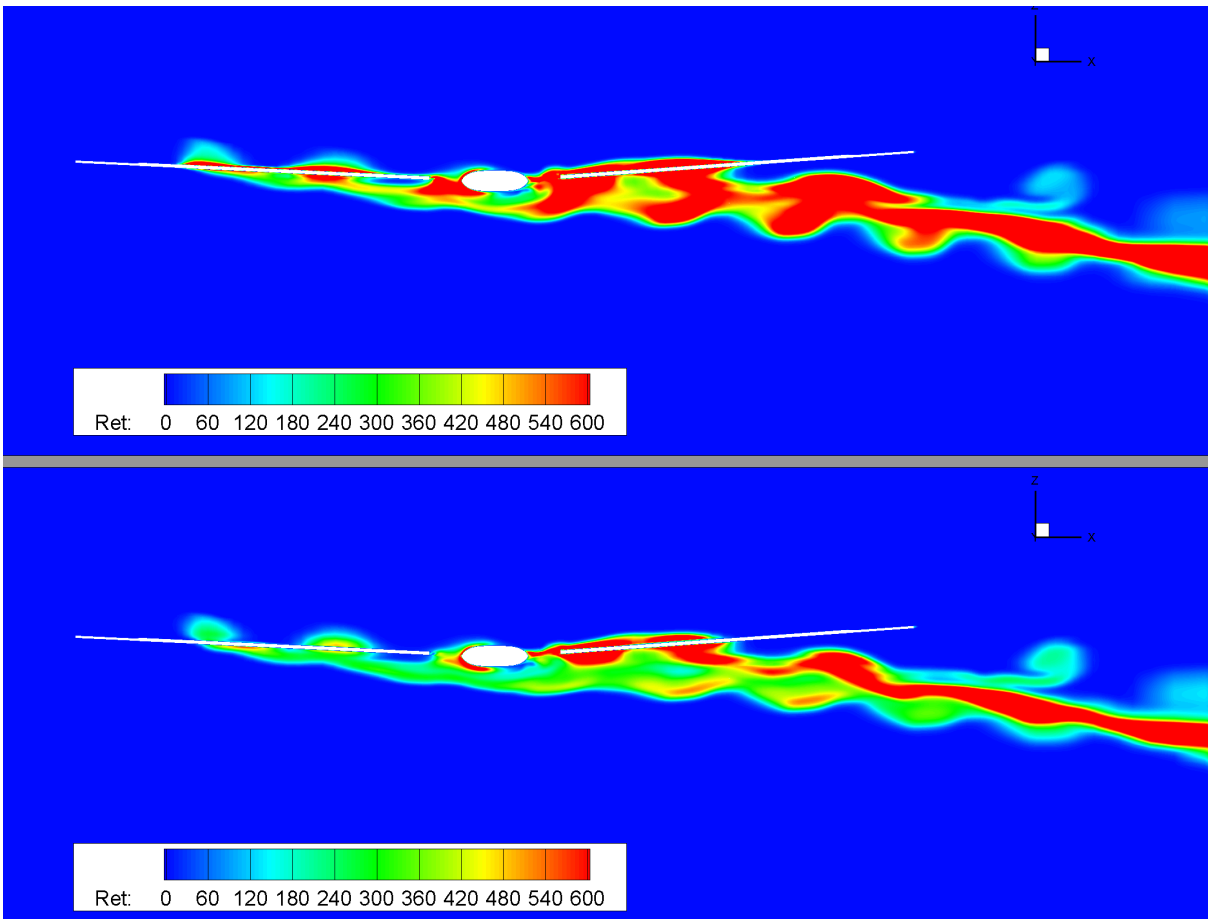

Figure 6.4: Turbulent viscosity contour sensitivity due to pk limiter (top=pk limiter off, bottom=pk limiter on) at $x/R = 0.0$ for the LBL blade at $\mu = 0.2$

6.2.4 Shaft Angle Sensitivity

The shaft angle sensitivity is assessed using the PSP validation cases computed using the shaft angle based on the propulsive force and the shaft angle based on the Heyson correction. For both shaft angles, the trimming routine was used to achieve the target thrust and minimize pitching/rolling coefficients. Example integrated load differences are shown in Table 6.6 for the PSP rotor blade at $\mu = 0.2$, $\mu = 0.35$ and $C_T = 0.00826$. The trim state differences are shown in Table 6.7.

Table 6.6: Shaft angle sensitivity on the integrated rotor loads for the PSP rotor blade at $C_T = 0.00826$ and $\mu = 0.2, 0.35$.

Case	μ	$C_{T_{trim}}$	C_Q	C_{M_x}	C_{M_y}
$\alpha_s = 1.885^o$	0.2	0.00827	4.271×10^{-4}	-7.505×10^{-7}	-1.339×10^{-5}
$\alpha_s = 3.363^o$	0.2	0.00828	4.629×10^{-4}	-5.185×10^{-6}	1.022×10^{-6}
$\alpha_s = 3.713^o$	0.35	0.00829	5.458×10^{-4}	1.113×10^{-5}	-1.242×10^{-4}
$\alpha_s = 5.095^o$	0.35	0.00833	6.069×10^{-4}	1.862×10^{-5}	-2.771×10^{-5}

Table 6.7: Shaft angle sensitivity on the rotor trim states for the PSP rotor blade at $C_T = 0.00826$ and $\mu = 0.2, 0.35$. Note, negative Fourier series used.

Case	μ	α_s	θ_0	θ_{1s}	θ_{1c}
Propulsive force, α_s	0.2	-1.885	6.911	3.584	-2.770
Heyson corrected, α_s	0.2	-3.363	7.292	3.716	-2.695
Heyson corrected, α_s	0.35	-3.7126	9.069	7.410	-2.722
Propulsive force, α_s	0.35	-5.095	9.921	7.724	-2.509

The shaft angle sensitivity has a fairly substantial effect on the rotor power, which is greater than differences seen by different turbulence models or grid refinement, especially at high advance ratios. The Heyson correction increases the required shaft angle at low advance ratio and decreases the shaft angle at high advance ratio. This correction is applied to account for the wind tunnel boundaries, based on potential flow theory. As seen from the integrated loads, the effect of this correction can alter the predicted rotor power by up to 10% at high advance ratio. For this reason, care must be taken when comparing CFD predictions with experimental data sets from facilities where the wall boundaries have an effect on the rotor loads. The validity of this correction can also be questioned for all experimental setups, however, in the present case, the Heyson corrected shaft angles lead to improved CFD predictions compared to experimental data (as will be seen later, in Section 6.3). An increase in the shaft angle due to a higher propulsive force leads to higher collective and slightly higher longitudinal cyclic angles to maintain the target thrust.

6.2.5 Installation Effects Sensitivity

The sensitivity due to installation effects is examined for the PSP rotor blade at $C_T = 0.00826$ and $\mu = 0.3, 0.35$. The ROBIN-mod7 fuselage was used for these investigations and was also used within the experiments of Overmeyer [227]. The ROBIN-mod7 geometry is composed of cross-sections defined analytically based on a set superellipses, with the coefficient data found in [334]. The coefficient data for the fuselage pylon was obtained from [256], whereas the rotor position with respect to the fuselage was found in [16]. A C code was written to generate a cloud of points that represent the fuselage shape. Curves for the cross-sections and the fuselage surfaces were generated through ICEM replay scripts. A grid of 3.1M cells was generated for the fuselage. The surface mesh for the fuselage and rotor blades is shown in Figure 6.5.

The installation effects sensitivity of the integrated loads for the PSP rotor blade at $C_T = 0.00826$ and $\mu = 0.3, 0.35$ is shown in Table 6.8, whereas the trim state differences are shown in Table 6.9.

The inclusion of the fuselage within the CFD simulations leads to a minor reduction in the torque coefficient. The simulations were trimmed to similar thrust coefficients and near zero pitching and rolling moments at the Heyson corrected shaft angles. Installation effects were

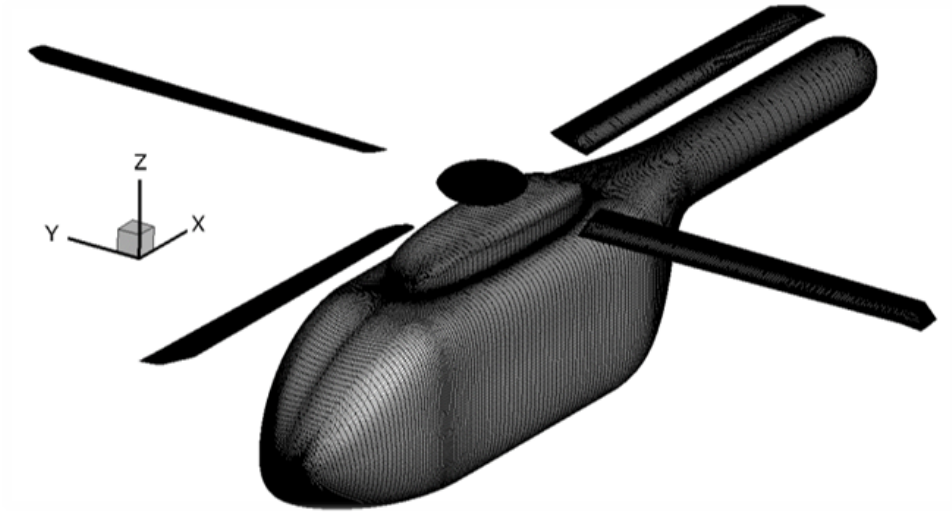

Figure 6.5: Computational surface mesh for the PSP rotor blade with the ROBIN-mod7 fuselage used for examination of the integrated loads sensitivity in forward flight due to installation effects.

Table 6.8: Installation effects sensitivity on the integrated rotor loads for the PSP rotor blade at $C_T = 0.00826$ and $\mu = 0.3, 0.35$.

Case	μ	$C_{T_{trim}}$	C_Q	C_{M_x}	C_{M_y}
Isolated Rotor	0.3	0.00831	5.100×10^{-4}	2.861×10^{-6}	-8.609×10^{-6}
Installed Rotor	0.3	0.00832	4.960×10^{-4}	1.128×10^{-5}	-9.446×10^{-6}
Isolated Rotor	0.35	0.00829	5.458×10^{-4}	1.113×10^{-5}	-1.242×10^{-4}
Installed Rotor	0.35	0.00830	5.346×10^{-4}	1.221×10^{-5}	-3.182×10^{-7}

Table 6.9: Installation effects sensitivity on the rotor trim states for the PSP rotor blade at $C_T = 0.00826$ and $\mu = 0.3, 0.35$. Note, negative Fourier series used.

Case	μ	α_s	θ_0	θ_{1s}	θ_{1c}
Isolated Rotor	0.3	-3.5941	8.318	5.987	-2.504
Installed Rotor	0.3	-3.5941	8.285	6.122	-3.109
Isolated Rotor	0.35	-3.7126	9.069	7.410	-2.722
Installed Rotor	0.35	-3.7126	9.115	7.538	-3.211

found to have a minor effect on the rotor collective and longitudinal cyclic angles, whereas an increase in the lateral cyclic angle was observed. This is further examined by extracting the rotor disk lift force differences (installed-isolated), shown in Figure 6.6.

The presence of the fuselage induces an upwash at the front of the rotor disk, increasing the local effective angle of attack and hence increasing the lift force. At the back of the rotor disk, the fuselage induces a downwash, leading to a reduction in the local effective angle of attack, as well as reduced lift force. These differences have an effect on the integrated pitching moment of the fuselage/rotor system leading to an increased lateral cyclic to maintain trim. Another aspect

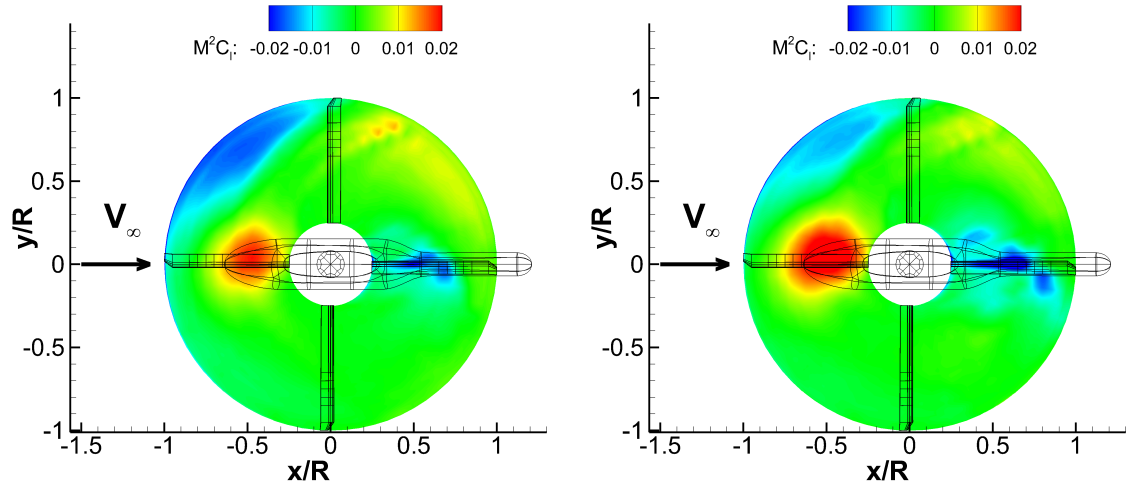

(a) $\mu = 0.3$ (b) $\mu = 0.35$

Figure 6.6: Rotor disk lift force differences (installed-isolated) between the installed and isolated simulations for the PSP rotor blade at $C_T = 0.00826$ and $\mu = 0.3, 0.35$.

is a slightly higher negative lift force at the blade tip as the blade moves from the advancing side to the front of the rotor disk, caused by the differences in trim state. The presence of the fuselage has a minor effect on the CFD solution, however, the sensitivity of installation effects will vary from rotor to rotor, depending on the rotor disk loading, rotor radius and size of the experimental facility. Comparisons with experimental data for the isolated and installed cases are discussed further in the next subsection.

6.3 Performance Predictions in Forward Flight - CFD Validation

The CFD performance predictions for the LBL, LBERP, PSP and AH-64A blades in forward flight are compared with experimental data in Figures 6.7-6.10. The performance is compared for the different designs in Chapter 7, Rotor Design - Pre-Optimisation Considerations, with the present discussion focused on CFD validation.

The CFD predictions are of reasonable accuracy for the Langley blades. For both LBL and LBERP blades, excellent agreement is obtained at high advance ratios with experimental data. At lower advance ratios, the torque coefficient is overpredicted, with a greater discrepancy for the LBL blade. As seen in the sensitivity studies, grid refinement and inclusion of the pk limiter led to a reduction of the predicted torque. However, the torque is still overpredicted (nominal grid with pk limiter shown in Figure 6.7). Based on the LBL and LBERP blades, the prediction of the low advance ratio case is more challenging compared to high advance ratio cases due to multiple near blade-vortex interactions and the requirement for a more accurate representation of the turbulence viscosity levels in the rotor wake.

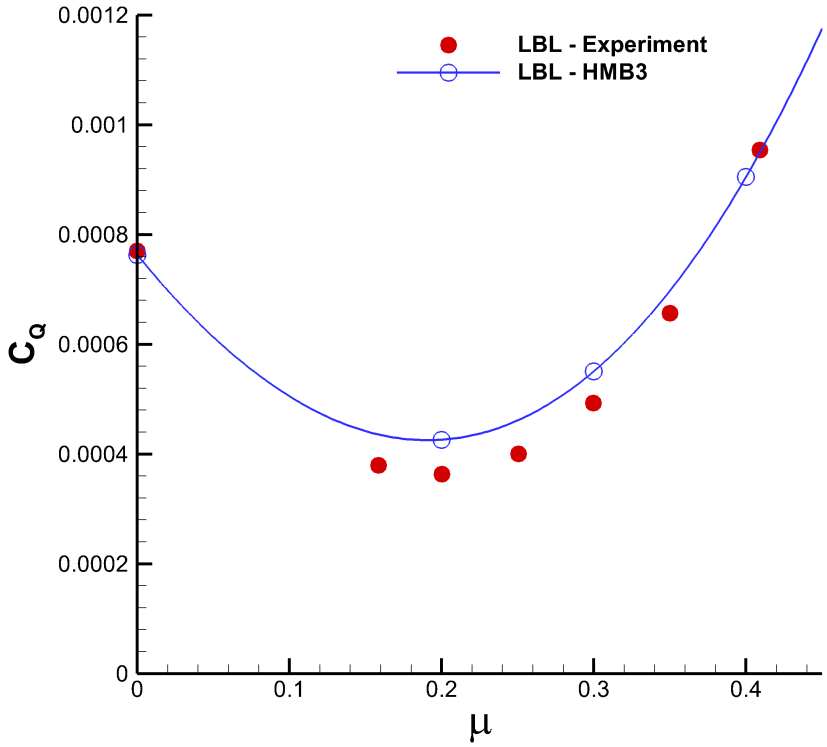

Figure 6.7: Performance predictions for LBL blade (Glasgow) in forward flight and comparison with experimental data of Yeager et al. [429].

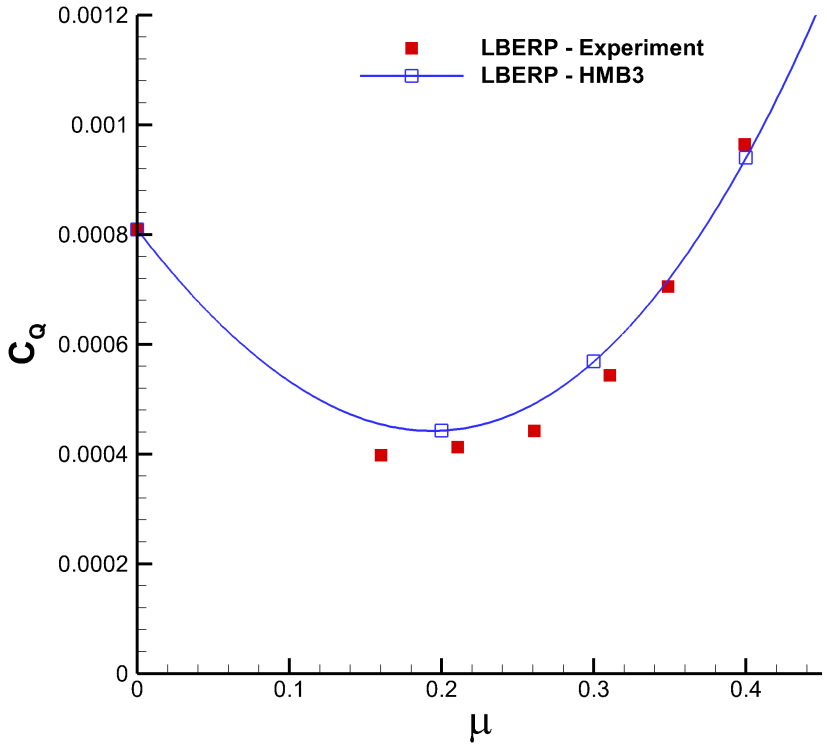

Figure 6.8: Performance predictions for LBERP blade (Glasgow) in forward flight and comparison with experimental data of Yeager et al. [429].

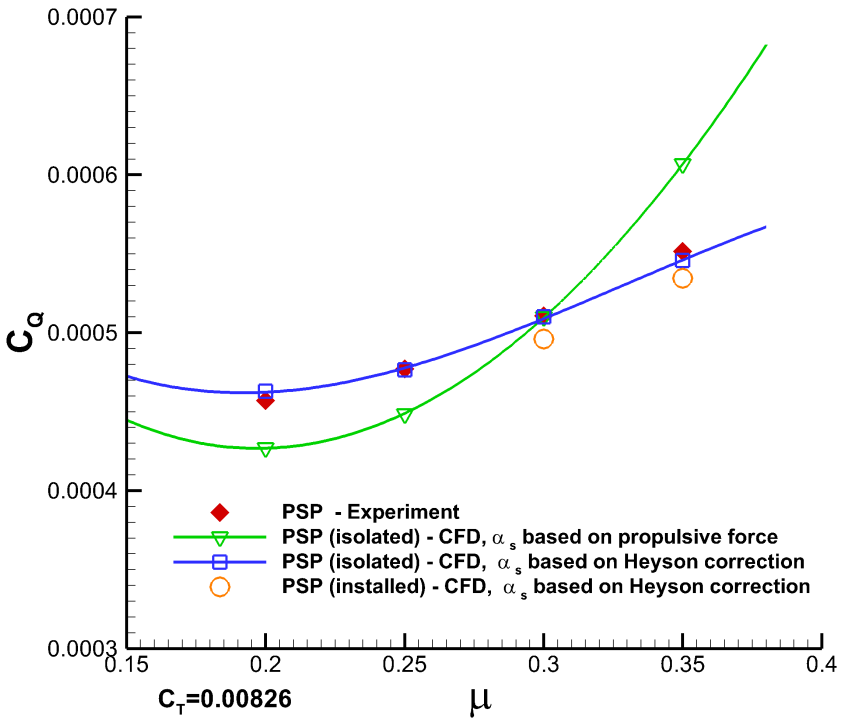

Figure 6.9: Performance predictions for PSP blade in forward flight and comparison with experimental data of Overmeyer [227].

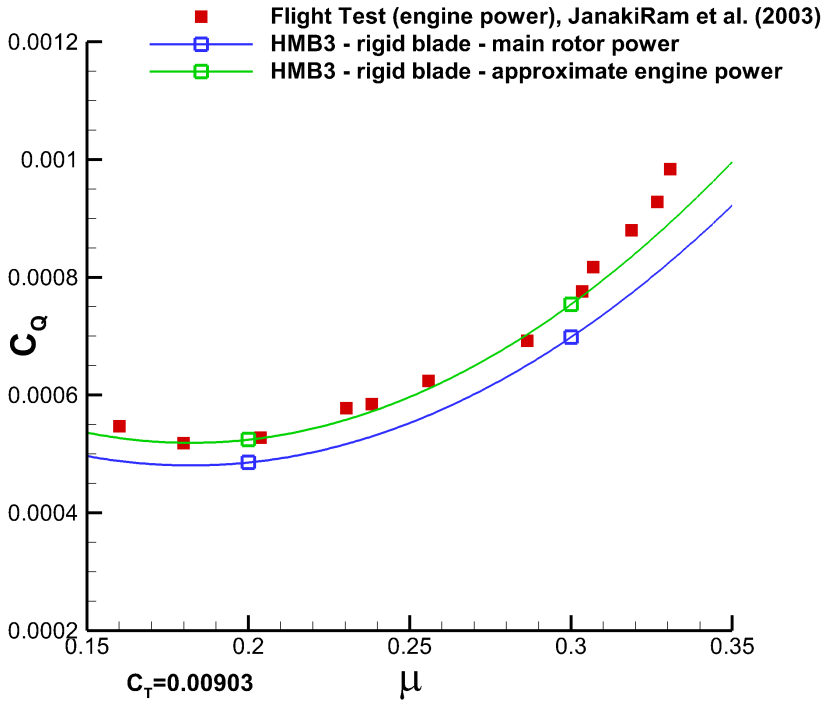

Figure 6.10: Performance predictions for AH-64A blade in forward flight and comparison with experimental data of JanakiRam et al. [168].

Further validation of the HMB3 solver was performed for the PSP rotor blade in forward flight. As can be seen in Figure 6.9, excellent agreement is obtained for the simulations using the Heyson corrected shaft angles across the examined advance ratios. The results based on the propulsive force shaft angle lead to a power underprediction in low-speed flight and power over-prediction at high speed. This shows the importance of correctly capturing the actual propulsive force generated by the rotor between experiment and CFD simulations for good data correlation. The inclusion of the fuselage leads to slightly worse correlation with experiments. However, as the rotor was modelled as rigid, the inclusion of aeroelastic effects could potentially slightly increase the torque coefficient predictions, leading to improved agreement with experiments. Another important aspect is that the experimental forward flight performance curve has a very shallow parabolic shape. From the minimum power point, with increasing advance ratio, the power increases much less rapidly when compared to the LBL and LBERP blades. Based on this data, the PSP rotor would be able to attain a high advance ratio before matching the available engine power.

Finally, the CFD predictions are compared with experimental data for the AH-64A blade. The integrated loads have reasonable agreement with flight test data, with an underprediction at both examined advance ratios. However, the main rotor power curve must be corrected for tail rotor power, auxiliary power (usually zero for experimental testing) and transmission losses for comparisons with experimental data. In this case, the same correction of 8% was applied to the power prediction as in the computations performed by Jones and Kunz [185]. This correction, however, is arbitrary and in reality the tail rotor power will vary with rotor advance ratio, leading to a high correction in hover and high-speed forward flight, and low correction at the minimum power point. After applying the correction, good agreement is obtained with experimental data with a minor underprediction at $\mu = 0.3$. However, as a full-scale rotor is simulated, aeroelastic effects may also have an impact on the power predictions. Based on the data seen here, however, it can be stated that the geometric shape is validated to a high level of confidence and that the uncertainty in the torque coefficient predictions is adequate to perform a rotor optimisation study.

Similarly, as in hover, no further experimental data is available for the four examined rotor blades designs in forward flight, apart from the experimental surface pressure for the PSP rotor blade at two azimuthal locations. The forward flight results are also analysed further from a rotor design perspective in Chapter 7, Rotor Design - Pre-Optimisation Considerations. Based on the torque coefficient predictions, however, it can be claimed that the HMB3 predictions are of good accuracy, with further improvements attainable with higher quality validation data. Further quantities are required for detailed CFD validation including rotor disk loads, surface pressure distributions and wake measurements.

6.4 PSP Surface Pressure Predictions in Forward Flight - CFD Validation

The forward flight pressure predictions for the PSP rotor blade are validated in this section. The CFD pressure predictions on the advancing and retreating blade sides and comparisons with experimental data [420] are presented in Figure 6.11.

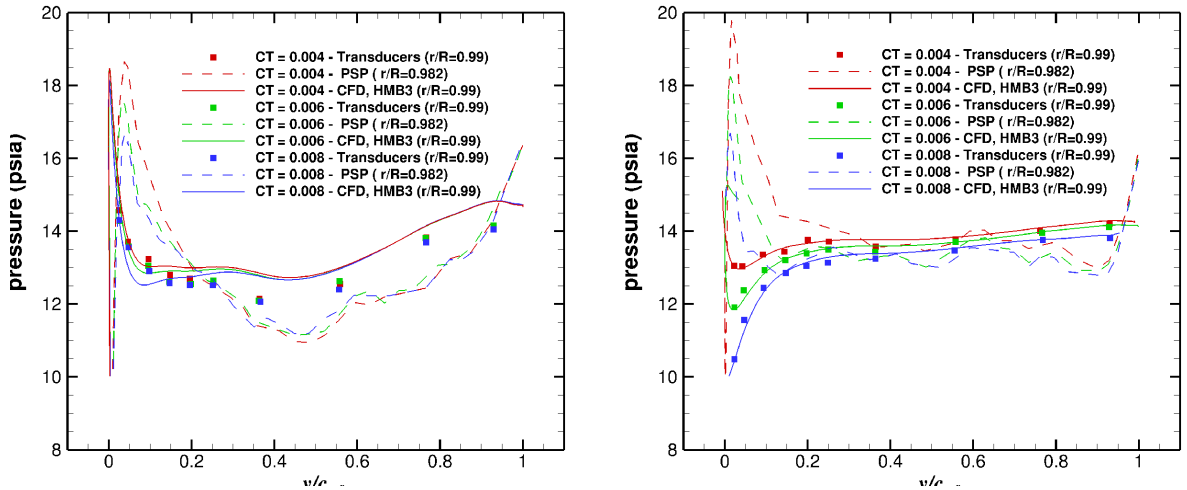

(a) Advancing blade side, $\psi = 101^o$ (b) Retreating blade side, $\psi = 262^o$

Figure 6.11: Surface pressure predictions for the PSP blade in forward flight at three thrust levels. Comparisons are shown for the advancing and retreating blade sides with experimental data from transducers and the PSP technique [420]

It can be seen that the CFD data agrees very well with the data from the pressure transducers. Excellent agreement is seen on the retreating blade side, whereas on the advancing side, the surface pressure is slightly overpredicted. This could potentially be due to elastic blade twist. The PSP data fails to capture the correct curve trends, which is especially visible on the retreating blade side, where the dynamic pressure is low. A certain error may be introduced into the comparisons due to the fact that the pressure using the PSP technique was extracted at $r/R = 0.982$, whereas the pressure transducers were installed at $r/R = 0.99$. The CFD predictions give further validation of the HMB3 solver, however, as with hover simulations, a more comprehensive experimental data set is required for in-depth validation. The data of Wong et al. [420] did not provide integrated loads, which were validated by comparisons with experimental data within the TTCP activity [227].

Chapter 7

Rotor design - Pre-Optimisation Considerations*

The main aim of this chapter is to compare the different rotor designs based on the simulations performed for CFD validation and assess the validity of these comparisons. Firstly, the use of standard performance metrics is investigated. Next, a solidity study is performed for the LBL and LBERP blades, to provide a high-fidelity analysis of the findings of Perry [299]. Following this, detailed comparisons are performed for four rotor blades: LBL, LBERP, PSP and AH-64A in hover and forward flight from a rotor design perspective. Additionally, an anhedral study is also performed for the LBL and LBERP blades in hover.

7.1 Performance Metrics

The typically used performance metrics are analysed first, in terms of their usage for comparing different rotor designs at a specific design point. In hover, the key efficiency parameter is the Figure of Merit (FoM) which relates the ideal power from momentum theory with the actual power required. The FoM is written in terms of dimensional units in equation 7.1.

$$FoM = \frac{C_T^{3/2}}{\sqrt{2}C_Q} = \frac{T\sqrt{DL}}{P\sqrt{2\rho}} \tag{7.1}$$

where DL (= T/A) is the rotor disk loading, T is the rotor thrust, P is the rotor power and A is the disk area.

Based on equation 7.1, rotors with a higher disk loading will achieve higher values of FoM due to the 3/2 power factor of the thrust coefficient. However, for high rotor efficiency, high power loading (defined as weight/power ratio) is sought for, and is maximized by minimizing

*A large portion of the work presented in this Chapter is published in T. Fitzgibbon et al., "Assessment of current rotor design comparison practices based on high-fidelity CFD methods," *The Aeronautical Journal*, Vol. 124, No. 1275, 2020, pp. 731-766, DOI: 10.1017/aer.2019.16

the disk loading and maximizing the FoM. The disk loading value, however, is usually set based on the vehicle class and sizing requirements. Rotors at high disk loading will be driven to higher values of FoM, due to a higher ratio between induced and profile power, as shown by Prouty [313]. Furthermore, a higher solidity (geometric) rotor will lead to a shift in the maximum FoM value to higher thrust coefficients by delaying the onset of stall. For this reason, the solidity (in many cases thrust-weighted) of a rotor is constrained in many hover optimisation studies [108, 158,214,221], when the objective is to maximize the FoM. This can be avoided by reformulating the objective as a power minimization problem at constant thrust. The power required at a specific weight is more important in real-life rotor design than the FoM value. To compare the different rotor designs, CFD simulations were performed in hover trimmed to a constant thrust coefficient of $C_T = 0.008$. The net thrust values are given in Table 7.1, based on CFD results, and hence account for the planform shape as well as solidity effects.

Table 7.1: Net thrust values for the four rotor blade designs in hover at $C_T = 0.008$ based on the scaled blades (scaled by a unit chord) used within the CFD simulations, the experimental values and values scaled to an equal rotor radius.

Blade	Net thrust based on a unit chord length	Net thrust based on experimental chord values	Net thrust scaled to an equal radius of 56.224 in. (1.428m)
LBERP	265.942 kN/m^2	2.864 kN	2.864 kN
LBL	232.277 kN/m^2	2.971 kN	2.971 kN
PSP	172.237 kN/m^2	3.300 kN	2.359 kN
AH-64A	283.094 kN/m^2	80.545 kN	3.069 kN

Firstly, net thrust values are presented assuming a unit chord length for all four rotor blades. These values are therefore primarily driven by the rotor blade tip Mach number and aspect ratio, hence not accounting for differences in planform shape. Based on this assumption, at a constant thrust coefficient, the LBERP net thrust is higher than the LBL blade due to a higher aspect ratio. The net thrust values for the PSP and AH-64A rotor blades are mainly driven by different blade tip Mach number compared to the LBL and LBERP blades. Further comparisons are performed whilst including the differences in planform shape. The actual experimental thrust values are presented based on the actual chord and radius for each of the rotor blades. The PSP rotor blade, delivers a higher net thrust compared to the LBL and LBERP blades, due to the higher rotor radius (66.5 in. compared to 56.224 in.). The AH-64A blade was tested at full-scale and therefore, a significantly higher net thrust is observed compared to the other three rotor blades. Finally, further observations are made by scaling all four rotor blades to an equal radius of 56.224 in. Firstly, it can be observed that even though the thrust-weighted solidity was matched between the LBL and LBERP blades, the LBL blade delivers a higher net thrust by 3.7% at a constant thrust coefficient. This is mainly due to the higher geometric solidity of the LBL blade. The net thrust produced by the PSP rotor blade is lower than for the other blades

due to the lower blade tip Mach number. Similarly, the AH-64A blade produces the highest net thrust due to the highest blade tip Mach number. As shown here, rotors at the same thrust coefficient can be operating at different net thrusts, due to different chord length and planform geometry. Nevertheless, the main reason for the higher FoM for the PSP rotor when compared to the Langley blade designs, comes from reduced compressibility effects due to the lower blade tip Mach number (0.58 compared to 0.628). For rotors operating at the same net thrust, higher FoM values are obtained at a lower blade tip Mach number (the lower limit of the blade tip Mach number is constrained by forward flight design considerations). Based on the interplay of many design parameters, the use of the FoM metric alone has its limitations when comparing different rotors for a particular design point, operating at different disk loadings, tip Mach numbers and net thrust values. For similar planforms and similar disk areas, the FoM comparison makes more sense.

In forward flight, the aerodynamic efficiency measure often used is the lift to drag ratio (L/D), shown in equation 7.2.

$$\frac{L}{D} = \frac{WV_\infty}{P} = \frac{C_L}{C_Q}\mu \tag{7.2}$$

where W is the weight of the helicopter, V_∞ is the flight speed and P is the rotor power, and μ is the rotor advance ratio.

In rotorcraft, this parameter is proportional to the power loading and flight speed of the helicopter. Rotors with high disk loading will generally have a lower power loading, and hence lower lift to drag ratio. Therefore, this parameter will favour rotor designs with low disk loading. The lift to drag ratio will decrease with increasing weight of the helicopter. Heavy-lift helicopters will generally have poor lift to drag ratios, however, may have a much wider flight envelope in terms of payload than lower loaded helicopters. Direct comparison of rotor designs in terms of lift to drag ratio is only valid for rotors with the same disk loading, as well as aircraft weight. Furthermore, this parameter does not directly account for differences in the generated propulsive force. For this reason, an equivalent lift to drag ratio, $(L/D)_e$, is also often used, defined in equation 7.3.

$$\left(\frac{L}{D}\right)_e = \frac{C_L}{C_Q/\mu - C_D} \tag{7.3}$$

where C_D is the drag coefficient which is equal to the propulsive force coefficient (assumed trim).

An additional simulation was performed for the PSP rotor blade trimmed to $C_T = 0.0081$ at $\mu = 0.4$ to compare the lift-to-drag ratios with the LBL and LBERP blades at a constant thrust coefficient. The calculated lift to drag ratios, as well as equivalent lift-to-drag ratios when scaled to two different full-scale helicopter rotors (UH-60A and AH-64) are shown in Table 7.2. This is done to demonstrate the L/D_e metric for full-scale rotors.

At a constant thrust coefficient of 0.0081, the PSP rotor blade generates 20% less net thrust

Table 7.2: Comparison of various lift-to-drag ratio values for the LBERP, LBL and PSP rotor designs at $C_T = 0.0081$ and $\mu = 0.4$. Same propulsive force coefficient assumed for the AH-64 and UH-60A helicopters.

Blade	LBERP	LBL	PSP
L/D	3.45	3.58	4.34
$(L/D)_e$ (UH-60A)	6.23	6.68	7.97
$(L/D)_e$ (AH-64A)	6.23	6.68	7.97

than the Langley blades (scaled to the same rotor radius), primarily due to the lower blade tip Mach number. This leads to a higher L/D ratio for the PSP rotor compared to the Langley blades. The equivalent lift to drag ratios are calculated by scaling the model-scale rotor blades to a full-scale radius. The drag coefficient is calculated based on the prescribed shaft angle (-7.449^o for the LBL and LBERP blades, -6^o for the PSP blade). Therefore, the propulsive force generated by the PSP rotor blade is lower than for the LBL and LBERP designs. The propulsive force required for the UH-60A and AH-64A helicopters was assumed as identical (although the equivalent flat plate areas will not be due to different rotor radii). The equivalent lift to drag ratio is the same for any helicopter as the value is only dependent on the rotor lift, torque and the required propulsive force. However, the AH-64A helicopter operates at a higher disk loading, and hence for a given thrust coefficient, the weight of the aircraft will be lower. Here, at $C_T = 0.0081$, the UH-60A operates at 22,132lbs whereas the Apache rotor operates at 18,362lbs. In fact, the condition of $C_T = 0.0081$ and $\mu = 0.4$ is outside the flight envelopes of both helicopters. Based on these observations it can be stated, that the L/D and $(L/D)_e$ values may be misleading for different rotor designs. The rotors must be compared for the same helicopter weight and disk loading to gain valuable insight.

Based on the analysis of FoM and lift-to-drag ratio, care must be taken when comparing rotors of different helicopters, due to different blade tip Mach numbers, disk loadings and net thrusts at a constant thrust coefficient. For this reason, when comparing rotors operating at different conditions, moving to the dimensional form of forces and moments may be more valuable. In optimisation studies, however, when the blade has a constant disk loading, radius and blade tip Mach number the FoM and lift-to-drag ratio parameters can be used as long as the objective function is correctly formulated.

7.2 Blade Solidity Study

The effects of rotor solidity matching, are examined for the LBERP and LBL blade designs. The blades tested by Yeager et al. [429] were matched based on thrust-weighted solidity. Here, an additional, scaled LBL blade is simulated to match the nominal solidity of the LBERP blade. This study is aimed at investigating the findings of Perry [299] who claimed that the definition of thrust weighted solidity is misleading. The solidity values for each of the blade designs are

presented in Table 7.3.

Table 7.3: Differences in the rotor solidity values for the LBERP, LBL and scaled LBL blade (LBLs).

Blade	LBERP	LBL	LBLs
Radius, R	56.224 in.	56.224 in.	56.224 in.
Chord, c_{ref}	4.086 in.	4.454 in.	4.086 in.
Aspect ratio, AR	13.76	12.62	13.76
Nominal solidity, $\sigma_N = N_b/(\pi R/c_{ref})$	0.0925	0.101	0.0925
Geometric solidity, $\sigma_G = \int_0^1 \sigma(r)dr$	0.096	0.101	0.0925
Thrust-weighted solidity, $\sigma_T = 3\int_0^1 \sigma(r)r^2dr$	0.101	0.101	0.0925

As can be seen in Table 7.3, the thrust-weighted solidity is matched between the LBL and LBERP blades, whereas the nominal solidity is matched between the LBLs and LBERP blades. The nominal solidity is based on the reference blade chord and blade radius and does not take into account the variation of chord along the blade radius. The geometric solidity considers the advanced planform shape, whereas the thrust-weighted solidity provides a higher weighting of blade area located further outboards, due to the r^2 term under the integral. Firstly, the effect on the hover performance is examined. The hover predictions are shown in Figure 7.1, based on thrust coefficient and blade loading (C_T/σ_G). For clarity, the experimental measurements are removed. The hover performance results indicate a performance loss at high thrust coefficients for the LBLs blade when compared to the nominal LBL blade. A similar peak FoM is obtained with a much sharper performance deterioration with increasing thrust. The LBLs blade has equal performance to the LBERP blade at a lower thrust coefficient when comparing with the LBL blade. When the FoM is based on blade loading the LBLs curve is slightly shifted with respect to the LBL curve as the geometric solidity of the LBLs blade is now lower than the LBERP blade. This leads to equal performance of the LBERP and LBLs blade at a slightly higher collective, hence the sharp drop in FoM is slightly delayed. To examine the cause behind this behaviour of the performance curves, the surface pressure and skin friction coefficient distributions along with skin friction lines are investigated at 13.5° collective for the LBL and LBLs blades, shown in Figure 7.2.

As can be seen from Figure 7.2, a stronger suction peak is seen inboards of the aerofoil transition as well as near the blade tip for the LBLs blade when compared to the LBL blade. This is due to the fact, that the load is distributed across a shorter chord leading to a sharper adverse pressure gradient. The pressure recovery at the trailing edge is also weaker indicating stronger stall for the LBLs blade. This also indicates that the LBLs blade will first encounter stall at a lower collective angle. The LBLs blade, therefore, has poorer performance than the LBL blade showing the effect of rotor solidity on the stall boundary.

Solidity effects are also examined in high-speed forward flight ($C_T = 0.0081, \mu = 0.4$), with integrated loads shown in Table 7.4.

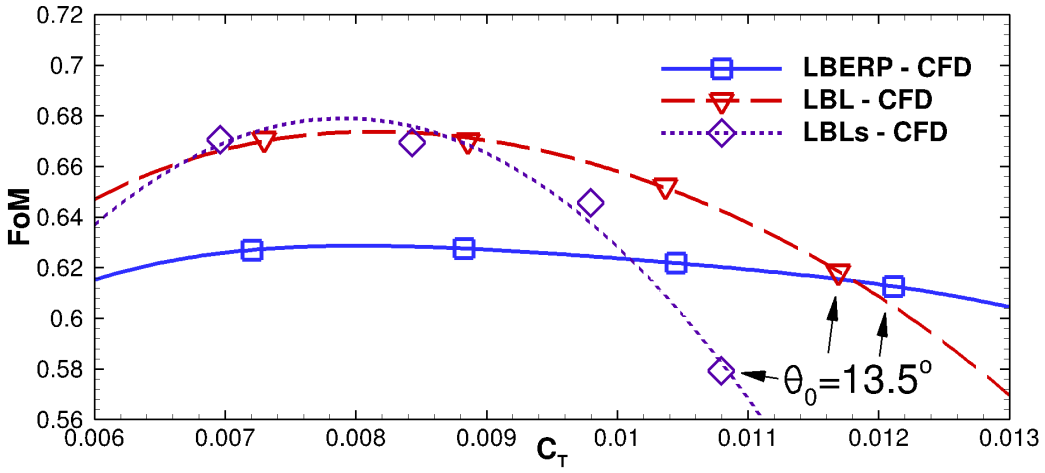

(a) FoM vs C_T

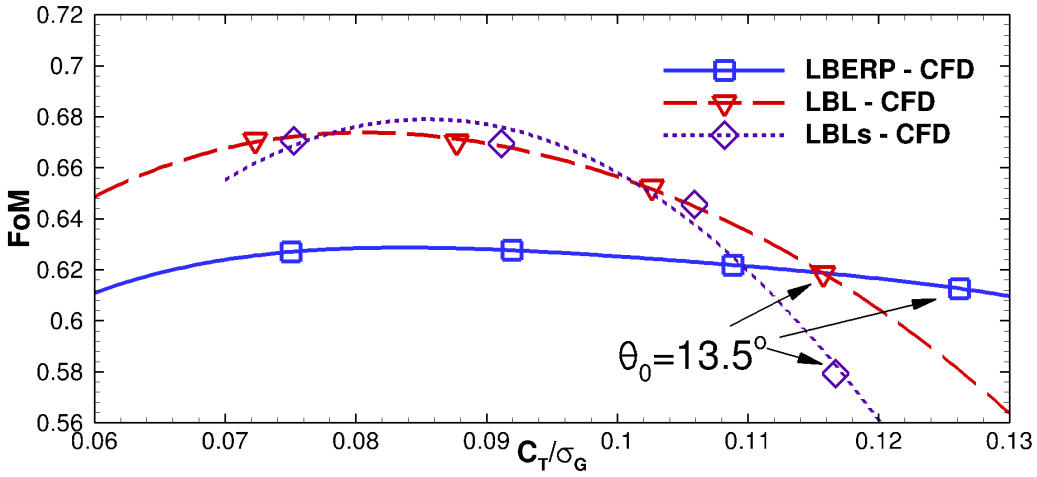

(b) FoM vs C_T/σ_G

Figure 7.1: Effects of rotor solidity matching (nominal vs thrust-weighted) on the hover performance of the LBERP and LBL blades based on thrust coefficient and blade loading.

Table 7.4: Solidity effects on the rotor forward flight performance at high-speed, $C_T = 0.0081, \mu = 0.4$

Blade	C_T	Net thrust	C_Q	ΔC_Q % rel. to LBERP
LBERP	8.085×10^{-3}	2.898 kN	9.396×10^{-4}	0.0%
LBL	8.081×10^{-3}	2.941 kN	9.049×10^{-4}	-3.693%
LBLs (before trim)	7.720×10^{-3}	2.767 kN	8.622×10^{-4}	-8.237%
LBLs (after trim)	8.065×10^{-3}	2.891 kN	9.524×10^{-4}	+1.362%

Based on Table 7.4 the baseline LBL blade is slightly better than the LBERP blade in terms of torque coefficient as predicted by the experiments. At the same trim state, the LBLs blade does not deliver the required thrust coefficient. This is not surprising due to the shorter chord of the blade and lower geometric solidity. After trimming to the required thrust coefficient the LBLs blade is worse than the LBERP blade. Here, a more extreme trim state is needed to attain the

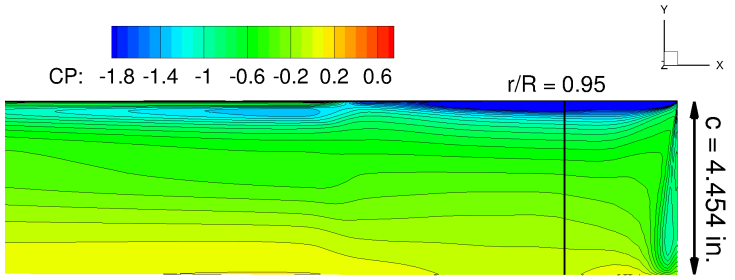

(a) C_P, LBL blade

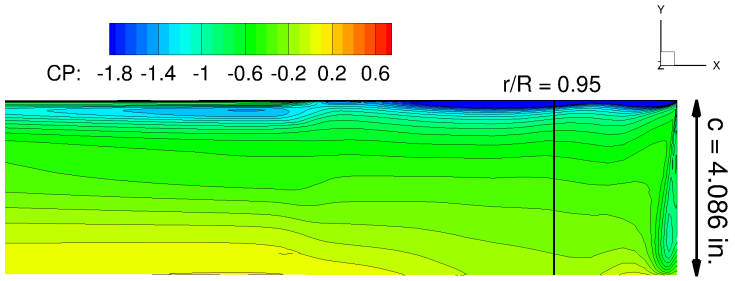

(b) C_P, LBLs blade

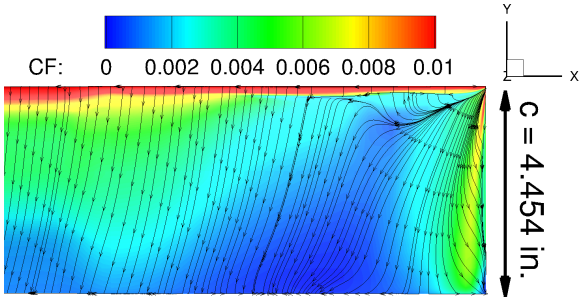

(c) C_F, LBL blade

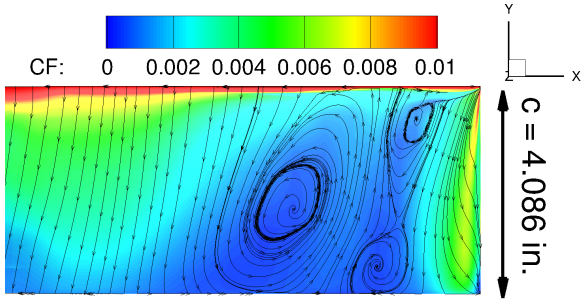

(d) C_F, LBLs blade

Figure 7.2: Surface pressure coefficient and skin friction distributions with skin friction lines near the blade tip for the LBL and LBLs blades at high thrust (13.5^o collective).

required thrust, with increased collective and longitudinal cyclic angles. On the retreating blade side, the blade pitch angle is increased by 1.51 degrees, leading to significantly higher power requirements, and hence worse performance compared to the LBERP design. This is confirmed by examining the skin friction lines shown in Figure 7.3 (to highlight flow separation).

A significantly higher separation region can be seen for the scaled LBL blade, especially at $240-260^o$ azimuthal locations. The lower blade solidity promotes stall on the retreating side leading to an increase in power. This statement is consistent with the findings of Perry [299], who compared the flight envelopes of a tapered planform with a BERP planform. As seen by Perry [299] the definition of thrust-weighted solidity can give misleading results and will promote planforms with lower area near the blade tip. In our case, the differences between the LBL and LBERP blades are not as drastic as those described by Perry (who compared a BERP with a tapered planform) [299] due to a lower area mismatch between the two blades. However,

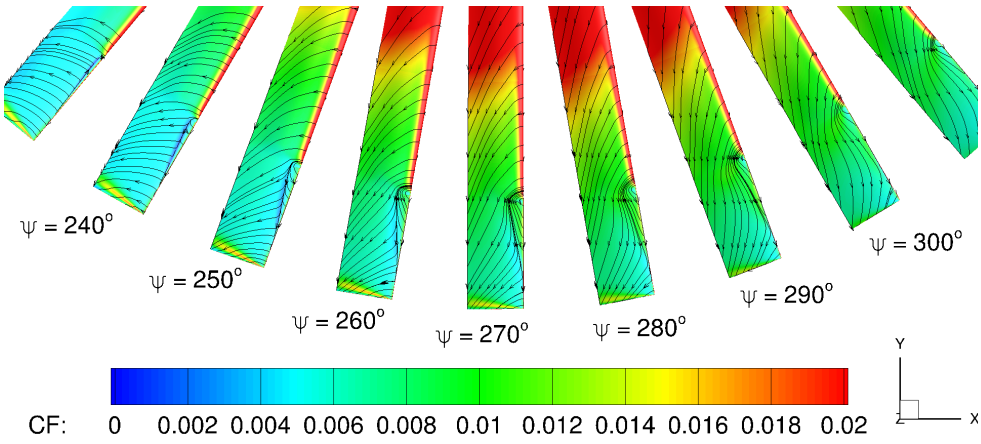

(a) Nominal LBL blade

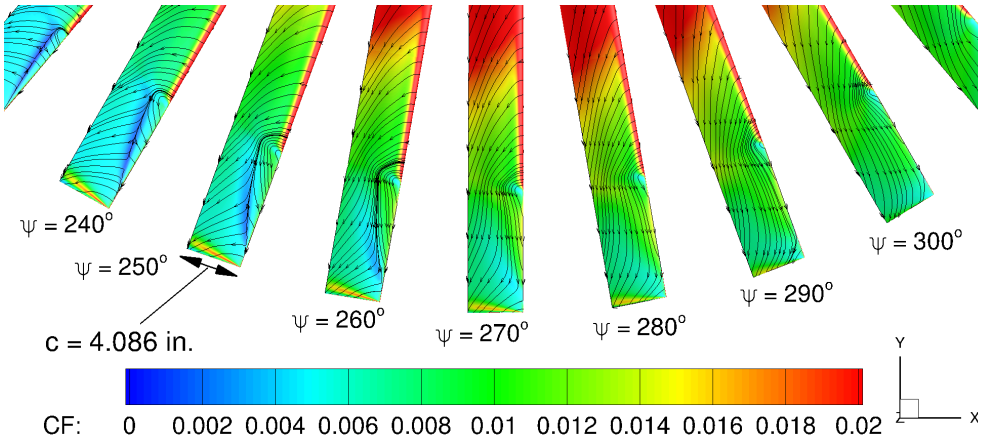

(b) Scaled LBL blade

Figure 7.3: Retreating side skin friction lines and skin friction coefficient distributions for the nominal and scaled LBL rotor blades.

the matching of thrust-weighted solidity still promotes the LBL blade as it delivers a higher net thrust by 1.5% at this condition when compared to the LBERP blade, purely due to larger chord. The main reason for the use of thrust-weighted solidity is to account for the additional blade weight of a blade with additional area near the blade tip, as seen for a BERP design. However, as stated by Perry [299] the weight increase is of second order due to the outer structure of the blade only being a light fairing. To generate the same thrust, the blade chord of the tapered blade would have to be increased by 7.5 % [299] which would incur much more significant weight penalties. Another aspect is that the success of the BERP rotor design did not only come from the planform but was also due to the advanced aerofoils which were designed with the planform shape. The use of the same aerofoils on a rectangular and BERP-like planform as seen for the LBL and LBERP blades may promote one of the blades.

7.3 Analysis of Different Rotor Designs in Hover

A further comparison of the different rotor designs is performed in hover. Firstly, qualitative comparisons are performed across a range of collective angles. Next, the four rotor designs are examined at $C_T = 0.008$, whilst taking into account the observations made for comparing different rotor designs at different blade tip Mach numbers and disk loading. Finally, an anhedral study is performed for the LBL and LBERP blades.

7.3.1 Comparisons Over a Range of Collectives

Firstly, a comparison of the different rotor designs is performed over a range of collective angles. The FoM curves versus C_T are compared in Figure 7.4 and versus blade loading (C_T/σ_G) in Figure 7.5.

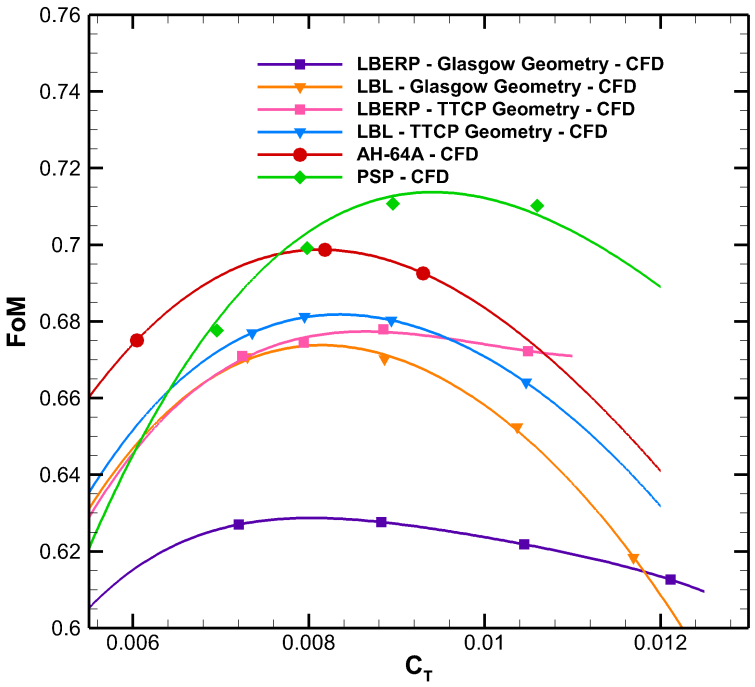

Figure 7.4: Comparison of the performance predictions based on thrust coefficient for the LBL (TTCP and Glasgow geometries), LBERP (TTCP and Glasgow geometries), PSP and AH-64A blades.

Firstly, the designs of the LBL and LBERP blades are compared in terms of performance. As discussed in Chapter 5.2.1, Geometric sensitivity for the LBL and LBERP blades, the differences for the Glasgow and TTCP geometries are much higher for the LBERP blade than the LBL blade. The Glasgow LBERP blade has the lowest performance based on C_T and C_T/σ_G of all blades. The performance of the TTCP LBERP blade is comparable with the Glasgow and TTCP LBL blade with a significantly higher FoM at higher thrust coefficients. The LBERP blade has a much flatter FoM curve for both Glasgow and TTCP geometries. This planform is able to

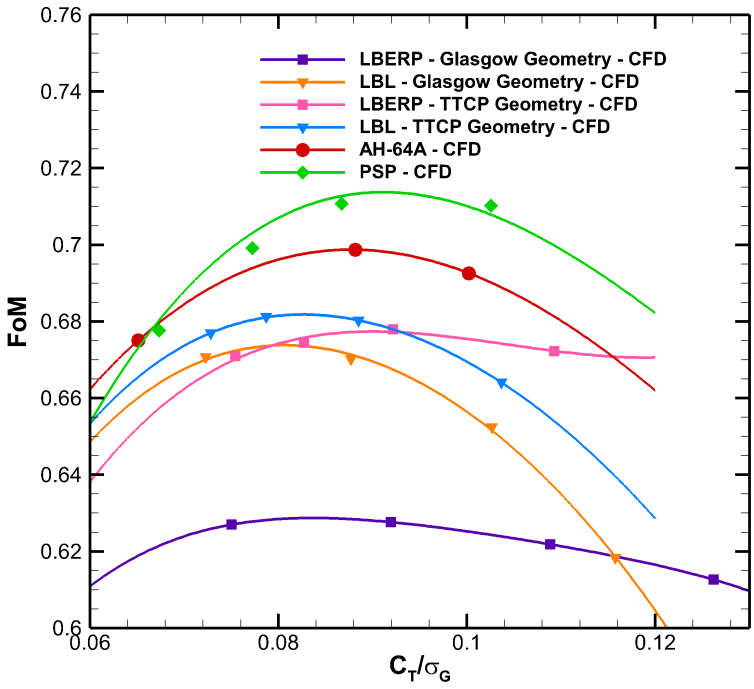

Figure 7.5: Comparison of the performance predictions based on blade loading for the LBL (TTCP and Glasgow geometries), LBERP (TTCP and Glasgow geometries), PSP and AH-64A blades.

operate at higher blade loading without significant losses in performance [298], [338]. This is due to the paddle-shape blade tip and the notch feature which prevents separation across the blade tip at significantly higher loading when compared to the rectangular LBL blade design. The high blade tip area, however, leads to an increased torque at lower blade loading reducing the LBERP blade performance compared to the other blades. When comparing the Glasgow LBL and LBERP geometries, the LBERP blade surpasses the LBL blade at a fairly high thrust coefficient of $C_T = 0.0118$, equivalent to a collective of nearly 13.5^o for the LBERP blade. When these blades are compared based on blade loading, this point occurs at an even lower collective for the LBERP blade, but similar value for the LBL blade. This is due to the fact that at a constant thrust coefficient, the LBERP blade operates at a higher blade loading, due to lower geometric solidity, when compared to the LBL blade. The FoM values for the PSP and AH-64A blades indicate significantly higher performance compared to the LBL and LBERP blades. The shape of the FoM curves is similar to the LBL blade as the performance decreases rapidly at higher thrust coefficients. A comparison based on the thrust coefficient indicates higher performance of the AH-64A blade at lower thrust than the PSP blade, with a peak FoM value at a much lower thrust. Based on blade loading, however, the AH-64A FoM peak value is shifted closer the peak FoM value of the PSP rotor blade. This is due to the lower geometric solidity of the AH-64A blade compared to the PSP rotor blade. The improved performance of the AH-64A and PSP rotor blades compared to the LBL blade can be explained by the incorporation of tip sweep leading to reduced compressibility effects. The AH-64A blade has a higher blade tip

Mach number than the Langley blades, which typically leads to reduced hover performance, however, the incorporation of tip sweep and potentially better aerofoil design, leads to higher overall performance compared to the LBL blade. Another factor is the higher disk loading of the AH-64A blade compared to the LBL and LBERP blades (when scaled to the same radius of 56.224 in.). The PSP rotor blade performance is even higher due to the higher linear blade twist value (-14^o compared to -9^o) and lower blade tip Mach number (0.58 compared to 0.65). This leads to a reduced loading at the tip of the blade and reduced compressibility effects, leading to higher rotor blade performance.

The four blade designs LBL (Glasgow), LBERP (Glasgow), PSP and AH-64A are analysed further by extracting the sectional loads at a range of collectives, shown in Figures 7.6-7.7. Both the sectional thrust and torque values are scaled by the local flow velocity and reference blade chord equal to the chord of the first aerodynamic section.

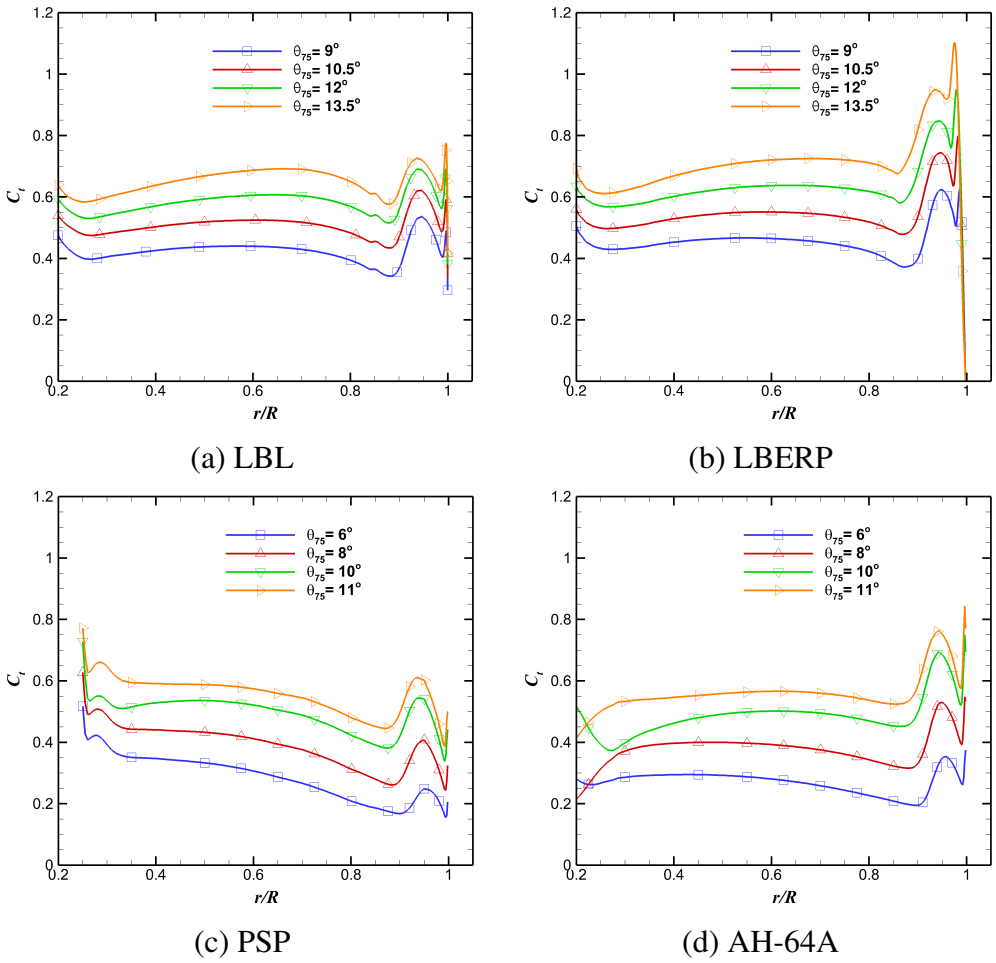

(a) LBL (b) LBERP

(c) PSP (d) AH-64A

Figure 7.6: Sectional thrust distributions in hover at a range of collective angles for the LBL (Glasgow), LBERP (Glasgow), PSP and AH-64A blade designs.

The sectional loads show fairly similar radial thrust distributions for all four blade designs. A high thrust is seen inboards due to the scaling with local velocity. The effect of the preceding blade tip vortex is also seen at approximately r/R=0.9 for all four rotor blades (the radial location

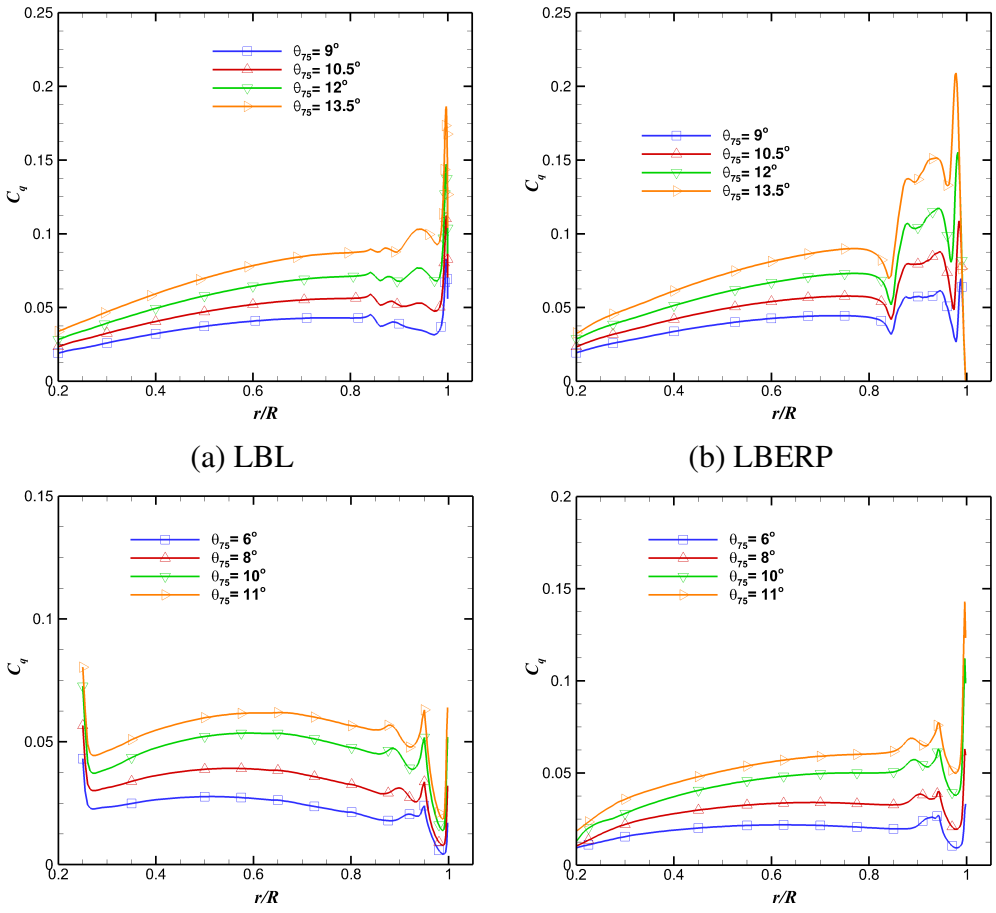

(a) LBL (b) LBERP

(c) PSP (d) AH-64A

Figure 7.7: Sectional torque distributions in hover at a range of collective angles for the LBL (Glasgow), LBERP (Glasgow), PSP and AH-64A blade designs.

shifts inboard with increasing thrust due to greater wake contraction). Inboard of the tip vortex, the local thrust is reduced due to a locally increased downwash, reducing the effective angle of attack, whereas outboard of the tip vortex, the local thrust is increased due to a locally increased upwash, increasing the effective angle of attack. The locally induced downwash and upwash effects occur due to the sense of rotation of the preceding blade tip vortex. Larger values of local thrust in the tip region can be seen for LBERP blade compared to the other blade due to paddle-shaped tip which generates a stronger downwash field. The blade tip shape is also responsible for a larger increase in thrust with increasing collective for the LBERP blade, especially when compared to the LBL blade, which leads to improved performance at higher collective angles. A slightly different slope of the thrust distribution can be seen for the PSP rotor blade compared to the other designs due to a higher linear blade twist angle of -14^o compared to -9^o. The increased blade twist also leads to a lower tip loading, as the load is shifted inboard. Greater differences between the four blade designs can be seen in the torque distributions. A typical rotor blade torque distribution can be seen for the LBL blade, with increasing torque outboards, with the peak value at the very tip of the blade. The effect of the aerofoil blending region

can also be seen with mild discontinuities in the curve smoothness at r/R = 0.84. The LBERP torque distributions show a decrease in torque coefficient at the notch, with an increase across the paddle-type blade tip. The high blade tip area is the main reason behind the increase in local torque and lower performance of the LBERP blade in hover. The PSP and AH-64A rotor blades show fairly similar torque distributions, with the swept blade tip leading to a rapid decrease in local torque. This effect is sharper for the PSP rotor blade, due to the greater sweep angle and tip taper, which reduces the loading at the blade tip. However, the radial stations at which the tip sweep is initiated see a sharp rise in local torque. The higher loading inboard for the PSP rotor blade also increases the torque inboard of the blade tip. Similarly, as for the thrust distributions, the preceding tip vortex also has an effect on the local torque, following the same trends as the local thrust. To analyse the sources behind the loading distributions for the four rotor blade designs, the surface pressure and skin friction distributions (along with skin friction lines) are extracted from the solutions, shown in Figures 7.8-7.11.

The surface pressure contours for the LBL blade are typical for a rectangular blade design. A sharp suction peak can be seen near the leading edge at the tip of the blade which leads to decreased performance compared to more modern blade designs such as a design with a parabolic blade tip. The region of high suction moves further inboard and grows in the chordwise direction with increasing collective. A secondary suction peak is also seen before the aerofoil transition region. The rapid aerofoil transition causes a non-smooth pressure distribution, which can especially be seen in Figure 7.8 (g). At the highest collective angle, the pressure contours indicate the onset of separation across the blade tip, as the blade pressure is no longer recovered at the trailing edge. The skin friction lines indicate a low level of shock-induced separation near the leading edge at the blade tip, for lower collective angles. This separation grows stronger with increasing collective, and the reattachment location is seen at an increased chordwise position. A significant amount of separation can be seen at the highest collective of 13.5^o indicating the onset of stall. This is the primary reason for the lower performance of this blade at 13.5^o collective compared to the LBERP design, which is able to operate at much higher collectives without developing stall. The surface pressure distribution for the LBERP blade also indicates two regions of high suction, which are inboard of the notch and round the swept tip. With increasing collective, these suction regions grow and propagate inboard and cover a larger portion of the paddle-shaped tip. The effect of the tip vortex is also clearly seen. With increasing collective, the tip vortex formation moves further inboard. The tip vortex separates inboards of the very tip of the blade, which is especially visible at high collective angles, due to a reduced pressure recovery near the trailing edge. This could be one of the causes for the poor performance of the LBERP blade, as the blade tip vortex is expected to form round the curved tip. Such behaviour of the tip vortex can be seen for the production BERP III and BERP IV blades based on the surface pressure distributions in hover (Euler computation) [321]. The early vortex separation for the LBERP blade is potentially attributed to the too low blade thickness in this region. Tapering

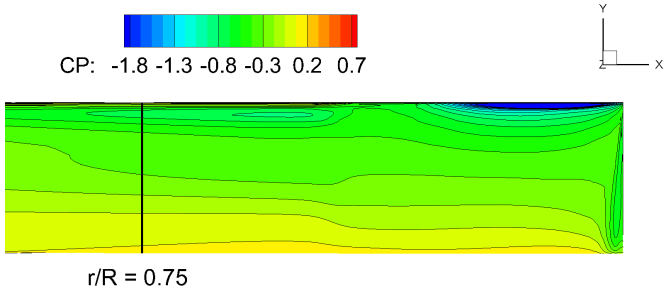

(a) C_P, $\theta_0 = 9^o$

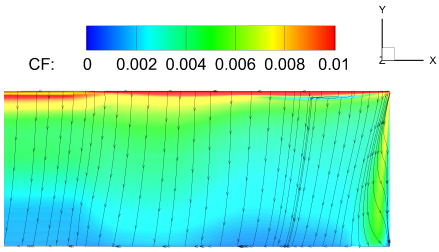

(b) C_F, $\theta_0 = 9^o$

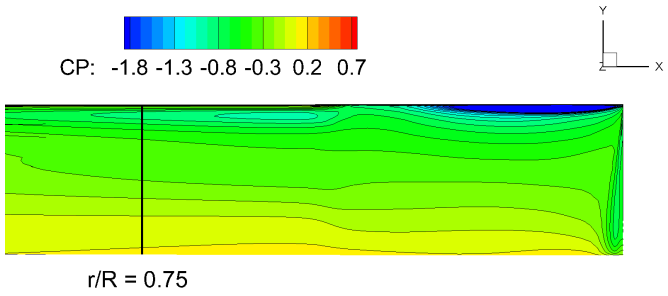

(c) C_P, $\theta_0 = 10.5^o$

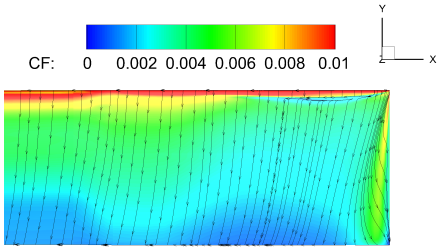

(d) C_F, $\theta_0 = 10.5^o$

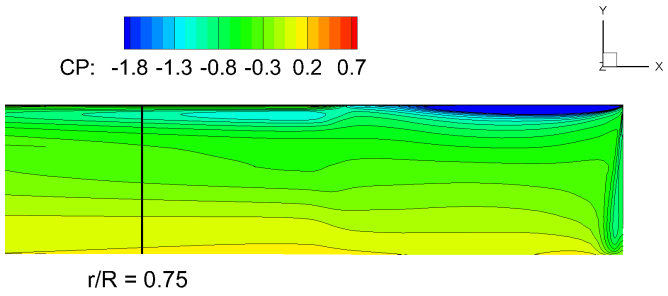

(e) C_P, $\theta_0 = 12^o$

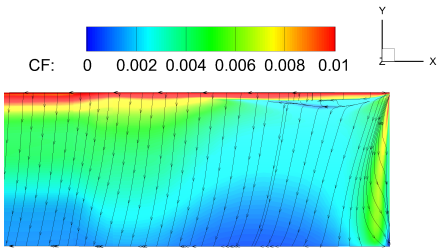

(f) C_F, $\theta_0 = 12^o$

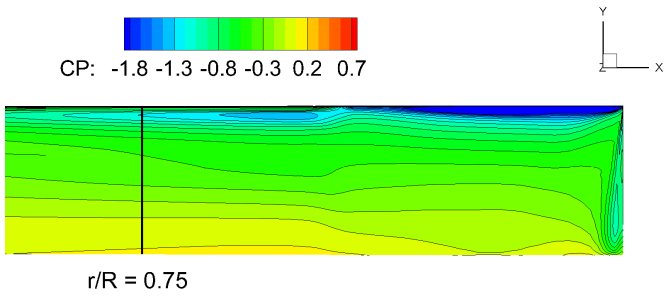

(g) C_P, $\theta_0 = 13.5^o$

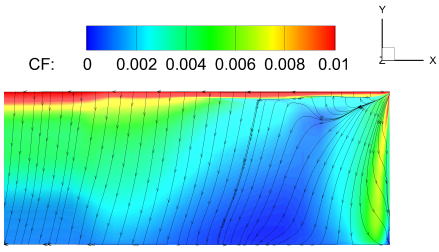

(h) C_F, $\theta_0 = 13.5^o$

Figure 7.8: Surface pressure and skin friction distributions along with skin friction lines for the LBL rotor blade in hover at four collectives.

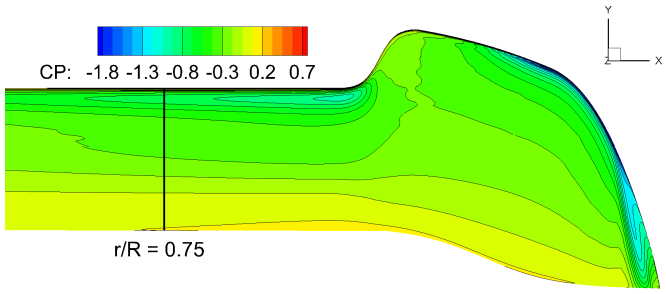

(a) C_P, $\theta_0 = 9^o$

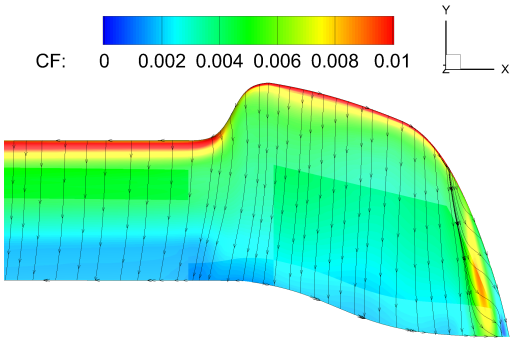

(b) C_F, $\theta_0 = 9^o$

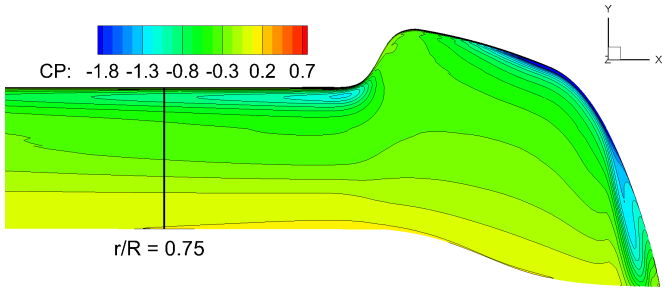

(c) C_P, $\theta_0 = 10.5^o$

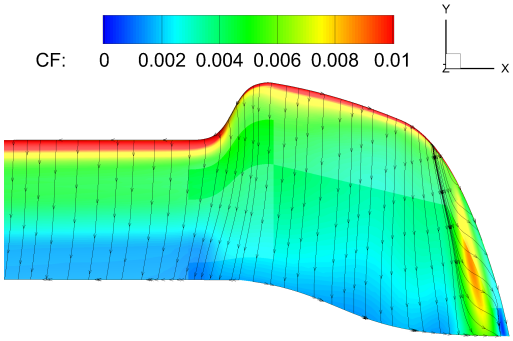

(d) C_F, $\theta_0 = 10.5^o$

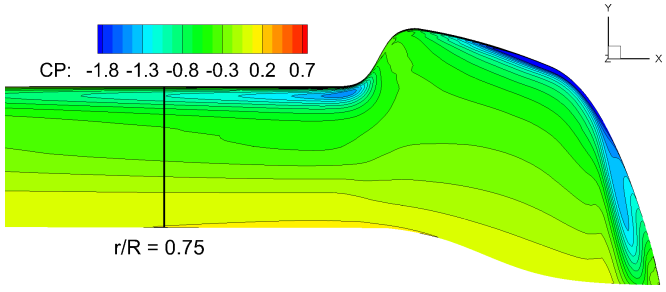

(e) C_P, $\theta_0 = 12^o$

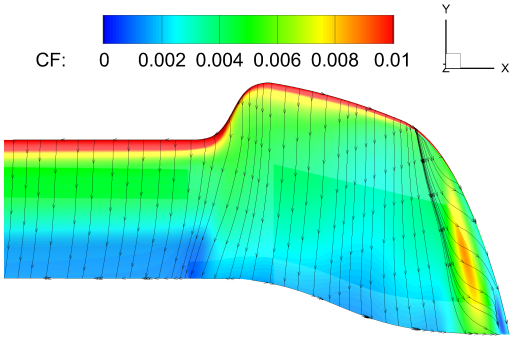

(f) C_F, $\theta_0 = 12^o$

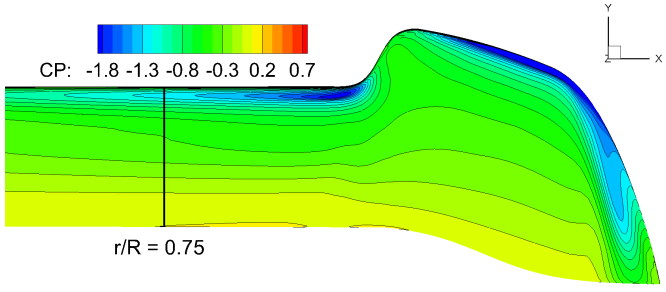

(g) C_P, $\theta_0 = 13.5^o$

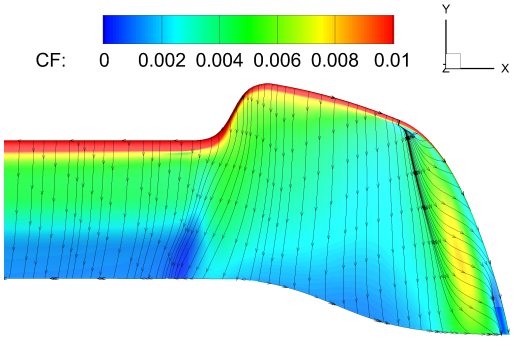

(h) C_F, $\theta_0 = 13.5^o$

Figure 7.9: Surface pressure and skin friction distributions along with skin friction lines for the LBERP rotor blade in hover at four collectives.

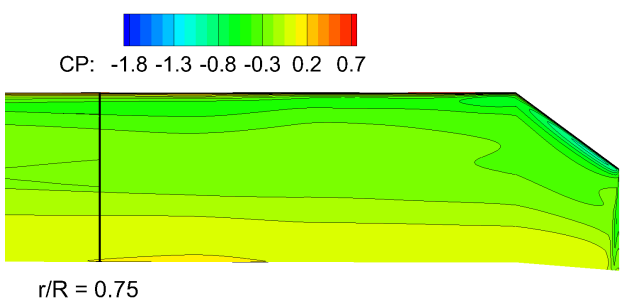

(a) C_P, $\theta_0 = 6^o$

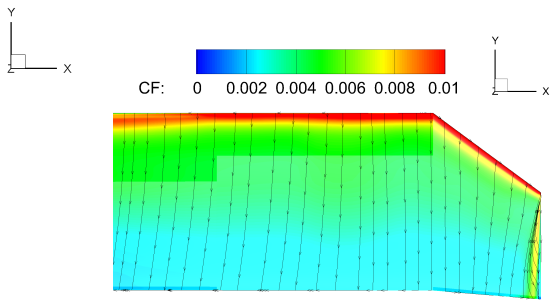

(b) C_F, $\theta_0 = 6^o$

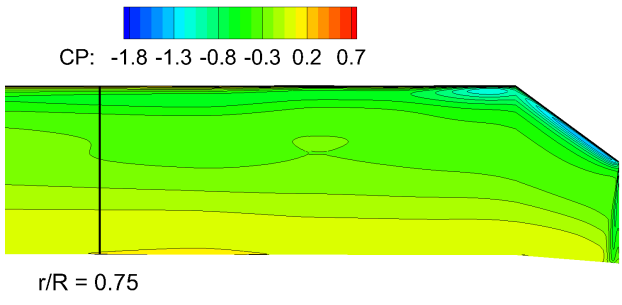

(c) C_P, $\theta_0 = 8^o$

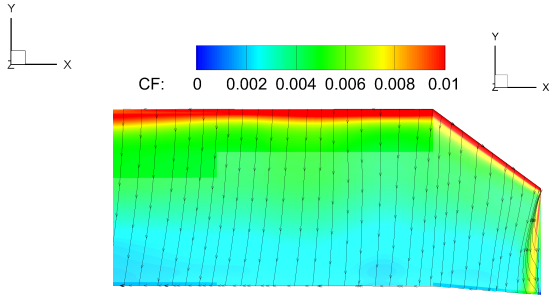

(d) C_F, $\theta_0 = 8^o$

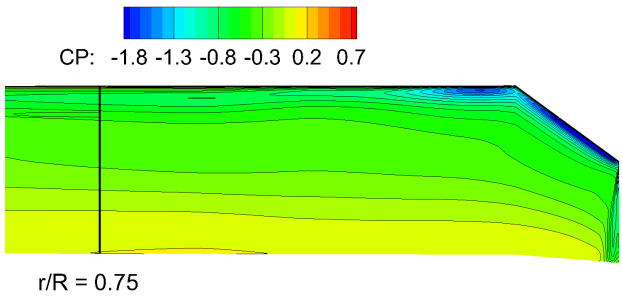

(e) C_P, $\theta_0 = 10^o$

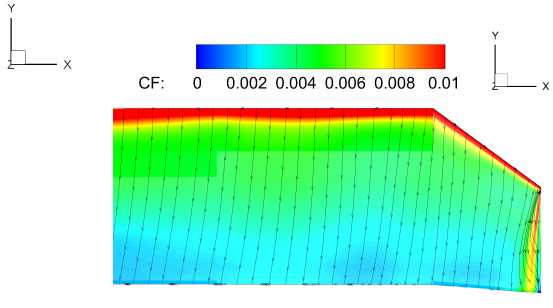

(f) C_F, $\theta_0 = 10^o$

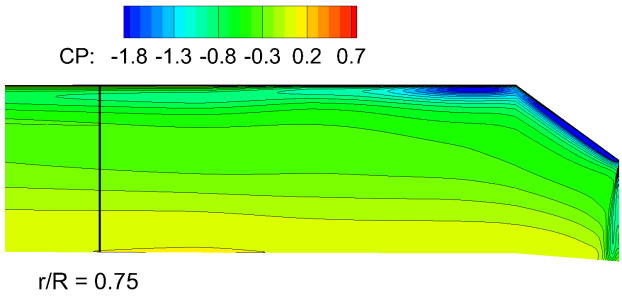

(g) C_P, $\theta_0 = 11^o$

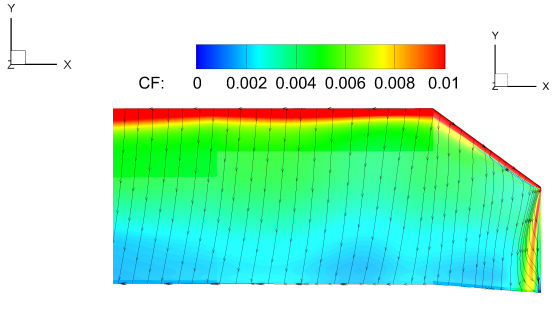

(h) C_F, $\theta_0 = 11^o$

Figure 7.10: Surface pressure and skin friction distributions along with skin friction lines for the PSP rotor blade in hover at four collectives.

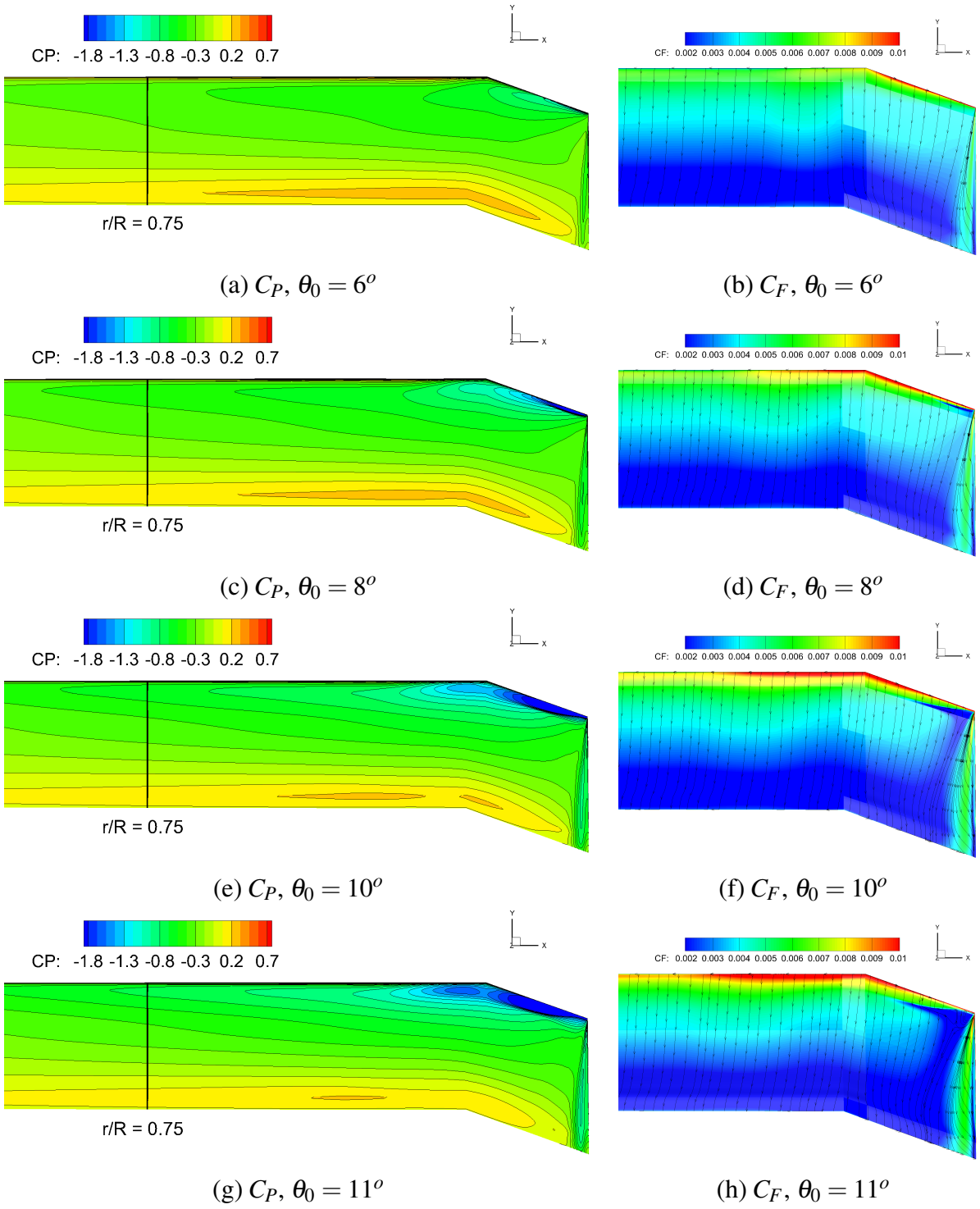

(a) C_P, $\theta_0 = 6^o$ (b) C_F, $\theta_0 = 6^o$

(c) C_P, $\theta_0 = 8^o$ (d) C_F, $\theta_0 = 8^o$

(e) C_P, $\theta_0 = 10^o$ (f) C_F, $\theta_0 = 10^o$

(g) C_P, $\theta_0 = 11^o$ (h) C_F, $\theta_0 = 11^o$

Figure 7.11: Surface pressure and skin friction distributions along with skin friction lines for the AH-64A rotor blade in hover at four collectives.

off the blade quadratically rather than linearly could potentially prevent this, leading to a more optimal blade thickness distribution. These tip vortex features are further highlighted by the skin friction contours and skin friction lines. The very tip of the blade is completely separated as indicated by the very low skin friction values (outboard of r/R = 0.99). Evidence of the notch vortex formation is also seen for the higher thrust case, as a drop in skin friction is seen. Finally, the LBERP blade only sees a low level of shock-induced separation at the highest examined collective at 13.5^o. The LBERP planform shape is more favourable than the LBL blade in terms of pressure distribution, however, the exact planform features are highly sensitive as seen in the comparison of the Glasgow and TTCP LBERP geometries (Section 5.2.1 Geometric sensitivity for the LBL and LBERP blades). The PSP rotor blade also has two key regions of high suction, which are placed along the swept blade tip and before the sweep initiation. The favourable effect of sweeping the blade tip is also highlighted. A reduced suction is seen when compared to the rectangular blade, with the sweep onset acting as an aerodynamic discontinuity. The more favourable pressure contours, however, are also due to the lower blade tip Mach number. Only at the highest collective, a weak shock-induced separation can be seen across the swept blade tip as indicated by the skin friction lines. No evidence of the onset of stall is seen, across the examined collectives. The lack of major adverse flow features for this planform lead to a high FoM across the examined collectives. Finally, the AH-64A blade surface pressure contours indicate a formation of a strong suction region at the leading edge of the blade near the blade tip. This region grows with increasing collective and propagates further inboard. At collective angles of 10° and 11°, a strong shock is formed at the leading edge, leading to increased power requirements. This feature could potentially be weakened through an optimisation study. The pressure contours are smooth showing no adverse effects of the aerofoil transition, and the effect of tip vortex is clearly seen. At the highest collective, a weaker pressure recovery can be observed at the trailing edge. The skin friction lines indicate fairly strong shock-induced separations, which reattach quickly. The effect of the trim tab on the HH02 aerofoil is also seen as a positive pressure coefficient can be seen near the trailing edge of the blade.

7.3.2 Comparisons at a Constant Thrust Coefficient

A more detailed comparison of the four different blade designs is performed at a constant thrust coefficient of $C_T = 0.008$. Firstly, similar results are extracted from the solutions as for the investigation across the range of collectives. The integrated loads for the four rotor blade designs at $C_T = 0.008$ are presented in Table 7.5.

The thrust coefficient values are close to $C_T = 0.008$ for all four rotor blades. The LBL blade produces a slightly higher net thrust (by 3.7%) than the LBERP blade, despite the fact that the thrust-weighted solidities were matched. The FoM values are fairly similar for the PSP and AH-64A blades, however, the net thrust (scaled to a radius of 56.224 in.) produced by the AH-64A blade is significantly higher when compared to the PSP blade. This is due to the

Table 7.5: Integrated loads for the LBL, LBERP, PSP and AH-64A rotor blades in hover at $C_T = 0.008$.

Blade	C_T	Net Thrust (scaled)	C_Q	*FoM*
LBL	0.00795	2.971 kN	0.0007356	0.6812
LBERP	0.00797	2.864 kN	0.0008030	0.6265
PSP	0.00797	2.359 kN	0.0007196	0.6991
AH-64A	0.00799	3.069 kN	0.0007211	0.6999

higher blade tip Mach number, and higher disk loading. The AH-64A exhibits significantly more adverse flow features compared to the PSP rotor blade, however, due to different operating conditions, the FoM value matches the performance PSP rotor blade. Another aspect is that the $C_T = 0.008$ condition is close to the maximum FoM value for the AH-64A blade, whereas the FoM curve keeps increasing for the PSP blade with the maximum FoM value occurring at approximately $C_T = 0.0094$. These differences are due to different blade tip Mach numbers and disk loading. Next, the sectional loads are analysed for the four rotor blades at $C_T = 0.008$, shown in Figure 7.12. The sectional loads are scaled by a unit chord of 1.0 equal to the chord of the first aerodynamic section.

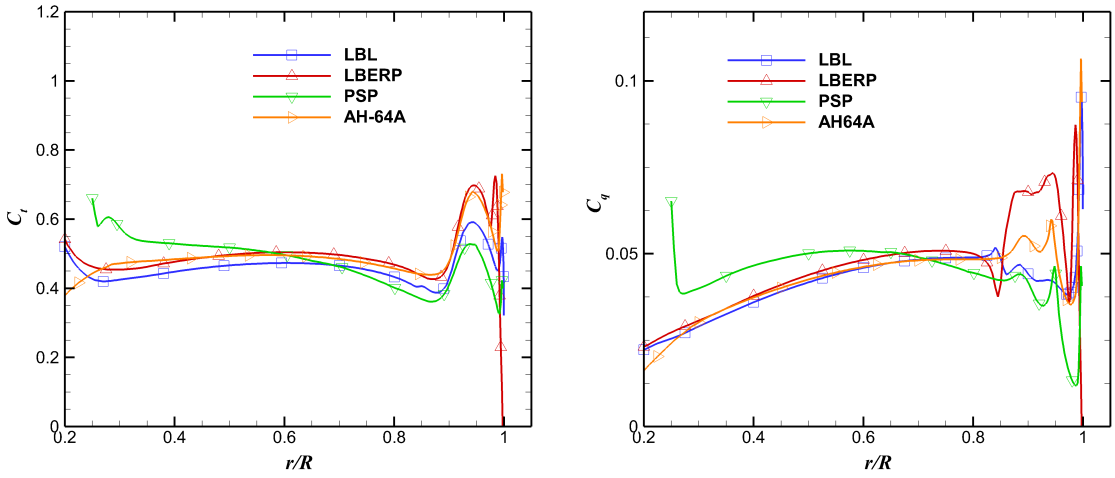

(a) Sectional thrust distribution (b) Sectional torque distribution

Figure 7.12: Comparison of the sectional load distributions at $C_T = 0.008$ for the LBL (Glasgow), LBERP (Glasgow), PSP and AH-64A blade designs.

The sectional thrust distributions indicate a similar blade loading for the four blade designs. Due to the scaling by local flow velocity, the loading at the root of the blade is augmented. The two peaks in the blade loading are due to the formation of the tip vortex as well as the effect of the preceding blade tip vortex. The peak thrust near the blade tip is the highest for the LBERP and AH-64A blades, leading to reduced hover performance. This is potentially due to the non-optimal thickness distribution across the tip of the LBERP blade and strong shock for the AH-64A blade. A certain shift in the thrust curve can be seen for the LBL blade, when

compared to the LBERP blade, due to the scaling with thrust-weighted solidity. The tip of the LBL blade is less loaded compared to the LBERP blade. The PSP rotor blade has a much more optimal loading distribution compared to the other three blades. This is primarily due to the higher blade twist of the blade (14 degrees compared to 9 degrees), as can be seen by the slope of the blade loading distribution curve. This leads to an offloading of the blade tip, and hence higher performance. The radial torque distributions show much greater differences. The LBERP blade geometry leads to a reduction in local torque at the notch, however, an increased torque is observed across the paddle type blade tip. A reduced peak is seen at the blade tip when compared to the LBL blade. The result of the aerofoil transition can also be seen for the LBL blade. A more uniformly distributed loading can once again be seen for the PSP blade. In particular, the swept blade tip leads to a significant drop in local torque. The shape of the AH-64A torque distribution is very similar to the PSP blade, due to a similar planform geometry, however, due to lower blade twist and no tip taper, the tip is more loaded with an increased torque across the blade tip. The inboard torque follows the trend of the Langley blades, as the AH-64A and Langley blades have the same blade twist. The surface pressure distributions are analysed next for the four blade designs at $C_T = 0.008$ shown in Figure 7.13.

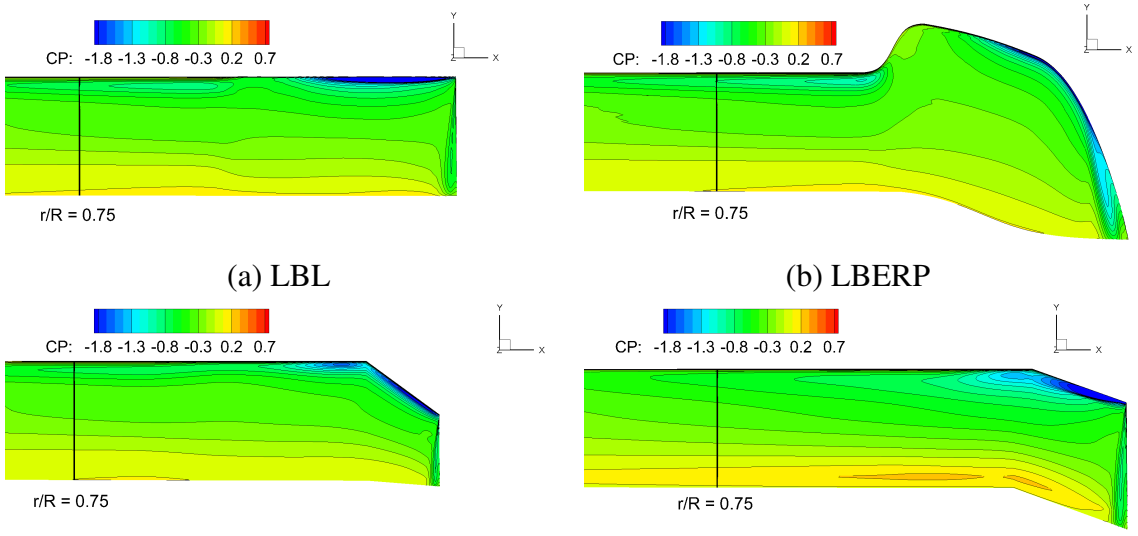

(a) LBL (b) LBERP

(c) PSP (d) AH-64A

Figure 7.13: Comparison of the surface pressure distributions at $C_T = 0.008$ for the LBL (Glasgow), LBERP (Glasgow), PSP and AH-64A blade designs.

Similar findings can be observed for the four rotor blade designs as in the analysis across a range of collectives. Comparing the four designs, the LBERP blade has a favourable pressure distribution with a high region of suction round the swept blade tip that covers a low portion of the local chord. The tip vortex roll-up, however, does not occur round the very tip of the blade, leading to a drop in performance. The AH-64A blade has a strong shock, which is stronger than for the rectangular LBL planform. However, this blade is operating at a higher blade tip Mach number and higher net thrust at $C_T = 0.008$. No shock can be seen for the PSP blade operating

at a lower blade tip Mach number compared to the other designs. The tip of the PSP blade is also offloaded leading to a much weaker effect of the tip vortex on the surface pressure distribution. The tip vortex formations are analysed next, in Figure 7.14 through contours of vorticity.

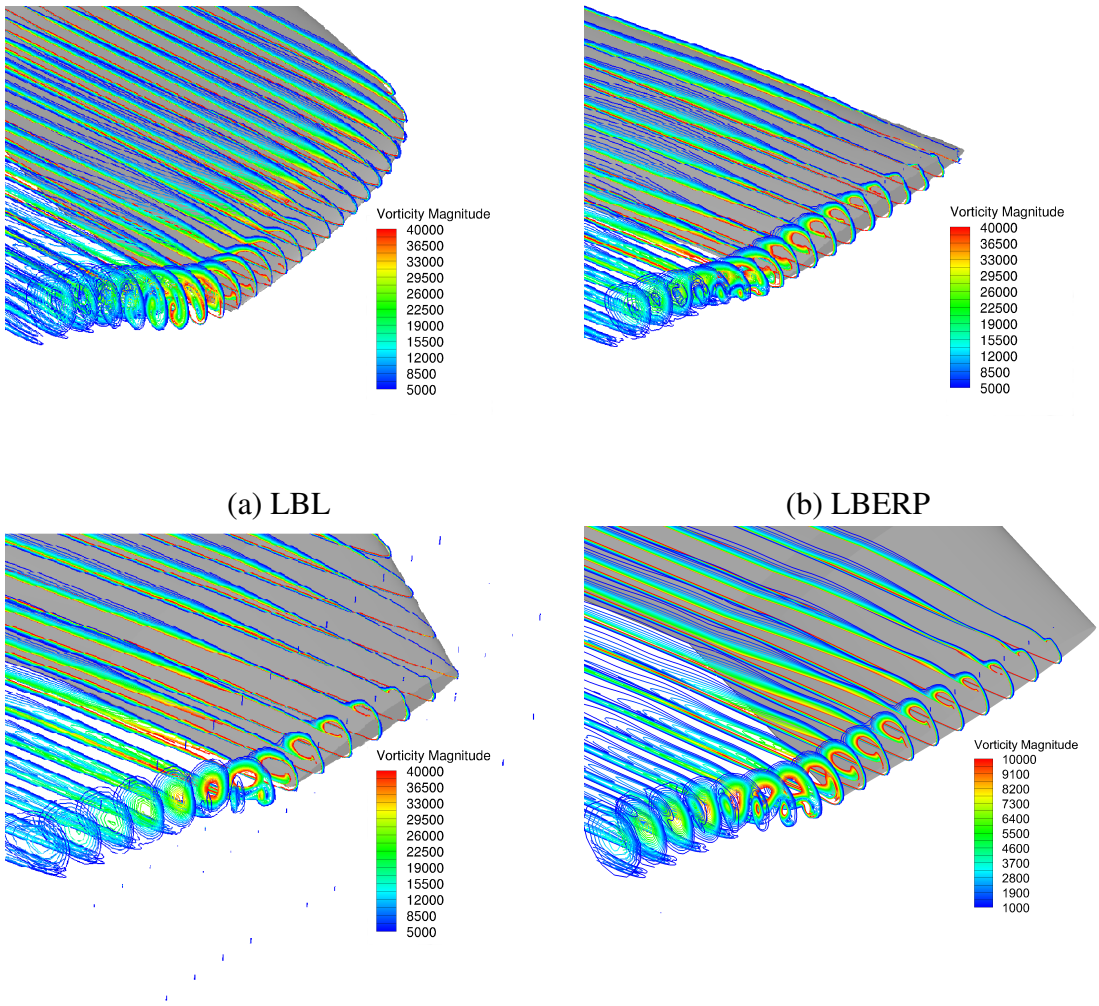

(a) LBL (b) LBERP

(c) PSP (d) AH-64A

Figure 7.14: Vortex formation comparison for the LBERP, LBL, PSP and AH-64A blade designs at $C_T = 0.008$ based on contours of vorticity.

For the LBERP blade, the onset of the tip vortex is located close to the edge of the blade tip, further inboards than for the other three blade designs. The tip vortex grows round the curved tip, moving towards the upper surface near the trailing edge of the blade. A typical vortex pair is formed from the lower and upper surfaces of the rotor blade. A strong secondary tip vortex structure (from the lower surface) is present in the main vortex core for a longer period for the LBERP blade compared to the other three blades. For the AH-64A, PSP and LBL blades, the tip vortex formation physics are similar, as the vortices form on the upper surface close to the blade leading edge. A stronger secondary vortex is seen for the AH-64A blade compared to the LBL or PSP blades. However, the vorticity is significantly lower for this blade as a full-scale blade chord is used to convert from dimensionless vorticity. Other differences in the tip vortex

formation are primarily due to planform geometry. The tip vortex for the PSP blade travels a shorter distance before separating at the blade trailing edge due to the blade tip taper (shorter distance between leading and trailing edge). The blade sweep of the PSP and AH-64A blades moves the vortex onset downstream along the chordwise direction. These features can have a significant effect on the loading at the blade tip and hence the rotor blade performance. The rotor wakes are analysed next, by comparing the wake visualisations using Q-criterion and the downwash fields at $\psi = 0^o$ shown in Figures 7.15-7.16.

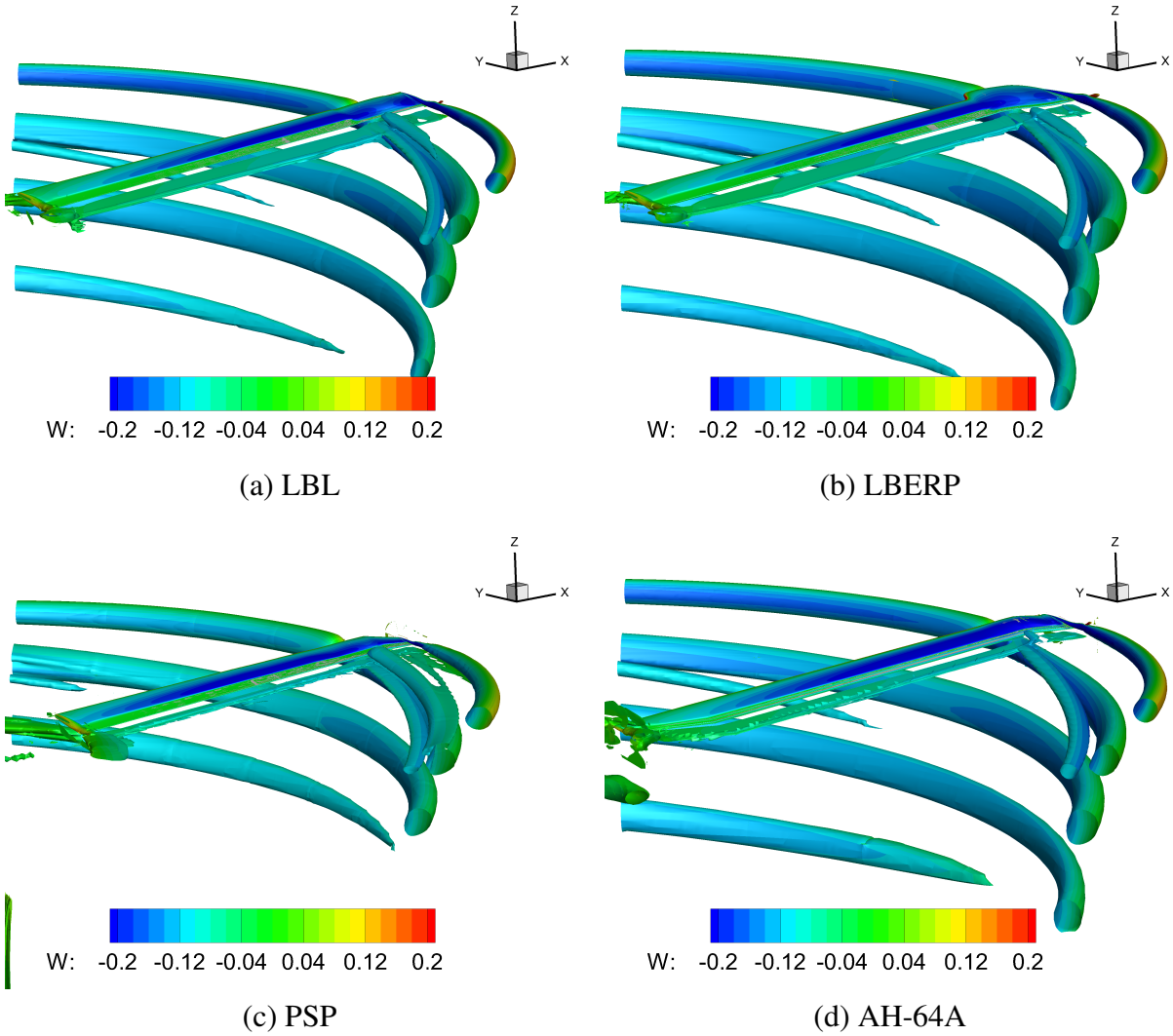

(a) LBL (b) LBERP

(c) PSP (d) AH-64A

Figure 7.15: Wake visualisation comparison for the LBERP, LBL, PSP and AH-64A blade designs at $C_T = 0.008$ based on isosurfaces of Q-criterion (value of 0.005).

The rotor wake visualisations and downwash fields indicate similar flow field structures for the four blade designs. The solutions capture four passages of the rotor blade tip vortex. A weak secondary vortical structure is also present further inboard for all for the LBL, LBERP and AH-64A designs. However, the further examination of the vorticity and velocity contours was not a clear indication of the presence of a secondary vortex at $C_T = 0.008$. The velocity

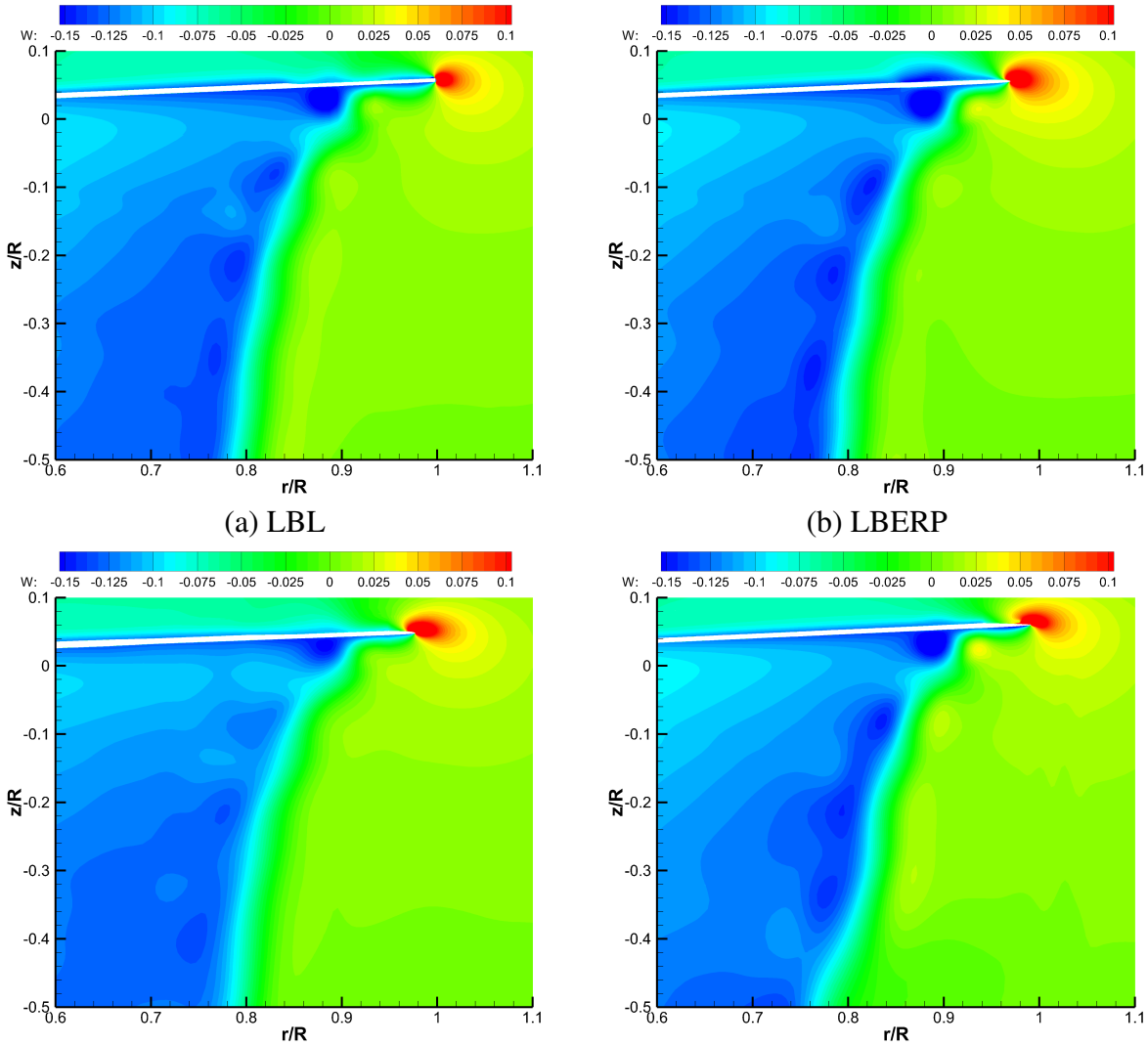

(a) LBL (b) LBERP

(c) PSP (d) AH-64A

Figure 7.16: Downwash velocity fields comparison at $\psi = 0^o$ for the LBERP, LBL, PSP and AH-64A blade designs at $C_T = 0.008$.

contours show a strong downwash on the upper surface of the blade tip, due to the interaction of the preceding tip vortex with the blade. The LBERP blade generates the tip vortex with the largest vortex core, but also a strong downwash field which is comparable to the downwash field of the AH-64A blade operating at a higher blade tip Mach number. The PSP downwash field is significantly weaker compared to the other designs, indicated by the velocity magnitude, but also a more horizontal orientation of the velocity contours.

7.3.3 Anhedral Study in Hover

The effect of anhedral is also examined, as performance improvements were shown for other blades such as the S-76 [173]. Here, we examine the performance improvements for the LBL and LBERP blades with 15 degrees parabolic anhedral at a single collective of 10.5 degrees. The

anhedral was initiated at 0.945R, where the raked tip begins for the Langley BERP blade. The grids for these blades were generated from the initial blade grids using a deformation method based on inverse distance weighting. The effect of anhedral on the rotor performance for the LBL and LBERP blades is shown in Table 7.6.

Table 7.6: Hover performance of standard LBERP and LBL blades, and blades with 15 degrees parabolic anhedral.

Blade	C_T	C_Q	*FoM*	**FoM %**
LBL	0.00885	0.000880	0.6702	-
LBERP	0.00882	0.000934	0.6276	-
LBL (anh)	0.00891	0.000849	0.6997	+4.4%
LBERP (anh)	0.00888	0.000883	0.6698	+6.7%

The tip anhedral increases the hover performance for both blades. For the LBL blade, a performance improvement of approximately 3 counts in FoM is achieved, whereas the LBERP blade sees an increase of over 4 counts. Therefore, it can be stated that blade anhedral is more beneficial for the LBERP geometry than the LBL blade. This is due to the fact that anhedral generally benefits highly loaded rotor blades, and the BERP-like geometry generates a stronger downwash field in the blade tip region compared to a rectangular blade. Similar observations were made by Brocklehurst and Barakos [64] in a review of helicopter blade tip shapes. The LBERP blade with 15 degrees achieved a similar FoM as for the standard LBL blade. The performance improvement due to anhedral, comes from a small increase in thrust and torque reduction. No experimental data exists to validate these results, however, the benefit of blade anhedral is also seen for the S-76 rotor blade [32]. To examine the sources of the beneficial action of anhedral, the surface pressure distributions and sectional loads are compared. The surface pressure distributions for the LBERP and LBL blades with and without anhedral are shown in Figure 7.17. The pressure coefficient is normalised by local flow velocity. The anhedral redistributes the loading along the blade leading to an offloading of the blade tip and higher loading inboard. This leads to a more optimal induced lift distribution and reduced overall torque. In fact, the blade anhedral acts similarly as an additional negative twist on the blade loading distribution. The differences in blade loading for the blades with and without anhedral are noticeably lower for the LBL blade. The aerofoil transition region can also be clearly seen in the surface pressure distributions, where the pressure iso-lines spread out. For the LBERP blade, a reduced suction at the blade tip can be observed (caused by the formation of the tip vortex). The suction, however, is increased in the blade notch region. This is highlighted further through the sectional load distributions, in Figure 7.18. The loads are normalised by local flow velocity and the reference blade chord taken as the chord of the first aerodynamic section.

The observations from the surface pressure distributions are confirmed by the sectional load distributions. The anhedral has a similar effect on the rotor thrust distributions, where a larger

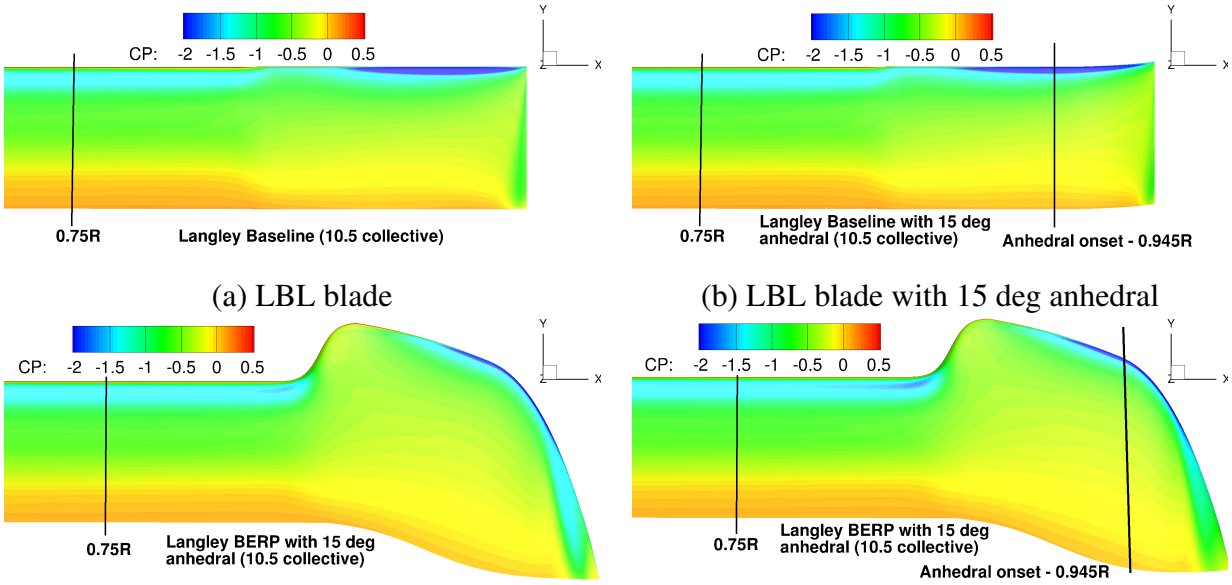

(a) LBL blade

(b) LBL blade with 15 deg anhedral

(c) LBERP blade

(d) LBERP blade with 15 deg anhedral

Figure 7.17: Comparison of the surface pressure distributions (normalised by local flow velocity) for the LBL and LBERP blades in hover with and without anhedral.

amount of thrust is generated inboard. The benefit of anhedral mainly comes from a reduction in torque at the blade tip, which is seen for both blades. For the LBERP tip, the largest reduction can be seen across the paddle-like blade tip, as well as at the very end of the tip where the tip vortex forms. For the LBL blade, the torque is reduced past the aerofoil transition region.

To investigate the differences in blade loading, the vertical tip vortex displacements are extracted from the solutions and are shown in Figure 7.19.

The vertical tip vortex displacements indicate that for the blades with anhedral, so called "vortex snaking" occurs, as the tip vortex initially moves upwards back towards the rotor disk in the initial wake ages before displacing downwards. This is due to the formation of much weaker tip vortices when compared to blades without anhedral. This behaviour was also observed by Brocklehurst and Barakos [64]. The typical change in the gradient of vortex descent is seen as the vortex passes the next blade at 90 degrees azimuth. The vertical miss distance is marginally higher for the blades with anhedral, however, this effect is not seen to be significant. In the later wake ages, the vortex displacement is similar for all blades, except for the LBL blade without anhedral which displaces at a slower rate. At this collective, the LBL blade produces a weaker downwash field near the blade tip compared to the LBERP blade. This also leads to a reduced effect on the tip vortex vertical displacements due to the introduction of anhedral. The vortex strength due to the introduction of anhedral is examined next and is shown in Figure 7.20.

For both blade designs, the addition of anhedral leads to a weaker tip vortex. The rotor blades were not trimmed to the same thrust coefficient, however, the values in Table 7.6 indicate a minor increase in thrust with the addition of anhedral. The LBERP blade generates a weaker blade tip vortex at this collective, despite operating at a higher thrust coefficient. The vortex radius before

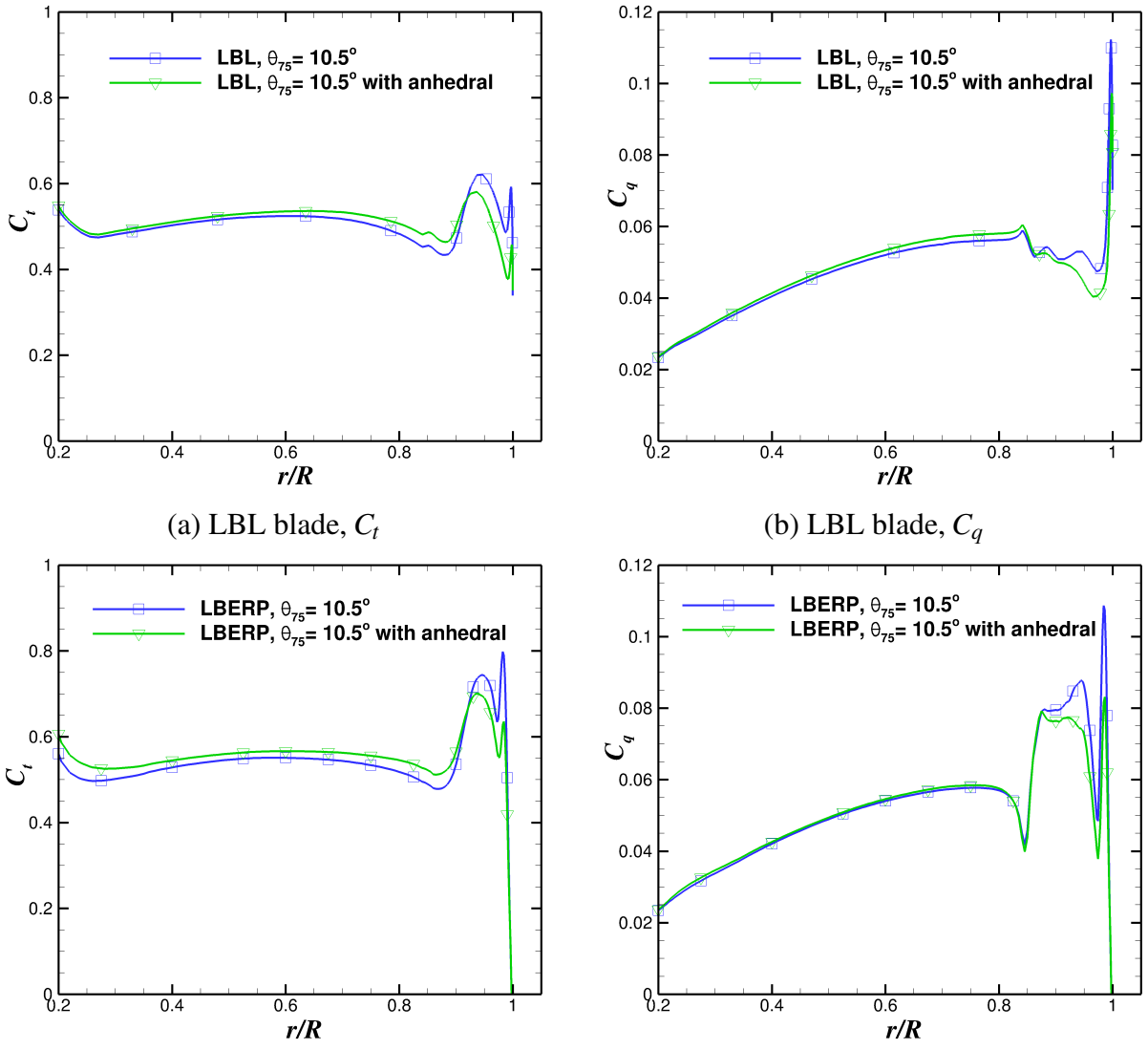

(a) LBL blade, C_t

(b) LBL blade, C_q

(c) LBERP blade, C_t

(d) LBERP blade, C_q

Figure 7.18: Comparison of sectional thrust and torque distributions for the LBL and LBERP blades in hover with and without anhedral.

interacting with the next blade is also clearly larger for the LBERP blade when compared to the LBL blade. Based on these observations, it can be seen that the LBERP tip vortex aerodynamics are favourable compared to the LBL blade, due to reduced interaction of the blade with the preceding blade tip vortices. The addition of anhedral further offloads the blade tip. The effects of anhedral also show that advanced planforms require careful computational optimisation. This is due to the strong sensitivity of the blade performance on geometric features such as anhedral, as shown for the LBL and BERP blades.

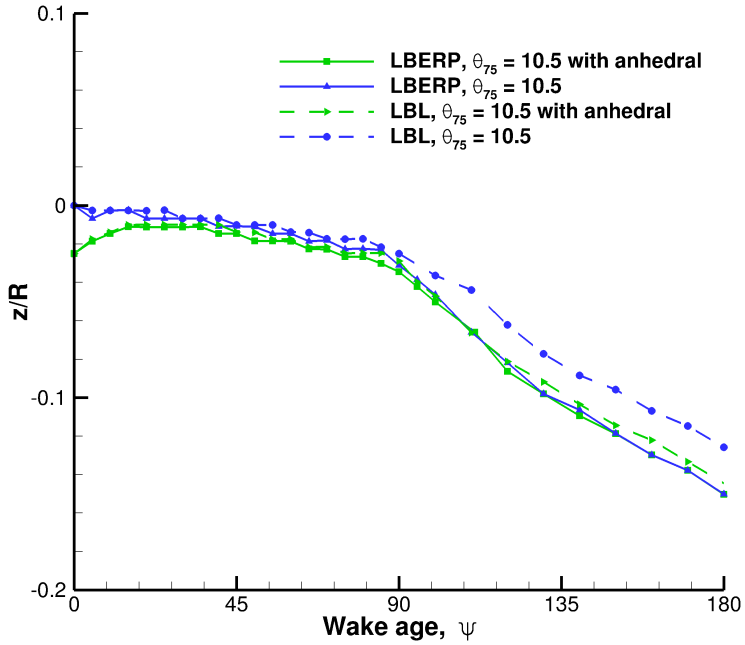

Figure 7.19: Comparison of the tip vertical vortex displacements for the LBL and LBERP blades in hover with and without anhedral.

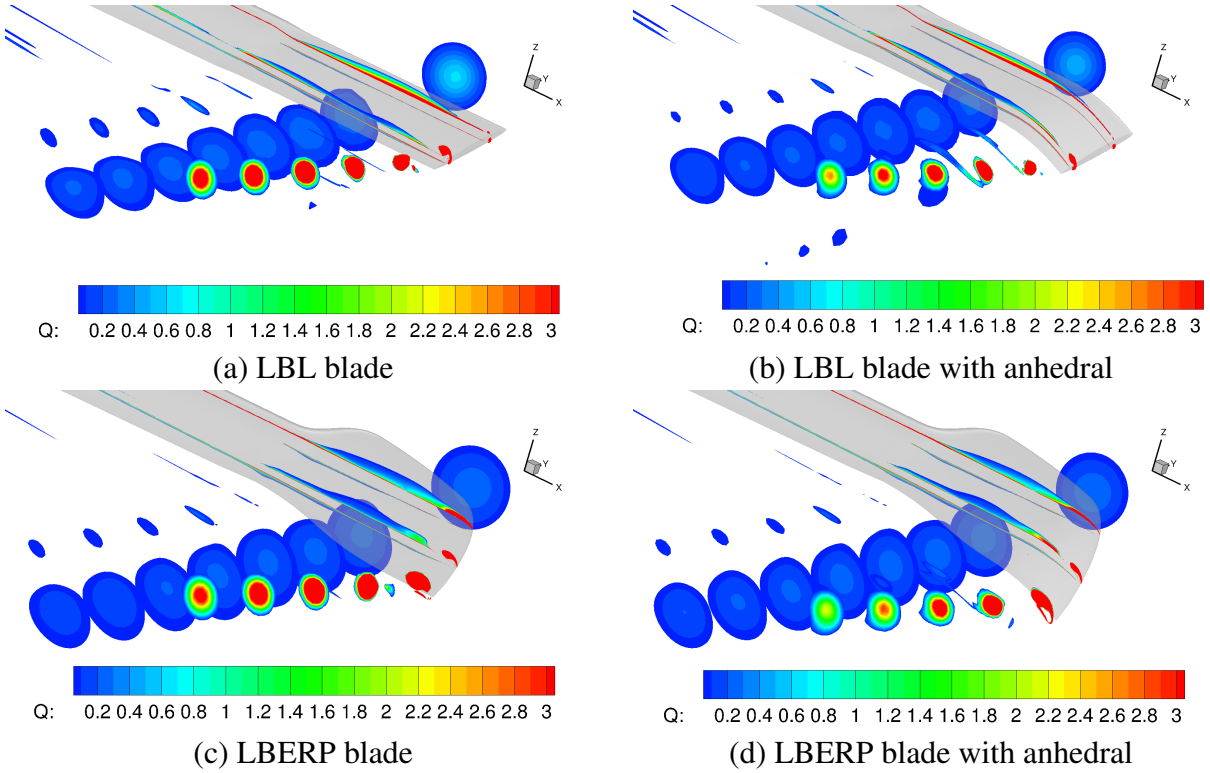

(a) LBL blade

(b) LBL blade with anhedral

(c) LBERP blade

(d) LBERP blade with anhedral

Figure 7.20: Comparison of vortex strength for the Langley blades with and without anhedral as indicated by a Q-criterion contour at various azimuthal locations. A cutoff below Q=0.02 is applied.

7.4 Analysis of Different Rotor Designs in Forward Flight

The four rotor blade designs are also compared in forward flight. Firstly, a qualitative analysis is performed across a range of advance ratios with a focus on the evolution of rotor disk loads and wake geometry with increasing flight speed for different designs. A more detailed analysis is performed at the same condition: $\mu = 0.4$, $C_T = 0.0081$ for the LBERP, LBL and PSP blades. The AH-64A blade is analysed in detail separately at $\mu = 0.3$, $C_T = 0.00903$ as it was selected for the optimisation process in Chapter 9.

7.4.1 Comparisons over a range of advance ratios

Firstly, the four designs are compared in terms of disk loads across different advance ratios, shown in Figures 7.21-7.24. The loads are scaled by a reference chord equal to the chord of the first aerodynamic section. The M^2C_L and M^2C_D represent force values normal and tangential directions (non-radial) to the rotor disk plane representing the local lift and drag values uncorrected for downwash effects (hence, thrust and torque/(local radius)).

The four rotor blade designs indicate similar trends in the disk loading with increasing advance ratio. At low advance ratio, the high lift regions are located at the back of the rotor disk and the retreating side. As the flight speed increases, the retreating side loading reduces, and the front of the rotor disk carries a larger portion of the lifting load. At high advance ratio (above $\mu = 0.35$), a region of negative lift force forms on the advancing side, seen for the LBL, LBERP and PSP rotor blades with the magnitude being highest for the PSP blade due to higher blade twist when compared to the other designs. The pitching moment loading is also similar for the different rotor designs. An increase in negative nose-down pitching moment is seen for all of the designs as the blade moves from the advancing side to the front of the rotor disk and with a positive nose-up pitching moment at the back of the rotor disk. The magnitudes of these high nose-down and nose-up pitching moment regions increase with increasing advance ratio. A region of increased nose-down pitching moment is also seen on the retreating side for the AH-64A blade due to dynamic stall present at the examined condition,($\mu = 0.3$, $C_T = 0.00903$), which is operating at a higher thrust than for the other examined designs. The in-plane drag force distributions show a region of high in-plane force at the back of the rotor disk at a low advance ratio, which propagates to the retreating side and front of the rotor disk with increasing advance ratio. In general, the loading trends are similar for the four blade designs, with the planform geometry having a more localised effect on the loads. These localised effects are analysed further in the next subsection where the designs are compared at $C_T = 0.0081$, $\mu = 0.4$. The similarity of the disk loads across different rotor designs is also dictated by similar wake visualisation features, as shown in Figures 7.25-7.27.

The wake geometries are similar for all four rotor blade designs and are more sensitive to flight condition than planform geometry. At low advance ratio, the preceding blade tip vortices

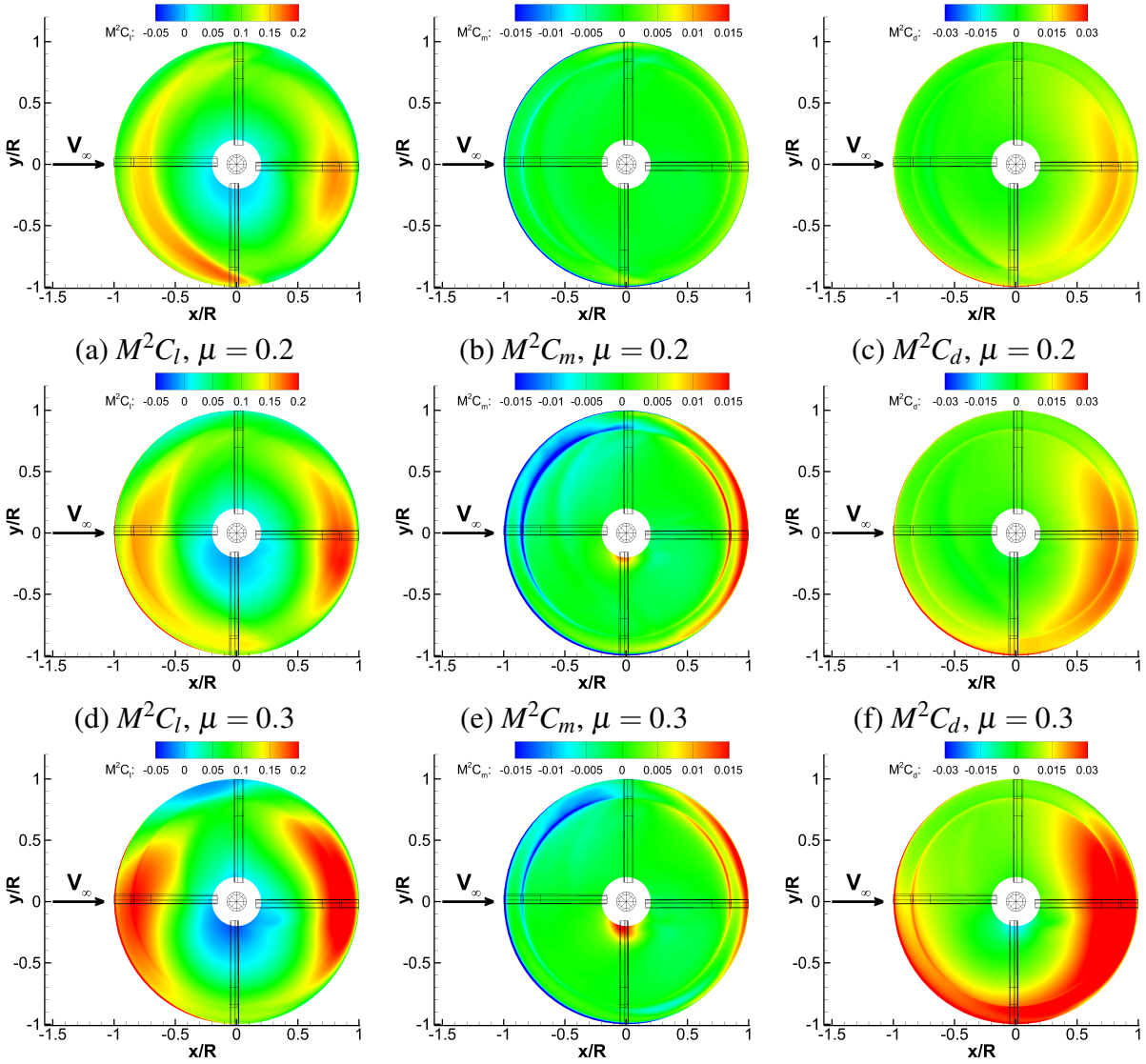

(a) M^2C_l, $\mu = 0.2$ (b) M^2C_m, $\mu = 0.2$ (c) M^2C_d, $\mu = 0.2$

(d) M^2C_l, $\mu = 0.3$ (e) M^2C_m, $\mu = 0.3$ (f) M^2C_d, $\mu = 0.3$

(g) M^2C_l, $\mu = 0.4$ (h) M^2C_m, $\mu = 0.4$ (i) M^2C_d, $\mu = 0.4$

Figure 7.21: Rotor disk loads in forward flight for the LBL rotor blade at $C_T = 0.0081$ and three advance ratios.

are entrained into two supervortices which form at each side of the rotor disk. A greater amount of blade vortex interactions can also be seen at low advance ratios. At a moderate advance ratio, the supervortices become weaker. The key feature at $\mu = 0.3$ for all blade designs is the blade vortex interaction on the retreating side with the vortex from the blade at the back of the rotor disk. This leads to a dynamic stall for the AH-64A blade operating at a higher thrust coefficient when compared to the other blades. This is typical of the highly loaded, moderate advance ratio flight condition. As the advance ratio increases further, this interaction no longer occurs at the blade tip vortex from the back of the rotor disk, does not reach the retreating blade, due to a greater mean flow velocity. At the highest advance ratio, the individual vortices are recognisable in the rotor wake and no supervortices form. The different blade designs can be seen to have an impact on the strength of the blade tip vortices and secondary structures present in the rotor

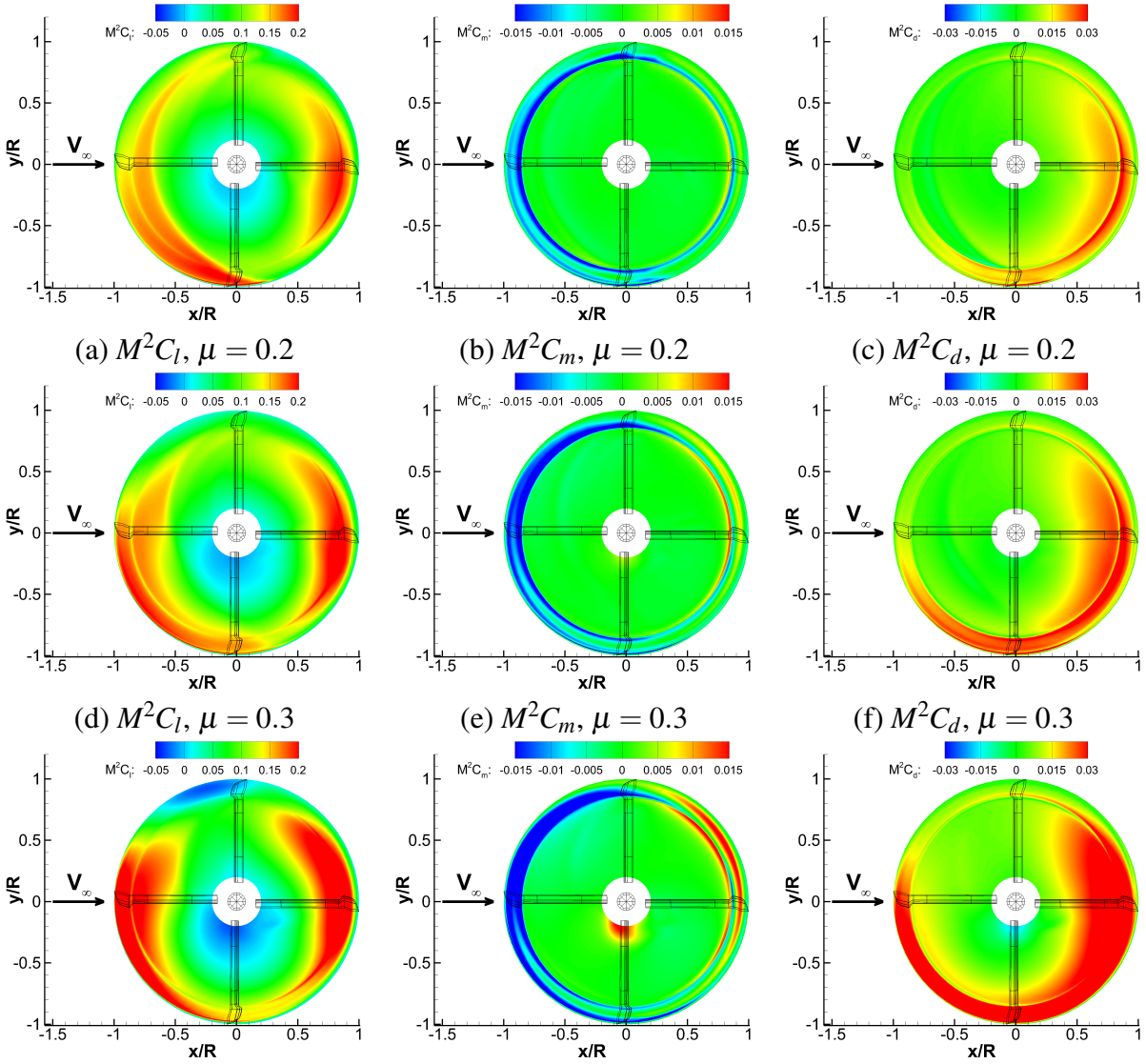

(a) M^2C_l, $\mu = 0.2$ (b) M^2C_m, $\mu = 0.2$ (c) M^2C_d, $\mu = 0.2$

(d) M^2C_l, $\mu = 0.3$ (e) M^2C_m, $\mu = 0.3$ (f) M^2C_d, $\mu = 0.3$

(g) M^2C_l, $\mu = 0.4$ (h) M^2C_m, $\mu = 0.4$ (i) M^2C_d, $\mu = 0.4$

Figure 7.22: Rotor disk loads in forward flight for the LBERP rotor blade at $C_T = 0.0081$ and three advance ratios.

wake. The vortex core from the back of the rotor disk is clearly larger for the LBERP blade than the LBL blade. Secondary vortical structures are present in the wake of the LBL blade geometry, due to sharp aerofoil transition or the presence of the notch feature for the LBERP blade. The PSP and AH-64A flowfields show no secondary structures in the rotor wakes. Finally, the downwash velocity magnitudes cannot be directly compared between different designs, as the downwash velocity is based on the reference free-stream velocity magnitude. To analyse the designs further, comparisons are attempted at a constant thrust coefficient and advance ratio, aimed at examining the effect of planform shape in greater detail.

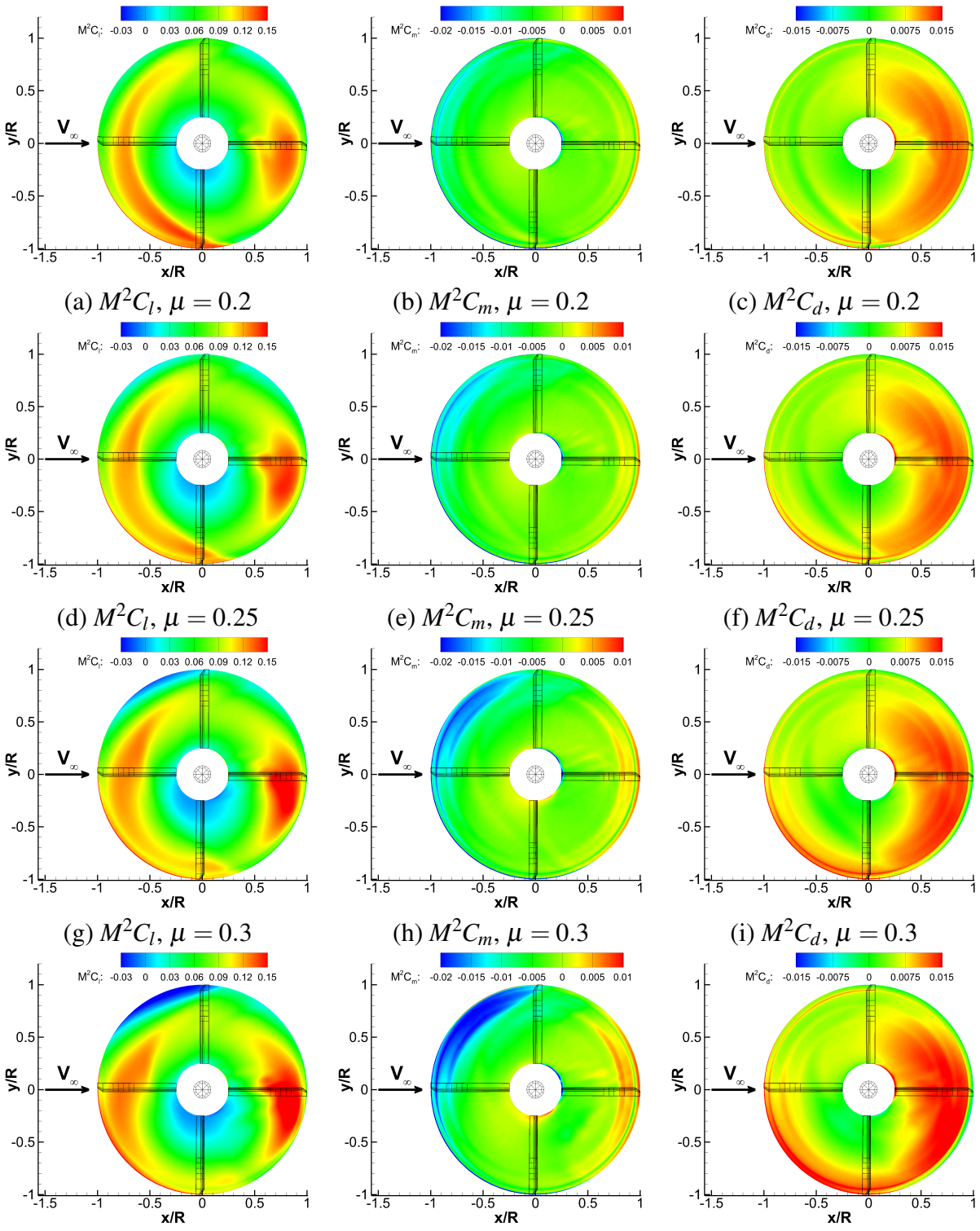

(a) M^2C_l, $\mu = 0.2$ (b) M^2C_m, $\mu = 0.2$ (c) M^2C_d, $\mu = 0.2$

(d) M^2C_l, $\mu = 0.25$ (e) M^2C_m, $\mu = 0.25$ (f) M^2C_d, $\mu = 0.25$

(g) M^2C_l, $\mu = 0.3$ (h) M^2C_m, $\mu = 0.3$ (i) M^2C_d, $\mu = 0.3$

(j) M^2C_l, $\mu = 0.35$ (k) M^2C_m, $\mu = 0.35$ (l) M^2C_d, $\mu = 0.35$

Figure 7.23: Rotor disk loads in forward flight for the PSP rotor blade at $C_T = 0.0083$ and four advance ratios.

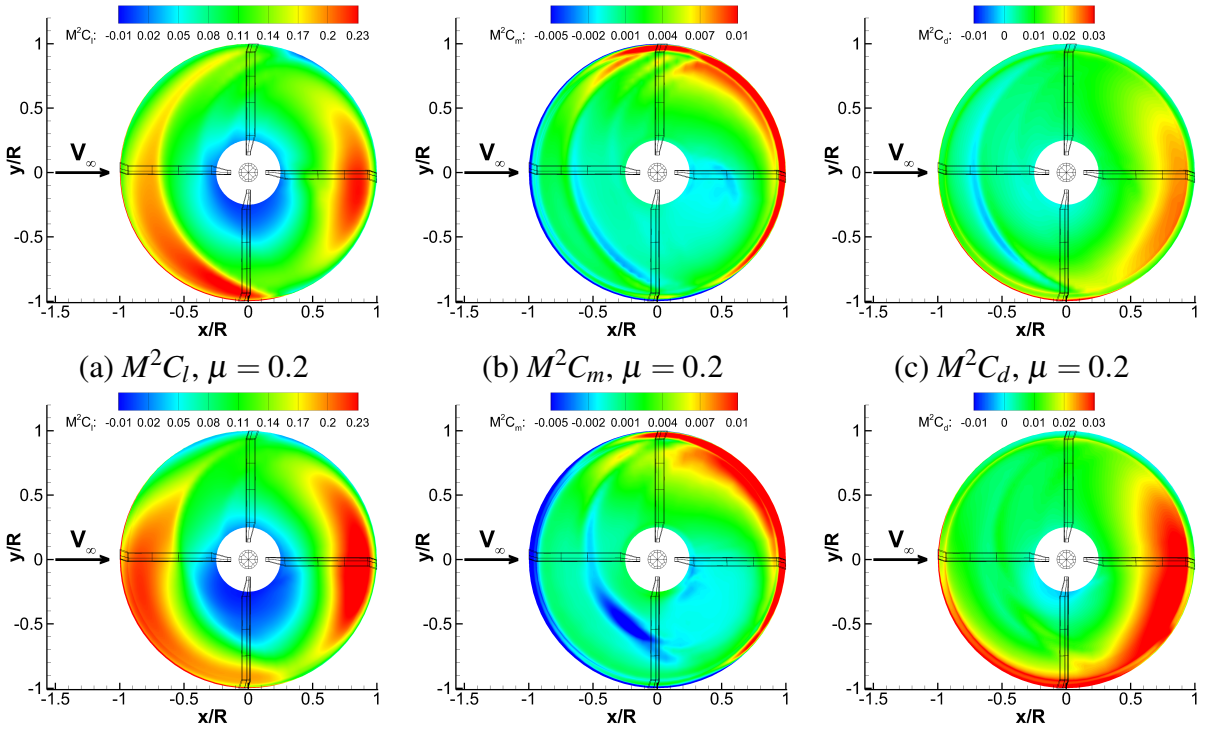

(a) M^2C_l, $\mu = 0.2$ (b) M^2C_m, $\mu = 0.2$ (c) M^2C_d, $\mu = 0.2$

(d) M^2C_l, $\mu = 0.3$ (e) M^2C_m, $\mu = 0.3$ (f) M^2C_d, $\mu = 0.3$

Figure 7.24: Rotor disk loads in forward flight for the AH-64A rotor blade at $C_T = 0.0093$ and two advance ratios.

7.4.2 Comparisons at a Constant Thrust Coefficient

A detailed comparison of the different rotor designs is performed at $C_T = 0.0081$, $\mu = 0.4$ for the LBL, LBERP and PSP blades. The AH-64A blade is analysed further in the next subsection, based on the baseline optimisation condition. The comparisons are primarily conducted in a qualitative manner due to different blade tip Mach numbers and radii, leading different net thrusts produced by each blade at a constant thrust coefficient. Firstly, the trim states are examined, shown in Table 7.7.

Table 7.7: Forward flight trim states for the LBL, LBERP and PSP blades at $C_T = 0.0081$, $\mu = 0.4$. Note, negative Fourier series used.

Blade	α_s	θ_0	θ_{1s}	θ_{1c}
LBL	-7.449	12.535	10.437	-4.022
LBERP	-7.449	12.920	10.891	-4.229
PSP	-6.0	11.124	9.229	-3.336

The trim states indicate lower collective and longitudinal cyclic angles for the PSP rotor blade when compared to the Langley blades. This is due to the fact that this rotor produces a lower net thrust for a given thrust coefficient (due to a lower blade tip Mach number). The matching of thrust-weighted solidity, which led to an increase in 9% chord for the LBL blade,

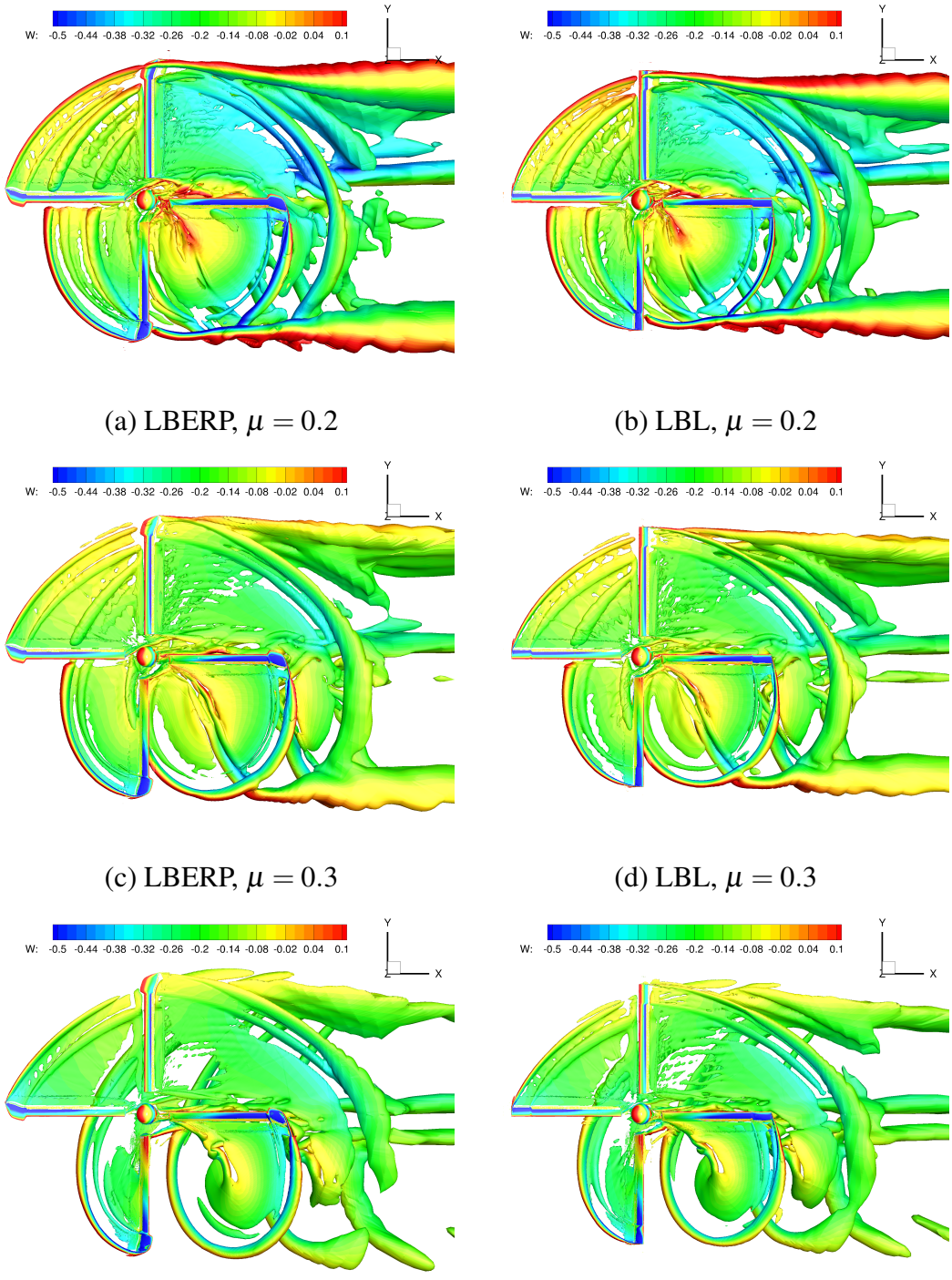

(a) LBERP, $\mu = 0.2$

(b) LBL, $\mu = 0.2$

(c) LBERP, $\mu = 0.3$

(d) LBL, $\mu = 0.3$

(e) LBERP, $\mu = 0.4$

(f) LBL, $\mu = 0.4$

Figure 7.25: Rotor wake visualization for LBL and LBERP rotor blades in forward flight at three advance ratios using an isosurface of Q-criterion (value of 0.002) coloured by downwash velocity W.

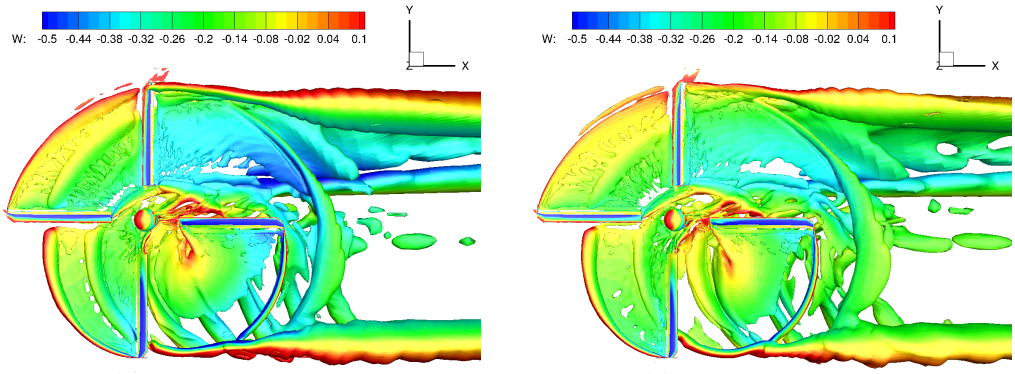

(a) $\mu = 0.2$ (b) $\mu = 0.25$

(c) $\mu = 0.3$ (d) $\mu = 0.35$

Figure 7.26: Rotor wake visualization for PSP rotor blade in forward flight at four advance ratios using an isosurface of Q-criterion (value of 0.002) coloured by downwash velocity W.

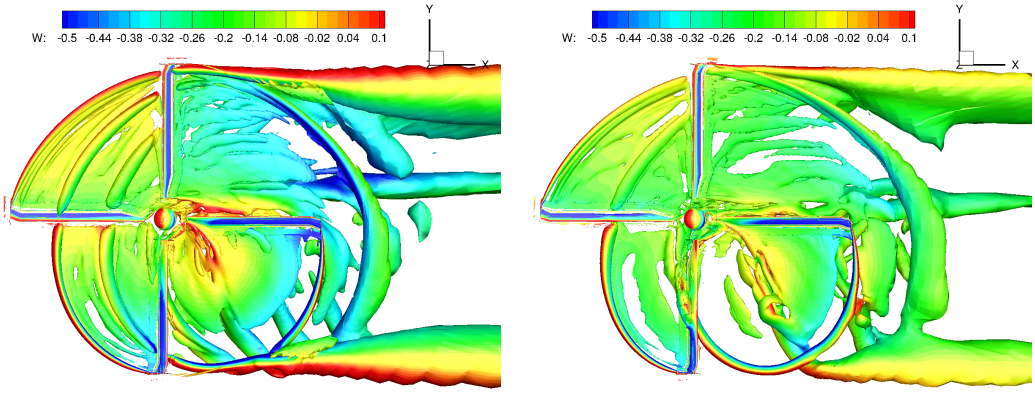

(a) $\mu = 0.2$ (b) $\mu = 0.3$

Figure 7.27: Rotor wake visualization for AH-64A rotor blade in forward flight at $C_T = 0.00903$ and two advance ratios using an isosurface of Q-criterion (value of 0.002) coloured by downwash velocity W.

leads to a slightly lower collective and longitudinal cyclic compared to the LBERP blade. The shaft, flapping and coning angles are prescribed.

The rotor disk blade loads are extracted for the three blade designs and shown in Figure 7.28. Note that the PSP blade loads are shown on a different scale compared to the Langley blades. All loads are scaled by the reference blade chord (equal to the chord of the first aerodynamic section), and the pitching moments are taken about the local quarter chord location (chord taken as normal to pitch axis).

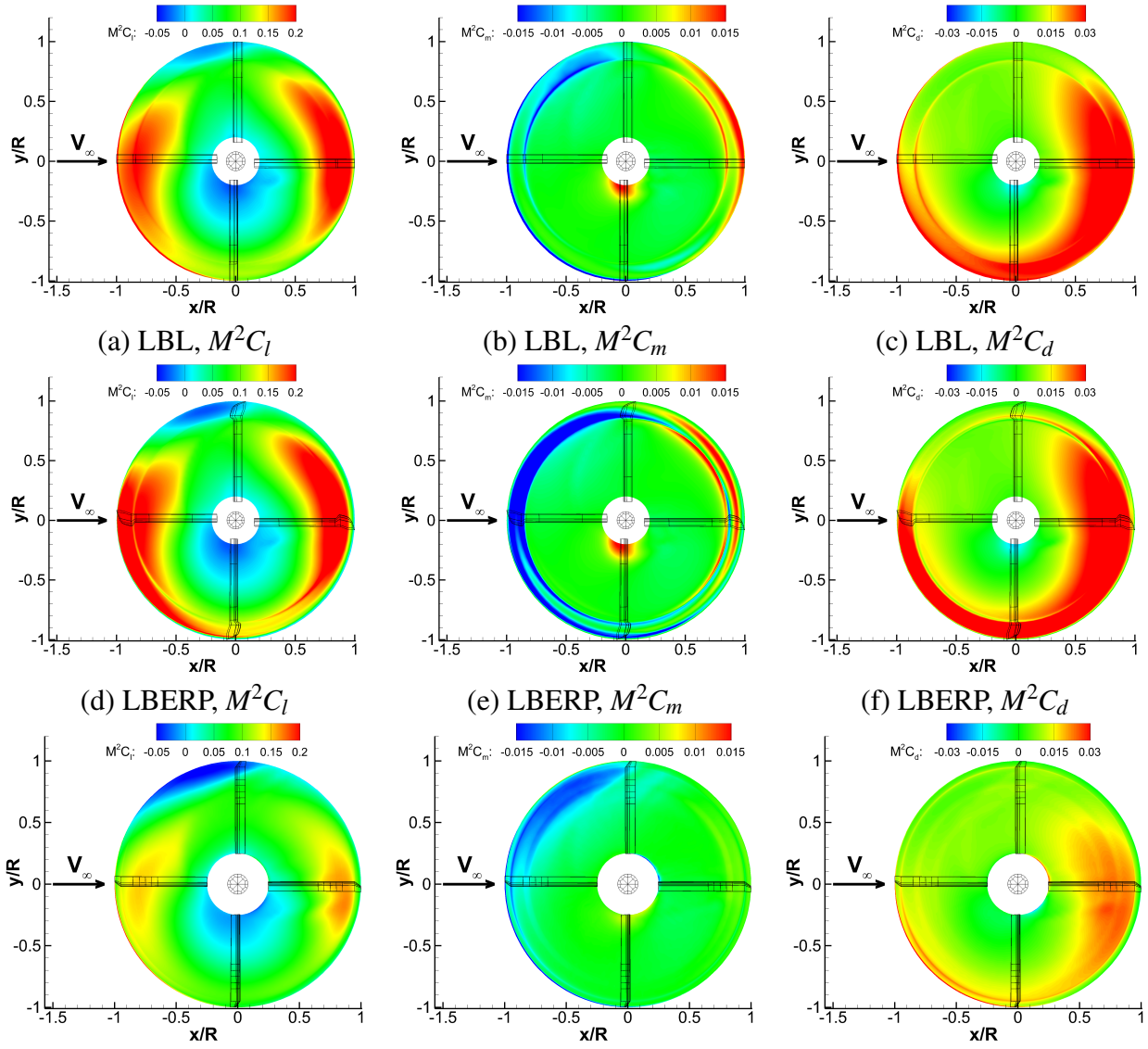

(a) LBL, M^2C_l (b) LBL, M^2C_m (c) LBL, M^2C_d

(d) LBERP, M^2C_l (e) LBERP, M^2C_m (f) LBERP, M^2C_d

(g) PSP, M^2C_l (h) PSP, M^2C_m (i) PSP, M^2C_d

Figure 7.28: Rotor disk blade load distributions for LBERP, LBL and PSP blades at $C_T = 0.0081, \mu = 0.4$. All loads are scaled by the reference blade chord, equal to the chord of the first aerodynamic section.

Figure 7.28 indicates fairly similar load distributions for the three blade designs, as shown in the disk loads analysis across different advance ratios. At the same thrust coefficient and advance ratio, the disk loads can still only be compared qualitatively, due to different blade tip Mach numbers and net thrusts produced by the three blade designs. The magnitudes of the disk loads are significantly lower for the PSP blade due to lower blade tip Mach number. The LBERP and LBL blades can be compared in greater detail, however, the matching of thrust weighted solidity will also impact the comparison. The normal force distributions indicate that the LBERP blade, provides a higher lifting force at the front of the rotor disk and on the retreating blade, when compared to the LBL blade, which is not surprising due to the tip shape (larger chord). At the back of the disk, high loading is seen across the paddle blade tip which reduces towards the very tip of the blade, leading to a more offloaded blade tip (last 5%R) when compared to the LBL blade. On the advancing blade, a slightly larger region of negative thrust can be seen. The extent of this region is significantly increased for the PSP rotor blade. This is predominantly, due to the higher twist of this rotor blade, leading to operation of the local aerofoil section in this region at higher negative angles of incidence. The LBERP planform leads to a greater negative pitching moment as the blade moves from the advancing side to the front of the rotor disk, when compared to the simpler LBL or PSP planforms. A much greater pitching moment variation can be seen for the LBERP blade compared to the other designs. This variation indicates, blade structural untwisting across the blade tip at the advancing side and increased twisting on the retreating side. This could have positive effects on the rotor performance, however, as the blade is modelled as rigid, structural deformations are not taken into account. The in-plane force distributions highlight the effect of the LBERP tip geometry, leading to a significantly higher in-plane force across the blade tip when compared to the LBL blade, which is especially visible at the front of the rotor disk. The planform geometry features, such as the sharp aerofoil transition of the LBL blade, the notch feature of the LBERP geometry and the sweep initiation of the PSP blade, also lead to certain discontinuities in the rotor disk loads, in particular, localised pitching moments. Based on the blade load distributions, it can be stated, that aeroelastic deflections will be important for simulation of advanced planforms, as a much larger variation of pitching moments is seen across the rotor blade tip, leading to much more significant elastic blade twist deformations. The blade loads are compared quantitatively for the LBL and LBERP blades, by extracting the azimuthal loads at r/R = 0.75, 0.9 and 0.975 which is shown in Figure 7.29.

As expected, at the r/R=0.75 radial station, the loads for the LBERP and LBL blades are very similar, as the shape of the planform and aerofoil sections are the same. The effect of the notch can be seen at this station in the slightly higher lift and in-plane forces at the front and back of the rotor disk. At the r/R=0.9 radial station, the LBERP blade starts to lift more at the back of the disk at the expense of high nose-down pitching moment on the advancing blade side and higher in-plane force at the back of the rotor disk. A higher in-plane force is also encountered on the retreating blade. At r/R=0.975 the LBERP blade obtains much higher lift force can be seen at

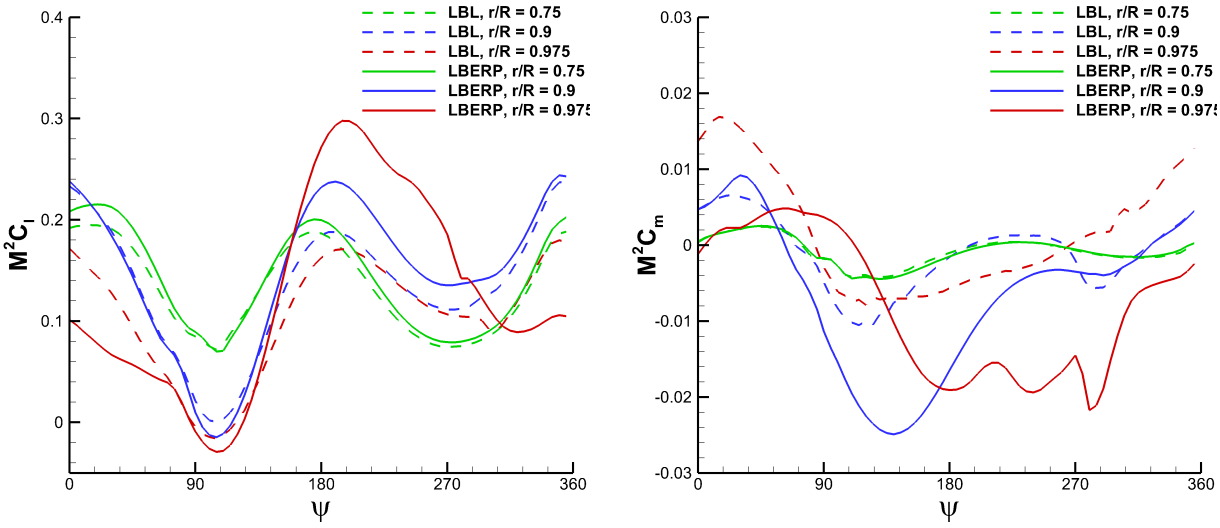

(a) M^2C_N (b) M^2C_M

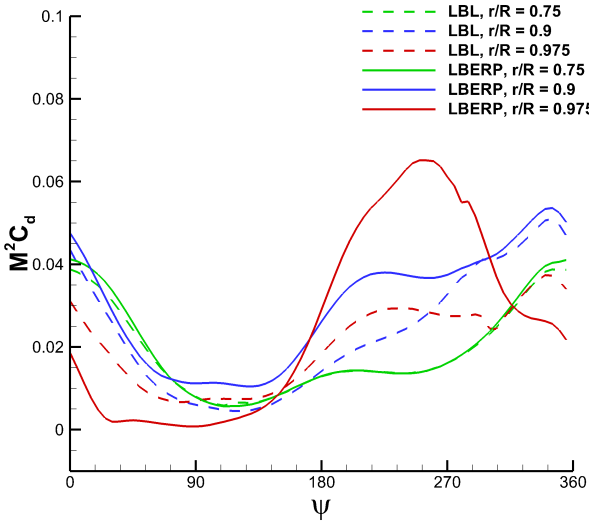

(c) M^2C_D

Figure 7.29: Comparison of the azimuthal loads at three radial stations for the LBL and LBERP blades at $C_T = 0.0081, \mu = 0.4$.

the back of the disk, leading a significantly higher in-plane force, however, on the retreating side a loss of lift is encountered, leading to a normal force and chordwise force reduction at the front of the disk. A certain level of oscillations exists in the pitching moment curve at r/R = 0.975 for the LBERP blade.

The advancing and retreating blade sides are examined in more detail for all three blade designs. The surface pressure coefficient distributions at 90^o azimuth along with the flow field streamlines and Mach number contours at r/R = 0.82 can be seen in Figure 7.30.

The surface pressure solutions on the advancing blades indicate strong shocks for both the LBERP and LBL blades. The notch geometry prevents the shock from propagating onto the blade tip surface through a reduction in the thickness/chord ratio. However, it can be seen that for the rectangular LBL blade, the shock also stops at a similar radial location. This is the

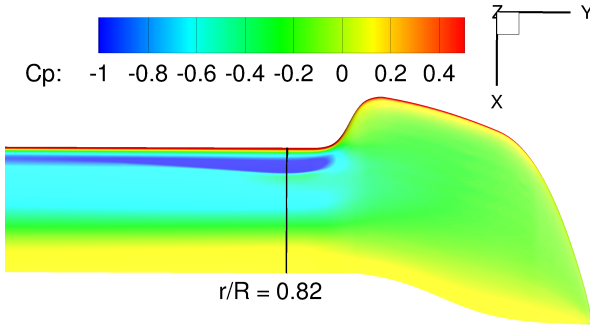

(a) LBERP, C_P distribution

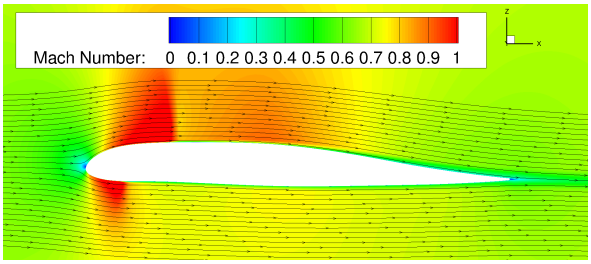

(b) LBERP, Mach contours

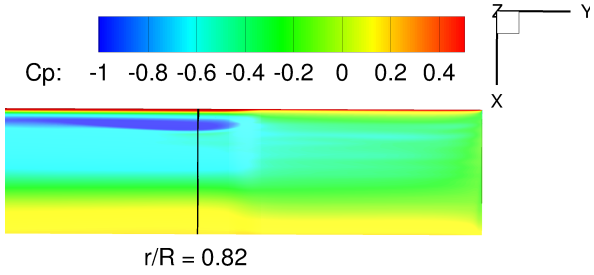

(c) LBL, C_P distribution

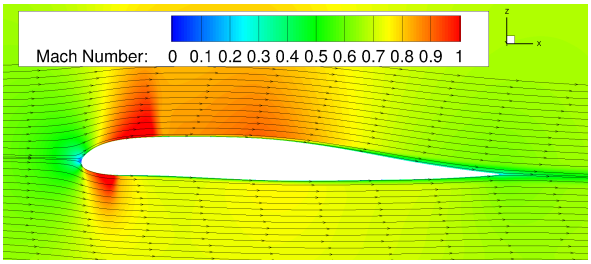

(d) LBL, Mach contours

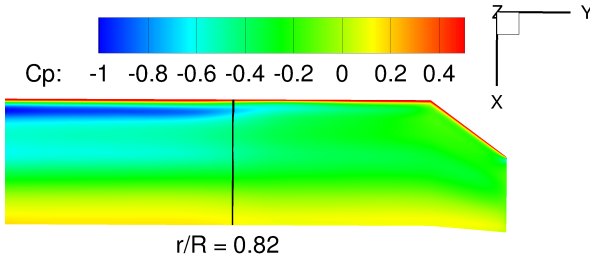

(e) PSP, C_P distribution

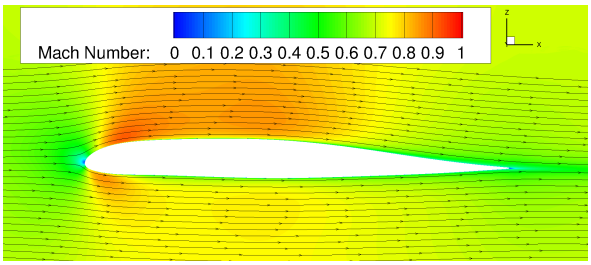

(f) PSP, Mach contours

Figure 7.30: Advancing side pressure distributions and flow field streamlines along with contours of Mach number at r/R = 0.82 for the LBERP, LBL and PSP rotor blades at $\mu = 0.4$, $C_T = 0.0081$.

position of the aerofoil transition (r/R=0.84-r/R=0.866). Another geometric design feature that may have a significant effect on the dissipation of the shock is the sudden change in the gradient of the blade twist curve. The twist is constant across both the LBL and LBERP blade tips, which generates an aerodynamic discontinuity at r/R = 0.866. Based on these observations, it is not surprising that both blades show similar values of normal and chordwise forces on the advancing blade side. The strong nose-down pitching moment for the LBERP blade, however, could give rise to significant pitch-link loads. The addition of blade anhedral could potentially reduce these strong pitching moment variations, due to reduced loading at the blade tip. The PSP blade surface pressure distribution indicates, that the region of high suction is reduced more gradually, as a shock does not form. This is expected due to the lower blade tip Mach number compared to

the other two blades. The Mach number contours show a larger chordwise extent of supersonic flow for the LBERP blade compared to the LBL design. The primary reason for this is associated with the stronger downwash field near the blade tip for the LBERP blade. A weaker shock also forms on the blade lower surface for both Langley blade designs. No evidence of shock-induced separation is seen on the blade upper surface for either blade design, with a small recirculation bubble present on the blade lower surface for the LBL and LBERP blades. The C_L values are close to zero for both blades due to the low local incidence of the aerofoil section. The PSP Mach contours only indicate the presence of the compression on both upper and lower surface, without the presence of a distinct shock, which is due to the lower blade tip Mach number. The retreating side flow physics are also examined in more detail. The surface pressure and skin friction coefficient distributions along with skin friction lines near the blade tip are shown in Figure 7.31.

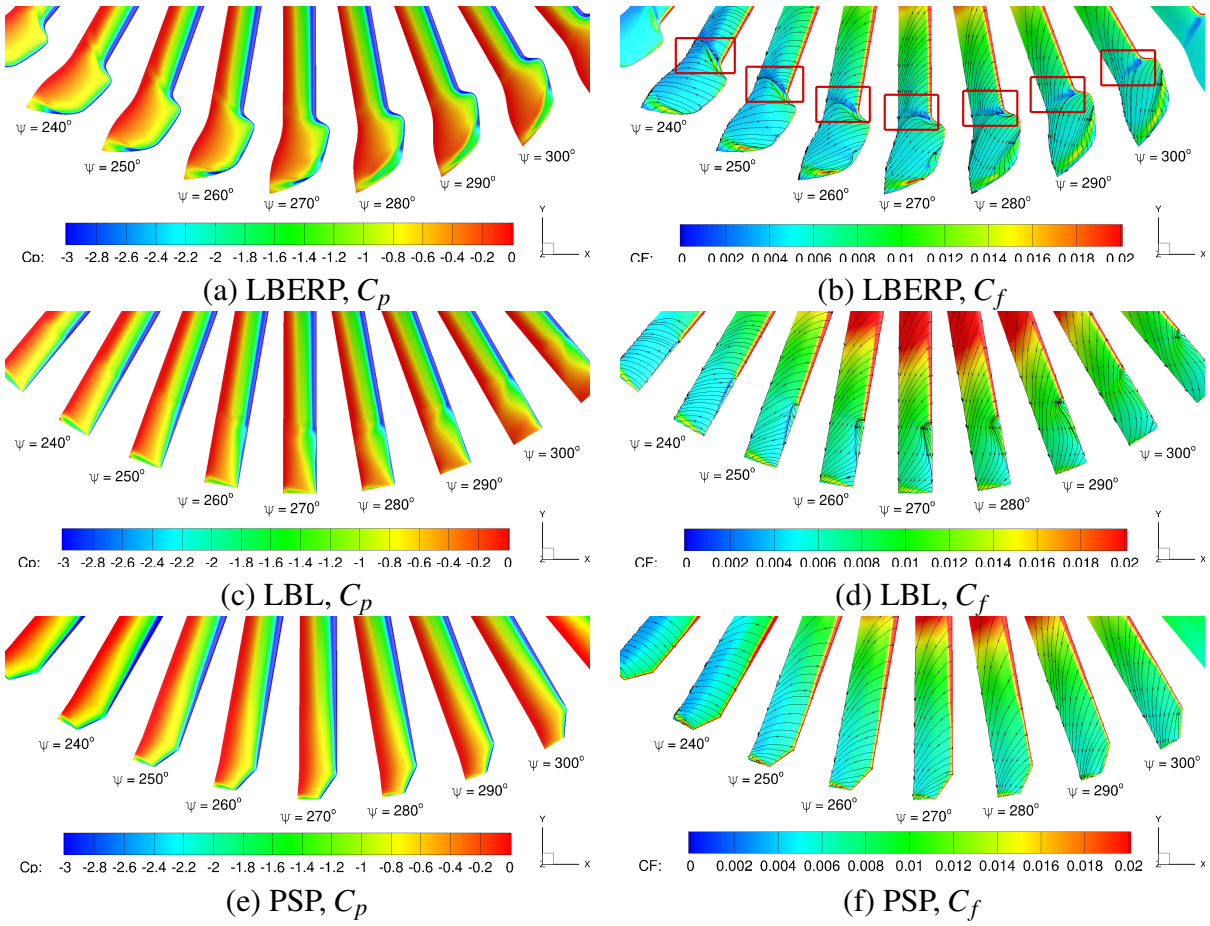

(a) LBERP, C_p (b) LBERP, C_f

(c) LBL, C_p (d) LBL, C_f

(e) PSP, C_p (f) PSP, C_f

Figure 7.31: Retreating side pressure and skin friction distributions along with skin friction lines for the LBERP, LBL and PSP rotor blades.

No evidence of dynamic stall was found for any of the blade designs in the high-speed forward flight condition. The loading distribution and skin friction lines on the retreating side for the LBERP blade indicate the presence of a notch vortex (highlighted with red boxes) which prevents propagation of separated flow to the blade tip. Due to the moderate thrust coefficient,

no significant separation is seen inboard of the notch and as expected the flow over the blade tip remains attached. At the very tip of the LBERP blade, changes can be seen in both the pressure distributions and skin friction lines. The tip vortex rolls up on the upper surface of the blade inboards of the very tip of the blade up to the 270^o azimuthal location. After passing the retreating side, a drop in skin friction can be observed, along with the skin friction lines oriented in a more spanwise direction. Here, the tip vortex rolls up round the curved blade tip and detaches further outboard. Once again, the thickness distribution across the very blade tip of this geometry could potentially have a significant effect on the flow physics in this region. The surface pressure distributions for the LBL blade shows a distinct drop in the suction pressure in the aerofoil transition region. As indicated by the skin friction lines, a separation bubble is present near the leading edge of the blade. The chordwise extent of this separation, however, is not very large, hence not leading to a drastic increase in the rotor power. While the steep reduction in aerofoil thickness and discontinuity in the blade twist led to promising features for the LBL blade on the advancing blade side, adverse flow features were found on the retreating side. However, these features would have a much more significant effect, if the LBL blade was simulated at the same geometric solidity as the LBERP blade, leading to more severe retreating side separation, and potentially dynamic stall. No flow features of major significance can be seen for the PSP rotor blade design showing that this rotor does not suffer from poor retreating blade performance due to the low blade tip Mach number. At a higher thrust level (or matched net thrust), however, this blade may stall more abruptly compared to the Langley blade designs due to lower blade tip area and lower tip speed.

7.4.3 Assessment of the Baseline AH-64A Blade Design

The AH-64A blade design is analysed separately, as this blade was selected as the baseline blade for the optimisation study. The conditions selected here, $C_T = 0.00903$ and $\mu = 0.3$, also matched the optimisation flight condition in forward flight. The focus of this section will be on the adverse flow features present for the AH-64A blade design, which could potentially be removed by performing the optimisation process. Firstly, the rotor disk loads are analysed in further detail, shown in Figure 7.32.

The rotor disk loads indicate a favourable lifting force distribution for the AH-64A blade design with high loading at the back and front of the rotor disk and no significant negative lifting force regions on the advancing side. A more favourable design would, however, potentially move the loading from the retreating side to the back or front of the rotor disk, leading to a reduced longitudinal cyclic angle requirement. The pitching moment distribution indicates a sharp drop in pitching moment due to dynamic stall on the retreating side. This is a highly adverse feature that could be weakened through an optimisation process. The regions of high in-plane force follow the trends of the lift force distribution, with the highest loading at the back of the rotor disk. While the tip loading is reduced at the front and back of the rotor disk, the tip

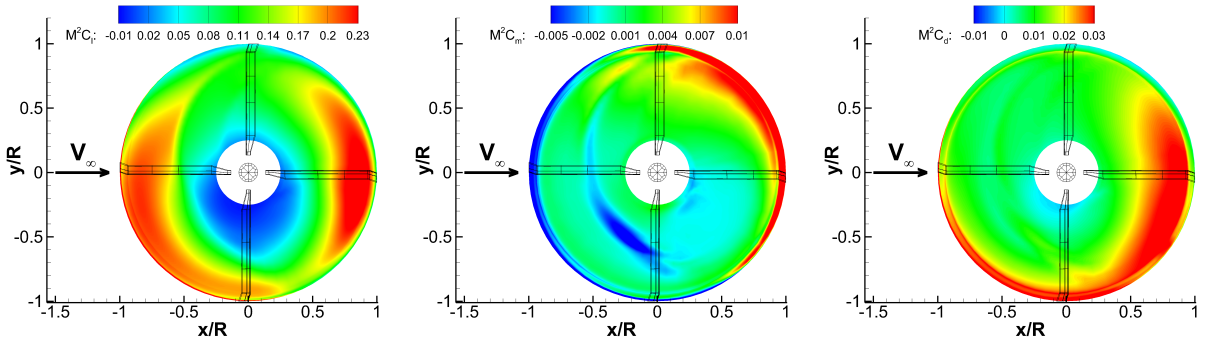

(a) M^2C_l (b) M^2C_m (f) M^2C_d

Figure 7.32: Rotor disk loads in forward flight for the baseline AH-64A rotor blade at $C_T = 0.0093$, $\mu = 0.3$.

is highly loaded on the retreating side, leading to a non-optimal spanwise loading distribution, which could also be improved during an optimisation process.

The advancing and retreating sides are analysed in further detail for the AH-64A blade. The surface pressure coefficient distributions at 90^o azimuth along with the flow field streamlines and Mach number contours at r/R = 0.82 can be seen in Figure 7.33.

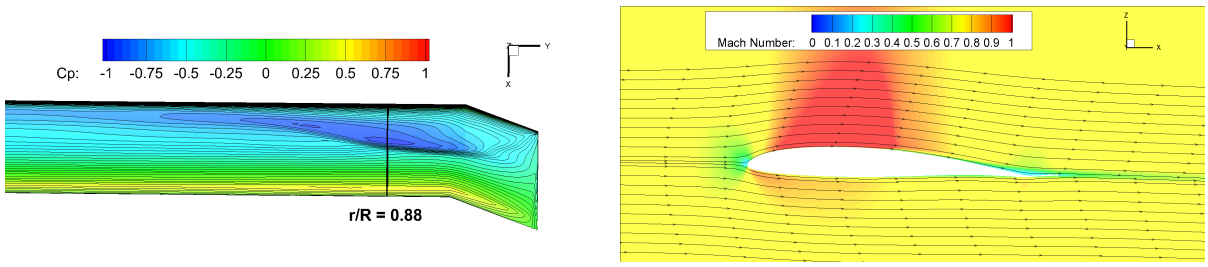

(a) AH-64A, C_P distribution (b) AH-64A, Mach contours

Figure 7.33: Advancing side pressure distributions and flow field streamlines along with contours of Mach number at r/R = 0.88 for the AH-64A rotor blade at $\mu = 0.3$, $C_T = 0.00903$.

The surface pressure distribution on the advancing side exhibits a strong shock for the AH-64A blade at $C_T = 0.00903$, $\mu = 0.3$. This shock is located further outboard than for the LBL or LBERP designs, and hence will have a greater impact on the rotor power. The region of high suction also has a greater chordwise extent, and therefore potentially affecting the blade pitching moments to a greater degree. This is confirmed for the Mach number contours, as the flow is supersonic for nearly half the rotor chord length. Compared to the other blade designs (LBL, LBERP, PSP), the stronger compressibility effects are not surprising for the AH-64A blade, which operates at a higher blade tip Mach number, and therefore even at a lower advance ratio of $\mu = 0.3$, exhibits similar advancing side characteristics. The impact of the higher blade loading of the AH-64A blade on the advancing side aerodynamics is fairly low, as typically the longitudinal cyclic is increased to reduce the advancing blade incidence angle. The strong advancing blade shock is an adverse flow feature which could potentially be removed through

computational optimisation. Although the thickness to chord ratio will play a large role here, planform shape features such as local chord, sweep and local twist angle are also of significance in weakening the advancing blade shock. The retreating side aerodynamics are also analysed for the AH-64A blade by extracting the surface pressure and skin friction distributions along with skin friction lines, shown in Figure 7.34

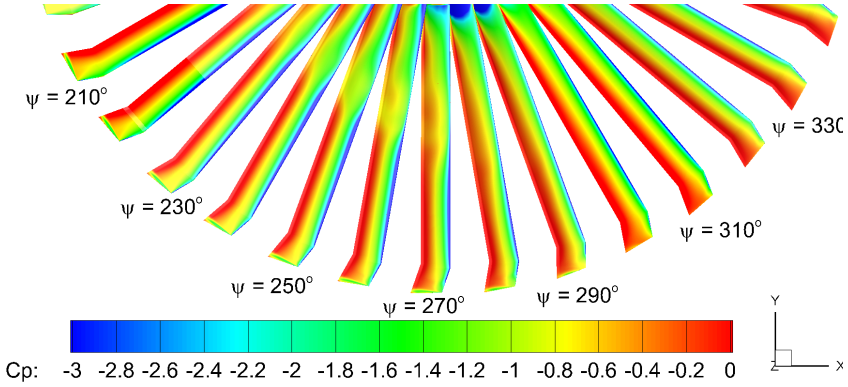

(a) C_p

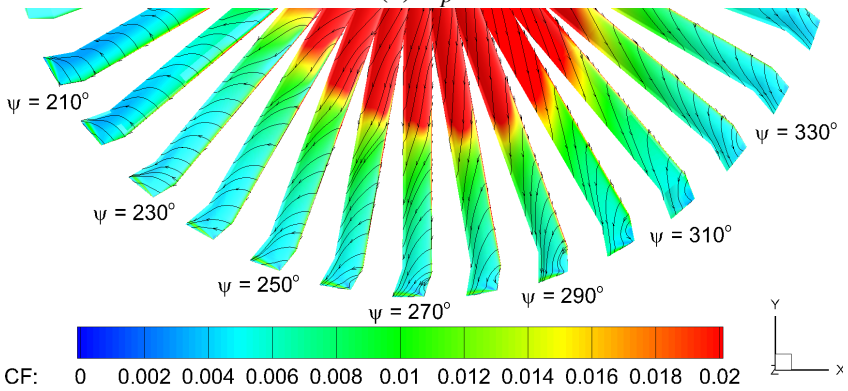

(b) C_f

Figure 7.34: Retreating side pressure and skin friction distributions along with skin friction lines for the AH-64A rotor blade at $C_T = 0.00903$ and $\mu = 0.3$.

The surface pressure distribution indicates the presence of dynamic stall in the mid-span region on the retreating side as a loss in suction is seen and the pressure is not fully recovered at the trailing edge. This phenomenon is especially seen at azimuthal stations from 240^o to 260^o, with further azimuthal stations from 270^o to 290^o exhibiting a better pressure recovery. The dynamic stall does not appear clearly on the skin friction plot, although a large degree of spanwise flow is seen in this region. However, the presence of this flow feature was verified in the wake visualisations across different advance ratios, and is highlighted again in Figure 9.17, where a clear interaction of the blade tip vortex from the back of the rotor disk is seen with the retreating blade. A significant localised drop in pitching moment was also an indicator of a dynamic stall event. This adverse flow feature, however, is primarily an effect of the flight condition and is present for many rotors at high lift and moderate advance ratio conditions. The weakening of the blade tip vortex or changes in the planform geometry (especially non-

planar features), could have an impact on this interaction and hence the strength of the dynamic stall. This is another adverse flow feature that could potentially be removed through the use of optimisation methods.

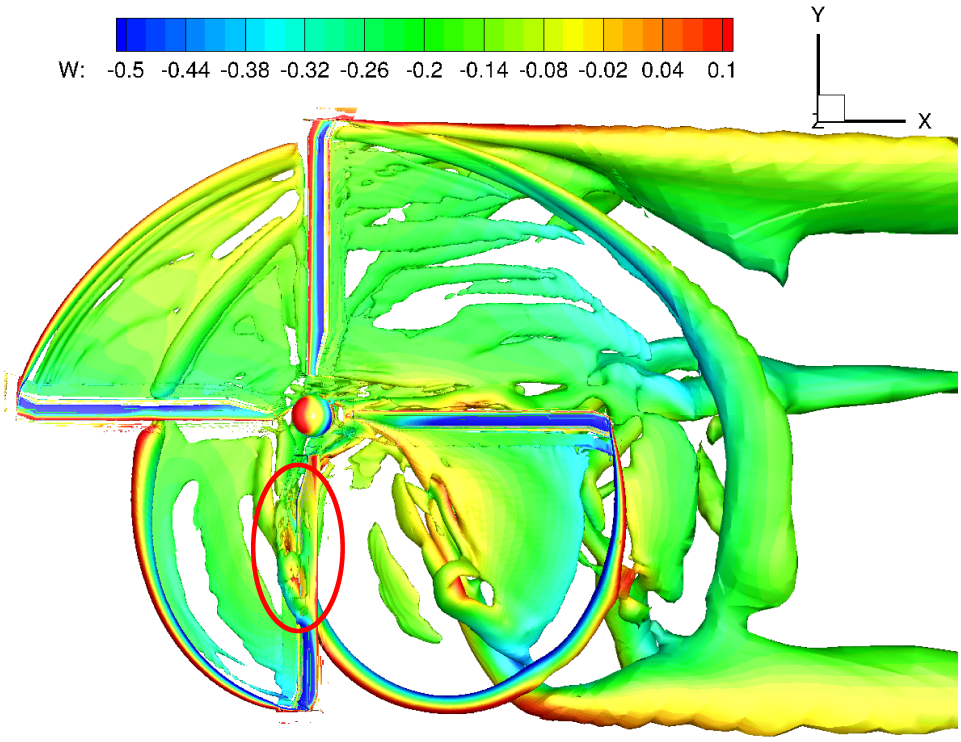

Figure 7.35: Rotor wake visualization for AH-64A rotor blade in forward flight at $\mu = 0.3$ and $C_T = 0.00903$ using an isosurface of Q-criterion (value of 0.002) coloured by downwash velocity W, with a highlighted dynamic stall event.

Chapter 8

Optimisation Framework Validation

This chapter presents the employed validation of CFD optimisation framework. Validation of the harmonic balance solver is presented, including a sensitivity study regarding the number of harmonic balance modes required to capture unsteady rotor loading. A verification of the adjoint sensitivities is also performed to verify the coupled harmonic balance adjoint implementation. Finally, an optimisation of a 2D aerofoil in DM/DT mode is performed to validate the entire optimisation framework.

8.1 Harmonic Balance Solver Validation

To validate the harmonic balance method, calculations are performed for the full-scale AH-64A rotor blade [168] with a varying number of harmonic balance modes (one, four and seven) and the results are compared with the time-marching predictions. The high thrust, moderate advance ratio case of $\mu = 0.3$, $C_T = 0.00903$ case is selected for this study, as was used for CFD validation. This condition exhibits highly nonlinear flow phenomena such as an advancing blade shock and retreating side dynamic stall, hence is considered as a very difficult case for the harmonic balance method. The harmonic balance calculations using one, four and seven harmonic balance modes were simulated for 15,000 iterations and showed good convergence of the rotor loads. The same trim state was used in the harmonic balance calculations obtained from the time-marching calculation shown in Table 6.2. The main aim of this section is to show the increase of the solution fidelity with an increasing number of harmonic balance modes, and determine how many modes are required to capture the rotor loading, advancing and retreating blade characteristics.

Firstly, the rotor disk load distributions are extracted from the time-marching and harmonic balance solutions, shown in Figure 8.1, for a qualitative assessment of the harmonic balance predictions of rotor blade loads.

The lift force distributions show good qualitative agreement. Even for one harmonic balance mode, the main lifting areas of the rotor disk are well predicted, with certain differences seen on

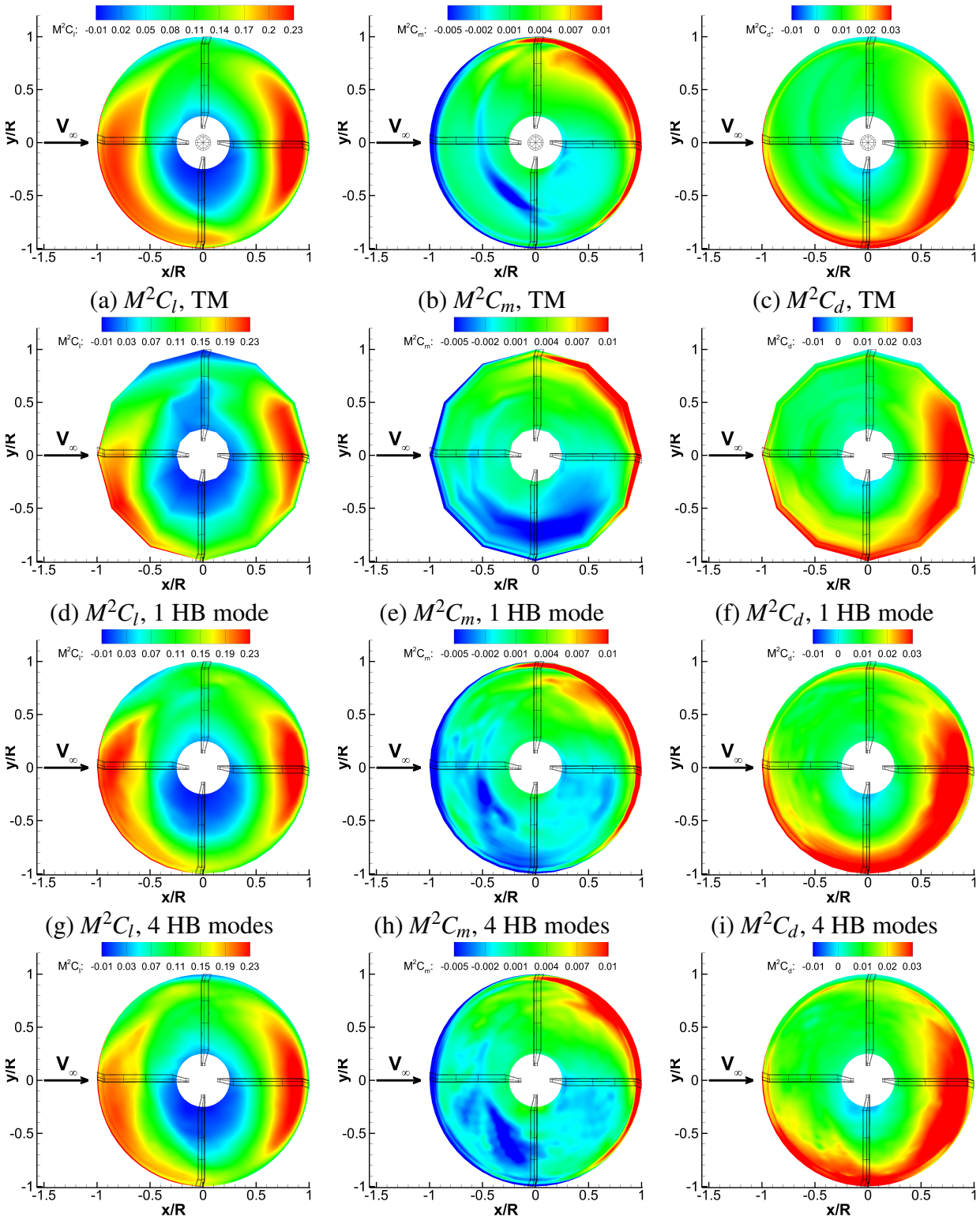

(a) M^2C_l, TM (b) M^2C_m, TM (c) M^2C_d, TM

(d) M^2C_l, 1 HB mode (e) M^2C_m, 1 HB mode (f) M^2C_d, 1 HB mode

(g) M^2C_l, 4 HB modes (h) M^2C_m, 4 HB modes (i) M^2C_d, 4 HB modes

(j) M^2C_l, 7 HB modes (k) M^2C_m, 7 HB modes (l) M^2C_d, 7 HB modes

Figure 8.1: Rotor disk loads distributions for the AH-64A rotor blade in forward flight at $\mu = 0.3$ and $C_T = 0.00903$ for a various number of harmonic balance modes and comparison to time-marching simulation predictions. TM=Time Marching, HB=Harmonic Balance

the advancing and retreating side. With four harmonic balance modes, the agreement improves in these regions. The seven mode calculation when compared to the four mode prediction, improves the agreement at the front of the rotor disk and advancing side, when compared to the time-marching calculation. The pitching moment distributions indicate a clear dynamic stall event in the mid span region on the retreating side, due to the strong nose-down pitching moment. With an increasing number of modes, the region of dynamic stall is captured in a more precise manner. However, based on the results it can be stated that a higher number of modes would be beneficial. The in-plane force distributions are also well captured, with the highest in-plane force at the back of the rotor disk and on the retreating side, predicted even for the one mode harmonic balance calculation. The magnitude of the in-plane force is, however, overpredicted especially on the retreating side and when compared to the time-marching calculation, with an improved agreement as the number of harmonic balance modes increases.

The results are compared in a more quantitative manner by extracting the azimuthal loads at three radial stations, shown in Figure 8.2

The lift force predictions are in very good agreement especially for the four mode and seven mode harmonic balance calculations. A certain phase shift can be seen on the advancing and retreating side due to the complex flow physics associated with the formation of the advancing blade shock and retreating blade dynamic stall. This can especially be seen in the pitching moment curves as certain nonlinearities associated with these features, lead to poorer predictions in these regions. A high number of modes is required to resolve these flow features more precisely. The in-plane force predictions are reasonable with a slight overprediction on the retreating side and across the blade tip on the advancing side. The overall trends and magnitude, however, are well captured.

A more detailed analysis is performed for the advancing and retreating blades. The surface pressure distribution on the advancing blade is shown in Figure 8.3.

The harmonic balance solutions capture the advancing side surface pressure with good agreement. The one mode solution does not predict the presence of the shock, whereas the four and seven mode harmonic balance solutions are much closer to the time-marching prediction. The four and seven mode harmonic balance solutions lead to a better capturing of the shock location. The seven mode solution, also, has an improved prediction of the blade loading further inboard. This is shown more quantitatively in Figure 8.4, through a chordwise surface pressure distribution at r/R = 0.90 and the radial normal force distribution. The surface pressure distribution shows that the four mode harmonic balance calculation captures the chordwise shock position very accurately, whereas the seven mode solution leads to an improved radial loading on the advancing side.

The retreating side is also analysed in more detail. The surface pressure distributions at 270^o azimuth are shown in Figure 8.5.

The predictions show that the location, and effect on blade loading of the dynamic stall

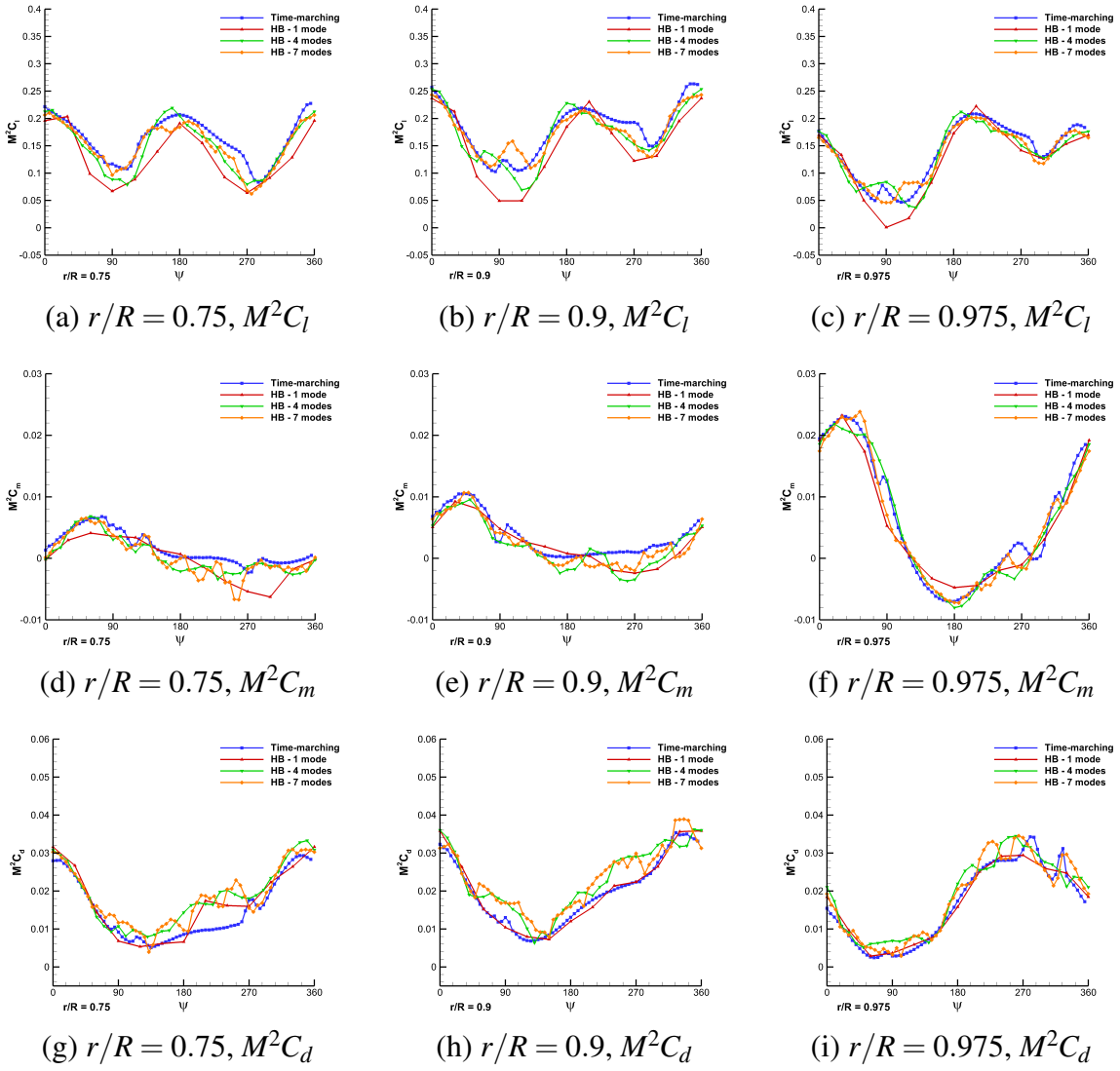

(a) $r/R = 0.75$, M^2C_l (b) $r/R = 0.9$, M^2C_l (c) $r/R = 0.975$, M^2C_l

(d) $r/R = 0.75$, M^2C_m (e) $r/R = 0.9$, M^2C_m (f) $r/R = 0.975$, M^2C_m

(g) $r/R = 0.75$, M^2C_d (h) $r/R = 0.9$, M^2C_d (i) $r/R = 0.975$, M^2C_d

Figure 8.2: Azimuthal loads at three radial stations for the AH-64A blade in forward flight at $C_T = 0.00903$ and $\mu = 0.3$ for the harmonic balance method with varying number of modes and comparison to time-marching predictions.

vortex is difficult to predict using the harmonic balance method. This is a highly nonlinear phenomenon which would require a very high number of modes to capture accurately. However, the seven mode calculation predicts the reduced blade loading near the trailing edge fairly well. This is also confirmed by the sectional pitching moments shown in Figure 8.6, as the location at which a nose-down pitching moment indicating the presence of dynamic stall is predicted very well for the seven mode harmonic balance case. Another important aspect, is that the loading is underpredicted at the blade tip on the retreating side for all the harmonic balance cases.

The results indicate that the harmonic balance method is a promising alternative to computationally expensive time-marching simulations. Very good predictions of the rotor loading were obtained in forward flight at significantly reduced computational costs. However, to accurately capture flow phenomena such as dynamic stall, a high number of modes are required. For

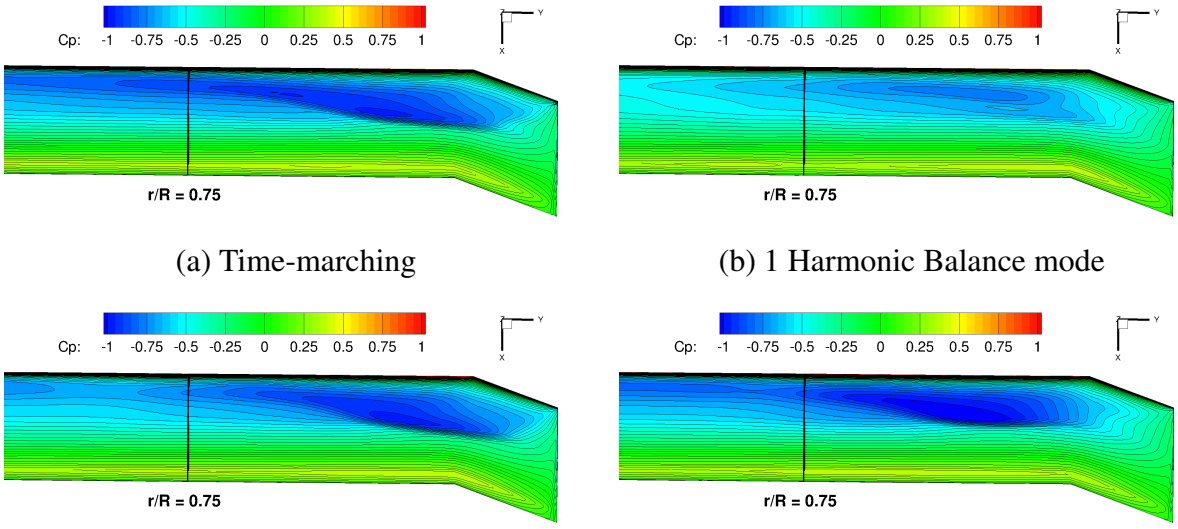

(a) Time-marching

(b) 1 Harmonic Balance mode

(c) 4 Harmonic Balance modes

(d) 7 Harmonic Balance modes

Figure 8.3: Surface pressure distributions on the advancing side for the AH-64A blade in forward flight at $C_T = 0.00903$ and $\mu = 0.3$ for the harmonic balance method with varying number of modes and comparison to time-marching predictions.

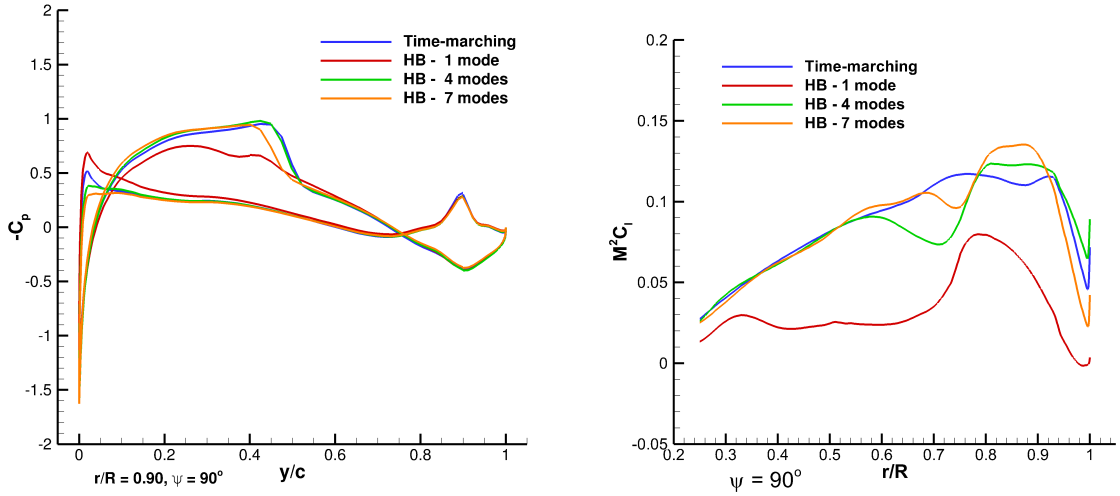

(a) C_P at r/R =0.90 and $\psi = 90°$

(b) Sectional lift force at $\psi = 90°$

Figure 8.4: Quantitative comparison of the chordwise surface pressure distribution at $\psi = 90°$ and sectional normal force on the advancing side for the AH-64A blade in forward flight at $C_T = 0.00903$ and $\mu = 0.3$ for the harmonic balance method with varying number of modes and comparison to time-marching predictions.

rotor design studies, the exact physics of these flow features are of less importance and the relative changes between different designs become significant. This makes the harmonic balance method well suited for optimisation studies as the method maintains the fidelity of Navier-Stokes methods, and captures the correct loading trends with only a few modes.

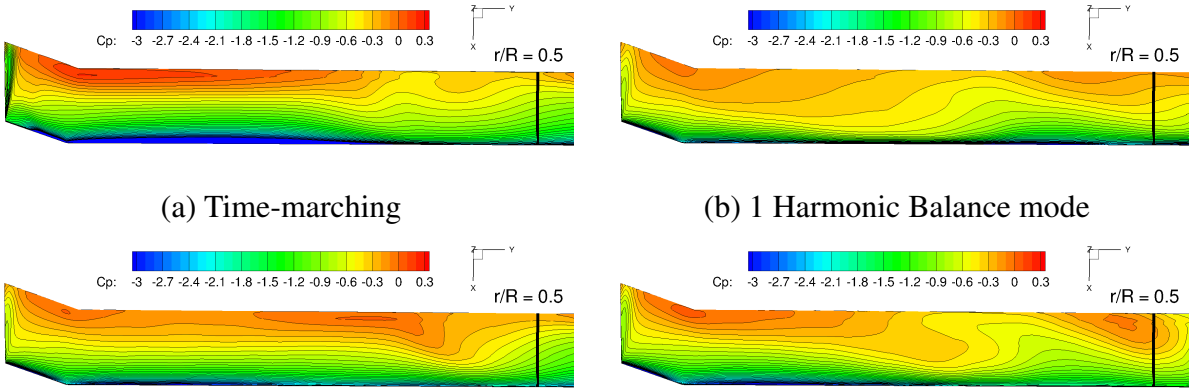

(a) Time-marching

(b) 1 Harmonic Balance mode

(c) 4 Harmonic Balance modes

(d) 7 Harmonic Balance modes

Figure 8.5: Surface pressure distributions on the retreating side for the AH-64A blade in forward flight at $C_T = 0.00903$ and $\mu = 0.3$ for the harmonic balance method with varying number of modes and comparison to time-marching predictions.

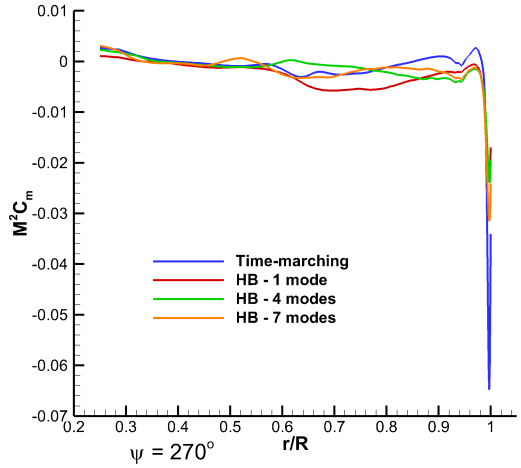

Figure 8.6: Sectional pitching moment distributions on the retreating side for the AH-64A blade in forward flight at $C_T = 0.00903$ and $\mu = 0.3$ for the harmonic balance method with varying number of modes and comparison to time-marching predictions.

8.2 Adjoint Sensitivity Validation

The aim of this section is to validate the adjoint harmonic balance implementation by comparing the adjoint gradient with finite differences. The effect of numerical modelling on the sensitivity values is also assessed including 1st order versus 3rd order adjoint gradients, Euler vs Navier-Stokes and number of harmonic balance modes.

8.2.1 Gradient Accuracy Study

Firstly, the gradient accuracy is assessed by comparing the adjoint harmonic balance gradients with 2nd order finite differences. Two cases were used to perform this validation: a pitching 2D aerofoil and a rotor in forward flight, which are described here.

Firstly, adjoint validation was performed for a 2D aerofoil case. The NACA0012 aerofoil was used for this purpose using a very coarse grid of 28,000 cells. The shape was parameterised using 12 CST coefficients (6 for upper and 6 for lower surface), and a perturbation of 10^{-4} was applied to the first coefficient of the upper surface. The case used two harmonic balance modes and was performed at a Mach number of 0.55 and Reynolds number of 10^6. A reduced frequency of k=0.1 was used along with a pitching schedule of $\alpha = 0^o + 5^o \sin(\omega t)$. The simulations achieved good levels of convergence as the harmonic balance solver converged by 7 orders of magnitude (both flow and turbulence residuals) and the adjoint solver converged by 8 orders of magnitude. A comparison between the adjoint and finite difference results is shown in Table 8.1.

Table 8.1: Comparison of gradient values for the pitching NACA0012 aerofoil, using the adjoint method and finite differences.

Gradient	Finite Differences	Adjoint	% difference
$dC_L/d\alpha_1$	0.256419	0.256765	-0.13%
$dC_D/d\alpha_1$	0.004520	0.004541	+0.46%
$dC_M/d\alpha_1$	0.038616	0.039010	+1.02%

Excellent agreement was seen between the adjoint and finite differences predictions, considering that the finite differences are only 2nd order accurate, and sensitive to the step size used.

A more complex case was also used to verify the adjoint harmonic balance implementation for rotors in forward flight. The AH-64A rotor was simulated at $C_T = 0.00903$ and $\mu = 0.3$ using a grid of 3.1 million cells. Due to the coarse mesh, the gradient values are not expected to be fully accurate, with the present investigation aimed at validation of the adjoint implementation. The trim state was taken from the fine grid calculation 6.2. The blade was parameterised using the description shown in Chapter 3.1.6, Blade Surface Parameterisation. A 10^{-3} perturbation was applied to the blade tip variables (twist, chord, sweep, anhedral) to obtain the 2nd order finite differences. The harmonic balance flow residual was converged by 5 orders of magnitude whereas the turbulence residual was converged by 3 orders of magnitude. The adjoint solver was converged by 1-2 orders of magnitude after 1,000 iterations. The moderate convergence of the harmonic balance and adjoint solvers, however, is not surprising due to a poor discretisation of a complex flow field, leading to large expansion ratios in regions of high velocity gradients. However, as the main purpose of this investigation is to validate the adjoint implementation, such convergence is acceptable for validation purposes as long as the adjoint sensitivities have

the correct sign and are of similar order as the finite difference predictions. This comparison is performed in Table 8.2, for the twist, chord, sweep and anhedral variables at the blade tip.

Table 8.2: Comparison of non-dimensional thrust and torque gradient values with respect to the blade design parameters (twist, chord, sweep, anhedral) at the blade tip for the baseline AH-64A rotor blade in forward flight at $C_T = 0.00903$ and $\mu = 0.3$ using the adjoint method and finite differences.

Gradient	Finite Differences	Adjoint
$dC_{Pz}/dtwist_{tip}$	25.002	21.949
$dC_{Mz}/dtwist_{tip}$	61.139	66.915
$dC_{Pz}/dchord_{tip}$	0.477	0.334
$dC_{Mz}/dchord_{tip}$	0.980	0.752
$dC_{Pz}/dsweep_{tip}$	-0.121	-0.040
$dC_{Mz}/dsweep_{tip}$	0.705	0.482
$dC_{Pz}/danhedral_{tip}$	0.383	0.142
$dC_{Mz}/danhedral_{tip}$	-1.123	-0.749

The gradient accuracy compared to finite differences is considered to be reasonable. For most design sensitivities, the adjoint values are consistently slightly lower than the finite difference results. The difficulty in comparing the adjoint gradients with finite differences is associated with the adequate perturbation step size. A low perturbation step size leads to significant round-off errors, whereas a high perturbation step size leads to high truncation errors. However, another aspect is the loads convergence for the harmonic balance solver, which are difficult to converge past the 3rd decimal digit (under 0.01% difference), thereby also having an effect on the finite difference gradient solution. This is the main reason why a smaller perturbation than 10^{-3} cannot be used, leading to a large truncation error. Additionally, the adjoint equations are not fully converged introducing another error in the present comparison. The adjoint gradient values, however, gave consistent results across different levels of convergence, hence this effect is not considered to change the design gradients drastically. The present comparison, although could be improved, proves that the gradient values are accurate enough to drive the design in the correct direction, as the sign and order of magnitude are well captured.

8.2.2 Modelling Sensitivity Study

Next, the effects of numerical modelling are examined, aimed at investigating the sensitivity of the design parameter gradients. The same case, as shown above, for validation of the adjoint gradient values is used. The AH-64A is simulated on a coarse grid of 3.1M cells at $C_T = 0.00903, \mu = 0.3$. Due to the coarse grid size, the significant non-linearity of the solution may not be captured, hence the modelling sensitivity shown here, may in fact be higher for a finer mesh. The effect of neglecting viscous effects was also examined for an Euler solution grid of 0.8M cells, with similar cell spacing in the chordwise and spanwise direction. Effects of the

adjoint solver order (1st vs 3rd) and neglection of viscous effects (Euler vs Navier-Stokes) are shown in Table 8.3.

Table 8.3: Effect of the adjoint solver order and neglection of viscous effects on the non-dimensional thrust and torque gradient values with respect to different design variables.

Gradient	**3rd order Adjoint Navier-Stokes**	**1st order Adjoint Navier-Stokes**	**3rd order Adjoint Euler**
$dC_{Pz}/dtwist_{tip}$	21.949	22.425	24.566
$dC_{Mz}/dtwist_{tip}$	66.915	68.839	48.322
$dC_{Pz}/dchord_{tip}$	0.334	0.336	0.317
$dC_{Mz}/dchord_{tip}$	0.752	0.658	0.893
$dC_{Pz}/dsweep_{tip}$	-0.040	-0.027	-0.063
$dC_{Mz}/dsweep_{tip}$	0.482	0.460	0.032
$dC_{Pz}/danhedral_{tip}$	0.142	-0.0963	0.523
$dC_{Mz}/danhedral_{tip}$	-0.749	-1.4686	-0.955

The effects of the 1st order adjoint solver and neglecting viscous effects are fairly small on the design sensitivities. The effects changing the twist and chord at the blade tip are well captured by both 1st order adjoint solution and Euler solutions, although the torque sensitivity with respect to tip twist is significantly reduced for the inviscid solution. The tip sweep torque sensitivity is significantly underpredicted for the Euler solution, whereas the 1st order adjoint solution overpredicts the torque sensitivity for the tip anhedral variable. The thrust sensitivity due to anhedral is also poorly predicted by the 1st order adjoint and slightly overpredicted by the inviscid computation. Therefore, a reasonable representation of the design gradients can be obtained through 1st order adjoint solution. The neglection of viscous effects, can have an impact on the design sensitivities (tip sweep), and will also impact the final optimum shape directly through different values of the objective and constraint functions, and therefore, cannot be simply neglected during an optimisation process. Next, the effect of the number of harmonic balance modes on the design sensitivities in examined for Navier-Stokes solutions based on 3rd order gradients, shown in Table 8.4.

The gradients of thrust and torque with respect to the design variables show a very low sensitivity due to the number of harmonic balance modes employed. The differences between the design gradients seen here, are of secondary order and could be due to the partial convergence of the adjoint equations. The gradient values, however, all show the same signs and similar magnitude with an increasing number of harmonic balance modes, hence the final shape would not be altered dramatically. However, a higher number of modes would potentially drastically change the values of the objective and constraint functions from the CFD simulation, especially if optimisation objectives that require higher frequency are to be obtained. Finally, the low sensitivity due to the number of harmonic balance modes, representing time discretisation may also be due to the poor spatial discretisation.

Table 8.4: Effect of the number of harmonic balance modes on the non-dimensional thrust and torque gradient values with respect to different design variables.

Gradient	1 HB mode	2 HB modes	4 HB modes	7 HB modes
$dC_{Pz}/dtwist_{tip}$	21.404	21.949	21.878	21.577
$dC_{Mz}/dtwist_{tip}$	64.363	66.915	67.958	68.125
$dC_{Pz}/dchord_{tip}$	0.335	0.334	0.348	0.346
$dC_{Mz}/dchord_{tip}$	0.792	0.752	0.766	0.785
$dC_{Pz}/dsweep_{tip}$	-0.033	-0.040	-0.044	-0.055
$dC_{Mz}/dsweep_{tip}$	0.431	0.482	0.444	0.386
$dC_{Pz}/danhedral_{tip}$	0.290	0.142	0.202	0.230
$dC_{Mz}/danhedral_{tip}$	-0.424	-0.749	-0.715	-0.640

Based on the adjoint sensitivity validation study, it can be stated that the obtained gradients are accurate enough to drive the design in the correct direction. Further improvements for the accuracy of the gradients are possible, through improvements in the harmonic balance convergence for more complex cases and further sensitivity verification studies. The numerical modelling sensitivities indicated a low sensitivity of the adjoint solver order, neglection of viscous effects and number of harmonic balance modes on the gradient values, however, these findings would need to be verified on a finer mesh. To verify the full adjoint-harmonic balance framework, an unsteady optimisation of a 2D aerofoil is performed in the next section.

8.3 Optimisation Framework Demonstration - 2D DM/DT Aerofoil Optimisation

The full optimisation framework is validated by performing an optimisation study for the HH02 aerofoil. The simulations are performed in 2D, in DM/DT mode, hence accounting for variation of pitch and local Mach number. The conditions are taken from the AH-64A rotor blade operating at $\mu = 0.3$ and $C_T = 0.00903$, based on the radial station at r/R=0.75. The pitching schedule is based on the trim state of the full 3D simulation, shown in Table 8.5. No correction for downwash or 3D wake effects was applied, hence an increased effective angle of attack is expected in the 2D simulation. The shaft angle from the forward flight simulation was also not taken into account. The simulations are performed using a 2D grid of 58,000 cells, giving a similar resolution of a 2D slice through the 3D full AH-64A rotor blade grid.

The pitching schedule and variation in Mach number for the DM/DT case is shown in Figure 8.7.

Table 8.5: Pitching schedule used for the DM/DT simulations of the HH02 aerofoil.

Parameter	Angle (deg)
Collective angle, θ_0	10.41278
Lateral cyclic, θ_{1s}	7.4214
Longitudinal cyclic, θ_{1c}	-3.0722

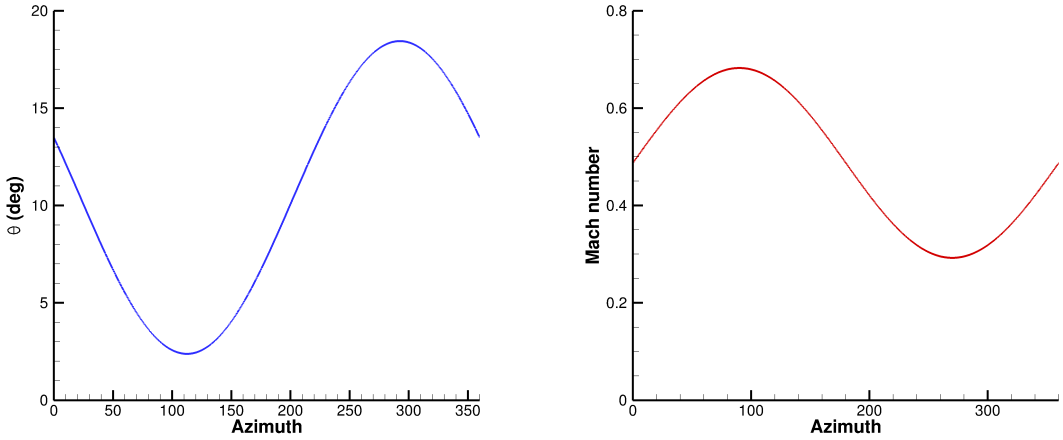

(a) Pitching schedule (b) Mach number schedule

Figure 8.7: Pitching and Mach number schedules for the HH02 DM/DT case.

8.3.1 HH02 aerofoil - Harmonic balance modes sensitivity

Before moving to the optimisation results, firstly, an assessment of how many harmonic balance modes are required to correctly capture the variation in blade loads is conducted. A time-marching simulation is performed for comparison with 1440 steps per cycle. The integrated loads are compared, in Table 8.7. Uncorrected and corrected CFD values are shown.

Table 8.6: Comparison of the integrated loads for the DM/DT HH02 aerofoil between the time-marching simulations and harmonic balance (HB) with different numbers of modes. Both uncorrected (uncor.) and corrected (cor.) CFD values are shown. Peak to peak value abbreviated as P-P.

Aerofoil	$\overline{C_L}$ (uncor.)	$\overline{C_D}$ (uncor.)	**P-P** C_M (uncor.)	$\overline{C_L}$ (cor.)	$\overline{C_D}$ (cor.)	**P-P** C_M (cor).
HH02 Time-Marching	1.0102	0.06099	0.1796	1.0865	0.09197	0.4121
HH02 HB 5 modes	0.9957	0.04893	0.0446	1.0511	0.06477	0.0868
HH02 HB 9 modes	0.9892	0.06097	0.1301	1.0545	0.08986	0.2089
HH02 HB 15 modes	1.0046	0.593	0.1586	1.0632	0.08357	0.2922

As the CFD simulations used the reference Mach number to calculate the loads, the coefficient values need to be corrected as follows:

$$C_L = C_L^{CFD} \frac{1}{\left[1 + \mu \left(\frac{R}{r}\right) sin(\omega t)\right]} \tag{8.1}$$

The application of this correction, therefore, reduces the error in the comparison between time-marching and harmonic balance simulations in the azimuthal angle from 0 to 180 degrees, and increases the error from 180 to 360 degrees. The comparisons between the time-marching and harmonic balance simulations show good agreement for the uncorrected load values when 9 or 15 harmonic balance modes are used, with a minor underprediction of the aerofoil peak to peak of the pitching moment. After the correction is applied the differences are greater. The agreement between time-marching and harmonic balance modes improves with an increasing number of modes, as expected. Potentially, a higher number of modes could be used for this highly nonlinear case to further improve the comparisons. The loads are analysed further, by extracting the values of the coefficients (corrected values) vs azimuthal angle, shown in Figures 8.8-8.10.

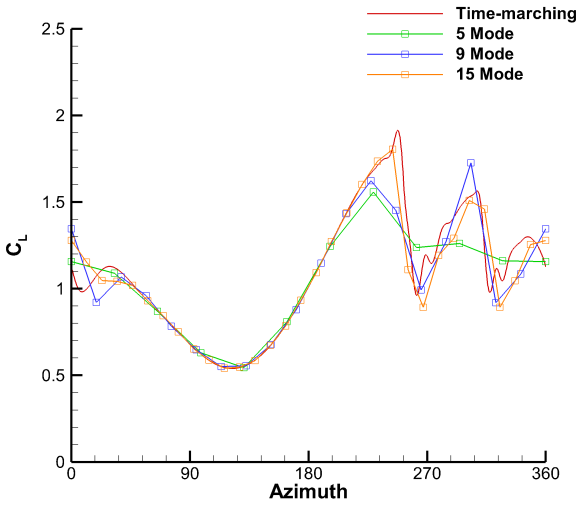

Figure 8.8: Lift coefficient vs azimuth for the HH02 DM/DT case with varying number of harmonic balance modes

Based on the obtained results it can be claimed that 9 harmonic balance modes is a good compromise between accuracy and computational cost. The 9 harmonic balance mode calculation captures the second stall event very accurately, seen by a rapid increase in drag and nose-down pitching moment. The first stall event is also captured, however, it is significantly weaker than in the time-marching simulation. The application of optimisation methods to this case, should lead to a design with significantly weakened stall events, leading to reduced drag and pitching moment.

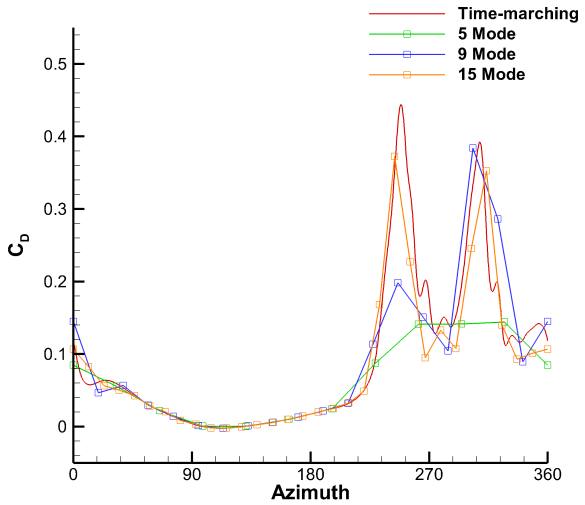

Figure 8.9: Drag coefficient vs azimuth for the HH02 DM/DT case with varying number of harmonic balance modes

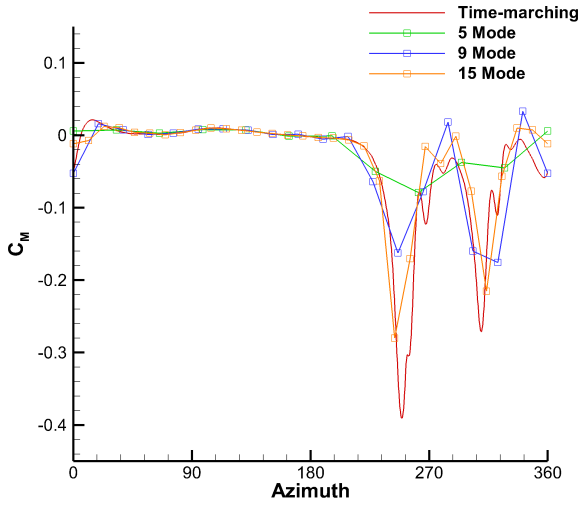

Figure 8.10: Moment coefficient vs azimuth for the HH02 DM/DT case with varying number of harmonic balance modes

8.3.2 HH02 Aerofoil - Optimisation Results

The HH-02 aerofoil was optimised at the same conditions as in the previous section. The objective function was formulated to minimize drag whilst constraining the lift and the peak-to peak pitching moment coefficients, as follows:

$$\begin{cases} \text{Minimize I} = \overline{C_D} \text{ subject to,} \\ \overline{C_L} = \overline{C_{L_{base}}} \\ \text{peak-to-peak } C_M <= \text{peak-to-peak } C_{M_{base}} \end{cases} \tag{8.2}$$

The peak-to-peak pitching moment constraint and drag objectives are likely to drive the

design in the same direction, as the high drop in pitching moment caused by the three stall events seen in Figure 8.10, lead to a large increase in drag. Therefore, the minimization of the drag coefficient should directly lead to a lower peak-to-peak pitching moment.

The aerofoil upper and lower surfaces are parameterised using a standard CST (Class-Shape Transformation) method, represented in equation 8.3.

$$\zeta(\psi) = C_{N_1}^{N_2}(\psi) \sum_{r=0}^{n} \alpha_r S_{r,n}(\psi) + \psi \zeta_{TE}. \tag{8.3}$$

The term $C_{N_1}^{N_2}(\psi)$ is called the "class function", and has the following general mathematical form:

$$C_{N_1}^{N_2}(\psi) = \psi^{N_1}(1-\psi^{N_2}). \tag{8.4}$$

The coefficients N_1 and N_2 define the behaviour of the parameterisation at the leading and trailing edges. Here, values of $N_1 = 0.5$ and $N_2 = 1.0$ are set to represent typically obtained aerofoil shapes,

The term $\sum_{r=0}^{n} \alpha_r S_{r,n}(\psi)$ is a polynomial expansion, with the Bernstein polynomial base used here. The Bernstein polynomials are defined as:

$$S_{r,n}(\psi) = K_{r,n} \psi^r (1-\psi)^{n-r}, \tag{8.5}$$

where

$$K_{r,n} = \begin{pmatrix} n \\ r \end{pmatrix} = \frac{n!}{r!(n-r)!}. \tag{8.6}$$

The linear function $\psi\zeta_{TE}$ is added to represent the thick trailing edge. The quantity $\zeta_{TE} = y_{TE}/c$ represents the coordinate of the aerofoil (upper or lower side) at the trailing edge. It follows that the trailing edge thickness is $\zeta_{TE,u} - \zeta_{TE,l}$, where the subscript u and l are used to denote quantities relative to the upper and lower side, respectively.

The polynomial coefficients α_r, $r = 0, \ldots, n$ appearing in formula (8.3) represent the design variables for the aerofoil. Eight coefficients each are used for the upper and lower surfaces of the aerofoil giving a total of 16 design parameters. Due to the fact that the HH-02 aerofoil has a trim tab, this sharp feature cannot be represented accurately using such a parameterisation method. The CST method leads to a smoothing in the tab region. A comparison of the tab region between the baseline and parameterised HH-02 aerofoils is shown in Figure 8.11. The parameterisation also leads to a reduced tab thickness before the trailing edge.

The optimisation process was performed for three iterations, with the harmonic balance solver converging by 5 orders of magnitude in 10,000 iterations and the adjoint solver converging by 6 orders of magnitude in 900 iterations. The optimised shape was not considered to be fully converged, with the main aim of this study to validate the adjoint harmonic balance implementation.

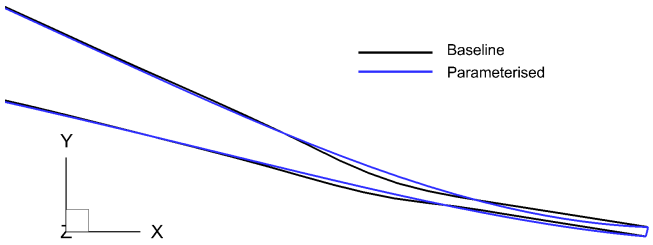

Figure 8.11: Comparison of the trim tabs of the baseline and parameterised HH-02 aerofoils.

The comparison of the integrated loads (corrected) between the baseline, parameterised and optimised aerofoils are shown in Table 8.7.

Table 8.7: Comparison of the integrated loads (corrected) between the baseline, parameterised and optimum HH-02 aerofoils.

Aerofoil	C_L	C_D	**P-P** C_M
HH02 Baseline	1.0545	0.08986	0.4121
HH02 Parameterised	1.0349	0.08823	0.4371
HH02 Optimised	1.06789	0.05898	0.2089

The parameterised HH02 aerofoil leads to a slightly lower integrated lift and drag coefficient when compared to the baseline HH02 aerofoil, which is due to the different trim tab shape. The optimised aerofoil leads to significant benefits over the baseline HH02 aerofoil. A minor increase in lift coefficient is seen along with a drop in drag coefficient by over 34 % and reduction in peak-to-peak pitching moment by nearly 50%. The optimised HH02 aerofoil shape is compared with the parameterised HH02 aerofoil in Figure 8.12.

The optimised aerofoil has a slightly larger thickness and leading edge radius. These features are primarily aimed at minimising the three dynamic stall events seen in the aerofoil loads. The differences in shape, however, are not large to not deteriorate the performance at other azimuthal locations, especially on the advancing side exhibiting transonic flow characteristics. To confirm the influence of the shape on the aerofoil loads, the baseline and optimised aerofoil coefficients are compared in Figures 8.13-8.15.

The aerofoil loads confirm that the optimisation process was primarily driven at weakening the three dynamic stall events. The optimised aerofoil leads to an increased lift coefficient and significantly reduced drag and negative pitching moment coefficients indicating much less severe stall events. At other azimuthal locations, the differences between the baseline and optimised aerofoil are minor. The dynamic stall on the baseline and optimised HH02 aerofoil is analysed further by extracting the surface pressure field along with the flow field streamlines at a number of azimuthal stations and is shown in Figure 8.16.

At the azimuthal station of $\psi = 208^o$, both aerofoils exhibit a very similar behaviour. As the aerofoil pitches up, a separation bubble forms at the trailing edge, sooner for the baseline

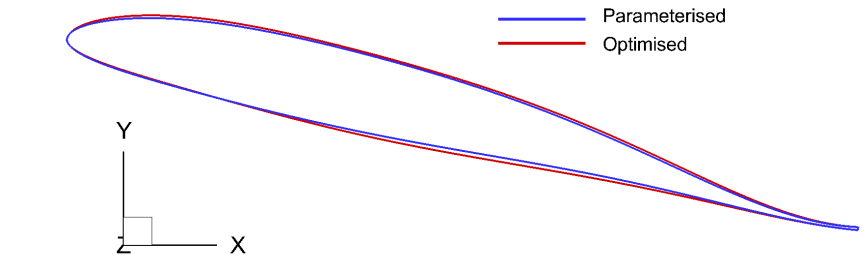

(a) Aerofoil

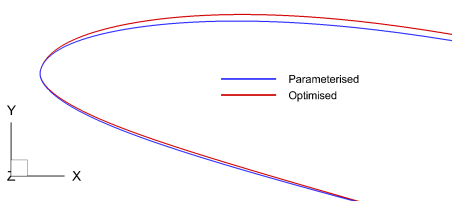

(b) LE region

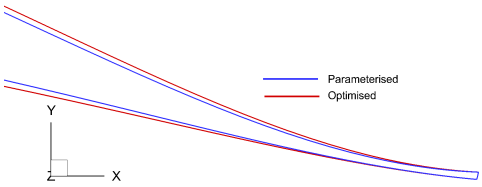

(c) TE region

Figure 8.12: Comparison of the optimised and parameterised baseline HH02 aerofoils.

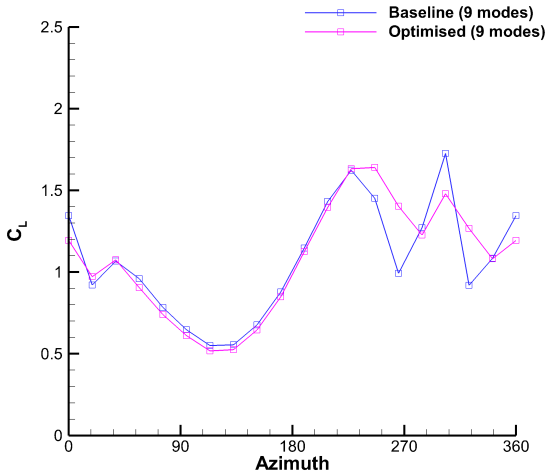

Figure 8.13: Lift coefficient vs azimuth for the HH02 DM/DT baseline and optimised aerofoils

aerofoil than for the optimised aerofoil, as seen at $\psi = 227^o$, where no recirculation region is present for the optimised aerofoil. In the next step captured by the harmonic balance method at $\psi = 246^o$, a much larger separation bubble is formed for the baseline aerofoil compared to the optimised aerofoil, which is similar to next step for the optimised aerofoil at $\psi = 265^o$. The behaviour of the optimised aerofoil is actually similar to the baseline aerofoil, but seems to delayed in pitch (and azimuth). Subfigures (h) and (j) show comparable flow features with a secondary recirculation forming below the main separation bubble. As the aerofoil pitch rate drops and starts to pitch down the flow reattaches for both baseline and optimised aerofoils. A second stall event is seen with similar flow features on both aerofoils seen in subfigures (k) and

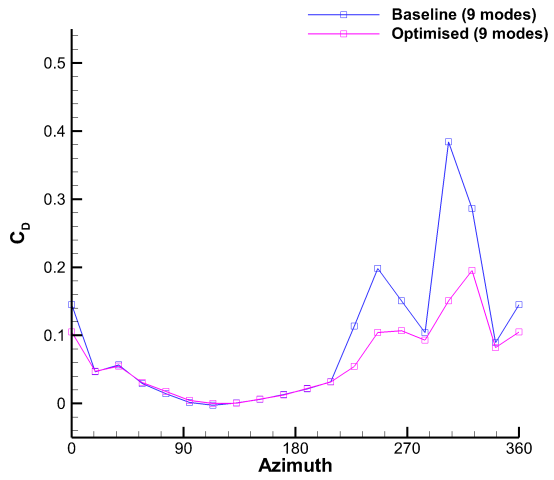

Figure 8.14: Drag coefficient vs azimuth for the HH02 DM/DT baseline and optimised aerofoils

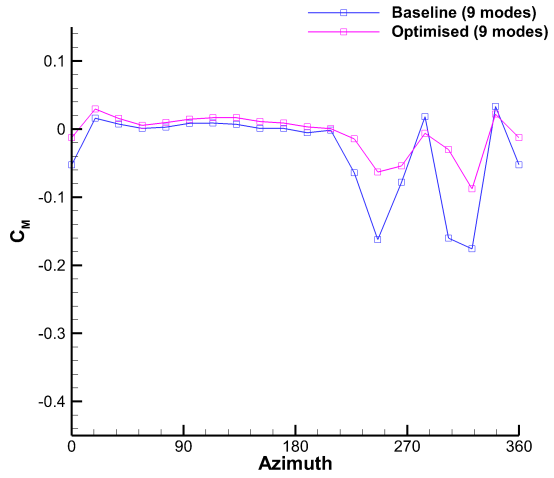

Figure 8.15: Moment coefficient vs azimuth for the HH02 DM/DT baseline and optimised aerofoils

(n). A massive recirculation region then forms for the baseline aerofoil, which is significantly smaller for the baseline aerofoil. A third minor stall event forms at the trailing edge, as the blade pitches rapidly downwards past $\psi = 360^o$. For both cases, the separation bubble seemed to remain attached throughout the stall cycle (verified by looking at the time-marching simulations), however, the optimised aerofoil led to delayed stall and hence smaller recirculation regions leading to reduced drag and peak-to-peak pitching moment. The sharp dynamic stall seen in the 2D cases was overpredicted when compared to 3D rotor simulations, as no correction was applied to the effective angle of attack due to downwash and unsteady wake effects. Despite this, the optimisation framework was successfully applied to the highly nonlinear and complex 2D unsteady case, thereby verifying the implementation of the adjoint harmonic balance method.

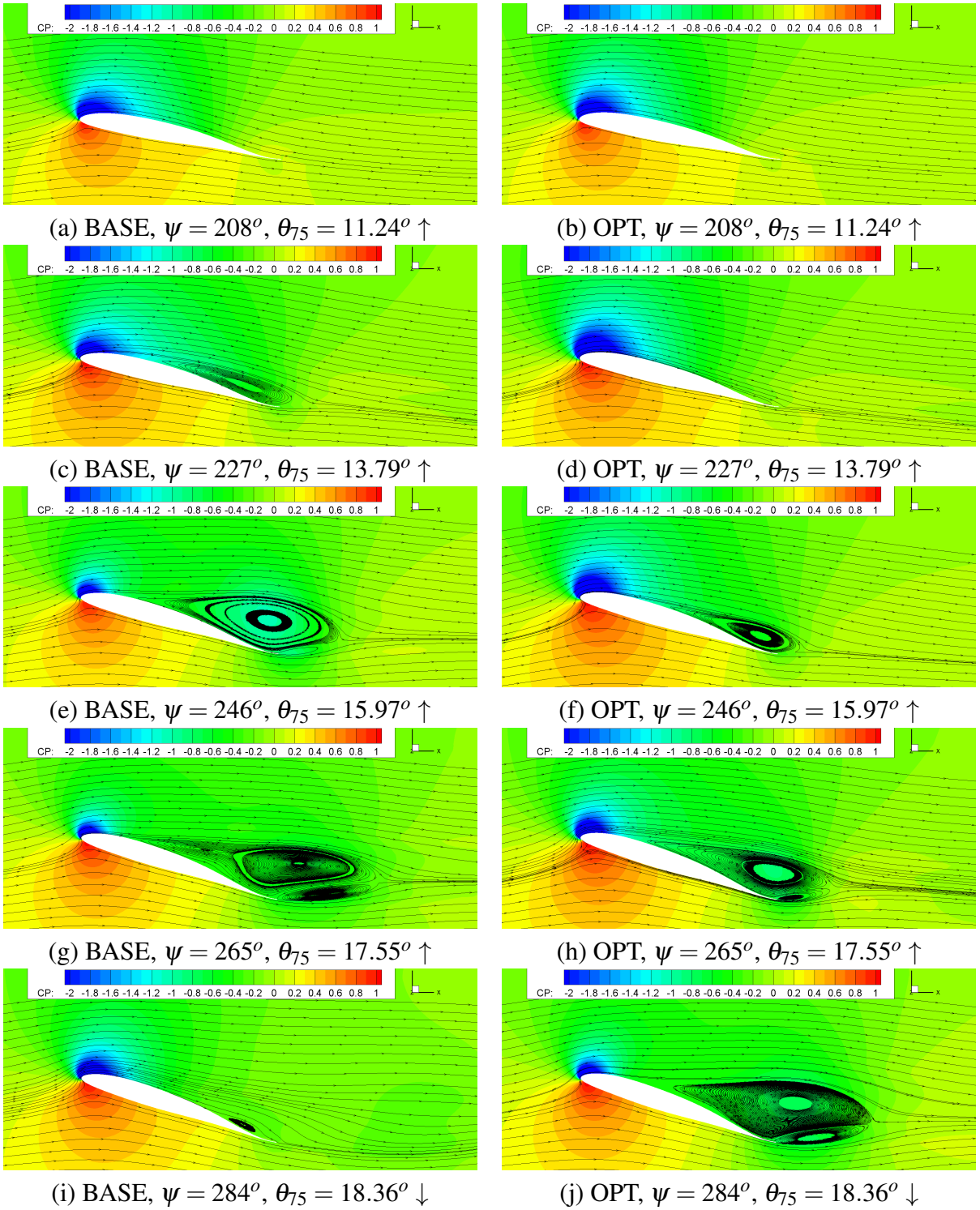

(a) BASE, $\psi = 208^o$, $\theta_{75} = 11.24^o \uparrow$

(b) OPT, $\psi = 208^o$, $\theta_{75} = 11.24^o \uparrow$

(c) BASE, $\psi = 227^o$, $\theta_{75} = 13.79^o \uparrow$

(d) OPT, $\psi = 227^o$, $\theta_{75} = 13.79^o \uparrow$

(e) BASE, $\psi = 246^o$, $\theta_{75} = 15.97^o \uparrow$

(f) OPT, $\psi = 246^o$, $\theta_{75} = 15.97^o \uparrow$

(g) BASE, $\psi = 265^o$, $\theta_{75} = 17.55^o \uparrow$

(h) OPT, $\psi = 265^o$, $\theta_{75} = 17.55^o \uparrow$

(i) BASE, $\psi = 284^o$, $\theta_{75} = 18.36^o \downarrow$

(j) OPT, $\psi = 284^o$, $\theta_{75} = 18.36^o \downarrow$

Figure 8.16: Comparison of the dynamic stall characteristics between the baseline (BASE) and optimised (OPT) HH02 aerofoils.

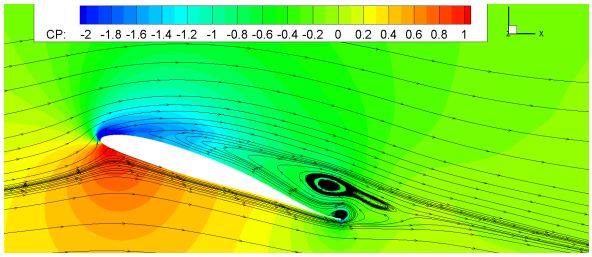

(k) BASE, $\psi = 303^o$, $\theta_{75} = 18.30^o \downarrow$

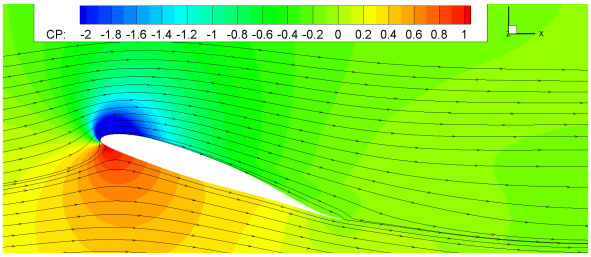

(l) OPT, $\psi = 303^o$, $\theta_{75} = 18.30^o \downarrow$

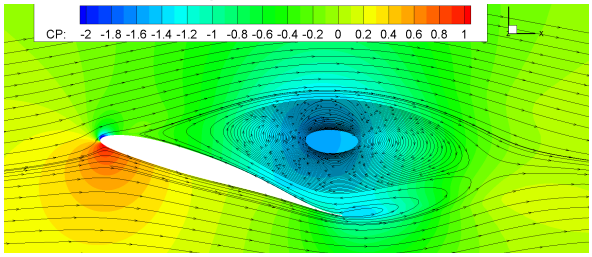

(m) BASE, $\psi = 322^o$, $\theta_{75} = 17.39^o \downarrow$

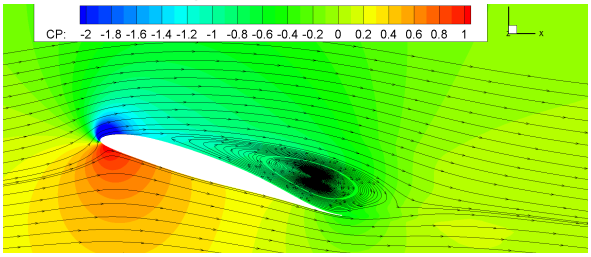

(n) OPT, $\psi = 322^o$, $\theta_{75} = 17.39^o \downarrow$

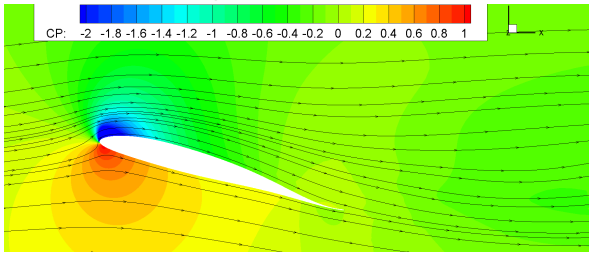

(o) BASE, $\psi = 341^o$, $\theta_{75} = 15.73^o \downarrow$

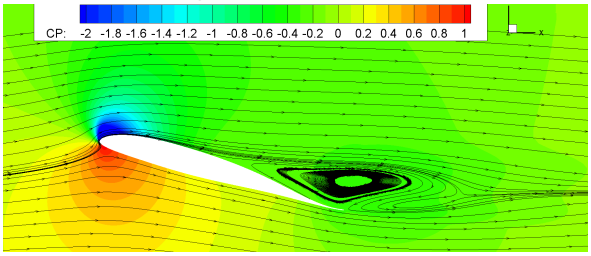

(p) OPT, $\psi = 341^o$, $\theta_{75} = 15.73^o \downarrow$

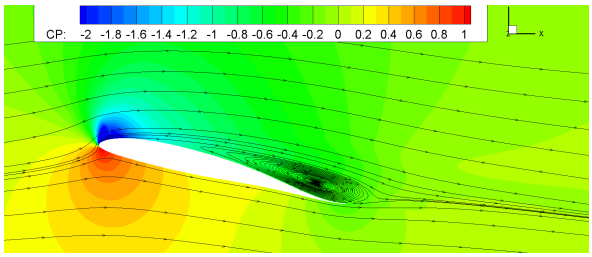

(q) BASE, $\psi = 360^o$, $\theta_{75} = 13.485^o \downarrow$

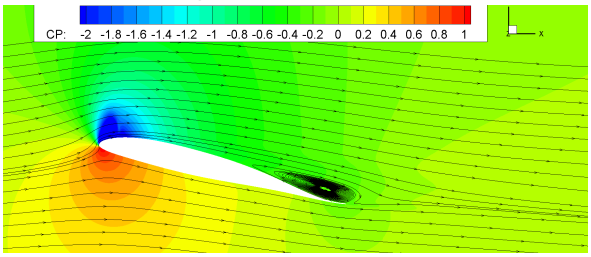

(r) OPT, $\psi = 360^o$, $\theta_{75} = 13.485^o \downarrow$

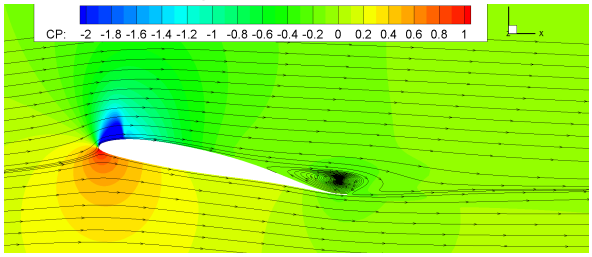

(s) BASE, $\psi = 19^o$, $\theta_{75} = 10.91^o \downarrow$

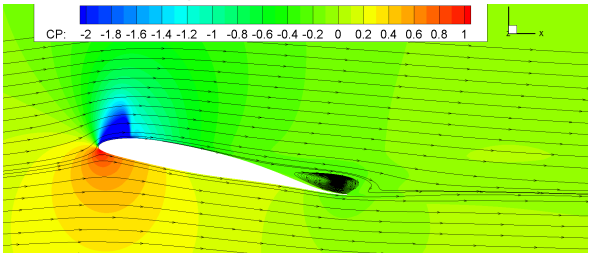

(t) OPT, $\psi = 19^o$, $\theta_{75} = 10.91^o \downarrow$

Figure 8.16: Comparison of the dynamic stall characteristics between the baseline (BASE) and optimised (OPT) HH02 aerofoils (continued).

Chapter 9

Rotor Blade Optimisation

This chapter focuses on the application of the adjoint-harmonic balance optimisation framework to a real-life rotor blade design, the AH-64A rotor blade. Firstly, the context of the research is reviewed, along with the baseline AH-64A rotor blade design. Next, the AH-64A blade is optimised in hover using the steady adjoint solver. Following this, an optimisation study is performed in forward flight, whilst constraining the key features that led to improvements in hover performance. The final blade design is also validated using time-marching calculations.

9.1 Introduction

The main aim of the present chapter is to assess the application of high-fidelity CFD in conjunction with optimisation methods for the design rotor blades in hover and forward flight. The adjoint-harmonic balance optimisation framework, outlined in Chapter 3, High-Fidelity Rotor Optimisation Framework, is used as an efficient approach of capturing the Navier-Stokes flow physics whilst minimising the computational costs. As examined in the literature survey, one of the objectives of the present is to examine rotor blade design at high blade loading, leading to the selection of the AH-64A blade as the baseline blade for the optimisation study. As shown in Chapter 7, the AH-64A blade suffers from a strong shock in hover at higher collective angles. In forward flight, at moderate advance ratio and high loading, an advancing blade shock is present along with a weak dynamic stall on the retreating side. The optimisation process is ultimately assessed against the ability to remove or weaken these adverse flow features. However, it must be highlighted, that the optimisation process is highly dependent on the parameterisation, objective function and trim constraints. Therefore, while the obtained designs provide a certain insight into favourable rotor design features, the optimised designs could potentially be improved further, which is elaborated on further, throughout the analysis of the optimal blade designs.

9.2 Optimisation in Hover

9.2.1 Optimisation Setup

Firstly, the AH-64A blade is optimised in hover using the steady-state adjoint solver and the steady state hover formulation. As discussed in Chapter 7.1, Performance Metrics, the Figure of Merit (FoM) metric is avoided as the objective of the optimisation study, due to its dependency on the rotor disk loading. Here, the objective function is reformulated to minimize the power whilst achieving a target thrust coefficient, as follows:

$$\begin{cases} \text{Minimize I} = C_Q \text{ subject to,} \\ C_T = C_{T_{base}} \end{cases} \tag{9.1}$$

This formulation of the objective function ensures that the optimum shape is obtained solely based on aerodynamics and allows to keep the rotor solidity as a free parameter. The increase in lifting capability can then be obtained by extrapolating the optimum power to the available power of the engine. The parameterisation of the blade includes blade twist, chord, sweep and anhedral variables as described in Chapter 3.1.6, Blade Surface Parameterisation, giving a total of 17 design variables. The AH-64A rotor blade is optimised at a single collective angle of 11 degrees, representing a high-lift condition ($C_T = 0.0093$). The same operating conditions and grid size are used, as in the validation study, giving a blade tip Mach number of 0.65 and Reynolds number of 7.98×10^6 and mesh size of 10.7M cells. All subsequent flow solutions in the optimisation study are initialised from the checkpoint file of the baseline AH-64A blade at 120,000 iterations, and are simulated for an additional 30,000 iterations. The first iteration of the optimisation process, therefore, simulates an AH-64A blade with a parabolic tip, labeled as the "Parameterised AH-64A blade". The differences between the baseline and parameterised AH-64A planform shapes are shown in Figure 9.1. The adjoint equations are solved using a nested Krylov-base solver FGMRES-DR(300,100)-GMRES(40). Here, 1000 adjoint iterations are deemed sufficient enough to drive the design in the correct direction, as shown in Chapter 9.2, Adjoint Sensitivity Validation. Full convergence of the adjoint equations was not sought for due to much higher adjoint solution times.

Figure 9.1: Difference between the baseline (in grey) and parameterised (in red) AH-64A blades

9.2.2 Hover Optimisation Results

The design history for the optimisation of the AH-64A blade in hover is shown in Figure 9.2.

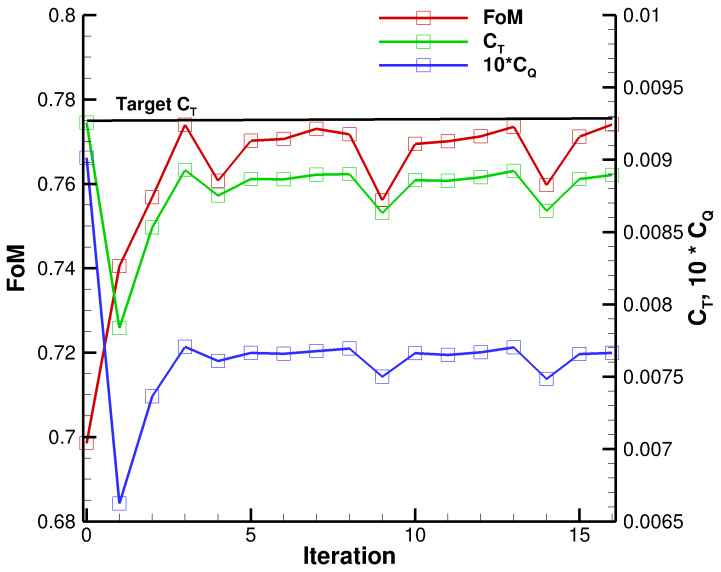

Figure 9.2: Hover optimisation history of the integrated loads with each iteration.

The optimisation history shows that a near optimal blade was obtained after three design iterations. The optimiser then tries to further minimize the power, but goes further away from the target thrust and follows up by reverting to a similar design. The thrust constraint is not fully met due to the highly nonlinear design space and a tolerance imposed on the constraint function. The optimised shape is compared to the baseline AH-64A blade in Figures 9.3-9.4.

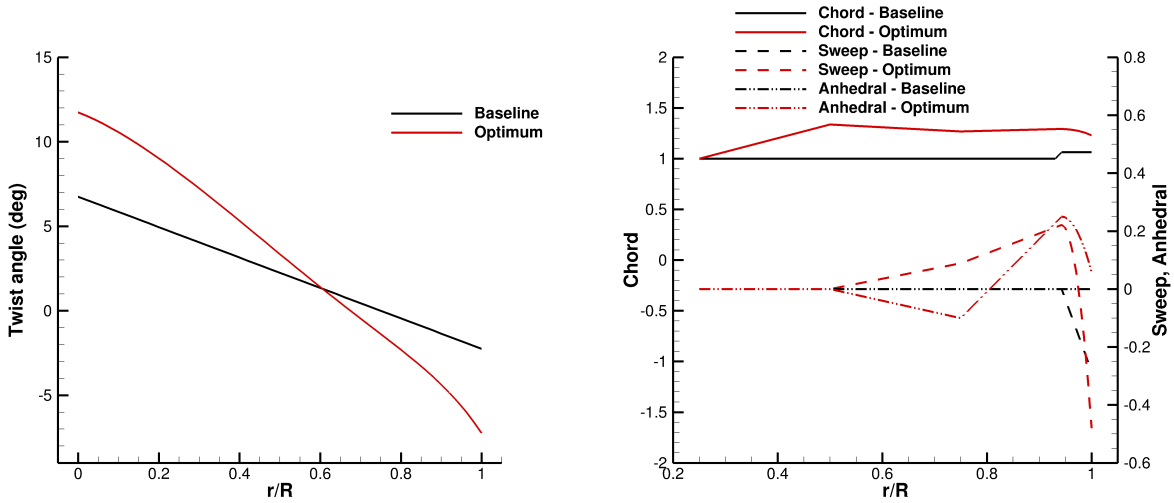

(a) Twist law

(b) Chord, Sweep and Anhedral laws

Figure 9.3: Comparison of baseline AH-64A and hover optimised geometric laws.

(a) Top view

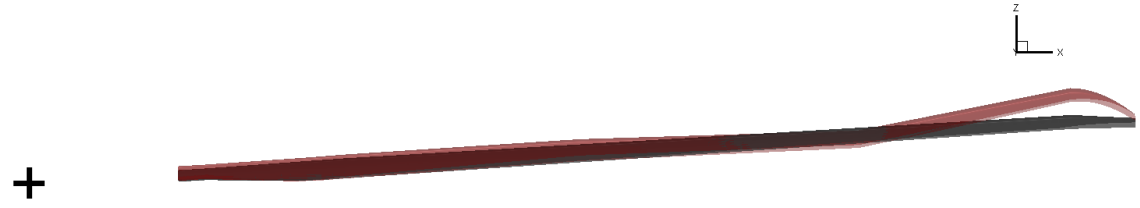

(b) Side view

Figure 9.4: Comparison between the baseline (black) and optimum (red) planform shapes for the AH-64A rotor blade in hover at 11 deg collective.

The new blade design has the maximum available blade twist with the upper and lower bounds reached at the blade root and tip respectively, leading to a close to linear blade twist of -19 degrees. A forward-backward swept blade shape is obtained with a significantly higher planform area than the baseline blade design. This is due to the imposed thrust constraint at a fixed collective. The interaction between the optimum planform shape and the collective angle should be examined further, as part of future work. In hover, higher blade twist is generally favourable for improved hover performance, however, more highly twisted blades, require a higher collective angle to achieve the same thrust coefficient. In this case, the main design feature that recovers the thrust is the high inboard chord, which may be reduced should the collective angle be included within the design parameters. The blade design also has a distinct dihedral-anhedral shape to minimize the interaction of the blades with the preceding blade tip vortices. The integrated loads for the baseline and optimised designs are shown in Table 9.1.

Table 9.1: Comparison of the integrated loads between the baseline, parameterised and optimum AH-64A planforms in hover

Planform	C_T	C_Q	FoM	**FoM difference**
AH-64A Baseline	0.00930	0.000911	0.696	-
AH-64A Parameterised	0.00925	0.000901	0.699	+0.3 counts
AH-64A Optimised	0.00890	0.000766	0.774	+7.8 counts
AH-64A Optimised (re-trimmed)	0.00929	0.000807	0.785	+8.9 counts

A benefit of 7.8 counts (0.01 = 1 count) is seen in FoM for the optimised blade design. A slightly lower thrust coefficient is seen during the optimisation process, hence the blade is re-trimmed to the required thrust. This leads to a benefit of 8.9 counts in FoM at the thrust of

the baseline blade. Based on the design gradients, the largest contributors to the increase in the hover performance are the dihedral-anhedral planform shape and the high blade twist. The exact shape of the planform is of less importance in hover conditions. The surface pressure distributions for the baseline and optimised blades are shown in Figure 9.5.

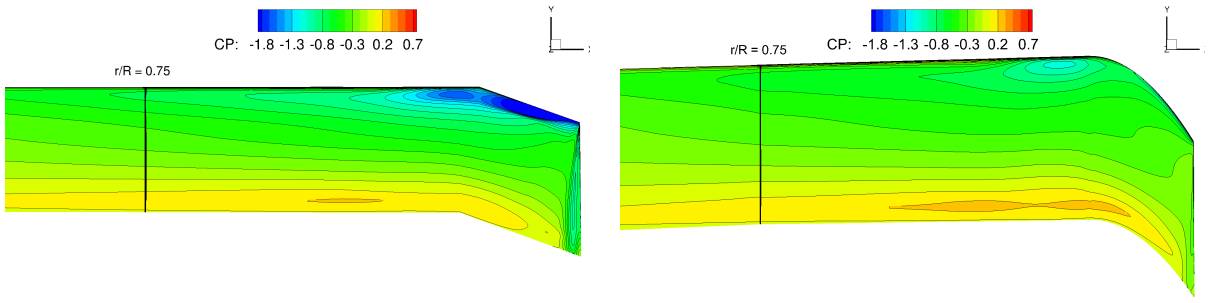

(a) Baseline planform (b) Optimised planform

Figure 9.5: Surface pressure distributions for the baseline and hover optimised AH-64A rotor blades at $C_T = 0.0093$.

The baseline AH-64A blade has a strong shock at 11 degrees collective, which is completely removed for the optimised blade. The new planform shape offloads the blade tip, shifting the load further inboard, leading to a more optimal surface pressure distribution and hence higher performance. This is further confirmed by the sectional load distributions shown in Figure 9.6.

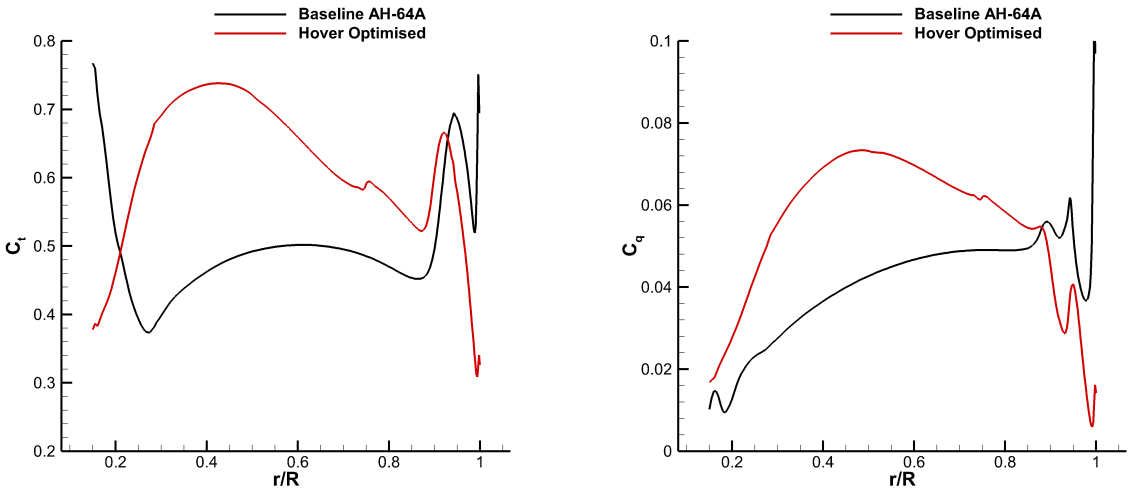

(a) Sectional thrust distribution (b) Sectional torque distribution

Figure 9.6: Sectional loads for the baseline and hover optimised AH-64A rotor blades at $C_T = 0.0093$.

The sectional loads show a significantly higher loading inboard and an offloaded blade tip. This leads to a more optimal loading distribution, and thus leading to a much higher FoM. Finally, the vortical structures are visualised in Figure 9.7.

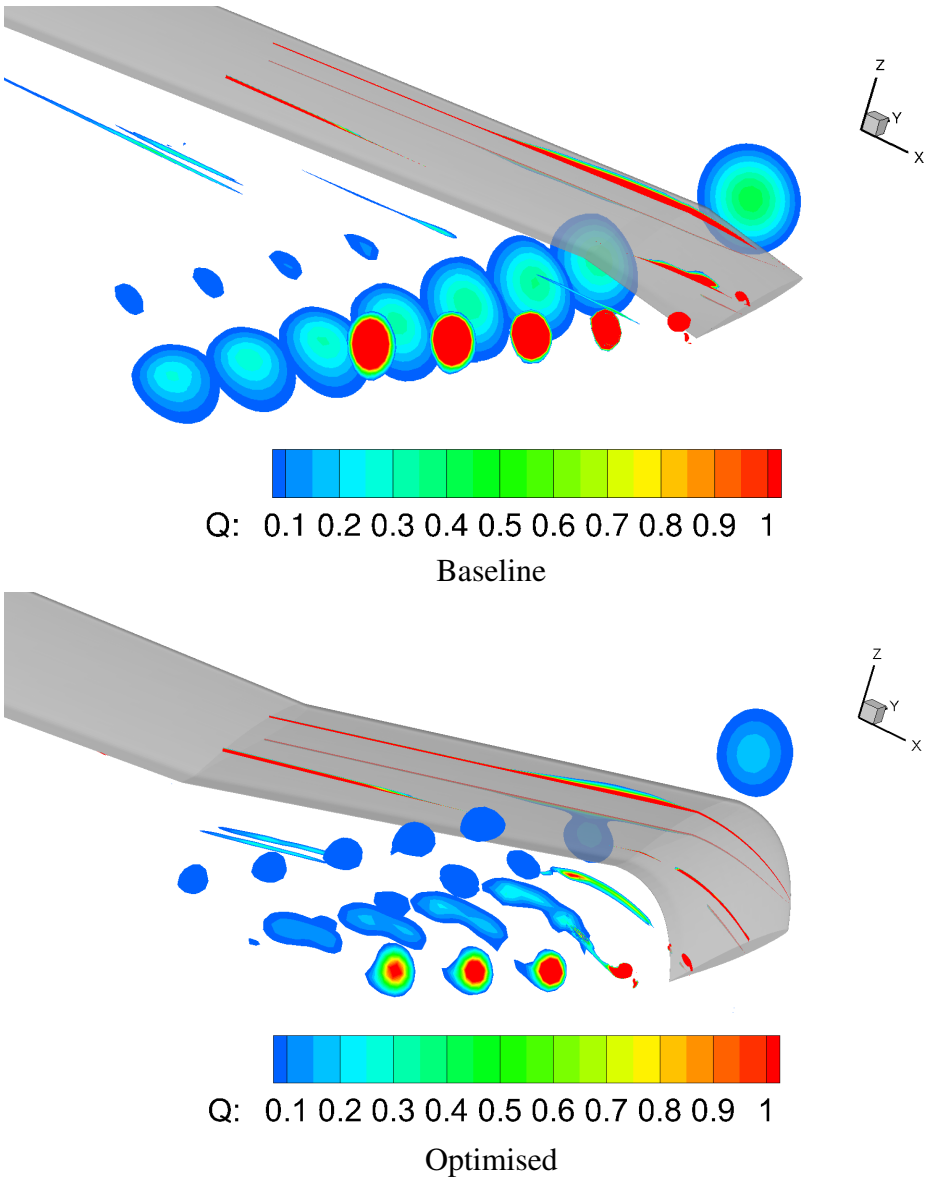

Figure 9.7: Blade tip vortices visualised by contours of Q-criterion (cut-off value of 0.05) for the baseline and hover optimised AH-64A planforms at $C_T = 0.0093$.

The offloaded blade tip produces a much weaker tip vortex, mainly due to the high blade twist and sharp blade tip anhedral. The distinct non-planar dihedral-anhedral shape minimizes the interaction of the blade vortex with the next blade. A discontinuity in the blade shape, however, leads to the shedding of an additional vortical structure where the anhedral starts. The hover optimised blade is analysed in forward flight in Section 9.4, Design Analysis and Validation.

9.3 Optimisation in Forward Flight

9.3.1 Optimisation Setup

The AH-64A blade is also optimised in forward flight using the harmonic balance adjoint framework. The moderate advance ratio, high lift condition of $\mu = 0.3$, $C_T = 0.00903$ used for CFD validation is selected for the optimisation study. In this case, a coarser grid of 13.1M cells is used with two harmonic balance modes. As a four-bladed rotor was used, this leads to a rotor solution snapshot every 18 degrees, with a full capturing of viscous and unsteady wake effects. The starting point for the optimisation process was a rectangular blade with the aerofoils of the AH-64A blade and the dihedral-anhedral distribution of the hover optimised blade. This design feature was carried on through to the forward flight design process as it was the main characteristic of the hover optimised blade that led to hover performance improvements. The same parameterisation was used as in hover, with the anhedral/dihedral parameters kept fixed, leading to 14 design parameters. As the twist design variable gradients were much larger than the other parameters due to radians used as units (5 deg = 0.0872665), the twist design variable bounds were rescaled to <-0.8,+0.8>, giving these design variable values of similar order as the other design parameters. This improved the behaviour of the optimiser in terms of convergence. Similarly as in hover, the optimisation problem was formulated as follows:

$$\begin{cases} \text{Minimize I} = C_Q \text{ subject to,} \\ C_T = C_{T_{base}} \end{cases} \tag{9.2}$$

The control angles were not included as design variables, hence various strategies were examined in terms of treatment of the shape updates and imbalance in roll/pitch caused by the new planform. In particular, simply optimising the design at a prescribed trim state or updating the trim state outside the optimisation loop were proven unsuccessful, as the optimiser typically reverted back to the initial design. This is due to large changes in the pitching and rolling moments caused by planform shape changes. The procedure which saw the best results included a strategy where the rotor was trimmed to the initial thrust coefficient of the new design (typically lower than $C_T = 0.00903$) whilst minimizing pitching and rolling moments. This procedure drove the optimisation process in the correct direction and ensured that the shape is updated based on both the thrust constraint and power objective. The differences in the trim state between design iterations, which are not directly seen by the optimiser algorithm, led to inaccuracies in the Hessian matrix update. For this reason, every few optimiser iterations, the design was re-trimmed to the target thrust of $C_T = 0.00903$, the Hessian matrix was discarded and the optimisation process was restarted. Therefore, the optimiser algorithm used the steepest descent method rather than the SLSQP algorithm in the steps where the Hessian was discarded to update the shape. Another key aspect of the optimisation setup was the lack of any constraints/objectives on the

pitching and rolling moments. Therefore, it can not be stated with full confidence whether the optimiser is driving the design to a better aerodynamic shape or a design that generates rolling and pitching moments that reduce the rotor power. In particular, it was found that designs which generated a positive integrated pitching moment and a rolling moment from the advancing side to the retreating side were beneficial to the rotor power. This is one of the difficulties associated with forward flight rotor optimisation, as the rotor power is actually more sensitive to the rotor trim state rather than the rotor shape. These aspects are considered whilst analysing the optimal design. Finally, the adjoint equations are not fully converged in between design iterations to minimize computational costs, however, as shown in Chapter 8.2, Adjoint sensitivity validation, the gradient values are accurate enough to drive the design in the correct direction.

9.3.2 Forward Flight Optimisation Results

The design history of the forward flight optimisation is shown in Figure 9.8. The thrust and torque coefficient values are normalised by the baseline AH-64A values.

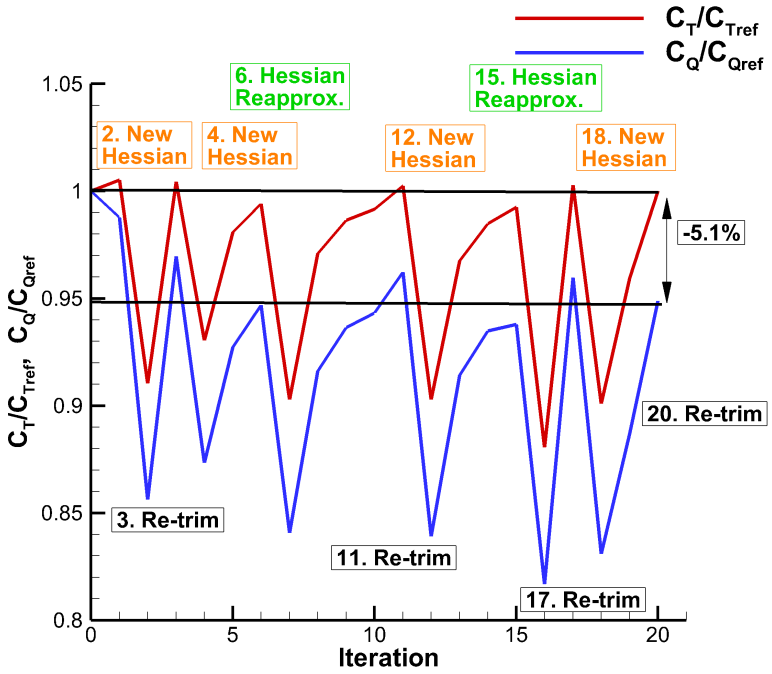

Figure 9.8: Forward flight optimisation history of the integrated loads with each iteration.

The design history shows an improvement of the objective function for the optimisation starting design when compared to the baseline AH-64A blade. A rectangular blade with the hover optimised dihedral-anhedral distribution was used as the baseline design here (iteration 1), leading to a 1.2% reduction in the torque coefficient. During the optimisation history, the optimisation was restarted three times at iterations 3, 11 and 17, by re-trimming the blade to $C_T = 0.00903$ and discarding the approximate Hessian. In all other iterations, the design was trimmed to the new design thrust with minimised pitching and rolling moments. In total, 10

adjoint evaluations were performed during the optimisation process (two for each new Hessian evaluation). As can be seen from the optimisation history, the nature of the SLSQP method leads to a number of function evaluations without a Hessian update. The optimiser typically breaks the thrust constraint by lowering the power, and then tries to recover the design to meet the constraint value. In this case, an optimised design was obtained after 20 design iterations, leading to a power improvement of 5.1% compared to the baseline AH-64A blade. This is significant given that the original aerofoil sections were kept. The final design is analysed in more detail with the geometric laws and planform shape shown in Figures 9.9-9.10.

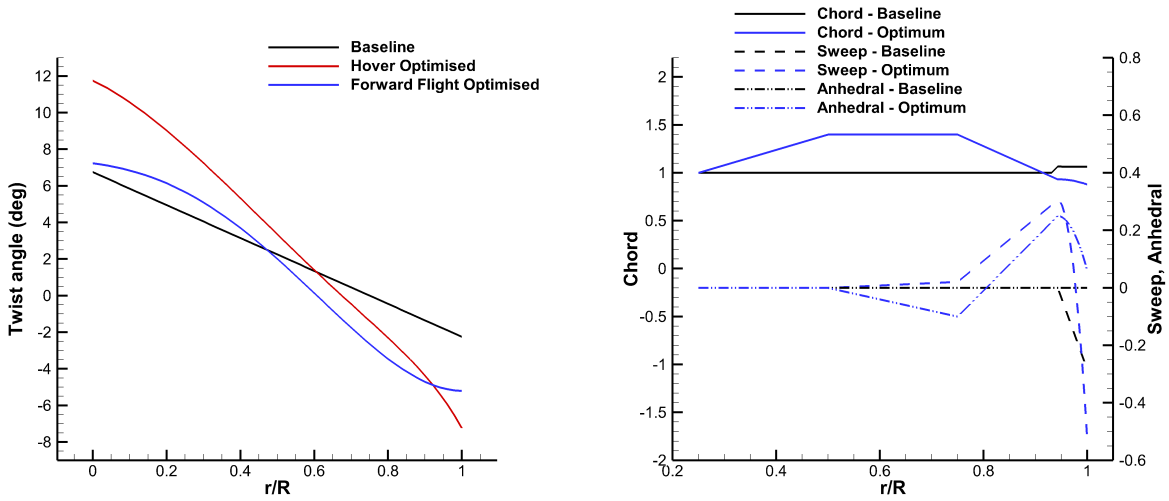

(a) Twist law

(b) Chord, Sweep and Anhedral laws

Figure 9.9: Comparison of baseline AH-64A and forward flight optimised geometric laws.

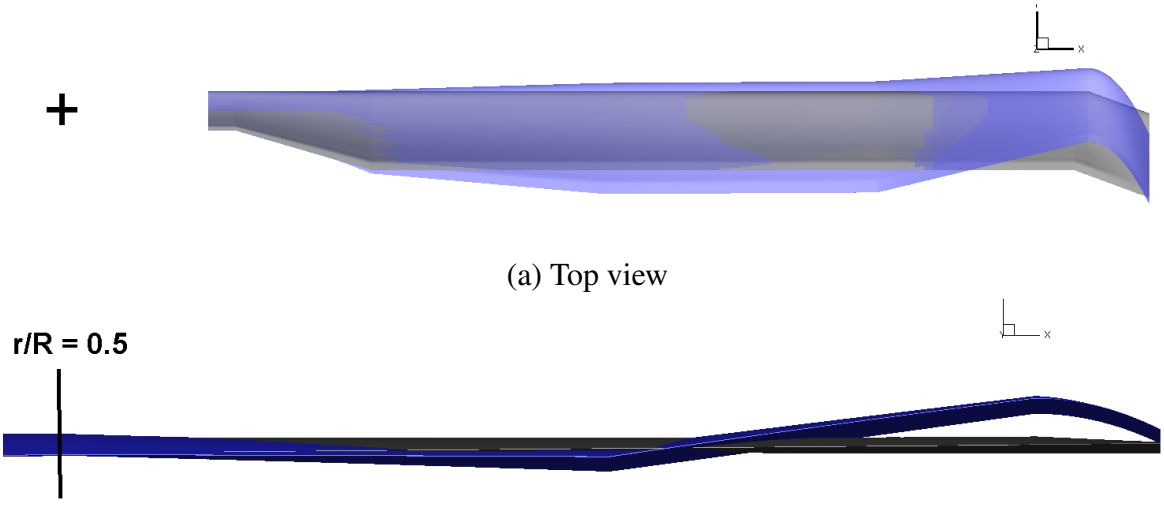

(a) Top view

(b) Side view

Figure 9.10: Comparison between the baseline (black) and forward flight optimised (blue) planform shapes for the AH-64A rotor blade in forward flight at $C_T = 0.00903$, $\mu = 0.3$.

As in hover, the optimiser leads to a design with increased blade twist. The twist slope of the forward flight optimised blade is similar to the hover optimised blade in the region of r/R=0.5 to r/R=0.8 and flattens out towards to blade tip. This feature increases the tip loading when compared to the hover optimised blade, however, the twist value is still significantly increased when compared to the baseline AH-64A design. The inboard twist is similar to the baseline design. Regarding, the chord distribution, the planform achieves the maximum chord inboard with a reduced chord across the blade tip. Compared to the hover optimised blade, the forward flight blade has a significantly lower blade tip area. The forward flight optimised blade also has a forward-backward sweep distribution, which is more aggressive when compared to the hover optimised design. It must, however, be noted that no integrated pitching moment constraints were present in the optimisation process, hence the blade may not be fully balanced in pitch. With each optimisation iteration, an increased forward-backward sweep was seen from one design to the next, with the sweep gradient values increasing with higher sweep angles. The forward sweep at r/R=0.943 indirectly also introduces backward sweep at r/R=1.0 (relative to that section). Therefore, the main reason for the forward-backward sweep may be a faster reduction of compressibility effects at the blade tip. The dihedral-anhedral distribution is retained from the hover design, however, based on the design gradients, blade tip dihedral seems to be more favourable in forward flight. This would, however, potentially lead to a reduction in the blade hover performance. Similarly, as in hover, the final planform shape may be influenced by the non-inclusion of trim variables within the optimisation process. A higher blade twist leads to the production of an unfavourable rolling moment on the rotor power, but is more beneficial aerodynamically, by offloading the blade tip. After re-trimming to the same thrust of the new design and minimizing the pitching and rolling moments, the power goes down further. This is mainly due to a lower longitudinal cyclic requirement for a highly twisted blade. The only features that increase the thrust of the blade are higher blade planform area or by modifying the angle of incidence along the span of the blade (blade twist). The reduced planform area and negative incidence at the blade tip led to a greater reduction in power than reduction in thrust. Hence, increasing the planform area inboard was seen as the main feature that recovers this thrust loss. However, the high planform area inboard may not be optimal, and should trim variables be included within the optimisation process, a better design may be found at a different trim state (for example lower blade area at a higher collective). Despite, the fact that the trim state variables were not included within the optimisation process, the final design still yields a 5.1% power benefit over the baseline blade. The source of the performance improvements is examined further, based on the harmonic balance solutions, by extracting the rotor disk loads shown in Figure 9.11. A comparison is made between the baseline parameterised AH-64A blade (with a parabolic blade tip), starting optimisation blade (rectangular with hover optimised dihedral-anhedral distribution) and the forward flight optimised blade. The loads are scaled by a reference chord equal to the chord of the first aerodynamic section. The M^2C_L and

M^2C_D represent force values normal and tangential directions (non-radial) to the rotor disk plane representing the local lift and drag values uncorrected for downwash effects (hence, thrust and torque/(local radius)).

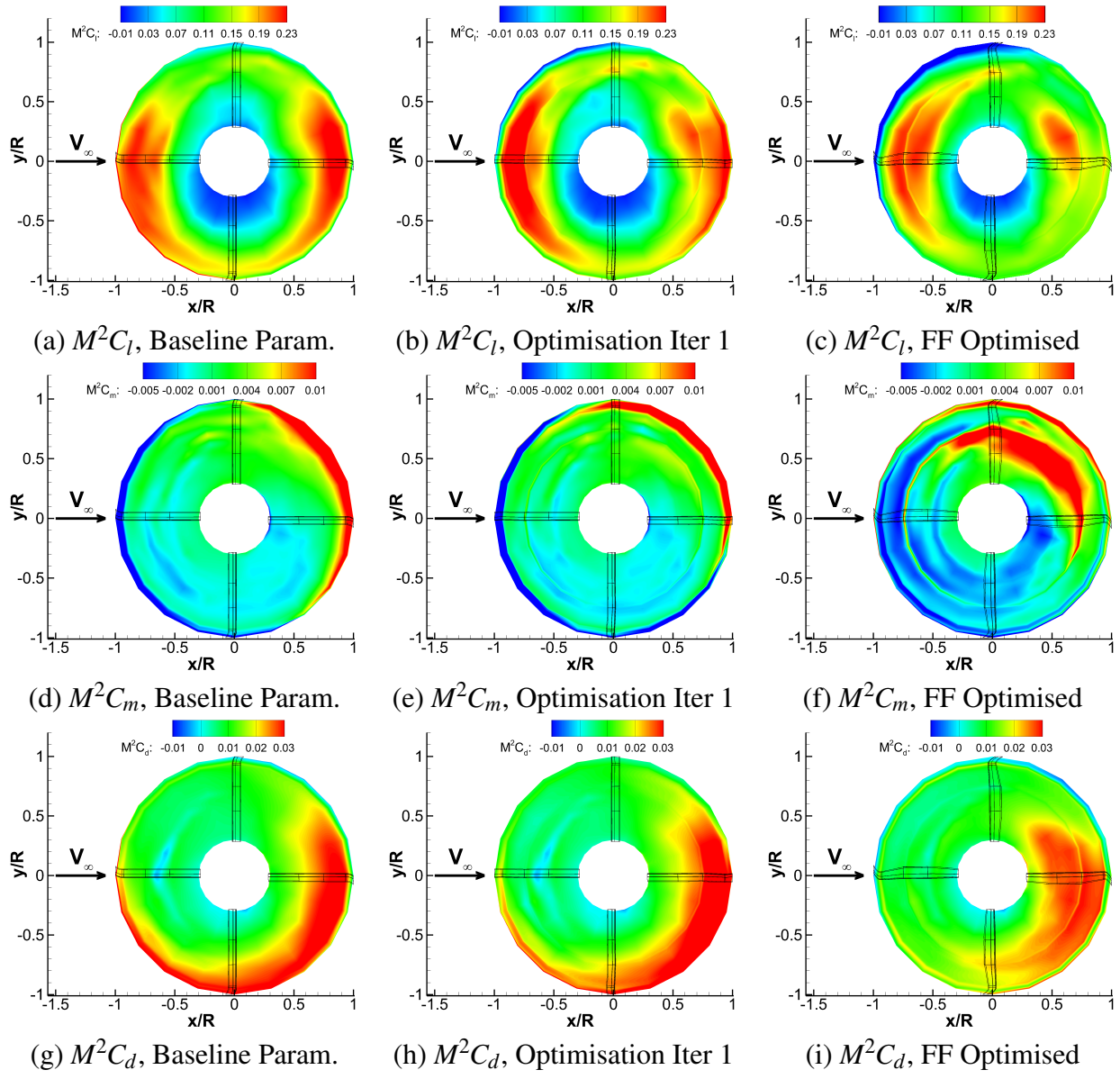

(a) M^2C_l, Baseline Param. (b) M^2C_l, Optimisation Iter 1 (c) M^2C_l, FF Optimised

(d) M^2C_m, Baseline Param. (e) M^2C_m, Optimisation Iter 1 (f) M^2C_m, FF Optimised

(g) M^2C_d, Baseline Param. (h) M^2C_d, Optimisation Iter 1 (i) M^2C_d, FF Optimised

Figure 9.11: Comparison of the rotor disk loads for the baseline parameterised (with parabolic blade tip), optimisation starting blade (rectangular with hover optimised dihedral-anhedral), and forward flight optimised AH-64A rotor blades in forward flight at $C_T = 0.00903$, $\mu = 0.3$ based on two mode harmonic balance solutions.

Firstly, it must be highlighted that loading for the baseline AH-64A blade based on 2 mode harmonic balance calculations is well captured when compared to time-marching calculations (shown in Section 7.4.3, Assessment of the Baseline AH-64A Blade Design, Figure 7.32). The largest differences are seen in the capturing of the negative pitching moment on the retreating side due to the dynamic stall caused by the interaction with the vortex of the preceding blade. The optimisation starting point disk loads highlight the action of the hover optimised dihedral-

anhedral distribution leading to a less loaded blade tip and higher loading inboard when compared to the baseline AH-64A blade. This can especially be seen on the advancing side, where a minor negative lift force is produced at the blade tip. These features are also caused by a different trim state, as the lateral cyclic is increased, leading to higher tip loading at the back of the rotor disk and lower tip loading at the front of the rotor disk. A discontinuity can also be seen in the loading at r/R=0.75 caused by the sharp introduction of the blade dihedral. The blade dihedral-anhedral distribution has a minor impact on the blade pitching moments with the region of negative pitching moment across the blade tip, moving towards the back of the rotor disk. The in-plane force distribution is fairly similar to the baseline blade with a lower in-plane force across the blade tip at the front of the rotor disk and higher in-plane force at the back of the rotor disk across the blade tip. This is primarily due to the higher lateral cyclic required to obtain trim, which may also be one of the reasons behind the improved rotor performance. Comparing the optimisation starting design and the forward flight optimised blade, the most obvious feature is the even more offloaded blade tip. The loading is increased inboard at the front and back of the rotor disk, whereas, the retreating side loading is significantly reduced. A negative lift force is generated on the advancing side at the blade tip. A greater variation in pitching moment is also seen, with the tip having a similar pitching moment behaviour as the optimisation starting point. A sharp positive pitching moment is also seen inboard as the blade moves from the back of the rotor disk to the advancing side. A large region of negative pitching moments can also be observed at the front of the rotor disk and on the retreating side. Finally, the in-plane force loading shows a significantly reduced drag force across the blade tip at all azimuthal stations, which is especially visible at the front of the rotor disk and on the retreating side. At the back of the rotor disk, the region of high in-plane force shifts inboard, following the lift force trends. Based on the harmonic balance solutions, the performance improvement is mostly coming from a redistribution of the loading inboard and offloading of the blade tip. This loading distribution also increases the lateral cyclic but also leads to a reduction in the longitudinal cyclic, leading to a power reduction due to a more uniform angle of incidence across the rotor disk. The trim state differences are analysed further in the next section, and compared with trim states obtained from time-marching calculations.

9.4 Design Analysis and Validation

In this section, time-marching calculations in forward flight are performed to assess the hover optimised blade and validate the forward flight optimised design. Both calculations are performed on the same grid used for CFD validation of the baseline AH-64A blade of 36.1M cells. The forward flight optimised blade is also simulated in hover at a range of collectives and compared to the baseline AH-64A and hover optimised blade at $C_T = 0.00903$. The time-marching calculations are performed for designs with a smoothed dihedral-anhedral distribution, where

sharp changes in curvature were seen, by using a third order Bezier curve between r/R = 0.75 and r/R = 0.943 as shown in Figure 9.12. A comparison of the predicted integrated loads for the baseline, hover optimised and forward flight optimised blades is shown in Table 9.2 in both hover and forward flight conditions.

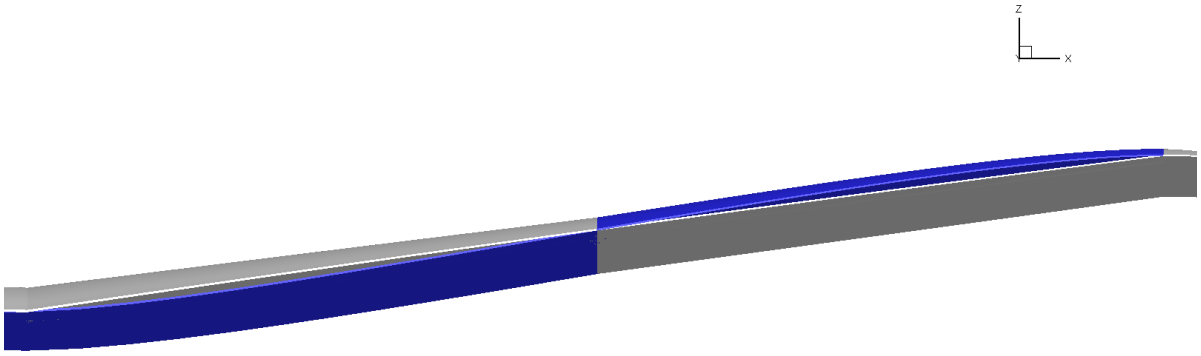

Figure 9.12: Smoothed anhedral distribution using a 3rd order Bezier curve between r/R =0.75 and r/R = 0.943.

Table 9.2: Comparison of the integrated loads between the baseline, hover optimised and forward flight optimised AH-64A planforms. Value in brackets represents performance benefit over baseline blade. A breakdown of the forward flight pressure (C_{Qp}) and viscous (C_{Qv}) torque components are also given.

Planform	**Baseline AH-64A**	**Hover optimised blade**	**Forward flight optimised blade**
Hover Figure of Merit (FoM) ($C_T = 0.0093$)	0.696 (-)	0.785 (+8.9 counts)	0.757 (+6.1 counts)
Forward flight, C_Q ($C_T = 0.00903, \mu = 0.3$)	6.984×10^{-4} (-)	6.866×10^{-4} (-1.69%)	6.529×10^{-4} (-6.51%)
C_{Qp}	6.097×10^{-4}	5.708×10^{-4}	5.462×10^{-4}
C_{Qv}	8.870×10^{-5}	1.158×10^{-4}	1.066×10^{-4}

As previously, discussed, the hover optimised blade leads to a large improvement of 8.9 counts in FoM in hover conditions. A minor improvement of 1.7% is seen in forward flight compared to the baseline AH-64A blade, which is due to a reduction in the pressure torque term through a redistribution of the blade loading due to the action of dihedral-anhedral and high blade twist. The viscous term is increased, which is a result of the more non-planar dihedral-anhedral planform. The forward flight optimised blade sees a slight drop in the hover performance improvement when compared to the hover optimised blade, however, the forward flight performance is improved by 6.5% when compared to the baseline AH-64A. The forward flight optimised blade has a slightly less negative twist angle at the blade tip and reduced tip chord when compared to the hover optimised blade, along with a sharper forward-backward sweep

distribution, leading to a further reduction in the pressure torque term. The viscous torque is also reduced compared to the hover optimised blade, primarily through a lower blade tip area, and lower inboard incidence angles. The performance improvement obtained through time-marching calculations is slightly higher than the optimisation result, due to differences between time-marching and two mode harmonic balance simulations as well as grid sizes (13.1M vs 36.1M cells). The harmonic balance calculations tend to overpredict the turbulent eddy viscosity levels in the wake compared to the time-marching calculations leading to reduced performance improvements between designs (to overcome this a higher number of modes would be required). Differences are also seen in the trim states, shown in Table 9.3. All calculations were within 1% of the required thrust and had close to zero pitching and rolling moments. The trim state differences between the baseline AH-64A, hover optimised and forward flight optimised blades are also analysed.

Table 9.3: Differences in the trim state, between different designs as well as time-marching (TM) and 2 mode harmonic balance (HB) calculations. Note: Negative Fourier series used.

Case	θ_0	θ_{1s}	θ_{1c}
Forward Flight, $C_T = 0.00903$**,** $\mu = 0.3$			
Baseline (TM)	10.413	7.421	-3.072
Baseline (HB)	10.873	7.904	-2.943
Hover Optimised (TM)	10.338	6.012	-4.018
Forward Flight Optimised (TM)	11.330	6.359	-3.855
Forward Flight Optimised (HB)	11.913	6.996	-3.599
Hover, $C_T = 0.0093$			
Baseline	11.0	0.0	0.0
Hover Optimised	11.194	0.0	0.0
Forward Flight Optimised	12.403	0.0	0.0

As can be seen in Table 9.3, the time-marching and harmonic balance calculations have differences in trim state of approximately 0.5-0.6 degrees in collective and longitudinal cyclic. A more extreme trim state is predicted by the harmonic balance calculations, which may reduce (in this case) the obtained performance benefits. Another aspect to highlight is the higher collective required by the forward flight optimised blade compared to the baseline and hover optimised blades to achieve the target thrust. This is due to the significantly reduced blade tip area and a lower inboard blade incidence compared to the hover optimised blade. Similarly, as for the hover optimised blade, however, the trim state for the forward flight optimised blade leads to a reduced longitudinal cyclic angle and increased lateral cyclic, which leads to a more uniform rotor disk blade incidence distribution. These trim state differences between the baseline and optimised designs are primarily due to the much higher blade twist of the hover and forward flight optimised blades, which lead to a shift of loading of the blade inboards. The collective requirement is also higher in hover condition for the forward flight optimised blade when compared

to the baseline AH-64A blade. The trim state was not directly optimised, but will have a large impact on the performance improvement, and should be optimised with the planform shape in the future. The hover and forward flight optimised blades are analysed further by comparing the rotor disk loads with the baseline AH-64A blade, based on time-marching calculations, shown in Figure 9.13. The loads are normalised by the reference chord of 1.0, equal to the chord of the first aerodynamic section.

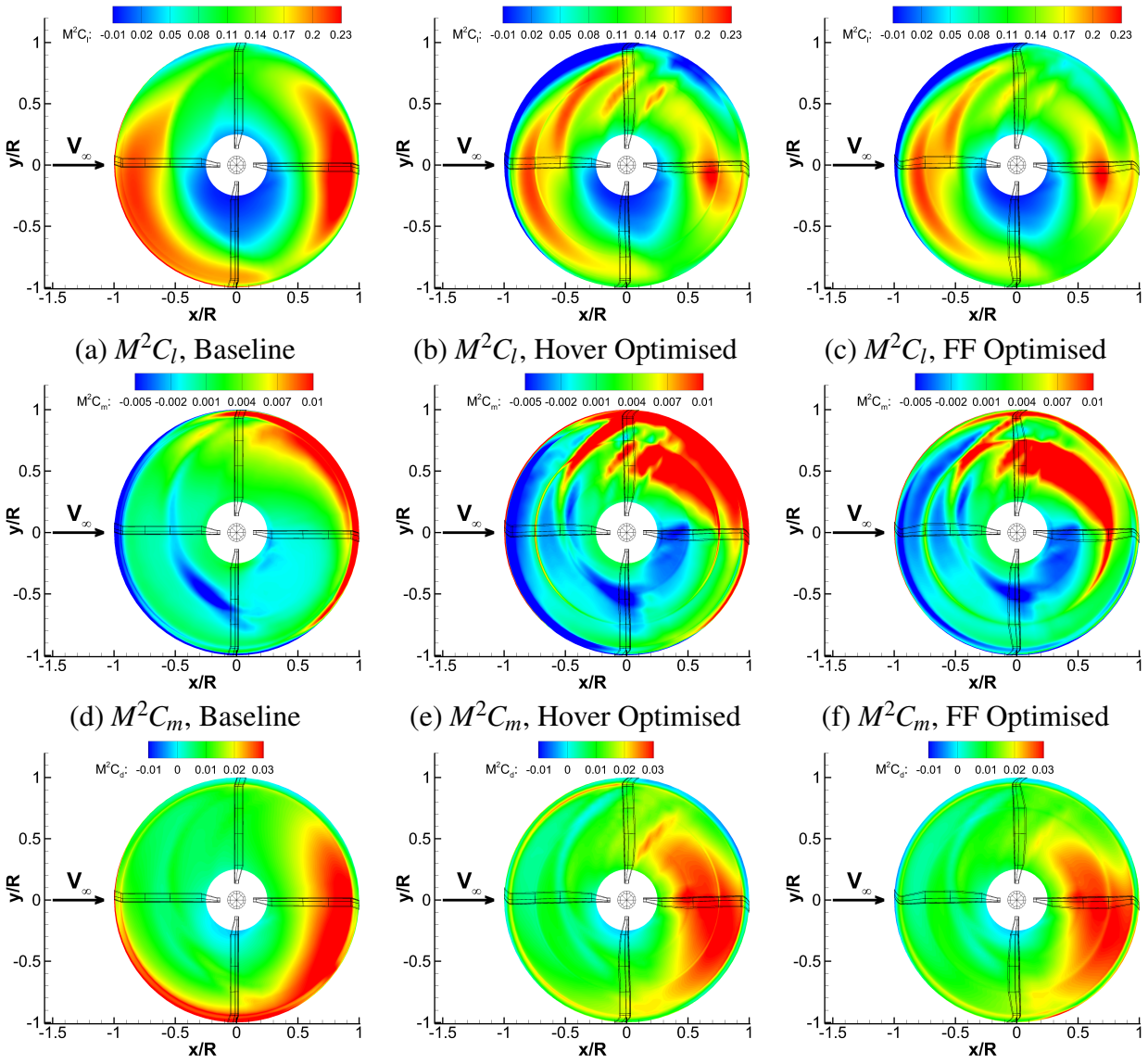

(a) M^2C_l, Baseline (b) M^2C_l, Hover Optimised (c) M^2C_l, FF Optimised

(d) M^2C_m, Baseline (e) M^2C_m, Hover Optimised (f) M^2C_m, FF Optimised

(g) M^2C_d, Baseline (h) M^2C_d, Hover Optimised (i) M^2C_d, FF Optimised

Figure 9.13: Comparison of the rotor disk loads for the baseline, hover optimised and forward flight (FF) optimised AH-64A rotor blades in forward flight at $C_T = 0.00903$, $\mu = 0.3$.

The disk loads indicate the presence of higher-harmonic content in the lift force loading as the blade passes from the advancing side to the front of the rotor disk for the hover and forward flight optimised blade. The magnitude of this harmonic content is weaker for the forward flight optimised blade. This higher frequency effect is not captured well in the harmonic balance

loading for the forward flight optimised blade, as seen in Figure 9.11. The high twist on the hover optimised blade leads to a negative normal force on the advancing side and as the blade passes from the back of the rotor disk to the advancing side. A similar observation can be made for the forward flight optimised blade, with a lower negative loading, due to a reduced twist angle at the blade tip. Similar loading can be seen for the hover and forward flight optimised blades at the front and back of the rotor disk, with a large portion of the load shifted inboard when compared to the baseline AH-64A blade. The optimised designs also have a much larger pitching moment variation compared to the baseline AH-64A blade. Certain discontinuities are also present in the pitching moment solution, due to the introduction of blade dihedral at 0.75R. The main difference between the hover and forward flight optimised blades, is a more negative blade tip pitching moment as the blade moves from the retreating side to the back of the rotor disk. A high positive pitching moment region in between r/R=0.75 and r/R=0.943 as the blade moves to the advancing side is also removed. Finally, the in-plane force distributions show reduced in-plane force at the front of the rotor disk and on the retreating side for the optimised designs when compared to the baseline AH-64A blade. Comparing the hover and forward flight optimised designs, the forward flight blade has a reduced in-plane force on the retreating side and as the blade moves from the back of the rotor disk to the advancing side. A sharp increase is also seen where the anhedral is introduced at r/R=0.943 on the advancing side for the hover optimised blade, which is significantly weaker for the forward flight optimised blade. The findings seen in the disk loads are analysed further by comparing the surface pressure distributions on the advancing and retreating blades, shown in Figure 9.14.

The advancing side characteristics indicate favourable behaviour of the hover optimised blade as the advancing blade shock is completely removed, when compared to the baseline AH-64A blade. The loading is increased inboard due to the higher blade twist, as indicated by the higher suction. The forward flight optimised blade shows a significantly weaker shock compared to the baseline AH-64A blade, however, this shock is not completely removed showing the potential for further improvements. The shock is moved further inboard and moved into the region of the HH02 aerofoil. The manner in which the optimisation was set up, however, maintained the aerofoil shape with chord changes, hence the thickness/chord ratio was maintained. The separation of chord and aerofoil thickness parameters may have increased the chord in this region, leading to a reduced thickness to chord ratio and therefore, potentially removing the shock completely. In this case, as the thickness to chord ratio was held constant, the optimiser reduced to local chord to reduce viscous effects and further offload the blade tip. Therefore, the reduction in blade tip area was found to be more beneficial to the rotor power than complete removal of the advancing blade shock. The forward sweep leads to a weakening of this shock, whereas the actual blade tip carries very little loading. The forward flight optimised blade is also operating at a slightly higher collective, when compared to the hover optimised blade. On the retreating side, the dynamic stall event is moved further inboard for both the hover and forward

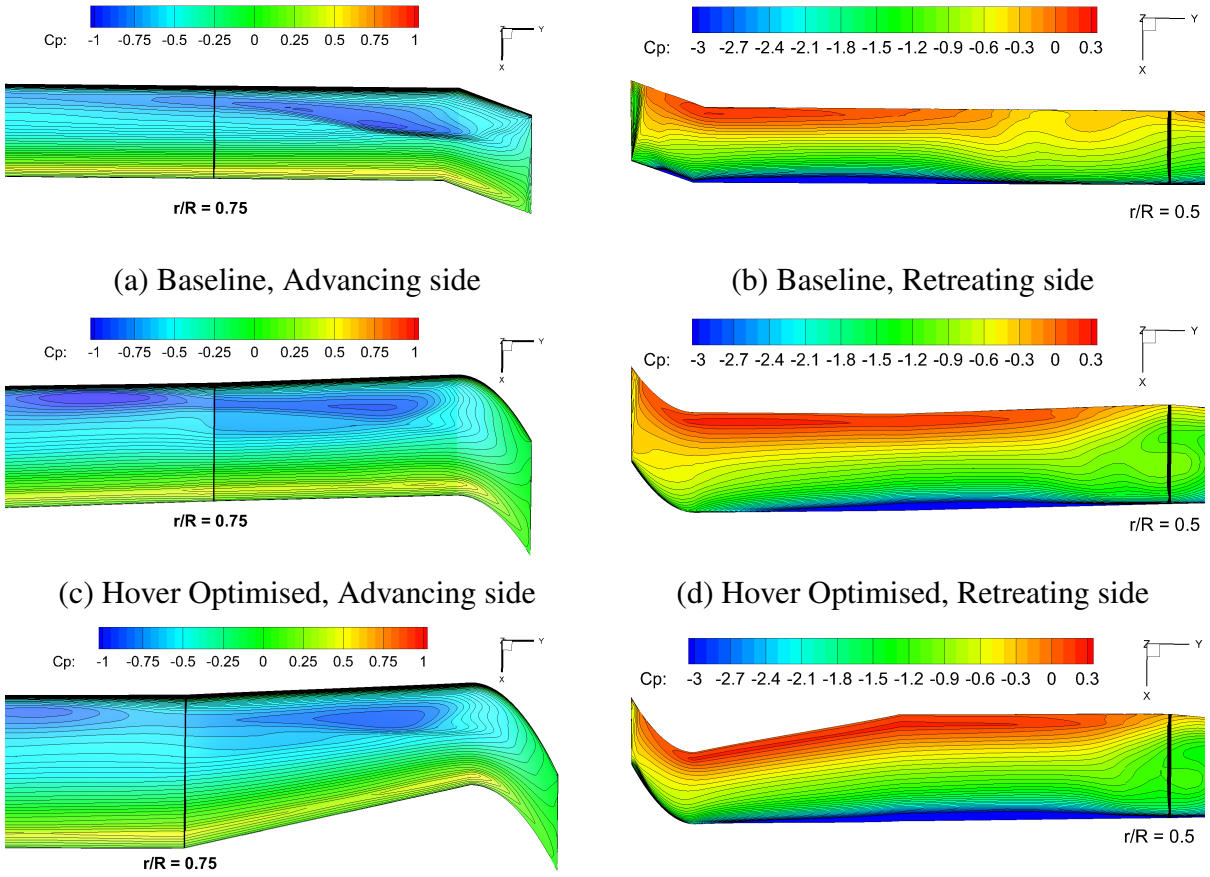

(a) Baseline, Advancing side

(b) Baseline, Retreating side

(c) Hover Optimised, Advancing side

(d) Hover Optimised, Retreating side

(e) FF Optimised, Advancing side

(f) FF Optimised, Retreating side

Figure 9.14: Comparison between the baseline, hover optimised and forward flight (FF) optimised advancing and retreating sides surface pressure distributions at $C_T = 0.00903, \mu = 0.3$.

flight optimised blades. This is primarily due to the offloaded blade tip, leading to much weaker tip vortices which are affected by the mean flow velocity (forward speed + rotation). The retreating side characteristics, however, were not accurately captured during the optimisation as only two modes were used within the harmonic balance calculations, hence the improvement of the retreating side aerodynamics was not a driver of the optimisation process. A higher number of harmonic balance modes would be required (5-7) to optimise a blade with an objective to minimize dynamic stall effects. Similarly, as on the advancing side, the blade tip is also significantly offloaded on the retreating side. Further analysis of the three blades is performed by comparing the azimuthal and sectional loads shown in Figures 9.15-9.16.

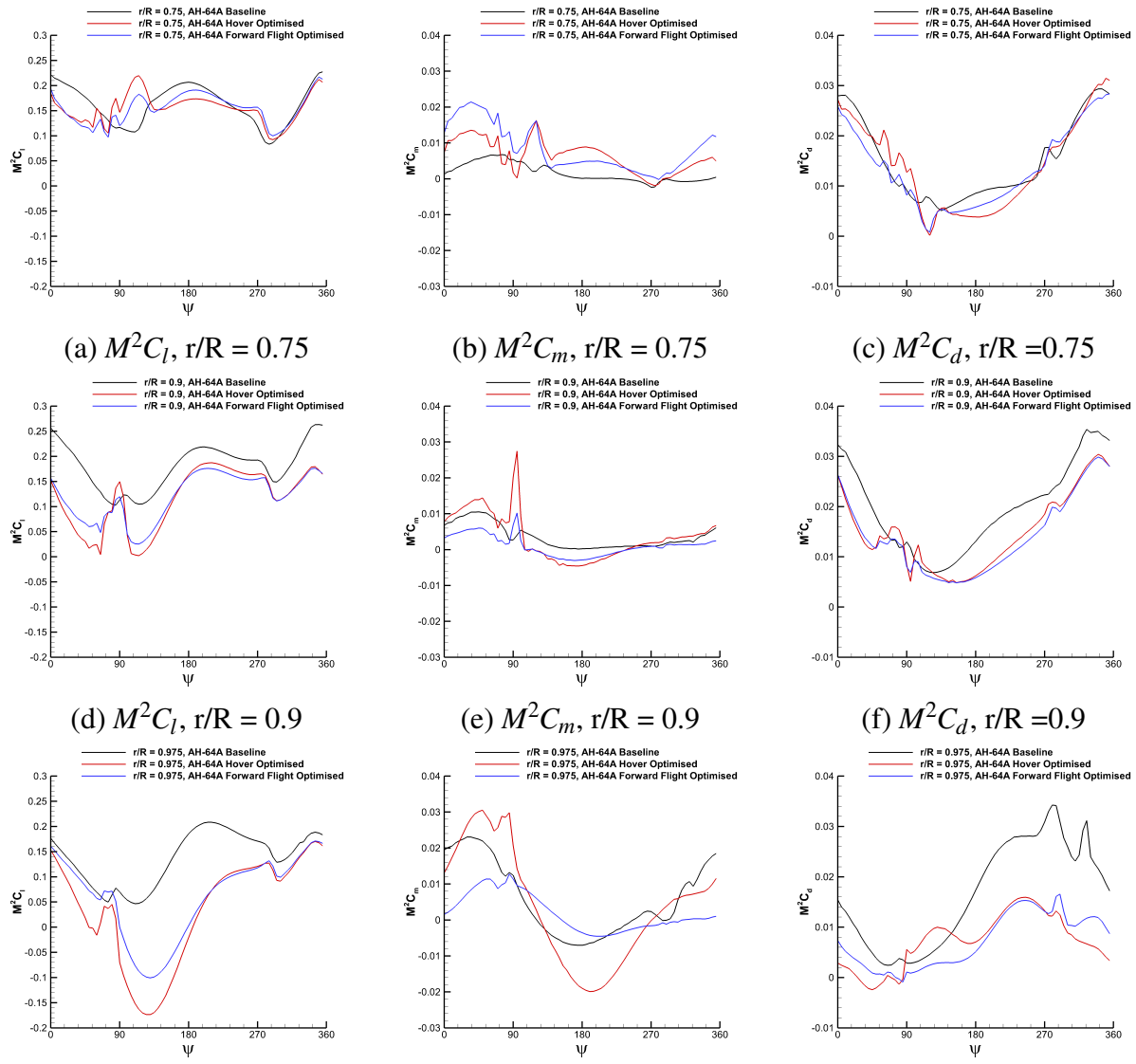

(a) M^2C_l, r/R = 0.75 (b) M^2C_m, r/R = 0.75 (c) M^2C_d, r/R =0.75

(d) M^2C_l, r/R = 0.9 (e) M^2C_m, r/R = 0.9 (f) M^2C_d, r/R =0.9

(g) M^2C_l, r/R = 0.975 (h) M^2C_m, r/R = 0.975 (i) M^2C_d, r/R =0.975

Figure 9.15: Azimuthal loads at three radial stations for the AH-64A baseline, hover optimised and forward flight optimised blades in forward flight at $\mu = 0.3$, $C_T = 0.00903$.

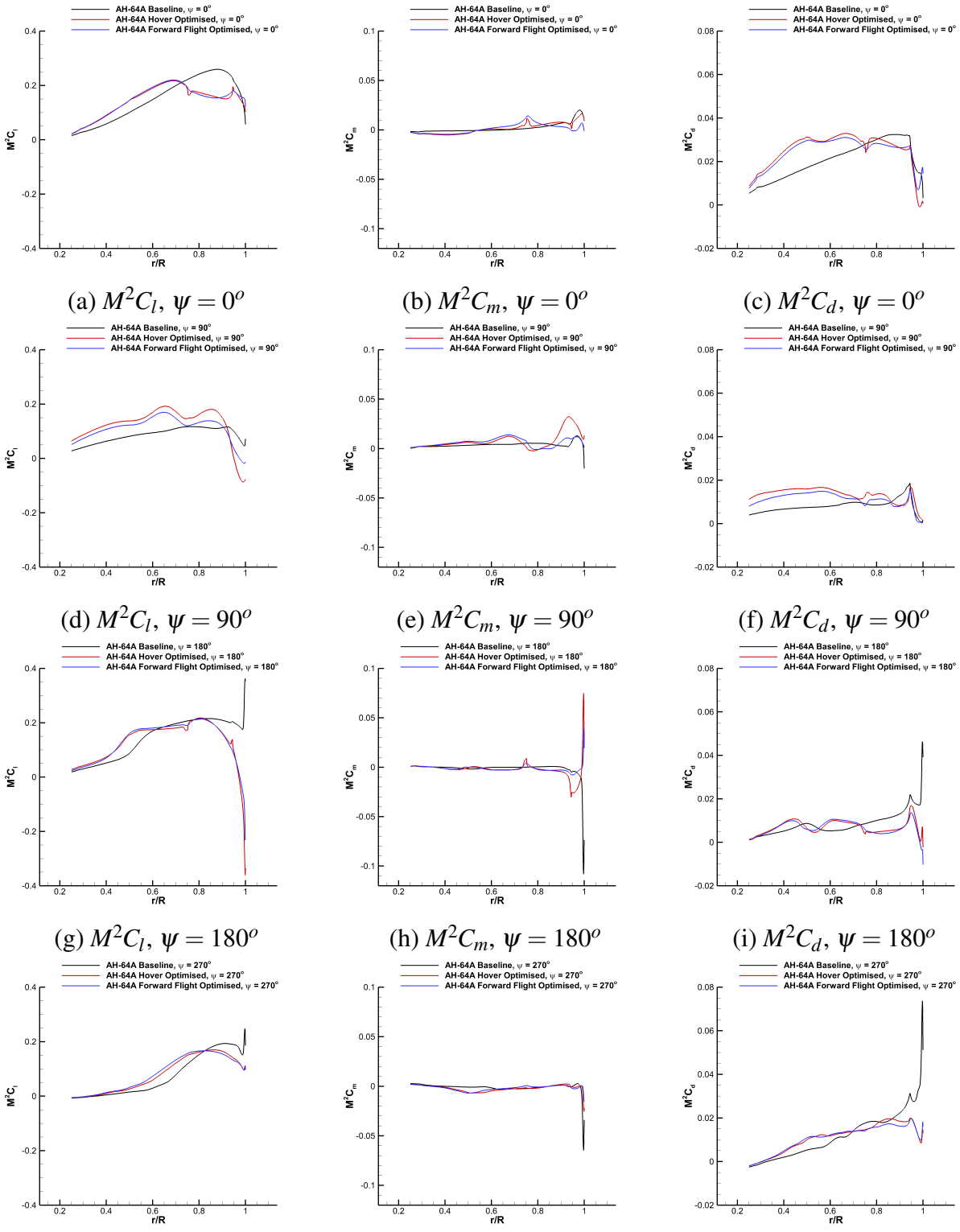

(a) M^2C_l, $\psi = 0^o$ (b) M^2C_m, $\psi = 0^o$ (c) M^2C_d, $\psi = 0^o$

(d) M^2C_l, $\psi = 90^o$ (e) M^2C_m, $\psi = 90^o$ (f) M^2C_d, $\psi = 90^o$

(g) M^2C_l, $\psi = 180^o$ (h) M^2C_m, $\psi = 180^o$ (i) M^2C_d, $\psi = 180^o$

(j) M^2C_l, $\psi = 270^o$ (k) M^2C_m, $\psi = 270^o$ (l) M^2C_d, $\psi = 270^o$

Figure 9.16: Sectional loads at four azimuthal locations for the AH-64A baseline, hover optimised and forward flight optimised blades in forward flight at $\mu = 0.3$, $C_T = 0.00903$.

The azimuthal loads indicate a significantly lower lift force in the blade tip region for the hover and forward flight optimised blades when compared to the baseline AH-64A blade. A significant drop in normal force can be seen for the hover optimised blade as the blade moves from the advancing side to the front of the rotor disk due to the high blade twist and anhedral implemented on this blade. This effect is weaker for the forward flight optimised blade, due to slightly lower blade twist at the tip, and hence higher tip loading. Increased harmonic content can be seen in both normal force and pitching moment plots, especially on the advancing side, for both hover and forward flight optimised blades. These effects, however, also appear to be weaker for the forward flight optimised blade. The forward flight optimised has slightly higher positive pitching moments in the inboard locations when compared to the hover optimised blade, with a reduced peak to peak pitching moment across the blade tip. Compared to the baseline AH-64A blade, the azimuthal in-plane force plots indicate a significantly lower in-plane force at the outboard stations for both optimised blades due to a more offloaded blade tip, with the greatest differences on the retreating side. Compared to the hover optimised blade, the forward flight optimised has a lower in-plane force across the blade tip on the advancing side but slightly higher at the back of the rotor disk. Further inboard, the forward flight optimised blade, has lower in-plane forces at most azimuthal angles, however, the differences are lower. The higher lateral cyclic also leads to a higher in-plane force at the back of the rotor disk and lower in-plane force at the front of the rotor disk, when compared to the hover optimised blade. The sectional loads highlight the effects of highly twisted blades with anhedral, leading to an offloaded blade tip and higher loading inboards. The forward flight blade removes certain negative effects of a highly offloaded blade tip, reducing the negative normal force on the advancing side as well as pitching moment variation. The in-plane force values generally follow the trends of the lift force observations. The reasons for the increased harmonic loading of the hover and forward flight optimised blades are examined further by extracting the wake visualisations using Q-criterion (value of 0.002), shown in Figure 9.17.

The offloaded blade tip of the hover and forward flight optimised blades leads to a significantly weaker tip vortices which interact with the next blade leading higher harmonic content rotor loads. As can be seen from Figure 9.17, further flow structures are shed from the blade, including multiple vortices due to the sharp dihedral-anhedral distribution. This is especially visible as the blade moves from the advancing side to the front of the rotor disk, where multiple blade vortex interactions are seen. The flow fields are very similar for the hover and forward flight optimised blades, hence the changes in loading are not a result of different flow features, but are directly an effect of different twist distributions and reduced tip planform area for the forward flight optimised blade. The exact increase in the oscillatory forcing is examined by extracting thrust force harmonic content, shown in Figure 9.18.

The 4/rev harmonic of the lift force is slightly increased for the hover optimised blade which is the main indicator of vibration. A slightly reduced value is seen for the forward flight opti-

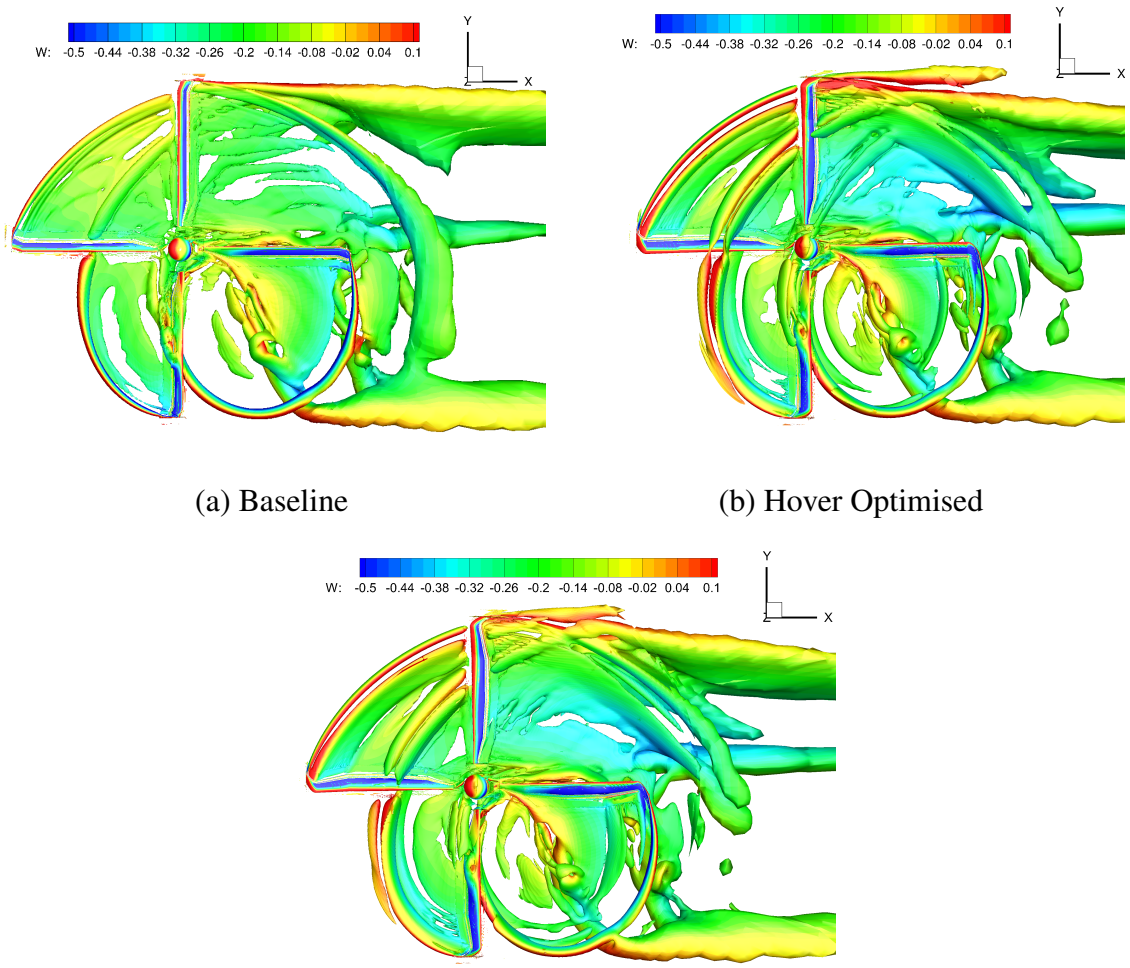

(a) Baseline

(b) Hover Optimised

(c) Forward Flight Optimised.

Figure 9.17: Rotor wake visualization for baseline, hover optimised and forward flight optimised AH-64A rotor blades in forward flight at $C_T = 0.00903$, $\mu = 0.3$ using an isosurface of Q-criterion (value of 0.002) coloured by downwash velocity W.

mised blade when compared to the hover optimised blade. The other lift forcing harmonics do not contribute to the fuselage vibration as they cancel each other out for a 4-bladed rotor, but can for example affect the blade root stresses. The new forward flight optimised blade design leads to an increase in the 1/rev and 3/rev harmonic but a reduction in the 2/rev harmonic. However, no objectives or constraints were imposed on such design requirements in the present study, hence this result is not unexpected. To capture higher frequency content a high number of harmonic balance modes would have to be included within the optimisation, leading to excessive computational costs.

The forward flight optimised design is also assessed in hover to ensure that the new design does not lead to a significant reduction in hover performance. The torque coefficient and figure of merit curves versus thrust coefficient are compared for the baseline and forward flight optimised

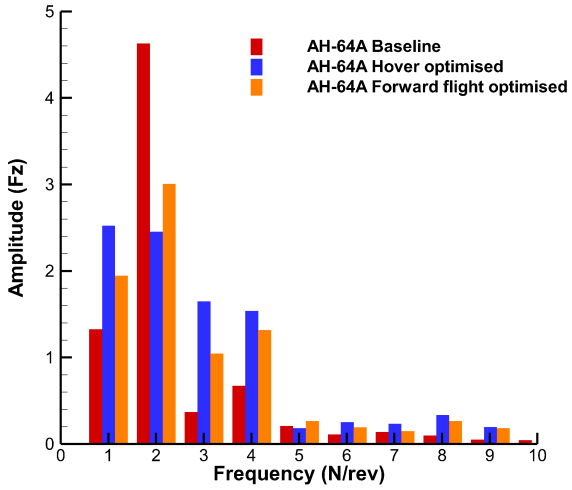

Figure 9.18: Vertical force vibratory components for the baseline, hover optimised and forward flight AH-64A rotor blades

blades in Figure 9.19.

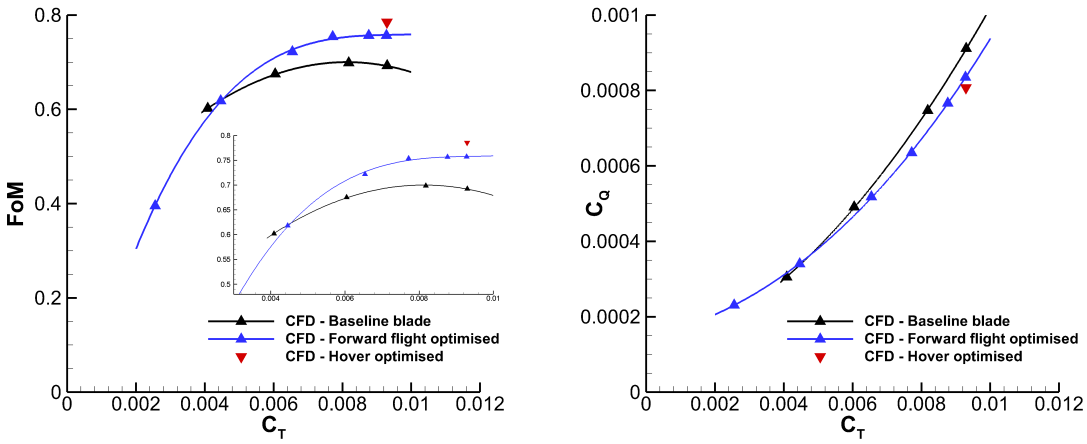

(a) *FoM* vs C_T (b) C_Q vs C_T

Figure 9.19: Comparison of the hover performance for the baseline and forward flight optimised AH-64A rotor blades.

The hover performance curves indicate a significant performance improvement over the baseline AH-64A blade, especially at higher thrust coefficients. The curve for the optimised blade shows a flatter FoM curve, with the peak FoM moved to a higher thrust coefficient. This is typical of rotors with higher solidity. However, as the objective function was to minimize power, the increased solidity is a feature of the optimal aerodynamic design. The forward flight optimised blade design sees a deterioration of 3 counts in FoM at $C_T = 0.0093$, compared to the hover-only optimised blade. This is primarily due to the fact that forward flight optimised blade requires a higher collective to achieve the target thrust when compared to the hover optimised and baseline AH-64A blades, due to the reduced blade tip area, and the reduced inboard

blade twist when compared to the hover optimised blade. At a constant torque coefficient the benefit in lifting capability can be seen from Figure 9.19 b). The evaluation of the forward flight optimised blade in hover is continued by examining the surface pressure distributions at $C_T = 0.0093$, shown in Figure 9.20.

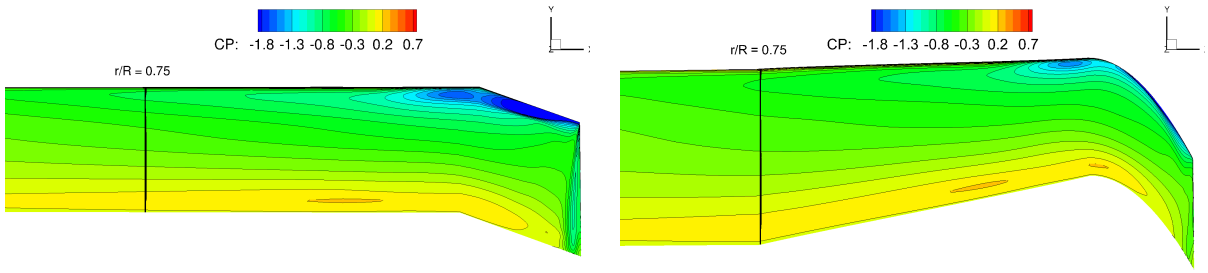

(a) Baseline planform (b) Optimised planform

Figure 9.20: Surface pressure distributions for the baseline and forward flight optimised AH-64A rotor blades at $C_T = 0.0093$.

Compared to the baseline AH-64A blade, the forward flight optimised blade has a much more favourable pressure distribution. Before the initiation of the swept tip, the region of high suction is significantly reduced. Across the parabolic blade tip, a very small region of high suction is seen with the formation of a weak shock. This feature is significantly weaker compared to the strong shock seen for the baseline AH-64A blade, however, this is the main reason behind the reduced hover performance compared to the hover optimised blade (surface pressure distribution seen in Figure 9.5 (b)). The combination of the lower blade tip area and higher collective angle lead to the performance deterioration. The effect on the sectional loading is examined in Figure 9.21.

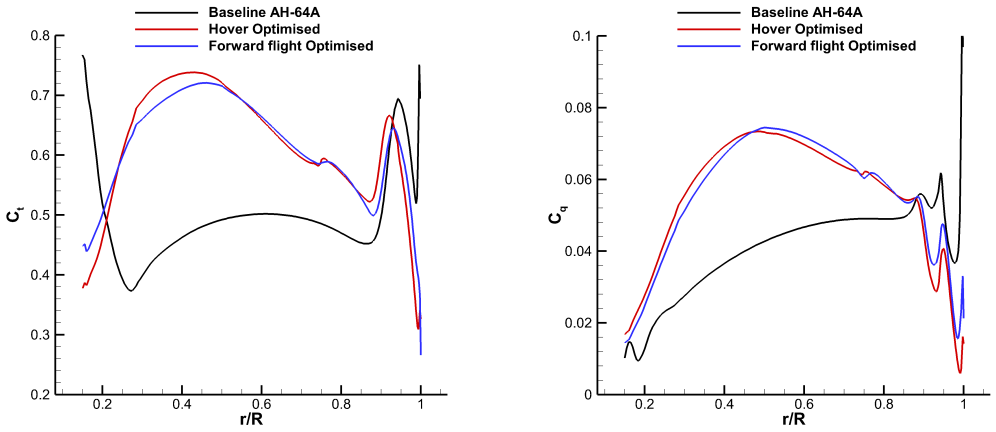

(a) Sectional thrust distribution (b) Sectional torque distribution

Figure 9.21: Sectional loads for the baseline, hover optimised and forward flight optimised AH-64A rotor blades at $C_T = 0.0093$.

The sectional loads for the forward flight optimised blade exhibit similar features as for the hover optimised blade, but to a lesser degree, when compared to the baseline AH-64A blade. The blade tip for the hover and forward flight optimised blade designs is more offloaded with a larger portion of the load moved inboards. The forward flight optimised blade tip is slightly more loaded than the hover optimised blade, due to the reduced blade twist angle at the tip (loads are scaled by reference chord of 1.0), which leads to a higher torque across the blade tip for the forward flight optimised blade.

Chapter 10

Conclusions and Future Work

This thesis examined aspects of advanced rotor blade design based on high fidelity computational dynamics in conjunction with optimisation methods. Two key phases of the research can be identified: the CFD validation phase and the rotor design phase. The CFD validation phase was aimed at assessing the sensitivities of different modelling aspects on the accuracy of the CFD performance predictions at modest computational costs. The rotor design phase focused on determining the key design features of a rotor blade that contribute to performance improvements in hover and forward flight. To examine the rotor design sensitivities a novel fully-turbulent overset adjoint harmonic balance optimisation framework was developed and demonstrated in a rotor design optimisation study. The conclusions and suggestions for future work from the present research are outlined in the next subsections.

10.1 Conclusions

During the validation phase, a number of rotor blades were simulated in hover and forward flight, including the LBL, LBERP, PSP and AH-64 blades, showing very good agreement of the performance predictions with experimental data, using modest computational resources. The sensitivity of several geometric and numerical modelling parameters was assessed and for the majority of cases, was found to be lower than the experimental data scatter. The high data scatter and the presence of only integrated loads in many experimental data sets calls for higher quality and more accurate experimental data to improve the fidelity of CFD predictions. For this reason, the use of higher fidelity representations of the rotor flow field than in the present research, such as the use of DES turbulence models or finer meshes may not be fully justified.

Regarding the hover modelling sensitivities, the use of different turbulence models and the steady state hover formulation was not seen to have a large effect on the performance predictions. The effect of the turbulence production limiter was found to be moderate leading to reduced power by reducing the turbulent eddy viscosity ratio levels in the rotor wake. Transitional effects were found to be greater than other numerical modelling parameters, however, are not

expected to have such a high impact in real flight scenarios due to greater freestream turbulence, gusts, vibration and presence of the erosion shield, when compared to idealised wind-tunnel conditions. The need for inclusion of transitional effects will, therefore, be case dependent, based on the experimental setup. A detailed experimental blade geometry definition is also key for CFD validation studies, as seen for the LBERP blade, where a high geometric rotor performance sensitivity was found between the Glasgow and TTCP geometries. In general, however, good agreement with experimental data can be obtained using the steady state hover formulation with a grid of around 10 million cells and the k-ω SST turbulence model.

The forward flight modelling sensitivities indicated a low impact of grid refinement and farfield wake resolution on the rotor loads. The effect of the turbulence production limiter was determined to be greater than in hover, due to improved resolution of the multiple near-blade vortex interactions, with a similar effect on the rotor power and turbulence flow field as in hover. This sensitivity, however, was reduced at higher advance ratio's. Installation effects were found to have a minor impact, leading to a slight reduction in rotor power. In general, good agreement with experimental data can be obtained for rotors in forward flight for grid sizes of approximately 30-40 million cells using the k-ω SST turbulence model, with low advance ratio cases requiring additional treatment of the rotor wake to reduce the turbulence eddy viscosity levels, such as a turbulence production limiter or rotational correction.

Based on the validation results, the standard performance metrics and use of the thrust-weighted solidity parameter were examined for comparing different rotor designs, along with a preliminary investigation of rotor design feature sensitivities. The figure of merit and lift-to-drag ratio metrics have their limitations when comparing rotors at different rotor disk loading, net thrust and blade tip Mach number. For such comparisons, operating in dimensional units such as net thrust and power provides more insight.

The blade solidity of the LBL and LBERP blades study proved that the definition of thrust-weighted solidity is misleading. Matching of thrust-weighted solidity between two blade designs will always favour the blade with a lower blade area across the blade tip in terms of stall envelope, due to a larger chord inboard. The comparison of different rotor designs should be performed based on nominal solidity (based on the chord inboard of the blade tip) to correctly predict the rotor stall envelopes solely based on the aerodynamic planform shape.

The preliminary design sensitivity analyses based on the CFD validation results showed that advanced planforms require computational optimisation as the geometric design features have a large impact on the flow features across the blade planform leading to changes in loading distribution, and hence performance. In hover, highly-twisted blades with a lower blade tip Mach number such as the PSP blade, were found to achieve higher figure of merit values. Blade tip anhedral was also found to be highly beneficial in hover, acting in a similar manner as additional blade twist, by redistributing the loading inboard and offloading the blade tip, leading to the production of a weaker tip vortex. The hover performance was also highly dependent on the clean

formation of the tip vortex which as seen in the comparison of the Glasgow and TTCP LBERP geometries. The forward flight advancing side analyses confirmed the beneficial qualities of a BERP-like geometry with a notch feature which prevents propagation of the advancing blade shock onto the blade tip through a reduction in thickness to chord ratio. Similar qualities, however, were observed for a rectangular blade through a sharp reduction in aerofoil thickness. On the retreating side, evidence of a notch vortex for the LBERP geometry was also seen, leading to reduced separation across the blade tip. The rotor blade planform geometric features were found to alter the rotor disk loading and pitching moment distributions in forward flight, leading to potential performance benefits.

The rotor design phase examined favourable rotor blade planform features in greater detail through the use of optimisation methods. For this purpose, an adjoint harmonic balance optimisation framework has been developed, enabling high-fidelity unsteady optimisation at moderate computational costs. The harmonic balance method was able to give an accurate representation of the rotor blade loading variation in forward flight with only a few harmonic balance modes at significantly lower computational costs making it a promising alternative to time-marching simulations. The adjoint implementation has also been verified by comparing the obtained gradients with finite differences, giving reasonable agreement, and leading to an efficient computation of the design sensitivities, at a cost of a base flow solution.

The present rotor design study showed the benefits of using a high fidelity CFD method in conjunction with optimisation methods. Various rotor design sensitivities were highlighted that would not be accurately represented if a lower fidelity method was used within the optimisation framework. In particular, high blade twist and a non-planar dihedral-anhedral planform were found to be the main drivers behind performance improvements in hover, with the exact planform shape (chord, sweep), being of less importance. In forward flight, increased blade twist is also beneficial in terms of rotor power, however, a non-linear distribution with a flattening of the twist curve towards the blade tip is preferred. In forward flight, the blade planform was found to be more important than in hover. The optimal chord distribution leads to higher inboard chord with a reduced blade tip area, which leads to a more optimal loading distribution and reduced profile power. A forward-backward sweep distribution maximises the possible backward tip sweep, leading to a reduction in compressibility effects. Although in this case, no constraints were imposed on the blade integrated pitching moment. The blade dihedral-anhedral distribution was not found to have a large impact on the rotor power in forward flight, however, the exact distribution should also be optimised in forward flight. The highly offloaded blade tip along with the sharp dihedral-anhedral distribution also led to higher harmonic loading, however, this aspect was not considered within the optimisation study and could be minimised by slightly higher blade tip loading and a smoother non-planar planform shape. Both hover and forward flight optimised blades featured certain similarities, as both optimisations led to designs with a highly offloaded blade tip and increased inboard loading. Forward-backward sweep was

found to be beneficial in both hover and forward flight, although this design feature had a lower impact in hover. Therefore, based on the current optimisation study, the hover and forward flight conditions are not as conflicting as typically reported in literature. Based on past designs seen in literature and the findings within the present optimisation study, a summary of past, present and a prediction of future rotor design features are shown in Table 10.1.

Table 10.1: Summary of rotor design features utilised in the past (1st,2nd,3rd generation), present (4th generation) and in the future (5th generation).

1st generation (1950s-1960s)	Rectangular planform, Examples: Bell UH-1, AH-1 Cobra, BO-105
2nd generation (1970s-1980s)	Swept and/or tapered blade tips (linear distribution), typically low blade twist (8-10 degrees) and rarely high blade twist (UH-60A), Examples: AH-64, S-76, UH-60A, A129; NOTE: BERP planform seen as ahead of its time, still relevant today due to highly advanced shape.
3rd generation (1990-2000s)	Swept, tapered blade tips sometimes with anhedral (non-linear distribution, typically parabolic), rarely non-linear inboard chord distribution, increased blade twist (10-14 degrees), Examples: AW139, S-92, EC145, EC225, Bell 429
4th generation (2010s)	Non-linear chord distribution along the whole planform with swept-anhedral blade tips (AW169, AW189, CH-53K), forward-backward sweep (the only example is the BLUE-EDGE blade, H160), dihedral-anhedral distribution (the only example is the ACRB blade, CH-47)
5th generation (2020 onwards)	High blade twist (15-20 degrees) with aeroelastically tailored blade deformation, wider use of non-planar planforms (dihedral-anhedral) and forward-backward swept planforms, morphing planform shapes and novel blade tip concepts (example: split winglet tip of Bell)

The present optimisation study was able to correctly identify favourable rotor design features that have only emerged in the past 10 years, including a forward-backward swept planform, as seen on the Blue-Edge blade utilised on the H160 helicopter and a dihedral-anhedral distribution as seen for the ACRB blade for the CH-47 aircraft. These are the only examples of rotor designs in industry that utilize these attributes. A wider use of these design characteristics is likely to be seen in the future. The use of non-planar planform designs apart from tip anhedral is not well researched with great potential offered by minimizing the blade vortex interactions in many flight conditions. The reduced blade tip area and tip anhedral are fairly standard today, and were also a result of the present optimisation study. Future blades are also likely to have a higher blade twist which would be adaptable through a passive pre-designed blade deformation through aeroelastic tailoring. Till date, highly twisted rotor blades with large offsets off the blade feathering axis have been avoided due to effects on structural loads and vibration. The

significant developments in coupled aerodynamic, structural and dynamic codes over the past years are, however, a key enabler of these more advanced planform features to be utilised more widely in the future.

Regarding, the methodology used in the present optimisation study, various observations can be made. The final planform was found to be dependent on the treatment of trim as the rotor control angles were not directly included within the optimisation process. Based on the present work, designs that achieve the target trim state at lower longitudinal cyclic and higher lateral cyclic angles are found to have higher performance, due to a more uniform angle of incidence across the rotor disk. The exact interplay between rotor collective, planform area and blade twist is not fully accounted for. With the inclusion of these features, however, the optimisation process is still likely to lead to a design with high inboard loading and an offloaded blade tip. This type of design leads to reduced induced power through a more optimal loading distribution as well as reducing the impact of the preceding blade tip vortices. The exact optimal loading must be achieved, whilst removing unwanted flow features such as the advancing blade shock or retreating blade stall. In the present study, the optimisation framework was successful at weakening these adverse effects, as demonstrated by the optimised designs, even though it was limited by the employed parameterisation and treatment of trim. In particular, the advancing side aerodynamic improvements were limited by maintaining the thickness to chord ratio as constant, whereas the retreating side aerodynamic improvements were limited by the low number of harmonic balance modes in the CFD solution. A limitation of the current framework also includes the high memory required for the adjoint harmonic balance solutions (13.1M cell grid with 2 harmonic balance modes and 200 Krylov vectors in the GMRES solver (FMGRES(200,40)-GMRES(50)) required 765GB of memory). Based on these limitations, suggestions are put forward for future work in the next subsection. Despite, the limitations of the employed optimisation framework, the present optimisation study, showed the capability of the adjoint harmonic balance method for the AH-64A blade. The developed method can be employed in many different optimisation studies, including different baseline designs, flight conditions and optimisation objective functions/constraints. A single harmonic balance adjoint calculation for a baseline design is also an extremely powerful tool outside an optimisation framework, as the designer can obtain the design sensitivities at a low cost, which can guide decisions based on engineering judgement.

10.2 Future Work

Based on the validation phase, the main aspect not covered in the present work are aeroelastic effects and their influence on the rotor performance predictions. The sensitivity of including aeroelasticity should be examined for different experimental data sets to assess when these effects can be neglected, by performing coupled CFD/CSD calculations. It is expected that the

performance of full-scale blades will be influenced to a higher degree when compared to model-scale blades with a typically stiffer.

The main areas of future work from the present research, however, arise from the rotor design phase and potential improvements within the developed optimisation framework:

As a first step using the current framework, coupled weighted sum objective optimisation should be performed for the AH-64A blade including multiple flight conditions: hover and forward flight. This would lead to a better balance of the imposed and optimised rotor design features across hover and forward flight.

Aeroelastic effects should be included in the optimisation framework. As a first step, the harmonic balance method should be coupled with a structural code to perform coupled CFD/CSD analyses, and the blade elastic deformation should be prescribed throughout the optimisation process without updating the blade structural properties. Following this, the blade structural properties should be included within the optimisation framework by performing fully-coupled aerostructural sensitivity analysis, which requires a differentiated structural solver.

The treatment of trim in the hover and forward flight optimisation studies should be modified, to include the rotor control angles as design variables, which should be optimised together with the blade planform shape. The adjoint calculations on top the thrust and torque sensitivities should also compute the propulsive force, pitching and rolling moment gradients with constraints on these variables imposed in the optimisation process.

The use of a more arbitrary blade surface parameterisation could lead to further performance improvements and discovery of more novel blade planform shapes. This could also lead to the evaluation of more advanced shapes such as BERP-like planforms. As a starting point, the parameterisation shown in Appendix A could be used based on a Bezier curve based representation of the planform and extending to parameterisation to include free-from deformation to modify to aerofoil shapes.

The use of multi-disciplinary objective functions within the optimisation process should also be considered. Apart from rotor performance, objectives that consider noise reduction, vibration, control loads, avoiding blade resonance, autorotation requirements, blade weight and structural integrity should be included. This would ensure that practical rotor designs are obtained that can be used in real-life. The use of such objective functions, however, requires the use of a large number of harmonic balance modes to capture higher frequency content and coupling with external solvers, such as structural or noise calculation codes.

Finally, improvements in the efficiency of the adjoint harmonic balance method should be examined aimed at reducing solution time and memory. Different linear solvers of the adjoint equations could be investigated, in particular, by examining improved preconditioning strategies that lead to reduced memory requirements when compared to the currently used nested GMRES solver. The adjoint convergence could also be improved by intelligent determination of the number of deflated Krylov vectors in the GMRES solver. Adaptive harmonic balance methods

should also be investigated to further reduce the cost of the primal CFD calculation.

Appendices

Appendix A

Bezier Parameterisation

A parameterisation based on Bezier curves has been developed for a more arbitrary representation of the rotor blade without constraining the local radial stations at which the design parameters are applied and the variable radial distribution. Further work is required regarding the design parameter and gradient scaling for efficient use with the SLSQP optimiser, which requires a well-scaled input for optimal convergence of the algorithm.

The method has been similarly implemented as the parameterisation method used in the AH-64A optimisation studies and is based on a mesh deformative method. The method generates a new rotor blade shape, deforms the existing baseline mesh and calculates the surface mesh sensitivities which are calculated analytically. The parameterisation is based on Bezier curves, which allow for a more arbitrary definition of the curves that define the blade properties compared to linear/parabolic distributions. The blade planform is parameterised using piecewise cubic Bezier curves defined as shown in equation A.1.

$$B(t) = \sum_{i=0}^{3} P_i b_{i,n}(t) \tag{A.1}$$

where P_i is the control point coordinate and $b_{i,n}$ is a Bernstein polynomial, which is defined as:

$$b_{i,n}(t) = \binom{n}{i} t^i (1-t)^{n-i}, i = 0,..,n \tag{A.2}$$

where n is the order of the polynomial, and $\binom{n}{i}$ is the binomial coefficient.

In this implementation, piecewise cubic Bezier curves are used to define the leading and trailing edge of the rotor blade. The leading edge is formed from five C1 continuous curves, whereas the trailing edge is formed from four. The graphical representation of a cubic Bezier curve, along with the shape of the basis functions (Bernstein Polynomials) is shown in Figure A.1.

Each cubic Bezier curve is formed from four points. Points P_0, P_3 are the curve end points, and points P_1, P_2 control the curve tangency at the end points. The (x,y) coordinates of each of

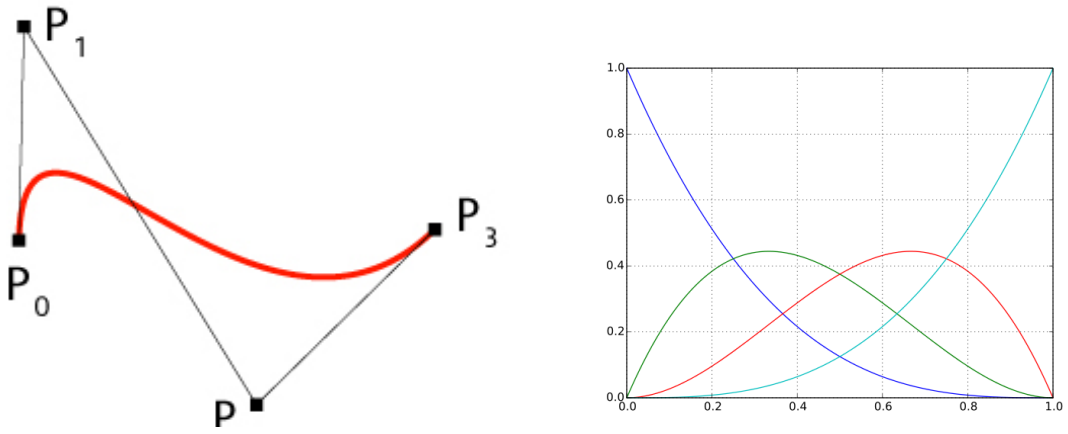

(a) Bezier curve formation (b) Basis functions for a cubic Bezier curve

Figure A.1: Cubic Bezier curves - graphical description of curve shape and basis functions.

the end points and control points will be optimised. An example application of this planform parameterisation to a rotor with a swept parabolic tip shape is shown in Figure A.2.

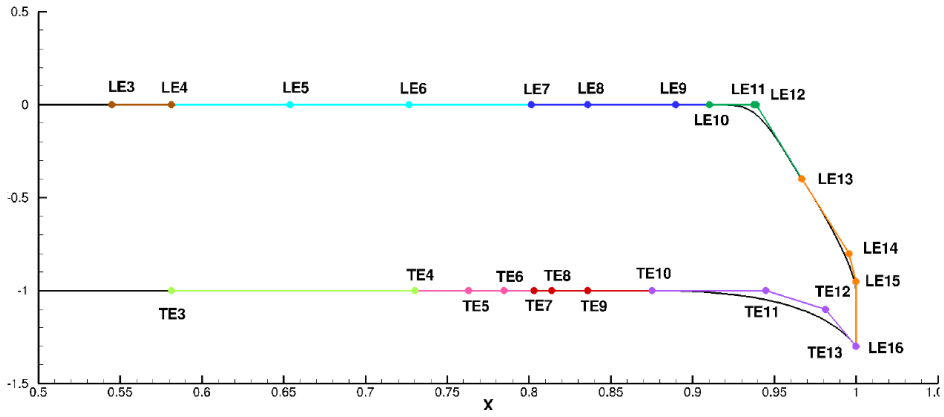

Figure A.2: Bezier curves parameterisation showing example control point locations for the leading and trailing edge curves.

The number of curves that define the leading and trailing edge curves can be controlled. The constraints of the curve parameters need to be carefully selected to ensure realistic planform shapes are obtained. In particular, a tangency condition is set between each of the cubic Bezier curves to ensure curve smoothness. Further examples of the present parameterisation based on legacy advanced rotor blades designed in industry are shown in Figure A.3. The positions of the Bezier Control points are also shown.

As can be seen in Figure A.3, fairly complex blade shapes can be obtained with the Bezier parameterisation method, allowing for exploration of novel rotor design spaces. However, the complex blade shape must also be adequately discretised leading to higher mesh size requirements than for simple planform representations. Similarly, the blade twist, thickness and anhedral-dihedral distributions can also be described using Bezier curves. The parameterisation method

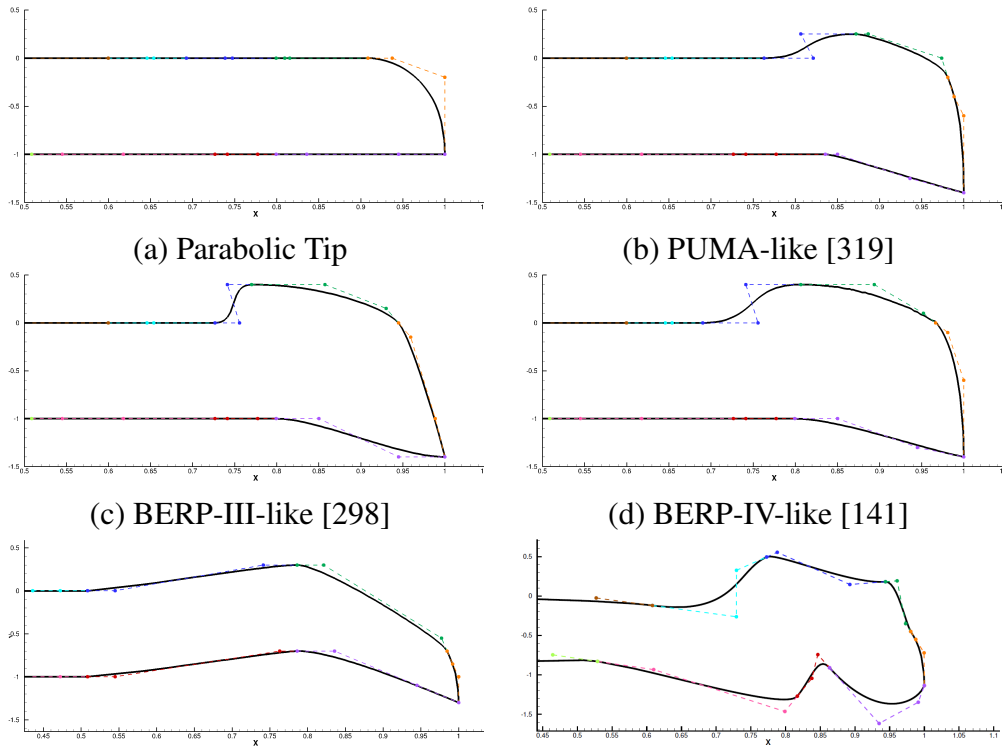

(a) Parabolic Tip

(b) PUMA-like [319]

(c) BERP-III-like [298]

(d) BERP-IV-like [141]

(e) Blue-Edge-like [39]

(f) Arbitrary design

Figure A.3: Different rotor blade designs that can be obtained using the developed parameterisation method.

also leads to a fairly high number of design parameters (around 50), which is not problematic for use with an adjoint method, as the adjoint solution cost is independent with respect to the number of design parameters. However, further scaling studies are required as the gradients of the Bezier curve end-points are much higher than the intermediate control points which control the shape of the curve. Finally, the exact normalisation procedure of the design parameters also needs to be explored.

Appendix B

Structural Modelling

Structural models have been generated in NASTRAN for the PSP and AH-64A blade for future coupled CFD/CSD analyses. A newly developed Middleware tool is used to interface HMB3 with NASTRAN. In this Appendix, the generation of the 1D-beam structural models for the PSP and AH-64A blades along with the assumptions made is presented. Initial work with the AH-64A 3D FEM structural model is also reported.

For both the PSP and AH-64A models, a similar approach was followed as in Wilkie et al. [415], who validated a NASTRAN structural model by performing a rotating shake test. For both blades, 1D beam models were generated using CBEAM elements as shown in Figure B.1. Rigid bar elements (RBAR) were used to visualise torsion of the beam. The root boundary condition was represented as free to rotate about the Y and Z axes, which represent the flapping and lead-lag motions. Elastic springs (CELAS2) was used to represent the lead-lag damper and a flapping spring was also included in the model for numerical stability. The stiffness values of the springs were adjusted to match the rigid lag and flap modes.

For the PSP rotor blade, the structural properties along the blade span used in the NASTRAN model were taken from [290]. Data is provided for the flapwise (EI_f), chordwise (EI_c), torsional (GJ) and axial (EA) stiffness values. Data for the structural offsets from the twist axis is also provided including offsets of the shear centre, centre of gravity and neutral axis. For NASTRAN input, quantities such as the chordwise and flapwise moments of area (I_c, I_f), torsional constant (J) and the sectional area (A) are required. Therefore, the values of Young's modulus (E) and Shear modulus (G) have to be estimated. Here, we use the axial stiffness data and the area of the whole aerofoil section to get the value of Young's modulus along the blade span. The Shear modulus is calculated based on a Poisson's ratio of 0.3. The structural offsets including the neutral axis offset (NA) and centre of gravity offset (CG) are with respect to the elastic axis. The structural inputs to the NASTRAN model are shown in Figure B.2.

The properties for the AH-64A blade were taken from Berry [47] and Straub [364]. Two beam models were generated for this blade, one representative of the model-scale AH-64A blade, and the second one based on the full-scale AH-64A blade (from ideally scaled structural

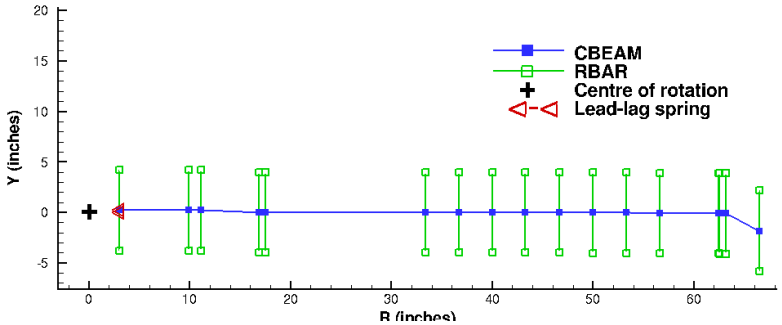

(a) PSP

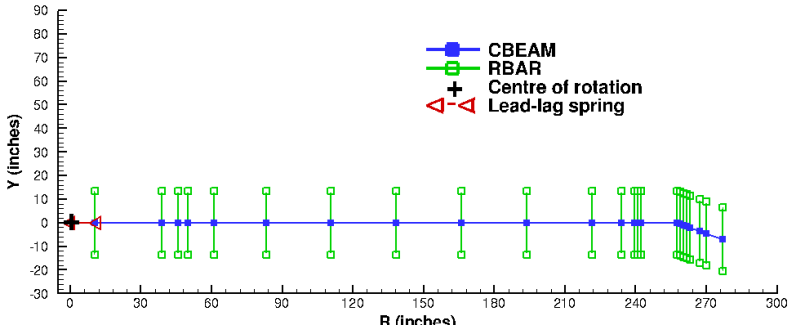

(b) AH-64A

Figure B.1: Structural models generated for the PSP and AH-64A rotor blades generated in NASTRAN.

properties). This was done using a set of scaling factors for the structural data. Similarly as for the PSP blade, the root boundary condition was represented as free to rotate in the flapping and lead-lag directions (at the flap hinge located at 11 in.). Clamping the blade at the lag hinge position (34.518 in.) leads to a significant overprediction of the first lag mode. Once again the values of the lead-lag and flapping springs were adjusted to match the frequencies of the rigid lag and flap modes. The blade structural properties are propagated in the structural model from the blade root inboard till the flap hinge. Similarly as for the PSP rotor blade, data in literature is given for the flapwise (EI_f), chordwise (EI_c) and torsional stiffnesses (GJ). Here, we assume a constant Young's modulus of $1.0 \times 10^7 lbf/in^2$ and a Poisson's ratio of 0.3. No axial stiffness data is available, hence the sectional area is taken as the area of the entire aerofoil. The neutral axis offsets are also unknown. The elastic axis is located at 24% c whereas the feathering axis is located 20% c [68, 208]. This offset is not taken into account and the feathering axis is taken as the reference axis for the NASTRAN model. The sectional mass inertia per unit length was also used in the model but is only known in the constant chord section (value of 12.871 $lbf - in$). The full-scale structural properties are shown in Figure B.3, whereas the model-scale CG offsets are also shown due to large differences compared to full-scale.

Both structural models for the PSP and AH-64A blades were simulated in NASTRAN using SOL 106 (nonlinear static analysis). The blade eigenmodes were extracted using the Modified

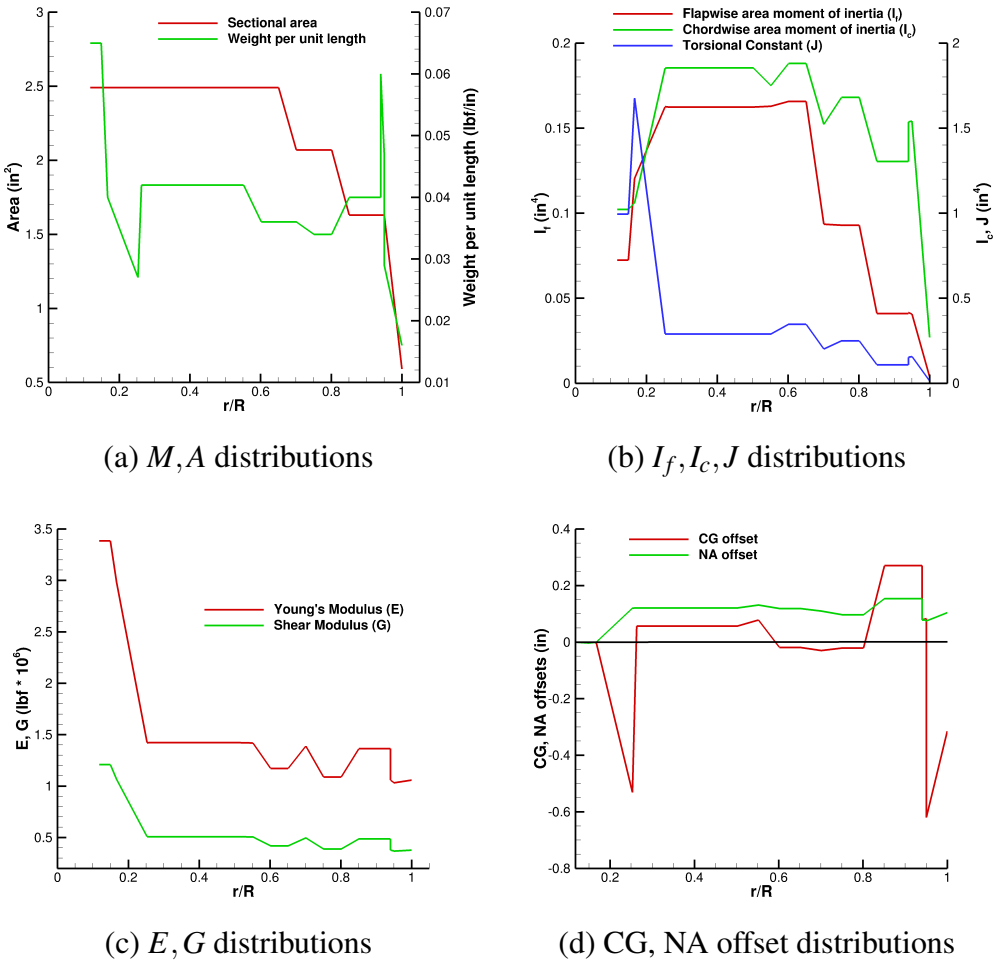

(a) M, A distributions

(b) I_f, I_c, J distributions

(c) E, G distributions

(d) CG, NA offset distributions

Figure B.2: Structural property distributions along the blade span used in the NASTRAN based on [290] for the PSP rotor blade.

Givens method (MGIV). The centrifugal loading is included in the structural model and applied through an RFORCE entry. The nominal rotational speed (Ω_{NOM}) for the PSP rotor blade is 1150 RPM, whereas 1065RPM and 288 RPM are used for the model-scale and full-scale AH-64A blade respectively. To examine the evolution of the blade eigenmodes and natural frequencies the NASTRAN models are simulated for normalised rotational speeds (Ω/Ω_{NOM}) from 0.2 to 1.2.

The evolution of the natural frequencies with normalised rotational speed for the PSP rotor blade is shown in Figure B.4. Unfortunately, no experimental data is available for this rotor blade, however, good agreement was obtained with the TTCP project partners. Similarly, no data is available for validation of the rotor mode shapes.

For the AH-64A rotor blade, experimental data is available for comparison in [208, 364]. Firstly, however, the evolution of the natural frequencies with normalised rotational speed are compared for the model-scale and full-scale blades [47] in Figure B.5.

The first three modes are in very good agreement for the model-scale and full-scale blade. The main differences occur for the 4th and 5th modes. The frequency coalescence occurs at a

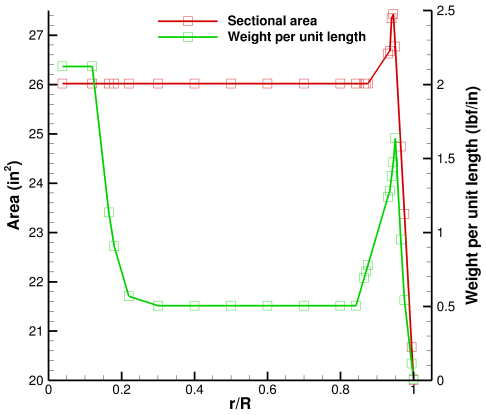

(a) M, A distributions

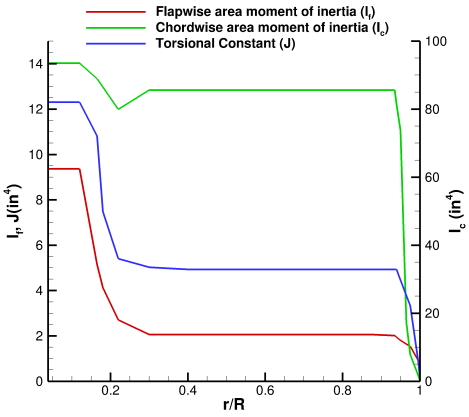

(b) I_f, I_c, J distributions

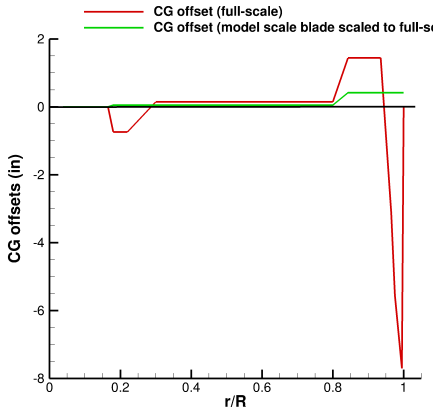

(c) CG distribution (full and model-scale (model-scale offsets scaled up)

Figure B.3: Structural property distributions along the blade span used in the NASTRAN based on [47].

lower normalised RPM for the full-scale blade. The main cause of this difference is attributed to the drastically different centre of gravity offsets along with the 1D beam model. The ideally scaled model blade also has a 20% lower torsional stiffness which may also have a minor effect. The full-scale AH-64A spoke diagram is analysed further by comparing the NASTRAN predictions with data of Kunz et al. [208] and Straub et al. [364], shown in Figure B.6.

Figure B.6 shows excellent agreement for the first three modes with both other computational studies [208, 364]. The higher frequency modes differ significantly between the two computational studies. The study of Kunz follows the full-scale AH-64A trends whereas the Straub trends are closer to the model scale blade, although these were reported as full-scale. The NASTRAN predictions for the 4th mode have very good agreement with the predictions from Kunz [208]. Modes 5-7 also follow the trends of Kunz, with the 5th mode frequencies overpredicted and 6th mode frequencies underpredicted. Experimental modal frequencies at the nominal RPM are also included in the report by Kunz [208]. These are presented in Table B.1 and compared with the NASTRAN predictions.

The agreement between NASTRAN and the published experimental data is very good. The

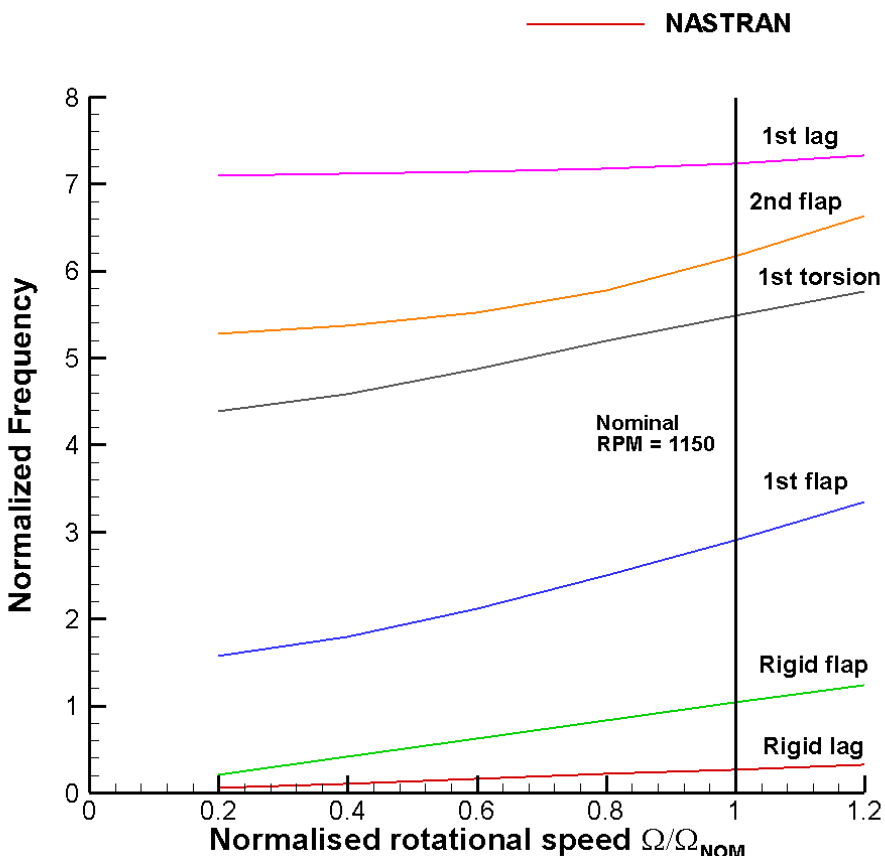

Figure B.4: Spoke diagram NASTRAN prediction for the PSP rotor blade.

Table B.1: Reported experimental frequency measurements during whirl tower testing [208] and comparisons with the NASTRAN predictions. The two first rigid modes are omitted.

Mode	**Experiment**	**Computed NASTRAN**
1st flap-bending	2.80/rev	2.83/rev
1st torsion	4.05-4.14/rev	4.09/rev
2nd flap-bending	4.90/rev	5.27/rev
1st chord-bending	6.55/rev	5.66/rev

1st flap-bending and 1st torsion frequencies are in excellent agreement. The 2nd flap-bending mode is slightly underpredicted with a large underprediction of the 1st chord-bending mode. These underpredictions could be due to the assumption in the lag hinge modelling or neglection of the offset of the elastic axis from the feathering axis. However, the key lower-frequency modes are well predicted, and these will have the largest impact on the net blade deflection that lead to changes in the rotor performance. The mode shapes are not analysed here, due to lack of experimental data for comparison.

Initial work has also been performed for 3D FEM modelling of the AH-64A blade. A 2D cross-sectional mesh was distributed within the TTCP activity for the HH-02 section including the composite layers, the leading edge tungsten weight, honeycomb and foamcore [226]. The

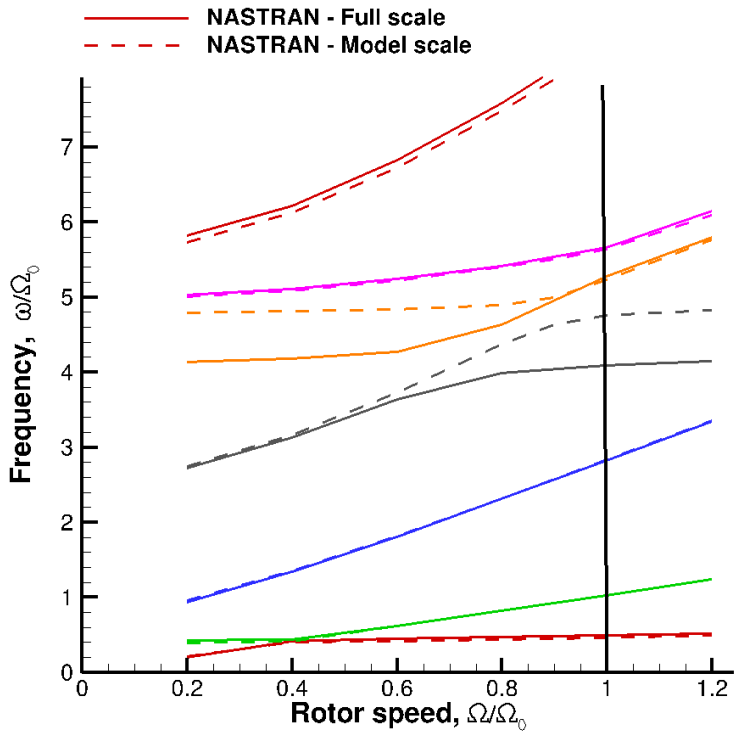

Figure B.5: Differences between model-scale and full-scale normalised frequency predictions.

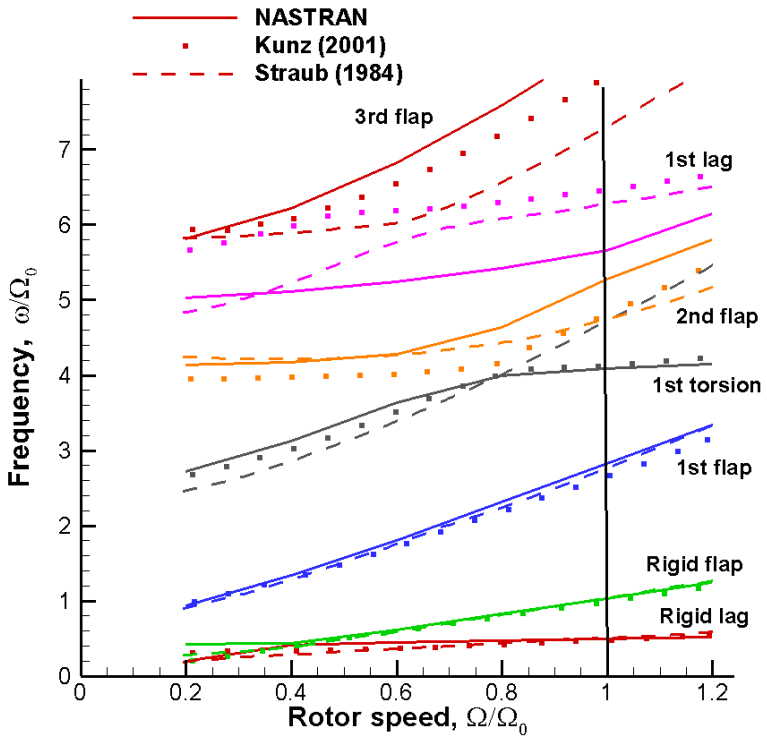

Figure B.6: Spoke diagram NASTRAN prediction for the AH-64A rotor blade and comparisons with data from two other computational studies [208, 364].

exact geometric structural layup and material properties were assumed based on past experience, and hence do not resemble any real blade design. This sectional mesh was used as a baseline starting point for the 3D FEM model. Firstly, the mesh was mapped onto the NACA64A006 section at the blade tip and the HH02 section at 0.943R with a longer chord (c = 1.060579c_{ref}). The baseline HH-02 and the NACA64A006 2D sectional meshes are shown in Figure B.7. For details on the material characteristics and material properties refer to [226].

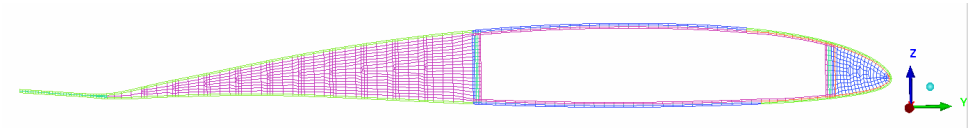

(a) Baseline HH-02 sectional mesh

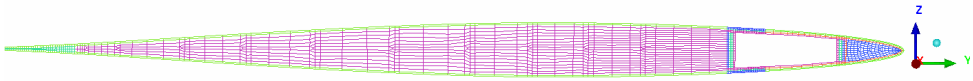

(b) NACA64A006 sectional mesh

Figure B.7: 2D sectional meshes for the HH-02 and NACA64A006 sections used within the 3D FEM structural model.

Using the sections in Figure B.7, a C code was written to read the sectional data (at stations r/R = 0.285, 0.931, 0.943, 1.0) and generate the connectivity between the nodes to generate the baseline 3D FEM mesh. Additional sections were obtained in the spanwise direction through linear interpolation (currently done manually in ICEM). The full 3D FEM mesh can be seen in Figure B.8.

The mesh shown in Figure B.8, is the baseline 3D FEM mesh with 326343 nodes (181 2D sections). A 2nd coarser model was also generated for faster simulation times with 55893 nodes (31 2D sections). CHEXA elements were used to model the volume elements with PSOLID property cards. The composite material is modelled using the PCOMPLS entry in NASTRAN with an option to specify the number and thickness of each individual ply. SOL 400 was used (advanced implicit nonlinear static analysis), for the eigenmodal analysis. Here, the Lanczos method is used as opposed to the Modified Givens Method for extraction of the eigenvalues due to much better performance with larger systems. The initial results for the coarse and baseline meshes along with comparisons with experimental data and the 1D beam model results are shown in Table B.2 at the nominal rotational speed.

The initial frequency predictions for the 3D FEM model show excellent frequency predictions for the first two rigid modes and fair agreement for the 1st flap-bending mode. The 1st torsion mode is highly overpredicted, however, it must be noted that the inclusion of the PCOMPLS elements with -45/0/45 composite ply angles increased the modal frequency of this mode from 3.65/rev to 5.12/rev showing the high sensitivity of this model to the composite layup. The higher frequency modes are overpredicted compared to the 1D-beam model. The 2D sectional layup, however, was fully assumed, hence the poorer agreement of the 3D FEM model is not

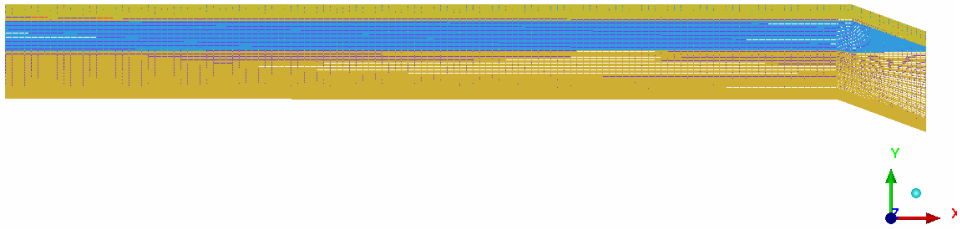

(a) View from the top

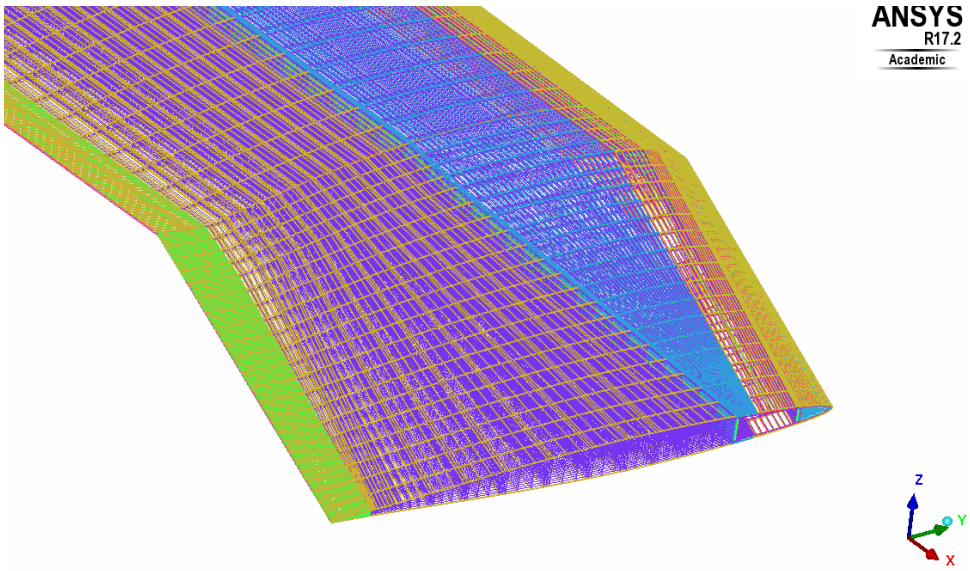

(b) Mesh in the blade tip region

Figure B.8: Baseline 3D FEM mesh for the AH-64A rotor blade.

Table B.2: Comparisons of the 3D FEM AH-64A frequency predictions with Reported experimental frequency measurements during whirl tower testing [208] 1D beam model predictions.

Mode	**Experiment**	**Beam model**	**Coarse 3D FEM**	**Baseline 3D FEM**
Rigid Lag	- (0.5 [208])	0.49/rev	0.508/rev	0.516/rev
Rigid Flap	- (1.04 [208])	1.03/rev	1.031/rev	1.031/rev
1st flap-bending	2.80/rev	2.83/rev	2.734/rev	2.739/rev
1st torsion	4.05-4.14/rev	4.09/rev	5.122/rev	5.124/rev
2nd flap-bending	4.90/rev	5.27/rev	5.616/rev	5.656/rev
1st chord-bending	6.55/rev	5.66/rev	7.023/rev	7.007/rev

surprising. Further work is required to iteratively adjust the 2D sectional layup for better agreement of the modal frequencies with the 1D-beam model. The 2D sectional properties could also be altered to match the sectional properties of the 1D beam model including weight and stiffness values reported in [47].

Bibliography

[1] Computational Modeling of Hovering Rotor and Wake Aerodynamics. *Journal of Aircraft*, 39(5).

[2] Conservative Full-Potential Model for Rotor Flows. *AIAA Journal*, 25(2).

[3] Efficient High-Resolution Wake Modelling Using the Vorticity Transport Equation. *AIAA Journal*, 43(7).

[4] Euler Calculations for Flow field of a Helicopter in Hover. *AIAA Journal*, 24(4).

[5] High-Order Essentially Nonoscillatory Schemes for Rotary-Wing Wake Computations. *Journal of Aircraft*, 41(2).

[6] Improved Method for Rotor Wake Coupling. *Journal of Aircraft*, 39(5).

[7] Lower-Upper Symmetric-Gauss-Seidel Method for the Euler and Naver-Stokes Equations. *AIAA Journal*, 26(9).

[8] Navier-Stokes calculations of hovering rotor flowfields. *Journal of Aircraft*, 25(10).

[9] Subsonic and Transonic Potential Flow over Helicopter Rotor Blades. *AIAA Journal*, 10(12).

[10] TURNS: A Free-Wake Euler/Navier-Stokes Numerical Method for Helicopter Rotors. *AIAA Journal*, 31(5).

[11] L. Ahaus, M. Wasikowski, JA. Morillo, and M. Louis. Loads Correlation of a Bell M429 Rotor Using CFD/CSD Coupling. In *69th Annual Forum of the American Helicopter Society*, Phoenix, AZ, USA, 2013.

[12] J. Ahmad and NM. Chaderijan. High-Order Accurate CFD/CSD Simulation of the UH-60 Rotor in Forward Flight. In *29th AIAA Applied Aerodynamics Conference*, Honolulu, Hawaii, USA, 2011.

[13] J. Ahmad and EPN. Duque. Helicopter Rotor Blade Computation in Unsteady Flows Using Moving Overset Grids. *Journal of Aircraft*, 33(1):54–60, 1996. DOI: 10.2514/3.46902.

[14] T. Albring, M. Sagebaum, and NR. Gauger. Efficient Aerodynamic Design using the Discrete Adjoint Method in SU2. In *AIAA Aviation 17th AIAA/ISSMO Multidisciplinary Analysis and Optimization Conference*, Washington, D.C., USA, 2016.

[15] D. Alfano, P. Cranga, V. Gareton, F. Guntzer, and JF. Hirsch. The Blue Edge^{TM} Blade Continuation. In *Vertical Flight SocietyâĂŹs 75th Annual Forum & Technology Display*, Philadelphia, PA, USA, 2019.

[16] BG. Allan and NW. Schaeffler. Numerical Investigation of Rotorcraft Fuselage Drag Reduction using Active Flow Control. In *67th Annual Forum of the American Helicopter Society*, Virginia Beach, VA, USA, 2011.

[17] CB. Allen and TCS. Rendall. Aerodynamic shape optimisation of hovering rotors using compressible CFD. *The Aeronautical Journal*, 115(1170):513–519, 2011. DOI: 10.1017/S0001924000006151.

[18] M. Allongue, HJ. Marze, and F. Potdevin. The Quiet Helicopter - From Research To Reality. In *American Helicopter Society 55th Annual Forum*, Montreal, Canada, 1999.

[19] A. Altmikus, S. Wagner, P. Beaumier, and G. Servera. A Comparison: Weak versus Strong Modular Coupling for Trimmed Aeroelastic Rotor Simulations. In *American Helicopter Society 58th Annual Forum*, Montreal, Canada, 2002.

[20] KB. Amer. Technical Note: High Speed Rotor Aerodynamics. *Journal of American Helicopter Society*, 34(1):63–63, 1989. DOI: 10.4050/JAHS.34.1.63.

[21] T. Aoyama, K. Kawachi, and S. Saito. Effect of Blade-Tip Planform on Shock Wave of Advancing Helicopter Blade. *Journal of Aircraft*, 32(5):955–961, 1995. DOI: 10.2514/3.46823.

[22] R. Arieli and M. Tauber. Computation of subsonic and transonic flow about lifting rotor blades. In *5th Atmospheric Flight Mechanics Conference for Future Space Systems*, Boulder, CO, USA, 1979.

[23] WE. Arnoldi. The Principle of Minimized Iterations in the Solution of the Matrix Eigenvalue Problem. *Quarterly of Applied Mathematics*, 9(1):17–29, 1951. DOI: 10.1090/qam/42792.

[24] O. Axelsson. *Iterative Solution Methods*. Cambridge University Press: Cambridge, MA, 1994.

[25] OA. Bachau and JU. Ahmad. Advanced CFD and CSD methods for multidisciplinary applications in rotorcraft problems. In *6th Symposium on Multidisciplinary Analysis and Optimization*, Bellevue, WA., USA, 1996.

[26] JD. Baeder. Passive Design for Reduction of High-Speed Impulsive Rotor Noise. In *52nd Annual Forum of the American Helicopter Society*, Washington, D. C., USA, 1996.

[27] A. Bagai. Aerodynamic Design of the X2 Technology Demonstrator^{TM} Main Rotor Blade. In *American Helicopter Society 64th Annual Forum*, Montreal, Canada, 2008.

[28] J. Bailly and D. Bailly. Multi-Fidelity Aerodynamic Optimization of a Helicopter Rotor Blade. In *42nd European Rotorcraft Forum*, Lille, France, 2016.

[29] J. Bailly and D. Bailly. Multifidelity Aerodynamic Optimization of a Helicopter Rotor Blade. *AIAA Journal*, 57(8):3132–3144, 2019. DOI: 10.2514/1.J056513.

[30] J. Bailly, B. Ortun, and Y. Delrieux. Recent Advances in Rotor Aerodynamic Optimization, Including Structural Data Update. *Journal of the American Helicopter Society*, 62(2):1–17, 2017. DOI: 10.4050/JAHS.62.022009.

[31] DT. Balch. Correlation of Full Scale Wind Tunnel Test Data with Model Rotor Test Data and Theory for a Modern Helicopter Main Rotor. In *American Helicopter Society 34th Annual Forum*, Washington, DC, USA, 1978.

[32] DT. Balch and J.Lombardi. Experimental Study of Main Rotor Tip Geometry and Tail Rotor Interactions in Hover, Vol I - Text and Figures. Technical report, National Aeronautics and Space Administration, 1985. NASA-CR-177336-Vol-1.

[33] DT. Balch and J. Lombardi. Experimental Study of Main Rotor Tip Geometry and Tail Rotor Interactions in Hover. Vol II - Run Log and Tabulated Data. Technical report, Sikorsky Aircraft Division, United Technologies Corporation, 1985. NASA-CR-177336.

[34] DT. Balch, A. Saccullo, and TW. Sheehy. Experimental Study of Main Rotor/Tail Rotor/Airframe Interactions in Hover - Volume I. Technical report, United Technologies Corporation, Sikorsky Aircraft Division, 1983. NASA-CR-166485.

[35] DA. Barrows, AW. Burner, AI. Abrego, and LE. Olson. Blade Displacement Measurements of the Full-Scale UH-60A Airloads Rotor. In *29th AIAA Applied Aerodynamics Conference*, Honolulu, Hawaii, USA, 2011.

[36] K. Baverstock. AgustaWestland's application of HMB to simulate the active Gurney flap. In *40th European Rotorcraft Forum*, Southampton, UK, 2014.

[37] P. Beaumier. A Coupling Procedure between a Rotor Dynamics code and a 3D Unsteady Full Potential Code. In *American Helicopter Society Aeromechanics Specialists Conference*, San Francisco, CA, USA, 1994.

[38] P. Beaumier, C. Kessler, Y. Delrieux, BG. van der Wall, M. Gervais, JF. Hircsh, K. Pengel, and P. Crozier. From ERATO Basic Research to the Blue EdgeTM Rotor Blade: an Example of Virtual Engineering? In *72nd Annual Forum of the American Helicopter Society*, West Palm Beach, FL, USA, 2016.

[39] M. Bebesel, A. D'Alascio, S. Schneider, S. Guenther, F. Vogel, C. Wehle, and D. Schimke. Bluecopter Demonstrator - An Approach to Eco-Efficient Helicopter Design. In *41st European Rotorcraft Forum*, Munich, Germany, 2015.

[40] GL. Bender, VL. Diekmann, JD. Ottomeyer, BD. Picasso III, and LB. Higgins. Engineering Design Test 4, YAH-64 Advanced Attack Helicopter . Technical report, United States Army Engineering Flight Activity, 1980. USAAEFA NO. 80-03.

[41] GL. Bender, GM. Yamakawa, MK. Herbst, PJ. Sullivan, RD. Robbins, and RA. Williams. Airworthiness and Flight Characteristics Test (A&FC) of the CH-47D Heclicopter. Technical report, United States Army Engineering Flight Activity, 1980. USAAEFA NO. 82-07.

[42] P. Beran, B. Stanford, and M. Kurdi. Sensitivity Analysis for Optimization of Dynamic Systems with Reduced Order Modeling. In *48th AIAA Aerospace Sciences Meeting*, Orlando, FL, USA, 2010.

[43] CR. Berezin and LN. Sankar. An Improved Navier-Stokes/Full-Potential Coupled Analysis for Rotors. *Journal of Mathematical and Computer Modeling*, 19(3), 1994.

[44] S. Bernstein. Demonstration du theoreme de Weierstrass fondee sur le calcul desprobabilites. *Comm. Kharkov Math. Soc.*, 13:1–2, 1912.

[45] JD. Berry. Wind Tunnel Testing of an Advanced UH-1 Type Rotor System. In *37th annual forum of the American Helicopter Society*, New Orleans, LA, 1981.

[46] JD. Berry. Performance Testing of a Main Rotor System for a Utility Helicopter at 1/4 scale. Technical report, National Aeronautic and Space Administration, 1982. NASA-TM-83274.

[47] JD. Berry. Helicopter Blade Dynamic Loads Measured During Performance Testing of Two Scaled Rotors. Technical report, National Aeronautics and Space Administration, 1987. NASA-TM-89053.

[48] MD. Betzina. Rotor Performance of an Isolated Full-Scale XV-15 Tiltrotor in Helicopter Model. In *American Helicopter Society Aerodynamics, Acoustics, and Test and Evaluation Technical Specialists Meeting*, San Francisco, California, USA, 2002.

[49] M. Biava and GN. Barakos. Optimisation of Ducted Propellers for Hybrid Air Vehicles Using High-Fidelity CFD. *The Aeronautical Journal*, 120(1232):1632–1657, 2016. DOI: 10.1017/aer.2016.78.

[50] M. Biava, M. Woodgate, and GN. Barakos. Fully implicit discrete-adjoint methods for rotorcraft applications. *AIAA Journal*, 54(2):735–748, 2016. DOI: 10.2514/1.J054006.

[51] RT. Biedron and EM. Lee-Rausch. Computation of UH-60A Airloads Using CFD/CSD Coupling On Unstructured Meshes. In *American Helicopter Society 67th Annual Forum*, Virginia Beach, VA , USA, 2011.

[52] RT. Biedron and EM. Lee-Rausch. Blade Displacement Predictions for the Full-Scale UH-60A Airloads Rotor. In *American Helicopter Society 70th Annual Forum*, Montreal, Canada, 2014.

[53] GJ. Bingham and KW. Noonan. Two-Dimensional Aerodynamic Characteristics of Three Rotorcraft Airfoils at Mach Numbers From 0.35 to 0.90. Technical report, National Aeronautics and Space Administration, 1982. NASA-TP-2000.

[54] Boeing. New chinook composite blades proven. http://www.boeing.com/features/2017/01/chinook-blades-01-17.page, 2017. [Online; accessed 29-April-2020].

[55] Boeing. New chinook composite blades proven. `http://www.boeing.com/features/2017/01/chinook-blades-01-17.page`, 2017. [Online; accessed 22-March-2018].

[56] OJ. Boelens, GN. Barakos, M. Biava, A. Brocklehurst, M. Costes, A. DâĂŹAlascio, M. Dietz, D. Drikakis, J. Ekaterinaris, I. Humby, W. Khier, B. Knutzen, J. Kok, F. LeChuiton, K. Pahlke, T. Renaud, T. Schwarz, R. Steijl, L. Sudre, H. van der Ven, L. Vigevano, and B. Zhong. The blind-test activity of the GOAHEAD project. In *33rd European Rotorcraft Forum*, Kazan, Russia, 2007.

[57] R. Boisard. Aerodyanmic Investigation of Rotor/Propeller Ineractions on a Fast Rotorcraft. In *44th European Rotorcraft Forum*, Delft, Netherlands, 2018.

[58] J. Bonet and J. Peraire. An Alternating Digital Tree (ADT) Algorithm for 3D Geometric Searching and Intersection Problems. *International Journal for Numerical Methods in Engineering*, 31(1):1–17, 1991. DOI: 10.1002/nme.1620310102.

[59] WG. Bousman and RM. Kufeld. UH-60A Airloads Catalog. Technical report, National Aeronautics and Space Administration, 2005. NASA/TM-2005-212827.

[60] WG. Bousman and T. Norman. Assessment of Predictive Capability of Aeromechanics Methods. In *American Helicopter Society Aeromechanics SpecialistâĂŹ Conference*, San Francisco, CA, USA, 2008.

[61] WG. Bousman, C. Young, N. Gilbert, F. Toulmay, W. Johnson, and MJ. Riley. Correlation fo PUMA Airloads - Lifting-Line and Wake Calculation. Technical report, National Aeronautics and Space Administration, 1989. NASA TM-102212.

[62] PO. Bowles, C. Matalanis, M. Battisti, BY. Min, BE. Wake, N. Tuozzo, and PF. Lorber. Full-Configuration CFD Analysis of the S-97 RAIDER^TM. In *Vertical Flight Society 75th Annual Forum & Technology Display*, Philadelphia, PE, USA, 2019.

[63] MA. Bremond, A. Cassier, and JM. Pouradier. Design and Wind Tunnel Testing of 1.5M Diamete Model Rotors. In *4th European Rotorcraft and Power Lift Aircraft Forum*, Stresa, Italy, 1978.

[64] A. Brocklehurst and G.N. Barakos. A review of helicopter rotor blade tip shapes. *Progress in Aerospace Sciences*, 56:35 – 74, 2013. DOI: 10.1016/j.paerosci.2012.06.003.

[65] A. Brocklehurst and EPN. Duque. Experimental and numerical study of the British Experimental Rotor Programme blade. In *Flight Simulation Technologies Conference and Exhibit, Guidance, Navigation, and Control and Co-located Conferences*, Dayton, OH, USA, 1990.

[66] A. Brocklehurst and AC. Pike. Reduction of BVI noise using a vane tip. In *American Helicopter Society specialists' conference on aerodynamics, dynamics and acoustics*, San Francisco, CA, USA, 1994.

[67] E. Brouwers, M. Fillman, and R. Deresz. Advanced AH-64 Compound Wind Tunnel Testing Overview. In *American Helicopter Society 75th Annual Forum*, Philadelphia, PA, USA, 2019.

[68] C. Callahan and FK. Straub. Design Optimization of Rotor Blades for Improved Performance and Vibration. In *American Helicopter Society 47th Annual Forum*, Phoenix, AZ, USA, 1993.

[69] MS. Campobasso and M. Giles. Stabilization of a linear flow solver for turbomachinery aeroelasticity by means of the recursive projection method. *AIAA Journal*, 42(9):1765–1774, 2004. DOI: 10.2514/1.1225.

[70] F. Cantariti, L. Dubuc, B. Gribben, M. Woodgate, KJ. Badcock, and BE. Richards. Approximate "Jacobians for the Solution of the Euler and Navier-Stokes Equations. Technical report, University of Glasgow, 1997. Internal Aero. Report 9705.

[71] FX. Caradonna and MP. Isom. Numerical Calculation of Unsteady Transonic Potential Flow over Helicopter Rotor Blades. *AIAA Journal*, 14(4):482–488, 1976. DOI: 10.2514/3.61387.

[72] FX. Caradonna and JJ. Philippe. The Flow over a Helicopter Blade Tip in the Transonic Regime. In *2nd European Rotorcraft and Powered Lift Aircraft Forum*, Buckeburg, Germany, 1976.

[73] FX. Caradonna and C. Tung. Experimental and Analytical Studies of a Model Helicopter Rotor in Hover. Technical report, National Aeronautics and Space Administration, 1980. NASA TM-81232.

[74] C. Castells, F. Richez, and M. Costes. A Numerical Analysis of the Dynamic Stall Mechanisms on a Helicopter Rotor from Light to Deep Stall. *Journal of the American Helicopter Society*, 65(2):1–24, 2020. DOI: 10.4050/JAHS.65.032005.

[75] NM. Chaderijan. Advances in Rotor Performance and Turbulent Wake Simulation using DES and Adaptive Mesh Refinement. In *Seventh International Conferences on Computational Fluid Dynamics (ICCFD7)*, Hawaii, USA, 2012.

[76] NM. Chaderijan. Numerical Simulation of Dynamic Stall Using Near-Body Adaptive Mesh Refinement. In *Tenth International Conference on Computational Fluid Dynamics (ICCFD10)*, Barcelona, Spain, 2018.

[77] S. Chae, K. Yee, C. Yang, T. Aoyama, S. Jeong, and S. Obayashi. Helicopter Rotor Shape Optimization for the Improvement of Aeroacoustic Performance in Hover. *Journal of Aircraft*, 47(5):1770–1783, 2010. DOI: 10.2514/1.C000283.

[78] IC. Chang, TR. Norman, and EA. Romander. Airloads Correlation of the UH-60A Rotor inside the 40- by 80-Foot Wind Tunnel. *International Journal of Aerospace Engineering*, 2014:1–19, 2014. DOI: 10.1155/2014/473989.

[79] IC. Chang, EA. Romander, M. Potsdam, and H. Yeo. Air-loads Prediction of a UH-60A Rotor inside the 40- by 80-Foot Wind Tunnel. In *American Helicopter Society Aeromechanics SpecialistâĂŹ Conference*, San Francisco, CA, USA, 2010.

[80] IC. Chang and C. Tung. Euler solution of the transonic flow for a helicopter rotor. In *25th AIAA Aerospace Sciences Meeting*, Reno, NV, USA, 1987.

[81] A. Chattopadhyay and TR. McCarthy. A multidisciplinary optimization approach for vibration reduction in helicopter rotor blades. *Journal of Computers & Mathematics with Applications*, 25(2):59–72, 1993. DOI: 10.1016/0898-1221(93)90223-I.

[82] CL. Chen, WJ. McCroskey, and S. Obayashi. Numerical solutions of forward-flight rotor flow using an upwind method. *Journal of Aircraft*, 28(6):374–380, 1991. DOI: 10.2514/3.46037.

[83] MC. Cheney Jr. The ABC Helicopter. In *AIAA/AHS VTOL Research, Design and Operations Meeting*, Atlanta, GA, USA, 1969.

[84] S. Choi, JJ. Alonso, E. van der Weide, and J. Sitaraman. Validation Study of Aerodynamic Analysis Tools for Design Optimization of Helicopter Rotors. In *25th AIAA Applied Aerodynamics Conference*, Miami, Florida, USA, 2007.

[85] S. Choi and A. Datta. CFD Prediction of Rotor Loads using Time-Spectral Method and Exact Fluid-Structure Interface. In *26th AIAA Applied Aerodynamics Conference*, Honolulu, Hawaii, USA, 2008.

[86] S. Choi and A. Datta. Time-Spectral Method for CFD Prediction of Helicopter Rotor Vibratory Loads. In *5th International Conference on CFD*, Seoul, Republic of Korea, 2008.

[87] S. Choi, K. Lee, MM. Potsdam, and JJ. Alonso. Helicopter Rotor Design Using a Time-Spectral and Adjoint-Based Method. *Journal of Aircraft*, 51(2):412–423, 2014. DOI: 10.2514/1.C031975.

[88] S. Choi, KH. Lee, JJ. Alonso, and A. Datta. Preliminary Study on Time-Spectral and Adjoint-Based Design Optimization of Helicopter Rotors. In *AHS SpecialistâĂŹs Conference on Aerodynamics*, San Francisco, CA, USA, 2008.

[89] DR. Clark and AC. Leiper. The Free Wake Analysis - A Method for the Prediction of Helicopter Rotor Hover Performance. In *American Helicopter Society 25th Annual Forum*, Washington, DC, USA, 1969.

[90] CD. Coffen and AR. George. Prediction of XV-15 Tiltrotor Discrete Frequency Aeroacoustic Noise with WopWop. Technical report, National Aeronautics and Space Administration, 1990. NASA CR-187684.

[91] CP. Coleman and WG. Bousman. Aerodynamic Limitations of the UH-60A Rotor. Technical report, National Aeronautics and Space Administration, 1996. NASA-TM-110396.

[92] S. Colonia, V. Leble, R. Steijl, and G. Barakos. Assessment and calibration of the γ-equation transition model for a wide range of reynolds numbers at low mach. *AIAA Journal*, 55(4):1126–1139, 2017. DOI: 10.2514/1.J055403.

[93] MR. Colonno, K. Naik, K. Duraisamy, and JJ. Alonso. An Adjoint-Based Multidisciplinary Optimization Framework for Rotorcraft Systems. In *12th AIAA Aviation Technology, Integration, and Operations (ATIO) Conference and 14th AIAA/ISSM*, Indianapolis, IN, USA, 2012.

[94] JL. Cross and ME. Watts. Tip Aerodynamics and Acoustics Test. Technical report, National Aeronautics and Space Administration, 1988. NASA Reference Publication 1179.

[95] HC. Curtiss Jr. and F. Carson. Performance of a Sikorsky S-61 with a New Main Rotor. In *29th European Rotorcraft Forum*, Friedrichshafen, Germany, 2003.

[96] A. Da Ronch, AJ. McCracken, KJ. Badcock, M. Widhalm, and MS. Campobasso. Linear frequency domain and harmonic balance predictions of dynamic derivatives. *AIAA Journal*, 50(3):694–707, 2013. DOI: 10.2514/1.C031674.

[97] A. Datta and I. Chopra. Validation of Aerodynamic and Structural Modeling using UH-60A Flight Test Data. In *American Helicopter Society 59th Annual Forum*, Phoenix, AZ, USA, 2003.

[98] A. Datta and I. Chopra. Prediction of UH-60A Dynamic Stall Loads in High Altitude Level Flight using CFD/CSD Coupling. In *American Helicopter Society 61st Annual Forum*, Grapevine, TX, USA, 2005.

[99] A. Datta and I. Chopra. Prediction of UH-60 Main Rotor Structural Loads using CFD/Comprehensive Analysis Coupling. In *32nd European Rotorcraft Forum*, Maastricht, Germany, 2006.

[100] A. Datta, J. Sitaraman, JD. Baeder, and I. Chopra. Analysis Refinements for Prediction of Rotor Vibratory Loads in High-Speed Forward Flight. In *American Helicopter Society 60th Annual Forum*, Baltimore, MD, USA, 2004.

[101] A. Datta, H. Yeo, and TR. Norman. Experimental Investigation and Fundamental Understanding of a Slowed UH-60 Rotor at High Advance Ratios. In *American Helicopter Society 67th Annual Forum*, Virginia Beach, Virginia, USA, 2011.

[102] A. Desopper, P. Lafon, and P. Ceron. Influence of the Control Law on the Performance of a Helicopter Model Rotor. In *15th European Rotorcraft Forum*, Amsterdam, The Netherlands, 1989.

[103] A. Desopper, P. Lafon, P. Ceroni, and JJ. Philippe. Ten Years of Rotor Flow Studies at ONERA. In *42nd Annual National Forum of the American Helicopter Society*, Washington, D. C., USA, 1996.

[104] A. Desopper, P. Lafon, JJ. Philippe, and J. Prieur. Effect of an Anhedral Sweptback Tip on the Performance of a Helicopter Rotor. In *13th European Rotorcraft Forum*, Arles, France, 1987.

[105] D. Desvigne, R. Coisnon, BR. Michel, A. Thomas, JP. Pinacho, and E. Roca-Leon. Multi-Objective Industrial Optimization of High-Speed Helicopter Main Rotor Blades with Dynamically-Adpated Structural Properties. In *45th European Rotorcraft Forum*, Warsaw, Poland, 2019.

[106] M. Dietz and O. Dieterich. Towards Increased Industrial Application of Rotor Aeroelastic CFD. In *35th European Rotorcraft Forum*, Hamburg, Germany, 2009.

[107] N. Donaldson and GC. Hall. AH-1 (HueyCobra) Helicopter Equipped with the XM35 Armament Subsystem (20mm Automatic Gun). Technical report, US Army Aviation Systems Test Activity, 1969. USAAVSCOM PROJECT NO. 68-31.

[108] A. Dumont, A. Le Pape, J. Peter, and S. Huberson. Aerodynamic Shape Optimization of Hovering Rotors Using a Discrete Adjoint of the Reynolds-Averaged Navier-Stokes Equations. *Journal of the American Helicopter Society*, 56(3):1–11, 2011. DOI: 10.4050/JAHS.56.032002.

[109] EPN. Duque. A Numerical Analysis of the British Experimental Rotor Program Blade. In *45th Annual Forum of the American Helicopter Society*, Boston, MA, USA, 1989.

[110] EPN. Duque and GR. Srinivasan. Numerical Simulation of a Hovering Rotor Using Embedded Grids. In *American Helicopter Society 48th Annual Forum*, Washington, DC, USA, 1992.

[111] RP. Dwight and J. Brezillon. Efficient and robust algorithms for solution of the adjoint compressible navierâĂŞstokes equations with applications. *International Journal of Numerical Methods in Fluids*, 60:365–389, 2008. DOI: 10.1002/fld.1894.

[112] TD. Economon, F. Palacios, and JJ. Alonso. Optimal Shape Design for Open Rotor Blades. In *30th AIAA Applied Aerodynamics Conference*, St. Louis, NO, USA, 2012.

[113] TD. Economon, F. Palacios, and JJ. Alonso. An Unsteady Continuous Adjoint Approach for Aerodynamic Design on Dynamic Meshes. In *AIAA Aviation 15th AIAA/ISSMO Multidisciplinary Analysis and Optimization Conference*, Atlanta, GA, USA, 2014.

[114] TA. Egolf, N. Hariharan, R. Narducci, and E. Reed. AIAA Standardized Hover Simulation: Hover Performance Prediction Status and Outstanding Issues. In *AIAA SciTech Forum, 55th Aerospace Sciences Meeting*, Grapevine, TX, USA, 2017.

[115] TA. Egolf and SP. Sparks. A Full Potential Rotor Analysis With Wake Influence Using an Inner-Outer Domain Technique. In *American Helicopter Society 42nd Annual Forum*, Washington, D. C., USA, 1986.

[116] K. Ekici, KC. Hall, and EH. Dowell. Computationally fast harmonic balance methods for unsteady aerodynamic predictions of helicopter rotors. *Journal of Computational Physics*, 227(12):6206–6225, 2008. DOI: 10.1016/j.jcp.2008.02.028.

[117] E. Fabiano and D. Mavriplis. Adjoint-based Aeroacoustic Design-Optimization of Flexible Rotors in Forward Flight. In *American Helicopter Society 72nd Annual Forum*, West Palm Beach, FL, USA, 2016.

[118] DW. Fanjoy and WA. Crossley. Aerodynamic Shape Design for Rotor Airfoils via Genetic Algorithm. In *53rd Annual Forum of the American Helicopter Society*, Virginia Beach, VA, USA, 1999.

[119] FF. Felker, MD. Betzina, and DB. Signor. Performance and Loads Data from a Hover Test of a Full-Scale XV-15 Rotor. Technical report, National Aeronautics and Space Administration, 1985. TM-86833.

[120] F. Frey, J. Thiemeier, C. Ohrle, M. Kessler, and E. Kramer. Aerodynamic Interactions on Airbus HelicoptersâĂŹ Compound Helicopter RACER in Cruise Flight. In *Vertical Flight Society 75th Annual Forum & Technology Display*, Philadelphia, PE, USA, 2019.

[121] F. Fusi, PM. Congedo, A. Guardone, and G. Quaranta. Robust aerodynamic optimization strategies for rotor blade morphing airfoils. In *41st European Rotorcraft Forum*, Munich, Germany, 2015.

[122] F. Fusi, A. Guardone, G. Quaranta, and PM. Congedo. Multifidelity Physics-Based Method for Robust Optimization Applied to a Hovering Rotor Airfoil. *AIAA Journal*, 53(11):3448–3465, 2015. DOI: 10.2514/1.J053952.

[123] S. Gates. Aerodynamic Analysis of Tiltrotors in Hovering and Propeller Modes Using Advanced Navier-Stokes Computations. In *39th European Rotorcraft Forum*, Moscow, Russia, 2013.

[124] M. Gervais and V. Gareton. Analysis of main rotor noise reduction due to novel planform design - The blue edge^{TM} blade. In *37th European Rotorcraft Forum*, Cascina Costa, Italy, 2011.

[125] AK. Gopinath, PS. Beran, and A. Jameson. Comparative Analysis of Computational Methods for Limit-Cycle Oscialltions. In *47th AIAA/ASME/ASCE/AHS/ASC Structures, Structural Dynamics and Materials Conference*, Newport, Rhode Island, USA, 2006.

[126] AK. Gopinath and A. Jameson. Time Spectral Method for Periodic Unsteady Computations over Two- and Three- Dimensional Bodies. In *43rd AIAA Aerospace Sciences Meeting and Exhibit*, Reno, NV, USA, 2005.

[127] RB. Gray. An Aerodynamic Analysis of a Single-Bladed Rotor in Hovering and Low-Speed Forward Flight as Determined from Smoke Studies of the Vorticity Distribution in the Wake. Technical report, Princeton Univ. Aeronautical Eng. Dept., 1956. Report No. 356.

[128] RB. Gray. The 1991 Alexander A. Nikolsky Lecture: Vortex Modeling for Rotor Aerodynamics. In *American Helicopter Society 47th Annual Forum*, Phoenix, AZ, USA, 1991.

[129] F. Guillet and JJ. Philippe. Flight Tests of a Sweptback Parabolic Tip on a Dauphin-365N. In *10th European Rotorcraft Forum*, The Hague, The Netherlands, 1984.

[130] F. Guntzer, V. Gareton, JP. Pinacho, and J. Caillet. Low Noise and Acoustic Testing of the Airbus Helicopter H-160B. In *45th European Rotorcraft Forum*, Warsaw, Poland, 2019.

[131] KC. Hall, JP. Thomas, and WS. Clark. Computation of Unsteady Nonlinear Flows in Cascades Using a Harmonic Balance Technique. *AIAA Journal*, 40(5):879–886, 2002. DOI: 10.2514/2.1754.

[132] RE. Hansford. Rotor Load Correlation with the British Experimental Rotor Program Blade. In *42nd Annual Forum of the American Helicopter Society*, Washington, D. C., USA, 1986.

[133] N. Hariharan. An Overview of Wake-Breakdown in High-Fidelity Simulations of Rotor in Hover. In *AIAA SciTech Forum, 58th Aerospace Sciences Meeting*, Orlando, FL, USA, 2020.

[134] N. Hariharan, J. Abras, and R. Narducci. Wake Breakdown of High-fidelity Simulations of a Rotor in Hover. In *AIAA SciTech Forum, 57th Aerospace Sciences Meeting*, San Diego, CA, USA, 2019.

[135] N. Hariharan, TA. Egolf, and L. Sankar. Simulation of Rotor in Hover: Current State and Challenges. In *AIAA SciTech Forum, 52th Aerospace Sciences Meeting*, National Harbor, Maryland, USA, 2014.

[136] N. Hariharan, R. Narducci, R. Jain, B. Wake, and J. Abras. Hover Prediction Workshop Newsletter. Technical report, AIAA Hover Prediction Working Group, March 2020.

[137] N. Hariharan, R. Narducci, E. Reed, and TA. Egolf. Helicopter Aerodynamic Modeling of Rotor with Tip-Shape Variations: AIAA Standardized Hover Evaluations. In *AIAA SciTech Forum, 54th Aerospace Sciences Meeting*, 2016.

[138] N. Hariharan, R. Narducci, E. Reed, and TA. Egolf. Helicopter Aerodynamic Modeling of Rotor with Tip-Shape Variations: AIAA Standardized Hover Evaluations. In *AIAA SciTech Forum, 54th Aerospace Sciences Meeting*, San Diego, CA, USA, 2016.

[139] N. Hariharan and LN. Sankar. Higher Order Numerical Simulation of Rotor Flowfield. In *American Helicopter Society 50th Annual Forum*, Washington, DC, USA, 1994.

[140] FD. Harris, JD. Kocurek, and TT. Mclarty. Helicopter Performance Methodology at Bell Helicopter Textron. In *American Helicopter Society 35th Annual Forum*, Washington, D. C., USA, 1979.

[141] R. Harrison, S. Stacey, and B. Hansford. BERP IV - The Design, Development and Testing of an Advanced Rotor Blade. In *American Helicopter Society 64th Annual Forum*, Montreal, Canada, 2008.

[142] J. Harse, JG. Yen, and R. Taylor. An Overview of Key Technology Thrusts at Bell Helicopter Textron. Technical report, National Aeronautics and Space Administration, 1988. N88-16657.

[143] L. Hascoët and V. Pascual. TAPENADE 2.1 User's Guide. Technical Report TR 300, Institut National de Recherche en Informatique et en Automatique, Sophia Antipolisi, France, 2004.

[144] S. He, E. Jonsson, CA. Mader, and JRRA. Martins. Aerodynamic Shape Optimization with Time Spectral Flutter Adjoint. In *AIAA SciTech Forum*, San Diego, CA, USA, 2019.

[145] S. He, AJ. Luder, CA. Mader, KJ. Maki, and JRRA. Martins. A Time-Spectral Adjoint Approach for Aerodynamic Shape Optimization Under Periodic Wakes. In *AIAA SciTech Forum*, Orlando, FL, USA, 2020.

[146] DR. Hoad and GC. Green. Helicopter noise research at the Langley V/STOL tunnel. Technical report, National Aeronautics and Space Administration, 1978. NASA CP 2052.

[147] M. Hollands, M. Kessler, A. Altmikus, and E. Kramer. Trade study: Influence of different blade shape designs on forward flight and hovering performance of an isolated rotor. In *37th European Rotorcraft Forum*, Cascina Costa, Italy, 2011.

[148] M. Hollands, M. Kessler, and E. Kramer. Influence of An-/Dihedral and of Different Blade Shapes on Performance and Aeroacoustics of an Isolated Rotor. In *38th European Rotorcraft Forum*, Amsterdam, Netherlands, 2012.

[149] TL. Holst and TH. Puliam. Overset Solution Adaptive Grid Approach Applied to Hovering Rotorcraft Flows. In *27th AIAA Applied Aerodynamics Conference*, San Antonio, TX, USA, 2009.

[150] H. Huang and K. Ekici. A discrete adjoint harmonic balance method for turbomachinery shape optimization. *Journal of Aerospace Science and Technology*, 39:481–490, 2014. DOI: 10.1016/j.ast.2014.05.015.

[151] H. Huber. Helicopter Flight Characteristics improvement through swept-tip rotor blades. In *Fifth European Rotorcraft and Powered Lift Aircraft Forum*, Amsterdam, The Netherlands, 1979.

[152] HB. Huber and C. Schick. MBB's BO 108 Design and Development. In *46th Annual Forum of the American Helicopter Society*, Washington, D. C., USA, 1990.

[153] A. Humpert and C. Schley. Design, Development and Flight Testing of the new EUROCOPTER EC145 Medium Twin. In *27th European Rotorcraft Forum*, Moscow, Russia, 2001.

[154] DK. Im and S. Choi. Helicopter Rotor Flow Analysis Using Mapped Chebyshev Pseudospectral Method and Overset Mesh Topology. *Journal of Mathematical Problems in Engineering*, 2018, 2018. DOI: 10.1155/2018/9745862.

[155] DK. Im, S. Choi, and H. Kwon. Unsteady rotor flow analysis using a diagonally implicit harmonic balance method and an overset mesh topology. *International Journal of Computational Fluid Dynamics*, 29(1):82–99, 2015. DOI: 10.1080/10618562.2015.1015525.

[156] M. Imiela. High-fidelity optimization framework for helicopter rotors. In *35th European Rotorcraft Forum*, Hamburg, Germany, 2009.

[157] M. Imiela. Investigation of Aeroelastic Effects for a Helicopter Main Rotor in Hover. In *36th European Rotorcraft Forum*, Paris, France, 2010.

[158] M. Imiela. High-fidelity optimization framework for helicopter rotors. *Journal of Aerospace Science and Technology*, 23(1):2–16, 2012. DOI: 10.1016/j.ast.2011.12.011.

[159] M. Imiela and G. Wilke. Passive Blade Optimization and Evaluation in Off-Design Conditions. In *39th European Rotorcraft Forum*, Moscow, Russia, 2013.

[160] NCG. Isaacs and RJ. Harrison. Identification of Retreating Blade Stall Mechanisms Using Flight Test Pressure Measurements. In *45th Annual Forum of the American Helicopter Society*, Boston, MA, USA, 1989.

[161] EW. Jacobs and MJ. Pollack. High Performance and Low Noise Characteristics of the Sikorsky S-76D^{TM} Helicopter. In *American Helicopter Society 69th Annual Forum*, Phoenix, AZ, USA, 2013.

[162] KE. Jacobson and MJ. Smith. Carefree Hybrid Methodology for Rotor Hover Performance Analysis. *Journal of Aircraft*, 55(1):52–65, 2018. DOI: 10.2514/1.C034112.

[163] R. Jain. CFD Performance and Turbulence Transition Predictions of an Installed Model-scale Rotor in Hover. In *AIAA SciTech Forum, 55th Aerospace Sciences Meeting*, Grapevine, TX, USA, 2017.

[164] R. Jain. Effect of Facility Walls and Blade Aeroelasticity on PSP Rotor Hover Performance Predictions. In *AIAA SciTech Forum, 56th Aerospace Sciences Meeting*, Kissimmee, Florida, USA, 2018.

[165] A. Jameson. Time-Dependent Calculations Using Multigrid, with Applications to Unsteady Flows past Airfoils and Wings. In *AIAA 10th Computational Fluid Dynamics Conference*, 1991.

[166] A. Jameson and S. Yoon. Lower-Upper Implicit Schemes with Multiple Grids for the Euler Equations. *AIAA Journal*, 25(7):929–935, 1987. DOI: 10.2514/3.9724.

[167] N. Butsuntorn A. Jameson. Time Spectral Method for Rotorcraft Flow. In *46th AIAA Aerospace Sciences Meeting and Exhibit*, Reno, NV, USA, 2008.

[168] R. JanakiRam, R. Smith, B. Charles, and A. Hassan. Aerodynamic Design of a New Affordable Main Rotor for the Apache Helicopter. In *American Helicopter Society 59th Annual Forum*, Phoenix, USA, 2003.

[169] M. Jarkowski, M. Woodgate, G. N. Barakos, and J. Rokicki. Towards consistent hybrid overset mesh methods for rotorcraft cfd. *International Journal for Numerical Methods in Fluids*, 74(8):543–576, 2014. DOI: 10.1002/fld.3861.

[170] B. Jayaraman and M. Potsdam. Effect of Fuselage and Wind Tunnel Wall on Full-Scale UH-60A Rotor Tip Vortex Prediction. In *AIAA Aviation, 34th Applied Aerodynamics Conference*, Washington, D. C., USA, 2016.

[171] J. Jeong and F. Hussain. On the identifiction of a vortex. *Journal of Fluid Mechanics*, 285:69–94, 1995. DOI: 10.1017/S0022112095000462.

[172] D. Jepson, R. Moffitt, K. Hilzinger, and J. Bissell. Analysis and Correlation of Test Data From an Advanced Technology Rotor System. Technical report, United Technologies Corporation, Sikorsky Aircraft Division, 1983. NASA-CR-3714.

[173] A. Jimenez and G. N. Barakos. Hover predictions of the s-76 rotor using hmb2- model to full-scale. In *AIAA SciTech Forum, 54th Aerospace Sciences Meeting*, San Diego, California, 2016.

[174] A. Jimenez-Garcia. *Development of Predictive Methods for Tiltrotor Flows*. PhD thesis, University of Glasgow, 2017.

[175] A. Jimenez-Garcia and GN. Barakos. Assessment of a high-order MUSCL method for rotor flows. *International Journal for Numerical Methods in Fluids*, 87(6):292–327, 2018. DOI: 10.1002/fld.4492.

[176] A. Jimenez-Garcia and GN. Barakos. Numerical Simulations on the PSP Rotor Using HMB3. In *AIAA SciTech Forum, 56th Aerospace Sciences Meeting*, Kissimmee, FL, USA, 2018.

[177] A. Jimenez-Garcia, M. Biava, GN. Barakos, K. Baverstock, S. Gates, and P. Mullen. Tiltrotor CFD Part II - aerodynamic optimisation of tiltrotor blades. *The Aeronautical Journal*, 121(1239):611–636, 2017. DOI: 10.1017/aer.2017.21.

[178] C. Johnson. *Optimisation of Aspects of Rotor Blades using Computational Fluid Dynamics*. PhD thesis, University of Liverpool, 2012.

[179] CS. Johnson and GN. Barakos. Optimizing Rotor Blades with Approximate British Experimental Rotor Programme Tips. *Journal of Aircraft*, 51(2):447–463, 2014. DOI: 10.2514/1.C032042.

[180] S. G. Johnson. The NLopt Nonlinear-Optimization Package, `http://ab-initio.mit.edu/nlopt`. Technical report.

[181] W. Johnson. Performance and Loads Data From a Wind Tunnel Test of a Full-Scale Rotor with Four Blade Tip Planforms. Technical report, National Aeronautics and Space Administration, 1980. NASA-TM-81229.

[182] W. Johnson. CAMRAD/JA: A Comprehensive Analytical Model of Rotorcraft Aerodynamics and Dynamics, Volumes 1-2. Technical report, Johnson Aeronautics, Palo Alto, California, 1988.

[183] W. Johnson. CAMRAD II: Comprehensive Analytical Model of Rotorcraft Aerodynamics and Dynamics, Volumes I-VI. Technical report, Johnson Aeronautics, Palo Alto, California, 1992-2002.

[184] W. Johnson. A History of Rotorcraft Comprehensive Analyses. In *American Helicopter Society 69th Annual Forum*, Phoenix, AZ, USA, 2013.

[185] HE. Jones and DL. Kunz. Comprehensive Modeling of the Apache in CAMRAD II. In *American Helicopter Society Structure Specialists' Meeting*, Williamsburg, VA, USA, 2001.

[186] WT. Jones, EJ. Nielsen, EM. Lee-Rausch, and CW. Acree Jr. Multi-point Adjoint-Based Design of Tilt-Rotors in a Noninertial Reference Frame. In *10th AIAA Multidisciplinary Design Optimization Conference*, National Harbor, MD, USA, 2014.

[187] K. Kampa, B. Enenkl, G. Polz, and G. Roth. Aeromechanic Aspects in the Design of the EC135. In *23rd European Rotorcraft Forum*, Dresden, Germany, 1997.

[188] W. Karush. Minima of functions of several variables with inequalities as side constraints. Master's thesis, University of Chicago, 1939.

[189] K. Kaufmann, MM. Muller, and AD. Gardner. Dynamic Stall Computations of Double-SweptRotor Blades. In *21st STAB/DGLR Symposium*, Darmstadt, Germany, 2018.

[190] HL. Kelley. Effects of Planform Taper on Hover Performance of an Advanced AH-64 Model Rotor. Technical report, National Aeronautics and Space Administration, 1987. NASA-TM-89145.

[191] HL. Kelley. Aerodynamic Performance of a 0.27-Scale Model of an AH-64 Helicopter With Baseline and Alternate Rotor Blade Sets. Technical report, National Aeronautics and Space Administration, 1990. NASA-TM-4201.

[192] GKW. Kenway, CA. Mader, P. He, and JRRA. Martins. Effective adjoint approaches for computational fluid dynamics. *Progress in Aerospace Sciences*, 110:1–26, 2019. DOI: 10.1016/j.paerosci.2019.05.002.

[193] GKW. Kenway and JRRA. Martins. High-fidelity aerostructural optimization considering buffet onset. In *AIAA Aviation 16th AIAA/ISSMO Multidisciplinary Analysis and Optimization Conference*, Dallas, TX, USA, 2015.

[194] C. Keys, F. Tarzanin, and F. McHugh. Effect of Twist on Helicopter Performance and Vibratory Loads. In *13th European Rotorcraft Forum*, Arles, France, 1987.

[195] CN. Keys, MA. McVeigh, L. Dadone, and FJ. McHugh. Estimation of Full-Scale Rotor Performance from Model Rotor Test Data. In *39th Annual Forum of the American Helicopter Society*, St. Louis, Missouri, USA, 1983.

[196] C. Kitaplioglu. Analysis of Small-Scale Rotor Hover Performance Data. Technical report, National Aeronautics and Space Administration, 1990. NASA-TM-102271.

[197] V. Klimchenko, A. Sridharan, and J. Baeder. CFD/CSD Study of the Aerodynamic Interactions of a Coaxial Rotor in High-Speed Forward Flight. In *AIAA Aviation, 35th AIAA Applied Aerodynamics Conference*, Denver, CO, USA, 2017.

[198] J. D. Kocurek and J. L. Tangler. A Prescribed Wake Lifting Surface Hover Performance Analysis. *Journal of the American Helicopter Society*, 22(1):24–35, 1977. DOI: 10.4050/JAHS.22.24.

[199] JD. Kocurek, FD. Harris, and LE. Berkowitz. Hover Performance Methodology at Bell Helicopter Textron. In *American Helicopter Society 36th Annual Forum*, Washington, D. C., USA, 1980.

[200] JD. Kocurek and JL. Tangler. A Prescribed Wake Lifting Surface Hover Performance Analysis. In *32nd Annual Forum of the American Helicopter Society*, Washington D.C, USA, 1976.

[201] N. Kondo, H. Nishmura, H. Nakamura, M. Aoki, T. Tsujiuschi, E. Yamakawa, T. Aoyama, and S. Saito. Preliminary Study of a Low Noise Rotor. In *23rd European Rotorcraft Forum*, Dresden, Germany, 1997.

[202] D. Kraft. A software package for sequential quadratic programming. Technical Report DFVLR-FB 88-28, Institut fur Dynamik der Flugsysteme, Oberpfaffenhoffen, Germany, 1988.

[203] D. Kraft. Algorithm 733: TOMP-Fortran Modules for Optimal Control Calculations. *ACM Transactions on Mathematical Software*, 20(3):262–281, 1994. DOI: 10.1145/192115.192124.

[204] RM. Kufeld, DL. Balough, JL. Cross, KF. Studebaker, CD. Jennison, and WG. Bousman. Flight Testing the UH-60A Airloads Aircraft. In *American Helicopter Society 50th Annual Forum*, Washington, DC, USA, 1994.

[205] HW. Kuhn and AW. Tucker. Nonlinear programming. In *2nd Berkeley Symposium*, Berkeley, USA, 1951.

[206] MR. Kumar and C. Venkatesan. Comparative Study of the Influence of Straight and Modified-Tip Rotor Blades on Loads and Control Response. In *40th European Rotorcraft Forum*, Southampton, UK, 2014.

[207] MR. Kumar and C. Venkatesan. Effects of rotor blade-tip geometry on helicopter trim and control response. *Aeronautical Journal*, 121(1239):637–659, 2017. DOI: 10.1017/aer.2017.15.

[208] DL. Kunz and HE. Jones. Modelling and Simulation of the Apache Rotor System in CAMRAD II. In *American Helicopter Society Structure Specialists' Meeting*, Williamsburg, VA, USA, 2001.

[209] A. J. Landgrebe. The Wake Geometry of a Hovering Rotor and its Influence on Rotor Performance. *Journal of the American Helicopter Society*, 17(4):3–15, 1972. DOI: 10.4050/JAHS.17.3.

[210] AJ. Landgrebe. An Analytical Method for Predicting Rotor Wake Geometry. In *AIAA, AHS VTOL Research, Design and Operations Meeting*, Atlanta,GA, USA, 1969.

[211] BH. Lau, AW. Louie, N. Griffiths, and CP. Sotiriou. Performance and Rotor Loads Measurements of the Lynx XZ170 Helicopter with Rectangular Blades. Technical report, National Aeronautics and Space Administration, 1993. TM-104000.

[212] BH. Lau, AW. Louie, and CP. Sotiriou. Correlation of the Lynx-XZ170 Flight-Test Results up to and Beyond the Stall Boundary. In *49th Annual Forum of the American Helicopter Society*, St. Louis, Missouri, USA, 1993.

[213] A. Le Pape. Numerical aerodynamic optimization of helicopter rotors: multi-objective optimization in hover and forward flight conditions. In *31st European Rotorcraft Forum*, Florence, Italy, 2005.

[214] A. Le Pape and P. Beaumier. Numerical Optimization of Helicopter Rotor Aerodynamic Performance in Hover. In *29th European Rotorcraft Forum*, Friedrichshafen, Germany, 2003.

[215] B. Lee, B. Govindarajan, and JD. Baeder. Methods for Efficient Resolution of Vortical Structures of an S-76 Rotor in Hover. In *AIAA SciTech Forum, 55rd Aerospace Sciences Meeting*, Grapevine, TX, USA, 2017.

[216] C. Lee, B. Charles, and D. Kidd. Wind-Tunnel Investigation of a Quater-Scale Two-Bladed High Performance Rotor in a Freon Atmosphere. Technical report, Bell Helicopter Company, 1971. USAAVLABS TN 70-58.

[217] SM. Lee, JH. Sa, SE. Heon, CJ. Kim, SH. Park, and KH. Chung. A response-surface methodology for rotor airfoil design with multiple design constraints. In *36th European Rotorcraft Forum*, Paris, France, 2010.

[218] EM. Lee-Rausch and RT. Biedron. FUN3D Airload Predictions for the Full-Scale UH-60A Airloads Rotor in aWind Tunnel. In *American Helicopter Society 69th Annual Forum*, Phoenix, AZ, USA, 2013.

[219] JI. Leffell, SM. Murman, and TH. Puliam. Time-Spectral Method for Overlapping Meshes. *AIAA Journal*, 55(10):3381–3398, 2017. DOI: 10.2514/1.J054850.

[220] JG. Leishman. *Principles of Helicopter Aerodynamics*. Cambridge Aerospace Series, 2nd edition, 2006.

[221] ER. Leon, A. Le Pape, JA. Desideri, D. Alfano, and M. Costes. Concurrent Aerodynamic Optimization of Rotor Blades Using a Nash Game Method. *Journal of the American Helicopter Society*, 61(2):1–13, 2016. DOI: 10.4050/JAHS.61.022009.

[222] Leonardo. Aw249 - new combat helicopter. `https://www.leonardocompany.com/en/products/aw249`, 2020. [Online; accessed 19-June-2020].

[223] D. Leusink, D. Alfano, P. Cinnella, and JC. Robinet. Aerodynamic rotor blade optimization at Eurocopter - a new way of industrial rotor blade design. In *51st AIAA Aerospace Sciences Meeting*, Grapevine, TX, USA, 2013.

[224] JS. Light. Results from an XV-15 Rotor Test in the National Full-Scale Aerodynamics Complex. In *53rd Annual Forum of the American Helicopter Society*, Virginia Beach, Virginia, USA, 1997.

[225] JW. Lim. Consideration of structural constraints in passive rotor blade design for improved performance. *Aeronautical Journal*, 119(1222):1513–1539, 2015. DOI: 10.1017/S0001924000011386.

[226] JW. Lim. Structural Sectional Input. Technical report, Aviation & Missile Center Aviation Development Directorate, March 2019.

[227] JW. Lim and AD. Overmeyer. Pressure Sensitive Paint (PSP) Rotor Blade Wind Tunnel Conditions. Technical report, U.S. Army Aviation Development Directorate, 2019. In Private.

[228] C. Liu and J. Nocedal. On the limited memory BFGS method for large scale optimization. *Math. Programming*, 45:503–528, 1989. DOI: 10.1007/BF01589116.

[229] LK. Loftin Jr. Theoretical and Experimental Data for a number of NACA 6A-Series airfoil sections. Technical report, National Aeronautics and Space Administration, 1948. NASA-TR-903.

[230] PF. Lorber. Aerodynamic Results of a Pressure-Instrumented Model Rotor Test at the DNW. In *American Helicopter Society 46th Annual Forum*, Washington, DC, USA, 1990.

[231] PF. Lorber, P. Bowles, E. Fox, ZK. Wang, B. Hein, and C. Matalanis. Wind Tunnel Testing for the SB1-DEFIANT^{TM} Joint-Multi-Role Technology Demonstrator. In *AHS International 73rd Annual Forum & Technology Display*, Fort Worth, TX, USA, 2017.

[232] PF. Lorber, GK. Law, JJ. O'Neill, C. Matalanis, and P. Bowles. Overview of the S-97 RAIDER^{TM} Scale Model Tests. In *American Helicopter Society 72nd Annual Forum*, West Palm Beach, FL, USA, 2016.

[233] PF. Lorber, BY. Min, C. Berezin, and BE. Wake. Interactional Aerodynamic Insight Obtained from Wind Tunnel Testing and Computational Analysis. In *AHS International 74th Annual Forum & Technology Display*, Phoenix, AZ, USA, 2018.

[234] PF. Lorber, J. O'Neill, FW. Kohlhepp, and SA. Woods. CH-53K Scale Model Aerodynamic Evaluation. In *American Helicopter Society 66th Annual Forum*, Phoenix, AZ, USA, 2010.

[235] B. Lutke, J. Nuhn, Y. Govers, and M. Schmidt. Design of a rotor blade-tip for the investigation of dynamic stall in the transonic wind-tunnel Gottingen. *Aeronautical Journal*, 120(1232):1509–1533, 2016. DOI: 10.1017/aer.2016.74.

[236] Z. Lyu, Z. Xu, and J. R. R. A. Martins. Benchmarking Optimization Algorithms for Wing Aerodynamic Design Optimization. In *8th International Conference on Computational Fluid Dynamics (ICCFD8)*, number ICCFD8-2014-0203, pages 1–18, Chengdu, China, 7 2014.

[237] CA. Mader, JRRA. Martins, JJ. Alonso, and E. van der Weide. ADjoint: An Approach for the Rapid Development of Discrete Adjoint Solvers. *AIAA Journal*, 46(4):863–873, 2008. DOI: 10.2514/1.29123.

[238] JB. Malone and JC. Narramore. BELLTECH - A Multi-Purpose Navier-Stokes Code for Rotor-Blade and Fixed-Wing Configurations. In *45th Annual Forum of the American Helicopter Society*, Boston, MA, USA, 1989.

[239] JB. Malone, JC. Narramore, and LN. Sankar. Airfoil Design Method Using the Navier-Stokes Equations. *Journal of Aircraft*, 28(3):216–224, 1991. DOI: 10.2514/3.46015.

[240] K. Mani, BA. Lockwood, and D. Mavriplis. Adjoint-based Unsteady Airfoil Design Optimization with Application to Dynamic Stall. In *American Helicopter Society 68th Annual Forum*, Fort Worth, TX, USA, 2012.

[241] K. Mani and DJ. Mavriplis. Geometry Optimization in Three-DimensionalUnsteady Flow Problems using the Discrete Adjoint. In *51st AIAA Aerospace Sciences Meeting including the New Horizons Forum and Aerospace Exposition*, Grapevine, TX, USA, 2013.

[242] RP. Marpu, LN. Sankar, TR. Norman, TA. Egolf, and S. Makinen. Analysis of the UH-60A Rotor Loads Using Wind Tunnel Data. In *51st AIAA Aerospace Sciences Meeting*, Grapevine, TX, USA, 2013.

[243] A. Massaro and E. Benini. Multi-Objective Optimization of Helicopter Airfoils Using Surrogate-Assisted Memetic Algorithms. *Journal of Aircraft*, 49(2):375–383, 2012. DOI: 10.2514/1.C001017.

[244] A. Massaro and A. D'Andrea. Multi-Point Aerodynamic Optimizaiton by Means of Memetic Algorithm for Design of Advanced Tiltrotor Blades. In *39th European Rotorcraft Forum*, Moscow, Russia, 2013.

[245] A. Massaro, A. D'Andrea, and E. Benini. Multiobjective-Multipoint Rotor Blade Optimization in Forward Flight Conditions Using Surrogate-Assisted Memetic Algorithms. In *37th European Rotorcraft Forum*, Cascina Costa, Italy, 2011.

[246] DJ. Mavriplis, Z. Yang, and N. Mundis. Extensions of Time Spectral Methods for Practical Rotorcraft Problems. In *50th AIAA Aerospace Sciences Meeting*, Nashville, Tennesee, 2012.

[247] MS. McCluer and JL. Johnson. Full-Span Tiltrotor Aeroacoustic Mdoel (FS TRAM) - Overview and Initial Testing. In *American Helicopter Society Aerodynamics, Acoustics, and Test and Evaluation Technical Specialists' Meeting*, San Francisco, CA, USA, 2002.

[248] M. McMullen, A. Jameson, and JJ. Alonso. Application of a Non-Linear Frequency Domain Solver to the Euler and Navier-Stokes Equations. In *40th Aerospac Sciences Meeting & Exhibit*, Reno, NV, 2002.

[249] MA. McVeigh and FJ. McHugh. Influence of Tip Shape, Chord, Blade Number, and Airfoil on Advanced Rotor Performance. *Journal of the American Helicopter Society*, 29(4):55–62, 1984. DOI: 10.4050/JAHS.29.55.

[250] ET. Meadowcroft and R. Jain. Improvements to Tandem-Rotor H-47 Helicopter Coupled CFD-CSD Full Aircraft Model. In *American Helicopter Society 72nd Annual Forum*, West Palm Beach, FL, USA, 2016.

[251] F. R. Menter. Two-equation eddy-viscosity turbulence models for engineering applications. *AIAA Journal*, 32(8):1598–1605, 1994. DOI: 10.2514/3.12149.

[252] F. R. Menter, P. E. Smirnov, T. Liu, and R. Avancha. A one-equation local correlation-based transition model. *Flow Turbulence Combust*, 95(4):583–619, 2015. DOI:10.1007/s10494-015-9622-4.

[253] FR. Menter and RB. Langtry. Correlation-based transition modeling for unstructured parallelized computational fluid dynamics codes. *AIAA Journal*, 47(12):2894–2906, 2009. DOI: 10.2514/1.42362.

[254] JR. Metlon and GC. Hall. Engineering Flight Test of the AH-1G Helicopter HueyCobra, Phase B Part1, Final Report. Technical report, US Army Aviation Test Activity, 1968. USATECOM PROJECT NO. 4-6-0500-01.

[255] BY. Min and B. Wake. Modified Hybrid NavierâĂŞStokes/Free-Wake Method for Hovering Rotor Analysis. *Journal of Aircraft*, 55(1):38–51, 2018. DOI: 10.2514/1.C034066.

[256] RE. Mineck and SA. Gorton and. Steady and Periodic Pressure Measurements on a Generic Helicopter Fuselage Model in the Presence of a Rotor. Technical report, National Aeronautics and Space Administration. NASA TM-2000-210286.

[257] A. Mishra, K. Mani, D. Mavriplis, and J. Sitaraman. Helicopter Rotor Design using Adjoint-based Optimization in a Coupled CFD-CSD Framework. In *American Helicopter Society 69th Annual Forum*, Phoenix, AZ, USA, 2013.

[258] A. Mishra, K. Mani, D. Mavriplis, and J. Sitaraman. Time-dependent adjoint-based aerodynamic shape optimization applied to helicopter rotors. In *American Helicopter Society 70th Annual Forum*, Montreal, Canada, 2014.

[259] S. Moffatt and N. Griffiths. Structural Optimisation and Aeroelastic Tailoring of the BERP IV Demonstrator Blade. In *65th Annual Forum of the American Helicopter Society*, Grapevine, Texas, 2009.

[260] A. Mohasebi and S. Nadarajah. An implicit and adaptive nonlinear frequency domain approach for periodic viscous flows. *Journal of Computational Physics*, 278:92–116, 2014. DOI: 10.1016/j.jcp.2014.08.022.

[261] JA. Morillo, R. Singh, and M. Wasikowski. Model Development and Integration of DYMORE at Bell Helicopter. In *64th Annual Forum of the American Helicopter Society*, Montreal, Canada, 2008.

[262] JA. Morillo, M. Summers, and JO. Bridgeman. Implementation of DYMORE (CSD)/OVERFLOW-2 (CFD) Loose-Coupling Methodology at BHTI. In *66th Annual Forum of the American Helicopter Society*, Phoenix, AZ, USA, 2010.

[263] PM. Morris, JD. Ottomeyer, LB. Higgins, GL. Bender, BD. Picasso III, and R. Savage. Airworthiness and Flight Characteristics Test - Part I, YAH-64 Attack Helicopter. Technical report, United States Army Engineering Flight Activity, 1981. USAAEFA NO. 80-17-1.

[264] M. Mosher. Acoustic Measurements of a Full-Scale Rotor with Four Tip Shapes Vol. 1: Text, Appendix A and Appendix B. Technical report, National Aeronautics and Space Administration, 1983. NASA-TM-85878.

[265] MM. Muller, T. Schwermer, H. Mai, and C. Stieg. Development of an innovative double-swept rotor blade-tip for the rotor test facility Goettingen. In *Deutscher Luft-und Raumfahrtkongress*, Friedrichshafen, Germany, 2018.

[266] A. Murashige, N. Kobiki, A. Tsuchihashi, H. Nakamura, K. Inagaki, and E. Yamakawa. ATIC Aeroacoustic Model Rotor Test at DNW. In *24th European Rotorcraft Forum*, Marseille, France, 1998.

[267] S. Nadarajah. Convergence studies of the time accurate and non-linear frequency domain methods for optimum shape design. *International Journal of Computational Fluid Dynamics*, 21(5-6):189–207, 2007. DOI: 10.1080/10618560701577328.

[268] R. Narducci. Industry Assessment of HPCMP CREATE^{TM}-AV Helios. In *53rd AIAA Aerospace Sciences Meeting*, Kissimmee, FL, USA, 2015.

[269] R. Narducci. Comparison of Steady-State and Time-Dependent Solutions for the S-76 Model-Scale Rotor in Hover. In *AIAA SciTech Forum, 55th Aerospace Sciences Meeting*, Grapevine, TX, USA, 2017.

[270] R. Narducci and H. Tadghighi. An Assessment of CREATE^{TM} AV Helios for Apache Hover and Forward Flight Simulations. In *54th AIAA Aerospace Sciences Meeting*, San Diego, CA, USA, 2016.

[271] JC. Narramore. Application of Computational Fluid Dynamics to the Design of the Bell 429. In *62nd Annual Forum of the American Helicopter Society*, Phoenix, AZ, USA, 2006.

[272] JC. Narramore, DA. Platz, and AG. Brand. Application of Computational Fluid Dynamics to the Design of the BA609. In *25th European Rotorcraft Forum*, Rome, Italy, 1999.

[273] JC. Narramore, LN. Sankar, and R. Vermeland. An Evaluation of a Navier-Stokes Code For Calculations of Retreating Blade Stall on a Helicopter Rotor. In *44th Annual Forum of the American Helicopter Society*, Washington, D. C., USA, 1988.

[274] JC. Narramore, J. Vadyak, and G. Shrewsbury. Navier-Stokes Computations of the Full V-22 Configuration Using Massively Parallel Computers. In *52nd Annual Forum of the American Helicopter Society*, Washington, D. C., USA, 1996.

[275] JC. Narramore and RD. Yeary. Airfoil Design and Analysis Using an Information Systems Approach. In *AIAA Fluid & Plasma Dynamics Conferece*, Snowmass, CO, USA, 1980.

[276] JC. Narramore, M. Yuce, and BJ. Thomas. Bell 429 Main Rotor Aerodynamic and Dynamic Development. In *66th Annual Forum of the American Helicopter Society*, Phoenix, AZ, USA, 2010.

[277] JS. Newman, EJ. Rickely, TL. Bland, and KR. Beattie. Noise Measurement Flight Test: Data/ Analyses Sikorsky S-76A Helicopter. Technical report, U.S Department of Transportation, Federal Aviation Administration, 1984. FAA-EE-84-6.

[278] JS. Newman, EJ. Rickley, TL. bland, and KR. Beattie. Noise Measurement Flgiht Test for Boeing Vertol 234/CH 47-D Helicopter . Technical report, Federal Aviation Administration, Office of Environment and Energy, Noise Abatement Division, Noise Technology Branch, 1984. FIA-EE-84-7.

[279] EJ. Nielsen and B. Diskin. Discrete Adjoint-Based Design for Unsteady Turbulent Flows On Dynamic Overset Unstructured Grids. *AIAA Journal*, 51(6):1355–1373, 2013. DOI: 10.2514/1.J051859.

[280] KW. Noonan. Aerodynamic Characteristics of Two Rotorcraft Airfoils Designed for Application to the Inboard Region of a Main Rotor Blade. Technical report, National Aeronautics and Space Administration, 1990. NASA-TP-3009.

[281] KW. Noonan. Aerodynamic Characteristics of a Rotorcraft Airfoil Designed for the Tip Region of a Main Rotor Blade. Technical report, National Aeronautics and Space Administration, 1991. NASA-TM-4264.

[282] KW. Noonan, WT. Yeager Jr, and JD. Singleton. Wind Tunnel Evaluation of a Model Helicopter Main-Rotor Blade with Slotted Airfoils at the Tip. Technical report, National Aeronautics and Space Administration, 2001. NASA/TP-2001-211260.

[283] TR. Norman, P. Shinoda, RL. Peterson, and A. Datta. Full-Scale Wind Tunnel Test of the UH60-A Airloads Rotor. In *American Helicopter Society 67th Annual Forum*, Virginia Beach, Virginia, USA, 2011.

[284] TR. Norman, PM. Shinoda, C. Kitaplioglu, SA. Jacklin, and A. Sheikman. Low-Speed Wind Tunnel Investigation of a Full-Scale UH-60 Rotor System. In *American Helicopter Society 58th Annual Forum*, Montreal, Quebec, Canada, 2002.

[285] S. Obayashi, K. Fujii, and S. Gavali. Navier-Stoke Simulation of Wind-Tunnel Flow Using LU-ADI Factorization Algorithm. In *International Workshop on Numerical Simulation of Compressible Viscous-Flow Aerodynamics*, Goettingen, Germany, 1987.

[286] C. Ohrle, U. Schaferlein, M. Kessler, and E. Kramer. Higher-order Simulations of a Compound Helicopter using Adaptive Mesh Refinement. In *AHS International 74th Annual Forum & Technology Display*, Phoenix, AZ, USA, 2018.

[287] B. Ortun, D. Petot, KV. Truong, and R. Ohayon. Towards a new generation of rotorcraft comprehensive analysis; coupling with CSM and CFD. In *34th European Rotorcraft Forum*, Liverpool, UK, 2008.

[288] S. Osher and S. Chakravarthy. Upwind schemes and boundary conditions with applications to euler equations in general geometries. *Journal of Computational Physics*, 50(3):447–481, 1983. DOI: 10.1016/0021-9991(83)90106-7.

[289] T. Ota, Y. Hashiguchi, and T. Tsukahara. BVI Noise Reduction Research with Canard Blade Tip. In *27th European Rotorcraft Forum*, Moscow, Russia, 2001.

[290] AD. Overmeyer. Pressure Sensitive Paint Rotor Blade Definition. Technical report, U.S. Army Aviation Development Directorate, 2016. In Private.

[291] AD. Overmeyer and PB. Martin. Measured Boundary Layer Transition and Rotor Hover Performance at Model Scale. In *55th Aerospace Sciences Meeting*, Grapevine, Texas USA, 2017.

[292] AD. Overmeyer and PB. Martin. The Effect of Laminar Flow on Rotor Hover Performance. In *73rd Annual Forum of the American Helicopter Society*, Fort Worth, TX, USA, 2017.

[293] K. Pahlke, M. Costes, AD. D'Alascio, C. Castellin, and A. Altmikus. CHANCE: A French-German Helicopter CFD-Project. In *ONERA-DLR Aerospace Symposium*, Toulouse, France, 2006.

[294] K. Pahlke and BG. van der Wall. Calculation of Multibladed Rotors in High-Speed Forward Flight with Weak Fluid-Structure-Coupling. In *27th European Rotorcraft Forum*, Moscow, Russia, 2001.

[295] Y. Park and O. Kwon. Simulation of unsteady rotor flow field using unstructured adaptive sliding meshes. *Journal of the American Helicopter Society*, 49(4):391–400, 2004. DOI: 10.4050/JAHS.49.391.

[296] AA. Parwani and JG. Coder. Effect of Laminar-Turbulent Transition Modeling on PSP Rotor Hover Predictions. In *AIAA SciTech Forum, 56th Aerospace Sciences Meeting*, Kissimee, FL, USA, 2018.

[297] B. Passe, A. Sridharan, and J. Baeder. Computational Investigation of Coaxial Rotor Interactional Aerodynamics in Steady Forward Flight. In *AIAA Aviation, 33rd AIAA Applied Aerodynamics Conference*, Dallas, TX, USA, 2015.

[298] FJ. Perry. Aerodynamics of the World Speed Record. In *43rd Annual Forum of the American Helicopter Society*, St. Louis, Missouri, 1987.

[299] FJ. Perry. Technical Note: The Contribution of Planform Area to the Performance of the BERP Rotor (Reply to Kenneth B. Amer). *Journal of American Helicopter Society*, 34(1):64–65, 1989. DOI: 10.4050/JAHS.34.64.

[300] J. Peter, F. Renac, A. Dumont, and M. Meheut. Discrete Adjoint Method for Shape Optimization and Mesh Adaptation in the elsA Code. Status and Challenges. In *3AF - 50th International Conference on Applied Aerodynamics*, Toulouse, France, 2015.

[301] JEV. Peter and RP. Dwight. Numerical sensitivity analysis for aerodynamic optimization: A survey of approaches. *Journal of Computers & Fluids*, 39:373–391, 2010. DOI: 10.1016/j.compfluid.2009.09.013.

[302] AE. Phelps III and SL. Althoff. Effects of Planform Geometry on Hover Performance of a 2-Meter-Diameter Model of a Four-Bladed Rotor. Technical report, National Aeronautics and Space Administration, 1986. NASA-TM-87607.

[303] JJ. Philippe and JJ. Chattot. Experimental and Theoretical Studies on Helicopter Blade Tips at ONERA. In *6th European Rotorcraft Forum*, Bristol, UK, 1980.

[304] DR. Polak and AR. George. Flowfield and Acoustic Measurements from a Model Tiltrotor in Hover. *Journal of Aircraft*, 35(6):921–929, 1998. DOI: 10.2514/2.2387.

[305] C. Polascek and P. Lafon. High-Speed Impulsive Noise and Aerodynamic Results for Rectangular and Swept Rotor Blade Tip Tests in S1-Modane Wind Tunnel. In *17th European Rotorcraft Forum*, Berlin, Germany, 1991.

[306] G. Polz and D. Schimke. New Aerodynamic Rotor Blade Design at MBB. In *Thirteenth European Rotorcraft Forum*, Arles, France, 1987.

[307] M. Postdam and T. Puliam. Turbulence Modeling Treatment for Rotorcraft Wakes. In *AHS Specialist's Conference on Aeromechanics*, San Francisco, CA, USA, 2008.

[308] M. Potsdam and RC. Strawn. CFD Simulations of Tiltrotor Configurations in Hover. *Journal of the American Helicopter Society*, 50(1):82–94, 2005. 10.4050/1.3092845.

[309] M. Potsdam, H. Yeo, and W. Johnson. Rotor Airloads Prediction using Loouse Aerodynamic/Structural Coupling. In *American Helicopter Society 60th Annual Forum*, Baltimore, MD, USA, 2004.

[310] M. Potsdam, H. Yeo, and R. Orniston. Performance and Loads Predictions of a Slowed UH-60A Rotor at High Advance Ratios. In *39th European Rotorcraft Forum*, Moscow, Russia, 2013.

[311] R. Prasad and S. Choi. Aerodynamic Shape Optimization for Flutter/LCO based design using Coupled Adjoint. In *AIAA SciTech Forum*, Orlando, FL, USA, 2020.

[312] J. Prieur and WR. Splettstoesser. ERATO-an ONERA-DLR Cooperative Programme on Aeroacoustic Rotor Optimisation. In *25th European Rotorcraft Forum*, Rome, Italy, 1999.

[313] RW. Prouty. *More Helicopter Aerodynamics*. PJS Publication Inc., Peoria, III, 1988.

[314] TR. Quackenbush, DB. Bliss, DA. Wachspress, and CC. Ong. Free Wake Analysis of Hover Performance Using a New Influence Coefficient Method. Technical report, National Aeronautics and Space Administration, 1990. NASA-CR-4309.

[315] M. Ramasamy, NP. Gold, and MJ. Bhagwat. Rotor Hover Performance and Flowfield Measurements with Untwisted and Highly-twisted Blades. In *36th European Rotorcraft Forum*, Paris, France, 2010.

[316] P. Rauch, M. Gervais, P. Cranga, A. Baud, JF. Hirsch, A. Walter, and P. Beaumier. Blue Edge^{TM}: The Design, Development and Testing of a New Blade Concept. In *American Helicopter Society 67th Annual Forum*, Virginia Beach, VA, USA, 2011.

[317] RJ. Renka. Multivariate Interpolation of Large Sets of Scattered Data. *ACM Trans. Math. Softw.*, 14(2):139–148, 1988. DOI: 10.1145/45054.45055.

[318] F. Richez. Analysis of Dynamic Stall Mechanisms in Helicopter Rotor Environment. *Journal of the American Helicopter Society*, 63(2):1–11, 2018. DOI: 10.4050/JAHS.63.022006.

[319] MJ. Riley and JV. Miller. Pressure Distributions on a Helicopter Swept Tip from Flight Tests and from Calculations. In *9th European Rotorcraft Forum*, Stresa, Italy, 1983.

[320] TW. Robers. Euler Equation Computations for the Flow over a Hovering Helicopter Rotor. Technical report, NASA, 1988. Contractor Report 177493.

[321] K. Robinson and A. Brocklehurst. BERP IV Aerodynamics, Performance and Flight Envelope. In *34th European Rotorcraft Forum*, Liverpool, UK, 2008.

[322] E. Roca-Leon, A.Le Pape, JA. Desideri, D. Alfano, and M. Costes. Concurrent Aerodynamic Optimization of Rotor Blades Using a Nash Game Method. In *American Helicopter Society 69th Annual Forum*, Phoenix, AZ, USA, 2013.

[323] P. Roesch. Aerodynamic Design of the Aerospatiale SA 365N Dauphin 2 Helicopter. In *6th European Rotorcraft and Powered Lift Aircraft Forum*, Bristol, UK, 1980.

[324] A. Rubino. *Reduced Order Models For Unsteady Fluid Dynamic Optimization of Turbomachinery*. PhD thesis, University of Delft, 2019.

[325] A. Rubino, M. Pini, P. Colonna, T. Albring, S. Nimmagadda, T. Economon, and J. Alonso. Adjoint-based fluid dynamic design optimization in quasi-periodic unsteady flow problems using a harmonic balance method. *Journal of Computational Physics*, 372:220–235, 2018. DOI: 10.1016/j.jcp.2018.06.023.

[326] AJ. Ruddell. Advancing Blade Concept (ABC^{TM}) Development. In *32nd Annual National V/STOL Forum of the American Helicopter Society*, Washington, D. C., USA, 1976.

[327] Y. Saad. A Flexible Inner-Outer Preconditioned GMRES Algorithm. *SIAM Journal on Scientific Computing*, 14(2):461–469, 1993. DOI: 10.1137/0914028.

[328] Y. Saad. *Iterative Methods for Sparse Linear Systems*. PWS Publishing, Boston, MA, 1996.

[329] Y. Saad and MH. Schultz. GMRES: A Generalized Minimal Residual Algorithm for Solving Nonsymmetric Linear Systems. *SIAM Journal on Scientific and Statistical Computing*, 7(3):856–869, 1986. DOI: 10.1137/0907058.

[330] LN. Sankar, JB. Malone, and Y. Tassa. A Strongly Implicit Procedure for Steady Three-Dimensional Transonic Potential Flows. *AIAA Journal*, 20(5):598–605, 1981. DOI: 10.2514/3.51117.

[331] LN. Sankar and D. Pritchard. Solution of transonic flow past rotor blades using the conservative full potential equation. In *3rd Applied Aerodynamics Conference*, Colorado Springs, CO, USA, 1985.

[332] LN. Sankar and C. Tung. Euler Calculations for Rotor Configurations in Unsteady Forward Flight. In *American Helicopter Society 42nd Annual Forum*, Washington, D. C., USA, 1986.

[333] A. Scandroglio, A. D'Andrea, and S. Melone. Numerical Analysis of Advanced-Innovative Tiltrotor Configurations. In *34th European Rotorcraft Forum*, Liverpool, UK, 2008.

[334] NW. Schaeffler, BG. Allan, C. Lienard, and A. Le Pape. Progress Towards Fuselage Drag Reduction via Active Flow Control: A Combined CFD and Experimental Effort. In *36th European Rotorcraft Forum*, Paris, France, 2010.

[335] KJ. Schlutz, W. Splettstoesser, B. Junker, W. Wagner, E. Schoell, G. Arnaud, E. Mercker, K. Pengel, and D. Fertis. A Parametric Wind Tunnel Test on Rotorcraft Aerodynamics and Aeroacoustics (HELISHAPE) - Test Procedures and Representative Results. In *22nd European Rotorcraft Forum*, Brighton, UK, 1996.

[336] T. Schwarz and K. Pahlke. The GOAHEAD project âĂŞ overview and selected results. In *36rd European Rotorcraft Forum*, Paris, France, 2010.

[337] MT. Scott and JC. Narramore. Navier - Stokes Correlation of a Swept Helicopter Rotor Tip at High Alpha. In *AIAA 22nd Fluid Dynamics, Plasma Dynamics & Lasers Conference*, Honolulu, Hawaii, USA, 1991.

[338] MT. Scott, D. Sigl, and RC. Strawn. Computational and Experimental Evaluation of Helicopter Rotor Tips for High-Speed Flight. *Journal of Aircraft*, 28(6):403–409, 1991. DOI: 10.2514/3.46041.

[339] G. Servera, P. Beaumier, and M. Costes. A weak coupling method between the dynamics code HOST and the 3D unsteady Euler code WAVES. *Journal of Aerospace Sciences & Technology*, 5(6):397–408, 2001. DOI: 10.1016/S1270-9638(01)01120-8.

[340] C. Sheng, J. Wang, and Q. Zhao. Improved Rotor Hover Predictions Using Advanced Turbulence Modeling. *Journal of Aircraft*, 53(4):1549–1560, 2016. DOI: 10.2514/1.C033512.

[341] D. Shepard. A Two-dimensional Interpolation Function for Irregularly-spaced Data. In *Proceedings of the 1968 23rd ACM National Conference*, pages 517–524, New York, 1968. Assoc. for Computing Machinery.

[342] PM. Shinoda. Full-Scale S-76 Rotor Performance and Loads at Low Speeds in the NASA Ames 80- by 120-Foot Wind Tunnel, Volume 1. Technical report, National Aeronautics and Space Administration, 1996. NASA-TM-110379.

[343] PM. Shinoda and W. Johnson. Performance Results from a Test of an S-76 Rotor in the NASA Ames 80-by-120 ft Foot Wind Tunnel. In *11th AIAA Applied Aerodynamics Conference*, Monterey, California, USA, 1993.

[344] PM. Shinoda, H. Yeo, and TR. Norman. Rotor Performance of a UH-60 Rotor System in the NASA Ames 80- by 120-Foot Wind Tunnel. In *American Helicopter Society 58th Annual Forum*, Montreal, Quebec, Canada, 2002.

[345] F. Sicot, A. Gomar, H. Dufour, and A. Dugeai. Time-Domain Harmonic Balance Method for Turbomachinery Aeroelasticity. *AIAA Journal*, 52(1):62–71, 2014. DOI: 10.2514/1.J051848.

[346] F. Sicot, G. Puigt, and M. Montagnac. Block-jacobi implicit algorithms for the time spectral method. *AIAA Journal*, 46(12):3080–3089, 2014. DOI: 10.2514/1.36792.

[347] JD. Sinsay and JJ. Alonso. Heuristic Discovery of Improved Rotor Designs. In *American Helicopter Society 74th Annual Forum*, Phoenix, AZ, USA, 2018.

[348] J. Sitaraman, JD. Baeder, and I. Chopra. Validation of UH-60A Rotor Blade Aerodynamic Characteristics using CFD. In *American Helicopter Society 59th Annual Forum*, Phoenix, AZ, USA, 2003.

[349] J. Sitaraman, A. Datta, JD. Baeder, and I. Chopra. Fundamental Understanding and Prediction of Rotor Vibratory Loads in High-Speed Forward Flight. In *29th European Rotorcraft Forum*, Friedrichschafen, Germany, 2003.

[350] Y. Skladanek, J. Hocquette, and P. Cranga. H160 Dynamics Development: Setting New Standards. In *Vertical Flight SocietyâĂŹs 75th Annual Forum & Technology Display*, Philadelphia, PA, USA, 2019.

[351] M. Smith. 2019 aro dynamic stall workshop. `http://www.msmith.gatech.edu/ARO`, 2019. [Online; accessed 21-May-2020].

[352] MJ. Smith, JW. Lim, BG. van der Wall, JD. Baeder, RT. Biedron, DD. Boyd Jr., B. Jayaraman, SN. Jung, and BY. Min. An Assessment of CFD/CSD Prediction State-of-the-Art Using the HART II InternationalWorkshop Data. In *American Helicopter Society 68th Annual Forum*, Fort Worth, TX, USA, 2012.

[353] WR. Splettstoesser, B. van der Wall, B. Junker, KJ. Schultz, P. Beaumier, Y. Delrieux, P. Lecontre, and P. Crozier. The ERATO Programme: Wind Tunnel Test Results and Proof of Design for an Aeroacoustically Optimised Rotor. In *25th European Rotorcraft Forum*, Rome, Italy, 1999.

[354] GR. Srinivasan, V. Raghavan, and EPN. Duque. Flowfield Analysis of Modern Helicopter Rotors in Hover by Navier-Stokes Method. In *International Technical Specialists Meeting on Rotorcraft Acoustics and Rotor Fluid Dynamics*, Philadeplhia, PA, USA, 1991.

[355] JD. Stanko, JG. Coder, and S. Schmitz. Shape Optimization of Rotorcraft Airfoils Using a Genetic Algorithm. In *American Helicopter Society 74th Annual Forum*, Phoenix, AZ, USA, 2018.

[356] W. Staruk, B. Jayaraman, and J. Sitaraman. Integrated 3D Structural Dynamics Using the CREATEâĎć-AV Helios v9 Rotorcraft Analysis Framework. In *AIAA Scitech 2019 Forum*, San Diego, CA, USA, 2019.

[357] JL. Steger, FC. Dougherty, and JA. Benek. Chimera Grid Scheme. In *ASME Mini-Symposium on Advances in Grid Generation*, Houston, TX, USA, 1983.

[358] R. Steijl and G. N. Barakos. Sliding mesh algorithm for cfd analysis of helicopter rotor-fuselage aerodynamics. *International Journal for Numerical Methods in Fluids*, 58(5):527–549, 2008. DOI: 10.1002/d.1757.

[359] R. Steijl, G. N. Barakos, and K. Badcock. A framework for cfd analysis of helicopter rotors in hover and forward flight. *International Journal for Numerical Methods in Fluids*, 51(8):819–847, 2006. DOI: 10.1002/d.1086.

[360] R. Steijl and GN. Barakos. CFD analysis of complete helicopter configurations âĂŞ lessons learnt from the GOAHEAD project. *Journal of Aerospace Sciences & Technology*, 19(1):58–71, 2012. DOI: 10.1016/j.ast.2011.01.007.

[361] J. Steinhoff, Y. Wenren, L. Wang, and FX. Caradonna. Application of Vorticity Confinement to Rotorcraft Flows. In *31st European Rotorcraft Forum*, Florence, Italy, 2005.

[362] T. Stokkermans, M. Voskuijl, L. Veldhuis, B. Soemarwoto, R. Fukari, and P. Eglin. Aerodynamic Installation Effects of Lateral Rotors on a Novel Compound Helicopter Configuration. In *AHS International 74th Annual Forum & Technology Display*, Delft, Netherlands, 2018.

[363] F. Straub, RD. Janakiram, T. Zientek, R. Maciolek, and T. Birchette. Conceptual Design of an Edgewise Mission Adaptive Rotor. In *American Helicopter Society 69th Annual Forum*, Phoenix, AZ, USA, 2013.

[364] FK. Straub, RA. Johnston, RE. Head, and HL. Kelley. Design and Development of a Dynamically Scaled Model AH-64 Main Rotor. In *10th European Rotorcraft Forum*, The Hague, The Netherlands.

[365] RC. Strawn, FX. Caradonna, and EPN. Duque. 30 Years of Rotorcraft Computational Fluid Dynamics Research and Development. *Journal of the American Helicopter Society*, 51(1):5–21, 2006. DOI: 10.4050/1.3092875.

[366] RC. Strawn, A. Desopper, J. Miller, and A. Jones. Correlation of PUMA Airloads - Evaluation of CFD Prediction Methods. Technical report, National Aeronautics and Space Administration, 1989. NASA TM-102226.

[367] RC. Strawn and C. Tung. The Predictions of Transonic Loading on Advancing Helicopter Rotors. Technical report, National Aeronautics and Space Administration, 1986. NASA TM-88238.

[368] RH. Stroub. An Investigation of a Full-Scale Rotor With Four Blade Tip Planform Shapes. Technical report, National Aeronautics and Space Administration, 1979. NASA-TM-78580.

[369] RH. Stroub, JP. Rabbott Jr, and CF. Niebanck. Rotor Blade Tip Shape Effects on Performance and Control Loads From Full-Scale Wind Tunnel Testing. *Journal of the American Helicopter Society*, 24(4), 1979. DOI: 10.4050/JAHS.24.28.

[370] H. Sugawara and Y. Tanabe. A Study of Rotor/Wing Aerodynamic Interaction at High Speed Flight on a Compound Helicopter. In *6th Asian/Austrailian Rotorcraft Forum/Heli Japan 2017*, Kanazwa, Japan, 2017.

[371] H. Sun and S. Lee. Response surface approach to aerodynamic optimization design of helicopter rotor blade. *International Journal for Numerical Methods in Engineering*, 64:125–142, 2005. DOI: 10.1002/nme.1391.

[372] H. Tadghighi. Helios Simulation of Rotors in Hover: The Boeing Company. In *52nd AIAA Aerospace Sciences Meeting*, National Harbor, MD, USA, 2014.

[373] CA. Tatossian, SK. Nadarajah, and P. Castonguay. Aerodynamic shape optimization of hovering rotor blades using a Non-Linear Frequency Domain approach. *Journal of Computers & Fluids*, 51(1):1–15, 2011. DOI: 10.1016/j.compfluid.2011.06.014.

[374] JJ. Thibert and J. Gallot. Advanced Research on Helicopter Blade Airfoils. In *6th European Rotorcraft Forum*, Bristol, UK, 1980.

[375] JP. Thomas, CH. Custer, EH. Dowell, and KC. Hall. Unsteady Flow Computation Using a Harmonic Balance Approach Implemented about the OVERFLOW 2 Flow Solver. In *19th AIAA Computational Fluid Dynamics*, San Antonio, TX, USA, 2009.

[376] JP. Thomas, EH. Dowell, and KC. Hall. Modeling Viscous Transonic Limit-Cycle Oscillation Behavior Using a Harmonic Balance Approach. *Journal of Aircraft*, 41(6):1266–1274, 2004. DOI: 10.2514/1.9839.

[377] MS. Torok and CR. Berezin. Aerodynamic and Wake Methodology Evaluation Using Model UH-60A Experimental Data. In *American Helicopter Society 48th Annual Forum*, Washignton, D. C., USA, 1992.

[378] KV. Truong. Modeling Aerodynamics for Comprehensive Analysis of Helicopter Rotors. In *42nd European Rotorcraft Forum*, Lille, France, 2016.

[379] N. Tuozzo, E. Fox, E. Eller, B. Mayrides, TA. Zientek, PF. Lorber, RP. Narducci, and T. Sproul. Analytic Tool Correlation Status for the Joint Multi-Role Technology Demonstrator Program. In *AHS International 73rd Annual Forum & Technology Display*, Fort Worth, TX, USA, 2017.

[380] G. D. van Albada, B. van Leer, and W. W. Roberts. A comparative study of computational methods in cosmic gas dynamics. *Astronomy and Astrophysics*, 108(1):76–84, 1982. DOI: 10.1007/978-3-642-60543-7.

[381] H. Van der Ven and OJ. Boelens. A framework for aeroelastic simulations of trimmed rotor systems in forward flight. In *29th European Rotorcraft Forum*, Marseille, France, 2004.

[382] BG. van der Wall, B. Junker, CL. Burley, TF. Brooks, Y. Yu, C. Tung, M. Raffel, H. Richard, W. Wagner, E. Mercker, K. Pengel, H. Holthusen, P. Beaumier, and Y. Delrieux. The HART II Test in the LLF of the DNW - a Major Step towards Rotor Wake Understanding. In *28th European Rotorcraft Forum*, Bristol, UK, 2002.

[383] BG. van der Wall, JW. Lim, MJ. Smith, SN. Jung, J. Bailly, JD. Baeder, and DD. Boyd Jr. The HART II international workshop: an assessment of the state-of-the-art in comprehensive code prediction. *CEAS Aeronautical Journal*, 4:223–252, 2013. DOI: 10.1007/s13272-013-0077-9.

[384] E. van der Weide, AK. Gopinath, and A. Jameson. Turbomachinery Applications with the Time Spectral Method. In *35th AIAA Fluid Dynamics Conference and Exhibit*, Toronto, Ontario, Canada, 2005.

[385] JR. van Gaasbeek. Validation of the Rotorcraft Flight Simulation Program (C81) Using Operational Loads Survey Flight Test Data. Technical report, Bell Helicopter Textron, 1980. USAAVRADCOM-TR-80-D-4.

[386] B. van Leer. Towards the ultimate conservative difference scheme. v.a second-order sequel to godunov's method. *Journal of Computational Physics*, 32(1):101–136, 1979. DOI: 10.1016/0021-9991(79)90145-1.

[387] BAO. Vieira, MP. Kinzel, and MD. Maughmer. CFD Hover Predictions Including Boundary-Layer Transition. In *AIAA SciTech Forum, 55th Aerospace Sciences Meeting*, Grapevine, TX, USA, 2017.

[388] MR. Visbal and DJ. Garmann. Effect of Sweep on Dynamic Stall of a Pitching Finite-Aspect-Ratio Wing. *AIAA Journal*, 57(8):3274–3289, 2019. DOI: 10.2514/1.J058206.

[389] S. Vitale, M. Pini, and P. Colonna. Multistage Turbomachinery Design Using the Discrete Adjoint Method Witihn the Open-Source Software SU2. *Journal of Propulsion and Power*, 36(3):465–478, 2020. DOI: 10.2514/1.B37685.

[390] NA. Vu, HJ. Kang, AI. Azamatov, JW. Lee, and YH. Byun. Aerodynamic Design Optimization of Helicopter Rotor Blades in Hover Performance Using Advanced Configuration Generation Method. In *35th European Rotorcraft Forum*, Hamburg, Germany, 2009.

[391] NA. Vu and JW. Lee. Aerodynamic Design Optimization of Helicopter Rotor Blades including Airfoil Shape for Forward Flight. *Journal of Aerospace Science and Technology*, 42:106–117, 2015. DOI: 10.1016/j.ast.2014.10.020.

[392] NA. Vu, JW. Lee, YH. Byun, and S. Kim. Aerodynamic Design Optimization of Helicopter Rotor Blades including Airfoil Shape. In *American Helicopter Society 66th Annual Forum*, Phoenix, AZ, USA, 2010.

[393] DA. Wachspress, KM. Yu, HA. Saberi, MJ. Hasbun, JC. Ho, and H. Yeo. Helicopter Rotor Airload Predictions with a Comprehensive Rotorcraft Analysis. In *American Helicopter Society 68th Annual Forum*, Fort Worth, TX, USA, 2012.

[394] AJ. Wadcock, GK. Yamauchi, and DM. Driver. Skin Friction Measurements on a Hovering Full-Scale Tilt Rotor. *Journal of the American Helicopter Society*, 44(4):312–319, 1999. DOI: 10.4050/JAHS.44.312.

[395] BE. Wake and LN. Sankar. Solutions of the NavierâĂŘStokes Equations for the Flow About a Rotor Blade. *Journal of the American Helicopter Society*, 34(2):13–23, 1989. DOI: 10.4050/JAHS.34.13.

[396] BE. Wake and LN. Sankar. Solutions of the NavierâĂŘStokes Equations for the Flow About a Rotor Blade. *Journal of American Helicopter Society*, 34(2):13–23, 1989. DOI: 10.4050/JAHS.34.13.

[397] BE. Wake, LN. Sankar, and SG. Lekoudis. A Strongly Implicit Procedure for Steady Three-Dimensional Transonic Potential Flows. *Journal of Aircraft*, 23(7):582–588, 1986. DOI: 10.2514/3.45347.

[398] JL. Walsh, WJ. LaMarsh II, and HM. Adelman. Fully Integrated Aerodynamic/Dynamic Optimization of Helicopter Rotor Blades. Technical report, National Aeronautics and Space Administration, 1992. NASA-TM-104226.

[399] JL. Walsh, KC. Young, JI. Pritchard, HM. Adelman, and WR. Mantay. Integrated Aerodynamic/Dynamic/Structural Optimization of Helicopter Rotor Blades Using Multilevel Decomposition. Technical report, National Aeronautics and Space Administration, 1995. NASA-TP-3465.

[400] B. Wang, Q. Zhao, X. Guohua, Y. Liang, and W. Junyi. Numerical analysis on noise of rotor with unconventional blade tips based on CFD/Kirchhoff method. *Chinese Journal of Aeronautics*, 26(3):572–582, 2013. DOI: 10.1016/j.cja.2013.04.045.

[401] L. Wang, B. Diskin, RT. Biedron, EJ. Nielsen, and OA. Bachau. High-Fidelity Multidisciplinary Sensitivity Analysis and Design Optimization for Rotorcraft Applications. *AIAA Journal*, 57(8):1–15, 2019. DOI: 10.2514/1.J056587.

[402] L. Wang, B. Diskin, LV. Lopes, EJ. Nielsen, EM. Lee-Rausch, and RT. Biedron. High-Fidelity Multidisciplinary Design Optimization of Low-Noise Rotorcraft. In *American Helicopter Society 75th Annual Forum*, Philadelphia, PA, USA, 2019.

[403] Q. Wang, P. Moin, and G. Iaccarino. Minimal repetition dynamic checkpointing algorithm for unsteady adjoint calculation. *SIAM Journal on Scientific Computing*, 31(4):2549–2567, 2009. DOI: 10.1137/080727890.

[404] Q. Wang and Q. Zhao. Rotor airfoil profile optimization for alleviating dynamic stall characteristics. *Journal of Aerospace Science & Technology*, 72:502–515, 2011. DOI: 10.1016/j.ast.2017.11.033.

[405] JM. Weiss, V. Subramanian, and KC. Hall. Simulation of Unsteady Turbomachinery Flows Using An Implicitly Coupled Nonlinear Harmonic Balance Method. In *ASME Turbo Expo 2011*, Vancouver, British Columbia, Canada, 2011.

[406] WH. Weller. Experimental Investigation of Effects of Blade Tip Geometry on Loads and Performance for an Articulated Rotor System. Technical report, National Aeronautics and Space Administration, 1979. NASA Technical Paper 1303.

[407] M. Wentrop, J. Yin, P. Kunze, T. Streit, JH. Wendisch, T. Schwarz, JP. Pinacho, K. Kicker, and R. Fukari. An overview of DLR compound rotorcraft aerodynamics and aeroacoustics activities within the CleanSky2 NACOR Project. In *AHS International 74th Annual Forum & Technology Display*, Phoenix, AZ, USA, 2018.

[408] PG. Wilby. The Development of Rotor Airfoil Testing in the UK. In *22nd European Rotorcraft Forum*, Brighton, UK, 1996.

[409] PG. Wilby. Shockwaves in the rotor world âĂŤ a personal perspective of 30 years of rotor aerodynamic developments in the UK. *The Aeronautical Journal*, 102(1013):113–128, 1998. DOI: 10.1017/S0001924000065404.

[410] PG. Wilby and JJ. Philippe. An Investigation of the Aerodynamics of an RAE swept tip using a model rotor. In *8th European Rotorcraft Forum*, Aix-En-Provence, France, 1982.

[411] DC. Wilcox. Reassessment of the scale-determining equation for advanced turbulence models. *AIAA Journal*, 28(11):1299–1310, 1988. DOI: 10.2514/3.10041.

[412] G. Wilke. Variable Fidelity Optimization of Required Power of Rotor Blades: Investigation of Aerodynamic Models and their Application. In *38th European Rotorcraft Forum*, Amsterdam, The Netherlands, 2012.

[413] G. Wilke. Multi-Objective Optimizations in Rotor Aerodynamics using Variable Fidelity Simulations. In *39th European Rotorcraft Forum*, Moscow, Russia, 2013.

[414] G. Wilke. Applying Multi-Objective Variable-Fidelity Optimization Techniques to Industrial Scale Rotors: Blade Designs for CleanSky. In *41st European Rotorcraft Forum*, Munich, Germany, 2015.

[415] WK. Wilkie, PH. Mirick, and CW. Langston. Rotating Shake Test and Modal Analysis of a Model Helicopter Rotor Blade. Technical report, National Aeronautics and Space Administration, 1997. NASA TM-4760.

[416] A. Wissink, M. Potsdam, V. Sankaran, J. Sitaraman, Z. Yang, and D. Mavriplis. A Coupled Unstructured-Adaptive Cartesian CFD Approach for Hover Prediction. In *American Helicopter Society 66th Annual Forum*, Phoenix, AZ, USA, 2010.

[417] WJ. McCroskey and KW. McAlister and LW. Carr and SL. Pucci. An Experimental Study of Dynamic Stall on Advanced Airfoil Sections Volume 1. Summary of the Experiment. Technical report, National Aeronautics and Space Administration, 1982. NASA-TM-84245.

[418] CC. Wolf, C. Schwarz, K. Kaufmann, AD. Gardner, D. Michaelis, J. Bosbach, D. Schanz, and A. SchrÃűder. Experimental study of secondary vortex structures in a rotor wake. *Experiments in Fluids*, 60(175), 2019. DOI: 10.1007/s00348-019-2807-1.

[419] OD. Wong, KW. Noonan, AN. Watkins, LN. Jenkins, and CS. Yao. Non-Intrusive Measurements of a Four-Bladed Rotor in Hover - A First Look. In *American Helicopter Society Aeromecganics Specialists' Conference*, San Francisco, California, USA, 2010.

[420] OD. Wong, AN. Watkins, KZ. Goodman, J. Crafton, A. Forlines, L. Goss, JW. Gregory, and TJ. Juliano. Blade Tip Pressure Measurements using Pressure Sensitive Paint. In *American Helicopter Society 68th Annual Forum*, Fort Worth, Texas, USA, 2012.

[421] TC. Wong. Application of CREATE^{TM}-AV Helios in an Engineering Environment: Hover Prediction Assessment. In *AIAA SciTech Forum, 55rd Aerospace Sciences Meeting*, Grapevine, TX, USA, 2017.

[422] MA. Woodgate and GN. Barakos. Implicit Computational Fluid Dynamics Methods for Fast Analysis of Rotor Flows. *AIAA Journal*, 50(6):1217–1244, 2012. DOI: 10.2514/1.J051155.

[423] S. Xue, B. Docker, J. Narramore, and ZX. Han. Integrated Aero-Acoustics Rotor Simulation and Design Optimization. In *12th AIAA/CEAS Aeroacoustics Conference (27th AIAA Aeroacoustics Conference)*, Cambridge, MA, USA, 2006.

[424] GK. Yamauchi, DB. Signor, ME. Watts, FJ. Hernandez, and P. LeMasurier. Flight Measurements of Blade-Vortex Interaction Noise Including Comparisons with Full-Scale Wind Tunnel Data. In *American Helicopter Society 49th Annual Forum*, 1993.

[425] Z. Yang, M. Sankar, M. Smith, and O. Bachau. Recent improvements to a hybrid method for rotors in forward flight. *Journal of Aircraft*, 39(5):804–812, 2002. DOI: 10.2514/2.3000.

[426] W. Yao and S. Marques. Prediction of Transonic Limit-Cycle Oscillations Using an Aeroelastic Harmonic Balance Method. *AIAA Journal*, 53(7):2040–2051, 2015. DOI: 10.2514/1.J053565.

[427] WT. Yeager Jr. and WR. Mantay. Wind-Tunnel Investigation of the Effects of Blade Tip Geometry on the Interaction of Torsional Loads and Performance for an Articulated Helicopter Rotor. Technical report, National Aeronautics and Space Administration, 1981. NASA-TP-1926.

[428] WT. Yeager Jr., WR. Mantay, ML. Wilbur, RG. Cramer JR, and JD. Singleton. Advanced Main-Rotor Blade Design for a Utility-Class Helicopter. Technical report, National Aeronautics and Space Administration, 1987. NASA-TM-89129.

[429] WT. Yeager Jr, KW. Noonan, JD. Singlton, ML. Wilbur, and PH. Mirick. Performance and Vibratory Loads Data From a Wind-Tunnel Test of a Model Helicopter Main-Rotor Blade With a Paddle-Type Tip. Technical report, National Aeronuatics and Space Administration, 1997. NASA-TM-4754.

[430] JG. Yen. Effects of Blade Tip Shape on Dynamics, Cost, Weight, Aerodynamic Performance, and Aeroelastic Response. In *19th European Rotorcraft Forum*, Cernobbio, Italy, 1993.

[431] H. Yeo and W. Johnson. Assessment of Comprehensive Analysis Calculation of Airloads on Helicopter Rotors. In *American Helicopter Society 4th Decennial SpecialistâĂŹs Conference on Aeromechanics*, San Francisco, CA, USA, 2004.

[432] H. Yeo and W. Johnson. Assessment of Comprehensive Analysis Calculation of Structural Loads on Rotors. In *American Helicopter Society 60th Annual Forum*, Baltimore, MD, USA, 2004.

[433] H. Yeo, M. Potsdam, B. Ortun, and K. Van Truong. High-Fidelity Structural Loads Analysis of the ONERA 7A Rotor. *Journal of Aircraft*, 54(5):1825–1839, 2017. DOI: 10.2514/1.C034286.

[434] N. Yeshala, A. Egolf, R. Vasilescu, and L. Sankar. Application of Higher Order Spatially Accurate Schemes to Rotors in Hover. In *24th AIAA Applied Aerodynamics Conference, Fluid Dynamics and Co-located Conferences*, San Francisco, CA, USA, 2006.

[435] S. Yoon, NM. Chaderijan nad TH. Puliam, and TL. Holst. Effect of Turbulence Modeling on Hovering Rotor Flows. In *AIAA Aviation, 45th AIAA Fluid Dynamics Conference*, Dallas, TX, USA, 2015.

[436] C. Young. The Prediction of Helicopter Rotor Hover Performance using a Prescribed Wake Analysis. Technical report, Aerodynamics Dept. R. A. E., 1976. C.P. No. 1341.

[437] HY. Yung. Rotor blade vortex interaction noise. *Progress in Aerospace Sciences*, 36(2):97–115, 2000. DOI: 10.1016/S0376-0421(99)00012-3.

[438] M. Zastawny. Presentation: Application of Turbulent Adjoint to Aerodynamic Design Problems. In *RAES: Aerodynamics Tools and Methods in Aircraft Design*, London, UK, 2019.

[439] K. Zhao, Z. Gao, J. Huang, and Q. Li. Aerodynamic optimization of rotor airfoil based on multi-layer hierarchical constraint method. *Chinese Journal of Aeronautics*, 29(6):1541–1552, 2016. DOI: 10.1016/j.cja.2016.09.005.

[440] Q. Zhao and G. Xu. A Study on Aerodynamic and Acoustic Characteristics of Advanced Tip-Shape Rotors. *Journal of the American Helicopter Society*, 52(3):201–213, 2007. DOI: 10.4050/JAHS.52.201.

[441] Q. Zhao, Z. Zhu, X. Yuan, and B. Wang. Aerodynamic Geometry Optimization of Coaxial Rigid Rotors in Forward Flight. In *American Helicopter Society 74th Annual Forum*, Phoenix, AZ, USA, 2018.

[442] BY. Zhou, T. Albring, NR. Gauger, CR. Ilario da Silva, TD. Economon, and JJ. Alonso. An Efficient Unsteady Aerodynamic and Aeroacoustic Design Framework Using Discrete Adjoint. In *AIAA Aviation 17th AIAA/ISSMO Multidisciplinary Analysis and Optimization Conference*, Washington, D. C., USA, 2016.

[443] C. Zhou, LN. Sankar, and P. Griffin. Effects of Anhedral on S-76 Hover Aerodynamics. In *AIAA SciTech 2019 Forum*, San Diego, CA, USA, 2019.

[444] Z. Zhu and Q. Zhao. Optimization for rotor blade-tip planform with low high-speed impulsive noise characteristics in forward flight. *Proceedings of the Institution of Mechanical Engineers, Part G: Journal of Aerospace Engineering*, 231(7):1312–1324, 2016. DOI: 10.1177/0954410016650908.

[445] J. Zibi. An Optimization Method Applied to the Aerodynamics of Helicopter Rotor Blades. In *21st European Rotorcraft Forum*, Moscow, Russia, 1995.

[446] J. Zibi, G. Defresne, and M. Costes. A Numerical Procedure for Aerodynamic Optimization of Helicopter Rotor Blades. In *18th European Rotorcraft Forum*, Avignon, France, 1992.

[447] C. Zwicker. Configuration and Program Status of Eurocopters's New Light Twin Helicoper EC135. In *19th European Rotorcraft Forum*, Cernobbio, Italy, 1993.